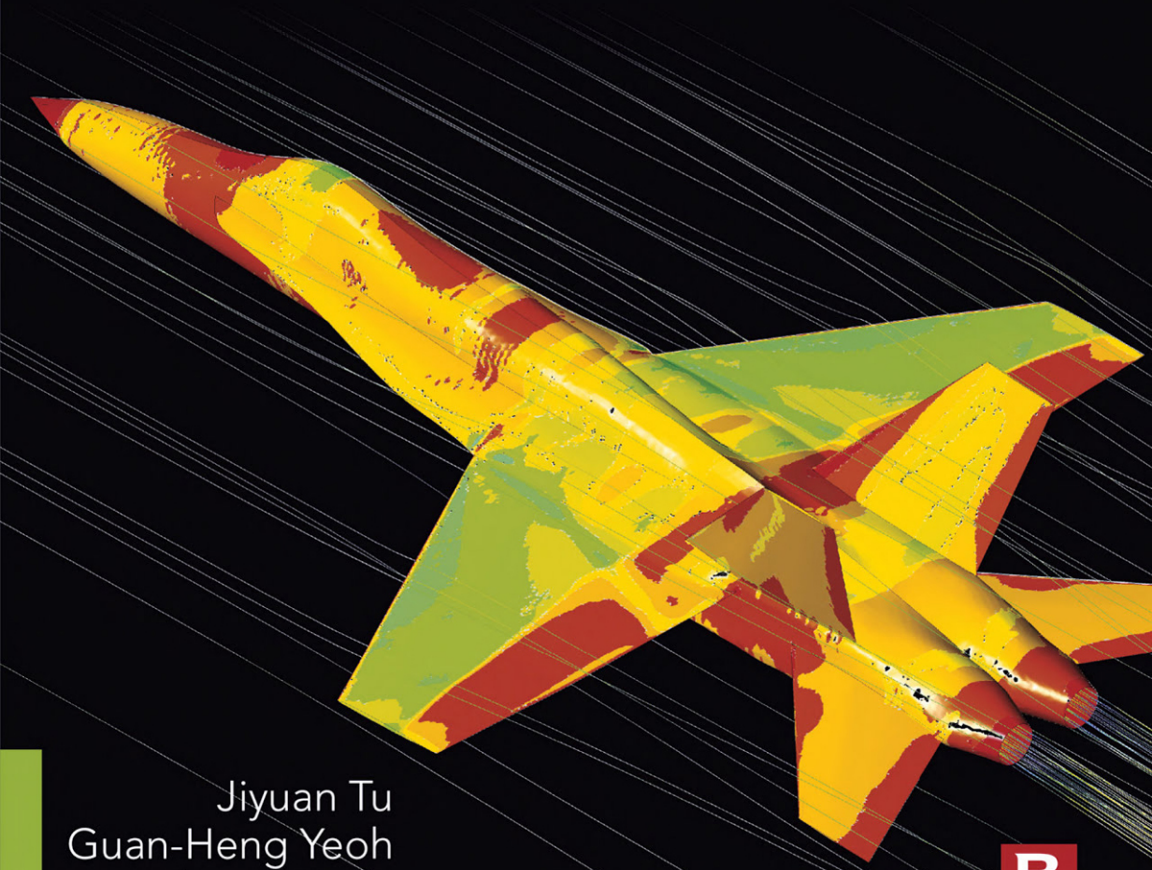
Computational Fluid Dynamics

THIRD EDITION

A Practical Approach



Jiyuan Tu
Guan-Heng Yeoh
Chaoqun Liu

B
H

Computational Fluid Dynamics

Computational Fluid Dynamics

A Practical Approach

Third Edition

Jiyuan Tu
RMIT University, Australia
University of New South Wales, Australia
Tsinghua University, P.R. China

Guan-Heng Yeoh
Australian Nuclear Science and Technology Organisation
University of New South Wales, Australia

Chaoqun Liu
University of Texas at Arlington, USA





Butterworth-Heinemann
An imprint of Elsevier

Butterworth-Heinemann is an imprint of Elsevier
The Boulevard, Langford Lane, Kidlington, Oxford OX5 1GB, United Kingdom
50 Hampshire Street, 5th Floor, Cambridge, MA 02139, United States

© 2018 Elsevier Ltd. All rights reserved.

No part of this publication may be reproduced or transmitted in any form or by any means, electronic or mechanical, including photocopying, recording, or any information storage and retrieval system, without permission in writing from the publisher. Details on how to seek permission, further information about the Publisher's permissions policies and our arrangements with organizations such as the Copyright Clearance Center and the Copyright Licensing Agency, can be found at our website: www.elsevier.com/permissions.

This book and the individual contributions contained in it are protected under copyright by the Publisher (other than as may be noted herein).

Notices
Knowledge and best practice in this field are constantly changing. As new research and experience broaden our understanding, changes in research methods, professional practices, or medical treatment may become necessary.

Practitioners and researchers must always rely on their own experience and knowledge in evaluating and using any information, methods, compounds, or experiments described herein. In using such information or methods they should be mindful of their own safety and the safety of others, including parties for whom they have a professional responsibility.

To the fullest extent of the law, neither the Publisher nor the authors, contributors, or editors, assume any liability for any injury and/or damage to persons or property as a matter of products liability, negligence or otherwise, or from any use or operation of any methods, products, instructions, or ideas contained in the material herein.

Library of Congress Cataloging-in-Publication Data
A catalog record for this book is available from the Library of Congress

British Library Cataloguing-in-Publication Data
A catalogue record for this book is available from the British Library

ISBN: 978-0-08-101127-0

For information on all Butterworth-Heinemann publications visit our website at https://www.elsevier.com/books-and-journals



Publisher: Katey Birtcher
Acquisition Editor: Steve Merken
Editorial Project Manager: Peter Jardim
Production Project Manager: Sruthi Satheesh
Cover Designer: Mark Rogers

Typeset by SPi Global, India

Preface for Third Edition

The acceptance of the first and second editions of our book by the CFD community has certainly been overwhelming and most welcomed ever since its publication. In response to the numerous reviews and suggestions, our third edition aims to further enhance and update the fast-growing subject, significant developments, and important applications of CFD. In this third edition, we have retained the materials that have been incorporated in the second edition and provided more discussion on some key topics. Not straying away from the primary focus to offer CFD users with a *suitable text* for *the right level* of assumed knowledge, we have slightly reorganized the structure of the second edition while maintaining the practical aspect in the understanding of CFD.

The significant changes in the third edition lie predominantly in the treatment of the fundamental physics of fluid flows and a new chapter focusing on mesh generation for CFD. Derivation and the generic form of the governing equations for compressible flows have been provided in Chapter 3. In retrospect, the form of equations is just an extension to the incompressible form of equations for CFD. The introduction of Chapter 4 on mesh generation looks into the key aspects relating to the use of structured, body-fitted, and unstructured meshes. We have also provided key practical guidelines of grid generation for CFD. More advanced grid generation approach such as moving meshes is also discussed.

In the second edition, we provided a summary of the basic ideas underpinning the utilization of finite element and spectral methods to solve the fluid flow equations. In this edition, we have further expounded on the description of these methods since they are still prevalently used in the main stream of CFD. To solve the discretized form of the governing equations, we have made every effort to discuss the important aspects of transportiveness and boundedness, which are important towards attaining stable and physical numerical solutions.

Considering the fast-paced development of computer hardware, we have included discussions on the increasing utilization of the graphical processing unit (GPU) in CFD. Also included in this edition are discussions on the use of hybrid CPU-GPU systems with the purpose of exploiting all available processing power and CPU memory resources for CFD calculations.

Jiyuan Tu
Guan-Heng Yeoh
Chaoqun Liu

Preface for Second Edition

The acceptance of the first edition of our book by the CFD community has certainly been overwhelming and most welcomed. We were extremely pleased by the positive feedback received even within a short period since its inception of publication. In response to the numerous comments, our second edition aims to further enhance and update the fast-growing subject, significant developments, and important applications of CFD. Not straying away by the primary focus to offer CFD users with a *suitable text* that is being pitched at *the right level* of assumed knowledge, the structure and systematic approach of the first edition have been retained in order to maintain practicality in understanding CFD.

In the treatment of the fundamental physics of fluid flows, we have added the generic form of the equations pertaining to compressible flows that in retrospective is an extension to the incompressible form of the equations for CFD.

At the time of writing the first edition, we have focused predominantly on the description of the most popular discretization approaches in CFD based on finite difference and finite volume. Recognizing that other discretization methods such as the finite element and spectral methods that are still available in the mainstream of CFD, we have provided a summary of the basic ideas underpinning the utilization of these methods to solve the fluid flow equations. To reflect the iterative approach that is also commonly being adopted to solve the systems of discretized equations in commercial CFD codes, a dedicated section on multigrid method has been written.

In the first edition, we have also identified a number of key sectors where CFD has been firmly established. They are aerospace, biomedical science and engineering, chemical and mineral processing, civil and environmental engineering, power generation, and sports. In this second edition, we further illustrate the application of CFD in the areas of metallurgy and nuclear safety. Considering the widespread of CFD throughout a number of significant engineering industries, the proper handling of complex geometries becomes ever more important in view of different types of meshing approaches that can be employed. Discussions on key aspects of structured, body-fitted, and unstructured meshes have been provided within the practical guidelines of grid generation.

Lastly, an alternative numerical approach based on the discrete element method has been added to the growing list of advanced topics in CFD.

Jiyuan Tu
Guan-Heng Yeoh
Chaoqun Liu

Preface for First Edition

Computational fluid dynamics (CFD), once the domain of academics, post-doctoral researchers, or trained specialists, is now progressively becoming more accessible to graduate engineers for research and development as well as design-oriented tasks in industry. Mastery of CFD in handling complex flow and heat industrial problems is becoming ever more important. Competency in such a skill certainly brings about a steep learning curve for practicing engineers, who constantly face extreme challenges to come up with solutions to fluid flow and heat-transfer problems without a priori knowledge of the basic concepts and fundamental understanding of fluid mechanics and heat transfer.

Today's engineers are almost certainly geared more towards the use of commercial CFD codes, such as ANSYS CFX, ANSYS FLUENT or STAR-CD. Without proper guidance, the use of these software packages poses risks likened to placing potent weaponry in the hands of poorly trained soldiers. There is every possibility of users with inadequate training causing more harm than good through flawed interpretations of results produced through such packages. This makes it ever more important that a sound knowledge and application in CFD is acquired. Furthermore, changing workplace environment has imposed constraints on users in discerning the pitfalls of CFD by osmosis and through frequent failures. The number of users who have had the luxury of being fully equipped and who were conscientious of the limitations of CFD from their own experiences is fast dwindling.

The purpose of this book is to offer CFD users with a *suitable text* pitches at *the right level* of assumed knowledge. CFD is a mathematically sophisticated discipline, and the authors' aim of this book has been to provide simple-to-understand descriptions of fundamental CFD theories, basic CFD techniques, and practical guidelines. It has never been our aim to overwhelm the reader with excessive mathematical and theoretical illustrations of computational techniques. Every effort has been made to discuss the material in a style to capture the reader's attention. The dominant feature of the present book is to maintain practicality in understanding CFD. In our lecturing experience on CFD, we have identified what it takes to present elementary concepts to initiate the student. This book incorporates specially designed *intuitive* and *systematic* worked-out CFD examples to enhance the learning process and also provides students with examples for practice to better comprehend the basic principles. It is hoped

that this approach will accomplish the purpose of offering *beginners* who are more focused on the *engineering practice* of CFD techniques.

The basic structure of this book is as follows:

***Chapter 1 presents an introduction to computational fluid dynamics and is specifically designed to provide the reader with an overview of CFD and its entailed advantages, the range of applications as a research tool on various facets of industrial problems, and the future use of CFD.

Chapter 2 aims to cultivate a sense of curiosity for the first-time user on how a CFD problem is currently handled and solved. The reader will benefit through the guidance of these basic processes using any commercial, shareware, and in-house CFD codes. More importantly, it serves as a guidepost for the reader to other chapters relating to the fundamental knowledge of CFD. Chapter 2 is a unique design compared with many traditional CFD presentations.

The basic thoughts and philosophy associated with CFD, along with an extensive discussion of the governing equations of fluid dynamics and heat transfer, are treated in Chapter 3. It is vitally important that the reader can fully appreciate, understand, and feel comfortable with the basic physical equations and underlying principles of this discipline, as they are its lifeblood. By working through the worked-out examples, the reader will have a better understanding of the equations governing the conservation of mass, momentum, and energy.

Computational solutions are obtained through two stages. The first stage deals with numerical discretization, which is examined in Chapter 4. Here, the basic numerics are illustrated with popular discretization techniques such as the finite-difference and finite-volume methods (adopted in the majority of commercial codes) for solving flow problems. The second stage deals with the specific techniques to solve algebraic equations. The pressure–velocity coupling scheme (SIMPLE and its derivatives) in this chapter forms the information core of the book. This scheme invariably constitutes the basis of most commercial CFD codes through which simulations of complex industrial problems have been successfully made.

The numerical concepts of stability, convergence, consistency, and accuracy are discussed in Chapter 5. As an understanding of the fundamental equations of fluid flow and heat transfer is the essence of CFD, it follows that the understanding of the techniques of achieving a CFD solution is the resultant substantive. This chapter will enable the reader to better assess the results produced when different numerical methodologies are applied.

The authors have included turbulence modelling in CFD, a subject not ordinarily treated in a book of this nature, but after careful considerations, we have felt it imperative to include it since *real-world applications of CFD* are turbulent in nature after all. In Chapter 6, the authors have therefore devised some practical guidelines for the reader to better comprehend turbulence modelling and other models commonly applied. The authors have also carefully designed worked-out examples that will assist students in the understanding of the complex modelling concept.

An increasing number of books and journals covering different aspects of CFD in mathematically abstruse terms are readily available mainly for specialists associated with industry. It follows that it is more helpful to include in Chapter 7 illustrations of the power of CFD through a set of industrially relevant applications on a significant range of engineering disciplines. Special efforts have been made in this chapter to stimulate the inquisitive minds of the reader through exposition of some pioneering applications.

Although the detailed treatment of advanced CFD techniques is usually outside the scope of a book of this nature, we have offered a general introduction to the basic concepts in Chapter 8, hoping in the process, to reap the benefits of whetting the appetite of readers for more to come in the evolutionary use of CFD in any new emerging areas of science and engineering.

Jiyuan Tu
Guan-Heng Yeoh
Chaoqun Liu

Acknowledgements

The material presented in this book has been partly accumulated from teaching the course *Introduction to Computational Fluid Dynamics* for senior undergraduate students at the School of Aerospace, Mechanical and Manufacturing Engineering at the Royal Melbourne Institute Technology University, Australia, and the course *Computational Fluid Dynamics* at the School of Mechanical and Manufacturing Engineering, University of New South Wales, Australia. For the students who have undertaken the course, we would like to thank them for providing us with many feedbacks to better design particular project topics and aid understanding in this subject. The authors would also like to thank many research students and colleagues who have generously assisted us in various ways.

For the first edition, we thank *Mr. Jonathan Simpson*, senior commissioning editor, and his colleagues at Elsevier Science and Technology who have offered us immense help both in their academic elucidation and professional skills in the publication process. Our special thanks are also given to *Dr. Risa Robinson*, Professor of Mechanical Engineering at the Rochester Institute of Technology, the United States, for reviewing the whole text and giving us invaluable suggestions and comments that we have incorporated in the book.

For the second edition, we would like to thank *Mr. Joe Hayton* and *Ms. Fiona Geraghty* from Elsevier Science and Technology for managing the project.

For the third edition, we extend our appreciation to *Mr. Steve Merken and Mr. Peter Jardim* from Elsevier Science and Technology for initiating the review process and guiding the project.

Dr. Tu would like to express his deep gratitude to his wife, *Xue*, and his son, *Tian*, who have provided their unflinching support in preparing and writing the text.

Dr. Yeoh would also like to acknowledge the untiring support of his wife, *Natalie*, and his daughters, *Genevieve*, *Ellana*, and *Clarissa*, for their understanding and encouragement during the seemingly unending hours spent in preparing and writing.

To all that have been involved, we extend our deepest heartfelt appreciation.

Chapter 1

Introduction

1.1 WHAT IS COMPUTATIONAL FLUID DYNAMICS

Computational fluid dynamics has certainly come of age in industrial applications and academia research. In the very beginning, this popular field of study, accredited by its infamous acronym CFD, was only renowned in high-technology engineering areas of aeronautics and astronautics, but now, it is becoming a rapidly adopted household methodology in solving complex problems in modern engineering practice. CFD, derived from different disciplines of fluid mechanics and heat transfer, is also finding its way into other important uncharted areas especially in process, chemical, civil, and environmental engineering. Construction of new and better improved system designs and optimization carried out on existing equipments through computational simulations are resulting in enhanced efficiency and lower operating costs. With the concerns of global warming and increasing world population, engineers in power generation industries are heavily relying on CFD to reduce development and retrofitting costs. These computational studies are currently being performed to address pertinent issues relating to technologies for clean and renewable power and meeting strict regulation challenges of emission control and substantial reduction of environmental pollutants.

Nevertheless, the basic question remains: what is actually *computational fluid dynamics*? In retrospect, it has certainly become a new branch integrating the disciplines of fluid mechanics not only with mathematics but also with computer science as illustrated in Fig. 1.1. Let us briefly discuss each of these individual disciplines. Fluid mechanics is essentially the study of fluids either in motion (fluid in dynamic mode) or at rest (fluid in stationary mode). CFD is particularly dedicated to the former, fluids that are in motion, and how the fluid flow behaviour influences processes that may include heat transfer and possibly chemical reactions in combusting flows. This directly infers to the *fluid dynamics* description appearing in the terminology. Additionally, the physical characteristics of the fluid motion can usually be described through fundamental *mathematical* equations, usually in partial differential form, which govern a process of interest and are often called governing equations in CFD (see Chapter 3 for more insights). In order to solve these *mathematical* equations, they are converted by *computer scientists* using high-level computer programming languages into computer programs or software packages. The *computational* part simply

Computational Fluid Dynamics. https://doi.org/10.1016/B978-0-08-101127-0.00001-5
© 2018 Elsevier Ltd. All rights reserved.

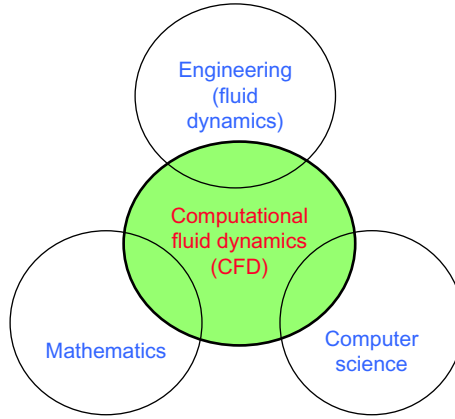


FIG. 1.1 The different disciplines contained within computational fluid dynamics.

means the study of the fluid flow through numerical simulations, which involves employing computer programs or software packages performed on high-speed digital computers to attain the numerical solutions. Another question arises: do we actually require the expertise of three specific people from each discipline—fluid engineering, mathematics, and computer science—to come together for the development of CFD programs or even to conduct CFD simulations? The answer is obviously not and more likely it is expected that this field demands a person who will proficiently obtain more or less some subsets of the knowledge from each discipline.

CFD has also become one of the three basic methods or approaches that can be employed to solve problems in fluid dynamics and heat transfer. As demonstrated in Fig. 1.2, each approach is strongly interlinked to each other and does not lie in isolation. Traditionally, both experimental and analytical methods

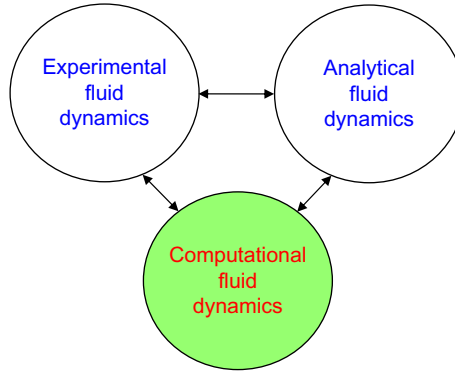


FIG. 1.2 The three basic approaches to solve problems in fluid dynamics and heat transfer.

have been used to study the various aspects of fluid dynamics and to assist engineers in the design of equipment and industrial processes involving fluid flow and heat transfer. With the advent of digital computers, the computational (numerical) aspect has emerged as another viable approach. Although the analytical method is still practised by many and experiments will continue to be significantly performed, the trend is clearly towards greater reliance on the computational approach for industrial designs, particularly when the fluid flows are very complex.

In the past, potential or novice users would probably learn CFD by investing a substantial amount of time writing their own computer programs. With the increasing demands from industries or even within academia to acquire the knowledge of CFD in a much shorter timeframe, it is not surprising that the interest in abandoning writing computer programs is escalating in favour of using more commercially available software packages. Multipurpose CFD programs are gradually earning the approval, and with the advancement of models to better encapsulate the flow physics, these software packages are also gaining wide acceptance. There are numerous advantages in applying these computer programs. Since the mundane groundwork of writing and testing of these computer codes has been thoroughly carried out by the 'developers' of respective software companies, today's potential or novice CFD users are comforted by not having to deal with these types of issues. Such a program can be readily employed to solve numerous fluid flow problems.

Despite the well-developed methodologies within the computational codes, CFD is certainly more than just being proficient in operating these software packages. Bearing this in mind, the primary focus of this book is thus oriented to better educate potential or novice users in employing CFD in a more judicious manner, equally supplementing the understanding of underlying basic concepts and the technical know-how in better tackling fluid flow problems. For other users who are inclined to pursue a postgraduate research study or are currently undergoing research through the development of new mathematical models to solve more complex flow problems, they should consult other CFD books (e.g. Fletcher, 1991; Anderson, 1995; Versteeg and Malalasekera, 1995) and our future book of which we intend to concentrate on presenting a step-by-step procedure of initially understanding the physics of new fluid dynamics problems at hand, developing new mathematical models to represent the flow physics, and implementing appropriate numerical techniques or methods to test these models in a CFD program.

CFD has indeed become a powerful tool to be employed either for pure/applied research or industrial applications. Computational simulations and analyses are increasingly performed in many fluid engineering applications that include aerospace engineering (airplanes, rocket engines, etc.), automotive engineering (reducing drag coefficients for cars and trucks, improving air intake in engines, etc.), biomedical engineering (blood flow in artificial hearts and through scents, breathing, etc.), chemical engineering (fluid flowing through

pumps and pipes, etc.), civil and environmental engineering (river restoration, pollutant dispersion, etc.), power engineering (improving turbine efficiency, wind farm sitting and performance prediction, etc.), and sports engineering (swimming equipment, golf swing mechanics, reducing drag in biking, etc.). Through CFD, one can gain an increased knowledge of how system components are expected to perform, so as to make the required improvements for design and optimization studies. CFD actually asks the question, what if…? before a commitment is undertaken to execute any design alteration. When one ponders the planet we live in, almost everything revolves in one way another around a fluid or moves within a fluid.

CFD is also revolutionizing the teaching and learning of fluid mechanics and thermal science in higher education institutions through visualization of complex fluid flows. Development of CFD-based software packages being more user-friendly is allowing students to visually reinforce the concepts of fluid flow and heat transfer. This software allows teachers to create their own examples or customize predefined existing ones. Using carefully constructed examples, students are introduced to the effective use of CFD for solving fluid flow problems and can instinctively develop an intuitive feel for the flow physics. In the next section, we discuss some important advantages and further expound on how CFD has evolved and is applied in practice.

1.2 ADVANTAGES OF COMPUTATIONAL FLUID DYNAMICS

With the rapid advancement of digital computers, CFD is poised to remain at the forefront of cutting-edge research in the sciences of fluid dynamics and heat transfer. Also, the emergence of CFD as a practical tool in modern engineering practice is steadily attracting much interest and appeal.

There are many advantages in considering CFD. Firstly, the theoretical development of the computational sciences focuses on the construction and solution of the governing equations and the study of various approximations to these equations. CFD presents the perfect opportunity to study specific terms in the governing equations in a more detailed fashion. New paths of theoretical development are realized of which could not have been possible without the introduction of this branch of computational approach. Secondly, CFD complements experimental and analytical approaches by providing an alternative cost-effective means of simulating real fluid flows. Particularly, CFD substantially reduces lead times and costs in designs and production compared with experimental-based approach and offers the ability to solve a range of complicated flow problems where the analytical approach is lacking. These advantages are realized through the increasing performance power in computer hardware and its declining costs. Thirdly, CFD has the capacity of simulating flow conditions that are not reproducible in experimental tests found in geophysical and biological fluid dynamics, such as nuclear accident scenarios or scenarios that are too huge or too remote to be simulated experimentally (e.g. Indonesian tsunami of 2004). Fourthly, CFD can provide rather detailed, visualized, and

comprehensive information when compared with analytical and experimental fluid dynamics.

In practice, CFD permits alternative designs to be evaluated over a range of dimensionless parameters that may include the Reynolds number, Mach number, Rayleigh number, and flow orientation. The utilization of such an approach is usually very effective in the early stages of development for fluid system designs. It may also prove to be significantly cheaper in contrast to the ever-increasing spiralling cost of performing experiments. In many cases, where details of the fluid flow are important, CFD can provide detailed information and understanding of the flow processes to be obtained, such as the occurrence of flow separation or whether the wall temperature exceeds some maximum limit. With technological improvements and competition requiring a higher degree of optimal designs and as new high-technological applications demand precise prediction of flow behaviours, experimental development may eventually be too costly to initiate. CFD presents an alternative option.

Nevertheless, the favourable appraisal of CFD thus far does not suggest that it will soon replace experimental testing as means to gather information for design purposes. It is rather considered of being complementary in solving fluid mechanics problems. For example, wind-tunnel testing is a typical piece of experimental equipment that still provides invaluable information for the simulation of real flows at reduced scale. For the design of engineering components especially in an aircraft that depends critically on the flow behaviour, carrying out wind-tunnel experiment remains an economically viable alternative over full-scale measurement. Wind tunnels are very effective for obtaining the global information of the complete lift and drag on a body and the surface distributions at key locations. In other applications where CFD still remains a relatively primitive state of development, experiment-based approach remains the primary source of information especially when complex flows such as multiphase flows, boiling, or condensation are involved.

In spite of the many upbeat assessments, the reader must also be fully aware of some inherent limitations of applying CFD. Numerical errors exist in computations; hence, there will be differences between the computed results and reality. Visualization of numerical solutions using vectors, contours, or animated movies of unsteady flows is by far the most effective way of interpreting the huge amount of data generated from the numerical calculation. However, there is a danger that an erroneous solution that may look good may not correspond to the expected flow behaviour! The authors have encountered numerous incorrect numerically produced flow characteristics that could have been interpreted as acceptable physical phenomena. Wonderfully bright colour pictures may provide a sense of realism of the actual fluid mechanics inside the flow system, but they are worthless if they are not quantitatively correct. Numerical results obtained must always be thoroughly examined before they are believed. Hence, a CFD user needs to learn how to properly analyse and make critical judgement on the computed results. This is one of the important aims of this book.

1.3 APPLICATION OF COMPUTATIONAL FLUID DYNAMICS

1.3.1 As a Research Tool

CFD can be employed to better understand the physical events or processes that occur in the flow of fluids around and within the designated objects. These events are closely related to the action and interaction of phenomena associated with dissipation, diffusion, convection, boundary layers, and turbulence. Whether the flows are incompressible or compressible, many of the most important aspects inside these types of flows are nonlinear and, as a consequence, often do not have any analytic solution. This motivates the need to seek numerical solutions for the partial differential equations, and it would seem, in hindsight, to invalidate the use of linear algebra for the classification of the numerical methods. Our experiences have nevertheless demonstrated that such is not the case.

CFD, analogous to wind-tunnel tests, can be employed as a *research tool* to perform *numerical experiments*. We examine one of these *numerical experiments*, garnered from our research investigation of Chen et al. (2003), in order to demonstrate the feasible use of CFD as a *research tool* and impart some understanding of this philosophy. Fig. 1.3A represents a 'snapshot' taken for an unsteady flow past two side-by-side cylinders at a given instant of time. In Fig. 1.3B, the comparative visualization of the numerical calculations based on a large-eddy-simulation model attests the power of CFD modelling to capture the complex flow characteristics. This example clearly illustrates how CFD can be utilized to better understand the observed flow structures and some important physical aspects of a flow field, similar to a real laboratory experiment. For the case of three side-by-side cylinders shown in Fig. 1.4, here again is another example of how CFD simulations can work harmoniously with experiments providing not only qualitative comparison but also a means to interpret some basic phenomenological aspects of the experimental condition. More importantly, *numerical experiments* can provide more comprehensive

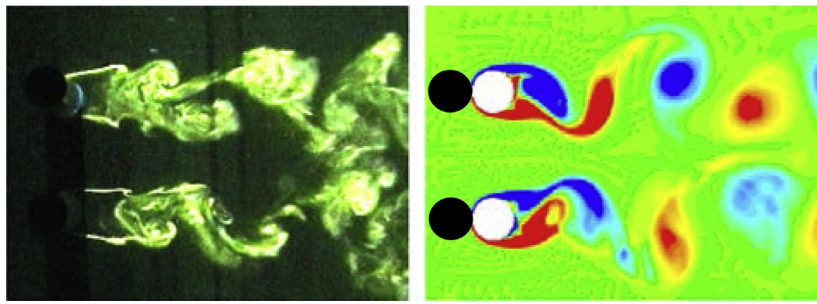


FIG. 1.3 Example of a CFD numerical experiment for a flow past two side-by-side cylinders—(A) experimental observation and (B) numerical simulation.

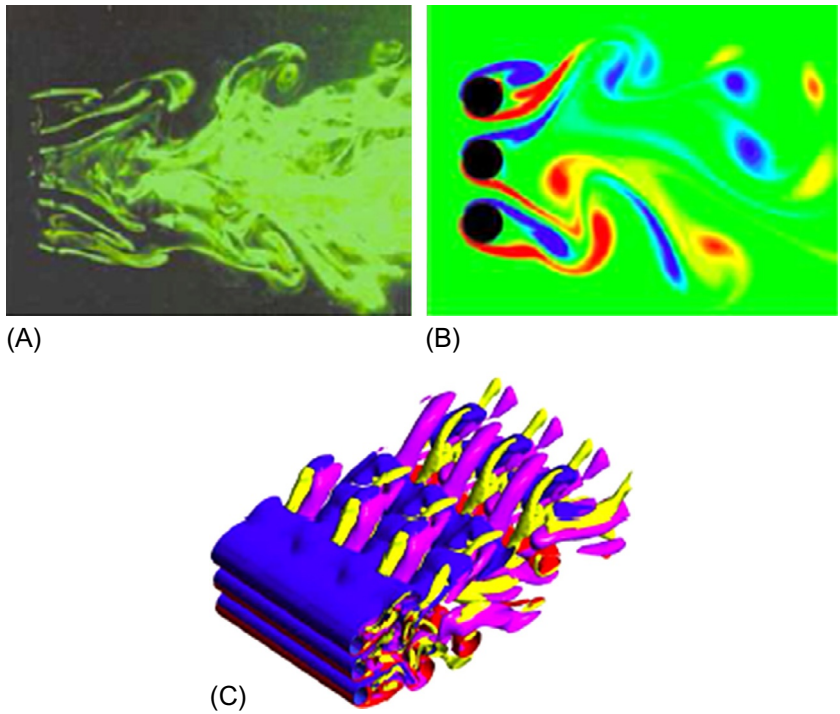


FIG. 1.4 Example of another CFD numerical experiment for a flow past three side-by-side cylinders—(A) experimental observation, (B) numerical simulation on a two-dimensional cross-sectional plane, and (C) three-dimensional representation of the fluid flow through numerical simulation.

information and details of the flow as visualized in three dimensions as shown in Fig. 1.4C when compared with laboratory experiments. These graphical examples clearly affirm the value of *numerical experiments* carried out within the framework of CFD.

1.3.2 As an Educational Tool

The educational spectrum of CFD generally ranges from advanced graduate course to a couple of days of software training. At the top of the spectrum, students are encouraged to develop numerical schemes and modelling challenging physical phenomena. Software training can be considered to be at the bottom of the spectrum where the focus is predominantly directed towards details of the software capability. Prior knowledge of CFD is normally assumed, and such a training is offered by companies for engineers to keep up with the latest advances in CFD. The philosophy of an undergraduate course at an introductory level lies in the middle of this spectrum. What is required is to expose

students to both theoretical foundation of CFD, beginning from the physical description of rather than the mathematics behind the governing equations and with a more focus on the physical interpretation of the flow physics such as boundary layer, separation, and boundary conditions. Software training is a secondary product of the learning process of which students will have to learn CFD by practice.

To meet the balance between theory and hands on, project-based learning (PBL) can be used in the course for the software training. The main mission is to expose students to essential CFD concepts and expand the learning experience with real-world applications, which is becoming an increasingly important skill in today's job market. Nowadays, ease of use and broad capability of commercial CFD software packages have enabled CFD to be brought down into the undergraduate classroom. With user-friendly graphical user interfaces guiding the students through stages of geometry creation and mesh generation, to be further exemplified in Chapter 2, computational simulations and viewing the results by means of vectors, contours, or animated movies, the teaching of CFD has never been so visually exhilarating and welcoming experience. Within these graphical user interfaces, line graphs are also provided to assist users to assess the CFD simulations by either tracking the convergence history or monitoring the surface distribution of certain fluid forces such as the lift force through the lift coefficient. The prime derivative of these graphical user interfaces is certainly more than just introducing CFD technology to undergraduates. They are intended of not only arousing students' interests to learn about the basic fluid dynamics and heat transfer but also enticing them to further extend their learning experience to other transport phenomena of all kinds that may exist in practice or in nature.

The authors believe that there are two prime benefits of exposing undergraduates to CFD. Firstly, the experience with a more hands-on approach as adopted to better understand the concepts of fluid flow and heat transfer deepens greatly the students' understanding of the fluid flow and the thermal phenomena. Particularly, the visualization capability greatly reinforces students' intuition of the flow and heat-transfer behaviour. Secondly, such an approach opens the door to new classes of problems that can be solved by undergraduates who are no longer limited by the narrow range of classical solutions of engineering fluid mechanics and heat transfer.

1.3.3 As a Design Tool

CFD, likewise as research and educational tools, is also becoming an integral part of engineering design and analysis environment in prominent industries. Companies are progressively seeking industrial solutions through the extensive use of CFD for the optimization of product development and processes and/or to predict the performance of new designs even before they are manufactured or implemented. Software applications can now provide numerical analyses and

solutions to pertinent flow problems through the employment of common desktop computers. As a viable design tool, CFD has assisted by providing significant and substantial insights into the flow characteristics within the equipment and processes required to increase production, improve longevity, and decrease waste. The increasing computer processing power is certainly revolutionizing the use of CFD in new and existing industries. These industrial solutions are expounded in the proceeding sections to further demonstrate the wide application of this specific technology in practice.

1.3.4 Aerospace

CFD has certainly enjoyed a long and illustrious history of development and application in the aerospace and defence industries. To maintain an edge in a very competitive environment, CFD is playing a crucial role in overcoming many challenges faced by these industries in improving flight and in solving a diverse array of designs. Indeed, many engineers would associate CFD with its well-known application to aerodynamics by the calculation of the lifting force on an aircraft wingspan. Nevertheless, as methods and resources have augmented in power and ease of use, practitioners have expanded the scope of application beyond the calculation of lift. Today, CFD is being applied to many greater difficult operational problems that were too unwieldy to analyse or solve with computational tools in the past.

The simulation of fluid pathlines in the vicinity of an F18 jet (left) and prediction of pressure coefficient contours at a 10 degree angle of attack around a supersonic missile system with grid fins (right) are illustrated in Fig. 1.5. These examples are just a small sampling of numerous applications in aerodynamic design and military application.

There are also other applications that CFD has been employed in resolving a number of complex operational problems in aircraft designs such as studying

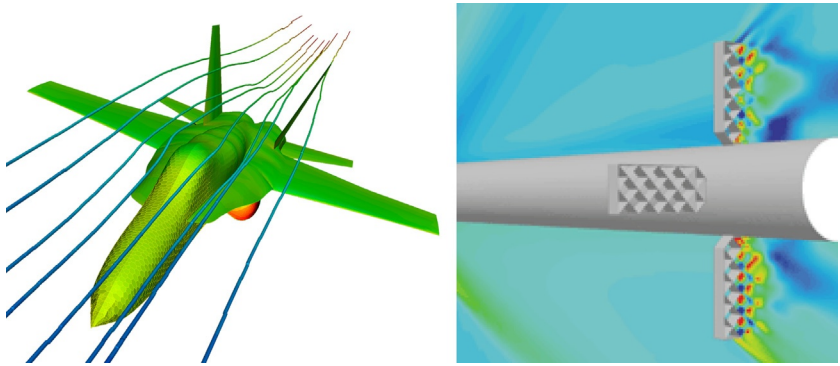


FIG. 1.5 Example of CFD results for applications in aerospace and defence industries. *(Courtesy of ANSYS-FLUENT and US Army Research Laboratory and ANSYS-FLUENT.)*

the impact of trailing vortices on the safe operation of successive aircraft taking off and landing on the runway as well as enhancing the passenger and crew comfort by improving cabin ventilation, heating, and cooling. Efforts to better understand and suppress the noise produced by heavy artillery and the safe operation of a military helicopter upon firing a missile that could impinge on the airframe or the tail rotor are just some other operational problems that CFD is increasingly being employed in military applications. As a versatile, robust, and powerful tool, CFD is rigorously meeting the broad physical modelling demands to investigate relevant complex phenomena in aerospace- and defence-related designs. CFD is undoubtedly becoming a household simulation tool within these industries. This is so as the need to save time and money by reducing development costs and accelerating time to market and improving the overall performance of system configurations are becoming more prevalent these days.

1.3.5 Automotive Engineering

Automobile engineers are increasingly relying on more simulation techniques to bring forth new vehicle design concepts to fruition. Computer-aided engineering has been at the forefront of creating innovative new internal systems that will better enhance the overall driving experience, improve driver and passenger comfort and safety, and advance fuel economy. CFD has long been an essential element in automotive design and manufacture. Besides the aerospace and aerodynamics industries, this branch of engineering has also embraced much of this technology in research and in practice; the use of CFD is thus well entrenched in many disciplines as the engineering simulation tool for even the most difficult challenges.

CFD in automotive engineering has provided many advantages. This technology has delivered the ability to shorten cycles, optimize existing engineering components and systems to improve energy efficiency and meet strict standards and specifications, improve in-car environment, and study the important external aerodynamics as illustrated in Fig. 1.6. Specifically, CFD has shown measurable results through decreasing emissions with powertrain and engine analyses; increasing fuel economy, durability, and performance through aerodynamic investigations; and increasing reliability of brake components. Like in the aerospace industry, CFD has been used to determine the effects of local geometry changes on the aerodynamic forces and provides a significant capability to directly compare a multitude of vehicle designs. This reduces the dependence on time-consuming expensive clay models and wind-tunnel experiments and delivers quicker design turnaround.

More importantly, CFD modelling has provided insights into features of in-cylinder flows that would otherwise be too difficult and expensive to obtain experimentally. Numerical simulations allow the ease of investigating different valve and port design that can lead to improved engine performance through

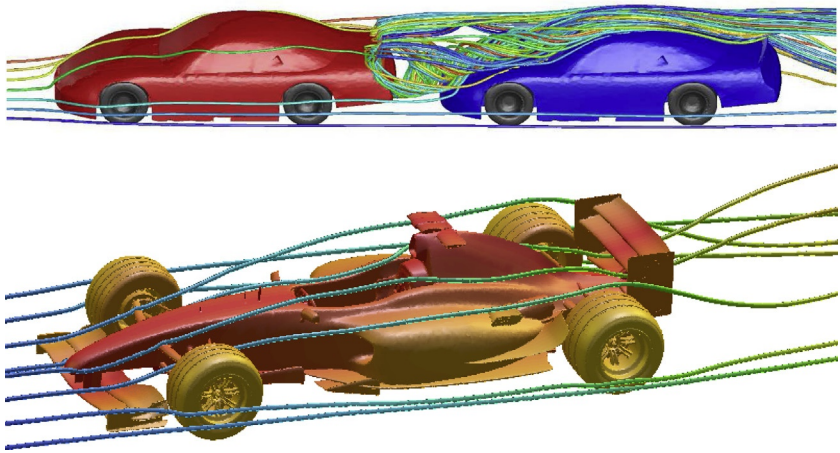


FIG. 1.6 Examples of automotive aerodynamics. *(Both courtesy of ANSYS-FLUENT.)*

better breathing and more induction change distribution. Within the cylinder itself, moving and deforming grids permit the means of simulating the piston and valve motion such as described by the example of Fig. 1.7 for a diesel internal combustion engine. The intake runner (blue) is on the left, and the exhaust runner (yellow) is on the right. Here, CFD allows engineers to understand how changes in port and combustion chamber design affect the engine performance such as volume efficiency or swirl and tumble characteristics. The flow physics described by the piston movement from the top dead centre down to the bottom dead centre and subsequently returning to its original position within the combustion chamber allows engineers to examine in detail the transient

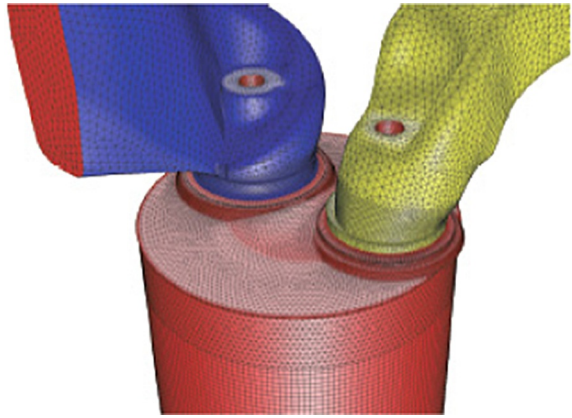


FIG. 1.7 Example of CFD applications in a diesel internal combustion engine. *(Courtesy of ANSYS-FLUENT, Internal Combustion Engine Design.)*

flow patterns inside the cylinder during the complete engine cycle. Cold flow simulations such as this address many challenging problems faced by engineers in the automotive industry. Through the application of dynamic mesh adaptation, CFD simulations of internal combustion engines are being performed with greater speed and the ease of use meeting the competitive progressive demands in the automotive industry.

1.3.6 Biomedical Science and Engineering

Medical researchers are nowadays relying on simulation tools to assist in predicting the behaviour of circulatory blood flow inside the human body. Computational simulations can provide invaluable information that is extremely difficult to be obtained experimentally, and they also allow many variations of fluid dynamics problems to be parametrically studied. Figs 1.8 and 1.9 illustrate just one of the many sample applications of CFD in the biomedical area where the blood flows through original stenosed and virtually stented arteries have been predicted herein. With the breadth of physical models and advances in areas of fluid-structure interaction, particle tracking, turbulence modelling, and better meshing facilities, rigorous CFD analysis is increasingly performed to study the fluid phenomena inside the human vascular system. Medical simulations of circulatory functions offer many benefits. They can lower the chances of postoperative

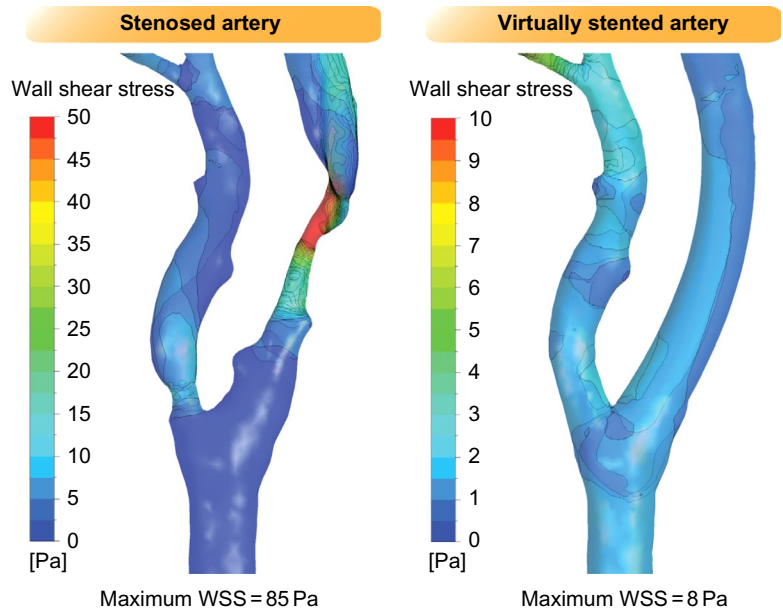


FIG. 1.8 Example of CFD prediction of wall shear stress (WSS) for original stenosed and virtually stented arteries.

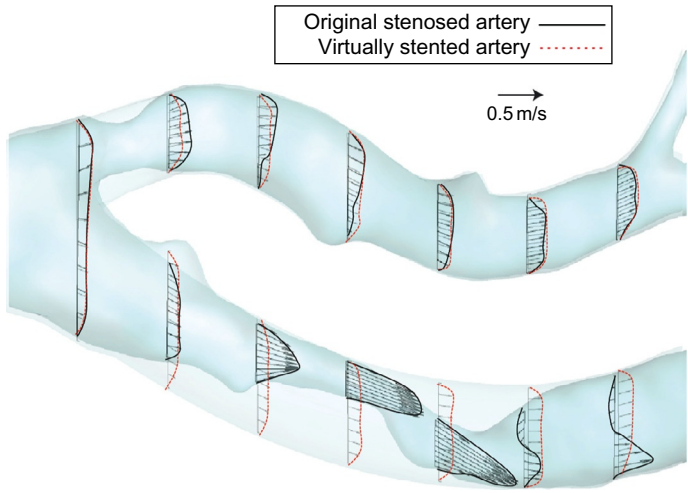


FIG. 1.9 Example of predicted velocity profiles for original stenosed and virtually stented arteries.

complications, assist in developing better surgical procedures, and deliver a good understanding of biological processes and more efficient and less destructive medical equipment such as blood pumps. For example, CFD is being increasingly employed via virtual prototyping to recommend the best design for surgical reconstructions such as carotid endarterectomy and to better understand the blood flow through an aneurysm in the abdominal artery.

CFD is also gaining an enormous interest in the pharmaceutical industries. With the ever-increasing pollution levels causing respiratory problems and frequent asthma attacks, the need has never been greater to predict and optimize inhaled therapies. CFD can provide essential insights by simulating the entire drug delivery process for particulate, aerosol, and gaseous drug types, from the inception of device design through the airways and down into the lungs of the pulmonary system. Through sophisticated multiphase models, the motion of aerosol droplets and drug particles and their transport/deposition characteristics within the airways are predicted to ascertain the drug concentration in the lungs as shown by the example exemplifying the modelling of particle formation/dispersion from nasal sprayers and particle transport/deposition in the nasal cavity in Fig. 1.10. In order to better emulate the actual fluid flow through the airways of the bronchial tree of the pulmonary system such as shown in Fig. 1.11, medical images obtained from accurate CT or MRI scans are converted into a geometrical model, which are subsequently used for advanced CFD flow simulations. Through these CFD simulations, deposition and uptake can thus be customized in a manner targeting particular drugs, delivery devices, diseases, and even individual patients. For example, Fig. 1.12 illustrates the predictions of pressure coefficient values for specific patient cases with and without asthma.

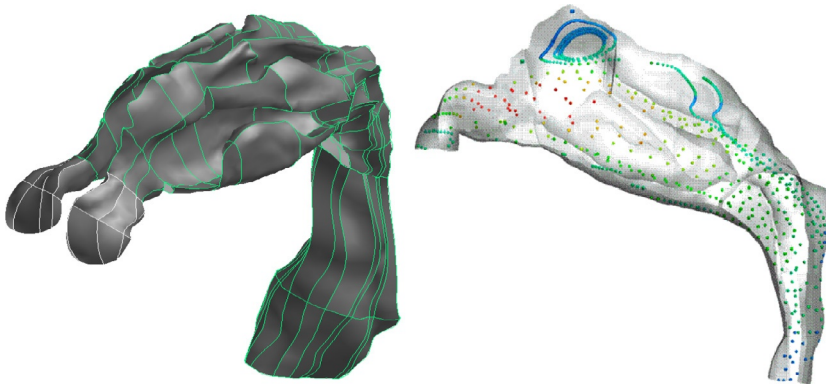


FIG. 1.10 Example of CFD application for particle formation/dispersion from nasal sprayers and particle transport/deposition in the nasal cavity.

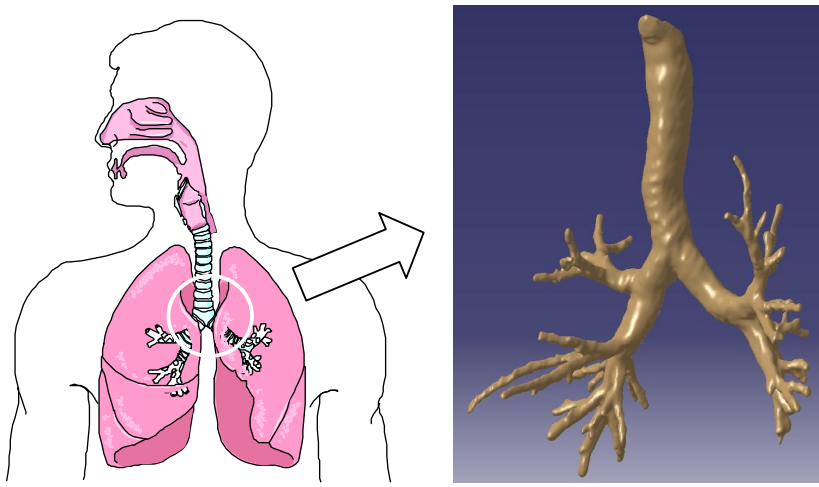


FIG. 1.11 Example of bronchial tree geometry created from CT data for CFD simulation.

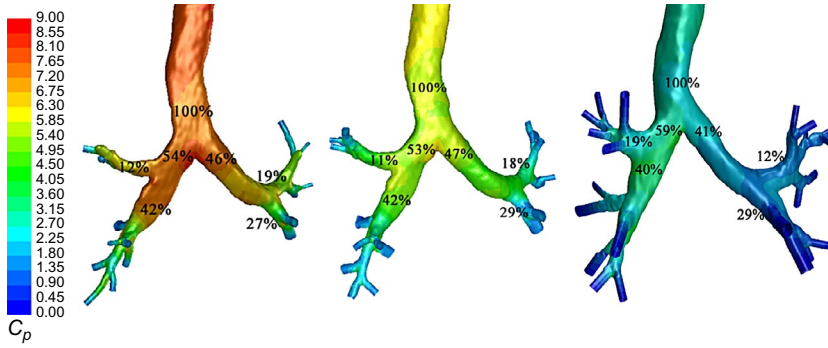


FIG. 1.12 Example of CFD prediction of pressure coefficient (C_p) values for specific patient cases with and without asthma.

As demands for new and better healthcare products continue to swell at a rapid pace, 'health' companies will be required to perform more research and develop promising new products. Within these diverse healthcare sectors that may include the aforementioned biomedical, pharmaceuticals, and other areas associated with medical equipment and 'general-health' personal products, CFD is becoming an important tool in the identification and improvement of new products to meet the surging market aided primarily by the ageing population.

1.3.7 Chemical and Mineral Processing

Many world necessities revolve around the chemical and mineral processing industries. By applying large quantities of heat and energy to physically or chemically deform raw materials, these industries have certainly helped to mould essential products for food and health as well as vital advanced technological equipments in computing and biotechnology. In the face of increasing industrial competitiveness, these industries are confronted with major challenges to meet the world's demands and needs for the present without compromising for the future. This translates into making the operational processes becoming more energy efficient, safer, and flexible whilst better containing and reducing emissions.

For example, improving the performance of gas-sparged stirred tank reactors is considered to be of paramount importance in the chemical industry. Fig. 1.13 presents contours of different bubble size distribution within the stirred tank accompanied by the local flow behaviour, indicated by velocity vectors, around one of the rotating blades. The detailed information of the transport of liquid and gases through the use of CFD and population balance approaches ensures that engineers have the best available possible data to work with in order to increase yield by improving fluid flows, thereby reducing operating costs and increasing system efficiency.

Also, in the world of manufacturing, no industry is more important than minerals, particularly in Australia. Mineral processing spans a wide range of activities, and many of these processes involve complex fluid flow, heat, and mass transfer phenomena inside aggressive and hostile environments. By modelling, optimizing, and improving processes such as *classification*, *separation*, and *filtration*, CFD is at the forefront of providing designs with greater efficiencies and significant production outputs. Fig. 1.14 illustrates a *separation* process in mineral processing that involves the use of gas cyclones and hydrocyclones. A gas cyclone is a commonly used apparatus that utilizes gravity and centrifugal force to separate solid particles from a gas stream. The hydrocyclone is a similar device; however, the operating fluid is liquid rather than a gas. Here, the generated centrifugal forces are strong enough to cause the solids to separate from the liquid of which these separated solids fall down under gravity into the accumulator vessel situated beneath the hydrocyclone. CFD simulations

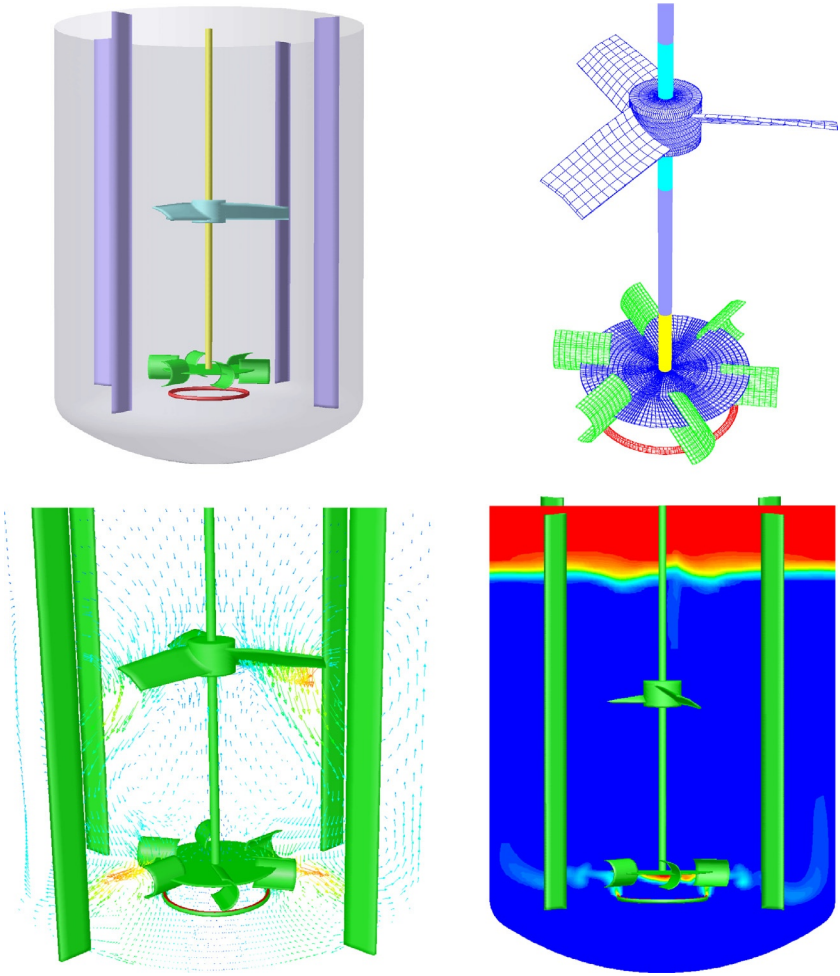
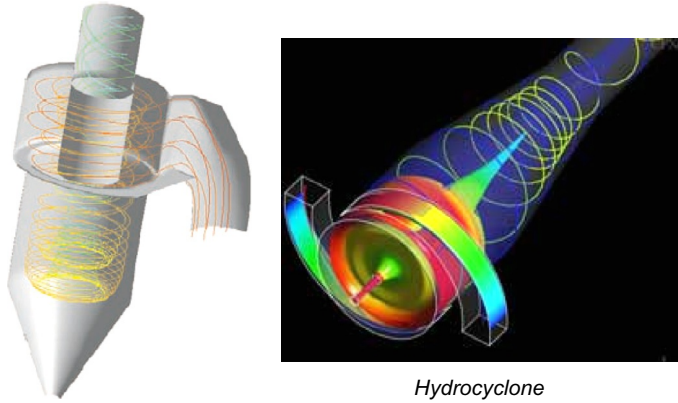


FIG. 1.13 Example of CFD application in the simulation of gas-sparged stirred tank reactor. *(Courtesy of ANSYS-FLUENT.)*

through application of advanced turbulence models are performed to ascertain the different flow physics within the cyclone geometry for the correct prediction of the fluid flows. The behaviour of the particulates can then be simulated using suitable particle transport models either employing the Eulerian or Lagrangian multiphase approach.

The above examples represent merely a tip of the iceberg of the many CFD applications in the processing industries. Advanced CFD is also heavily involved in other important manufacturing sectors such as extraction metallurgy and oil, gas, and petrochemical industries. The recent advances in modelling capabilities of CFD have indeed opened up many opportunities to achieve



Gas cyclone

Hydrocyclone

FIG. 1.14 Example of CFD application in the simulation of gas cyclone and hydrocyclone. *(Courtesy of ANSYS-FLUENT and ESSS and Petrobras, ANSYS-CFX.)*

significant technological strides in the complex and demanding world of the chemical and process industries. Primarily, CFD is playing a crucial role in extrapolating a process from laboratory and pilot plant scale to the industrial plant scale by combining different processes into smaller compact and efficient units instead of treating them individually. This has produced an upgrade in the efficiency of a plant with the same existing constraints.

1.3.8 Civil and Environmental Engineering

Governments, research institutes, and corporations are actively seeking ways to meet environmental legislations and guarantees by decreasing waste whilst maintaining acceptable production levels fuelled by increasing market demands. In many cases, CFD simulations have been at the heart of resolving many environmental issues. For instance, CFD has been used to predict the pollutant plume being dispersed from a cooling tower subject to wind conditions as shown in Fig. 1.15.

In addition, CFD can assist especially in ensuring compliance to strict regulations during the early design stages of construction. Fig. 1.16 represents the preconstruction for a new 22 m tank at a water treatment plant. Owing to the huge construction cost that may exceed millions of dollars, virtual computer-aided models can be built and analysed at a fraction of time and cost by exploring all aspects of design before construction is commenced. To determine the feasibility of such a construction, flow modelling is also performed (also shown in Fig. 1.16), which provides insights into the flow behaviour for the proposed tank that would not have been possible through physical modelling. The added understanding gained from CFD simulation provides

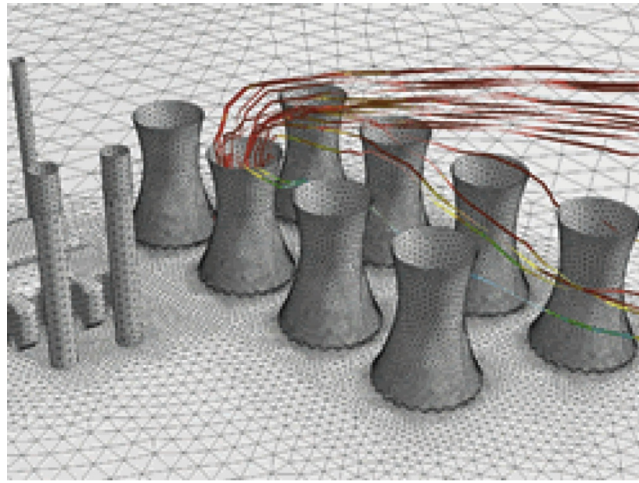


FIG. 1.15 Example of CFD application to plume dispersion from a cooling tower. *(Courtesy of ANSYS-FLUENT.)*



FIG. 1.16 Example of CFD application to the construction of a new tank at a water treatment plant. The top right-hand corner figure describes the CFD simulation of the water tank that will be installed within the excavated construction site. *(Courtesy of MMI Engineering.)*

confidence in the design proposal, thus avoiding the added costs of oversizing and overspecification whilst reducing risk.

Concerns of an architectural structure exposed to environmental elements have recently brought about an important study on the flow of air and water around the Itsukushima torii (gate), a large 17 m high wooden structure, located in the sea near Hiroshima, Japan, as illustrated in Fig. 1.17. By using the dynamic mesh model to periodically move a wall so as to act as a wave generator and a volume of fluid model to track the air–water interface to replicate the

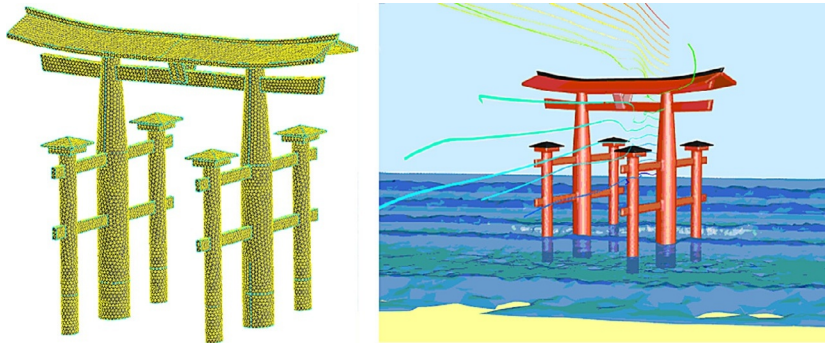


FIG. 1.17 Example of CFD application to the flow of air and water around the Itsukushima torii (gate) located in the sea near Hiroshima, Japan. *(Courtesy of ANSYS-FLUENT.)*

motion of the sea waves, significant insights to the flow characteristics around the architectural structure were realized. The ability to capture and better understand all the associated flow processes has certainly allowed environmental engineers the foundation whereby to better assess the environmental impacts on the existing structure.

1.3.9 Metallurgy

Metallurgical processes involve materials that flow in different forms (solid, liquids, gases, and their mixtures) from part or one of the equipment to another. Some of the typical processes include the extraction of metals from various types of iron ore to hot metal and from hot metal to steel, from copper concentrates to pure copper, and from aluminium scrap to pure aluminium or its alloys. These processes are generally complicated due its multiphase, high temperature, and highly reactive nature. The complex phenomena of flow, heat, and mass transport and heterogeneous chemical reactions play very important roles in determining the overall performance of large-scale reactors that accommodate such processes.

In recent times, CFD has been found very useful in studying various metallurgical processes and various aspects of a specific process. Through CFD, it has shown to provide an insightful understanding of an existing process, modification, and optimization of the operation and design in an existing process and new process development. It is worthwhile mentioning that metallurgical processes are by nature challenging for CFD modelling since a lot of the phenomena have not yet been properly described or incorporated into the general CFD framework. Nevertheless, many new and significant developments of multiphysics models are taking place to aptly simulate increasing complicated industrial processes involving flow and transport of mass, momentum, energy, and chemical species in multiphase and high-temperature reactive systems.

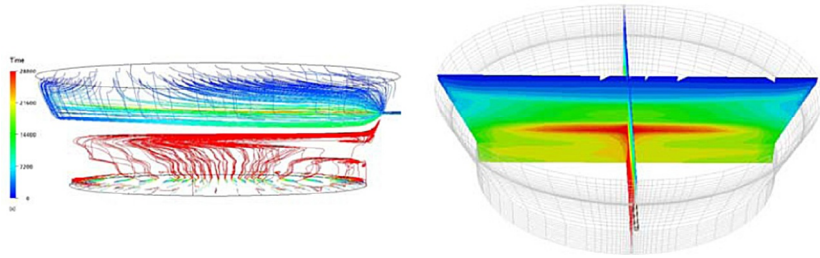


FIG. 1.18 Example of CFD application to predict molten iron flow (left, timeline) and carbon dissolution (right, concentration) in the blast furnace hearth. *(After Yang, Y.X., Zhou, B., Post, J.R., Scheepers, E., Reuter, M.A., Boom, R., 2006. Computational fluid dynamics simulation of pyrometallurgical processes. In: 5th International Conference on CFD in the Minerals and Process Industries. CSIRO, Melbourne, Australia.)*

The use of CFD in simulating heterogeneous and slow dissolution of packed bed code particles is illustrated in Fig. 1.18. In this example, the predicted flow pattern of molten iron and carbon dissolution in the blast furnace hearth is obtained through the population balance model coupled with the flow model. By tracking the local changes in size distribution and bed porosity, many aspects related to different initial coke size distributions, the use of inert versus reactive coke types, and the use of a mix of different code types can be investigated. Another example is the application of CFD for the redesigning of off-gas systems at different ferrosilicon production plants in order to assess operating conditions and the qualitative effects of different process parameters. A typical simulation is depicted in Fig. 1.19 where the coloured surface represents the interface of the flames and the colours represent the flame temperature. Such prediction assists in better understanding the off-gas combustion, gas collection in the hood, transport and burnout of soot and charge particles, carbon loss, heat transfer, and particle deposition on channel walls.

1.3.10 Nuclear Safety

During the last decade, the need for more accurate computational models for relevant safety analyses of nuclear facilities has sparked an escalating interest in CFD to feasibly predict a number of important flow phenomena, which otherwise may not have been possible through other simplified approaches. Some specific problems such as arising from pressurized thermal shock, coolant mixing, and thermal stripping as well as containment issues in nuclear reactors have certainly motivated enormous research activities for the application of CFD to analyse such problems.

CFD calculations have been performed for coolant mixing in pressurized water reactors. This problem has significant interest to the nuclear community, particularly in attempting to understand the stationary and transient mixing of coolant in stream line break and boron dilution scenarios where the mixing



FIG. 1.19 Example of CFD application to the flow of gas in an off-gas system at furnace 1 at Elkem Thamshavn, Norway. *(After Johansen, S.T., 2003. Mathematical modeling of metallurgical processes. In: 3rd International Conference on CFD in the Minerals and Process Industries. CSIRO, Melbourne, Australia.)*

phenomena have tremendous impact on the economical operation and structural integrity of such facilities. Fig. 1.20 illustrates the case of a pump start-up due to a strong impulse-driven flow at the inlet nozzle where the horizontal part of the flow dominates in the downcomer in a pressurized water reactor. CFD predictions gave in-depth insights on the injection that is distributed into two main jets where the maximum of the tracer concentration at the core inlet appears at the opposite part of the loop the tracer is injected. In relation to small break loss of coolant accident, slug flow that can occur in the cold leg of pressurized water reactor is potentially hazardous. Strong oscillating pressure levels form behind the liquid slugs can significantly affect and subsequently weaken the structure of the system. The calculated slug in a horizontal channel determined through the inhomogeneous multiphase model is in good agreement with the experiment such as exemplified in Fig. 1.21. Although the entrainment of small bubbles in the front of the slug could not be observed, the characteristic of the slug front wave rolling over and breaking is clearly identified. Based on the impending need for analysis of long, large-scale, and transient problems, the capability of CFD for performing full containment analysis is still currently out of reach with the available computational power and resources. Nevertheless, the use of CFD in addressing the transport of gases in multicompartment geometry

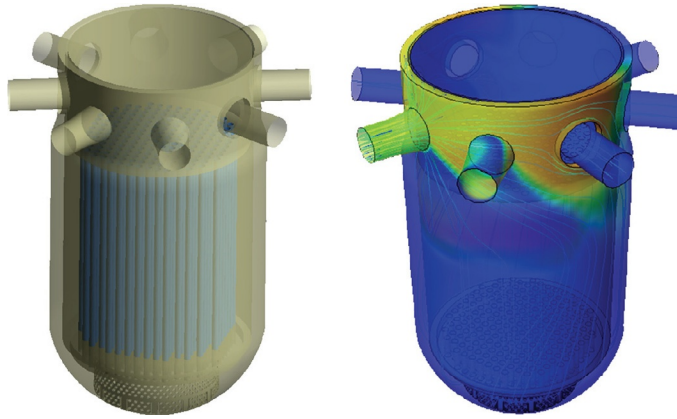


FIG. 1.20 Example of CFD application to the prediction of turbulent mixing in the ROCOM test facility during boron dilution transients (start-up of the first coolant pump). *(After Höhne, T., Krepper, E., Rohde, U., 2010. Application of CFD codes in nuclear reactor safety analysis. Sci. Technol. Nucl. Ins. (Article ID 198758).)*

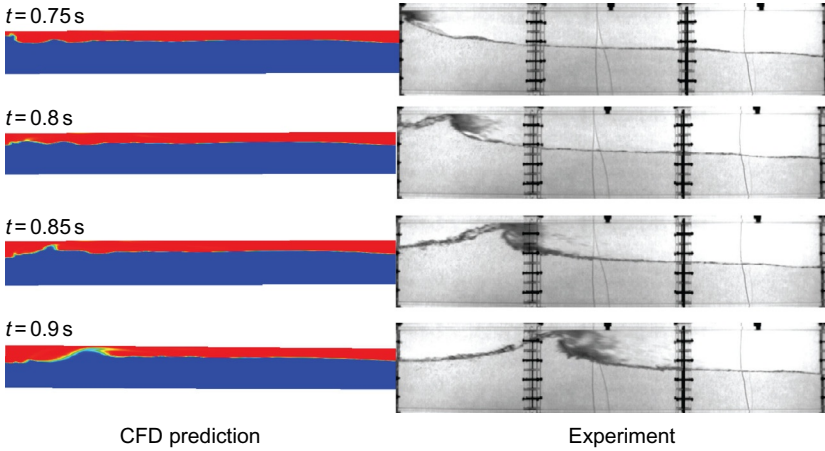


FIG. 1.21 Example of CFD application to predicting stratified flow in the cold leg of pressurized water reactor. *(After Höhne, T., Krepper, E., Rohde, U., 2010. Application of CFD codes in nuclear reactor safety analysis. Sci. Technol. Nucl. Ins. (Article ID 198758).)*

remains realistically achievable, and CFD with a detailed sufficient mesh can give reliable answers on issues relevant to containment simulation.

1.3.11 Power Generation and Renewable Energy

In an increasingly competitive energy market, utilities and equipment manufacturers are turning to CFD to provide a technological edge through a better

understanding of the equipment and processes within these industries. Although traditional electric power generation sources are still widely used, renewable power source such as wind energy is emerging as a potential alternative to power generation. To maximize return on investment, CFD is being employed to optimize the turbine blades for generating constant power under varying wind conditions as demonstrated by a typical three-dimensional simulation of the hydraulics in a complete wind turbine depicted in Fig. 1.22. CFD is also the only technology that has proved to accurately model wind farm resource distribution especially for highly complex terrain with steep inclines as shown in the same figure. Importantly, CFD has allowed the positioning of turbines throughout an area to achieve efficient wind capture and to minimize wake interaction. Wind resource assessments through CFD have allowed engineers to better study the economic viability of wind farms where accurate results are needed in order to reduce the financial risk.

The abundance of coal in many parts of the world such as Australia has made this raw mineral a popular fuel over many years in the power generation industries (see Fig. 1.23). Within these industries, the burning of coal in large furnaces has largely been associated with the release of environmentally harmful and hazardous pollutants such as CO, NOx, SOx, and mercury. To meet strict state, national, and international regulations, CFD simulations have greatly assisted engineers to identify areas where deficiencies in design occurred. More importantly, the causes of these ineffective operations can be established in order to reduce emissions in a cost-effective manner. With this information, design improvements or operating strategies can be implemented to maintain satisfactory levels of residual carbon in ash and achieve better flexibility in plant operation. For example, a boiler operation is optimized



FIG. 1.22 Example of CFD application in predicting the airflow over a wind turbine in the vicinity of a proposed wind farm.

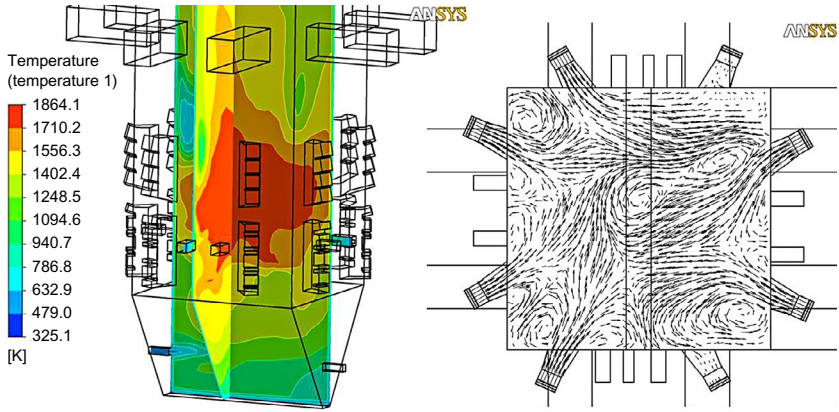


FIG. 1.23 Example of CFD simulation on an industrial pulverized coal furnace.

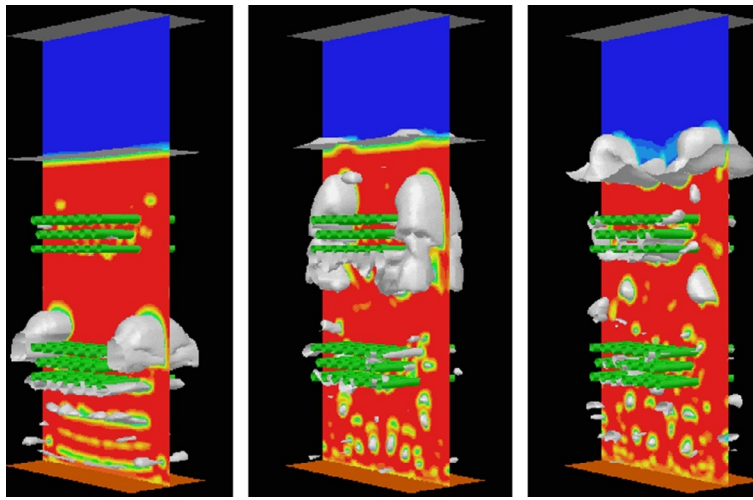


FIG. 1.24 Example of CFD simulation of bubbles in fluidized coal bed. *(Courtesy of ANSYS-FLUENT, Coal Gasification.)*

through reduction of fuel consumption, pollutant emissions, slagging, and degradation of the tubes, whilst downtime is reduced through prolonged component life. For clean power technologies, gasification offers the promise of increased generation efficiency and reduced emissions. Simulations can be performed to meet the modelling needs of this important technology as typified by the combusting fluidized coal bed in addition to other relevant unit operations as demonstrated in Fig. 1.24. By combining complete system simulations and detailed three-dimensional component analysis, engineers are at the liberty of making better design decisions and, ultimately, products of improved quality at low manufacturing costs.

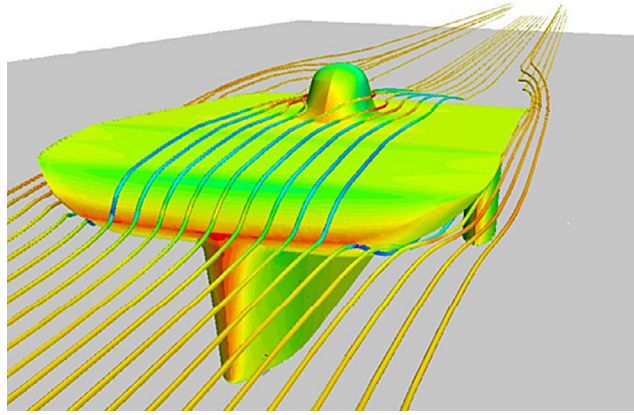


FIG. 1.25 Example of CFD simulation of airflow over SolarFox 3. *(Courtesy of http://www.ucl.ac.uk/solarfox/vehicles_main/SolarFox_3.)*

SolarFox 3, a highly competitive, fast car as shown in Fig. 1.25, is the latest vehicle being developed by the University College London team that has been created to run solely on solar energy. CFD simulations have proved to be useful in designing the outer body, wheel fairings, and canopy. The shape of the vehicle has been specifically crafted to significantly reduce the drag, and the teardrop curvature of the wheel fairings and canopy contributes to its aerodynamic profile. All materials on the vehicle have been carefully chosen to ensure that the overall weight is kept to a minimum. By minimizing the weight, a low rolling resistance is thus achieved that promotes a higher acceleration of the vehicle. The monocrystalline solar cells are divided into three arrays in accordance with the curvature of the upper body that allows for maximum solar energy absorption.

1.3.12 Sports

Very recently, one of the most innovative uses of CFD in the sports arena is to 'design' the optimum stroke to achieve peak propulsive performance for elite swimmers as demonstrated by the example in Fig. 1.26. In aspiring to attain the extra edge, USA Swimming, the national governing body for competitive swimming in the United States, commissioned CFD investigations to evaluate the flow around the hand and forearm of a swimmer during the propulsion phases of the freestyle and butterfly strokes. By applying CFD, steady-state lift and drag forces for the hand and arm are determined through applying sophisticated turbulence model and adaptive meshing. For this example, the force coefficients, evaluated at angles of attack ranging from −15 to 195 degree, and for various states of water turbulence, were found to compare very well with coefficients developed experimentally in a wind tunnel, a tow tank, and a flume.

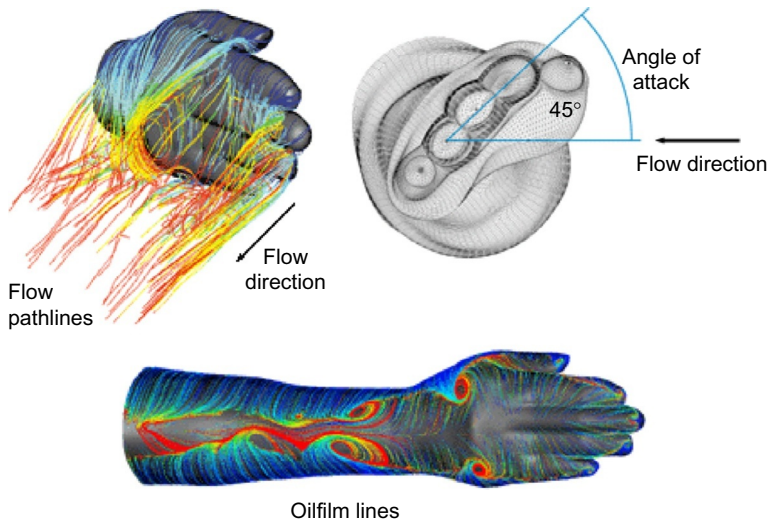


FIG. 1.26 Example of CFD application for designing the optimum stroke. *(Courtesy of USA Swimming, Honeywell Engines and Systems, and ANSYS-FLUENT.)*

The successful comparison of the simulated results with experimental data thus validates the chosen CFD modelling technique.

In the swimming literature, the hand is often compared to an aerofoil; a polar diagram developed from CFD analyses shows otherwise where the aerodynamic efficiency of the hand has been ascertained to be significantly less than that of an aerofoil of similar aspect ratio. At velocities reached by swimmers in competitive racing, flow pathlines predicted through CFD reveal a highly three-dimensional flow with significant boundary layer separation. Large vortices form on the downstream side of the hand, and smaller tip vortices twirl off the fingertips in a manner similar to those flowing from aircraft wings or turbine blades. By undertaking further assessments, CFD analyses can further study the effects of arm and hand acceleration and deceleration on the swimmer's ability to generate propulsive forces.

Cycling presents another sports arena where CFD has played a major role in designing the best possible bike to shave crucial milliseconds off the athletes' times. The Sports Engineering Research Group (SERG) at the University of Sheffield working closely with British Cycling have provided the British cycling team the means of constructing the fastest 'legal' bike in the world. During the Olympic Games, they won a total of four medals—two gold, one silver, and one bronze—a fantastic achievement for British cyclists. Their winning edge was solely attributed to SERG's aerodynamic optimization performed on the bike. Through CFD, SERG redesigned the Olympic bikes' forks and handlebar arrangement. CFD also helped the team to choose the most streamline design for the aerodynamic helmet as exemplified in Fig. 1.27.

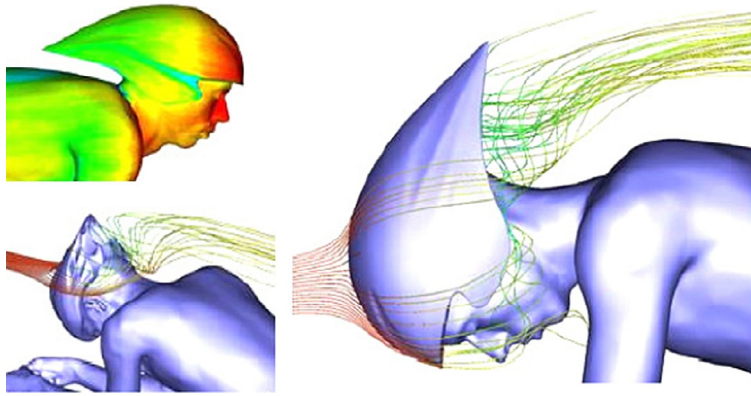


FIG. 1.27 Example of CFD simulation on designing the ultimate aerodynamic helmet. *(Courtesy of Sports Engineering at CSES, Sheffield Hallam University and ANSYS-FLUENT.)*

By better understanding the flow pathlines over the aerodynamic helmet, a range of helmet designs were manufactured to accommodate different head styles achieving the ultimate cycling efficiency. SERG's recommendations ensured that the British cycling team had the competitive advantage in their quest for gold.

1.4 THE FUTURE OF COMPUTATIONAL FLUID DYNAMICS

We are witnessing a renaissance of computer simulation technology in many industrial applications. This changing landscape is partly attributed by the rapid evolution of CFD techniques and models. For example, state-of-the-art models for simulating complex fluid mechanics problems such as jet flames, buoyant fires, multiphase, and/or multicomponent flows are now being progressively applied especially through the availability of multipurpose commercial CFD computer programs. The increasing usage of these types of codes in industries is a clear testimony whereby very demanding practical problems are now being analysed by CFD. With decreasing hardware costs and rapid computing times, engineers are increasingly relying on this reliable yet easy-to-use CFD tool for delivering accurate results as already described by the examples as described in the previous sections.

Additionally, significant advances in virtual technology and electronic reporting are allowing engineers to swiftly view and interrogate the CFD predictions and make necessary assessments and judgements on a given engineering design. In industries, CFD will eventually be so entrenched in the design process that new product development will evolve towards 'zero prototype engineering'. Such a conceptual design approach is not a mere flight of the imagination but rather a reality in the foreseeable future especially in the automotive industry. Looking ahead, full-vehicle CFD models with underhood,

climate control, and external aerodynamics will eventually be assembled into one comprehensive model to solve and analyse vehicle designs in hours instead of days. Time-dependent simulations will be routinely performed to investigate every possible design aspect. Other related 'cosimulation' areas in ascertaining the structural integrity and aeroacoustics of the vehicle will also be computed concurrently alongside with the CFD models. Engineering judgement will be consistently exercised on the spot through *real-time* assessments of proposed customized design simulations in selecting the most optimum vehicle.

In the area of research, the advances in computational resources are establishing large-eddy simulation (LES) as the preferred methodology for many turbulence investigations of fundamental fluid dynamics problems. Since all real-world flows are inherently unsteady, LES provides the means of obtaining such solutions and is gradually replacing traditional two-equation models in academia research. The demand of LES modelling is steadily growing. LES has made significant inroads especially for single-phase fluid flows. In combustion research, LES has also gained much respectability particularly in capturing the complex flame characteristics due to better accommodating the unsteadiness of the large-scale turbulence structure affecting the combustion process. Although much efforts have been focused in developing more robust CFD models to predict complicated multiphase physics involving gas–liquid, gas–solid, liquid–solid, or gas–liquid–solid flows, LES remains in its infant stage of application to cater for these types of flow problems. Instead, two-equation turbulence models are still very prevalent in order to account the turbulence within such flows. LES may be adopted as the preferred turbulence model for multiphase flows in the future, but in the meantime, the immediate need is to further develop more sophisticated two-equation turbulence models to resolve such kinds of flows.

Based on current computational resources, numerical calculations performed through LES can be rather long and arduous due to large number of grid nodal points required for computations. However, the ever-escalating trend of fast computing in a foreseeable future will permit such calculations to be performed in a more regular frequency. Also, with the model gradually moving away from the confines of academic research into the industry environment, it is not entirely surprising that LES will eventually become a household methodology for investigating many physical aspects of practical industrial flows. There are many challenging prospects for the use of CFD in industry and research. Perhaps, we can ponder towards the day where all turbulence flow problems can be resolved directly without the consideration of any models. Direct numerical simulation (DNS) of turbulent flows in academia research and possibly in some facets of industrial applications may well become a *distinct certainty* instead of a *distinct impossibility*.

1.5 SUMMARY

The array of examples illustrated in this introductory chapter clearly depicts how CFD has evolved through decades through rigorous development of numerical techniques. Despite the long standing usage within academic circles, Computational fluid dynamics, better known by its acronym CFD, is flourishing in many industrial sectors. This unprecedented occurrence is partly due to the increasing availability and accessibility of multipurpose commercial computer programs. These codes have certainly fuelled much of the swelling demand for industrial CFD applications. CFD research is also at the crossroads of progressive usage. Escalating computational power has permitted the ability to incorporate more sophisticated models to better resolve increasingly complex flow transport phenomena. As multipurpose commercial codes become a more commonplace in many educational institutions, they are revolutionizing the way by which CFD is being taught. Lately, simpler versions of these codes are being developed into dedicated educational tools for teaching and learning purposes. They are greatly assisting potential and novice users to learn CFD without them *reinventing the wheel* (i.e. duplicating their efforts in writing and debugging their own computational codes).

CFD computation usually involves the generation of a set of numbers or digits that will hopefully provide a realistic approximation of a real-life fluid system. Nevertheless, the main outcome of any CFD exercise is that the reader acquires an improved understanding of the flow behaviour for the system in question. The main ingredients of learning CFD are to gain experience and a thorough understanding of the flow physics and the fundamentals of the numerical techniques and models. Additionally, practical guidelines for good operating practice are ever more needed to increase competency in the use of this powerful tool. The intention of this book is therefore specifically written to address all of the aforementioned issues and to better equip the reader with the necessary background material for a good understanding of the internal workings inside a CFD code and its successful operation.

In the next chapter, we begin by discovering and coming to grips with how a CFD code works through the various elements that constitute a complete CFD analysis. Since a greater emphasis has been placed within this book on the practicality of CFD, many practical steps and aspects exemplifying the important elements of CFD analysis will be highlighted. The primary aim is to expose the reader to numerous operations that occur behind many existing commercial and shareware computer codes. With the surging demand for CFD to solve a spectrum of fluid-related problems, the aptitude to properly employ and apply this methodology has never been so important in the current climate.

REVIEW QUESTIONS

1.1 From which industry has CFD emerged from?
1.2 Which three disciplines CFD is derived from?
1.3 Traditionally, CFD has been used to solve aerospace and automotive engineering applications such as drag and lift for airplanes and cars, what examples can you think of where CFD is being used within nontraditional fluid engineering applications?
1.4 What are some of the advantages of using CFD?
1.5 What are the limitations and disadvantages of using CFD?
1.6 What CFD measurements can be obtained to assist the designs for safety and comfort in passenger airplanes?
1.7 What detailed results can be achieved in modelling of F18 jets that are difficult to achieve in experiments?
1.8 How is CFD being used as a research tool, a design tool, and an educational tool in academic fields, such as thermal fluids?
1.9 What aspect of CFD provides an advantage to allow better understanding of fluid flow and heat transfer?
1.10 How can CFD reduce development costs in time to market during design stage?
1.11 How would CFD be used to reduce drag in automotive engineering?
1.12 Why would parametric studies using CFD be more effective than large-scale wind-tunnel experiments?
1.13 Can CFD investigate piston engines in the automotive engineering? How would this be possible, computationally?
1.14 The biomedical science field is turning to CFD to resolve flows within human airway and vascular systems. What advantages does CFD hold over experiments in obtaining these numerical results?
1.15 What can CFD provide for evaluating surgical reconstructions for blood flows in arteries?
1.16 What other technologies are involved so that CFD can be performed on inside the human body?
1.17 What details can CFD capture in the simulation of hydrocyclones, a process commonly used in the minerals industry?
1.18 What types of flow can CFD model that investigates the separation process in mineral processing?
1.19 How is CFD being used in the civil and environmental industry?
1.20 How is CFD being employed in understanding metallurgical processes?
1.21 In metallurgy studies, CFD is able to model many phases at once (solid, liquid, and gas) known as multiphase modelling. Can you think of other multiphase problems that CFD could possibly be used for?
1.22 What kind of problems has CFD being applied for nuclear safety analyses?

1.23 What type of two applications CFD being used in the power generation industry? What kind of data is collected and how is this useful in increasing the efficiency in power generation?
1.24 What important parameters would you look for when modelling wind farms using CFD?
1.25 How can CFD influence the way swimmers in improving their swimming strokes?
1.26 What competitive edge can CFD give to a cycling team?
1.27 In the future, to what extent will CFD be involved within the product development process in manufacturing?
1.28 What is the future of CFD?

Chapter 2

CFD Solution Procedure: A Beginning

2.1 INTRODUCTION

With the widespread availability and ease of accessibility of many commercial, shareware, and in-house computer codes, today's CFD users will most probably acquire their necessary skills and knowledge rather differently from yesterday's CFD users. Such codes have become very prevalent, prominent, and widely used in many fields of academia, industrial sectors, and major research centres. It is therefore not surprising that potential or novice CFD users would be more inclined nowadays to resort to these available codes for learning CFD. The evolution of commercial codes towards more user-friendly environments and applications certainly reflects such demand.

Applying ready-developed CFD codes has certain advantages. Potential or novice users can initially treat these codes as black boxes (from the perspective of a student setting and not in a professional setting) and operate them with the main intentions of just practicing and familiarizing the many important features of these codes. Without any prior basic CFD knowledge, a first-time user can perform the necessary operations that involve setting up a fluid problem, solving the numerical problem, and managing some graphical representation of the results attained. Although the process can be regarded as very mechanically and laboriously driven, the exposure for a first-time user to CFD is not an intimidating or a daunting experience. Interested users are generally curious, and they are usually motivated to further investigate the mysterious aspects that are contained within these black boxes.

Fostering and cultivating the keenness and eagerness of interested users in learning CFD are important ingredients of maturing these users as eventual expert CFD users. The acquired skills and expertise fulfil the requirements of being competent and knowledgeable in analyzing and interpreting the computational solution whether it is physically realistic and numerically accurate. There have been many pitfalls in the past where the overexposure of hardcore mathematical formulations of the fluid flow equations and their numerical representations has certainly caused much angst amongst first-time users. More often than not, these users have become rather frustrated, disillusioned, and lamented at the prospect of learning CFD. However, CFD lies in the core

Computational Fluid Dynamics. https://doi.org/10.1016/B978-0-08-101127-0.00002-7
© 2018 Elsevier Ltd. All rights reserved.

comprehension of the fundamental principals concerning the fluid flow processes and analyzing the computational solutions. The integration of practical experience with theoretical knowledge to learning CFD is therefore tantamount. The practical side of CFD, in arousing and sustaining the level of enthusiasm of new users, shares the same foundational importance with the theoretical component in equipping these new users with the required level of CFD knowledge in better tackling fluid flow problems.

This book attempts to reconcile the two diametrically opposing approaches in teaching CFD. We begin by introducing the reader's perspective as a first-time user to the salient features that are common in many commercial and possibly in some shareware CFD codes. These codes are usually structured around the robust numerical algorithms that can tackle fluid flow problems. Almost all current commercial and possibly in some shareware CFD packages include user-friendly graphical user interface (GUI) applications and environments to input problem parameters and to examine the computed results. Hence, these codes provide a complete CFD analysis consisting of three main elements:

- *Preprocessor*
- *Solver*
- *Postprocessor*

This chapter, in retrospect, is intended to address the many practical steps and aspects that are exemplified in these three important elements in the attempt of uncovering the numerous operations beneath many of the shareware and commercial CFD codes. Fig. 2.1 presents a framework that illustrates the interconnectivity of the three aforementioned elements within the CFD analysis. The functions of these three elements will be examined in more detail in the subsequent sections within this chapter.

2.1.1 Shareware CFD

Today's CFD users have the luxury to download possible shareware or freeware CFD codes from certain websites through the internet. Under the website of http://www.cfd-online.com/Links/soft.html, the link offers the reader, under the software category, a catalogue of CFD codes listed as shareware products through the *shareware*, *freeware* option link.

Nevertheless, first-time CFD users may wish to search the internet to gain an immediate access to an interactive CFD code. First-time users may be required to register themselves in order to freely access the interactive CFD code. The website provides simple CFD flow problems for first-time users to solve and allows colourful graphical representation of the computed results. More advanced users may wish to visit an excellent web portal to acquire all the necessary aspects related to CFD in http://www.cfd-online.com/.

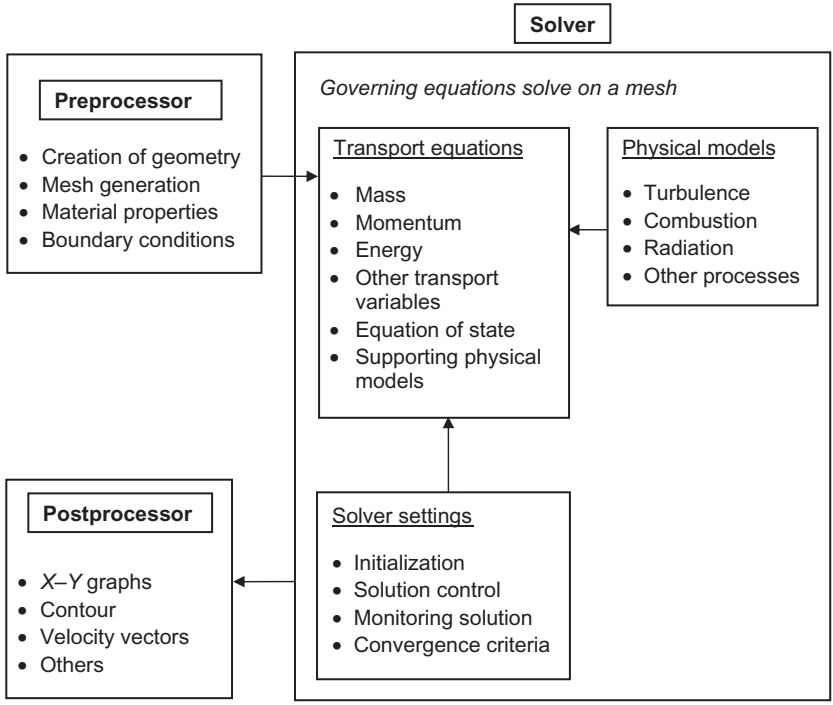


FIG. 2.1 The interconnectivity functions of the three main elements within a CFD analysis framework.

2.1.2 Commercial CFD

Under the software category of the web link http://www.cfd-online.com/Links/soft.htm/, the reader may wish to uncover the list of commercial codes that are currently available in the market through the *commercial* option link. Table 2.1 presents the internet links of some of the popular commercial CFD packages; it is by no means an exhaustive list. Commercial CFD vendors have invested much time, effort, and expense in the concerted development of user-friendly GUIs to make CFD very accessible and facilitate its usage and application in handling very complex fluid flow problems. We present some typical GUIs that a first-time user may experience and encounter in the course of employing a number of the commercial CFD packages tabulated in Table 2.1. The two interface fronts chosen are those that have been developed by ANSYS CFX and ANSYS FLUENT and they are illustrated in Figs 2.2 and 2.3. These interface fronts given below are not to be construed as an endorsement of these specific products, but we simply treat them as GUI examples for illustration purposes. Other commercial packages tabulated in Table 2.1 would most likely have similar user-friendly interface fronts of appealing graphical appearances and

TABLE 2.1 Internet Links to Some Popular Commercial CFD Packages

Developer	Code	Distributor Web Address
ANSYS, Inc.	CFX	http://www.ansys.com/
ANSYS, Inc.	FLUENT	http://www.fluent.com/
CD-adapco	STAR-CCM+	http://www.cd-adapco.com/
CHAM	PHOENICS	http://www.cham.co.uk/
COMSOL, Inc.	COMSOL	http://www.comsol.com/
ESI Group	CFD-ACE+	http://www.esi-group.com/
Flow Science	FLOW-3D	http://www.flow3d.com/

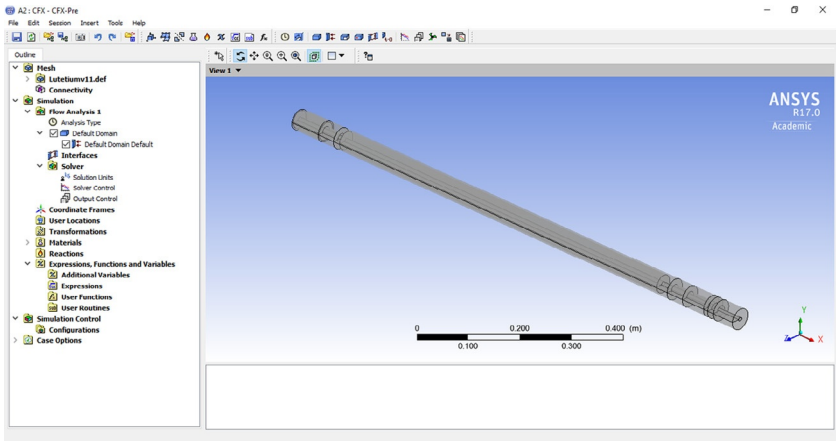


FIG. 2.2 A typical ANSYS CFX graphical user interface.

features such as possessed by the two aforementioned commercial packages. Whilst using these packages, the user will attempt to navigate through these interface fronts by accomplishing a certain number of basic steps to set up and solve the flow problem and obtain a CFD solution. These steps will be described and discussed in the next section.

2.2 PROBLEM SETUP—PREPROCESS

2.2.1 Creation of Geometry—Step 1

The first step in any CFD analyses is the definition and creation of geometry of the flow region, that is the *computational domain* for the CFD calculations.

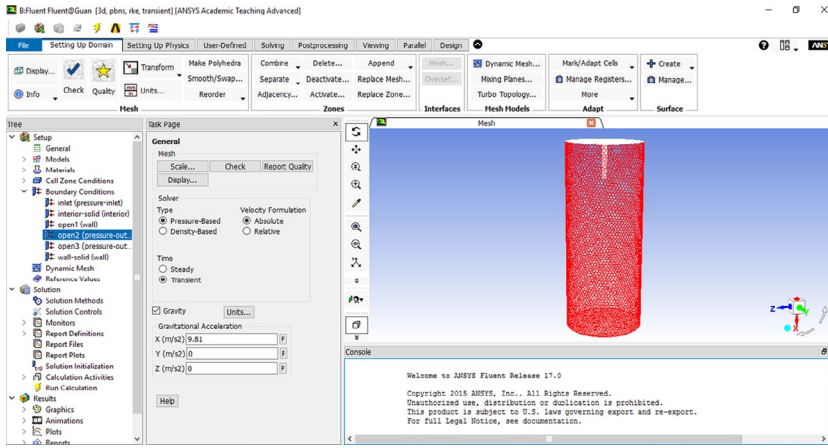


FIG. 2.3 A typical ANSYS FLUENT graphical user interface.

Let us consider two flow cases: a fluid flowing between two stationary parallel plates and a fluid passing through two cylinders in an open surrounding. It is important that the reader should always acknowledge the real physical flow representation of the problem that is to be solved as demonstrated by the respective *physical domains* in Figs 2.4 and 2.5. For the purpose of illustration, we designate the former and latter cases as Case 1 and Case 2. We shall assume that the two cylinders in Case 2 have the same length as the width W of the overall domain. We shall also assume that the width W of both flows within the three-dimensional *physical domains* is sufficiently large in order that the flows can be taken to be invariant along this transverse direction. Hence, Case 1 and

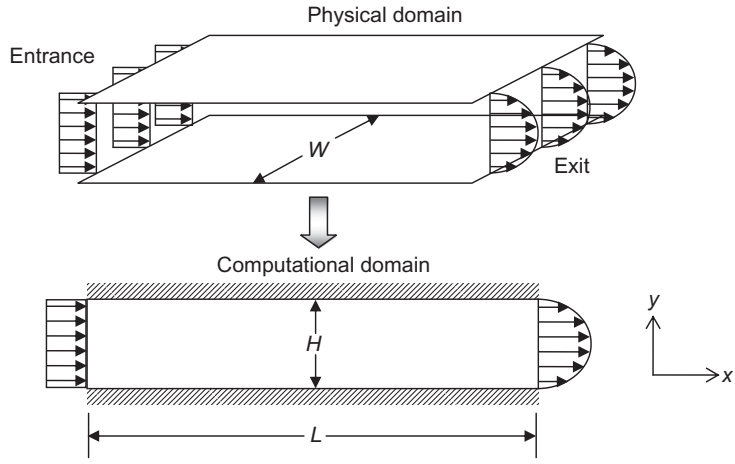


FIG. 2.4 Case 1: Fluid flowing between two stationary parallel plates.

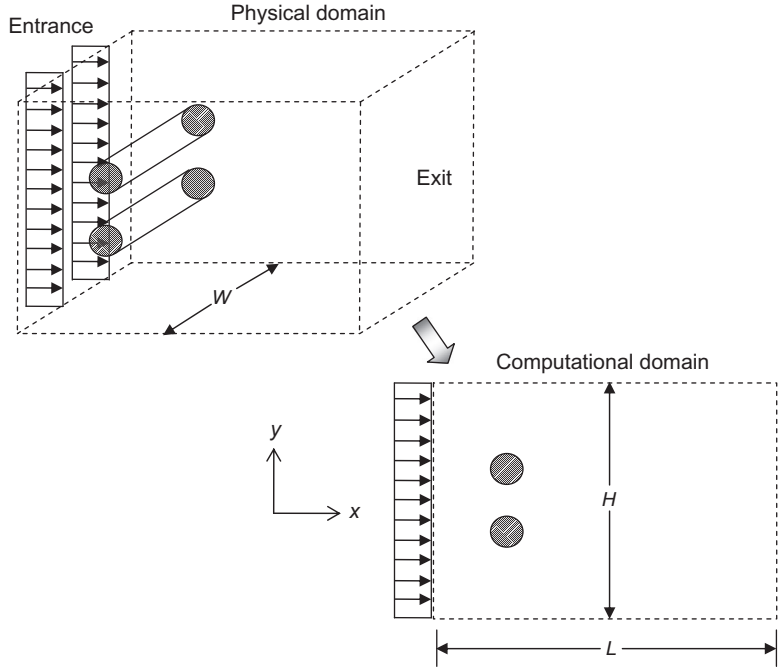


FIG. 2.5 Case 2: Fluid passing over two cylinders in an open surrounding.

Case 2 can simply be considered as two-dimensional *computational domains* for CFD calculations. These two flow cases will be repeatedly taken as illustrative examples to demonstrate the various basic steps that are involved in preprocess, solver, and postprocess stages.

There are certain distinct dissimilarities in the nature of these two flow problems. Case 1 represents an *internal flow* problem, whilst Case 2 is taken typically of an *external flow* scenario. In both cases, the fluid enters at the left boundary and exits at the right boundary of the *computational domains*. The main difference between these two flows is accentuated by the top and bottom boundaries, which brings about the classification of *internal* and *external flows*. In Case 1, the fluid flow is bounded within a domain of rigid walls as represented by the horizontal external walls of the two stationary parallel plates. That is not the characteristic of the fluid flow in Case 2 as the fluid can either take the inflow or outflow boundary conditions at the top and bottom boundaries.

One important aspect that the reader should always take note in the creation of the geometry for CFD calculations is to allow the flow dynamics to be sufficiently developed across the length L of these computational domains. For Case 1, we require the flow to be *fully developed* as it exits the domain. The physical interpretation and meaning of the concept of *fully developed* will be

expounded in Chapter 3. For Case 2, we require to encapsulate the occurrence of complex *wake-making* development that persists behind the two cylinders as the flow passes over these cylinders. This phenomenon is analogous to the formation and shedding of vortices that are commonly experienced for flow past a cylinder. In this particular case, the top and bottom boundary effects may influence the flow passing over these two cylinders; the height H of the domain needs to be prescribed at a distance to sufficiently remove any of these boundary effects on the fluid flow surrounding the two cylinders but still manageable for CFD calculations. More practical guidance on this issue will be addressed in Chapter 6.

2.2.2 Mesh Generation—Step 2

The second step that is mesh generation constitutes one of the most important steps during the preprocess stage after the definition of the domain geometry. CFD requires the subdivision of the domain into a number of smaller, nonoverlapping subdomains in order to solve the flow physics within the domain geometry that has been created; this results in the generation of a *mesh* (or grid) of *cells* (elements or control volumes) overlaying the whole domain geometry. The essential fluid flows that are described in each of these cells are usually solved numerically so that the discrete values of the flow properties such as the velocity, pressure, temperature, and other transport parameters of interest are determined. This yields the CFD solution to the flow problem that is being solved. The accuracy of a CFD solution is strongly influenced by the number of cells in the mesh within the computational domain. Whilst, in general, increasing the number of cells will improve the accuracy of the solutions, it is also influenced by many other factors, such as the type of mesh, the order of accuracy of the numerical method, and the adequacy of the techniques chosen to the physics of the problem. However, the accuracy of a solution is strongly dependant on the imposed limitations dominated by the computational costs and calculation turnover times. Issues concerning numerical accuracy and computational efficiency will be explored in Chapter 5.

Majority of the time spent in industry on a CFD project is usually devoted in successfully generating a mesh for the domain geometry. Most commercial CFD codes have developed their own dedicated CAD-style interface and/or facilities to import data from solid modeller packages such as PARASOLID, PRO/ENGINEER, SOLID EDGE, SOLIDWORKS, and UNIGRAPHICS to maximize productivity and allow the ease for geometry creation. The mesh for the created geometry can be subsequently realized through in-built powerful mesh generators that reside within these respective codes. Nevertheless, the reader should be well aware that it is still up to the skills of the CFD user to design a mesh that is a suitable compromise between the desired accuracy and solution cost. The generation of an appropriate mesh for CFD calculations will be further discussed in Chapter 6.

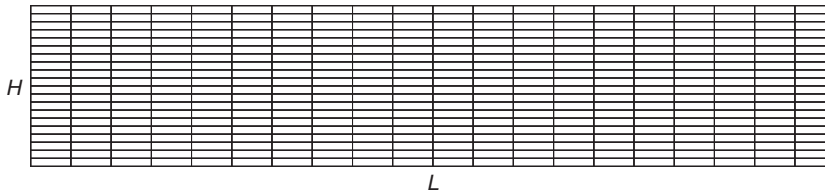


FIG. 2.6 Structured meshing for fluid flowing between two stationary parallel plates.

The mesh generation step is illustrated for Case 1 and Case 2. For relatively simple geometries such as the created geometry domain for Case 1, an overlay mesh of *structured* cells that generally comprise a regular distribution of rectangular cells can be readily realized. Fig. 2.6 shows a mesh of 20 (L) × 20 (H) cells resulting in a total number of 400 cells allocated for the Case 1 geometry. For more complex geometries, the meshing by triangular cells allows the flexibility of mesh generation for geometries having complicated shape boundaries. Fig. 2.7 illustrates a typical distribution of triangular cells within the computational domain for Case 2 geometry with a mesh totalling 16,637 cells mapping the whole flow domain.

The specific type of meshes represented in Case 1 and Case 2 domain geometries should be construed as just illustrative examples for the intended purpose of demonstrating the mesh generation step. It is not unprecedented and rather legitimate to interchangeably use an *unstructured* mesh in place of a *structured* mesh for Case 1 and vice versa for Case 2. It is also not uncommon and in some practices a requirement to embrace a combination of *structured* and *unstructured* meshes for more realistic simulations within flow domains that may include many inherent complex geometrical intricacies. More practical guidance on mesh generation will be provided in Chapter 6.

2.2.3 Selection of Physics and Fluid Properties—Step 3

Many industrial CFD flow problems may require solutions to very complex physical flow processes such as the accommodation of complicated chemical

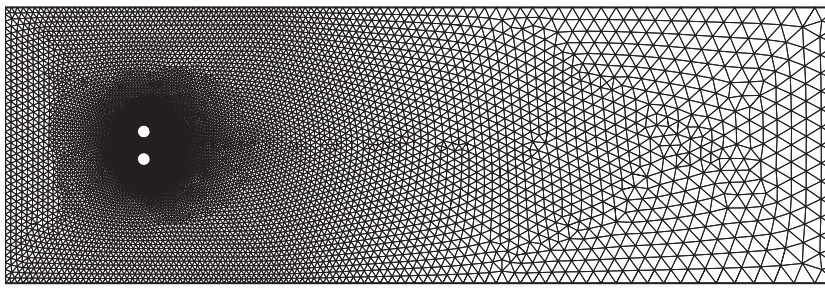


FIG. 2.7 Unstructured meshing for fluid passing over two cylinders in an open surrounding.

reactions in combusting fluid flows. The inclusion of combustion and possibly radiation models in the CFD calculations are generally prerequisites to the successful modelling of these types of flows. Combustion and radiation processes have the tendency to strongly influence the local and global heat transport, which consequently affect the overall fluid dynamics within the flow domain. It is therefore imperative that a CFD user carefully identifies the underlying flow physics that is unique to the particular fluid flow system.

For clarity and ease of reference, a flowchart highlighting the various flow physics that may be encountered within the framework of CFD and heat transfer processes is presented in Fig. 2.8. Under the main banner of *Computational Fluid Dynamics and Heat Transfer*, a CFD user declares initially whether simulations to the fluid flow system are to be attained for *transient/unsteady* or *steady* solutions. He/she subsequently defines which class of fluids that the flows may belong: *inviscid* or *viscous*. *Inviscid* fluid flows are generally compressible, and the consideration of fluid compressibility in the flow physics can usually be handled through the *panel method*. *Viscous* fluid flows can, however, exist in their *laminar* or *turbulent* state. Under these two flow conditions, prior knowledge of whether the fluids are *compressible* or *incompressible* is required. The classification of *internal* and *external* flows for viscous fluids allows the user to appropriately treat these types of flow problems in a manner that has been discussed in Section 2.2.1. Also, the transport of heat may contribute

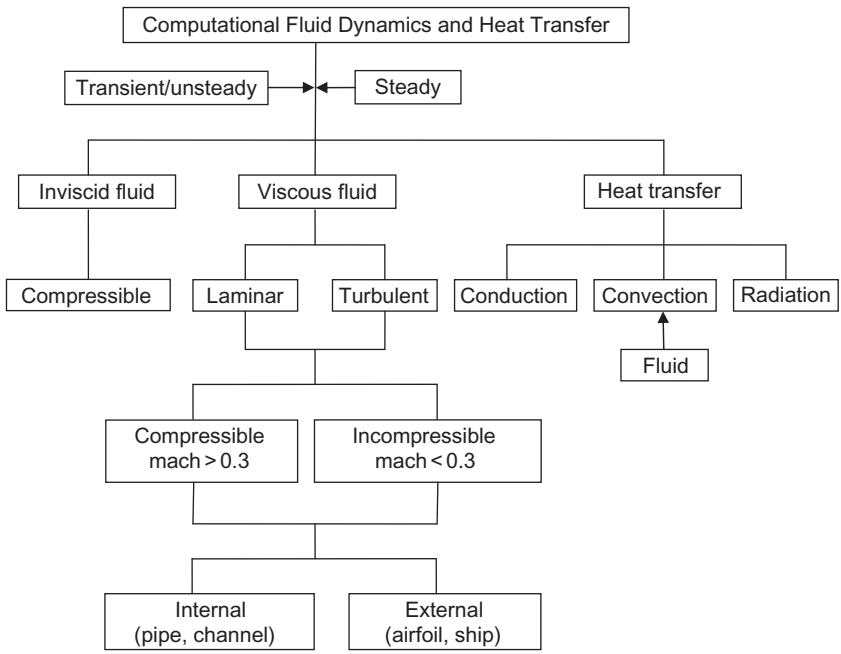


FIG. 2.8 A flowchart encapsulating the various flow physics in CFD.

significantly to the fluid flow process, which comprises of three heat transfer modes: *conduction*, *convection*, and *radiation*. For convection, the dominant mode of *heat transfer* will more likely to be driven by the *convective* fluid flow rather than by other modes of *conduction* and *radiation*. Nevertheless, there are circumstances where *radiation* and *convection* can coexist and dominate the *heat transfer* especially in the expansion of fires.

Let us review the various basic steps that have been described thus far for the preprocess stage. In step 1, we have created two-dimensional computational domains for Case 1 and Case 2. Step 2 illustrates the generation of an overlay mesh of structured cells for Case 1 and unstructured cells of different sizes for Case 2. Step 3, the current step in the preprocess stage, consists of the identification and formulation of the flow problems in terms of the physical phenomena. A CFD user must select the appropriate flow physics, as discussed above, in order to correctly simulate the characteristics of the fluid flow. For simplicity, a steady CFD solution is considered for Case 1 and Case 2, and the fluid flows in both cases can be taken to be viscous, laminar, incompressible, and isothermal (without heat transfer). It is rather important that setting up the flow physics is also accompanied by ascertaining what fluid is used within the flow domain. For example, air or water has its own unique fluid and thermal properties. Appropriate properties are therefore required to be assigned to correctly define the particular fluid in this preprocess step. Fluid properties such as *density* and *viscosity* (dynamic) can usually be imposed through the GUIs in many commercial CFD codes.

2.2.4 Specification of Boundary Conditions—Step 4

The complex nature of many fluid flow behaviours has important implications in which boundary conditions are prescribed for the flow problem. A CFD user needs to define appropriate conditions that mimic the real physical representation of the fluid flow into a solvable CFD problem.

The fourth step in the preprocess stage deals with the specification of permissible boundary conditions that are available for impending simulations. Evidently, where there exist *inflow* and *outflow* boundaries within the flow domain, suitable fluid flow boundary conditions are required to accommodate the fluid behaviour entering and leaving the flow domain. The flow domain may also be bounded by *open* boundaries. Although the intricacies of *open* boundary conditions are still subject to much theoretical debate, this boundary condition remains the simplest and cheapest form to prescribe when compared with other theoretically more satisfying selections in CFD. Appropriate boundary conditions are also required to be assigned for external stationary *solid wall* boundaries that bound the flow geometry and the surrounding walls of possible internal obstacles within the flow domain.

We illustrate the applications of the aforementioned boundary conditions to Case 1 and Case 2 for CFD calculations. Schematic descriptions of the boundary

conditions are respectively demonstrated in Fig. 2.9 for Case 1 and Fig. 2.10 for Case 2.

In Section 2.2.3, the considerations of a viscous fluid, laminar, incompressible, and isothermal assumed for the purpose of illustration in both Case 1 and Case 2 require the prescription of only the fluid velocity on all the bounding

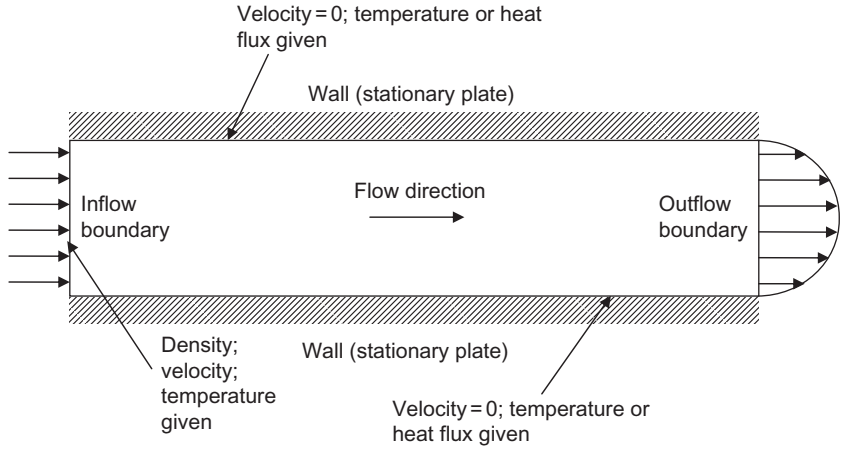


FIG. 2.9 Boundary conditions for an internal flow problem: Case 1.

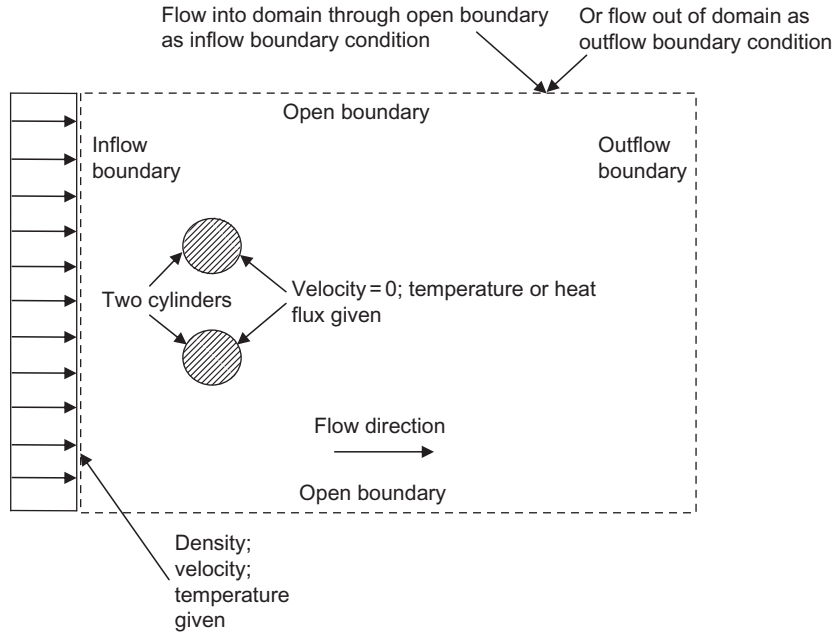


FIG. 2.10 Boundary conditions for an external flow problem: Case 2.

walls of the computational domain. By definition, the velocities are zero for the external stationary *solid walls* bounding the flow domain in Case 1 (see Fig. 2.9) and the two cylindrical motionless *solid walls* in Case 2 (see Fig. 2.10). For the *inflow* boundary conditions, the user is required to ascertain the inlet fluid velocity in order to stipulate the fluid entering into both of these flow domains. At the *outflow* boundaries indicating the fluid departure, only one outlet condition typically a specified relative pressure is imposed. A far-field flow boundary condition can be imposed for the open boundaries that apply either the inflow or outflow boundary conditions. Care should always be exercised in handling these *open* boundaries where they have to be defined far enough away from the region of interest within the solution domain in order to obtain physically meaningful results.

Nevertheless, for a general fluid flow case where the transport of heat is dominant within the flow domain as may be experienced by the flows in Case 1 and Case 2, the user is obliged to prescribe the surface boundaries of the flow domains and obstacles either by the given temperature or heat flux distributions as shown in Figs 2.9 and 2.10. In compressible-like flows such as buoyancy-driven flows and combusting flows such as fire where there exists a strong density variation with temperature, the density emerges as part of the solution everywhere within the flow domains. The density corresponding to the particular fluid flowing into these domains at the inflow boundaries needs to be specified and is usually determined directly from the imposed temperature and pressure. However, no boundary conditions are required for the density at the outflow boundaries since the fluid density replicates the outgoing fluid characteristics through these boundaries. For the open boundaries such as in Case 2, the density can either be represented by the inflow or outflow boundary conditions.

General-purpose CFD codes also often allow the prescription of inflow and outflow pressure or mass flow rate boundary conditions. By setting fixed pressure values, sources and sinks of mass placed at the boundaries ensure the correct mass flow into and out of the solution zone across the constant pressure boundaries. It is also feasible to allocate directly sources and sinks of mass at the boundaries by the mass flow rates instead of pressures to retain the overall mass balance for the flow domain. To take advantage of special geometrical features that the solution region may possess, *symmetric* and *cyclic* boundary conditions can be employed to speed up the computations and enhance the computational accuracy by placing additional number of cells to the simplified geometry. Fig. 2.11 shows the boundary geometry for which symmetry boundary condition can be imposed for Case 1, whilst Fig. 2.12 illustrates a generic geometry where cyclic boundary conditions may be useful. The physical meanings of the various boundary conditions that have described herein to close the fluid flow system will be expounded in Chapter 3.

Thus far, we have concentrated the application of various boundary conditions that only pertain to *subsonic* fluid flows—flows below the speed of sound.

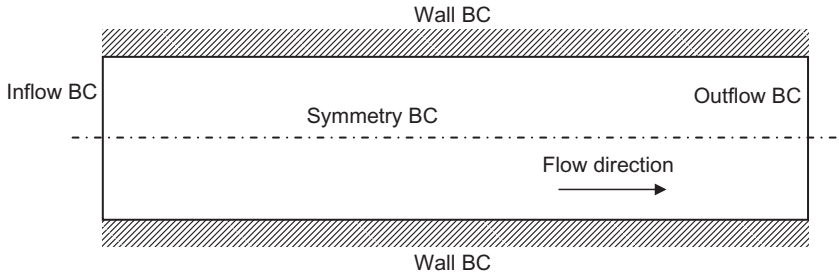


FIG. 2.11 Definition of symmetry boundary condition for Case 1.

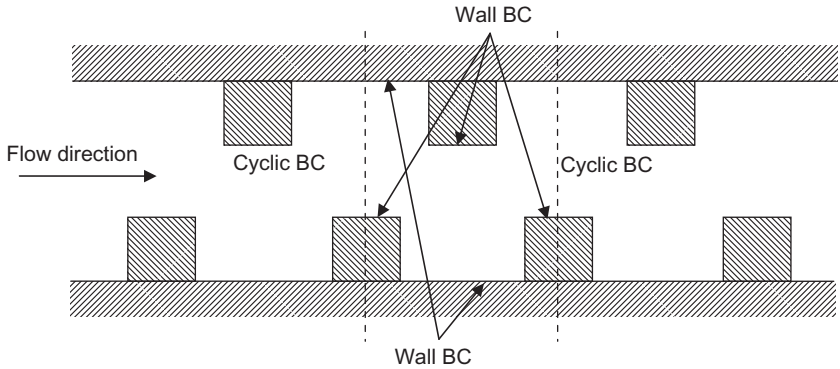


FIG. 2.12 Definition of cyclic boundary condition for a generic geometry.

There is another broad range of fluid flows that can possibly achieve speeds near to and above the speed of sound, which they are generally classified as *hypersonic*, *transonic*, and *supersonic* fluid flows. The prevalence of such complex flows is evident in many aerodynamic investigations. At these high speeds, the viscous regions in the flow are usually exceedingly thin, and the enveloping flow in a large part of the solution domain behaves effectively inviscid. Applying boundary conditions predominantly for viscous flow to a largely dominated inviscid flow may yield unphysical behaviour of the shockwaves propagating through the flow domain. Physical description and application of boundary conditions for *supersonic* flows will be covered in Chapters 3 and 7. For additional details, interested readers are advised to refer to Fletcher (1991) and Anderson (1995) for more discussions and prescriptions of the boundary conditions for fluid flows that are *hypersonic* and *transonic*. Majority of the commercial codes make claims and boast the capability to resolve all fluid flow regimes—*subsonic*, *transonic*, and/or *supersonic*. They usually, however, perform most effectively below the speed of sound, that is *subsonic*, as a consequence of the boundary conditions outlined above.

2.3 NUMERICAL SOLUTION—CFD SOLVER

The appropriate usage of either an in-house or a commercial CFD code commands the core understanding of the underlying numerical aspects inside the *CFD solver*. This section focuses on the treatment of the solver element. A *CFD solver* can usually be described and envisaged by the solution procedure presented in Fig. 2.13. The prerequisite processes in the solution procedure that have implications on the computational solution are *initialization*, *solution control*, *monitoring solution*, *CFD calculation*, and *checking for convergence*. A CFD user whether applying in-house or commercial codes needs to gain the necessary insights and knowledge pertaining to the workings of these prerequisite processes in order to skillfully utilize the many solver features and better navigate the underlying 'black box' operations that reside in many of these codes.

2.3.1 Initialization and Solution Control—Step 5

The fifth step of the CFD analysis encompasses two prerequisite processes within the CFD solver that are *initialization* and *solution control*.

Firstly, the underlying physical phenomena in real fluid flows that are generally complex and non-linear within such flows usually require the treatment of the key phenomena to be resolved through an iterative solution approach. Iterative procedure generally involves all the discrete values of the flow properties such as the velocity, pressure, temperature, and other transport parameters of

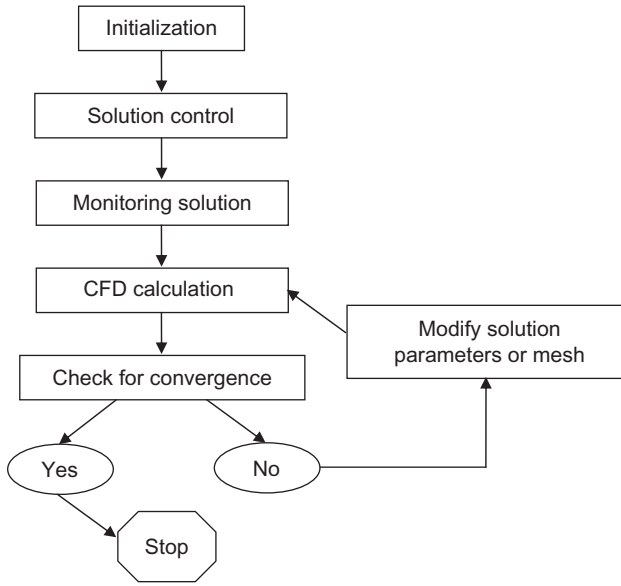


FIG. 2.13 An overview of the solution procedure.

interest to be *initialized* before calculating a solution. In theory, initial conditions can be purely arbitrary. However, in practice, there are certain advantages to impose initial conditions *intelligently*. Good initial conditions are crucial to the iterative procedure; two reasons on why the reader as a CFD user should undertake the appropriate selection of initial conditions are the following:

- If the initial conditions are closed to the final steady-state solution, the quicker the iterative procedure will converge and results in shorter computational time.
- If the initial conditions are far away from reality, the computations will result in longer computational efforts to reach the desired convergence. Also, improper initial conditions may lead to the iterative procedure misbehaving and possibly 'blowing up' or diverging.

Secondly, the setting up of appropriate parameters in the *solution control* usually entails the specification of appropriate *discretization* (*interpolation*) *schemes* and selection of suitable *iterative solvers*.

Almost all well-established and thoroughly validated general-purpose commercial codes adopt the *finite volume method* (Chapter 5) as their standard numerical solution technique. The algebraic forms of equations governing the fluid flow within these codes are usually approximated by the application of finite-difference-type approximations to a finite volume cell in space. At each face of the cell volume, surface fluxes of the transport variables that are required can be determined through different interpolation schemes. Some of the common interpolation schemes are *first-order upwind*, *second-order upwind*, *second-order central*, and *quadratic upstream interpolation convective kinetics* (*QUICK*). The inability of the *central* scheme to identify the flow direction results in the formulation of other schemes such as *upwind* or *QUICK*, which means the interpolation methods are biased on the upstream occurrence of the fluid flow and thus accounts for the flow direction. The choice of a higher order interpolation scheme may achieve the desired level of accuracy that needs to be evaluated at the cell faces. Solution procedures such as SIMPLE, SIMPLEC, or PISO algorithm are popular in many commercial codes. The method is geared towards guaranteeing correct linkage between the pressure and velocity, which predominantly accounts for the mass conservation within the flow domain. At present, our intention is not to dwell into the many underlying numerical properties but rather to present simply the choice of interpolation schemes and pressure-velocity coupling methods that are offered as standard options in many CFD codes. It is imperative that some background knowledge on the appropriate selection of these options is acquired before any CFD calculation is performed. More discussions and practical guidance on the many numerical issues pertaining to the application of interpolation schemes and pressure-velocity coupling methods will be provided in Chapters 4 and 6.

Iterative solvers so-called number crunching engines for numerical calculations are employed to resolve the algebraic equations. Nowadays, robust solvers

such as algebraic multigrid (AMG) algorithm and conjugate gradient methods are standard features in many commercial codes. Other popular solvers such as strongly implicit procedure (SIP) of Stone's method and TDMA line-by-line procedure are also prominently employed amongst many users in the CFD community. More descriptions of these solvers are provided in Chapter 5.

Solver controlling parameters that exist inside these solvers in commercial codes tend to be optimally configured for efficient matrix calculations. The desired performance can usually be achieved through the default settings prescribed within these codes.

Step 5 hereby completes the specification of various relevant physical features pertaining to the intended fluid flow process of a CFD problem. To exemplify the *CFD calculation* process of the solution procedure in Fig. 2.13, Case 1 and Case 2 fluid flow problems described in Section 2.1.1 are revisited to demonstrate the iterative operations that are typically visualized through the ANSYS CFX and ANSYS FLUENT GUIs in the next proceeding step below. We conveniently employ the default settings of the interpolation schemes and pressure–velocity coupling methods and retain the optimal controlling parameters that govern the performance of the iterative solvers to simply illustrate the important features of the numerical computations.

2.3.2 Monitoring Convergence—Step 6

The sixth step of the CFD solver involves the interlinking operations of three prerequisite processes: *monitoring solution*, *CFD calculation*, and *checking for convergence*. Two aspects that characterize a successful CFD computational solution are *convergence* (Chapter 5) of the iterative process and *grid independence* (Chapters 5 and 6).

Convergence can usually be assessed by progressively tracking the *imbalances* that are accentuated by the advancement of the numerical calculations of the algebraic equations through each iteration step. These *imbalances* measure the overall conservation of the flow properties; they are also commonly known as the so-called *residuals* (Chapters 4 and 5) that are generally viewed through commercial code GUIs. Examples of these GUIs by ANSYS CFX and ANSYS FLUENT that represent the downward trends of the *residuals* for Case 1 are illustrated in Figs 2.14 and 2.15, respectively. These downward tendencies clearly point to the *continual removal* as opposed to *possible accumulation* of any unwanted *imbalances* thereby causing the iterative process to *converge* rather than to *diverge*. A *converged* solution is achieved when the residuals fall below some *convergence criteria* or *tolerance* (Chapter 5) that is preset inside the solver controlling parameters of the iterative solvers. We indicate different default settings of the *tolerance values* (Chapter 5) that are used by ANSYS CFX and ANSYS FLUENT to terminate the iterative process. They are prescribed at values of 1×10^{-4} and 1×10^{-3}, respectively, as shown in Figs 2.14 and 2.15. A converged solution is obtained rather quickly from either

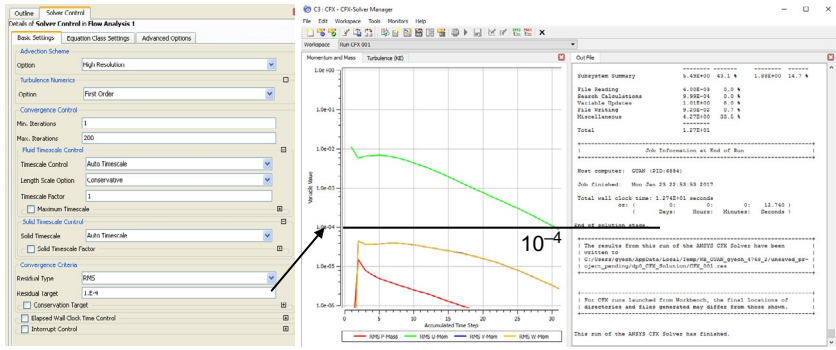


FIG. 2.14 Typical ANSYS CFX GUIs for monitoring convergence corresponding to the prescribed convergence criteria.

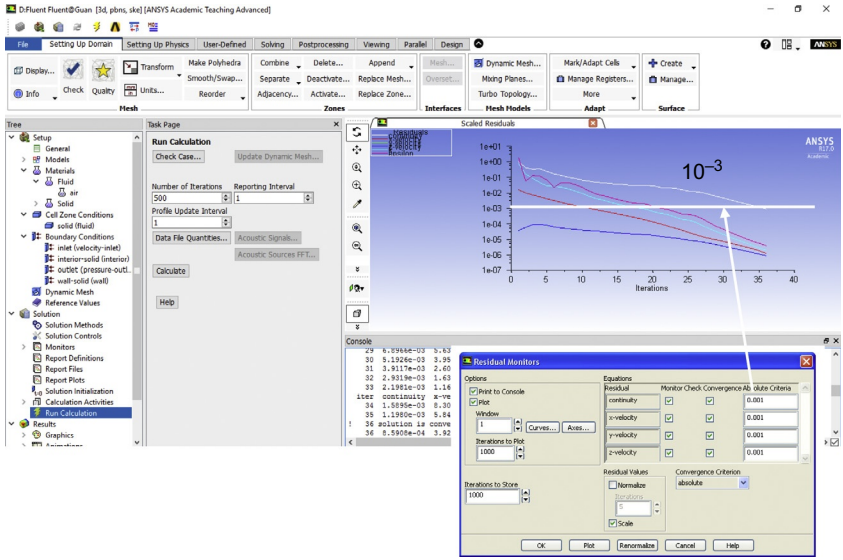


FIG. 2.15 Typical FLUENT GUIs for monitoring convergence corresponding to the prescribed convergence criteria.

ANSYS CFX or ANSYS FLUENT because of the sheer nature of the flow in Case 1 being rather straightforward. Besides examining the *residuals*, the user may use other monitoring variables such as the lift, drag, or moment force to ascertain the convergence of the numerical computations. Fig. 2.16 shows the lift coefficient (Cl) history for Case 2 employing the commercial code ANSYS FLUENT. It is not surprising that the fluid flow process in Case 2 being more complicated than Case 1 requires more iterations to reach *convergence*. No appreciable change to the lift coefficient is observed after 700 iterative steps, and the computational solution is thus deemed to be converged at about 1000

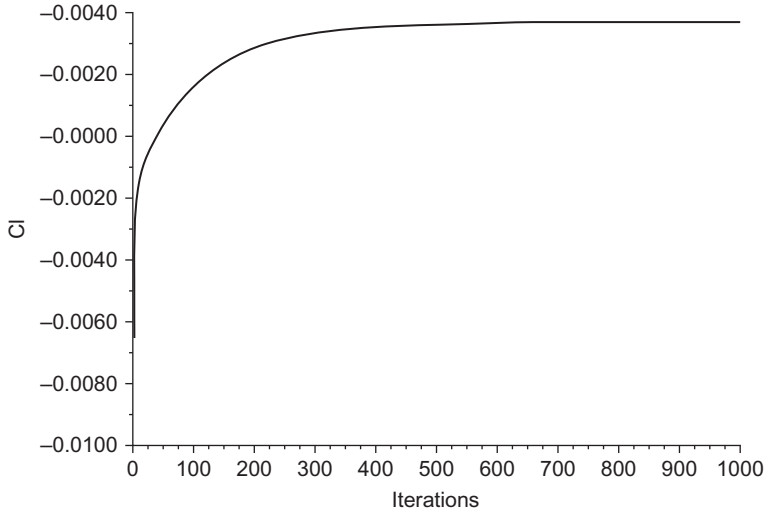


FIG. 2.16 Monitoring the solution convergence through the lift coefficient history.

iterations as the lift coefficient plateaus to a fixed value of around 0.0035. In addition to monitoring residual and variable histories, the user is well advised to also check the overall mass balance and possibly heat balance for the fluid flow system within the computational domain. The net imbalance should be minimized as low as possible to ensure adequate property conservation.

Progress towards a converged solution can be greatly assisted by the careful selection of various *underrelaxation factors* (Chapter 5). Most commercial codes adopt some form of *underrelaxation factors* to enhance the *stability* of the numerical procedure and ensure the *convergence* of the iterative process. The incorporation of *underrelaxation factors* into the system of algebraic equations that govern the fluid flow is intended to significantly moderate the iteration process by limiting the change in each of the transport variable from one iterative step to the next. There are no straightforward guidelines for pertinent choices of these factors. More often than not, in-depth experience on the selection of appropriate values of these factors can only be gained by the extensive investigation on a variety of flow problems.

Estimating the *errors* (Chapter 5) introduced by an inadequate mesh design for a general flow can be rather arduous. Preparing a good initial mesh design usually requires the preknowledge or insight to the expected properties of the flow. In dealing with the coarseness of a mesh, the only way to eliminate the *errors* is to embrace the procedure of successive refinement of an initially coarse mesh until certain key results exhibit no appreciable changes. This process forms part of the extended arm within the solution procedure as described in Fig. 2.17. A systematic search of *grid-independent* results generally leads to the accomplishment of high-quality CFD solutions.

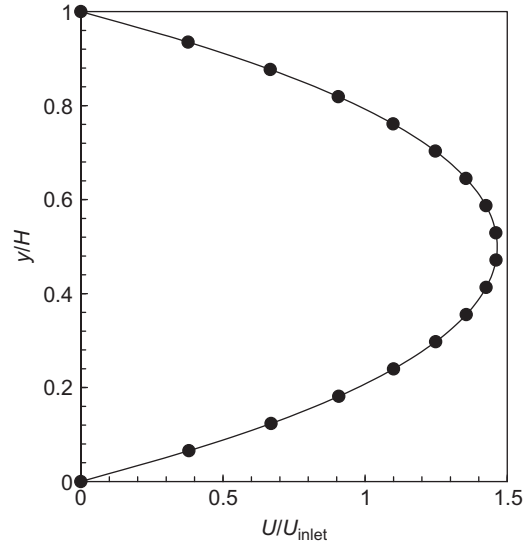


FIG. 2.17 *X–Y* plot of a parabolic laminar velocity profile at the fully developed region for Case 1.

The reader should take note that the many aspects such as *convergence*, *convergence criteria or tolerance values*, *residuals*, *stability*, *errors*, *underrelaxation factors*, and *grid independence* greatly underpin the many numerical considerations for the simulation of a CFD problem. These conceptual terminologies may be rather difficult to fathom at this juncture. Nevertheless, supplementary discussions will be provided later in other chapters to adjunct the knowledge of the basics already attained herein.

2.4 RESULT REPORT AND VISUALIZATION—POSTPROCESS

CFD has a reputation of generating vivid graphical images and, whilst some of them are promotional that are usually displayed in stunning and superb colourful outputs, the ability to present the computational results effectively is an invaluable design tool. In this section, we concentrate on some essential computer graphical techniques frequently encountered in the presentation of CFD data. The majority of ways that the CFD results are emphasized graphically can be classified under different categories. Each of these categories, to be discussed below, assists the CFD user to better analyze and visualize the many relevant physical characteristics within the fluid flow problem.

Commercial CFD codes such as ANSYS CFX, ANSYS FLUENT, and STAR-CD often incorporate impressive visualization tools within their user-friendly GUIs to allow users to graphically view the results of a CFD calculation at the end of a computational simulation. There also exist, however, many excellent stand-alone applications of independent computer graphical software

TABLE 2.2 Internet Links to Some Popular Computer Graphical Software Packages

Developer	Code	Distributor Web Address
Advanced Visual Systems	AVS, Gsharp, Toolmaster	http://www.avs.com/
Amtec Engineering	TECPLOT	http://www.amtec.com/
CEI	ENSIGHT	http://www.ceintl.com/
IBM (free, apparently)	OpenDX	http://www.opendx.org/
Intelligent Light	FIELDVIEW	http://www.ilight.com
Numerical Algorithms Group (NAG)	IRIS Explorer	http://www.nag.co.uk/
Visual Numerics	PV-WAVE	http://www.roguewave.com/
Kitware	ParaView	http://www.paraview.org/
Department of Energy (DOE) Advanced Simulation and Computing Initiative (ASCI)	VisIt	https://wci.llnl.gov/

packages that the reader may opt to utilize for his/her CFD applications. Table 2.2 presents a list of some currently available graphical packages. Majority of these packages cater for various computer platforms although some may only operate primarily in UNIX systems. Some of the commercial packages such as FIELDVIEW, TECPLOT, and ENSIGHT have been specifically developed for postprocessing CFD results, whilst others are more general-purpose visualization tools that may be equally applied for CFD applications. For simple graphical representations, the use of an open-source plotting package such as GNUPLOT is popular amongst many researchers in the CFD community. It can be obtained freely through the internet website: http://www.gnuplot.info/.

For the remainder of this section, we demonstrate the different categories that can be applied to illustrate a CFD solution through a popular versatile computer graphical software package, namely, TECPLOT. These categories will be mainly exemplified in the context of the solutions obtained from our previously defined flow cases: Case 1, a fluid flowing between two stationary parallel

plates, and Case 2—a fluid passing through two cylinders in an open surrounding. An overview of these categories may also assist the reader to be more accustomed to how a CFD solution can be processed and visualized within a commercial code at the end of a simulation.

The use of TECPLOT for our graphical representations of the CFD results should not be interpreted as being skewed towards the endorsement of a specific product. Rather, we aim to simply provide the reader example of a standard graphics software approach. With the rapid evolution of new graphical techniques, probing the flow behaviour inside a CFD problem may well be better achieved through other software packages. At that occasion, it is entirely up to the reader's choice to employ the appropriate graphics software package for their perusal.

2.4.1 *X–Y* Plots

These plots are mainly two-dimensional graphs that represent the variation of one dependent transport variable against another independent variable. They can usually be drawn by hand or more conveniently by many plotting packages. Such *X–Y* plots are the most precise and quantitative way to present the numerical data. Often, laboratory data are gathered by straight-line traverses. These graphs are therefore a popular way of directly comparing the numerical data with the experimental measured values. Also, logarithmic scales allow the identification of important flow effects occurring especially in the vicinity of solid boundaries. These graphs are widely used for presenting line profiles of velocity and for plots of surface quantities such as pressure and skin-friction coefficient. They are usually meant to be very easily identifiable; the reader can readily read the results without resorting to any mental or arithmetic interpolation.

An *X–Y* plot of a laminar velocity profile at the *fully developed* region for Case 1 is shown in Fig. 2.17. The significance of a parabolic profile characterizes the flow physics typically experienced for a fluid flowing within a parallel-plate channel. Another possible way of visualizing the development of the fluid flow is through the use of successive two-dimensional graphical profiles as shown for Case 1 in Fig. 2.18. The flow distribution gradually changes from a uniform profile specified at the entrance boundary (left) to a parabolic profile

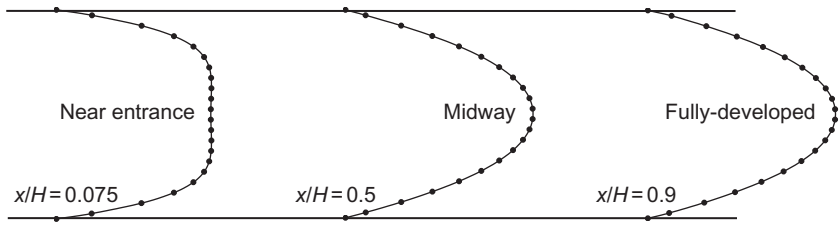


FIG. 2.18 Successive two-dimensional velocity profiles of a developing flow for Case 1.

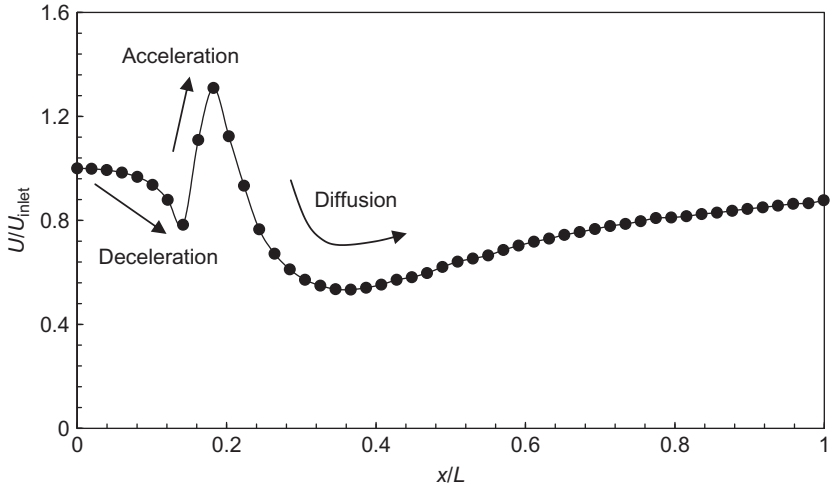


FIG. 2.19 *X–Y* plot of the normalized horizontal velocity along the length *L* midway between two cylinders for Case 2.

as it travels downstream towards the channel exit boundary (right). More discussions on the physical aspects of this simple flow will be further expounded in Chapter 3. For the more complex flow structure of Case 2, the normalized horizontal velocity profile along the entire length of the computational domain, as shown in Fig. 2.19, can be represented at the mid-height location to better illustrate the deceleration and acceleration characteristics of the flow behaviour as the fluid passes over the two cylinders. Further downstream, the fluid flow subsequently diffuses and recovers partially towards the free-stream condition near the exit boundary (right). The observed physical aspects of this particular flow will be further explored in Chapter 3.

2.4.2 Vector Plots

A vector plot provides the means whereby a vector quantity is displayed at discrete points (usually velocity) with arrow whose orientation indicates direction and whose size indicates magnitude. It generally presents a perspective view of the flow field in two dimensions. In a three-dimensional flow field, different slices of two-dimensional planes containing the vector quantities can be generated in different orientations to better scrutinize the global flow phenomena. If the mesh densities are considerably high, the CFD user can either interpolate or reduce the numbers of output locations to prevent the clustering of these arrows 'obliterating' the graphical plot.

Fig. 2.20 illustrates a typical velocity vector plot representing the fluid flowing along the parallel-plate channel. This plot gives an alternative view of the developing flow previously envisaged in Fig. 2.17. The different colours

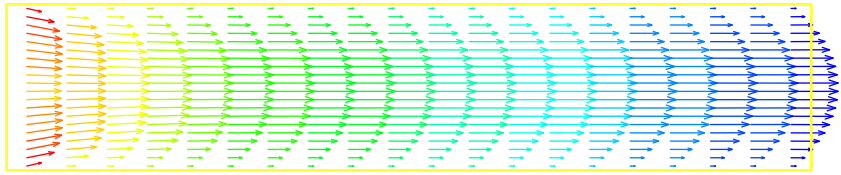


FIG. 2.20 Velocity vectors showing the flow development along the parallel-plate channel for Case 1.

represented in the vector plot depict the composite association of the velocity vectors with another dependent transport variable. For this particular flow case, we have arbitrarily chosen the distribution of dynamic pressure within the flow domain that impels the fluid flow. The range of colours displayed in the plot indicates the distribution between high (red) and low (blue) pressures that are effective inside the fluid flow process. Nevertheless, the CFD user can also freely select other transport variables that better emphasize significant physical aspects of the flow phenomena. For example, where heat transfer may be important, the velocity vectors can be coupled with the temperature distribution to illustrate the transport of hot fluid within the flow domain.

For the complex wake-developing flow of Case 2, the velocity vectors, as presented in Fig. 2.21, emphasize the presence of localized recirculation vortices as the fluid passes over and separates behind the proximity of the two cylinders. At the mid-height location, the varying sizes of the velocity vectors illustrating the approaching flow at upstream, transitional flow in the vicinity of the two cylinders, and departing flow at downstream clearly demonstrate

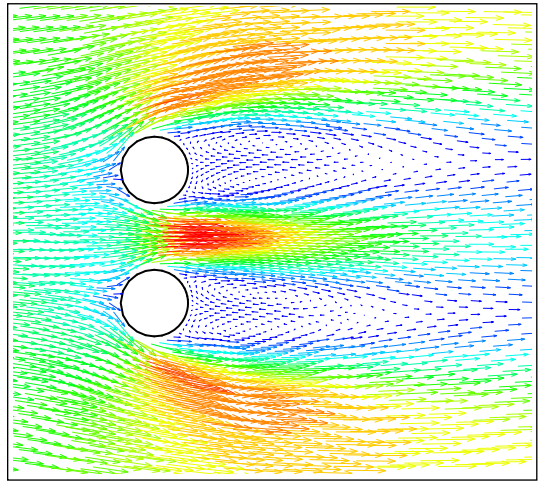


FIG. 2.21 Velocity vectors accentuating the localized wake recirculation zones behind the two cylinders for Case 2.

the three distinct flow characteristics of deceleration, acceleration, and diffusion observed in Fig. 2.19. Here again like in Case 1, the array of the colour spectrum that is displayed here illustrates the spatial distribution of the dynamic pressure.

2.4.3 Contour Plots

Contour plotting presents another useful and effective graphical technique that is frequently utilized in viewing CFD results. It is not surprising to imagine the proliferation of contour plots ever since the advent of the computer. In CFD, contour plots are one of the most commonly found graphical representations of data. A contour line (also known as *isoline*) can be described as a line indicative of some property that is constant in space. The equivalent representation in three dimensions is an *isosurface*. In contrast to *X–Y* plots, contour plots like vector plots provide a global description of the fluid flow encapsulated in one view. Generally, contours are plotted such that the difference between the numerical value of the dependent transport variable from one contour line to an adjacent contour line is held constant. The use of contour plots is usually not targeted for precision evaluation of the numerical values between contour lines. Although some mental and/or numerical interpolation can be performed between the contour lines in space, it is to say the very least an imprecise process. The actual numerical values represented by the *isolines* of these plots are sometimes less important than their overall disposition. In practice, the contours are usually linearly scaled. However, to better capture the hidden details in some small regions within the flow field, the reader may be required to intrepidly employ other type of scaling choices to reveal these isolated flow behaviours. For the contour plots where the intervals are the same, then, clustering of these lines indicates rapid changes in the flow quantities. Such plots are particularly useful especially in locating propagating shocks and discontinuities.

Figs 2.22 and 2.23 are examples of *flooded* contour plots for Case 1. Here, a constant flow-field property of any transport variable is denoted by the constant

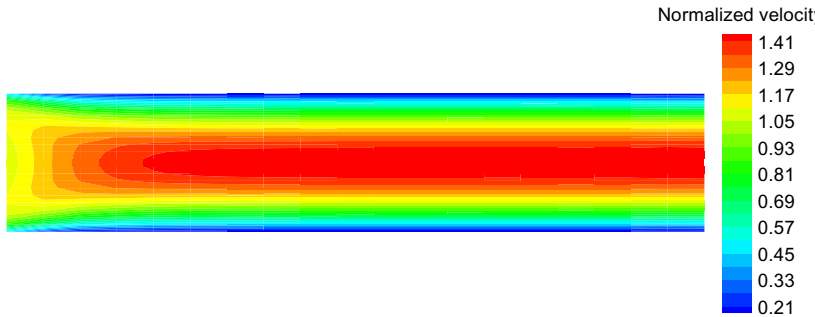


FIG. 2.22 Flooded contours on a rainbow-scale colour map for the distribution of Case 1 normalized velocity.

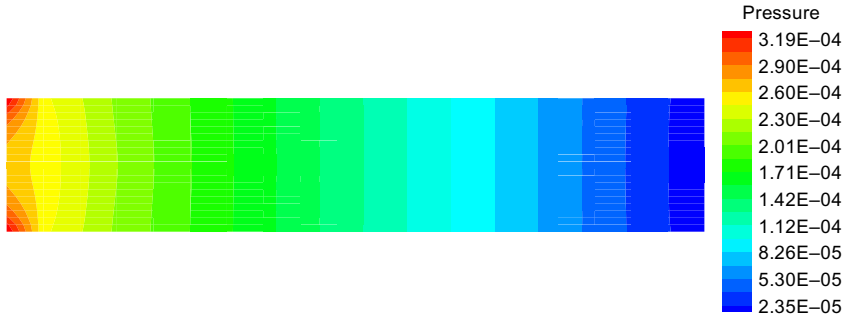


FIG. 2.23 Flooded contours on a rainbow-scale colour map for the distribution of Case 1 dynamic pressure.

intensity of the colour shading. In these two plots, the so-called 'rainbow-scale' colour map is employed to illustrate the distributions of the dimensionless resultant velocity normalized with respect to the inlet velocity and the dynamic pressure within the flow domain. The changing flooded contours near the entrance (left boundary) in Fig. 2.22 further confirm the development of the fluid flow as previously observed by the successive velocity profiles in the X–Y plot in Fig. 2.18 and velocity vector plot in Fig. 2.20. In contrast, no appreciable change of the velocity is observed near the exit (right boundary). The successive reduction of the pressure as indicated by the contour plot in Fig. 2.23 demonstrates the pressure gradient driving the fluid flow from the source imposed at the left boundary towards the sink located at the right boundary of the parallel-plate channel. At this point, we would like to draw the reader's attention of the colour map represented by the pressure contour plot that is associated with the array of colours represented by the velocity vectors in Fig. 2.20.

Figs 2.24 and 2.25 further exemplify another type of contour plots for the flow-field situation characterizing the flow-field situation of Case 2. The former illustrates the line contour representation of the pressure coefficient, whilst the latter demonstrates the dynamic pressure distribution by a 'grey-scaled' colour map flooded contour for the complex flow around the two cylinders. In both figures, contours that are tightly clustered around the two cylinders clearly indicate the presence of vigorous flow activity as the fluid passes over the top and bottom cylinders. The manifestation of positive and negative pressure coefficients accompanied by the high and low dynamic pressures in the vicinity of the two cylindrical surfaces causes the flow stream velocities to change significantly across the curved surfaces. If the pressure *decreases* in the downstream direction, then the boundary layer thickness reduces; this case is termed as a *favourable pressure gradient*. If, however, the pressure *increases* in the downstream direction, then the boundary layer thickens rapidly; this case is termed as an *adverse pressure gradient*. This adverse pressure gradient together with the action of the shear forces acted at a sufficient length cause the boundary layer to

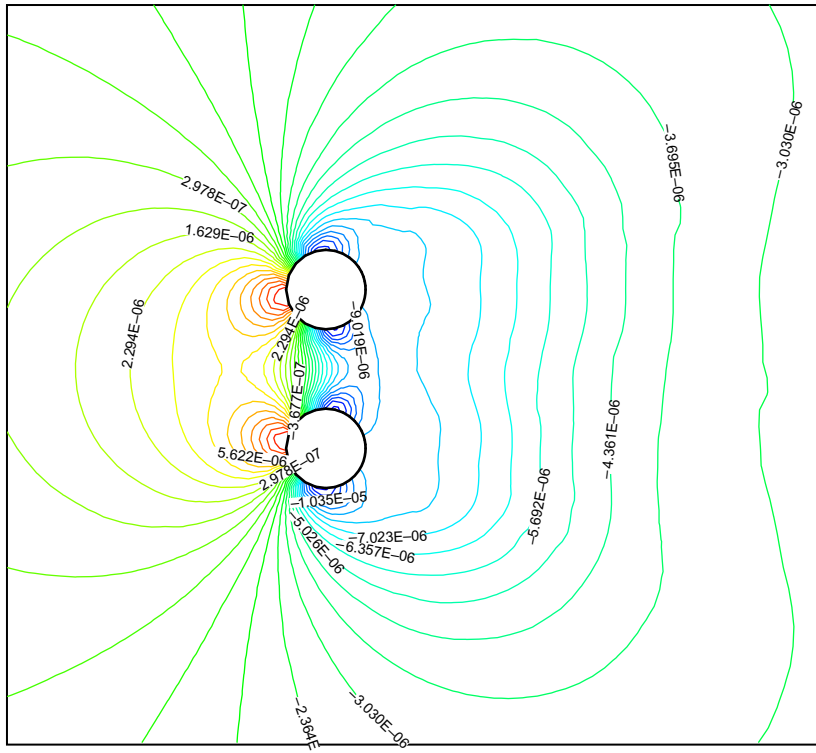


FIG. 2.24 Line contours on a rainbow-scale colour map for the distribution of Case 2 pressure coefficient.

come to rest. The flow separates from the surface leading to the formation of reversed flow eddies as represented by the apparent recirculation vortices (wakes) seen in the velocity vector plot of Fig. 2.21. More physical explanations of these flow behaviours will be further discussed in Chapter 3.

2.4.4 Other Plots

The application of *streamlines* in the preprocessing CFD stage, as in all aspects of fluid dynamics, is another exceptional tool for examining the nature of a flow either in two or three dimensions. By definition, *streamlines* are parallel to the mean velocity vector where they trace the flow pattern using *massless* particles. For an example, they can generally be obtained by integrating the spatial three velocity components expressed in a three-dimensional Cartesian frame: $dx/dt = u$, $dy/dt = v$, and $dz/dt = w$. For edification purpose, the reader may well benefit at this point of time to be accustomed to other existing terminologies synonymous to *streamlines* that are widely used in many graphical software

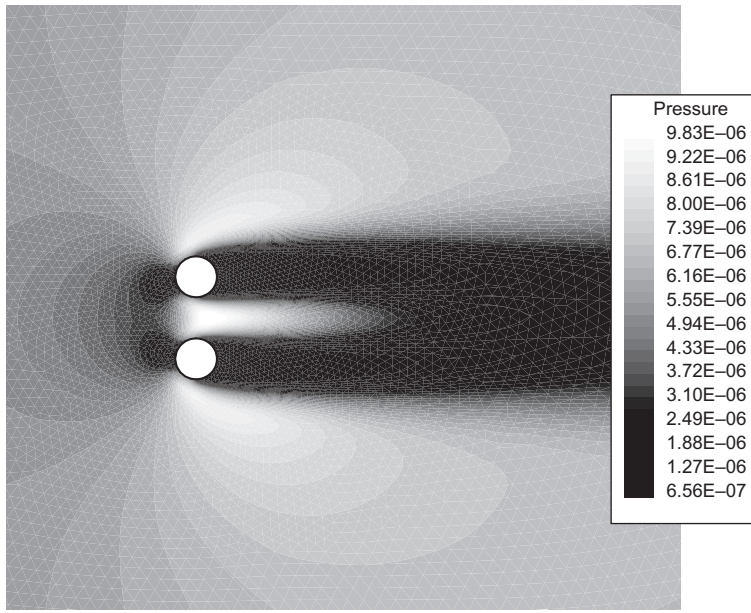


FIG. 2.25 Flooded contours on a grey-scale colour map for the distribution of Case 2 dynamic pressure.

packages. They are *streamtraces*, *streaklines*, or *pathlines*. In more complex flow problems such as multiphase flows that involve the transport of solid particles, the *particle tracks* associated with the discrete particles of certain diameter and mass being injected inside the parent fluid fall in this same category. Here, important information on the particle residence time, particle velocity magnitude, and other properties can be duly extracted. An example of a streamline plot illustrated in Fig. 2.26 defines the basic flow topology of localized recirculation zones behind the two cylinders as previously identified from the velocity vector plot in Fig. 2.26. This tool can often reveal important features that could be obscured in some isolated flow regimes, which is clearly demonstrated by a more definitive representation of the observed wake-developing vortices through the streamline plot. Like in the velocity vector plot, the colour spectrum corresponds to the spatial distribution of the dynamic pressure.

2.4.5 Data Report and Output

It is generally impractical to view the *raw data* of a CFD simulation especially on a mesh that may entail thousands or millions of grid points except possibly on a reasonably small 'mapped' grid. Other alphanumeric reporting approaches need however to be adopted of which such reports may be helpful to qualitatively check the attained numerical solution and/or extract the quantitative

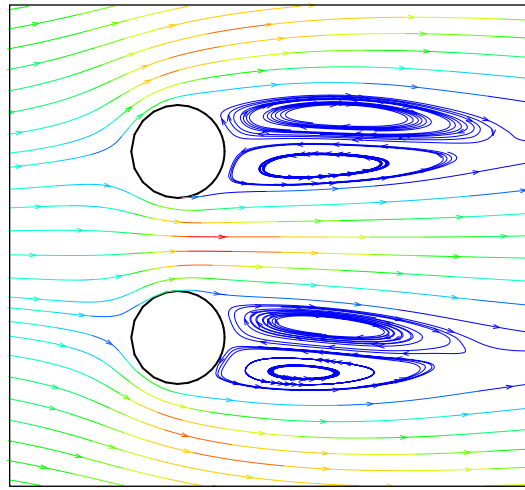


FIG. 2.26 Streamline plot emphasizing the definitive localized wake recirculation zones behind the two cylinders for Case 2.

results for post analysis purposes. Important variables such as surface fluxes, forces, and integrals can be evaluated at each respective boundary encompassing the computational domain. Some relevant data of significant interest are the evaluation of the mass flux in/out of each boundary that provides a clear indication of whether mass is conserved within the flow domain and the determination of the components of forces/moments on a surface such as wall shear stresses that may reveal important features connected with the flow physics of separation/reattachment/impingement. In some fluid mechanics problems, the transient/unsteady nature of a flow may be important. Data of a number of pertinent transport variables can be tracked and dumped into format/unformatted files to adequately describe the time-development response of the fluid flow process.

2.4.6 Animation

CFD data lend itself very neatly to the animation category—*moving pictures* of the data produced through the CFD simulation. Animation, as with other graphical display tool, represents not only a technical record of quantitative results; it is an artistic work of art. Some examples that animation has assisted in enhancing the physical representation of the fluid flow processes are the movement of particles with the fluid in multiphase flows, moving geometries such as mixing tanks, and shock propagation in high-speed flows. Nowadays, a collection of short-length animated videos or movies bristling with multiple frames of brightly colourful representations of CFD simulations can be found in many internet websites. It is undoubtedly an effective visualization tool for education

and marketing purposes. The ever-increasing availability of these *moving pictures* is indeed a tribute to the tireless efforts of computer graphical developers for *bringing the fluid flow to life*. Example of animated CFD results of a developing free-standing fire within a flickering period can be found in Chapter 8; the reader may well choose to advance to Chapter 8 to view those results that illustrate the puffing behaviour and other physical aspects of the fire dynamics in better appreciating the pivotal role of animation in CFD.

2.5 SUMMARY

This chapter has been purposefully written to expose potential or novice users to a powerful tool or technique for tackling problems associated with fluid flows. We have intended to capture the quintessence of how the CFD discipline has evolved; the prevalence of many commercial, shareware, and in-house computer codes is unquestionably a true testimonial of the dynamically evolving discipline. The widespread availability of these codes has certainly provided a favourable environment for students or new users learning CFD. Our intention throughout this chapter has been to provide proper guidance and possible supplementary knowledge emphasizing the many practical aspects within the framework of CFD analysis.

Although reference has been made to a number of commercial codes, this chapter is not intended to replace the user manuals of the CFD codes. The descriptions and explanations of many basic practical steps that may be akin to extracting the necessary parts or sections of a user manual are predominantly geared to assist the reader to achieve the goal of attaining the eventual computational solution. At the completion of this chapter, we strongly encourage the reader to begin applying any available CFD codes even without any *prior* knowledge of the fundamentals in order that he/she familiarizes with the many facets of CFD.

A complete CFD analysis consists of *preprocessor*, *solver*, and *postprocessor*. It simply encompasses the procedures of appropriately setting up the flow problem, solving and monitoring the solution, and analyzing the CFD results at the end of the simulation. Nevertheless, in the midst of these rather mechanically driven 'black box' operations, there are many underlying fundamental principals beneath each of these three elements. The reader at this moment may wish to carefully review the many basic practical steps that have been carried out in handling Case 1 and Case 2 flow problems within this chapter. Whilst performing the review, a list of questions presented below may assist the reader to contemplate and perhaps be more aware of the numerous theoretical and numerical issues that are profoundly embedded inside the CFD analysis, which are the following:

- What are the physical flow processes of the CFD problem? (Chapter 3)
- How is the flow physics described in mathematical equations? (Chapter 3)

- What are the equations governing the fluid flow and heat transfer? (Chapter 3)
- Why are boundary conditions important and how are they applied? (Chapter 3)
- What are the physical meanings of the boundary conditions? (Chapter 3)
- Why does a flow domain require to be subdivided into many smaller non-overlapping subdomains or a computational mesh/grid? (Chapter 4)
- What types of meshes that are commonly encountered in CFD? (Chapter 4)
- How are the mathematical equations solved? (Chapter 5)
- How are computational methods/techniques employed? (Chapter 5)
- What is the meaning of monitoring curves? (Chapter 6)
- How is the numerical procedure terminated? (Chapter 6)
- What are solution errors? (Chapter 6)
- How is a computational solution assessed to be correct, numerically accurate, and physically meaningful? (Chapter 6)
- When dealing with more complex flow problems, are there any other available methods/techniques or practical experiences or general guidelines that can assist in overcoming convergence difficulties? (Chapter 7)
- Are there any additional illustrative examples using CFD and how the solution can be better analyzed? (Chapter 8)
- What are the future advancements in CFD? (Chapter 9)

Various chapters indicated above at the end of each question are primarily intended to guide the reader where the theoretical and numerical considerations of CFD will be established in other chapters of this book. These chapters are aimed to comprehensively answer these questions whilst acknowledging the many practical aspects that have been covered in this chapter. Needless to say, applying CFD in practice goes hand in hand with the understanding of the basic equations governing the fluid flow process. These equations are based on conservation laws and theories. Discussions of their physical significance and implications as well as respective formulations are addressed in the next chapter.

REVIEW QUESTIONS

2.1 How are commercial codes allowing CFD analyses to be carried out with ease for the novice user?

2.2 What are the main elements involved in a complete CFD analysis?

2.3 Why is it important to correctly define the computational domain for the fluid flow problem? Give an example of this.

2.4 What is the consequence of using a very fine mesh (i.e. a very large number of cells) compared with using a coarse mesh (i.e. a small number of cells)?

2.5 What is the main difference between a structured and unstructured mesh and when are they applied to physical domains?

2.6 What types of boundary conditions can be imposed on the computational domain?
2.7 What type of boundary can be used for a computational boundary that represents an open physical boundary?
2.8 What advantages can a *symmetry* boundary condition and a *cyclic* boundary condition provide and when can they be applied?
2.9 What is the main purpose of a *CFD solver*?
2.10 What are the advantages of providing intelligent values for the initial solution?
2.11 What is an iteration process and how is it performed?
2.12 What does the convergence criterion control?
2.13 What is the main purpose of the *postprocessing* stage?
2.14 What are the advantages of using *X–Y* plots? Give examples of what CFD results *X–Y* plots can capture.
2.15 Why contour plots are best used to display the distribution of a variable?
2.16 What is the meaning of a streamline? What advantages do they have over other plot types?

Chapter 3

Governing Equations for CFD: Fundamentals

3.1 INTRODUCTION

CFD is fundamentally based on the *governing equations* of fluid dynamics. They represent mathematical statements of the *conservation laws of physics*. The purpose of this chapter is to introduce the derivation and discussion of these equations, where the following physical laws are adopted:

- Mass is conserved for the fluid.
- Newton's second law, the rate of change of momentum equals the sum of forces acting on the fluid.
- First law of thermodynamics, the rate of change of energy equals the sum of rate of heat addition and the rate of work done on the fluid.

It is important that anyone concerned with CFD possesses some understanding of the physical phenomena of fluid motion, as it is these phenomena that CFD analyzes and predicts. All of CFD is based on these equations; we must therefore begin our understanding at the most basic description of the fluid flow processes and the meaning and significance of each of the *terms* within them. After these equations are obtained, forms particularly suited for use in formulating CFD solutions will be delineated. The physical aspects of the boundary conditions and their appropriate mathematical statements will also be developed since the appropriate *numerical* form of the physical boundary condition is strongly dependent on the particular mathematical form of the governing equations and numerical algorithm used. At the completion of this chapter, it is the authors' endeavour to remove some of the underlying mysteries surrounding the prediction of a fluid in motion through computer-based tools and to replace with a solid understanding of the equations governing the fluid transport.

3.2 THE CONTINUITY EQUATION

3.2.1 Mass Conservation

One conservation law that is pertinent to fluid flow is *matter may neither be created nor destroyed*. Consider an arbitrary control volume V fixed in space and time in Fig. 3.1. The fluid moves through the fixed control volume, flowing

Computational Fluid Dynamics. https://doi.org/10.1016/B978-0-08-101127-0.00003-9
© 2018 Elsevier Ltd. All rights reserved.

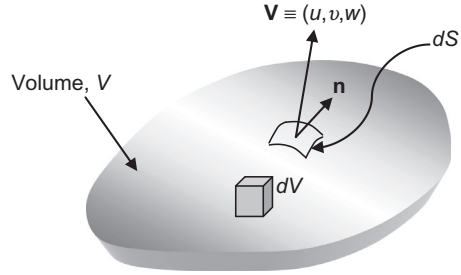


FIG. 3.1 Finite control volume fixed in space.

across the control surface. *Mass conservation* requires that the rate of change of mass within the control volume is equivalent to the mass flux crossing the surface S of volume V. In *integral form*,

$$\frac{d}{dt}\int_V \rho dV = -\int_S \rho \mathbf{V}\cdot\mathbf{n}dS \tag{3.1}$$

where $\mathbf{n}$ is the unit normal vector. We can apply Gauss's divergence theorem that equates the volume integral of a divergence of a vector into an area integral over the surface that defines the volume. This is stated as

$$\int_V div\rho\mathbf{V}dV = -\int_S \rho\mathbf{V}\cdot\mathbf{n}dS \tag{3.2}$$

Using the above theorem, the surface integral in Eq. (3.1) may be replaced by a volume integral, hence, the equation becomes

$$\int_V \left[\frac{\partial\rho}{\partial t} + \nabla\cdot(\rho\mathbf{V})\right]dV = 0 \tag{3.3}$$

where $\nabla\cdot(\rho\mathbf{V}) \equiv div\ \rho\mathbf{V}$. Since Eq. (3.3) is valid for any size of volume V, the implication is that

$$\frac{\partial\rho}{\partial t} + \nabla\cdot(\rho\mathbf{V}) = 0 \tag{3.4}$$

Eq. (3.4) is the *mass conservation*. In the Cartesian coordinate system, it can be expressed as

$$\frac{\partial\rho}{\partial t} + \frac{\partial(\rho u)}{\partial x} + \frac{\partial(\rho v)}{\partial y} + \frac{\partial(\rho w)}{\partial z} = 0 \tag{3.5}$$

where the fluid velocity $\mathbf{V}$ at any point in the flow field is described by the local velocity components u, v, and w, which are, in general, functions of location (x, y, z) and time (t).

Alternatively, consider the scenario of a fluid flowing between two stationary parallel plates as illustrated in Fig. 3.2. An infinitesimal small control volume $\Delta x\Delta y\Delta z$ fixed in space (enlarged to the right of the figure) is analyzed

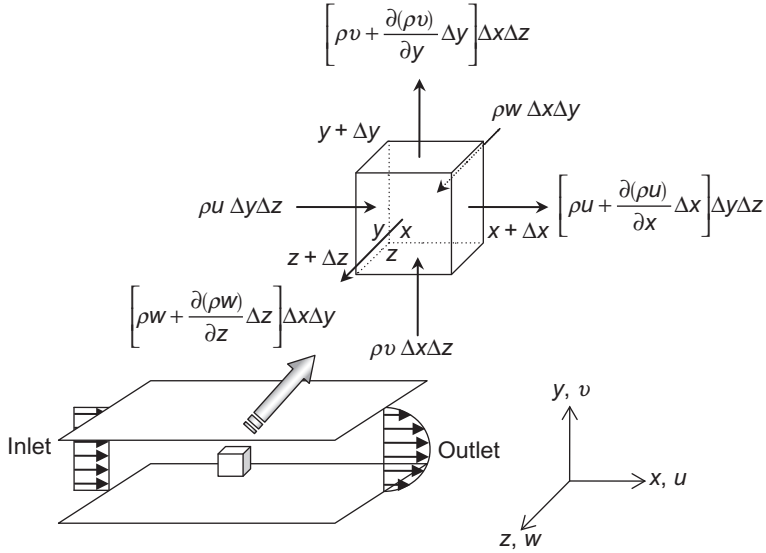


FIG. 3.2 The conservation of mass in an infinitesimal control volume of a fluid flow between two stationary parallel plates.

where the *mass conservation* statement applies to the (u, v, w) flow field. Transport due to such motion is often referred to as *advection*. The conservation law requires that, for unsteady flow, *the rate of increase of mass within the fluid element equals the net rate at which mass enters the control volume* (inflow–outflow), in other words,

$$\frac{dm}{dt} = \sum_{in} \dot{m} - \sum_{out} \dot{m} \tag{3.6}$$

The rate at which mass enters the control volume through the surface perpendicular to x may be expressed as $(\rho u)\,\Delta y\Delta z$, where ρ is the local density of the fluid and similarly through the surfaces perpendicular to y and z as $(\rho v)\,\Delta x\Delta z$ and $(\rho w)\,\Delta x\,\Delta y$, respectively. The rate at which the mass leaves the surface at $x+\Delta x$ may be expressed through Taylor expansion as

$$\left[(\rho u) + \frac{\partial(\rho u)}{\partial x}\Delta x\right]\Delta y\Delta z + O(\Delta x, \Delta V) \quad \text{where} \quad \Delta V = \Delta x\Delta y\Delta z \tag{3.7}$$

Similarly, the rate at which mass leaves the surfaces at $y+\Delta y$ and $z+\Delta z$ may also be expressed as

$$\begin{aligned} &\left[(\rho v) + \frac{\partial(\rho v)}{\partial y}\Delta y\right]\Delta x\Delta z + O(\Delta y, \Delta V) \quad \text{and} \\ &\left[(\rho w) + \frac{\partial(\rho w)}{\partial z}\Delta z\right]\Delta x\Delta y + O(\Delta z, \Delta V) \end{aligned} \tag{3.8}$$

Since the mass of the fluid element m is given by $\rho\ \Delta x\Delta y\Delta z$, Eq. (3.6) becomes

$$\frac{\partial(\rho\Delta x\Delta y\Delta z)}{\partial t} = (\rho u)\Delta y\Delta z + (\rho v)\Delta x\Delta z + (\rho w)\Delta x\Delta y - \left[(\rho u) + \frac{\partial(\rho u)}{\partial x}\Delta x\right]\Delta y\Delta z - \left[(\rho v) + \frac{\partial(\rho v)}{\partial y}\Delta y\right]\Delta x\Delta z - \left[(\rho w) + \frac{\partial(\rho w)}{\partial z}\Delta z\right]\Delta x\Delta y + \Delta V\ O(\Delta x, \Delta y, \Delta z) \tag{3.9}$$

In the limit, cancelling terms and dividing by the constant size $\Delta x\Delta y\Delta z$, we obtain

$$\frac{\partial\rho}{\partial t} + \frac{\partial(\rho u)}{\partial x} + \frac{\partial(\rho v)}{\partial y} + \frac{\partial(\rho w)}{\partial z} = 0 \tag{3.10}$$

Eq. (3.10) is exactly the same form as derived in Eq. (3.5). This equation is precisely the *partial differential form* of the *continuity equation*. We have shown that the integral form in Eq. (3.1) can, after some manipulation, yield the partial differential form. This specific differential form is usually called the *conservation form*. Both Eqs (3.1) and (3.10) are in conservation form; the manipulation performed does not alter the situation.

In Chapter 2, a two-dimensional CFD analysis is performed for a channel flow that is described by the fluid flow between two stationary parallel plates (see Fig. 3.2). This is made possible by the assumption that the dimension in the z coordinate direction is sufficiently large in order that the flow remains invariant along this coordinate direction. For a variable fluid property—varying density ρ—the continuity equation for a compressible flow in two dimensions is given by

$$\frac{\partial\rho}{\partial t} + \frac{\partial(\rho u)}{\partial x} + \frac{\partial(\rho v)}{\partial y} + \cancelto{0}{\frac{\partial(\rho w)}{\partial z}} = 0 \quad \text{or} \quad \boxed{\frac{\partial\rho}{\partial t} + \frac{\partial(\rho u)}{\partial x} + \frac{\partial(\rho v)}{\partial y} = 0} \tag{3.11}$$

Flow invariant in the z direction

If the fluid is taken to be incompressible, the density ρ is constant, that is the spatial and temporal variations in density are neglected relative to those velocity components of u, v, and w. We can obtain the continuity equation in two dimensions for an incompressible flow as

$$\cancelto{0}{\frac{\partial\rho}{\partial t}} + \rho\left(\frac{\partial u}{\partial x} + \frac{\partial v}{\partial y} + \cancelto{0}{\frac{\partial w}{\partial z}}\right) = 0 \quad \text{or} \quad \boxed{\frac{\partial u}{\partial x} + \frac{\partial v}{\partial y} = 0} \tag{3.12}$$

constant density

Flow invariant in the z direction

3.2.2 Physical Interpretation

Let us examine the physical meaning of the continuity equation of Eq. (3.12) as applied to an infinitesimal small control volume for the two-dimensional case of the fluid flow between two parallel plates to illustrate the fundamental physical principle. Two situations are considered.

Consider the first situation, if $\partial u/\partial x > 0$, then the velocity at the surface at $x+\Delta x$ is greater than the velocity at the surface x, that is $u(x+\Delta x) > u(x)$. Since more fluid is physically *leaving* the control volume than *entering* along the x direction, there should be more fluid *entering* than *leaving* along the y direction. Here, $\partial v/\partial y < 0$ and the velocity at the surface $y+\Delta y$ are less than the velocity at the surface y, that is $v(y+\Delta y) < v(y)$.

Alternatively, for the second situation, if $\partial u/\partial x < 0$, then the velocity at the surface at $x+\Delta x$ is less than the velocity at the surface x, that is $u(x+\Delta x) < u(x)$. Since more fluid is physically *entering* the control volume than *leaving* along the x direction, there should be more fluid *leaving* than *entering* along the y direction. Here, $\partial v/\partial y > 0$, and the velocity at the surface $y+\Delta y$ is greater than the velocity at the surface y, that is $v(y+\Delta y) > v(y)$.

Both situations satisfy the continuity equation: $\partial u/\partial x + \partial v/\partial y = 0$ (*mass conservation*).

Example 3.1

Consider a laminar boundary layer that can be approximated as having a velocity profile $u(x) = U_\infty y/\delta$ where $\delta = cx^{1/2}$, c is a constant, U_∞ is the free-stream velocity, and δ is the boundary layer thickness. With reference to the two-dimensional fluid flow over a flat plate as shown in Fig. 3.1.1 below, determine the velocity v (vertical component) inside the boundary layer.

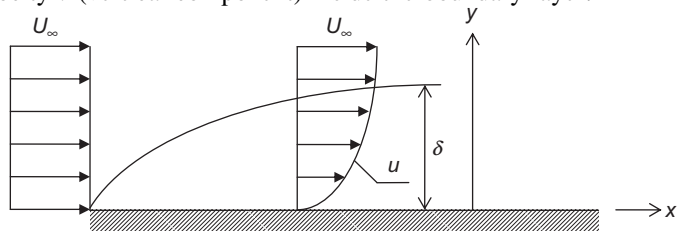


FIG. 3.1.1 Two-dimensional flow over a flat plate.

Solution: As the boundary layer grows downstream, the horizontal velocity u is gradually slowed down due to viscous effect and the no-slip condition at the surface of the flat plate. In order to satisfy the continuity equation, the vertical velocity v should be positive and acting to remove the fluid away from the boundary layer.

We begin the analysis by substituting the velocity profile $u(x)$ into Eq. (3.12), yielding

$$\frac{\partial}{\partial x}\left(\frac{U_\infty y}{cx^{1/2}}\right)+\frac{\partial v}{\partial y}=0\Rightarrow-\frac{U_\infty y}{2cx^{3/2}}=-\frac{\partial v}{\partial y}$$

Integrating the vertical velocity v with respect to y, the equation becomes

$$v=\frac{U_\infty y^2}{4cx^{3/2}}=\left(\frac{U_\infty y}{cx^{1/2}}\right)\left(\frac{y}{4x}\right)=\frac{uy}{4x}$$

Discussion: This physically means that the velocity ratio $v/u=y/4x$ increases away from the surface at a fixed x location, that is it decreases further downstream at a fixed y location. At the edge of the boundary layer, $y=\delta=cx^{1/2}$, the velocity ratio v/u equals to $c/4x^{1/2}$. If the constant c is assumed unity, the boundary layer thickness δ and the velocity ratio v/u as a function of the horizontal distance x from the leading edge of the flat plate can be described, and they are illustrated in Figs 3.1.2 and 3.1.3. The latter figure further illustrates the decrease of the velocity ratio v/u further downstream of the fluid flow over the flat plate. At some downstream distance x, the change in the horizontal u velocity is appreciably small. Here, $\partial u/\partial x\rightarrow 0$ that also leads to $\partial v/\partial y\rightarrow 0$ hence satisfying the continuity equation (3.12).

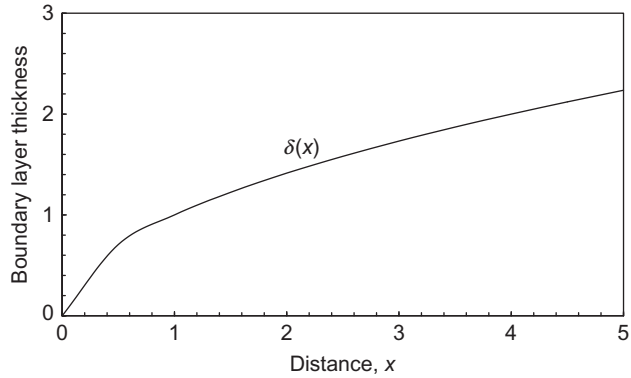


FIG. 3.1.2 Boundary layer thickness δ as a function of the horizontal distance x.

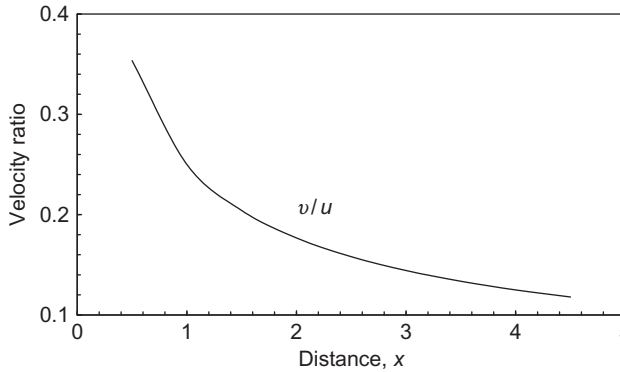


FIG. 3.1.3 Velocity ratio v/u as a function of the horizontal distance x.

Example 3.2

Consider the CFD case in Chapter 2 for the steady two-dimensional incompressible, laminar flow between two stationary parallel plates with the following dimensions: height $H = 0.1$ m and length $L = 0.5$ m. Using CFD, plot the velocity vector along the channel length. Discuss the physical meaning of the continuity equation by plotting the velocity components u and v close to the bottom wall surface along the channel length with the working fluid taken as air and a uniformly distributed velocity profile of 0.01 m/s applied at the channel inlet (u_{in}).

Solution: The problem is described as follows:

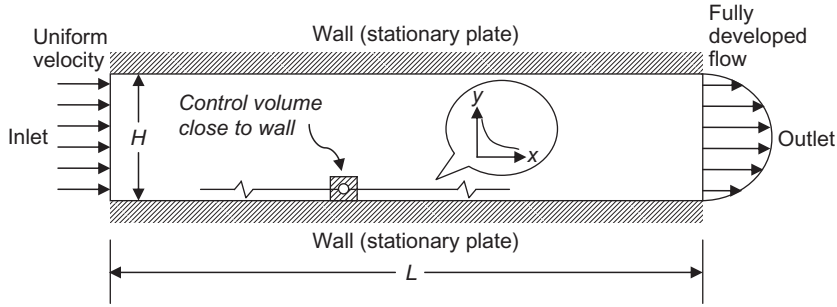


FIG. 3.2.1 Two-dimensional laminar flow between two stationary parallel plates.

From the CFD simulation, the flow field along the channel length is illustrated in Fig. 3.2.2. It is observed that the flow gradually changes from a uniform profile at the inlet surface to a parabolic profile as it travels downstream along the channel.

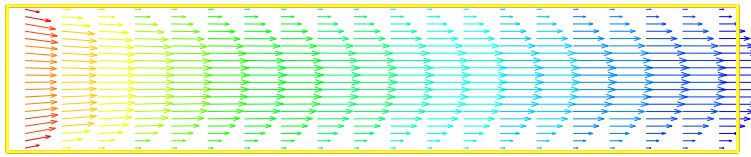


FIG. 3.2.2 Velocity profile distribution along the channel length.

The resultant velocity profiles of u and v close to the bottom wall surface along the channel length are given in Figs 3.2.3 and 3.2.4.

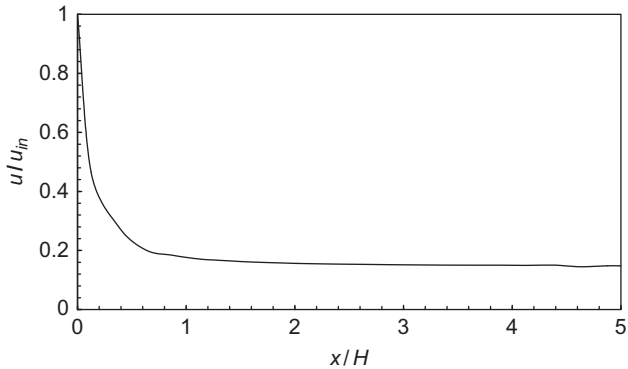


FIG. 3.2.3 Horizontal velocity u profile along the channel length.

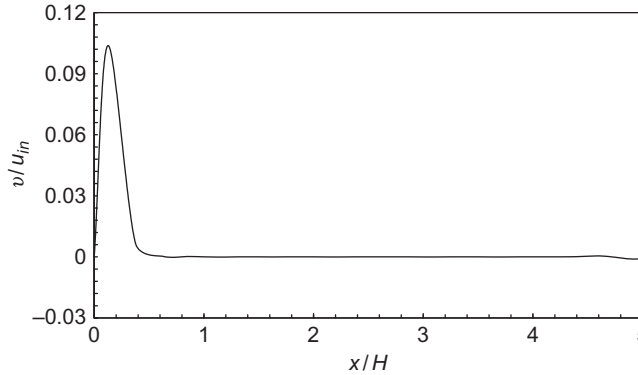


FIG. 3.2.4 Vertical velocity v profile along the channel length.

Discussion: It is observed that within the *hydrodynamic entrance region*, that is $x < 3H$, the horizontal velocity u decreases along the channel length. This means that $\partial u/\partial x < 0$ close to the wall surface. The airflow is slowed along the x direction due to the no-slip boundary condition imposed near the wall as it flows over the wall surface. More fluid is therefore physically entering than leaving the flow domain along the x direction. At the same time, there should be more fluid leaving than entering along the y direction; the vertical velocity v increases, which implies that $\partial v/\partial y > 0$, in order to conserve the mass. On the other hand, when the flow is in the *fully developed region*, that is $x \geq 3H$, it is observed that the horizontal velocity u does not appreciably change along the x direction, that is $\partial u/\partial x = 0$. In accordance with the continuity equation, $\partial v/\partial y$ must also be zero within this flow region. This is clearly reflected by the constant vertical velocity v as shown in Fig. 3.2.3 in the *fully developed region*. The physical meanings of the *hydrodynamic entrance region* and *fully developed region* are further discussed in Example 3.5.

3.2.3 Comments

In most Fluid Mechanics textbooks, the principal of mass conservation is often explained by a fluid flowing in a pipe; see Fig. 3.3 below. The mass entering a pipe, denoted by the mass flow rate $\dot{m}_1$, is equivalent to the product of the density, inlet velocity, and cross-sectional area, that is $\rho u_1 A_1$. This mass must equal to the mass flow rate leaving the pipe, which is denoted by $\dot{m}_2$ given as $\rho u_2 A_2$. If we take, for instance, that the cross-sectional areas are the same for both the inlet and outlet surfaces of the pipe, that is $A_1 = A_2$, and based on the mass conservation, the outlet velocity u_2 must equal to the inlet velocity u_1. If the cross-sectional areas are different at both ends of the pipe, take for example, $A_1 = 2A_2$, then $u_2 = 2u_1$, which means that the flow is *accelerated*. On the other hand, if $A_1 = ½A_2$, then $u_2 = ½\, u_1$, which means that the flow is *decelerated*.

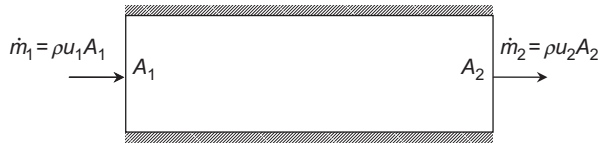


FIG. 3.3 A pipe flow scenario.

This principal of mass conservation as applied to the whole domain in one dimension is also applicable to any small control volume that is used in CFD to numerically solve the partial differential equations. In two dimensions, the mass flow may not be conserved in one direction, but overall, it will be conserved throughout the control volume by either removing or adding the mass in the other direction. It is important to persevere with the physical meaning of the mathematical equations in mind when studying and analyzing CFD results—a philosophy that we urge the reader to embrace. Indeed, this philosophy is extrapolated to all mathematical equations and operations encompassing any physical problems. We have explored to some great length the physical meaning of the continuity equation (3.12), and in the following sections, we will further explore the effects of various terms such as the *advection* and *diffusion* in the other mathematical equations. Whatever they are, we strongly encourage the reader at all times to continuously adopt the philosophy of understanding the physical meaning of the terms in the equations that are being dealt with.

3.3 THE MOMENTUM EQUATION

3.3.1 Force Balance

In deriving this physical law, we begin by considering the fluid element as described in Fig. 3.2 for mass conservation. *Newton's second law of motion* states that the sum of forces, which is acting on the fluid element, as illustrated in Fig. 3.4, equals to the product between its mass and acceleration of the element. There are essentially three scalar relations along the x, y, and z directions of the Cartesian frame of which the fundamental law can be invoked. We begin by considering the x component of Newton's second law,

$$\sum F_x = ma_x \tag{3.13}$$

where F_x and a_x are the force and acceleration along the x direction. The acceleration a_x at the right-hand side of Eq. (3.13) is simply the time rate change of u, which is given by the substantial derivative (see Appendix A for a more detailed description). Thus,

$$a_x = \frac{Du}{Dt} \tag{3.14}$$

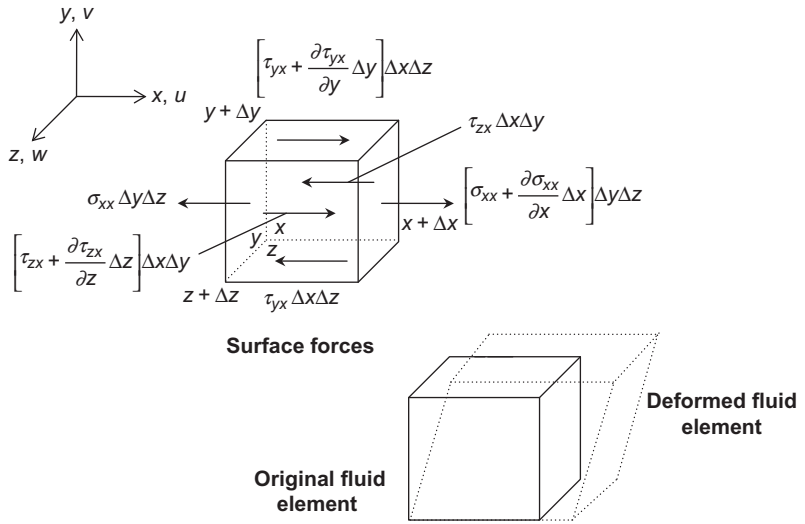


FIG. 3.4 Surface forces acting on the infinitesimal control volume for the velocity component u. Deformed fluid element due to the action of the surface forces.

Recalling that the mass of the fluid element m is $\rho\Delta x\Delta y\Delta z$, the rate of increase of x-momentum is

$$\rho\frac{Du}{Dt}\Delta x\Delta y\Delta z \tag{3.15}$$

On the left-hand side of Eq. (3.13), there are two sources of this force that the moving fluid element experiences. They are *body forces* and *surface forces*. The type of body forces that may influence the rate of change of the fluid momentum are gravity, centrifugal, Coriolis, and electromagnetic forces. These effects are usually incorporated by introducing them into the momentum equations as additional source terms to the contribution of the surface forces. The surface forces for the velocity component u as seen in Fig. 3.4 that deform the fluid element are due to the normal stress σ_{xx} and tangential stresses τ_{yx} and τ_{zx} acting on the surfaces of the fluid element. Combining the sum of these surface forces on the fluid element (see Appendix A for a more detailed derivation) and the time rate change of u from Eq. (3.15) into Eq. (3.13), the x-momentum equation becomes

$$\rho\frac{Du}{Dt} = \frac{\partial \sigma_{xx}}{\partial x} + \frac{\partial \tau_{yx}}{\partial y} + \frac{\partial \tau_{zx}}{\partial z} + \sum F_x^{body\ forces} \tag{3.16}$$

In a similar fashion, the y-momentum and z-momentum equations can be obtained as

$$\rho\frac{Dv}{Dt} = \frac{\partial \tau_{xy}}{\partial x} + \frac{\partial \sigma_{yy}}{\partial y} + \frac{\partial \tau_{zy}}{\partial z} + \sum F_y^{body\ forces} \tag{3.17}$$

and

$$\rho\frac{Dw}{Dt}=\frac{\partial\tau_{xz}}{\partial x}+\frac{\partial\tau_{yz}}{\partial y}+\frac{\partial\sigma_{zz}}{\partial z}+\sum F_z^{body\ forces} \tag{3.18}$$

The normal stresses σ_{xx}, σ_{yy}, and σ_{zz} in Eqs (3.16)–(3.18) are due to the combination of pressure p and normal viscous stress components τ_{xx}, τ_{yy}, and τ_{zz} acting perpendicular to the control volume. The remaining terms contain the tangential viscous stress components. In many fluid flows, a suitable model for the viscous stresses is introduced. They are usually a function of the local deformation rate (or strain rate) that is expressed in terms of the velocity gradients. The formulation of the appropriate stress–strain relationships for a Newtonian fluid is found in Appendix A.

Based on the concept of *substantial derivative* as illustrated in Appendix A, the *conservative* form of Eqs (3.16)–(3.18) can now be rewritten as

$$\frac{\partial(\rho u)}{\partial t}+\frac{\partial(\rho uu)}{\partial x}+\frac{\partial(\rho vu)}{\partial y}+\frac{\partial(\rho wu)}{\partial z}=\frac{\partial\sigma_{xx}}{\partial x}+\frac{\partial\tau_{yx}}{\partial y}+\frac{\partial\tau_{zx}}{\partial z}+\sum F_x^{body\ forces} \tag{3.19}$$

$$\frac{\partial(\rho v)}{\partial t}+\frac{\partial(\rho uv)}{\partial x}+\frac{\partial(\rho vv)}{\partial y}+\frac{\partial(\rho wv)}{\partial z}=\frac{\partial\tau_{xy}}{\partial x}+\frac{\partial\sigma_{yy}}{\partial y}+\frac{\partial\tau_{zy}}{\partial z}+\sum F_y^{body\ forces} \tag{3.20}$$

$$\frac{\partial(\rho w)}{\partial t}+\frac{\partial(\rho uw)}{\partial x}+\frac{\partial(\rho vw)}{\partial y}+\frac{\partial(\rho ww)}{\partial z}=\frac{\partial\tau_{xz}}{\partial x}+\frac{\partial\tau_{yz}}{\partial y}+\frac{\partial\sigma_{zz}}{\partial z}+\sum F_z^{body\ forces} \tag{3.21}$$

with the appropriate stress–strain relationships for a Newtonian fluid proposed in Appendix A.

For the two-dimensional case of the fluid flow between parallel plates (the flow being invariant along the z direction), the momentum equations with the inclusion of the stress–strain relationships for a compressible flow can be written as

$$\underbrace{\frac{\partial(\rho u)}{\partial t}}_{local\ accelration}+\underbrace{\frac{\partial(\rho uu)}{\partial x}+\frac{\partial(\rho vu)}{\partial y}}_{advection}=-\underbrace{\frac{\partial p}{\partial x}}_{pressure\ gradient}+\underbrace{\frac{\partial}{\partial x}\left(\mu\frac{\partial u}{\partial x}\right)+\frac{\partial}{\partial y}\left(\mu\frac{\partial u}{\partial x}\right)}_{diffusion}$$

$$+\underbrace{\frac{\partial}{\partial x}\left(\mu\frac{\partial u}{\partial x}\right)+\frac{\partial}{\partial y}\left(\mu\frac{\partial v}{\partial x}\right)+\frac{\partial}{\partial x}\left[\lambda\left(\frac{\partial u}{\partial x}+\frac{\partial v}{\partial y}\right)\right]}_{extra\ stress}+\underbrace{\sum F_x^{body\ forces}}_{body\ forces} \tag{3.22}$$

$$\underbrace{\frac{\partial(\rho v)}{\partial t}}_{\text{local acceleartion}} + \underbrace{\frac{\partial(\rho uv)}{\partial x} + \frac{\partial(\rho vv)}{\partial y}}_{\text{advection}} = - \underbrace{\frac{\partial p}{\partial y}}_{\text{pressure gradient}} + \underbrace{\frac{\partial}{\partial x}\left(\mu\frac{\partial v}{\partial x}\right) + \frac{\partial}{\partial y}\left(\mu\frac{\partial v}{\partial y}\right)}_{\text{diffusion}}$$

$$+ \underbrace{\frac{\partial}{\partial x}\left(\mu\frac{\partial u}{\partial y}\right) + \frac{\partial}{\partial y}\left(\mu\frac{\partial v}{\partial y}\right) + \frac{\partial}{\partial y}\left[\lambda\left(\frac{\partial u}{\partial x} + \frac{\partial v}{\partial y}\right)\right]}_{\text{extra stress}} + \underbrace{\sum F_y^{\text{body forces}}}_{\text{body forces}} \tag{3.23}$$

Alternatively, for the case for a *constant property* fluid flow, which implies that the density and viscosity are constants and in the absence of body forces particularly due to gravity (e.g. no density variation due to buoyancy), the momentum equations with the inclusion of the stress–strain relationships for an incompressible flow can be reduced to

$$\underbrace{\frac{Du}{Dt}}_{\text{acceleration}} = - \underbrace{\frac{1}{\rho}\frac{\partial p}{\partial x}}_{\text{pressure gradient}} + \underbrace{\nu\frac{\partial^2 u}{\partial x^2} + \nu\frac{\partial^2 u}{\partial y^2}}_{\text{diffusion}} + \frac{\partial}{\partial x}\left[\lambda\underbrace{\left(\underbrace{\frac{\partial u}{\partial x} + \frac{\partial v}{\partial y}}_{\text{continuity equation}} = 0\right)}\right]$$

$$+ \nu\frac{\partial}{\partial x}\left[\underbrace{\frac{\partial u}{\partial x} + \frac{\partial v}{\partial y}}_{\text{continuity equation}} = 0\right] + \underbrace{\frac{\partial \nu}{\partial x}\frac{\partial u}{\partial x} + \frac{\partial \nu}{\partial y}\frac{\partial v}{\partial x}}_{\text{constant property}} = 0 + \underbrace{\sum F_x^{\text{body forces}}}_{\text{body forces}} = 0$$

$$\underbrace{\frac{Dv}{Dt}}_{\text{acceleration}} = - \underbrace{\frac{1}{\rho}\frac{\partial p}{\partial y}}_{\text{pressure gradient}} + \underbrace{\nu\frac{\partial^2 v}{\partial x^2} + \nu\frac{\partial^2 v}{\partial y^2}}_{\text{diffusion}} + \frac{\partial}{\partial y}\left[\lambda\underbrace{\left(\underbrace{\frac{\partial u}{\partial x} + \frac{\partial v}{\partial y}}_{\text{continuity equation}} = 0\right)}\right]$$

$$+ \nu\frac{\partial}{\partial y}\left[\underbrace{\frac{\partial u}{\partial x} + \frac{\partial v}{\partial y}}_{\text{continuity equation}} = 0\right] + \underbrace{\frac{\partial \nu}{\partial x}\frac{\partial u}{\partial y} + \frac{\partial \nu}{\partial y}\frac{\partial v}{\partial y}}_{\text{constant property}} = 0 + \underbrace{\sum F_y^{\text{body forces}}}_{\text{body forces}} = 0$$

or

$$\underbrace{\frac{\partial u}{\partial t}}_{\text{local acceleration}} + \underbrace{u\frac{\partial u}{\partial x} + v\frac{\partial u}{\partial y}}_{\text{advection}} = - \underbrace{\frac{1}{\rho}\frac{\partial p}{\partial x}}_{\text{pressure gradient}} + \underbrace{\nu\frac{\partial^2 u}{\partial x^2} + \nu\frac{\partial^2 u}{\partial y^2}}_{\text{diffusion}} \tag{3.24}$$

$$\underbrace{\frac{\partial v}{\partial t}}_{\text{local acceleration}} + \underbrace{u\frac{\partial v}{\partial x} + v\frac{\partial v}{\partial y}}_{\text{advection}} = - \underbrace{\frac{1}{\rho}\frac{\partial p}{\partial y}}_{\text{pressure gradient}} + \underbrace{\nu\frac{\partial^2 v}{\partial x^2} + \nu\frac{\partial^2 v}{\partial y^2}}_{\text{diffusion}} \tag{3.25}$$

where ν is the kinematic viscosity ($\nu = \mu/\rho$). Eqs (3.22)–(3.25) derived from *Newton's second law* describe the conservation of momentum in the fluid flow and are also known as the Navier-Stokes equations. For ease of describing the physical significance of each of the terms in the momentum equations, Eqs (3.24) and (3.25) are examined in the next section to provide suitable explanations for the terms within.

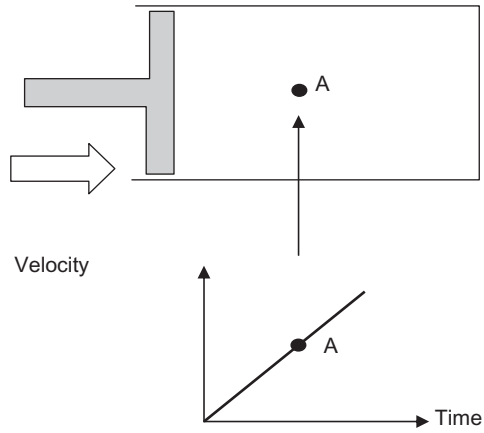


FIG. 3.5 The motion of fluid in a piston mechanism.

3.3.2 Physical Interpretation

Consider the motion of the fluid of a piston compressing the air within the enclosed cylinder. From the viewpoint of point A in Fig. 3.5, the fluid is locally accelerating due to the increase of the air velocity within the shrinking volume changing in time. In relation to the x-momentum equation (3.24), this is represented by the *acceleration* term $\partial u/\partial t$ for the horizontal velocity component u. Similarly, if the motion of fluid of the piston is inverted vertically, the local rate of increase of the air velocity is represented by the term $\partial v/\partial t$, which denotes the local *acceleration* of the vertical component v of Eq. (3.25).

The above example describes the motion of the fluid changing locally with time. We further explore the physical meaning of the fluid accelerating locally in space. Consider the motion of fluid through a venturi as indicated in Fig. 3.6. As the fluid travels between the locations B and C along the x direction and assuming that the velocity in itself is not fluctuating with time, the horizontal velocity component u has a local *acceleration* in space where the velocity is

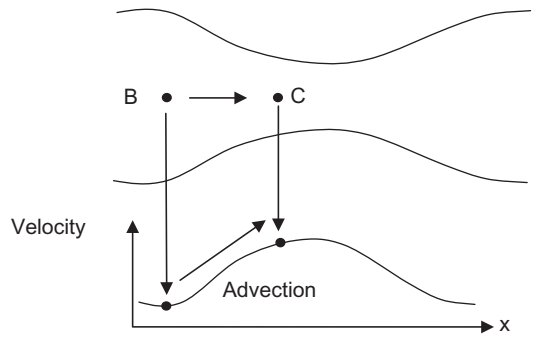


FIG. 3.6 The motion of fluid through a venturi.

accelerating between the incremental distance of locations B and C, that is the velocity gradient in the term $u\partial u/\partial x$ of Eq. (3.24) is increasing. Similarly, if the venturi is vertically oriented, then the vertical velocity component v has a local *acceleration* gradient in space where the velocity gradient in the term is $v\partial v/\partial y$ is increasing between the incremental distance of locations B and C. We usually refer to the fluid sweeping past point B and on its way to point C in the flow field as the *advection* term of the momentum equations.

We further investigate the physical interpretations of the pressure gradient and diffusion terms in the momentum equations (3.24) and (3.25) in the following examples below.

Example 3.3

Consider an incompressible, inviscid, laminar flow past a circular cylinder of diameter d in Fig. 3.3.1. The flow variation along the approaching stagnation streamline (A–B) can be expressed as

$$u(x) = U_\infty \left(1 - \frac{R^2}{x^2}\right)$$

With reference to Eqs (3.24) and (3.25), determine the total acceleration experienced by the fluid as it flows along the stagnation streamline. Also, determine the pressure distribution along the streamline by deriving Bernoulli's equation and the stagnation pressure at the stagnation point.

Solution: For an inviscid flow, the shear stresses are zero, that is $\tau = 0$ for all shear stresses. The diffusion terms are therefore zero. Along the stagnation streamline, the vertical velocity component v is zero. Also, since the continuity equation applies, and considering x-momentum equation (3.24), the following terms drop off from the equation:

$$\frac{\partial u}{\partial t} + u\frac{\partial u}{\partial x} + \cancel{v\frac{\partial u}{\partial y}}^{=0} = -\frac{1}{\rho}\frac{\partial p}{\partial x} + \cancel{\nu\frac{\partial^2 u}{\partial x^2}}^{=0} + \cancel{\nu\frac{\partial^2 u}{\partial y^2}}^{=0}$$

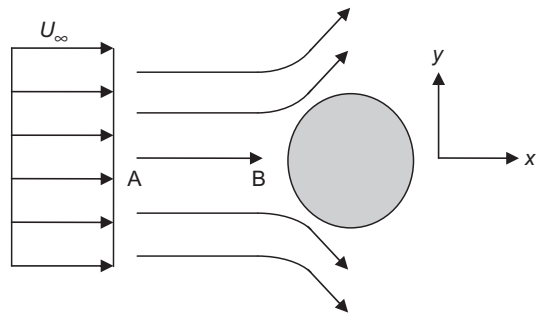


FIG. 3.3.1 Fluid motion over a circular cylinder.

The above equation reduces to

$$\frac{\partial u}{\partial t}+u\frac{\partial u}{\partial x}=-\frac{1}{\rho}\frac{\partial p}{\partial x}$$

The total acceleration of the fluid comprises of the sum of the local *acceleration* and *advection* terms and is driven by the pressure gradient in the x direction. Assuming that the upstream velocity $U_\infty = 1$ m/s and a radius $R = 1$ m, the total acceleration is given by

$$a_x=\frac{\partial u}{\partial t}+u\frac{\partial u}{\partial x}=\left(1-\frac{1}{x^2}\right)\left(\frac{2}{x^3}\right)$$

The equation derived represents another form of the momentum equation that is Euler's equation of the fluid flow. For a steady flow, Bernoulli's equation can be obtained by integrating the equation along a streamline. In other words,

$$u\frac{\partial u}{\partial x}=-\frac{1}{\rho}\frac{\partial p}{\partial x}\Rightarrow\frac{p(x)}{\rho}+\frac{u^2(x)}{2}=\frac{p_\infty}{\rho}+\frac{U_\infty^2}{2}$$

The above equation can be rearranged and taking the upstream pressure p_∞ to be atmospheric, it becomes

$$p(x)-p_{atm}=\frac{\rho}{2}\left(U_\infty^2-u^2(x)\right)=\frac{\rho}{2}\left[1-\left(1-\frac{1}{x^2}\right)^2\right]$$

Discussion: Along the streamline, the velocity profile $u(x)$ given above can be represented by the profile described in Fig. 3.3.2. The velocity drops very rapidly as the fluid approaches the cylinder. At the surface of the cylinder, the velocity is zero (stagnation point), and the surface pressure is a maximum.

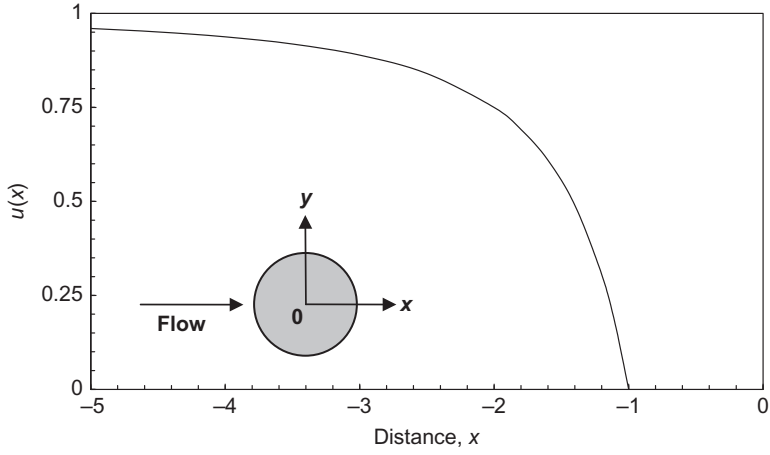


FIG. 3.3.2 Velocity profile $u(x)$ along the stagnation streamline.

The total acceleration profile depicted in Fig. 3.3.3 also shows the strong deceleration of the fluid as it approaches the cylinder. The maximum deceleration occurs at $x = -1.29$ m with a magnitude of -0.372 m/s^2.

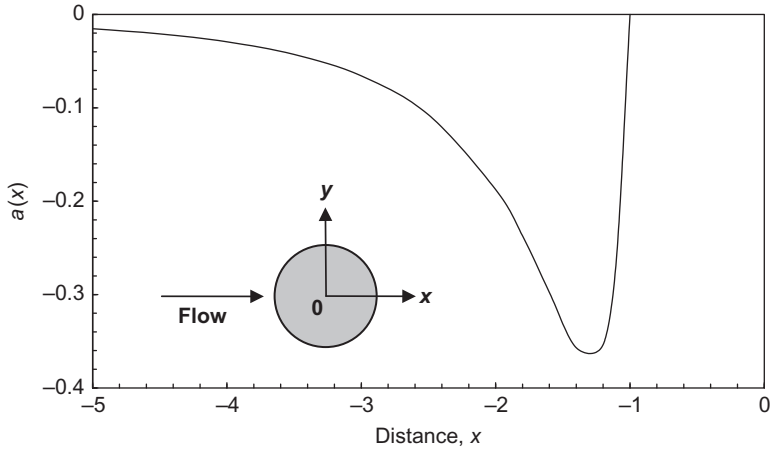


FIG. 3.3.3 Total acceleration profile $a(x)$ along the stagnation streamline.

The pressure difference $p(x) - p_{atm}$ derived above is illustrated in Fig. 3.3.4 demonstrates that the pressure increases as the fluid approaches the stagnation point. With the density ρ taken to be unity, it reaches the maximum value of 0.5, that is $p_{stag} - p_{atm} = (1/2)\rho U_\infty^2$ as $u(x) \to 0$ near the stagnation point.

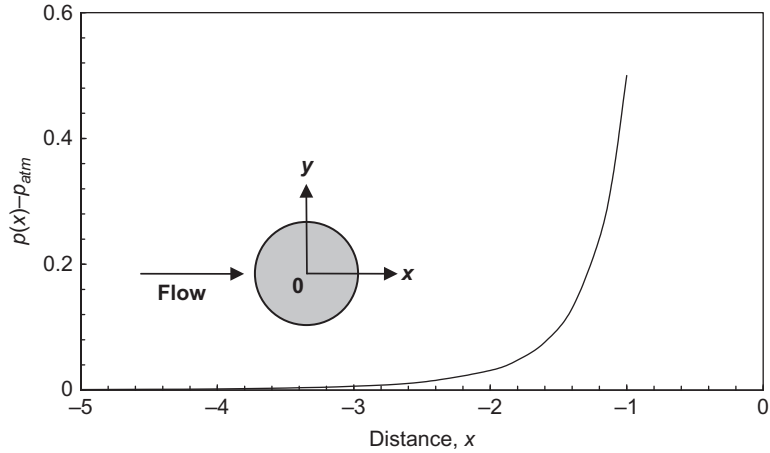


FIG. 3.3.4 Pressure difference $p(x) - p_{atm}$ along the stagnation streamline.

Example 3.4

Consider a steady incompressible laminar flow through the parallel-plate channel as investigated in Example 3.2. For a constant property fluid with a fully

developed flow, determine the velocity profile subject to the boundary condition where the vertical component v is zero everywhere.

Solution: The horizontal velocity component u depends only on x. The axial dependence on the horizontal velocity may be obtained by solving the appropriate form of the x-momentum equation (3.24). Since the vertical component v is zero everywhere, the continuity equation (3.13) reduces to

$$\frac{\partial u}{\partial x}+\underbrace{\frac{\partial v}{\partial y}}_{=0}=0 \quad \Rightarrow \quad \frac{\partial u}{\partial x}=0$$

This indicates that the velocity u is only a function of y. The x-momentum equation (3.24) becomes

$$\underbrace{\frac{\partial u}{\partial t}}_{=0}+u\underbrace{\frac{\partial u}{\partial x}}_{=0}+v\underbrace{\frac{\partial u}{\partial y}}_{=0}=-\frac{1}{\rho}\frac{\partial p}{\partial x}+\nu\underbrace{\frac{\partial^2 u}{\partial x^2}}_{=0}+\nu\frac{\partial^2 u}{\partial y^2}$$

Since $\nu=\mu/\rho$, the above equation reduces to

$$\frac{\partial^2 u}{\partial y^2}=\frac{1}{\mu}\frac{\partial p}{\partial x}$$

Hence, the momentum conservation requirement is just a simple balance between the shear and pressure forces in this case. Integrating once yields the velocity gradient $\partial u/\partial y$ with respect to y

$$\frac{\partial u}{\partial y}=\frac{1}{\mu}\frac{\partial p}{\partial x}y+C_1$$

Integrating again yields the horizontal velocity u with respect to y

$$u(y)=\frac{1}{2\mu}\left(\frac{\partial p}{\partial x}\right)y^2+C_1y+C_2$$

It is noted that the pressure gradient $\partial p/\partial x$ is treated as a constant as far as the integration is concerned since it is not a function of y (we can refer to the y-momentum equation later in this example).

The two boundary conditions required to determine the constants C_1 and C_2 are

$$u=0 \quad \text{at} \quad y=\frac{H}{2} \quad (\text{no slip})$$
$$\frac{\partial u}{\partial y}=0 \quad \text{at} \quad y=0 \quad (\text{symmetry})$$

From the symmetry condition, based on the velocity gradient $\partial u/\partial y$ with respect to y, the constant C_1 is zero.

$$0=\frac{1}{\mu}\left(\frac{\partial p}{\partial x}\right)\cdot 0+C_1 \Rightarrow C_1=0$$

The constant C_2 can be determined by applying the no-slip condition above into velocity profile $u(y)$ equation. Therefore,

$$0 = \frac{1}{2\mu}\left(\frac{\partial p}{\partial x}\right)\left(\frac{H}{2}\right)^2 + C_2 \Rightarrow C_2 = -\frac{1}{2\mu}\left(\frac{\partial p}{\partial x}\right)\left(\frac{H}{2}\right)^2$$

The velocity profile $u(y)$ becomes

$$u(y) = \frac{1}{2\mu}\left(\frac{\partial p}{\partial x}\right)y^2 - \frac{1}{2\mu}\left(\frac{\partial p}{\partial x}\right)\left(\frac{H}{2}\right)^2 \Rightarrow$$

$$u(y) = \frac{3}{2}\frac{H^2}{12\mu}\left(-\frac{\partial p}{\partial x}\right)\left[1 - \frac{y^2}{(H/2)^2}\right] \Rightarrow$$

$$u(y) = \frac{3}{2}U_m\left[1 - \frac{y^2}{(H/2)^2}\right] \tag{3.4A}$$

In this equation, the average velocity U_m is given as

$$U_m = \frac{H^2}{12\mu}\left(-\frac{\partial p}{\partial x}\right) \tag{3.4B}$$

The volume flow rate q passing between the plates can be obtained from the relationship

$$q = U_m H = -\frac{H^3}{12\mu}\left(\frac{\partial p}{\partial x}\right) \tag{3.4C}$$

The pressure gradient $\partial p/\partial x$ is negative, as the pressure decreases in the direction of the flow. If we let Δp represent the pressure drop between the inlet and outlet of the channel at a distance l apart, then

$$\frac{\Delta p}{l} = -\frac{\partial p}{\partial x}$$

and the volume flow rate can be expressed as

$$q = \frac{H^3 \Delta p}{12\mu L}$$

The flow is proportional to the pressure gradient, inversely proportional to the viscosity, and strongly dependent on the gap width ($\sim H^3$). In terms of the average velocity, it becomes

$$U_m = \frac{H^2}{12\mu}\frac{\Delta p}{l}$$

The above equations provide convenient relationships for relating the pressure drop along the channel between the parallel plates and the rate of flow or

average velocity. The maximum velocity U_{max} occurs midway ($y=0$) between the two plates so that

$$U_{max} = \frac{3}{2} U_m$$

Based on the boundary condition where the vertical component v is zero everywhere and if the body force due to gravity is considered in the y-momentum equation (3.19), the equation becomes

$$\cancel{\frac{\partial v}{\partial t}}^{=0} + u\cancel{\frac{\partial v}{\partial x}}^{=0} + v\cancel{\frac{\partial v}{\partial y}}^{=0} = -\frac{1}{\rho}\frac{\partial p}{\partial y} + \nu\cancel{\frac{\partial^2 v}{\partial x^2}}^{=0} + \nu\cancel{\frac{\partial^2 v}{\partial y^2}}^{=0} - g \quad \Rightarrow$$

Gravity

$$\frac{\partial p}{\partial y} = -\rho g$$

The gravitational force acts downwards, which results in the negative body force being represented in the above equation. This equation can be integrated to yield

$$p = -\rho g y + \{C_3 = f(x)\}$$

which shows that the pressure varies hydrostatically in the y direction. The constant C_3 in the above equation can be expressed by a function $f(x)$ where it can be related to the varying pressure gradient $\partial p/\partial x$ along the x direction and some reference pressure p_o.

$$f(x) = \left(\frac{\partial p}{\partial x}\right) x + p_o$$

where p_o is at a location $x = y = 0$, and the pressure variation throughout the fluid can be obtained from

$$p = -\rho g y + \left(\frac{\partial p}{\partial x}\right) x + p_o \tag{3.4D}$$

Discussion: Details of a steady, laminar flow between infinite parallel plates are completely predicted by the solution formulated above from the Navier-Stokes equations. For instance, if the pressure gradient, viscosity, and plate spacing are specified, then the velocity profile can be determined and those for the average velocity and flow rate—Eqs (3.4A), (3.4B), and (3.4C). Also, for a given fluid and reference pressure p_o, the pressure at any point can be predicted—Eq. (3.4D). The physical significance of the velocity distribution as seen in Eq. (3.4A) is that the profile is *parabolic*. The CFD simulation of Example 3.2 also predicts this particular velocity profile. The *parabolic* profile has been confirmed by many experiments where one of such by Nakayama (1988) experimentally displayed a line of bubbles resembling a parabolic shape

occurring at the downstream end of a channel. This fully developed flow distribution is known as the *Hagen-Poiseuille flow*, after the first two investigators who reported this flow behaviour (Sutera and Skalak, 1993). This relatively simple example of an exact solution illustrates the detail information about the flow field that can be obtained. The resultant velocity profile above being *parabolic* has physical implications as it is a typical distribution experienced for laminar flows in parallel channels.

Example 3.5

Consider the two-dimensional CFD case of an incompressible laminar flow between two stationary parallel plates to illustrate the physical meaning of the momentum equations. Here, the dimensions of the channel flow are given as height $H = 0.1$ m and length $L = 1$ m. Using CFD, discuss the development of the velocity profiles between the inlet and the *hydrodynamic entry length* (L_E) with air (density $\rho = 1.2$ kg/m^3) as the working fluid, for the following conditions:

(a) A fixed inlet velocity $u_{in} = 0.01$ m/s and dynamic viscosities $\mu_1 = 4 \times 10^{-5}$ kg/m s and $\mu_2 = 10^{-5}$ kg/m s.
(b) A fixed dynamic viscosity $\mu = 4 \times 10^{-5}$ kg/m s and inlet velocities $u_{in1} = 0.01$ m/s and $u_{in2} = 0.04$ m/s.

Solution: The problem is described as follows:

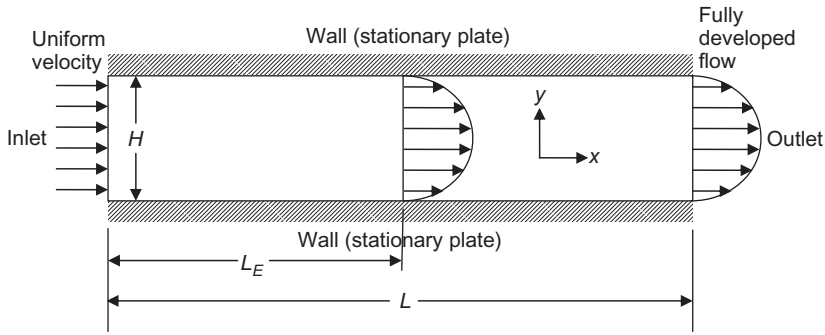


FIG. 3.5.1 Hydrodynamic entry length (L_E) location from the inlet surface in a two-dimensional laminar flow between two stationary parallel plates.

(a) By definition, the region from the inlet surface to the point at which the boundary layer merges at the centerline is called the *hydrodynamic entrance region*, and the length of this region is called the *hydrodynamic entry length*. This entrance region is also referred as the *hydrodynamically developing flow* since the velocity profile is still developing. Beyond this region, the velocity profile is fully developed and remains unchanged; it is called the *fully developed region*. The fluid flow at this instance is considered to be fully developed.

Based on the CFD simulation, the velocity profiles at different downstream locations x/H from the inlet surface for varying dynamic viscosities are given in

Figs 3.5.2 and 3.5.3. The former refers to the case where the flow has a higher dynamic viscosity than the latter.

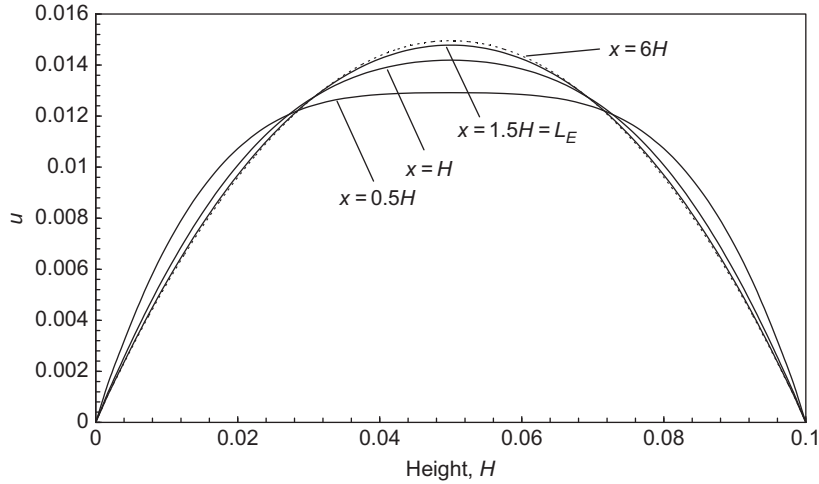


FIG. 3.5.2 Case A—velocity profiles at different locations of x/H for $u_{in} = 0.01$ m/s and dynamic viscosity $\mu_1 = 4 \times 10^{-5}$ kg/m s.

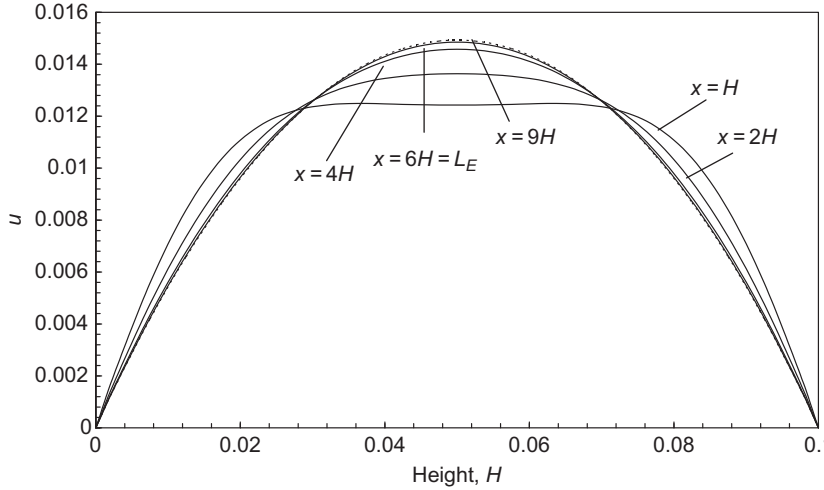


FIG. 3.5.3 Case B—velocity profiles at different locations of x/H for $u_{in} = 0.01$ m/s and dynamic viscosity $\mu_2 = 10^{-5}$ kg/m s.

(b) The velocity profiles at different downstream locations x/H from the inlet surface for varying inlet velocities are given in Figs 3.5.4 and 3.5.5. The former refers to the case where the flow has a lower velocity than the latter. The case presented in Fig. 3.5.4 is obviously exactly the same as the case presented above in Fig. 3.5.2. It is repeated here for comparison with the higher velocity case.

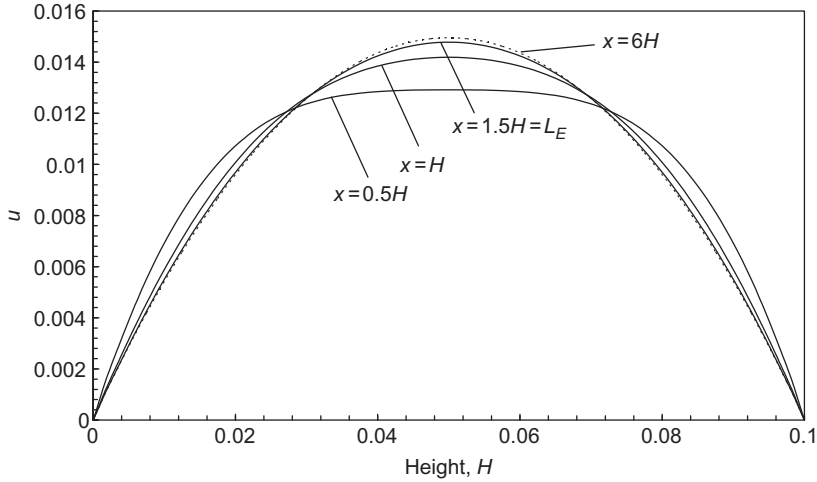


FIG. 3.5.4 Case C—velocity profiles at different locations of x/H for $u_{in1} = 0.01$ m/s and dynamic viscosity $\mu = 4 \times 10^{-5}$ kg/m s.

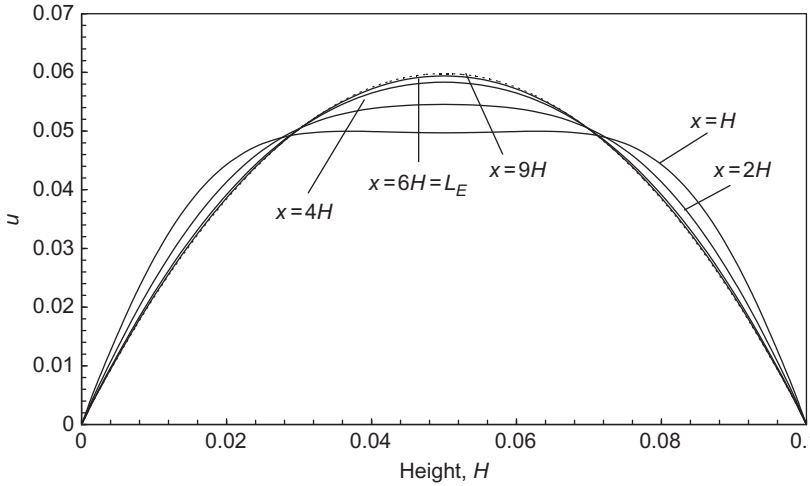


FIG. 3.5.5 Case D—velocity profiles at different locations of x/H for $u_{in2} = 0.04$ m/s and dynamic viscosity $\mu = 4 \times 10^{-5}$ kg/m s.

Discussion: We rewrite the steady two-dimensional x-momentum equation (3.24) as follows:

$$\underbrace{\rho u \frac{\partial u}{\partial x} + \rho v \frac{\partial u}{\partial y}}_{inertia} = \underbrace{-\frac{\partial p}{\partial x}}_{pressure} + \underbrace{\mu \left(\frac{\partial^2 u}{\partial x^2} + \frac{\partial^2 u}{\partial y^2} \right)}_{friction}$$

By comparing the results in Fig. 3.5.2 (Case A) with Fig. 3.5.3 (Case B), where the same *inertia* force is applied, it can be seen that the higher dynamic viscosity apparent in Case A produces a higher *friction* force that inhibits the fluid momentum. This leads to a quicker transition of the flow to a fully developed stage at a shorter distance. Case B has less frictional resistance thus allowing a slower development of the hydrodynamic boundary layer and reaches fully developed flow at a longer distance. The pressure gradients are the same for both of these cases. However, when the fluid has the same *friction* forces as demonstrated by the results in Fig. 3.5.4 (Case C) and Fig. 3.5.5 (Case D), the results for the higher velocity, that is higher *inertia* force, are surprisingly exactly the same as those of the case of higher *friction* force in Fig. 3.5.3. The higher *inertia* force in Case C yields the effect of reaching the same *hydrodynamic entry length* as imposing a higher *friction* due to the higher wall shear stress resisting the fluid flow as in Case A. All the cases investigated demonstrated the relative physical contributions of the *inertia* and *friction* forces competing with each other to conserve the momentum transfer.

3.3.3 Comments

The principal of conservation of momentum has been explored with investigations of the various contributions from the *advection* and *diffusion* terms in the momentum equations that affect the fluid flow. The reader should be aware of the importance of keeping the physical meaning of the mathematical equations in mind and the roles they play in CFD analyses. In CFD, the concept of *dynamic similarity* is frequently adopted. This involves normalizing the mathematical equations to yield the nondimensional governing equations. For instance, we have observed from the previous CFD Example 3.5 that through the various combinations of different inlet velocities and dynamic viscosities, the same fluid flow effect is obtained in reference to the development of the flow in yielding the same *hydrodynamic entrance region*. We can now even change the air density from $\rho_1 = 1.2$ kg/m^3 to $\rho_2 = 4.8$ kg/m^3 whilst fixing the inlet velocity and dynamic viscosity at 0.01 m/s and $\mu = 4 \times 10^{-5}$ kg/m s, respectively; the same results are obtained. This is because the increase of density contributes to the increase of the inertia force, which has the same effect as increasing the inlet velocity. There appears to be some homogeneity of the fluid flow behaviour that results in the combination of these physical variables. One important nondimensional parameter that describes the flow characteristics is the Reynolds number (Re), which is defined as the ratio of the *inertia force* over the *friction force*, that is

$$Re = \frac{Inertia\ Force}{Friction\ Force} = \frac{\rho u_{in} H}{\mu} \tag{3.26}$$

It is observed that Eq. (3.26) encapsulates the three variables, density, dynamic viscosity, and inlet velocity. Through different combinations of these

variables, the same *hydrodynamic entrance region* will be achieved if the resultant Reynolds number is the same. Another important use of the Reynolds number is to indicate whether the flow is laminar or turbulent. For a channel flow, the flow will remain laminar if the critical Reynolds number is below 1400. Further physical interpretation of this nondimensional parameter will be demonstrated in Example 3.9.

3.4 THE ENERGY EQUATION

3.4.1 Energy Conservation

The equation for the conservation of energy is derived from the consideration of the *first law of thermodynamics*:

$$\begin{aligned}\text{Time rate of change of energy} = \text{Net rate of heat added } &\left(\sum \dot{Q}\right) \\ + \text{Net rate of work done } &\left(\sum \dot{W}\right)\end{aligned} \tag{3.27}$$

As discussed in Appendix A, the time rate of change of any arbitrary variable property ϕ is defined as *the product between the density and the substantial derivative of* ϕ. In keeping with our derivation of the Navier-Stokes (the momentum equations), we will refer again to the elemental volume in the Cartesian frame as previously described in Fig. 3.2. The time rate of change of energy for the moving fluid element is just simply

$$\rho \frac{DE}{Dt} \Delta x \Delta y \Delta z \tag{3.28}$$

The two terms represented by $\Sigma \dot{Q}$ and $\Sigma \dot{W}$ describe the net rate of heat addition to the fluid within the control volume and the net rate of work done by surface forces on the fluid. We first consider the effects in the x direction as illustrated in Fig. 3.7. The rate of work done and heat added in the y and z directions automatically follows from the analysis of the x direction.

The rate of work done on the control volume in the x direction is equivalent to the product between the surface forces (caused by the normal viscous stress σ_{xx} and tangential viscous stresses τ_{yx} and τ_{zx}) with the velocity component u. The formulae for the net rate work done in this direction and for the other coordinate directions due to the contributions of the normal and tangential surface forces are detailed in Appendix A. When we combine all the contributions of the surface forces in the x, y, and z directions and substituting these expressions along with the time rate of change of energy E, from Eq. (3.28) into Eq. (3.27), the *nonconservative* form of equation for the conservation of energy is given as

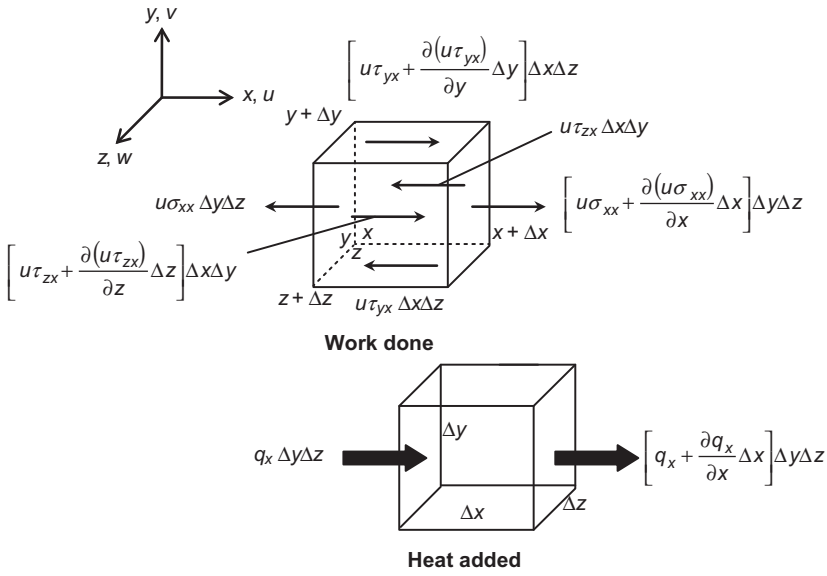


FIG. 3.7 Work done by surface forces on the fluid and heat added to the fluid within the infinitesimal control volume. Only the fluxes in the x direction are shown.

$$\rho\frac{DE}{Dt}=\frac{\partial(u\sigma_{xx})}{\partial x}+\frac{\partial(v\sigma_{yy})}{\partial y}+\frac{\partial(w\sigma_{zz})}{\partial z}+\frac{\partial(u\tau_{yx})}{\partial y}+\frac{\partial(u\tau_{zx})}{\partial z}+\frac{\partial(v\tau_{xy})}{\partial x}+\frac{\partial(v\tau_{zy})}{\partial z}$$
$$+\frac{\partial(w\tau_{xz})}{\partial x}+\frac{\partial(w\tau_{yz})}{\partial y}-\frac{\partial q_x}{\partial x}-\frac{\partial q_y}{\partial y}-\frac{\partial q_z}{\partial z} \tag{3.29}$$

The energy fluxes q_x, q_y, and q_z in Eq. (3.29) can be formulated by applying *Fourier's law of heat conduction* that relates the heat flux to the local temperature gradient:

$$q_x=-\lambda\frac{\partial T}{\partial x}\quad q_y=-\lambda\frac{\partial T}{\partial y}\quad q_z=-\lambda\frac{\partial T}{\partial z} \tag{3.30}$$

where λ is the thermal conductivity. By substituting Eq. (3.30) into Eq. (3.29) and applying the normal stresses described in Appendix A, Eq. (3.29) becomes

$$\rho\frac{DE}{Dt}=\frac{\partial}{\partial x}\left[\lambda\frac{\partial T}{\partial x}\right]+\frac{\partial}{\partial y}\left[\lambda\frac{\partial T}{\partial y}\right]+\frac{\partial}{\partial z}\left[\lambda\frac{\partial T}{\partial z}\right]-\frac{\partial(up)}{\partial x}-\frac{\partial(vp)}{\partial y}-\frac{\partial(wp)}{\partial z}+\Phi \tag{3.31}$$

The effects due to the viscous stresses in Eq. (3.31) are described by the dissipation function Φ that can be shown to be

$$\Phi=\frac{\partial(u\tau_{xx})}{\partial x}+\frac{\partial(u\tau_{yx})}{\partial y}+\frac{\partial(u\tau_{zx})}{\partial z}+\frac{\partial(v\tau_{xy})}{\partial x}+\frac{\partial(v\tau_{yy})}{\partial y}+\frac{\partial(v\tau_{zy})}{\partial z}$$
$$+\frac{\partial(w\tau_{xz})}{\partial x}+\frac{\partial(w\tau_{yz})}{\partial y}+\frac{\partial(w\tau_{zz})}{\partial z}$$

The dissipation function represents a source of energy due to deformation work done on the fluid. This work is extracted from the mechanical energy that causes fluid movement, which is converted into heat.

Based on the concept of *substantial derivative* as described in Appendix A, the *conservative* form of the energy equation can be rewritten as

$$\frac{\partial(\rho E)}{\partial t}+\frac{\partial(\rho uE)}{\partial x}+\frac{\partial(\rho vE)}{\partial y}+\frac{\partial(\rho wE)}{\partial z}=\frac{\partial}{\partial x}\left[\lambda\frac{\partial T}{\partial x}\right]+\frac{\partial}{\partial y}\left[\lambda\frac{\partial T}{\partial y}\right]+\frac{\partial}{\partial z}\left[\lambda\frac{\partial T}{\partial z}\right]$$
$$-\frac{\partial(up)}{\partial x}-\frac{\partial(vp)}{\partial y}-\frac{\partial(wp)}{\partial z}+\Phi \tag{3.32}$$

Thus far, we have not defined the specific energy E of a fluid. Often the energy of a fluid is defined as the sum of the *internal energy*, *kinetic energy*, and *gravitational potential energy*. We can regard the gravitational force as a body force and include the effects of potential energy changes as a source term. The energy equation for a *compressible flow* is often rearranged to give an equation for the *enthalpy*, which can be written in the form of

$$\frac{\partial(\rho h)}{\partial t}+\frac{\partial(\rho uh)}{\partial x}+\frac{\partial(\rho vh)}{\partial y}+\frac{\partial(\rho wh)}{\partial z}=\frac{\partial p}{\partial t}+\frac{\partial}{\partial x}\left[\lambda\frac{\partial T}{\partial x}\right]+\frac{\partial}{\partial y}\left[\lambda\frac{\partial T}{\partial y}\right]+\frac{\partial}{\partial z}\lambda\left[k\frac{\partial T}{\partial z}\right]+\Phi \tag{3.33}$$

More detail discussion regarding the relationship between the specific energy E and enthalpy h can be found in Appendix A and in the textbook of Çengel (2003).

For a two-dimensional *compressible flow*, the equation for the conservation of energy can be reduced to

$$\underbrace{\frac{\partial(\rho h)}{\partial t}}_{\text{local acceleration}}+\underbrace{\frac{\partial(\rho uh)}{\partial x}+\frac{\partial(\rho vh)}{\partial y}}_{\text{advection}}=\underbrace{\frac{\partial p}{\partial t}}_{\text{local pressure time derivative}}+\underbrace{\frac{\partial}{\partial x}\left[\lambda\frac{\partial T}{\partial x}\right]+\frac{\partial}{\partial y}\left[\lambda\frac{\partial T}{\partial y}\right]}_{\text{diffusion}}+\Phi \tag{3.34}$$

Let us also consider for the special case where the fluid is incompressible. For such flows in most practical fluid engineering problems, the local pressure time derivative $\partial p/\partial t$ and the dissipation function Φ can be neglected. Based on the definition of enthalpy, h can be reduced to C_pT where C_p is the specific heat and is assumed to be constant. With the temperature being invariant along the z direction and the thermal conductivity λ is constant, the equation for the conservation of energy in two dimensions for an *incompressible flow* can be expressed as

$$\underbrace{\rho C_p\frac{Dh}{Dt}}_{\text{acceleration}}=\underbrace{\lambda\frac{\partial^2 T}{\partial x^2}+\lambda\frac{\partial^2 T}{\partial y^2}}_{\text{diffusion}}$$

or

$$\underbrace{\frac{\partial T}{\partial t}}_{\text{local acceleration}} + \underbrace{u\frac{\partial T}{\partial x} + v\frac{\partial T}{\partial y}}_{\text{advection}} = \underbrace{\frac{\lambda}{\rho C_p}\frac{\partial^2 T}{\partial x^2} + \frac{\lambda}{\rho C_p}\frac{\partial^2 T}{\partial y^2}}_{\text{diffusion}} \tag{3.35}$$

3.4.2 Physical Interpretation

Physically, Eq. (3.35) defines the temperature of a differential fluid control volume as it travels past a point taking into consideration the local acceleration derivative (where the temperature in itself may be fluctuating with time at a given point) and also the advection derivative (where the temperature changes spatially from one point to another). To reinforce the physical meaning of these derivatives, imagine you are sitting on a high seat, close to the ceiling in a sauna room, where the buoyant heat flow causes the air to be hottest. You decide to move to a lower seat in the sauna and make your way down to the floor. As you descend, the air is a little cooler, and you experience a temperature decrease—this is analogous to the *advection* derivative in Eq. (3.35). Additionally, as you sit on the lower seat, the sauna door opens as someone enters and you feel a sudden rush of cold air. The temperature around you immediately drops for that moment—this is analogous to the local *acceleration* derivative in Eq. (3.35). The net temperature change you experience is therefore a combination of both the act of descending the highest seat to the floor and also the rush of cool air as the sauna door opens.

The remaining term in Eq. (3.35) represents the temperature flow due to heat conduction (the *diffusion* derivative), which the thermophysical property k is the thermal conductivity of the fluid. We examine the physical interaction of this term with the previous two derivatives. To further reinforce the physical meaning, imagine the problem concerning the fluid flowing between parallel plates in Fig. 3.2 of which the plates are now heated. If the surrounding fluid velocity is very low, the surrounding fluid temperature within the channel increases due to the heat flowing from the flat plate into the bulk fluid—this is analogous to the heat conduction through the heat *diffusion* derivative dominating over the local *acceleration* and *advection* derivatives of the fluid. However, if the surrounding fluid velocity is high, the heat of the fluid is carried away by the relatively cooler fluid. The high temperatures are only found near the hot surface of the flat plates—this is analogous to the local *acceleration* and *advection* derivatives dominating over the heat *diffusion* derivative.

Example 3.6

To illustrate the application of the energy equation (3.35), consider the steady heat conduction across an infinite long solid slab with a finite thickness as

illustrated in Fig. 3.6.1. Determine the analytical expressions based on the boundary conditions:

(a) $x=0$, $T=T_0$, and $x=L$, $T=T_L$
(b) $x=0$, $T=T_0$, and $x=L$, $\dot{q}_L=-k\frac{\partial T(L)}{\partial x}$.

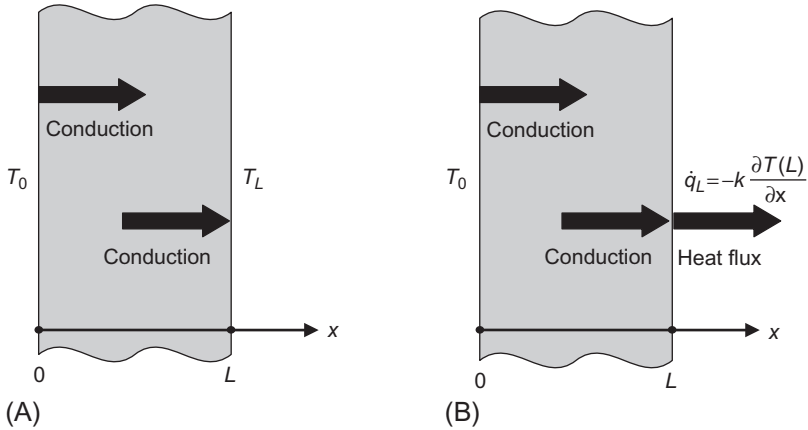


FIG. 3.6.1 Heat conduction across the solid slab subjected to various temperature boundary conditions.

Solution: Since the heat transfer is steady and it is a solid problem, the acceleration and advection terms in Eq. (3.34) vanish.

$$\cancel{\frac{\partial T}{\partial t}}^{=0}+u\cancel{\frac{\partial T}{\partial x}}^{=0}+v\cancel{\frac{\partial T}{\partial y}}^{=0}=\frac{\lambda}{\rho C_p}\frac{\partial^2 T}{\partial x^2}+\frac{\lambda}{\rho C_p}\frac{\partial^2 T}{\partial y^2}$$

The above equation reduces to

$$\frac{\partial^2 T}{\partial x^2}+\frac{\partial^2 T}{\partial y^2}=0$$

For an infinite long slab, we can restrict ourselves to a one-dimensional analysis; the equation can be further simplified to

$$\frac{\partial^2 T}{\partial x^2}+\cancel{\frac{\partial^2 T}{\partial y^2}}^{=0}=0 \quad \Rightarrow \quad \frac{\partial^2 T}{\partial x^2}=0$$

Integrating the differential equation once with respect to x yields

$$\frac{\partial T}{\partial x}=C_1$$

where C_1 is an arbitrary constant. Subsequent integration of the above equation yields

$$T(x) = C_1 x + C_2$$

which is the analytical expression of the differential equation. The general solution contains two unknown constants C_1 and C_2. We need two equations that can be determined through the boundary conditions imposed on the left and right surfaces of the solid slab.

Analysis: (a) For this case, the left-side boundary condition is applied to the general solution by replacing the x's by zero and $T(x)$ by T_0. In other words,

$$T_0 = C_1 \times 0 + C_2 \Rightarrow C_2 = T_0$$

The right-side boundary condition is applied by replacing the x's by L and $T(x)$ by T_L, which gives

$$T_L = C_1 L + C_2 \Rightarrow T_L = C_1 L + T_0 \Rightarrow C_1 = \frac{T_L - T_0}{L}$$

Substituting the C_1 and C_2 expressions into the general solution, we obtain

$$T(x) = \frac{T_L - T_0}{L} x + T_0$$

(b) For case b, the left-side boundary condition is the same as in part (a). Thus,

$$C_2 = T_0$$

On the right-side boundary condition, a heat flux $\dot{q}_L$ is specified rather than a specified temperature T_L. Noting that

$$\frac{\partial T}{\partial x} = C_1$$

the application of the boundary condition yields

$$-\lambda \frac{\partial T(L)}{\partial x} = \dot{q}_L \Rightarrow -\lambda C_1 = \dot{q}_L \Rightarrow C_1 = -\frac{\dot{q}_L}{\lambda}$$

Substituting, the above equations into the general solution, we obtain

$$T(x) = -\frac{\dot{q}_L}{\lambda} x + T_0$$

Discussion: The above equations are the analytical solutions for the temperature distribution across the finite thickness L in the solid slab. They satisfy not only the one-dimensional partial differential form of the energy equation but also the two specified boundary conditions. Both general solutions exhibit a linear distribution whose slopes are $T_L - T_0/L$ and $-\dot{q}_L/k$, respectively. During the integration process in establishing the general one-dimensional partial differential form of the energy equation, the thermal diffusivity $\alpha = \lambda/\rho C_p$

disappears. This may imply to the reader that the heat conduction across the slab is not influenced by any thermophysical properties such as the thermal conductivity k, density ρ, and specific heat C_p of the solid material. Nevertheless, in part (b), the final expression of the general solution demonstrates the influence of the material thermal conductivity that is obtained from the physical boundary condition based on Fourier's law. A better understanding of the types of physical boundary conditions for the temperature will be addressed later at the end of this chapter.

Example 3.7

Consider a two-dimensional CFD case of the incompressible laminar flow between two stationary parallel plates to illustrate the physical meaning of the energy equation. Using CFD and the dimensions of height $H = 0.1$ m and length $L = 1$ m, with air as the working fluid (density $\rho = 1.2$ kg/m^3), a specified uniform temperature of 330 K at the inlet, and a wall temperature maintained at 300 K, discuss the development of the temperature profiles between the inlet and the *thermal entry length* (L_T) for the following cases:

(a) A fixed inlet velocity $u_{in} = 0.01$ m/s and thermal conductivities $\lambda_1 = 0.04$ W/m K and $\lambda_2 = 0.01$ W/m K

(b) A fixed thermal conductivity $\lambda = 0.04$ W/m K and inlet velocities $u_{in1} = 0.01$ m/s and $u_{in2} = 0.1$ m/s

Solution: The problem is described as follows:

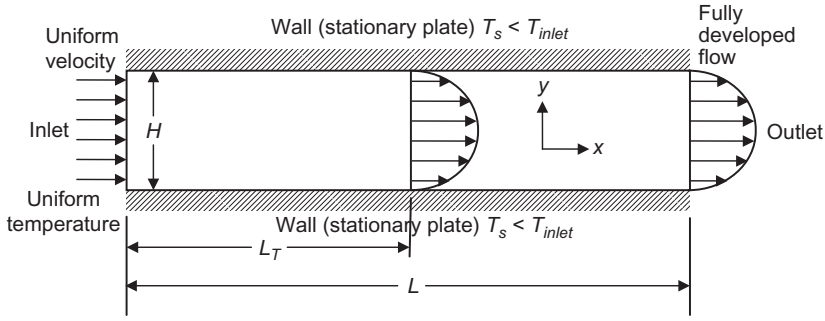


FIG. 3.7.1 Thermal entry length (L_T) location from the inlet surface in a two-dimensional laminar flow between two stationary parallel plates.

(a) By definition, the region from the inlet surface to the point at which the thermal boundary layer merges at the centerline is called the *thermal entrance region*, and the length of this region is called the *thermal entry length*. Flow in this entrance region is also called the *thermally developing flow* since the dimensionless temperature profile, $(T_s - T)/(T_s - T_m)$ where T_m denotes the mean temperature, is still developing. Beyond this region, the dimensionless temperature profile is fully developed and remains unchanged. Similar to the

fluid flow, the region in which the flow is thermally developed and thus both the velocity and dimensionless temperature profiles remain unchanged is called *fully developed flow*.

Based on the CFD simulation, the dimensionless temperature profiles at different downstream locations x/H from the inlet surface for varying thermal conductivities are given in Figs 3.7.2 and 3.7.3. The former refers to the case where the flow has a higher thermal conductivity than the latter.

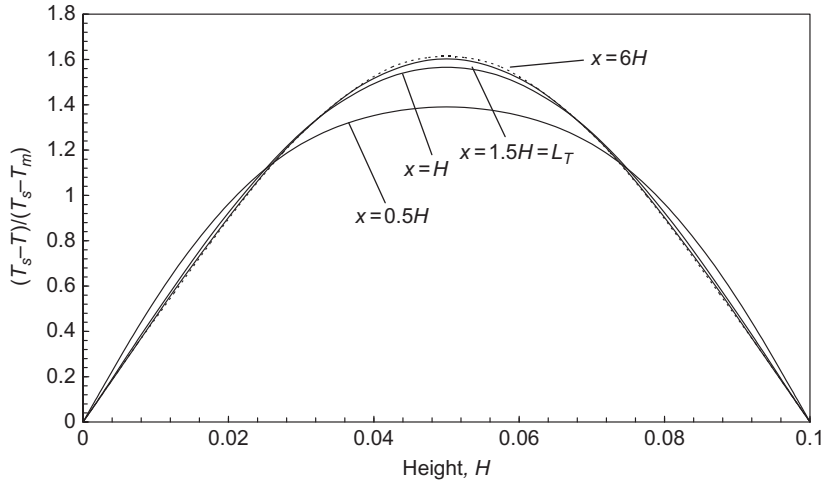


FIG. 3.7.2 Dimensionless temperature profiles at different locations of x/H for $u_{in}=0.01$ m/s and thermal conductivity $\lambda_1=0.04$ W/m K.

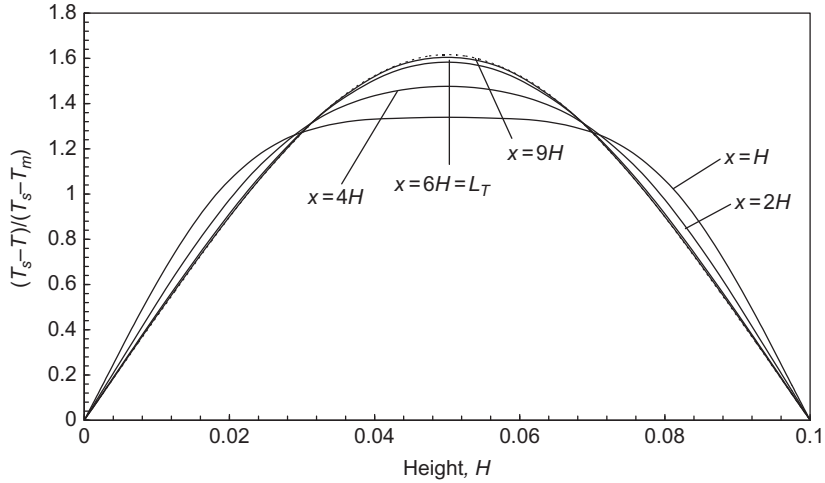


FIG. 3.7.3 Dimensionless temperature profiles at different locations of x/H for $u_{in}=0.01$ m/s and thermal conductivity $\lambda_2=0.01$ W/m K.

(b) The temperature profiles at different downstream locations x/H from the inlet surface for varying inlet velocities are given in Figs 3.7.4 and 3.7.5. The former refers to the case where the flow has a lower velocity than the latter. For comparison purposes, the case presented in Fig. 3.7.4 is of course exactly the same as the case presented above in Fig. 3.7.2 and is repeated here against the higher velocity case.

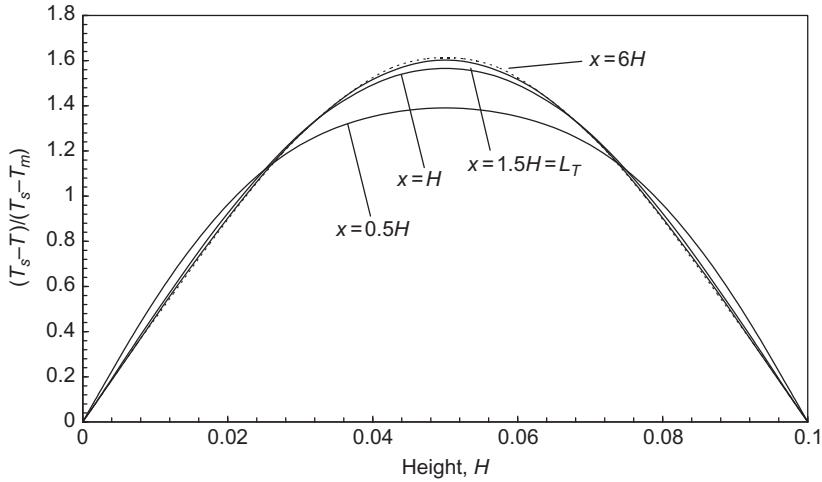


FIG. 3.7.4 Dimensionless temperature profiles at different locations of x/H for $u_{in1} = 0.01$ m/s and thermal conductivity $\lambda = 0.04$ W/m K.

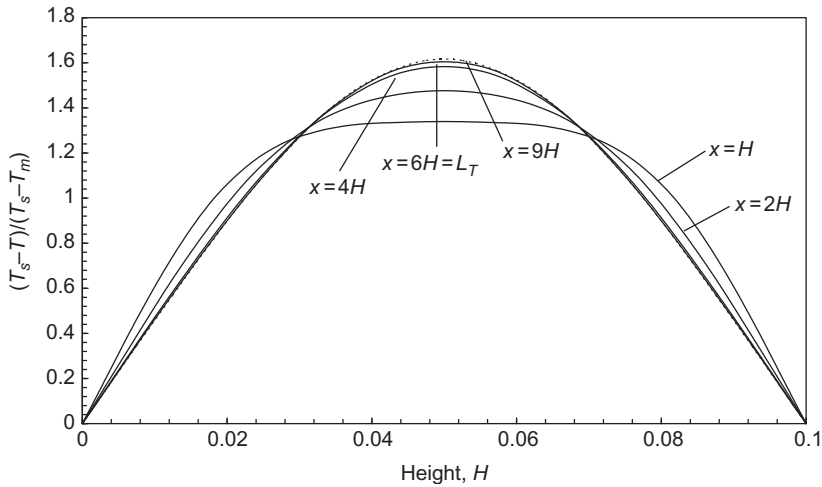


FIG. 3.7.5 Dimensionless temperature profiles at different locations of x/H for $u_{in2} = 0.1$ m/s and thermal conductivity $k = 0.04$ W/m K.

Discussion: As in the previous Example 3.5 for the momentum equations, we can rewrite the steady two-dimensional energy equation (3.34) as follows:

$$\underbrace{u\frac{\partial T}{\partial x}+v\frac{\partial T}{\partial y}}_{advection}=\underbrace{\frac{\lambda}{\rho C_p}\left(\frac{\partial^2 T}{\partial x^2}+\frac{\partial^2 T}{\partial y^2}\right)}_{diffusion}$$

The competition between the *advection* and *diffusion* in the energy equation is highlighted from the above results through the variation of the thermal conductivities and inlet velocities. For the case of a higher thermal conductivity, the *diffusion* term dominates. This leads to a shorter thermal entry length (i.e. the fully developed stage is reached at a shorter distance) due to a quicker development of the thermal boundary layer. This appears to have the same effect as that for the case of a higher *friction* force that inhibits the fluid momentum. However, a lower thermal conductivity induces less resistance to the heat flow thus allowing a slower development of the thermal boundary layer, and the flow reaches the fully developed stage at a longer distance. With a higher inlet velocity, this culminates in a higher *advection* overcoming the *diffusion* effect of the heat flow resulting in a longer development of the thermal entry length. It is noted that the thermal entry lengths for all the cases in the current example correspond exactly to the same hydrodynamic entry lengths obtained in Example 3.5. More explanation on the relationship between these hydrodynamic and thermal behaviours is given in the next section. All the cases investigated demonstrated the relative physical contributions of the *advection* and *diffusion* effects competing with each other to conserve the energy transfer.

3.4.3 Comments

Here, the principal of conservation of energy, like in the conservation of momentum, has been explored with investigations of the various contributions of the *advection* and *diffusion* terms in the energy equation. Through Example 3.7, there also appears to be some homogeneity for the thermal behaviour that results in the combination of the various flow variables. The dimensionless parameter previously introduced in Section 3.3.3, the Reynolds number (Re), depicts the contribution between the *inertia force* and the *friction force*, which describes the flow characteristics. Here, we introduce another important dimensionless parameter, the Prandtl number (Pr), which denotes the ratio of the *molecular diffusivity of momentum* over the *molecular diffusivity of heat*, that is

$$Pr=\frac{\text{Molecular diffusivity of momentum}}{\text{Molecular diffusivity of heat}}=\frac{\nu}{\alpha}=\frac{\mu C_p}{\lambda} \tag{3.36}$$

During laminar flow, the magnitude of the dimensionless Prandtl number is a measure of the relative growth of the velocity and thermal boundary layers. For fluids with $Pr\approx 1$, such as gases, the two boundary layers essentially coincide with each other. From Example 3.7, if the specific heat of air is taken to be 1000 J/kg, various combinations of the dynamic viscosity and thermal

conductivity of air can enable the Prandtl number to be unity. Here, the two boundary layers coincide with each other, and the same hydrodynamic and thermal entry lengths are obtained. For fluids with $Pr \gg 1$, such as water or oils, the velocity boundary layer outgrows the thermal boundary layer, whilst the opposite is true for fluids with $Pr \ll 1$ such as liquid metals. In thermal flow problems, we can therefore infer that the heat transfer characteristics are controlled by the combination of the Prandtl number and Reynolds number (representing the *advection* term). Further interpretation of the Prandtl number will be demonstrated in Example 3.9.

3.5 THE ADDITIONAL EQUATIONS FOR TURBULENT FLOW

3.5.1 What is Turbulence

Many if not most flows of engineering significance are turbulent in nature. The turbulent flow regime is, therefore, not only of theoretical interest among academics but also a problematic source for engineers who need to capture the effects of turbulence in solving everyday problems.

Flows in the laminar regime are completely described by the continuity and momentum equations as aforementioned. In simple cases, they can be solved analytically (Examples 3.1, 3.3, and 3.4). More complex flows may have to be tackled numerically with CFD techniques. It is well known that small disturbances associated with disturbances in the fluid streamlines of a laminar flow can eventually lead to a chaotic and random state of motion—a turbulent condition. These disturbances may originate from the free stream of the fluid motion or induced by the surface roughness where they may be amplified in the direction of the flow, in which case turbulence will occur. The onset of turbulence depends on the ratio of the inertia force to viscous force, which is indicated by the Reynolds number, Eq. (3.20). At low Reynolds number, inertia forces are smaller than the viscous forces. The naturally occurring disturbances are dissipated away, and the flow remains laminar. At high Reynolds number, the inertia forces are sufficiently large to amplify the disturbances, and a transition to turbulence occurs. Here, the motion becomes intrinsically unstable even with constant imposed boundary conditions. The velocity and all other flow properties are varying in a random and chaotic way.

Turbulence is associated with the existence of *random fluctuations* in the fluid. This behaviour can be exemplified by a typical point velocity measurement as a function of time at some location in the turbulent flow shown in Fig. 3.8. The random nature of flow precludes computations based on the equations that describe the fluid motion. Although the conservation equations remain applicable, the dependent variable such as the transient velocity distribution in Fig. 3.8 must be interpreted as an instantaneous velocity—a phenomena that is impossible to predict as the fluctuating velocity occurs randomly with time. Instead, the velocity can be decomposed into a steady mean value

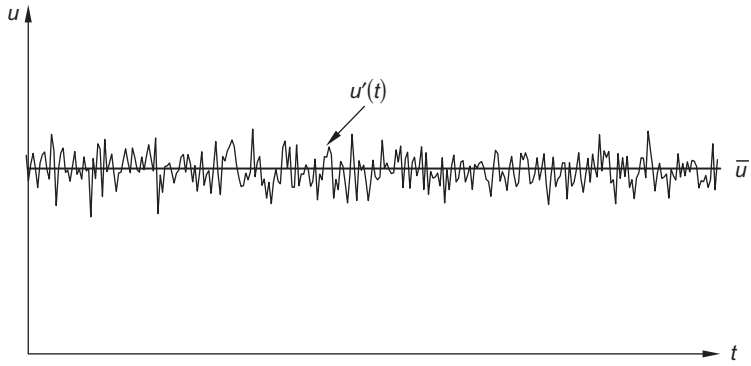


FIG. 3.8 Velocity fluctuating with time at some point in a turbulent flow.

$\bar{u}$ with a fluctuating component $u'(t)$ superimposed on it: $u(t) = \bar{u} + u'(t)$. In general, it is most attractive to characterize a turbulent flow by the mean values of flow properties ($\bar{u}$, $\bar{v}$, $\overline{w}$, $\overline{p}$, etc.) with its corresponding statistical fluctuating property (u', v', w', p', etc.).

Turbulent fluctuations always have a *three-dimensional* spatial character. Visualizations of turbulent flows have revealed rotational flow structures, so-called turbulent eddies, with a wide range of length and velocity scales called turbulent scales. The largest eddies have a characteristic velocity and a characteristic length of the same order as the velocity and length scale of the mean flow. This suggests that for turbulent flows where $ul \gg \nu$ (i.e. inertia effects dominate viscous effects), the largest eddies whose scales are comparable with the mean flow are dominated by inertia effects rather than the viscous effects. The large eddies are therefore effectively inviscid. Transport of eddies is attained by the extraction of energy from the mean flow by a process called vortex stretching. The presence of velocity gradients in the mean flow causes deformation of the fluid such as, shear and linear strain and rotation that 'stretch' eddies that are appropriately aligned by forcing one end of the eddies to move faster than the other. During vortex stretching, the angular momentum is conserved, and the stretching work done by the mean flow on the large eddies provides the energy that maintains the turbulence. These larger eddies then breed new instabilities creating smaller eddies that are transported mainly by vortex stretching from the larger eddy rather than from the mean flow. Thus, the energy is handed down from the larger eddy to the smaller eddy. This process continues until the eddies become so small that viscous effects become important, (the eddy length scales $ul \ll \nu$). Work is performed against the action of the viscous stresses, so that the energy associated with the eddy motions is dissipated and converted into thermal internal energy. The continual transfer of energy from the larger eddy to smaller and smaller eddies is termed as *energy cascade*. Larger eddies are flow-dependent as they are generated from mean flow

characteristics; thus, their turbulent scales are large compared with viscosity causing the structure of the eddy to be highly *anisotropic* (i.e. varying in all directions). Small eddies have much smaller turbulent scales (with scales up to the order of 10^{-4}) compared with viscosity causing the flow to be *isotropic* since the diffusive effects of viscosity dominate and smear out the directionality of the flow structure.

3.5.2 *k-ε* Two-Equation Turbulence Model

There is a crucial difference when modelling the physical phenomena between laminar and turbulent flow. For the latter, the appearance of turbulence eddies occurs over a wide range of length scales. A typical flow domain having a cross-sectional area of 0.1 m by 0.1 m with a high Reynolds number turbulent flow might contain eddies down to 10 or 100 μm in size. In order to describe the flow processes at all length scales, we would require computing meshes of 10^9–10^{12} grid points. Also, the fastest events can take place with a frequency of the order 10 kHz, which we would need to discretize time into steps of about 100 μs.

With the present day computing power, the computing requirements for a direct numerical solution (DNS) of the time-dependent Navier-Stokes equations of fully turbulent flows at high Reynolds numbers are still truly phenomenal. Meanwhile, engineers require computational procedures that can supply adequate information about the turbulent processes but wish to avoid the need to predict all the effects associated with each and every eddy in the flow. This category of CFD users is almost always satisfied with information about the time-averaged properties of the flow (e.g. mean velocities, mean pressures, and mean stresses). Since engineers are content to focus their attention on mean quantities, by adopting a suitable time-averaging operation on the momentum equations, we are able to discard all details concerning the state of the flow contained in the instantaneous fluctuations. This process, of obtaining mean quantities, can be applied on the compressible, two-dimensional equations of continuity and the *conservative* forms of momentum and energy that produce the time-averaged governing equations or more popularly known as the Reynolds-averaged Navier-Stokes (RANS) equations given by

$$\frac{\partial \rho}{\partial t} + \frac{\partial(\rho \overline{u})}{\partial x} + \frac{\partial(\rho \overline{v})}{\partial y} = 0 \tag{3.37}$$

$$\frac{\partial(\rho \overline{u})}{\partial t} + \frac{\partial(\rho \overline{u}\,\overline{u})}{\partial x} + \frac{\partial(\rho \overline{v}\,\overline{u})}{\partial y} = -\frac{\partial \overline{p}}{\partial x} + \frac{\partial}{\partial x}\left(\mu \frac{\partial \overline{u}}{\partial x}\right) + \frac{\partial}{\partial y}\left(\mu \frac{\partial \overline{u}}{\partial y}\right) + \frac{\partial}{\partial x}\left[\mu \frac{\partial \overline{u}}{\partial x}\right] + \frac{\partial}{\partial y}\left[\mu \frac{\partial \overline{v}}{\partial x}\right] - \left[\frac{\partial\left(\rho \overline{u'u'}\right)}{\partial x} + \frac{\partial\left(\rho \overline{u'v'}\right)}{\partial y}\right] \tag{3.38}$$

$$\frac{\partial(\rho v)}{\partial t}+\frac{\partial(\rho\overline{u}\overline{v})}{\partial x}+\frac{\partial(\rho\overline{v}\overline{v})}{\partial y}=-\frac{\partial\overline{p}}{\partial y}+\frac{\partial}{\partial x}\left(\mu\frac{\partial\overline{v}}{\partial x}\right)+\frac{\partial}{\partial y}\left(\mu\frac{\partial\overline{v}}{\partial y}\right)+\frac{\partial}{\partial x}\left[\mu\frac{\partial\overline{u}}{\partial y}\right]+\frac{\partial}{\partial y}\left[\mu\frac{\partial\overline{v}}{\partial y}\right]-\left[\frac{\partial\left(\rho\overline{u'v'}\right)}{\partial x}+\frac{\partial\left(\rho\overline{v'v'}\right)}{\partial y}\right] \tag{3.39}$$

$$\frac{\partial\left(\rho\overline{T}\right)}{\partial t}+\frac{\partial\left(\rho\overline{u}\overline{T}\right)}{\partial x}+\frac{\partial\left(\rho\overline{v}\overline{T}\right)}{\partial y}=\frac{\partial}{\partial x}\left(\frac{k}{C_p}\frac{\partial\overline{T}}{\partial x}\right)+\frac{\partial}{\partial y}\left(\frac{k}{C_p}\frac{\partial\overline{T}}{\partial y}\right)-\left[\frac{\partial\left(\rho\overline{u'T'}\right)}{\partial x}+\frac{\partial\left(\rho\overline{v'T'}\right)}{\partial y}\right] \tag{3.40}$$

where $\bar{u}$, $\overline{v}$, $\overline{p}$, and $\overline{T}$ are mean values and u', v', p', and T' are turbulent fluctuations. The equations above are similar to those formulated for laminar flows, except for the presence of additional terms of the form $\overline{a'b'}$. As a result, we have three additional unknowns (in three dimensions, we will have nine additional unknowns), known as the Reynolds stresses, in the time-averaged momentum equations. Similarly, the time-averaged temperature equation shows extra terms $\overline{u'T'}$ and $\overline{v'T'}$ (in three dimensions, we have an extra term $\overline{w'T'}$). For incompressible, two-dimensional equations of continuity and the *nonconservative* forms of momentum and energy, the time-averaged governing equations can be expressed as

$$\frac{\partial\overline{u}}{\partial x}+\frac{\partial\overline{v}}{\partial y}=0 \tag{3.41}$$

$$\frac{\partial\overline{u}}{\partial t}+\frac{\partial(\overline{u}\overline{u})}{\partial x}+\frac{\partial(\overline{v}\overline{u})}{\partial y}=-\frac{1}{\rho}\frac{\partial\overline{p}}{\partial x}+\frac{\partial}{\partial x}\left(\nu\frac{\partial\overline{u}}{\partial x}\right)+\frac{\partial}{\partial y}\left(\nu\frac{\partial\overline{u}}{\partial y}\right)+\frac{\partial}{\partial x}\left[\nu\frac{\partial\overline{u}}{\partial x}\right]+\frac{\partial}{\partial y}\left[\nu\frac{\partial\overline{v}}{\partial x}\right]-\left[\frac{\partial\left(\overline{u'u'}\right)}{\partial x}+\frac{\partial\left(\overline{u'v'}\right)}{\partial y}\right] \tag{3.42}$$

$$\frac{\partial v}{\partial t}+\frac{\partial(\overline{u}\overline{v})}{\partial x}+\frac{\partial(\overline{v}\overline{v})}{\partial y}=-\frac{1}{\rho}\frac{\partial\overline{p}}{\partial y}+\frac{\partial}{\partial x}\left(\nu\frac{\partial\overline{v}}{\partial x}\right)+\frac{\partial}{\partial y}\left(\nu\frac{\partial\overline{v}}{\partial y}\right)+\frac{\partial}{\partial x}\left[\nu\frac{\partial\overline{u}}{\partial y}\right]+\frac{\partial}{\partial y}\left[\nu\frac{\partial\overline{v}}{\partial y}\right]-\left[\frac{\partial\left(\overline{u'v'}\right)}{\partial x}+\frac{\partial\left(\overline{v'v'}\right)}{\partial y}\right] \tag{3.43}$$

$$\frac{\partial\overline{T}}{\partial t}+\frac{\partial\left(\overline{u}\overline{T}\right)}{\partial x}+\frac{\partial\left(\overline{v}\overline{T}\right)}{\partial y}=\frac{\partial}{\partial x}\left(\frac{k}{\rho C_p}\frac{\partial\overline{T}}{\partial x}\right)+\frac{\partial}{\partial y}\left(\frac{k}{\rho C_p}\frac{\partial\overline{T}}{\partial y}\right)-\left[\frac{\partial\left(\overline{u'T'}\right)}{\partial x}+\frac{\partial\left(\overline{v'T'}\right)}{\partial y}\right] \tag{3.44}$$

where the term $k/\rho C_p$ in Eq. (3.44) is the thermal diffusivity α of the fluid.

The time-averaged equations can be solved if the Reynolds stresses and extra temperature transport terms can be related to the mean flow and heat quantities. It was proposed by Boussinesq (1868) that the Reynolds stresses could be linked to the mean rates of deformation. We obtain

$$-\rho\overline{u'u'} = 2\mu_T\frac{\partial\overline{u}}{\partial x} - \frac{2}{3}\rho k; \quad -\rho\overline{v'v'} = 2\mu_T\frac{\partial\overline{v}}{\partial y} - \frac{2}{3}\rho k; \quad -\rho\overline{u'v'} = \mu_T\left(\frac{\partial\overline{v}}{\partial x} + \frac{\partial\overline{u}}{\partial y}\right) \tag{3.45}$$

The right-hand side is analogous to *Newton's law of viscosity*, except for the appearance of the turbulent or eddy viscosity μ_T and turbulent kinetic energy k.

In Eq. (3.45), the turbulent momentum transport is assumed to be proportional to the mean gradients of velocity. Similarly, the turbulent transport of temperature is taken to be proportional to the gradient of the mean value of the transported quantity. In other words,

$$-\rho\overline{u'T'} = \Gamma_T\frac{\partial\overline{T}}{\partial x}; \quad -\rho\overline{v'T'} = \Gamma_T\frac{\partial\overline{T}}{\partial y} \tag{3.46}$$

where Γ_T is the turbulent diffusivity. Since the turbulent transport of momentum and heat is due to the same mechanisms—eddy mixing—the value of the turbulent viscosity can be taken to be close to that of turbulent viscosity μ_T. Based on the definition of the turbulent Prandtl number Pr_T, we obtain

$$Pr_T = \frac{\mu_T}{\Gamma_T}$$

Experiments have established that this ratio is often nearly constant. Most CFD procedures assume this to be the case and use values of Pr_T around unity.

Since the complexity of turbulence in most engineering flow problems precludes the use of any simple formulae, it is possible to develop similar transport equations to accommodate the turbulent quantity k and other turbulent quantities one of which is the rate of dissipation of turbulent energy ε. Here, we indicate the form of a typical two-equation turbulence model that is commonly used in handling many turbulent fluid engineering problems, the *standard k-ε model* by Launder and Spalding (1974).

Some preliminary definitions are required first. The turbulent kinetic energy k and rate of dissipation of turbulent energy ε can be defined and expressed in Cartesian tensor notation as

$$k = \frac{1}{2}u_i'u_i' \quad \text{and} \quad \varepsilon = \nu_T\overline{\left(\frac{\partial u_i'}{\partial x_j}\right)\left(\frac{\partial u_i'}{\partial x_j}\right)} \quad \text{where } i,j = 1,2,3$$

From the local values of k and ε, a local turbulent viscosity μ_T can be evaluated as

$$\mu_T = \rho C_\mu\frac{k^2}{\varepsilon} \tag{3.47}$$

and the kinematic turbulent or eddy viscosity is denoted by $\nu_T = \mu_T/\rho$.

By substituting the Reynolds stress expressions in Eqs (3.38), (3.39), (3.42), and (3.43) and the extra temperature transport terms in Eqs (3.40) and (3.44), removing the overbar that is by default indicating the average quantities, we obtain the compressible form of governing equations as

$$\frac{\partial \rho}{\partial t}+\frac{\partial(\rho u)}{\partial x}+\frac{\partial(\rho v)}{\partial y}=0 \tag{3.48}$$

$$\frac{\partial(\rho u)}{\partial t}+\frac{\partial(\rho uu)}{\partial x}+\frac{\partial(\rho vu)}{\partial y}=-\frac{\partial p}{\partial x}+\frac{\partial}{\partial x}\left[(\mu+\mu_T)\frac{\partial u}{\partial x}\right]+\frac{\partial}{\partial y}\left[(\mu+\mu_T)\frac{\partial u}{\partial y}\right]+\frac{\partial}{\partial x}\left[(\mu+\mu_T)\frac{\partial u}{\partial x}\right]+\frac{\partial}{\partial y}\left[(\mu+\mu_T)\frac{\partial v}{\partial x}\right] \tag{3.49}$$

$$\frac{\partial(\rho v)}{\partial t}+\frac{\partial(\rho uv)}{\partial x}+\frac{\partial(\rho vv)}{\partial y}=-\frac{\partial p}{\partial y}+\frac{\partial}{\partial x}\left[(\mu+\mu_T)\frac{\partial v}{\partial x}\right]+\frac{\partial}{\partial y}\left[(\mu+\mu_T)\frac{\partial v}{\partial y}\right]+\frac{\partial}{\partial x}\left[(\mu+\mu_T)\frac{\partial u}{\partial y}\right]+\frac{\partial}{\partial y}\left[(\mu+\mu_T)\frac{\partial v}{\partial y}\right] \tag{3.50}$$

$$\frac{\partial(\rho T)}{\partial t}+\frac{\partial(\rho uT)}{\partial x}+\frac{\partial(\rho vT)}{\partial y}=\frac{\partial}{\partial x}\left[\left(\frac{\mu}{Pr}+\frac{\mu_T}{Pr_T}\right)\frac{\partial T}{\partial x}\right]+\frac{\partial}{\partial y}\left[\left(\frac{\mu}{Pr}+\frac{\mu_T}{Pr_T}\right)\frac{\partial T}{\partial y}\right] \tag{3.51}$$

and the incompressible form of governing equations as

$$\frac{\partial u}{\partial x}+\frac{\partial v}{\partial y}=0 \tag{3.52}$$

$$\frac{\partial u}{\partial t}+\frac{\partial(uu)}{\partial x}+\frac{\partial(vu)}{\partial y}=-\frac{1}{\rho}\frac{\partial p}{\partial x}+\frac{\partial}{\partial x}\left[(\nu+\nu_T)\frac{\partial u}{\partial x}\right]+\frac{\partial}{\partial y}\left[(\nu+\nu_T)\frac{\partial u}{\partial y}\right]+\frac{\partial}{\partial x}\left[(\nu+\nu_T)\frac{\partial u}{\partial x}\right]+\frac{\partial}{\partial y}\left[(\nu+\nu_T)\frac{\partial v}{\partial x}\right] \tag{3.53}$$

$$\frac{\partial v}{\partial t}+\frac{\partial(uv)}{\partial x}+\frac{\partial(vv)}{\partial y}=-\frac{1}{\rho}\frac{\partial p}{\partial y}+\frac{\partial}{\partial x}\left[(\nu+\nu_T)\frac{\partial v}{\partial x}\right]+\frac{\partial}{\partial y}\left[(\nu+\nu_T)\frac{\partial v}{\partial y}\right]+\frac{\partial}{\partial x}\left[(\nu+\nu_T)\frac{\partial u}{\partial y}\right]+\frac{\partial}{\partial y}\left[(\nu+\nu_T)\frac{\partial v}{\partial y}\right] \tag{3.54}$$

$$\frac{\partial T}{\partial t}+\frac{\partial(uT)}{\partial x}+\frac{\partial(vT)}{\partial y}=\frac{\partial}{\partial x}\left[\left(\frac{\nu}{Pr}+\frac{\nu_T}{Pr_T}\right)\frac{\partial T}{\partial x}\right]+\frac{\partial}{\partial y}\left[\left(\frac{\nu}{Pr}+\frac{\nu_T}{Pr_T}\right)\frac{\partial T}{\partial y}\right] \tag{3.55}$$

The term ν/Pr appearing in the temperature equation (3.55) is obtained from the definition of the laminar Prandtl number that is already defined in Eq. (3.36) as $Pr=\nu/\alpha$ where $\alpha=k/\rho C_p$. Interestingly, the time-averaged equations above have the same form as those developed for the laminar equations except for the additional turbulent viscosity found in the diffusion and nonpressure gradient

terms for the momentum equations and also found in the diffusion term for the energy equation. Hence, the solution to turbulent flow in engineering problems entails greater diffusion that is imposed by the turbulent nature of the fluid flow.

Additional differential transport equations that are required for the standard k-ε model, for the case of a variable fluid property in *conservative* form, are given by

$$\frac{\partial(\rho k)}{\partial t}+\frac{\partial(\rho u k)}{\partial x}+\frac{\partial(\rho v k)}{\partial y}=\frac{\partial}{\partial x}\left(\frac{\mu_T}{\sigma_k}\frac{\partial k}{\partial x}\right)+\frac{\partial}{\partial y}\left(\frac{\mu_T}{\sigma_k}\frac{\partial k}{\partial y}\right)+P-D \tag{3.56}$$

$$\frac{\partial(\rho \varepsilon)}{\partial t}+\frac{\partial(\rho u \varepsilon)}{\partial x}+\frac{\partial(\rho v \varepsilon)}{\partial y}=\frac{\partial}{\partial x}\left(\frac{\mu_T}{\sigma_\varepsilon}\frac{\partial \varepsilon}{\partial x}\right)+\frac{\partial}{\partial y}\left(\frac{\mu_T}{\sigma_\varepsilon}\frac{\partial \varepsilon}{\partial y}\right)+\frac{\varepsilon}{k}(C_{\varepsilon 1}P-C_{\varepsilon 2}D) \tag{3.57}$$

with the destruction term D is given by $\rho\varepsilon$ and the production term P formulated as

$$P=2\mu_T\left[\left(\frac{\partial u}{\partial x}\right)^2+\left(\frac{\partial v}{\partial y}\right)^2\right]+\mu_T\left(\frac{\partial u}{\partial y}+\frac{\partial v}{\partial x}\right)^2-\frac{2}{3}\mu_T\left(\frac{\partial u}{\partial x}+\frac{\partial v}{\partial y}\right)^2 -\frac{2}{3}\rho\mu_T k\left(\frac{\partial u}{\partial x}+\frac{\partial v}{\partial y}\right)$$

For the case of a constant fluid property, the differential transport equations in *nonconservative* form are expressed as

$$\frac{\partial k}{\partial t}+u\frac{\partial k}{\partial x}+v\frac{\partial k}{\partial y}=\frac{\partial}{\partial x}\left(\frac{\nu_T}{\sigma_k}\frac{\partial k}{\partial x}\right)+\frac{\partial}{\partial y}\left(\frac{\nu_T}{\sigma_k}\frac{\partial k}{\partial y}\right)+P-D \tag{3.58}$$

$$\frac{\partial \varepsilon}{\partial t}+u\frac{\partial \varepsilon}{\partial x}+v\frac{\partial \varepsilon}{\partial y}=\frac{\partial}{\partial x}\left(\frac{\nu_T}{\sigma_\varepsilon}\frac{\partial \varepsilon}{\partial x}\right)+\frac{\partial}{\partial y}\left(\frac{\nu_T}{\sigma_\varepsilon}\frac{\partial \varepsilon}{\partial y}\right)+\frac{\varepsilon}{k}(C_{\varepsilon 1}P-C_{\varepsilon 2}D) \tag{3.59}$$

where the destruction term D is given by ε and the production term P is formulated as

$$P=2\nu_T\left[\left(\frac{\partial u}{\partial x}\right)^2+\left(\frac{\partial v}{\partial y}\right)^2\right]+\nu_T\left(\frac{\partial u}{\partial y}+\frac{\partial v}{\partial x}\right)^2$$

The physical significance of the above equations is *the rate of change and the advection transport of k or ε equals the diffusion transport combined with the rate of production and destruction of k or ε*. The equations contain five adjustable constants C_μ, σ_k, σ_ε, $C_{\varepsilon 1}$, and $C_{\varepsilon 2}$. These constants have been arrived at by comprehensive data fitting for a wide range of turbulent flows (Launder and Spalding, 1974):

$$C_\mu=0.09,\quad \sigma_k=1.0,\quad \sigma_e=1.3,\quad C_{\varepsilon 1}=1.44,\quad C_{\varepsilon 2}=1.92$$

The production and destruction of turbulent kinetic energy are always closely linked in the k-equations (3.56) and (3.58). The dissipation rate ε is large where the production of k is large. The model equations (3.56) and (3.58) assume that the production and destruction terms are proportional to the production and destruction terms of the k-equation. Adoption of such terms ensures that ε increases rapidly if k increases rapidly and that it decreases sufficiently fast to avoid nonphysical (negative) values of turbulent kinetic energy if k decreases. The factor ε/k in the production and destruction terms makes these terms dimensionally correct in the ε-equations (3.57) and (3.59).

Example 3.8

Consider the two-dimensional CFD case of the flow between two stationary parallel plates to demonstrate the laminar and turbulent nature of the fluid flow. Using CFD with the dimensions of height $H = 0.1$ m and length $L = 10$ m of the channel, observe the velocity and viscosity profiles in the fully developed region with the working fluid taken as air (density $\rho = 1.2$ kg/m^3 and dynamic viscosity $\mu = 2 \times 10^{-5}$ kg/m s) for inlet velocities of $u_{in1} = 0.02$ m/s and $u_{in2} = 1$ m/s.

Solution: The problem is described as follows:

For an inlet velocity of $u_{in1} = 0.02$ m/s, the Reynolds number determined from Eq. (3.26) is given as 120. The flow is laminar. However, for an inlet velocity of $u_{in2} = 1$ m/s, the Reynolds number is calculated to be 6000. This Reynolds number is well above the critical Reynolds number of 1400, hence, the flow is turbulent.

Based on the CFD simulation, the laminar and turbulent velocity profiles in the fully developed region are given in Fig. 3.8.2.

The laminar (dynamic) and turbulent viscosities corresponding to the same location of the velocity profiles are shown in Fig. 3.8.3.

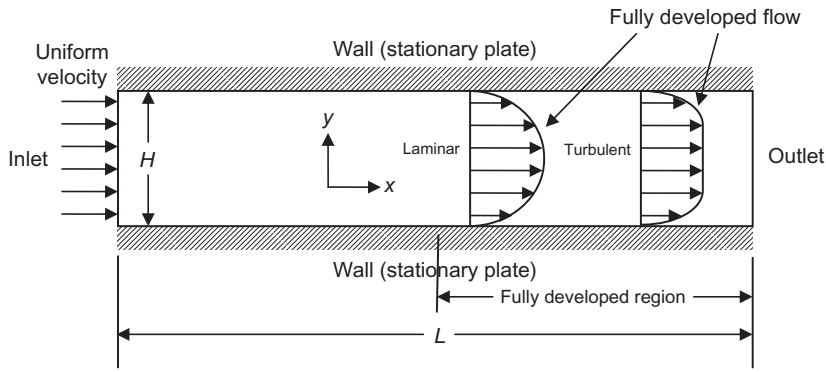


FIG. 3.8.1 Illustration of a laminar and turbulent flow in a two-dimensional fluid flow between two stationary parallel plates.

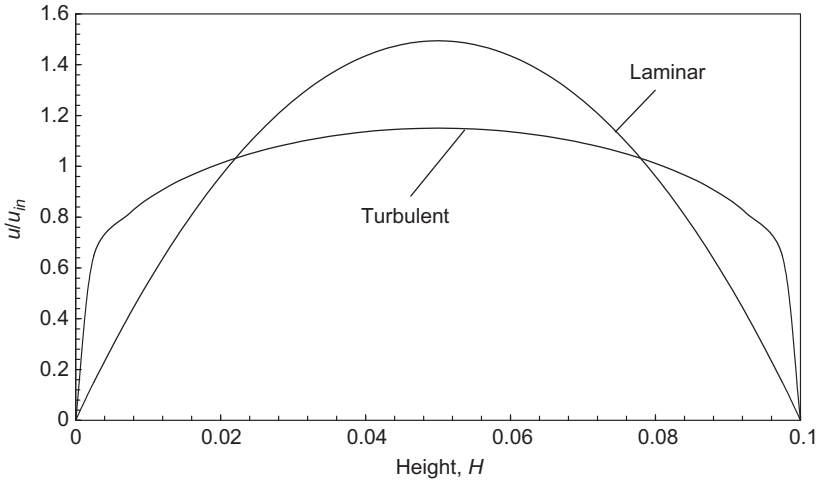


FIG. 3.8.2 Laminar and turbulent velocity profiles in the fully developed region.

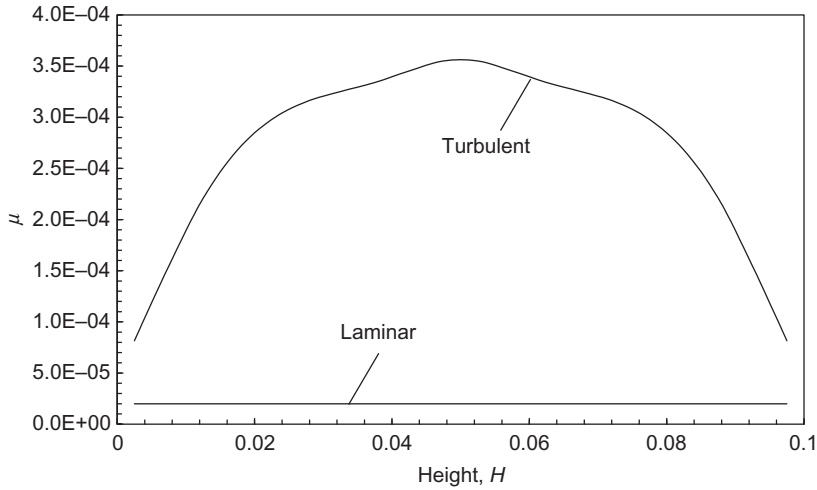


FIG. 3.8.3 Laminar and turbulent viscosities in the fully developed region.

Discussion: It is observed that there is a significant difference in the flow structure for the laminar and turbulent flow regimes. In the fully developed region, the velocity profile for laminar flow is parabolic, but the velocity profile for turbulent flow is rather blunt primarily at the centre of the channel with a steep velocity gradient near the wall surface. The turbulent velocity profile being blunt or flat at the centre is due to the effect of the high turbulent viscosity diffusing the flow in the momentum equations (this is exemplified in Fig. 3.8.3 where the turbulent viscosity is significantly higher by order of magnitudes than the laminar (dynamic) viscosity at the centre of the channel). To further illustrate the physical characteristics of the turbulent viscosity that is derived in

Eq. (3.36), profiles of the turbulent kinetic energy and dissipation along the height of the channel at the same location of the velocity profiles are plotted, which are respectively depicted in Figs 3.8.4 and 3.8.5. The results show that the turbulent kinetic energy k and dissipation rate ε peaking near the walls. Away from the wall and towards the centre of the channel, the kinetic energy decreases but at a slower rate than the dissipation rate. Even though the kinetic energy is high near the wall, the dissipation rate is much higher thereby resulting in a lower turbulent viscosity. At the centre, the kinetic energy is higher than the dissipation rate, which indicates a greater generation of turbulence thereby resulting in a higher turbulent viscosity.

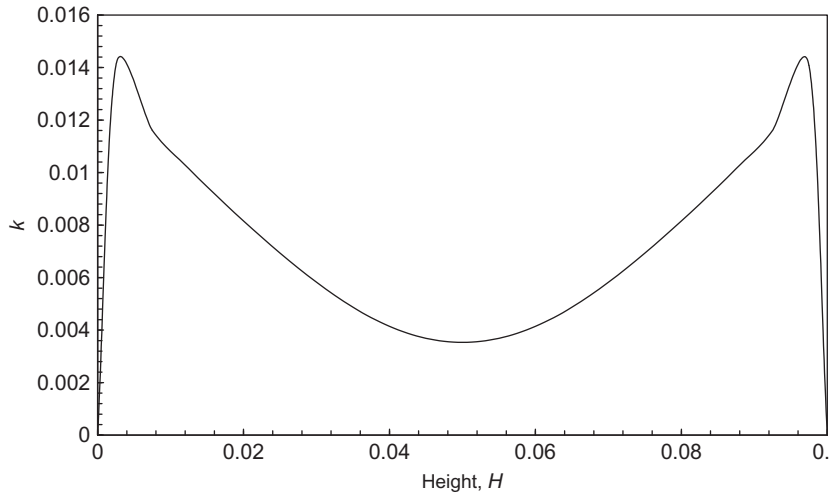


FIG. 3.8.4 Kinetic energy k profile for the turbulent flow in the fully developed region.

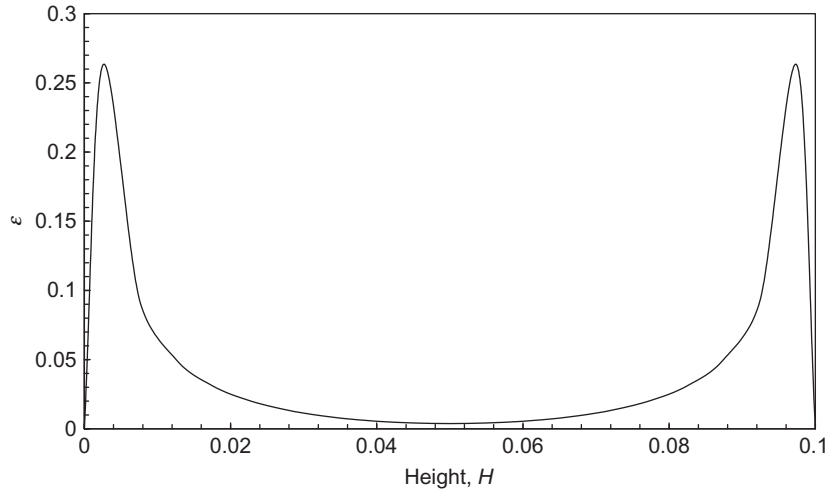


FIG. 3.8.5 Dissipation rate ε profile for the turbulent flow in the fully developed region.

3.5.3 Comments

The two-equation k-ε model is the most widely used and validated turbulence model. The model's performance has been assessed against a number of practical flows. It has achieved notable successes in predicting thin shear layers, boundary layers, and duct flows without the need for case-by-case adjustment of the model constants. It has also been shown that the two-equation k-ε model performs extremely well where the Reynolds shear stresses are important in confined flows. This accommodates a wide range of flows with industrial engineering applications, which explains the model's popularity among CFD users. Extension of the model to incorporate the buoyancy effects has led to application of the models to study environmental flows such as pollutant dispersion in the atmosphere and in lakes and modelling of enclosure fires.

Despite the many successful applications in handling industrial problems, the standard k-ε model demonstrates only moderate agreement when predicting unconfined flows. The weakness of the model is particularly amplified for weak shear layers—far-wake and mixing-layer unconfined separated flows. Also, for the case of the axisymmetric jets in stagnant surroundings, the spreading rate is severely overpredicted where in major parts of these flows, the rate of production of the turbulent kinetic energy is much less than the rate of dissipation. The difficulties can, however, be overcome by making *ad hoc* adjustments to the model constants, thereby reducing the model's generality and robustness.

Numerous problems are also experienced with the model in predicting swirling flows and flows with large, rapid, extra strains (e.g. highly curved boundary layers and diverging passages) since the model is unable to fully describe the subtle effects of the streamline curvature on turbulence. One major weakness of the standard k-ε model is the assumption of an *isotropic* eddy viscosity. Owing to the deficiencies of the treatment of the normal stresses, secondary flows that exist in long noncircular ducts, which are driven by anisotropic normal Reynolds stresses, could not be predicted. Finally, the model is oblivious to body forces due to rotation of the frame of reference.

3.6 GENERIC FORM OF THE GOVERNING EQUATIONS FOR CFD

From the governing equations derived above for either the laminar or turbulent conditions, there are significant commonalities between these various equations. Here, we will present the three-dimensional form of the governing equations for the conservation of mass, momentum, energy, and the turbulent quantities. If we introduce a general variable ϕ and expressing all the fluid flow equations in the conservative *incompressible* form, the equation can be written as

$$\frac{\partial \varphi}{\partial t}+\frac{\partial (u\varphi)}{\partial x}+\frac{\partial (v\varphi)}{\partial y}+\frac{\partial (w\varphi)}{\partial z}=\frac{\partial}{\partial x}\left[\Gamma\frac{\partial \varphi}{\partial x}\right]+\frac{\partial}{\partial y}\left[\Gamma\frac{\partial \varphi}{\partial y}\right]+\frac{\partial}{\partial z}\left[\Gamma\frac{\partial \varphi}{\partial z}\right]+S_{\varphi} \quad (3.60)$$

whilst in the conservative *compressible* form, the equation is given by

$$\frac{\partial (\rho\phi)}{\partial t}+\frac{\partial (\rho u\phi)}{\partial x}+\frac{\partial (\rho v\phi)}{\partial y}+\frac{\partial (\rho w\phi)}{\partial z}=\frac{\partial}{\partial x}\left[\Gamma\frac{\partial \phi}{\partial x}\right]+\frac{\partial}{\partial y}\left[\Gamma\frac{\partial \phi}{\partial y}\right]+\frac{\partial}{\partial z}\left[\Gamma\frac{\partial \phi}{\partial z}\right]+S_{\phi} \quad (3.61)$$

Eqs (3.60) and (3.61) are the so-called the transport equations for the property ϕ. Each of them illustrates the various physical transport processes occurring in the fluid flow: the *local acceleration* and *advection* terms on the left-hand side are, respectively, equivalent to the *diffusion* term (Γ = diffusion coefficient) and the *source* term (S_{ϕ}) on the right-hand side. Tables 3.1 and 3.2 present the governing equations for the incompressible and compressible flows in the Cartesian framework. In order to bring forth the common features, we have, of course, combined the terms that are not shared between the equations inside the source terms. It is noted that the additional source terms in the momentum equations S_u', S_v', and S_w' comprise of the pressure and nonpressure gradient terms and other possible sources such as gravity that influence the fluid motion, whilst the additional source term S_T in the energy equation may contain heat sources or sinks within the flow domain. It is also noted that the production P in the incompressible form of the turbulence equations can be obtained from its compressible counterpart via invoking the incompressible form of the continuity equation and division by constant density.

For compressible flow, the density and temperature can be evaluated through the equations of state, which provide the linkage between the energy equation and those of the mass and momentum equations. For a perfect gas, the following equations of state are $p=\rho RT$ where R is the gas constant and $e=C_vT$ where C_v is the specific heat of constant volume. For the dynamics viscosity and thermal conductivity, the variables can usually be determined via a linear or polynomial dependence on temperature.

This equation is usually used as the starting point for computational procedures in either the finite difference or finite volume methods. Algebraic expressions of this equation for the various transport properties are formulated and hereafter solved. For incompressible flow, by setting the transport property ϕ equal to 1, u, v, w, T, k, ε and selecting appropriate values for the diffusion coefficient Γ and source terms S_{ϕ}, we obtain the special forms presented in Table 3.3 for each of the partial differential equations for the conservation of mass, momentum, energy, and the turbulent quantities. In Table 3.4, by setting the transport property ϕ equal to 1, u, v, w, h, k, ε and selecting appropriate values for Γ and S_{ϕ}, we nonetheless obtain the special forms presented in Table 3.4 for the compressible form of the partial differential equations for the conservation of mass, momentum, energy, and the turbulent quantities.

TABLE 3.1 Governing Equations for Incompressible Flow in Cartesian Coordinates

Mass conservation	
(m)	$\frac{\partial u}{\partial x}+\frac{\partial v}{\partial y}+\frac{\partial w}{\partial z}=0$
Momentum equations	
(M_x)	$\frac{\partial u}{\partial t}+\frac{\partial (uu)}{\partial x}+\frac{\partial (vu)}{\partial y}+\frac{\partial (wu)}{\partial z}=\frac{\partial}{\partial x}\left[(\nu+\nu_T)\frac{\partial u}{\partial x}\right]+\frac{\partial}{\partial y}\left[(\nu+\nu_T)\frac{\partial u}{\partial y}\right]+\frac{\partial}{\partial z}\left[(\nu+\nu_T)\frac{\partial u}{\partial z}\right]+\left(S_u=-\frac{1}{\rho}\frac{\partial p}{\partial x}+S'_u\right)$
(M_y)	$\frac{\partial v}{\partial t}+\frac{\partial (uv)}{\partial x}+\frac{\partial (vv)}{\partial y}+\frac{\partial (wv)}{\partial z}=\frac{\partial}{\partial x}\left[(\nu+\nu_T)\frac{\partial v}{\partial x}\right]+\frac{\partial}{\partial y}\left[(\nu+\nu_T)\frac{\partial v}{\partial y}\right]+\frac{\partial}{\partial z}\left[(\nu+\nu_T)\frac{\partial v}{\partial z}\right]+\left(S_v=-\frac{1}{\rho}\frac{\partial p}{\partial y}+S'_v\right)$
(M_z)	$\frac{\partial w}{\partial t}+\frac{\partial (uw)}{\partial x}+\frac{\partial (vw)}{\partial y}+\frac{\partial (ww)}{\partial z}=\frac{\partial}{\partial x}\left[(\nu+\nu_T)\frac{\partial w}{\partial x}\right]+\frac{\partial}{\partial y}\left[(\nu+\nu_T)\frac{\partial w}{\partial y}\right]+\frac{\partial}{\partial z}\left[(\nu+\nu_T)\frac{\partial w}{\partial z}\right]+\left(S_w=-\frac{1}{\rho}\frac{\partial p}{\partial z}+S'_w\right)$
Energy equation	
(E)	$\frac{\partial T}{\partial t}+\frac{\partial (uT)}{\partial x}+\frac{\partial (vT)}{\partial y}+\frac{\partial (wT)}{\partial z}=\frac{\partial}{\partial x}\left[\left(\frac{\nu}{Pr}+\frac{\nu_T}{Pr_T}\right)\frac{\partial T}{\partial x}\right]+\frac{\partial}{\partial y}\left[\left(\frac{\nu}{Pr}+\frac{\nu_T}{Pr_T}\right)\frac{\partial T}{\partial y}\right]+\frac{\partial}{\partial z}\left[\left(\frac{\nu}{Pr}+\frac{\nu_T}{Pr_T}\right)\frac{\partial T}{\partial z}\right]+S_T$
Turbulence equations	
(k)	$\frac{\partial k}{\partial t}+\frac{\partial (uk)}{\partial x}+\frac{\partial (vk)}{\partial y}+\frac{\partial (wk)}{\partial z}=\frac{\partial}{\partial x}\left[\frac{\nu_T}{\sigma_k}\frac{\partial k}{\partial x}\right]+\frac{\partial}{\partial y}\left[\frac{\nu_T}{\sigma_k}\frac{\partial k}{\partial y}\right]+\frac{\partial}{\partial z}\left[\frac{\nu_T}{\sigma_k}\frac{\partial k}{\partial z}\right]+(S_k=P-D)$
(ε)	$\frac{\partial \varepsilon}{\partial t}+\frac{\partial (u\varepsilon)}{\partial x}+\frac{\partial (v\varepsilon)}{\partial y}+\frac{\partial (w\varepsilon)}{\partial z}=\frac{\partial}{\partial x}\left[\frac{\nu_T}{\sigma_\varepsilon}\frac{\partial \varepsilon}{\partial x}\right]+\frac{\partial}{\partial y}\left[\frac{\nu_T}{\sigma_\varepsilon}\frac{\partial \varepsilon}{\partial y}\right]+\frac{\partial}{\partial z}\left[\frac{\nu_T}{\sigma_\varepsilon}\frac{\partial \varepsilon}{\partial z}\right]+\left(S_\varepsilon=\frac{\varepsilon}{k}(C_{\varepsilon 1}P-C_{\varepsilon 2}D)\right)$
where	$P=2\nu_T\left[\left(\frac{\partial u}{\partial x}\right)^2+\left(\frac{\partial v}{\partial y}\right)^2+\left(\frac{\partial w}{\partial z}\right)^2\right]+\nu_T\left[\left(\frac{\partial u}{\partial y}+\frac{\partial v}{\partial x}\right)^2+\left(\frac{\partial v}{\partial z}+\frac{\partial w}{\partial y}\right)^2+\left(\frac{\partial w}{\partial x}+\frac{\partial u}{\partial z}\right)^2\right]$ and $D=\varepsilon$

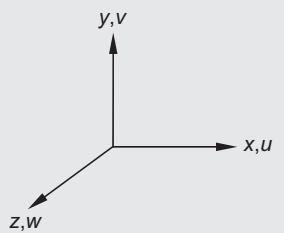


TABLE 3.2 Governing Equations for Compressible Flow in Cartesian Coordinates

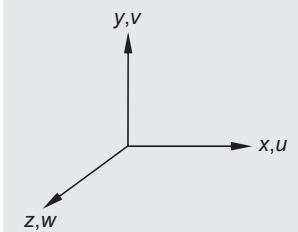
Mass conservation	
(m)	$\frac{\partial \rho}{\partial t}+\frac{\partial(\rho u)}{\partial x}+\frac{\partial(\rho v)}{\partial y}+\frac{\partial(\rho w)}{\partial z}=0$
Momentum equations	
(M_x)	$\frac{\partial(\rho u)}{\partial t}+\frac{\partial(\rho uu)}{\partial x}+\frac{\partial(\rho vu)}{\partial y}+\frac{\partial(\rho wu)}{\partial z}=\frac{\partial}{\partial x}\left[(\mu+\mu_T)\frac{\partial u}{\partial x}\right]+\frac{\partial}{\partial y}\left[(\mu+\mu_T)\frac{\partial u}{\partial y}\right]+\frac{\partial}{\partial z}\left[(\mu+\mu_T)\frac{\partial u}{\partial z}\right]+\left(S_u=-\frac{\partial p}{\partial x}+S'_u\right)$
(M_y)	$\frac{\partial(\rho v)}{\partial t}+\frac{\partial(\rho uv)}{\partial x}+\frac{\partial(\rho vv)}{\partial y}+\frac{\partial(\rho wv)}{\partial z}=\frac{\partial}{\partial x}\left[(\mu+\mu_T)\frac{\partial v}{\partial x}\right]+\frac{\partial}{\partial y}\left[(\mu+\mu_T)\frac{\partial v}{\partial y}\right]+\frac{\partial}{\partial z}\left[(\mu+\mu_T)\frac{\partial v}{\partial z}\right]+\left(S_v=-\frac{\partial p}{\partial y}+S'_v\right)$
(M_z)	$\frac{\partial(\rho w)}{\partial t}+\frac{\partial(\rho uw)}{\partial x}+\frac{\partial(\rho vw)}{\partial y}+\frac{\partial(\rho ww)}{\partial z}=\frac{\partial}{\partial x}\left[(\mu+\mu_T)\frac{\partial w}{\partial x}\right]+\frac{\partial}{\partial y}\left[(\mu+\mu_T)\frac{\partial w}{\partial y}\right]+\frac{\partial}{\partial z}\left[(\mu+\mu_T)\frac{\partial w}{\partial z}\right]+\left(S_w=-\frac{\partial p}{\partial z}+S'_w\right)$
Energy equation	
(E)	$\frac{\partial(\rho h)}{\partial t}+\frac{\partial(\rho uh)}{\partial x}+\frac{\partial(\rho vh)}{\partial y}+\frac{\partial(\rho wh)}{\partial z}=\frac{\partial}{\partial x}\left[\lambda\frac{\partial T}{\partial x}\right]+\frac{\partial}{\partial y}\left[\lambda\frac{\partial T}{\partial y}\right]+\frac{\partial}{\partial z}\left[\lambda\frac{\partial T}{\partial z}\right]+\frac{\partial}{\partial x}\left[\frac{\mu_T}{\mathrm{Pr}_T}\frac{\partial h}{\partial x}\right]+\frac{\partial}{\partial y}\left[\frac{\mu_T}{\mathrm{Pr}_T}\frac{\partial h}{\partial y}\right]+\frac{\partial}{\partial z}\left[\frac{\mu_T}{\mathrm{Pr}_T}\frac{\partial h}{\partial z}\right]+\frac{\partial p}{\partial t}+\Phi+S_T$
Turbulence equations	
(k)	$\frac{\partial(\rho k)}{\partial t}+\frac{\partial(\rho uk)}{\partial x}+\frac{\partial(\rho vk)}{\partial y}+\frac{\partial(\rho wk)}{\partial z}=\frac{\partial}{\partial x}\left[\frac{\mu_T}{\sigma_k}\frac{\partial k}{\partial x}\right]+\frac{\partial}{\partial y}\left[\frac{\mu_T}{\sigma_k}\frac{\partial k}{\partial y}\right]+\frac{\partial}{\partial z}\left[\frac{\mu_T}{\sigma_k}\frac{\partial k}{\partial z}\right]+(S_k=\rho(P-D))$
(ε)	$\frac{\partial(\rho\varepsilon)}{\partial t}+\frac{\partial(\rho u\varepsilon)}{\partial x}+\frac{\partial(\rho v\varepsilon)}{\partial y}+\frac{\partial(\rho w\varepsilon)}{\partial z}=\frac{\partial}{\partial x}\left[\frac{\mu_T}{\sigma_\varepsilon}\frac{\partial \varepsilon}{\partial x}\right]+\frac{\partial}{\partial y}\left[\frac{\mu_T}{\sigma_\varepsilon}\frac{\partial \varepsilon}{\partial y}\right]+\frac{\partial}{\partial z}\left[\frac{\mu_T}{\sigma_\varepsilon}\frac{\partial \varepsilon}{\partial z}\right]+\left(S_\varepsilon=\rho\frac{\varepsilon}{k}(C_{\varepsilon 1}P-C_{\varepsilon 2}D)\right)$
	
where	$P=2\mu_T\left[\left(\frac{\partial u}{\partial x}\right)^2+\left(\frac{\partial v}{\partial y}\right)^2+\left(\frac{\partial w}{\partial z}\right)^2\right]+\mu_T\left[\left(\frac{\partial u}{\partial y}+\frac{\partial v}{\partial x}\right)^2+\left(\frac{\partial v}{\partial z}+\frac{\partial w}{\partial y}\right)^2+\left(\frac{\partial w}{\partial x}+\frac{\partial u}{\partial z}\right)^2\right]-\frac{2}{3}\mu_T\left(\frac{\partial u}{\partial x}+\frac{\partial v}{\partial y}+\frac{\partial w}{\partial z}\right)^2-\frac{2}{3}\rho\mu_T k\left(\frac{\partial u}{\partial x}+\frac{\partial v}{\partial y}+\frac{\partial w}{\partial z}\right)$ and $D=\varepsilon$

TABLE 3.3 General Form of Governing Equations for Incompressible Flow in Cartesian Coordinates

Φ	Γ_Φ	S_Φ
1	0	0
u	$\nu+\nu_T$	$-\frac{1}{\rho}\frac{\partial p}{\partial x}+S'_u$
v	$\nu+\nu_T$	$-\frac{1}{\rho}\frac{\partial p}{\partial y}+S'_v$
w	$\nu+\nu_T$	$-\frac{1}{\rho}\frac{\partial p}{\partial z}+S'_w$
T	$\frac{\nu}{Pr}+\frac{\nu_T}{Pr_T}$	S_T
k	$\frac{\nu_T}{\sigma_k}$	$P-D$
ε	$\frac{\nu_T}{\sigma_\varepsilon}$	$\frac{\varepsilon}{k}(C_{\varepsilon 1}P-C_{\varepsilon 2}D)$

TABLE 3.4 General Form of Governing Equations for Compressible Flow in Cartesian Coordinates

Φ	Γ_Φ	S_Φ
1	0	0
u	$\mu+\mu_T$	$-\frac{\partial p}{\partial x}+S'_u$
v	$\mu+\mu_T$	$-\frac{\partial p}{\partial y}+S'_v$
w	$\mu+\mu_T$	$-\frac{\partial p}{\partial z}+S'_w$
h	$\frac{\mu_T}{Pr_T}$	$\frac{\partial}{\partial x}\left[\lambda\frac{\partial T}{\partial x}\right]+\frac{\partial}{\partial y}\left[\lambda\frac{\partial T}{\partial y}\right]+\frac{\partial}{\partial z}\left[\lambda\frac{\partial T}{\partial z}\right]+\frac{\partial p}{\partial t}+\Phi+S_T$
k	$\frac{\mu_T}{\sigma_k}$	$P-D$
ε	$\frac{\mu_T}{\sigma_\varepsilon}$	$\frac{\varepsilon}{k}(C_{\varepsilon 1}P-C_{\varepsilon 2}D)$

Although we have systematically walked through the derivation of the complete set of governing equations in detail from basic conservation principles, the final general form pertaining to the fluid motion, heat transfer, etc. conforms simply to the generic form of Eq. (3.60) for incompressible flow and Eq. (3.61) for compressible flow. These equations are important generic transport equations as they can accommodate increasing complexity within the CFD model for solving more complicated problems generally found in engineering applications.

Let us focus on some typical complex engineering flow problems that are of significant interest such as multistep combustion processes of swirling turbulent reactive flows in combustors and multiphase flows involving interactions between gas bubbles and liquids in bubble columns. Solutions to these processes can easily be obtained by modelling them through additional transport equations expressed in the simple generic form of Eq. (3.60) for incompressible flow and Eq. (3.61) for compressible flow. For reactive flows, the transport of the various *chemical species* can be handled by the additional scalar quantities representing each of the reactive species and appropriately formulating the reaction rates in the source terms to account for the chemical reaction processes that are occurring. For bubbly flows, additional transport equations of the *number density* can be formulated and solved for the various gas bubble sizes that migrate alongside with the liquid in the bubble columns.

Understanding CFD is not meant to be an arduous process. On the contrary, Eqs (3.60) and (3.61), originally formulated from first principles, reinforce the adherent *simplicity* that is embraced for any transport property that may be required to be solved within the CFD framework.

In Sections 3.3.3 and 3.4.3, we introduced the dimensionless parameters such as the Reynolds number (Re) and Prandtl number (Pr) that may be useful to describe some similar physical phenomena of the flow and heat transfer processes. It will be demonstrated in the next example that the governing equations of mass, momentum, and energy can be nondimensionalized to reduce the number of parameters that appear in the equations. Other similar characteristics of the fluid flow are also discussed.

Example 3.9

Consider the *dynamic similarity* of the partial differential equations that govern a two-dimensional CFD case for a steady incompressible laminar flow between two stationary parallel plates. The channel dimensions are height $H = 0.1$ m and length $L = 1$ m. This is the same model geometry as previously investigated in Examples 3.7 and 3.8.

(a) Nondimensionalize the continuity, momentum, and energy equations given by Eqs (3.12), (3.24), (3.25), and (3.35), respectively.

(b) Using CFD, determine the flow field for both air and water with the same Reynolds number whilst adjusting the inlet velocity. Discuss the velocity profiles in the fully developed region.

(c) Also determine the temperature field for both air and water with the same Reynolds number as in part (b). Discuss the nondimensional temperature profiles in the fully developed region with a prescribed uniform temperature of 330 K at the inlet and a wall temperature specified at 300 K.

Solution: (a) The nondimensional form of the governing equations (and boundary conditions) can be achieved by dividing all the dependent and independent flow variables by relevant and meaningful constant quantities. For lengths, the variable can be divided by a characteristic length H (which is the width of the channel), all velocities by a reference velocity u_{in} (which is the inlet velocity), pressure by ρu_{in}^2 (which is twice the dynamic pressure for the channel), and temperature by a suitable temperature difference (which is $T_\infty - T_s$ for the channel). We therefore obtain

$$x^* = \frac{x}{H},\quad y^* = \frac{y}{H},\quad u^* = \frac{u}{u_{in}},\quad v^* = \frac{v}{u_{in}},\quad p^* = \frac{p}{\rho u_{in}^2} \quad \text{and} \quad T^* = \frac{T - T_s}{T_\infty - T_s}$$

where the asterisks denote the nondimensional variables. Introducing these variables into the governing equations of mass, momentum, and energy produces

$$\frac{\partial u^*}{\partial x^*} + \frac{\partial v^*}{\partial y^*} = 0 \quad - \quad \text{continuity}$$

$$u^*\frac{\partial u^*}{\partial x^*} + v^*\frac{\partial u^*}{\partial y^*} = \frac{1}{Re}\left(\frac{\partial^2 u^*}{\partial x^{*2}} + \frac{\partial^2 u^*}{\partial y^{*2}}\right) - \frac{\partial p^*}{\partial x^*} \quad - \quad x - \text{momentum}$$

$$u^*\frac{\partial v^*}{\partial x^*} + v^*\frac{\partial v^*}{\partial y^*} = \frac{1}{Re}\left(\frac{\partial^2 v^*}{\partial x^{*2}} + \frac{\partial^2 v^*}{\partial y^{*2}}\right) - \frac{\partial p^*}{\partial y^*} \quad - \quad y - \text{momentum}$$

$$u^*\frac{\partial T^*}{\partial x^*} + v^*\frac{\partial T^*}{\partial y^*} = \frac{1}{RePr}\left(\frac{\partial^2 T^*}{\partial x^{*2}} + \frac{\partial^2 T^*}{\partial y^{*2}}\right) \quad - \quad \text{energy}$$

Discussion: A major advantage of nondimensionalizing the governing equations is the significant reduction of parameters to be considered. By grouping the dimensional parameters, originally 8 (H, u_{in}, T_∞, T_s, k, ρ, μ, and C_p), the nondimensionalized problem now involves only just two parameters (Re and Pr). Hence, for a given geometry, problems having the same values for the similarity parameters will have identical solutions. Another advantage of the use of similarity parameters is that results from a large number of experiments can be grouped and reported conveniently in terms of such parameters.

(b) The physical significance of the Reynolds number (Re) is investigated herein. As previously defined in Eq. (3.20), this dimensionless number requires the values of density (ρ) and dynamic viscosity (μ). For air, the values are $\rho = 1.2$ kg/m^3 and $\mu = 2 \times 10^{-5}$ kg/m s, whilst for water, they are $\rho = 1000$ kg/m^3 and $\mu = 10^{-3}$ kg/m s. If a laminar flow, for example $Re = 120$, is assumed for both fluids, the inlet velocities for air and water are 0.02 m/s and 0.0012 m/s.

Based on CFD simulations, the axial dimensional and nondimensional velocity profiles for air and water in the fully developed region are given in Figs 3.9.2 and 3.9.3.

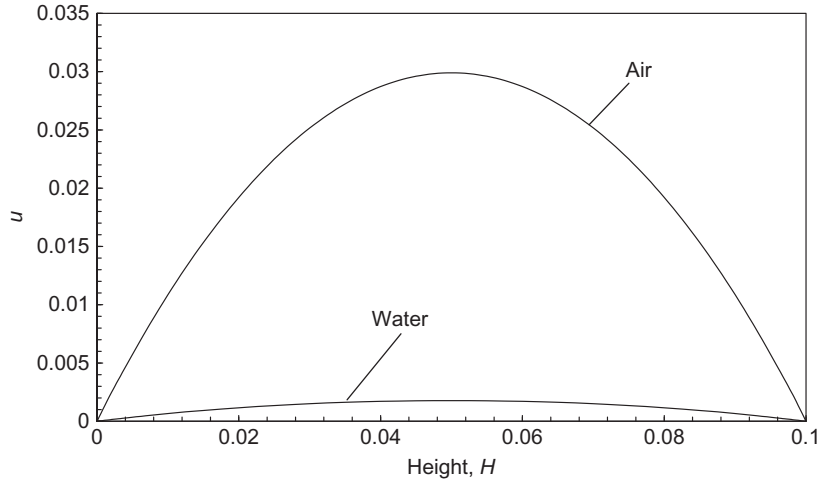


FIG. 3.9.2 Dimensional axial velocity profiles in the fully developed region.

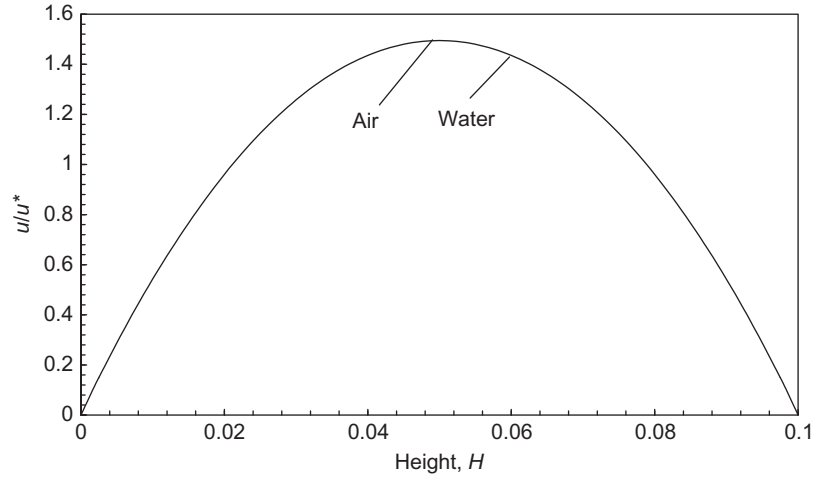


FIG. 3.9.3 Nondimensional axial velocity profiles in the fully developed region.

Discussion: Although the two flows have different fluid properties, one being air whilst the other is water, we obtain the same flow behaviour. This is because they have the same Reynolds numbers, and the nondimensional governing equations of the *x-momentum* and *y-momentum* are identical, which leads to the same numerical results. If we consider another fluid mechanics example that is the flow of air or water over a flat plate (Fig. 3.9.4) having different lengths but with the same inlet velocities at the same Reynolds numbers, these two geometrically similar bodies have the same physical phenomena since they have the same friction coefficients (C_f).

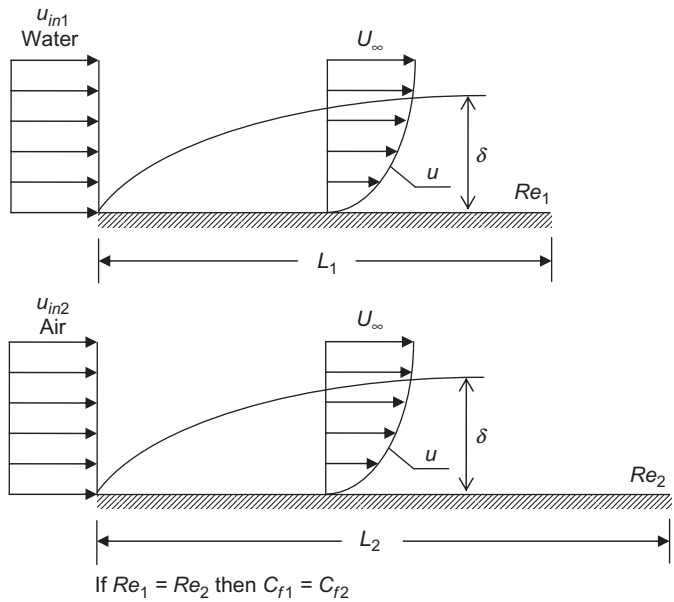


FIG. 3.9.4 Two geometrically similar bodies having the same friction coefficients at the same Reynolds numbers.

(c) The physical significance of the Prandtl number (Pr) is subsequently investigated herein. As previously defined in Eq. (3.35), it requires the values of the kinematic viscosity (ν) and thermal diffusivity (α). For air, the values are $\nu = 1.667 \times 10^{-5}$ m^2/s and $\alpha = 1.667 \times 10^{-5}$ m^2/s whilst for water $\nu = 1 \times 10^{-6}$ m^2/s and $\alpha = 1.435 \times 10^{-7}$ m^2/s. This yields $Pr = 1$ for air and $Pr \approx 7$ for water.

Based on the CFD simulations, the nondimensional temperature profiles for air and water in the fully developed region are given in Fig. 3.9.5.

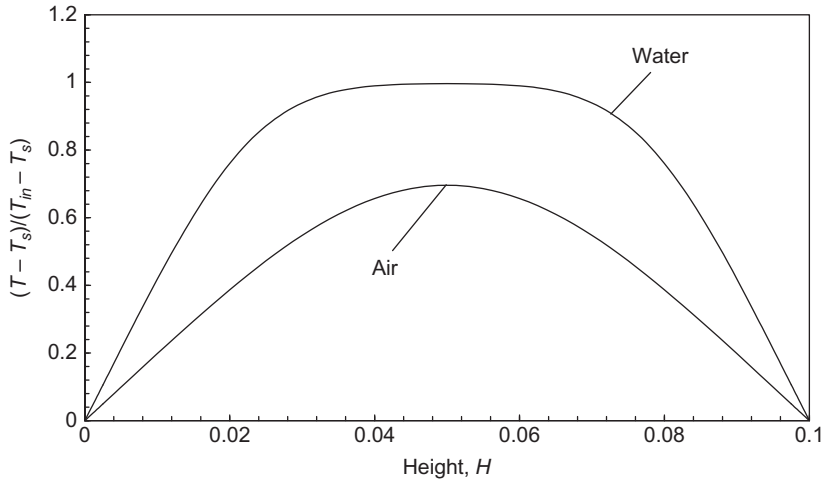


FIG. 3.9.5 Nondimensional temperature profiles in the fully developed region.

Discussion: With reference to the energy *diffusion* term, $1/Re\,Pr$ in the nondimensional energy equation, the Reynolds number of air and water is the same; however, the Prandtl number of air is found to be much less than water leading to heat flow being diffused more in air than in water. Therefore, with less *diffusion*, more *advection* is encouraged in water than in air, which leads to a higher temperature in the fully developed region. Nevertheless, we have the same momentum *diffusion* for the velocity fields since the Reynolds numbers are the same for both fluids in the *x-momentum* and *y-momentum* equations; both fluids therefore have the same velocity profiles.

3.7 PHYSICAL BOUNDARY CONDITIONS OF THE GOVERNING EQUATIONS

In Chapter 2, we have introduced various types of boundary conditions that are required in order to perform the numerical calculations of fluid flow in a channel. Here, we explore the physical meanings of the boundary conditions that were applied and other important boundary conditions that may be required to close the fluid flow system.

The continuity, momentum, energy, and turbulent quantity equations above govern the flow and heat transfer of a fluid. They are the same equations whether the flow is over high-rise buildings or bridges, through subsonic wind tunnels, or within various narrow channels of intricate electronic components in a computer box. However, the flow fields are quite *different* for each of these cases, although the governing equations are the *same*. The reason for the difference lies in the specification of the *boundary conditions*. The boundary conditions and sometimes the *initial conditions* strongly dictate the particular solutions to be obtained from the governing equations. For example, when all the geometrical shapes of the high-rise buildings are treated, when certain physical boundary conditions are applied on the surfaces, and when appropriate boundary conditions are imposed on the far free stream, then the resulting solution of the governing partial differential equations listed in Table 3.1 will yield the complex flow field over the high-rise buildings. In contrast, the solution of the flow field within heated channels in a computer box demands other physical boundary conditions. For example, the specific geometrical shape and locations of air entrainment and exhaust ports within the computer box.

We have formulated the governing equations that have been developed and described in the previous sections. However, the real driver for any particular solution is the boundary conditions. This creates particular significance especially in CFD as any numerical solution of the governing equations must result in a strong and compelling numerical representation of the proper boundary conditions.

Let us now review the physical boundary conditions for a subsonic viscous flow. We focus initially on the so-called *no-slip* condition. Here, the boundary condition on a solid surface assumes zero relative velocity between the surface and the fluid immediately at the surface. If the surface is stationary, with the

flow moving past it, then all the velocity components can be taken to be zero. In other words,

$$u = v = w = 0 \quad \text{at the surface} \tag{3.62}$$

In Chapter 2 and Examples 3.2, 3.5, 3.7, 3.8, and 3.9, we were introduced to the inflow boundary condition for a channel flow. The solution of the governing equations for any of the transport property ϕ for most flows requires at least one velocity component to be given at the inflow boundary. For the channel flow, this is provided by the *Dirichlet* boundary condition on the velocity in the x direction:

$$u = f \quad \text{and} \quad v = w = 0 \quad \text{at the inflow boundary} \tag{3.63}$$

where f can either be specified as a constant value or a velocity profile at the surface. Computationally, *Dirichlet* conditions can be applied accurately as long as f is continuous. We were also introduced in Chapter 2 and in Examples 3.2, 3.5, 3.7, 3.8, and 3.9 the use of an outflow boundary condition. Commonly, outflow boundaries are positioned at locations where the flow is approximately unidirectional and where surface stresses take known values. In a fully developed flow exiting from the channel, there is no change in the velocity component in the direction across the boundary. To satisfy stress continuity, the shear forces along the surface are taken to be zero; this gives the outflow condition

$$\frac{\partial u}{\partial n} = \frac{\partial v}{\partial n} = \frac{\partial w}{\partial n} = 0 \quad \text{at the outflow boundary} \tag{3.64}$$

where n is the direction normal to the surface, which for the channel flow problem is the x direction. This condition is usually known as the *Neumann* boundary condition. Physically, in reference to the continuity equation (3.12), it is clear that the appropriate boundary conditions (3.62), (3.63), and (3.64) that are imposed at any location on the surface of the channel walls in Chapter 2 close the system mathematically and satisfy local and overall mass conservation.

There is an analogous *no-slip* condition associated with the temperature at the surface. If the material temperature of the surface is denoted by T_w, then the temperature fluid layer immediately in contact with the surface is also T_w. In a given problem where the wall temperature is known, *Dirichlet* boundary condition applies and the fluid temperature is

$$T = T_w \quad \text{at the wall} \tag{3.65}$$

The application of this boundary condition was illustrated by Example 3.6, part (a), and Examples 3.8 and 3.9. However, if the wall temperature is not known (e.g. if the temperature is changing as a function of time due to the heat transfer to or from the surface), then Fourier's law of heat condition can be

applied to provide the necessary boundary condition at the surface. If we denote the instantaneous wall heat flux as q_w, then according to Fourier's law

$$q_w = -\left(k\frac{\partial T}{\partial n}\right)_w \quad \text{at the wall} \tag{3.66}$$

The application of this boundary condition was also illustrated by the same Example 3.6 but for part (b). Here, the changing surface temperature T_w is responding to the thermal response of the wall material through the heat transfer to the wall q_w. This type of boundary condition, as far as the flow is concerned, is a boundary condition of the temperature *gradient* at the wall. For the case where there is no heat transfer to the surface, this wall temperature, by definition is called an adiabatic wall temperature T_{adia}. The proper boundary condition comes from Eq. (3.66) with $q_w = 0$, hence

$$\left(\frac{\partial T}{\partial n}\right)_w = 0 \quad \text{at the wall} \tag{3.67}$$

This condition falls in line with the *Neumann* boundary condition for the velocity at the outflow boundaries. On the inflow and outflow boundaries of the flow domain, it is common to have the temperature specified at the inflow boundary and the adiabatic condition adopted at the outflow boundary.

Other commonly used boundary conditions include the open boundary condition. If we refer back to the description of the boundary conditions for the flow over high-rise buildings at the beginning of this section, the far free-stream boundary requires the application of an open boundary, which simply states that the normal gradient of any of the transport property ϕ is zero, that is $\partial\phi/\partial n = 0$. Gresho and Sani (1990) reviewed the intricacies of open boundary conditions in an incompressible flow and states that there are some *theoretical concerns* regarding this boundary condition. However, its success in CFD practice left them to recommend it as the simplest and cheapest method when compared with theoretically more satisfying selections. Furthermore, symmetric and cyclic boundary conditions can be employed to take advantage of special geometrical features of the solution region. For the symmetry boundary condition, the normal velocity at the surface is zero, whilst the normal gradients of the other velocity components are zero, where the latter condition also applies for any scalar quantity. For the cyclic boundary condition, the transport property of the one surface ϕ_1 is equivalent to the transport property of the second surface ϕ_2, that is $\phi_1 = \phi_2$ depending on which two surfaces of the flow domain experience periodicity.

For the turbulent quantities, *Dirichlet* and *Neumann* boundary conditions for the turbulent kinetic energy k and its dissipation ε are usually applied at the inflow and outflow boundaries. However, special treatment of the boundary conditions for k and ε is required to properly account for the laminar sublayer that exists near the wall surface in turbulent flow. We will further discuss in detail the wall treatment for the turbulent quantities in Chapter 6.

For a supersonic flow, *Dirichlet* and *Neumann* boundary conditions can be applied at the inflow boundary but not at the outflow boundary. All variables and properties at the outflow boundary are determined from the upstream flow. If the flow is assumed to be inviscid, the flow velocity is usually taken to be a finite, nonzero value at the solid surface. This means that the wall shear stress is zero. Also, there cannot be any mass flow into and out of the wall. The component velocity perpendicular to the wall is thus zero, and the flow at the surface is tangent to the solid surface.

3.8 SUMMARY

In this chapter, we have formulated the mathematical basis for a comprehensive general purpose model of fluid flow and heat transfer from the basic principles of conservation of mass, momentum, and energy. The governing equations are derived by the consideration of an infinitesimal small control volume to conserve mass and energy, and that the net force acting on the control volume is equivalent to the time rate of change of linear momentum. Although we have employed the Newtonian model of viscous stresses to close the system of equations, the accommodation of fluids having nonNewtonian characteristics can be easily incorporated within the framework of these equations. The appearance of viscosity and other thermophysical properties such as the density, thermal conductivity, and specific heat in the governing equations may vary with local conditions, and to account for these effects is a straightforward process.

The reader was also introduced to some aspects of turbulence modelling, which resulted in the derivation of the widely applied two-equation k-ε model. This turbulence model still comes highly recommended for general purpose CFD computations and is the default model used in many commercial codes.

Whether the fluid flow is laminar or turbulent, there are significant commonalities between these conservation equations. This leads to the formulation of the generic form of the governing equations accompanied by a discussion of the physical boundary conditions commonly employed within the CFD framework to close the fluid flow system. A road map to encapsulate all these aforementioned aspects, beginning from the conception of the fluid flow and ending with the system of equations to be solved, is shown in Fig. 3.9 below.

The means of obtaining a solution to these governing equations are discussed in the next chapter. We will present some of the basic computational techniques that can be employed to solve such partial differential equations. The equations presented in this chapter are usually regarded as the starting point for the application of the many *discretization* procedures predicting the fluid motion and heat transfer processes, which will be further elaborated in the next chapter.

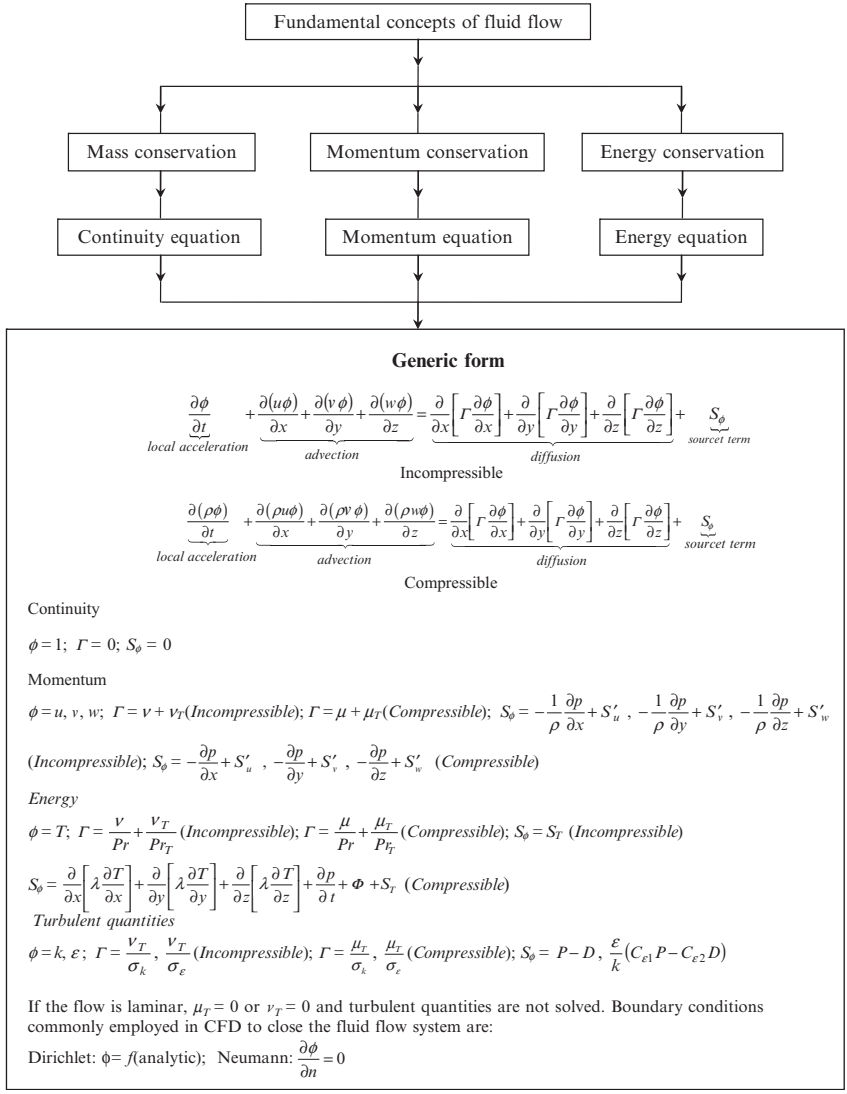


FIG. 3.9 The road map for this chapter.

REVIEW QUESTIONS

3.1 Simplify the general continuity equation: $\dfrac{\partial \rho}{\partial t} + \dfrac{\partial (\rho u)}{\partial x} + \dfrac{\partial (\rho v)}{\partial y} + \dfrac{\partial (\rho w)}{\partial z} = 0$, for a two-dimensional constant density case.

3.2 In a converging nozzle, the flow accelerates due to the narrowing geometry. Discuss the changes in the velocity gradients $\frac{\partial u}{\partial x}$ and $\frac{\partial v}{\partial y}$ during the flow (assume a constant density).

3.3 What is Newton's second law of motion?

3.4 Write a force balance equation for all the forces acting on a differential control volume.

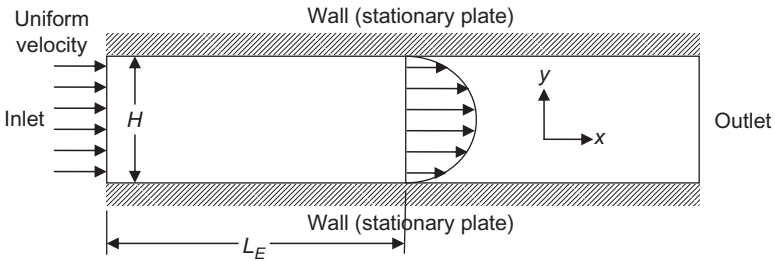
3.5 For the momentum of a fluid property in the x direction, discuss how the local acceleration $\frac{\partial u}{\partial t}$ and the advection terms $u\frac{\partial u}{\partial x}+v\frac{\partial u}{\partial y}$ contribute to the overall transport of the fluid.

3.6 A simplified one-dimensional inviscid, incompressible, laminar flow is defined by the following momentum equation in the x direction: $\frac{\partial u}{\partial t}+u\frac{\partial u}{\partial x}=-\frac{1}{\rho}\frac{\partial p}{\partial x}$. Name each term and discuss their contribution to the flow.

3.7 The momentum of a fluid in the y direction is given by the following equation: $\frac{\partial v}{\partial t}+u\frac{\partial v}{\partial x}+v\frac{\partial v}{\partial y}=-\frac{1}{\rho}\frac{\partial p}{\partial y}+\nu\frac{\partial^2 v}{\partial x^2}+\nu\frac{\partial^2 v}{\partial y^2}-g$. Discuss the forces that act to transport the fluid.

3.8 What are the differences between the momentum equation in question 3.7 and the following momentum equation: $\rho u\frac{\partial u}{\partial x}+\rho v\frac{\partial u}{\partial y}=-\frac{\partial p}{\partial x}+\mu\left(\frac{\partial^2 u}{\partial x^2}+\frac{\partial^2 u}{\partial y^2}\right)$.

3.9 The hydrodynamic length for a channel flow shown below is equal to L_e when air is used ($u_{in}=0.03$ m/s, $\mu_1=1.65\times10^{-5}$ kg/m s, and $\rho=1.2$ kg/m^3). To obtain the same hydrodynamic length for water, what inlet velocity is required ($\mu_1=1.003\times10^{-3}$ kg/m s, $\rho=1000$ kg/m^3).



3.10 The Reynolds number is a ratio of two fluid properties. What are they?

3.11 If the Reynolds is very high ($Re\gg10{,}000$), what does this suggest? If it is very low ($Re\ll100$), what does this imply?

3.12 Which fluid property changes from a constant to a variable when the fluid is considered a compressible flow?

3.13 Write down the continuity equation for a compressible and incompressible flow. What differences do you notice in the equations?

3.14 For an incompressible flow, what two fluid properties affect density variation? What general equation relates these two properties to the density?

3.15 Explain the first law of thermodynamics.

3.16 Name the sources of energy that contribute to the energy equation.

3.17 Write an equation for the energy balance using the sources of energy defined in question 3.11 for the first law of thermodynamics.

3.18 Apply *Fourier's law of heat conduction* to obtain the heat flux in the x direction.

3.19 Write the equation that defines the substantial derivative for the transport of temperature in terms of the local acceleration derivative and the advection derivative of temperature and why?

3.20 If a car travels across a warmer environment, the car body will experience a sudden rise of temperature. Is this an example of the local *acceleration* derivative or *advection* derivative at work?

3.21 In what type of situation can you simplify the general 2-D energy equation $\frac{\partial T}{\partial t}+u\frac{\partial T}{\partial x}+v\frac{\partial T}{\partial y}=\frac{k}{\rho C_p}\frac{\partial^2 T}{\partial x^2}+\frac{k}{\rho C_p}\frac{\partial^2 T}{\partial y^2}$ to reach the well-known Laplace's equation $\frac{\partial^2 T}{\partial x^2}+\frac{\partial^2 T}{\partial y^2}=0$.

3.22 Obtain the general analytical solution for Laplace's equation for a one-dimensional case.

3.23 The Prandtl number is a ratio of two fluid properties. What are they?

3.24 Fluids such as oils have a high Prandtl number ($Pr \gg 1$). What does this suggest?

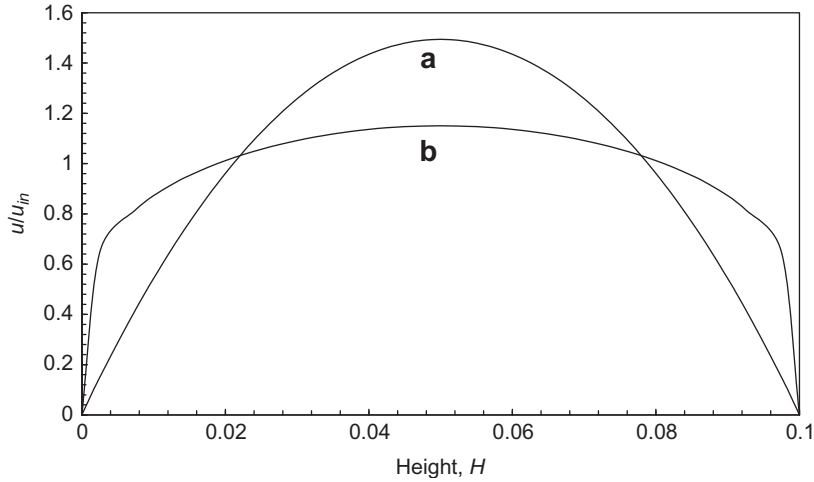
3.25 What is the significance of the Prandtl number equaling to 1 in terms of entry lengths.

3.26 What is the *energy cascade* process in turbulence?

3.27 Why do large eddies tend to be anisotropic in nature? Why are small-scaled eddies isotropic in nature?

3.28 The use of direct numerical simulation (DNS) remains a problem for engineering applications. Why?

3.29 Which profile as indicated below is the laminar or turbulent velocity profile?



3.30 From question 3.26, describe the shape of the turbulent velocity profile? Explain why the profile is so different from the laminar profile?

3.31 For incompressible flow, the nondimensional transport equation can be simplified as $u\dfrac{\partial u}{\partial x}=\dfrac{1}{Re}\dfrac{\partial^2 u}{\partial x^2}$. Provide an explanation why for a laminar flow, the diffusion term (the right-hand side of the equation) will be more dominant than the convective term (the left-hand side of the equation). At a highly turbulent flow, the situation is opposite, why?

3.32 Indicate the terms in the following general equation: $u\dfrac{\partial \phi}{\partial x}=\Gamma\dfrac{\partial^2 \phi}{\partial x^2}+S_\phi$.

3.33 The equation in question 3.29 represents a transport process for the property ϕ. Under what circumstances can this equation be applied?

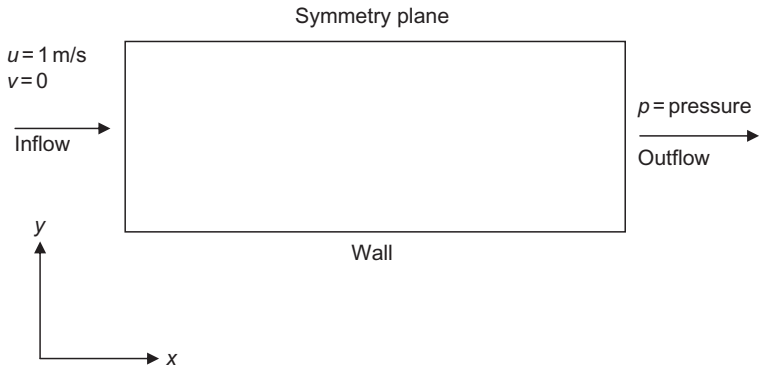
3.34 Spot the errors in the equation below. (Hint: It is a 3-D x-momentum equation.)

$$\frac{\partial u}{\partial t}+\frac{\partial(uu)}{\partial x}+\frac{\partial(vu)}{\partial x}+\frac{\partial(uu)}{\partial z}=\frac{\partial}{\partial x}[(\nu+\nu_T)\frac{\partial u}{\partial x}]+\frac{\partial}{\partial y}\left[(\nu+\nu_T)\frac{\partial u}{\partial x}\right]+$$
$$\frac{\partial}{\partial z}\left[(\nu+\nu_T)\frac{\partial u}{\partial x}\right]+\left(S_u=-\frac{1}{\rho}\frac{\partial p}{\partial x}+S_u'\right)$$

3.35 Referring to the diagram below, answer the following questions.

(a) At the wall, what is the value of u and v?

(b) At the symmetry plane, what is the value of u, v, and p?



Chapter 4

CFD Mesh Generation: A Practical Guideline

4.1 INTRODUCTION

Mesh or grid generation represents an important consideration in attaining the numerical solutions to the governing partial differential equations of the CFD problem. We would like to stress that the term grid or mesh is generally used interchangeably with identical meaning throughout this chapter. In Chapter 2, grid generation has been viewed as one of the key important considerations during the preprocess stage following the definition of a domain geometry. The aspect of grid generation is an important numerical issue where the specific mesh for a given flow problem can determine the *success* or *failure* in obtaining a computational solution. Principally, it must be fine enough to provide an adequate resolution in capturing the important flow features and geometrical structures. For flows with bounded walls, it is recommended that recirculation vortices or steep flow gradients within the viscous boundary layers are properly resolved through locally refining or clustering the mesh in the vicinity of wall boundaries. Mesh concentration may also be required for fluid flows having high shear and/or high-temperature gradients. Furthermore, the quality of the mesh has significant implications on the convergence and stability of the numerical simulation and accuracy of the computational result. These grid generation issues will be examined in this chapter.

What is a mesh in the context of CFD? By definition, a mesh in itself consists of an arrangement of discrete number of points overlaying the whole domain geometry. Through the subdivision of this domain, a number of smaller mesh or grid cells are thereby generated. It is therefore generally expected that the discretized domain is required to adequately resolve the important physics and to capture all the geometrical details of the domain within the flow region. Designing a suitable mesh is certainly by no means trivial. The quest to yield a well-constructed mesh deserves as much attention as prescribing the necessary physics to the flow problem. Because of this, grid generation, as it is commonly known by within the CFD community, has become a separate entity by itself and remains a very active area of research and development.

In retrospective, grid generation represents only a means to an end. It forms a necessary tool for the computational simulation of physical flow phenomena

Computational Fluid Dynamics. https://doi.org/10.1016/B978-0-08-101127-0.00004-0
© 2018 Elsevier Ltd. All rights reserved.

and processes. At the same time, grid generation can also be regarded as an art and a scientific requirement from a technological standpoint. Focusing on the discipline of mathematics, the role of mathematics provides a pathway for the essential foundation to move the grid generation process from a user-intensive craft or skill to an automated system. There are both art and science in the design of mathematics but unfortunately not for grid generation since there are no inherent conservation laws that can be utilized for the derivation of CFD governing equations described in Chapter 3. Therefore, grid generation is essentially not unique, but rather, it must be designed. In this chapter, some practical guidelines through proper illustrations will be provided for the design of suitable mesh systems that would be appropriate for CFD calculations.

Historically, early computing machines such as digital computers being limited in resources have focused mainly on CFD problems having regular domains. The use of rectangular Cartesian meshes has therefore been the preferred choice due to the adoption of a *discretization* approach such as the finite-difference method. In essence, such a rectangular lattice structure provides easy identification of neighbouring grid points. The derivatives of the partial differential equations of the CFD problem can be directly approximated via the use of these neighbouring grid points. Another form of a regular lattice that also promotes easy identification of neighbouring grid points especially in the ability of handling irregular domains is the curvilinear coordinate systems. Generally speaking, an orthogonal curvilinear system represents the special case of a rectangular Cartesian system. As a matter of fact, curvilinear coordinate system can be considered to be logically rectangular, and it is conceptually no different from the Cartesian coordinate system. For the consideration of domains that are nonetheless highly irregular, the nature of filling the domain by cells of general shapes has brought about the application of unstructured meshes. A network of such cells is made to purposefully fill any arbitrary shaped domains, and each of these cells represents an entity unto itself. With the advancement of digital computers, another *discretization* approach such as the finite-element method has been the nature of its construction of these general shaped cells. With regards to commonly encountered CFD problems, the finite-volume method is nonetheless the preferred *discretization* approach. The use of finite-volume method in the majority of currently developed commercial CFD codes stems basically from the conceptually identical representation of the control volume approach that has been considered for the derivation of the governing equations.

Grid generation process has certainly matured to the point where the use of commercial codes is generally recommended over the construction computer codes by end users performing computational simulation. We would like to draw the reader to many existing commercial CFD codes in the market having their own inbuilt powerful mesh generators, and there is also a choice of a number of independent grid generation packages such as GRIDGEN by Pointwise (www.pointwise.com) and GRIDPRO by Program Development Company (www.gridpro.com) for the reader's perusal. Although these independent grid

generation packages and the different inbuilt mesh generators in the commercial CFD codes have been designed to be very user-friendly and easy to utilize, the prerequisite to proficiently managing these software packages still relies on the reader's aptitude to operate them properly. In spite of this particular feature being available in commercial CFD codes or independent software packages, some understanding of the process of grid generation especially for the underlying principles, mathematics, and technology remains however relevant and important. It is from this standpoint that this chapter is geared towards a basic understanding of different types of mesh systems and how the reader can best adopt these different types of mesh systems to attain appropriate solutions for specific CFD problems being solved. At the very least, this chapter will serve to provide the reader with sufficient background knowledge and philosophy of grid generation in the prospect of handling more sophisticated flow configurations.

4.2 TYPES OF MESHES

4.2.1 Structured Mesh

Of all the techniques that currently exist for grid generation, the simplest is the creation of a structured mesh. For the purpose of illustration and a demonstration on how a mesh can be generated, let us consider a fluid flowing within a rectangular conduit. In the first instance, a uniformly distributed Cartesian mesh can be conveniently generated where the spacing of the grid points along the x direction is uniform and the spacing of the points along the y direction is also uniform such as illustrated in Fig. 4.1. An exploded view of a section of the discrete mesh in the x–y plane is also drawn to further demonstrate the arrangement of the discrete points within the domain. We would like the reader to pay attention to the regular-shaped four-nodal grid points of the rectangular element as described in Fig. 4.1.

In a two-dimensional structured mesh, the grid points are normally addressed by the indices (i, j) where the index i represents points that run in the x direction whilst the index j represents points that run in the y direction. If (i, j) are the indices for the point P, the neighbouring points immediately to the right, to the left, directly above, and directly below are defined by increasing or reducing one of the indices by unity. By allocating appropriate discrete values for Δx_i and Δy_j, the coordinates in the x direction and y direction inside the physical space can henceforth be incrementally determined, resulting in a rectangular mesh covering the whole domain.

For uniformly distributed grid points, the spacing of Δx_i or Δy_j is essentially a single representative value in the x direction or y direction. For nonuniformly distributed grid points, the spacing of Δx_i or Δy_j can however effectively take a number of discrete values; hence, we could have easily generated a mesh with totally unequal spacing in the x direction or y direction. For example, a finely

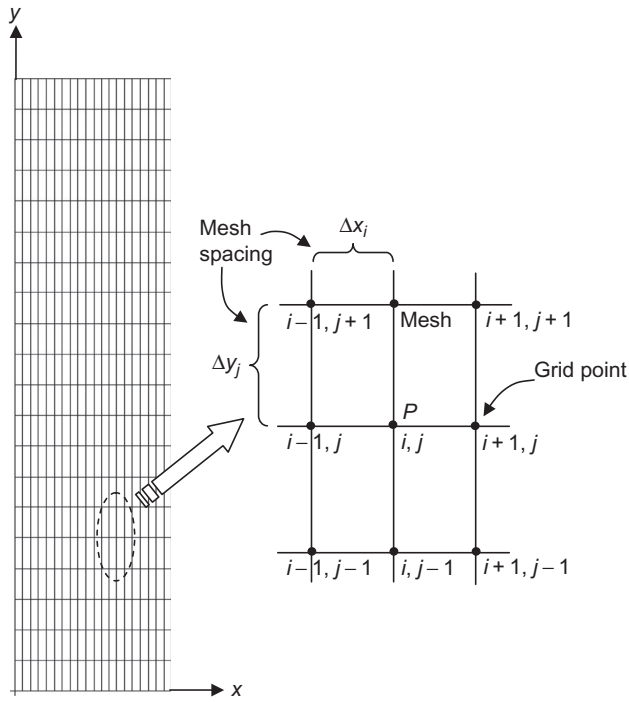


FIG. 4.1 A uniform rectangular mesh.

spaced mesh in the x direction can be generated to adequately resolve the viscous boundary layer of the flow in the vicinity of the wall geometry, whilst a uniformly spaced mesh is retained in the y direction as shown in Fig. 4.2. This particular arrangement is usually regarded as a 'stretched' or 'concentrated' mesh where the grid points could be considered of being *biased* towards the wall boundaries.

In three dimensions, any grid point in space can now be addressed by the indices (i, j, k) where the introduction of index k represents points that run in the z direction. The consideration of an additional dimension requires now the knowledge of the spacing of Δz_k in addition to the spacing of Δx_i and the spacing of Δy_j to construct the appropriate mesh covering the three-dimensional geometry.

4.2.2 Body-Fitted Mesh

Consider the following problem of a flow inside a 90° bend such as illustrated in Fig. 4.3. In order to apply an orthogonal mesh such as a structured mesh to the geometry, compromises are required to be made especially on the curved section through characterizing the boundaries through staircase-like steps.

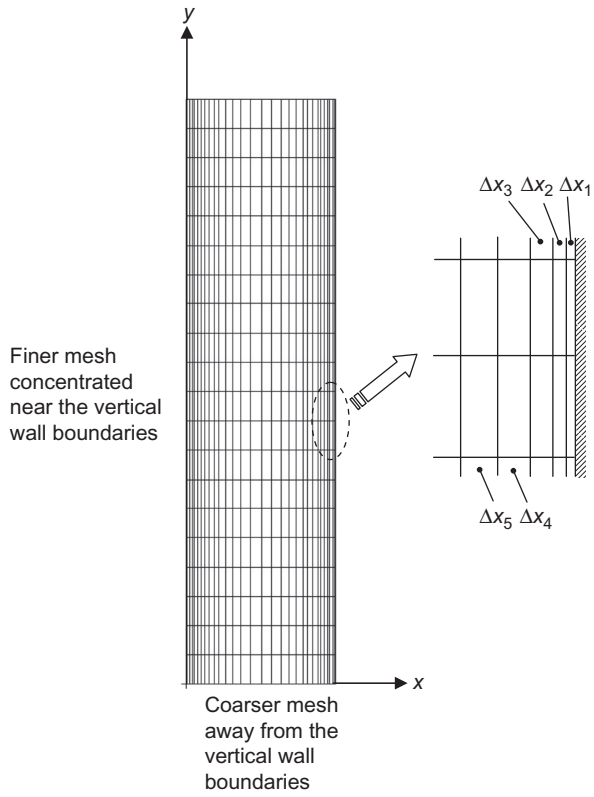


FIG. 4.2 A nonuniform rectangular mesh.

Nevertheless, such an approach raises two kinds of problems. Firstly, such an approximate boundary description is tedious and rather time-consuming to be set up. Secondly, the steps at the boundary may introduce errors in computations of the wall stresses, heat fluxes, boundary-layer effects, etc. The treatment of the boundary conditions at stepwise walls generally requires a fine Cartesian mesh to cover the wall regions, but the requirement of the highly regular structure of grid lines may cause further wastage of computer storage due to unnecessary refinement in interior regions that they are of minimal interest. This example clearly shows that mesh systems that are based on Cartesian coordinate systems have severe limitations in irregular geometries. It would therefore be more advantageous to work with meshes that can handle curvature and geometrical complexity more naturally.

When a body-fitted mesh is applied to the 90° bend geometry, let us alternatively consider that the walls coincide with lines of constant η (see Fig. 4.4). Location along the geometry, say from A to B or D to C, subsequently corresponds to specific values of ξ in the computational domain. Corresponding

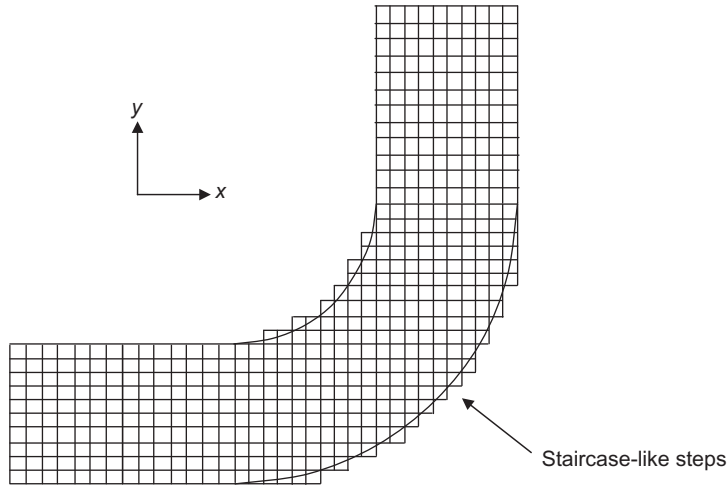


FIG. 4.3 An example of a mesh using staircase-like steps for the 90° bend geometry.

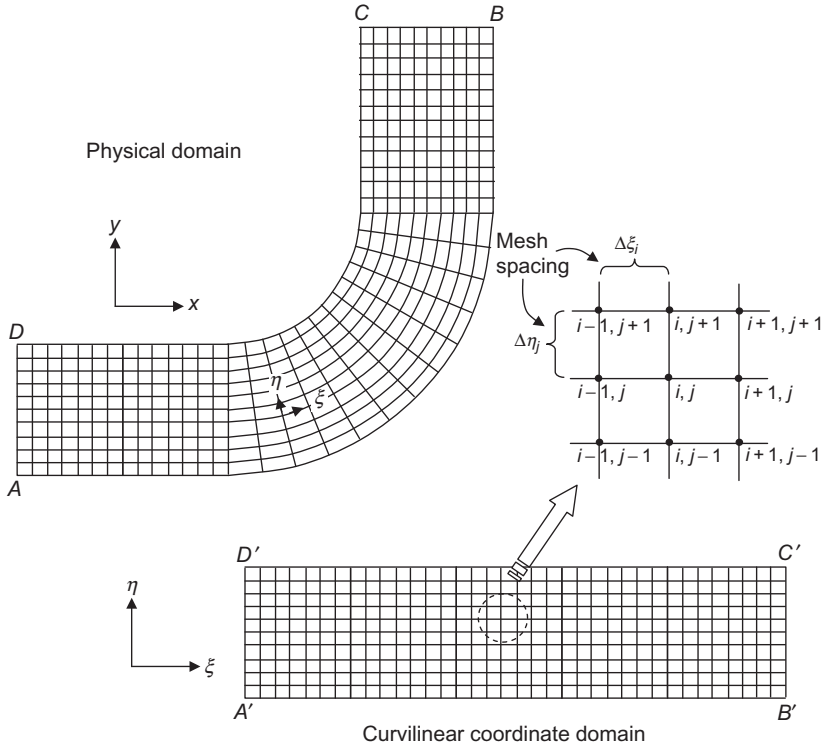


FIG. 4.4 An example of a body-fitted or curvilinear mesh for the 90° bend geometry and corresponding computational geometry.

points on AB and CD connected by a particular η line will have the same value of ξ_i but different η values. At a particular point (i, j) along this η line, $\xi = \xi_i$ and $\eta = \eta_j$. A corresponding point $x = x\,(\xi_i, \eta_j)$ and $y = y\,(\xi_i, \eta_j)$ in the computational domain exists in the physical domain.

In Fig. 4.4, the transformation of the 90° bend geometry should be defined such that there is a one-to-one correspondence between the rectangular mesh in the computational domain and the curvilinear mesh in the physical domain. The algebraic forms of the governing equations for the flow problems are carried out in the computational domain that has uniform spacing of $\Delta\xi$ and uniform spacing of $\Delta\eta$. Computed information is then directly fed back to the physical domain via a one-to-one correspondence of grid points. Because of the need to solve the equations in the computational domain, the governing equations are required to be expressed in terms of the curvilinear coordinates rather than the Cartesian coordinates, which means that they must be transformed from (x, y) to (ξ, η) as the new independent variables.

The mesh construction of the internal region of the 90° bend geometry can normally be achieved via two approaches. On one hand, the Cartesian coordinates may be algebraically determined through interpolation from the boundary values. This methodology requires no iterative procedure, and it is computationally inexpensive. On the other hand, a system of partial differential equations of the respective Cartesian coordinates may be solved numerically with the set of boundary values as boundary conditions in order to yield a highly smooth mesh in the physical domain. The former is commonly known as the transfinite interpolation method, and the latter is typically the elliptic grid generation method (Smith, 1982; Thompson et al., 1982).

The method of transfinite interpolation according to Gordon and Thiel (1982) consists of generating the interior mesh from the boundary grid data using appropriate interpolation functions or 'blending' functions. In multiple dimensions, the method can be easily developed by merely extending the one-dimensional interpolation function. Defining the position vector $\mathbf{r} \equiv (x, y)$, one-dimensional interpolation between two boundaries on a varying index i can be expressed as

$$\mathbf{r}_{i,j} = f_i \mathbf{r}_{1,j} + (1 - f_i)\mathbf{r}_{I,j} \tag{4.1}$$

where f_i varies monotonically from $f_1 = 0$ to $f_I = 1$ for $i = 1, 2, \ldots, I$. Analogous expressions involving function g_j applies for the interpolation in the j direction for $j = 1, 2, \ldots, J$. The interpolation operation given by Eq. (4.1) can be defined as the 'projector' P^i, that is,

$$\mathbf{r}_{i,j} = P^i = f_i \mathbf{r}_{1,j} + (1 - f_i)\mathbf{r}_{I,j} \tag{4.2}$$

Based on Eq. (4.2), two-dimensional transfinite interpolation can be effectively provided by the following relationship:

$$\mathbf{r}_{i,j} = P^i + P^j - P^i P^j \tag{4.3}$$

where

$$P^iP^j = f_i g_j \mathbf{r}_{I,J} + f_i\left(1-g_j\right)\mathbf{r}_{I,1} + (1-f_i)g_j\mathbf{r}_{1,J} + (1-f_i)\left(1-g_j\right)\mathbf{r}_{1,1} \tag{4.4}$$

For simplicity, the blending functions f_i and g_j may be taken to be linear: $f_i = (i-1)/(I-1)$ and $g_j = (j-1)/(J-1)$. They may also be formulated with added complexity to concentrate more grid nodal points near the boundaries of the physical domain or to include the specification of derivative boundary conditions to force the grid lines to intersect the boundaries orthogonally of the physical domain. On the latter aspect, the method of transfinite interpolation based on Hermite interpolation by Shih et al. (1995), which allows specification of derivatives at the end points of curves, has shown to generate high-quality meshes where the orthogonality of the grid lines intersecting the boundaries can be appropriately realized.

For the elliptic grid generation method, the interior mesh can be constructed via the numerical evaluation of the Poisson equation that can be written in the form

$$\frac{\partial^2\xi}{\partial x^2} + \frac{\partial^2\xi}{\partial y^2} = P(\xi,\eta) \tag{4.5}$$

$$\frac{\partial^2\eta}{\partial x^2} + \frac{\partial^2\eta}{\partial y^2} = Q(\xi,\eta) \tag{4.6}$$

where P and Q are functions that are generally unknown at the beginning of the grid generation procedure. They can be either specified externally or determined from the boundary-point distributions to control the spacing and orientation of the grid lines. If the functions of P and Q are set to zero, Eqs (4.5) and (4.6) reduce to the homogeneous Laplace equation. It can be readily shown by calculus of variations that a mesh generated as the solution of the Laplace equation is the smoothest possible mesh that can be attained. The actual solution of Eqs (4.5) and (4.6) needs however to be performed in the computational domain of which the roles of x and y are required to be switched as the dependent variables whilst ξ and η as the independent variables. Hence, the partial differential equations are transformed in this domain to

$$\alpha\frac{\partial^2 x}{\partial\xi^2} - 2\beta\frac{\partial^2 x}{\partial\xi\partial\eta} + \gamma\frac{\partial^2 x}{\partial\eta^2} + \alpha P(\xi,\eta)\frac{\partial x}{\partial\xi} + \gamma Q(\xi,\eta)\frac{\partial x}{\partial\eta} = 0 \tag{4.7}$$

$$\alpha\frac{\partial^2 y}{\partial\xi^2} - 2\beta\frac{\partial^2 y}{\partial\xi\partial\eta} + \gamma\frac{\partial^2 y}{\partial\eta^2} + \alpha P(\xi,\eta)\frac{\partial y}{\partial\xi} + \gamma Q(\xi,\eta)\frac{\partial y}{\partial\eta} = 0 \tag{4.8}$$

where

$$\alpha = \left(\frac{\partial x}{\partial\eta}\right)^2 + \left(\frac{\partial y}{\partial\eta}\right)^2,$$

$$\beta = \left(\frac{\partial x}{\partial \xi}\right)\left(\frac{\partial x}{\partial \eta}\right) + \left(\frac{\partial y}{\partial \xi}\right)\left(\frac{\partial y}{\partial \eta}\right),$$

$$\gamma = \left(\frac{\partial x}{\partial \xi}\right)^2 + \left(\frac{\partial y}{\partial \xi}\right)^2$$

Eqs (4.3) and (4.4) are merely elliptic partial differential equations with ξ and η as independent variables and x and y as dependent variables (Thompson et al., 1982). Bear in mind that Eqs (4.3), (4.7), and (4.8) have *nothing* to with the *physics* of the flow field. They are just simply algebraic and elliptic partial differential equations that ξ and η have been chosen to relate to x and y. This constitutes a transformation from the physical to the computational domain—a one-to-one correspondence of grid nodal points.

4.2.3 Unstructured Mesh

In addition to the use of a body-fitted mesh, an unstructured mesh could be constructed to fill the interior region of the 90° bend geometry (see Fig. 4.5). In the figure shown, there appears to be no regularity to the arrangement of the cells in the overlay mesh. Herein, the cells are totally unstructured oriented, and there are no coordinate lines that correspond to the curvilinear directions ξ and η such as in a body-fitted mesh. Maximum flexibility is thus allowed in matching the cells especially with highly curved boundaries, and required cells can be purposefully inserted to resolve the flow regions where they matter most such as in areas of high gradients. Triangle and tetrahedral meshing are by far the most common forms of unstructured grid generation.

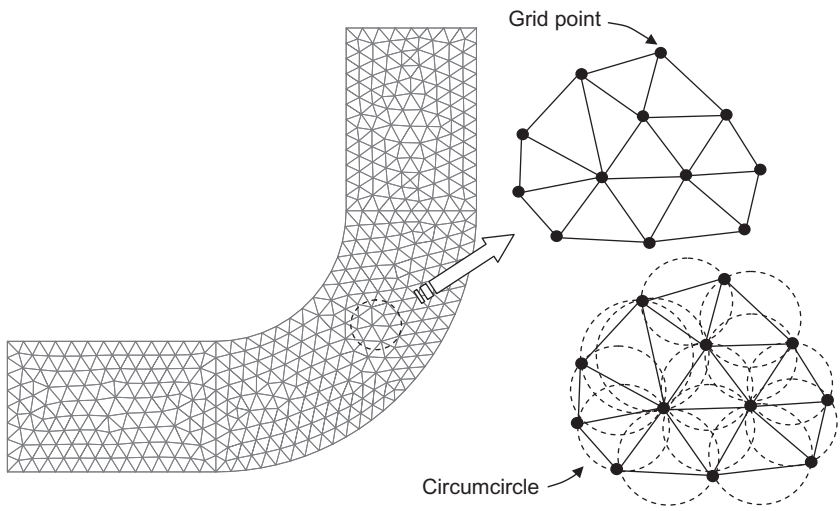


FIG. 4.5 An example of a triangular mesh for the 90° bend geometry.

As depicted in Fig. 4.5, the initial set of boundary nodes of the geometry can be effectively triangulated according to the Delaunay triangulation criterion. Here, the most important property of a Delaunay triangulation is that it has the *empty circumcircle* (*circumscribing circle*) *property* (Shewchuk, 2002). By definition, the circumcircle of a triangle is the unique triangle that passes through its three vertices. The Delaunay triangulation of a set of vertices can therefore be regarded as the triangulation (usually, but not always, unique) in which every triangle has an empty circumcircle—meaning that the circle encloses no vertex of the triangulation. It can be shown that the circumcircle of every Delaunay triangle of the mesh generated for the 90° bend geometry is empty. All algorithms for computing Delaunay triangulations rely on the fast operations for detecting when a grid point is within a triangle's circumcircle and an efficient data structure for storing triangles and edges. The most straightforward way of computing the Delaunay triangulation is to repeatedly add one vertex at a time, then retriangulating the affected parts thereafter. When a vertex is added, a search is done for all triangles' circumcircles containing the vertex. Then, those triangles are removed whose circumcircles contain the newly inserted point. All new triangulation is then formed by joining the new point to all boundary vertices of the cavity created by the previous removal of intersected triangles. Delaunay triangulation techniques based on point insertion extend naturally to three dimensions by considering the *circumsphere* (*circumscribing sphere*) associated with a tetrahedron. In hindsight, the Delaunay method is normally more efficient than the advancing-front method owing to the simplicity of the algorithm. The reader is strongly encouraged to refer to an excellent review paper by Mavriplis (1997) and a book by de Berg et al. (2000) for a more thorough understanding on the basic concepts of Delaunay triangulation and meshing.

Relying on Delaunay triangulation alone does not however resolve the many extensive problems concerning the application of generating an unstructured mesh. In particular, Delaunay method tends to maximize the minimum angle of the triangle, but the angle may be too small and might not conform to the domain boundaries. The obvious solution is to add more vertices, but the question remains, 'where should they be inserted?' This has brought about much concerted developments of a number of Delaunay refinement algorithms. For the particular refinement algorithm proposed by Chew (1989), the order of insertion that is based on the minimum angle of any triangle proceeds until the minimum angle is greater than the predefined minimum ($\approx 30°$). Such an approach has shown to yield high-quality meshes, albeit without any guarantees of grading or size optimality. The problem was rectified by Ruppert (1993) where an algorithm was introduced to produce a mesh with good grading and size optimality.

Other meshing algorithms in unstructured grid generation have also been introduced including the advancing-front method (Lo, 1985; Gumbert et al., 1989; Marcum and Weatherill, 1985) and quadtree/octree method (Yerry and Shepard, 1984; Shepard and Georges, 1991).

The main idea of the advancing-front method is to generate an unstructured mesh through the adding of individual elements one at a time to an existing front of generated elements. Once the boundary nodes are generated, these edges form the initial front that is to be advanced out into the field. Triangular cells are formed on each line segment, and, in turn, these cells create more line segments on the front. The front thus constitutes a stack, and edges are continuously added to or removed from the stack. The process terminates when the stack is empty, which is when all fronts have merged upon each other and the domain is entirely covered. For three-dimensional grid generation, a surface grid is first constructed by generating a two-dimensional triangular mesh on the surface boundaries of the domain. This mesh forms the initial front, which is then advanced into the physical space by placing new points ahead of the front and forming tetrahedral elements. The required intersection checking now involves triangular front faces rather than edges as in the two-dimensional case.

Alternatively, quadtree/octree method involves the generation of an unstructured mesh through a recursive subdivision of the physical space down to a prescribed (spatially varying) resolution. The vertices of the resulting quadtree or octree structure are used as grid points, and the tree quadrants or octants are divided up into triangular or tetrahedral elements, in two or three dimensions, respectively. It should however be mentioned that the quadtree/octree cells intersecting the boundary surfaces and the vertices at boundaries must somehow be required to be displaced or wrapped in order to coincide with the boundary. The method is relatively simple and inexpensive and produces good quality mesh in interior regions of the domain. One drawback of the method is that it has a tendency of generating an irregular cell distribution near boundaries.

Another unstructured mesh system that is graining significant interest in CFD calculations is the employment of a mesh containing *polyhedral* cells. A polyhedral mesh can be created by combining tetrahedral cells into polyhedral ones. Considering the tetrahedral mesh that has been generated for the 90° bend geometry in Fig. 4.5, a polyhedral mesh such as shown in Fig. 4.6 can be created via cell agglomeration, which results in a considerable reduction of the overall cell count. More importantly, cell agglomeration has the capacity of improving the original mesh by converting particular regions with highly skewed tetrahedral cells to polyhedral, thereby improving mesh quality. The use of a polyhedral mesh also leads to quicker convergence of the numerical solution. A clear potential benefit of applying polyhedral mesh is that it allows the flexibility of an unstructured mesh to be applied to a complex geometry without the computational overheads associated with a large tetrahedral mesh. The application of polyhedral meshing is gaining significant traction in the computational fluid dynamics community. Polyhedral meshing has been shown thus far to have considerable advantages over tetrahedral meshing with regards to the attained accuracy and efficiency of numerical computations.

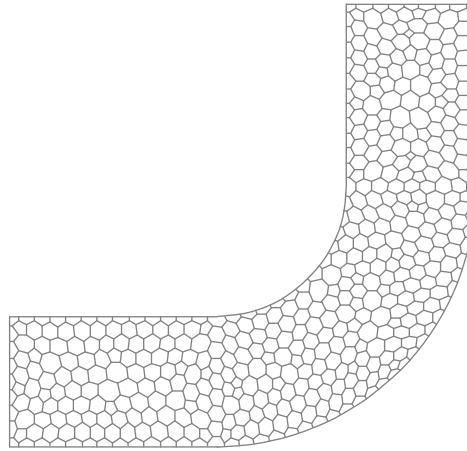


FIG. 4.6 A grid consisting of polyhedral cells of the 90° bend geometry.

4.3 COMMENTS ON MESH TOPOLOGY

Application of a *structured* mesh in any aspect of grid generation has certain advantages and disadvantages. The advantage of such a mesh is that the points of an elemental cell can be easily addressed by a double of indices (i, j) in two dimensions or a triple of indices (i, j, k) in three dimensions. The connectivity is straightforward because cells adjacent to a given elemental face are identified by the indices and the cell edges form continuous mesh lines that begin and end on opposite elemental faces as illustrated in Fig. 4.7. In two dimensions, the central cell is connected by four neighbouring cells. In three dimensions, the central cell is connected by six neighbouring cells. It also allows easy data management, and connectivity occurs in a regular fashion, which makes programming easy. Nevertheless, the reader should note that the disadvantage of adopting such a mesh particularly for more complex geometries is the increase in grid nonorthogonality or skewness that can cause unphysical solutions due to the transformation of the governing equations. The transformed equations that accommodate the nonorthogonality acts as the link between the structured coordinate system (such as Cartesian coordinates) and the body-fitted coordinate system and contains additional terms, thereby augmenting the cost of numerical calculations and difficulties in programming. Because of this, such a mesh may also affect the accuracy and efficiency of the numerical algorithm that is being applied.

One special case on the cleverly use of a *structured* mesh is the adoption of block-structured or multiblock meshes. Through this approach, the mesh of the domain in question is now assembled from a number of structured blocks being attached to one another. Here, the attachments of each face of adjacent blocks may be regular (i.e. having matching cell faces) or arbitrary (i.e. having nonmatching cell interfaces) as exemplified in Fig. 4.8. Generation of grids

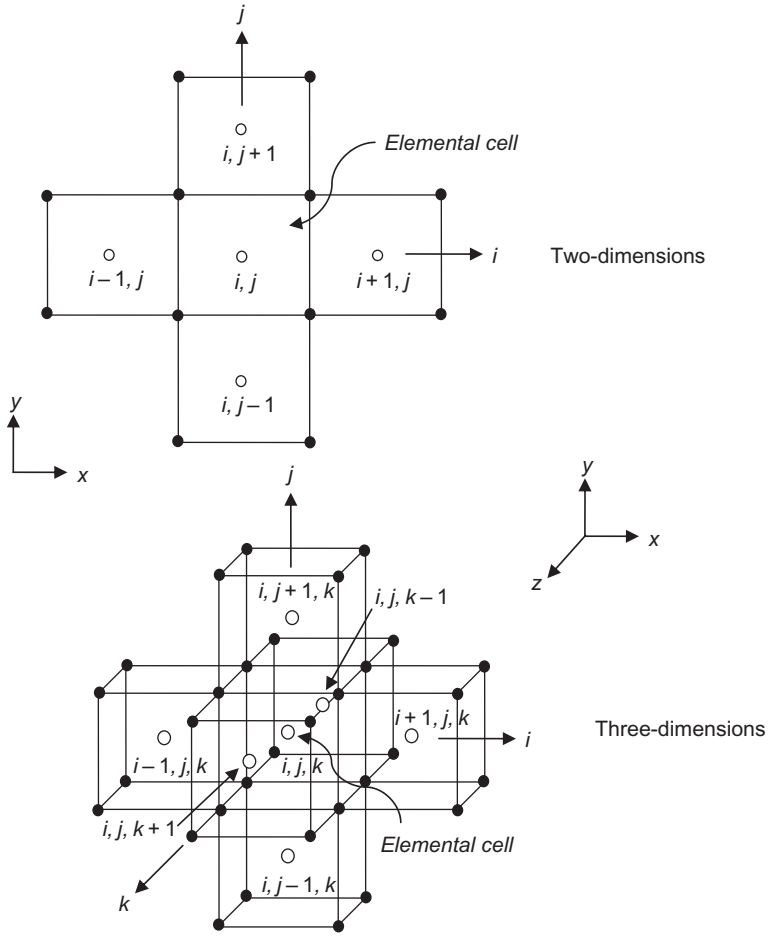


FIG. 4.7 Nodal indexing of elemental cells in two and three dimensions for a structured mesh.

especially with nonmatching cell interfaces is certainly much simpler than the creation of a single-block mesh fitted to the whole domain and to circumvent the increase in grid nonorthogonality or skewness of the grid cells. Such an approach offers great flexibility in determining the best grid topology for each of the subdivided blocks. The reader may select appropriate grid topology based on structured H-, O-, or C-grid, to fill each block. Fig. 4.9 presents an example of an H-grid designed for the flow calculation in a symmetry segment of a staggered tube bank. It is also possible to remove the highly skewed cells for a circular cylinder through the use of an O-grid as exemplified in Fig. 4.10.

On the other hand, the use of an *unstructured* mesh has become more prevalent and widespread in many CFD applications. Majority of commercial codes nowadays are based on the use of *unstructured* meshing whereby the cells are

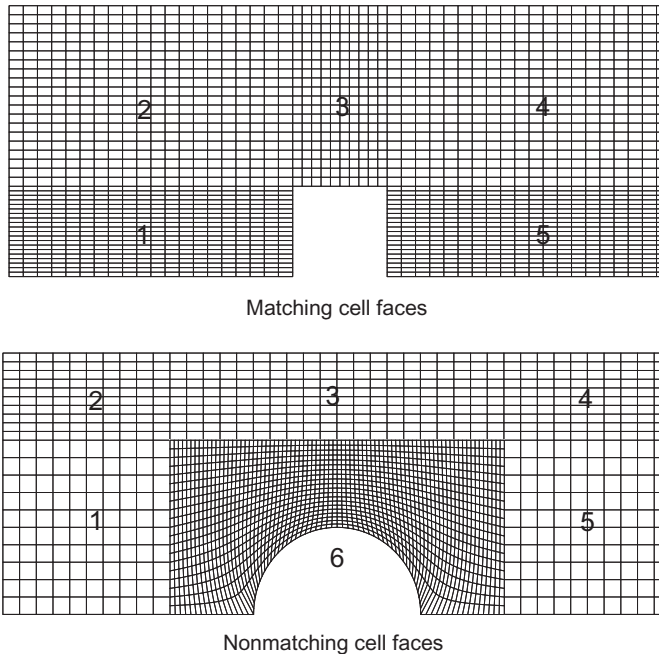


FIG. 4.8 Multiblock-structured mesh with matching and nonmatching cell faces.

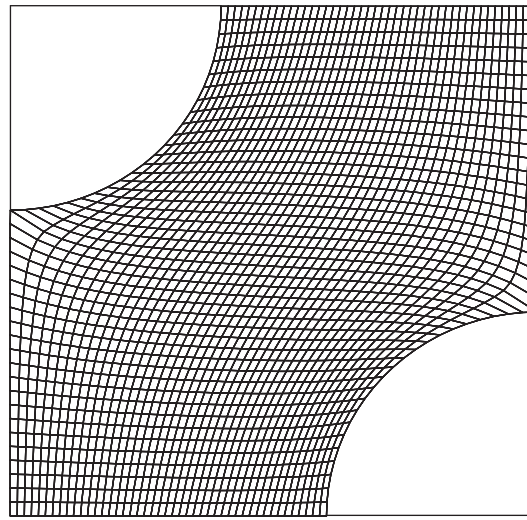


FIG. 4.9 The generation of a structured H-grid for the flow calculation in a symmetry segment of a staggered tube bank.

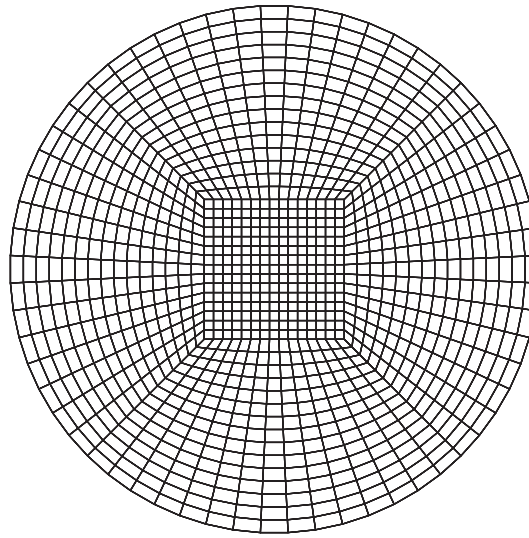


FIG. 4.10 The generation of a structured O-grid for a circular cylinder.

allowed to be assembled freely within the computational domain. The connectivity information for each face thus requires appropriate storage in some form of a table. The most typical shape of an *unstructured* element is a triangle in two dimensions or a tetrahedron in three dimensions. Nevertheless, any other elemental shape including quadrilateral or hexahedral cells is also possible. *Unstructured* meshes are certainly well suited for handling arbitrary shape geometries especially for domains having high-curvature boundaries. Fig. 4.11 illustrates the interior of a circular cylinder that has been filled by the overlaying of *structured* and *unstructured* meshes. For such a geometrical feature, the *structured* body-fitted nonorthogonal grid has a tendency to generate highly skewed cells at the four vertices as indicated in Fig. 4.11, since the interior of the domain must be built to satisfy the geometrical constraints imposed by the domain boundary. This type of mesh generally leads to numerical instabilities and deterioration of the computational results. It may have been more preferable to remesh the geometry with an *unstructured* triangular mesh (see Fig. 4.11).

In spite of the favourable features of *unstructured* meshing, the reader should be aware of a number of disadvantages that exist with the employment of such a mesh for CFD simulations. In comparison with *structured* mesh, the points of an elemental cell for an *unstructured* mesh generally cannot be simply treated or addressed by a double of indices (i, j) in two dimensions or a triple of indices (i, j, k) in three dimensions. An elemental cell may have an arbitrary number of neighbouring cells attaching to it making the data treatment and connection arduously complicated. More importantly, triangular (two-dimensional) or tetrahedral (three-dimensional) cells in comparison with quadrilateral

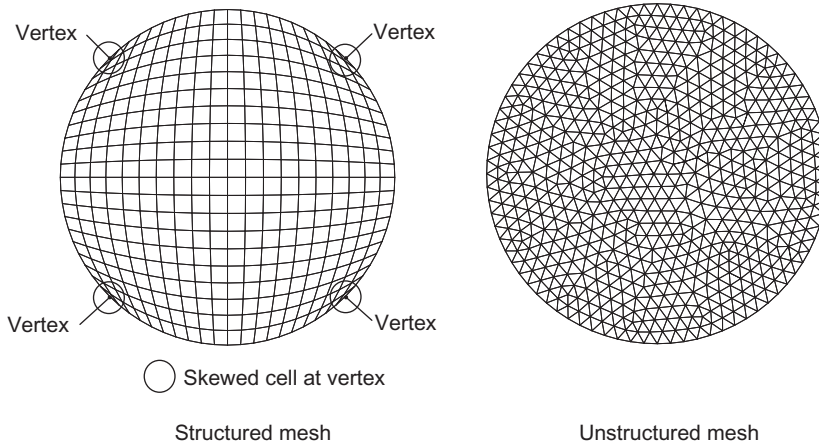


FIG. 4.11 A structured and an unstructured mesh for a circular cylinder.

(two-dimensional) or hexahedral (three-dimensional) cells are usually ineffective to resolve wall boundary layers. In most cases, the grid yields very long thin triangular or tetrahedral cells adjacent to the wall boundaries, thereby creating major problems in the approximation of the diffusive fluxes. Another disadvantage in connection with data treatment and connectivity of elemental cells is the requirement of more complex solution algorithms to solve the flow-field variables. This may result in increased computational times to obtain a solution and erode the gains in computational efficiency.

The use of hybrid grids that combine different element types such as triangular and quadrilateral in two dimensions or tetrahedra, hexahedra, prisms, and pyramids in three dimensions can provide maximum flexibility in matching mesh cells with the boundary surfaces and allocating cells of various element types in other parts of the complex flow regions. As a common practice, grid quality is usually enhanced through the placement of quadrilateral or hexahedral elements in resolving boundary layers near solid walls, whilst triangular or tetrahedral elements or polyhedral cells such as exemplified in Fig. 4.6 are generated for the rest of the flow domain. This generally leads to both accurate solutions and better convergence for the numerical solution methods. Fig. 4.12 illustrates an example of a mesh consisting of quadrilateral elements near the walls and triangular elements for the rest of the flow domain. Note again that the idea of a 'stretched' mesh as previously considered for the rectangular conduit in Fig. 4.2 has been constructed in the vicinity of the wall boundaries for the 90° bend geometry.

4.4 LOCAL MESH REFINEMENT

One local mesh refinement technique that is widely used in many CFD applications is the concept of a stretched grid in the near vicinity of domain walls.

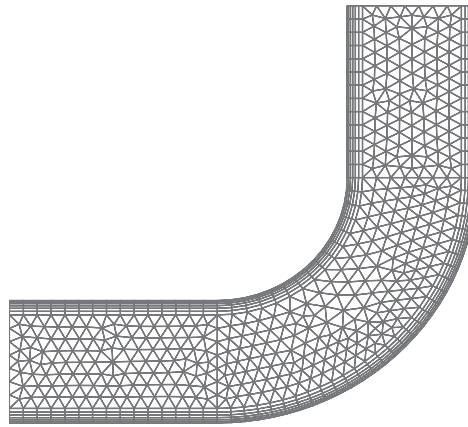


FIG. 4.12 A grid consisting of structured quadrilateral elements near the walls and unstructured triangular elements in the remaining part of the 90° bend geometry.

For a viscous flow bounded with solid boundaries, the need to cluster a large number of small cells within the physical boundary layer is more than just attempting to minimize the truncation error with the closely spaced grid points. Rather, it is a matter of utter importance that the actual flow physics is appropriately encapsulated.

Let us revisit the case for the fluid flowing between two stationary parallel plates as investigated in previous chapters. In a real physical flow, the existence of a developing boundary layer will grow in thickness as the fluid enters the left boundary and migrates downstream along the bottom wall of the domain such as illustrated in Fig. 4.13. By denoting the local thickness of the boundary layer as δ, where $\delta = \delta\ (x)$, it is evidently clear that the use of a coarse uniform mesh misses the physical boundary layer. The predicted *viscous-like* velocity profile shown at some point downstream in the fully developed region is simply due to the application of the no-slip boundary condition at the bottom wall. In contrast, the coarse stretched grid at the very least captures some of the essential features of the actual physical boundary layer. It is therefore not surprising that the accuracy of the computational solution is greatly influenced by the grid distribution inside the boundary layer region. We can further investigate this by imposing the concept of *consistency* to be discussed in Chapter 5 for the incompressible mass conservation in two dimensions where the truncation error yields the following:

$$\frac{\Delta x^2}{6}\frac{\partial^3 u}{\partial x^3} + \frac{\Delta y^3}{6}\frac{\partial^3 v}{\partial y^3} \tag{4.9}$$

If the solution error is expected to follow the truncation error, it is imperative that the grid needs to be appropriately refined in order to sufficiently resolve the

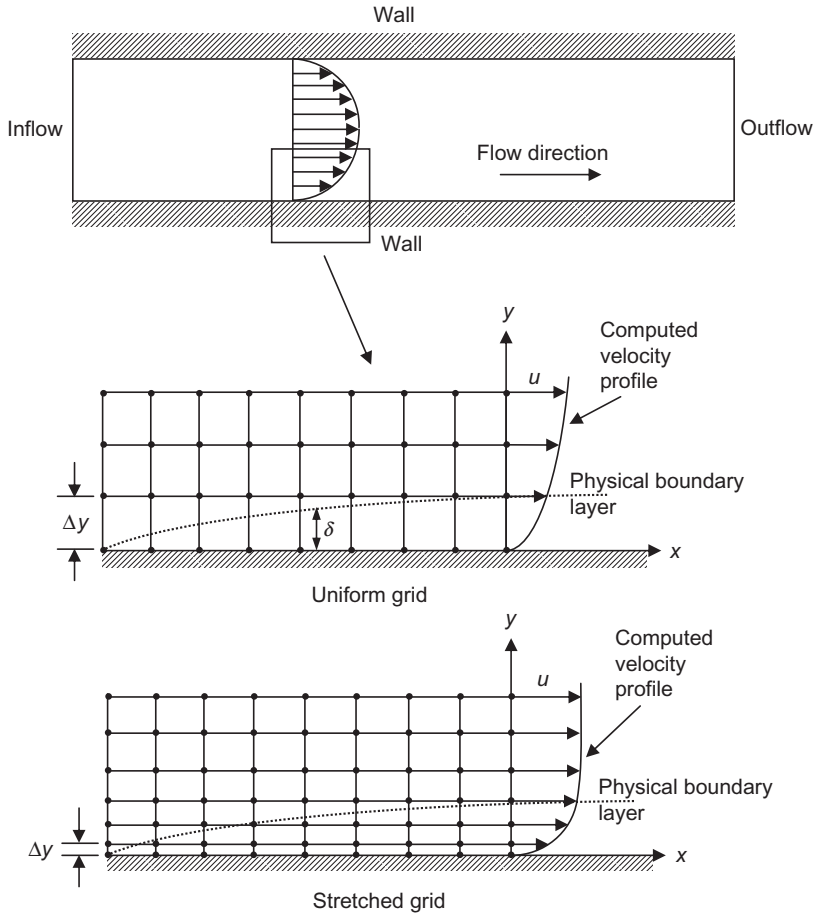


FIG. 4.13 Two schematic illustrations demonstrating the need for local refinement in the near vicinity of the bottom wall to resolve the physical boundary layer.

steep gradient of the velocity profile that exists within this region. This will help to minimize the solution error associated with the truncation error.

Local mesh refinement is also important to better resolve specific fluid dynamics problems such as upward stagnation flow and the backward-facing step geometry. The latter is one of the basic geometries used commonly in many engineering applications to better understand the phenomena of flow separation, flow reattachment, and free shear jet. The placement of stretched grids along both the horizontal and vertical directions to encapsulate the essential feature of the recirculation vortex is illustrated in Fig. 4.14.

Whilst applying the stretched grid described above, one useful consideration is to exercise care in avoiding sudden changes of the grid size away from the

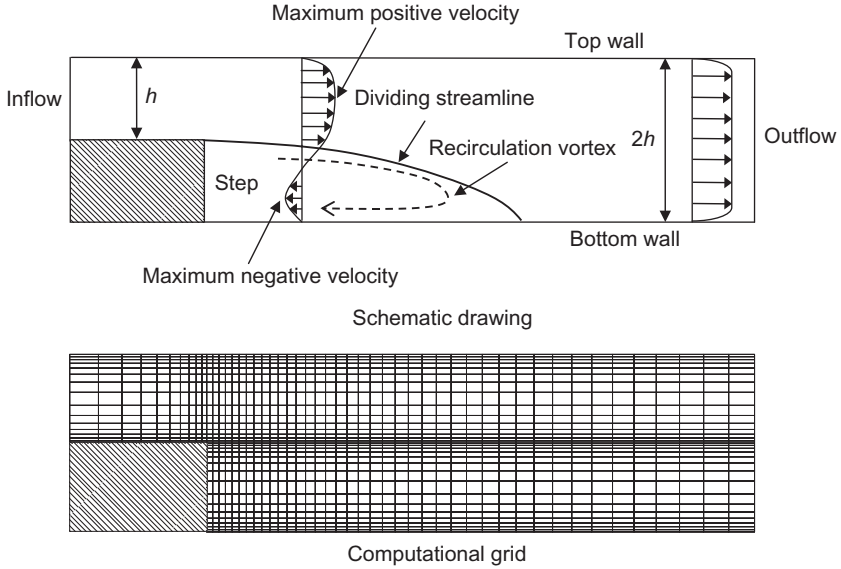


FIG. 4.14 A schematic drawing for the backward-facing step geometry and the computational grid to capture the essential feature of the recirculation vortex.

domain boundary. The mesh spacing should be continuous, and grid-size discontinuities should be removed as much as possible in regions of large flow changes, particularly when dealing with multiblock meshing of arbitrary mesh coupling, nonmatching cell faces, or extended changes of element types. Discontinuity in the grid size destabilizes the numerical procedure due to the accumulation of truncation errors in the critical flow regions. These errors usually contain the diffusive terms (second-order derivatives) where the discretization imposed on these derivatives requires very smooth grid changes. Making sure that the grid changes slowly and smoothly away from the domain boundary and within the domain interior will assist in overcoming divergence tendencies of the numerical calculations. It is also worthwhile noting that most inbuilt mesh generators in commercial codes and independent grid generation packages have the means of prescribing suitable mesh stretching or expansion ratios (rates of change of cell size for adjacent cells). The specification of these ratios should always be negotiated within the codes' requirements whilst generating the appropriate stretched grid.

By the mere construction of a stretched grid, the local refinement technique provides the possibilities of allocating additional grid nodal points to resolve the important fluid flow action and reducing or removing the grid nodal points from other regions where there is little or no action. Nevertheless, it should be noted that a stretched grid is an algebraically generated grid prescribed prior to the solution of the flow field being calculated. The question that needs to be carefully addressed is whether the generated stretched grid sufficiently captures the

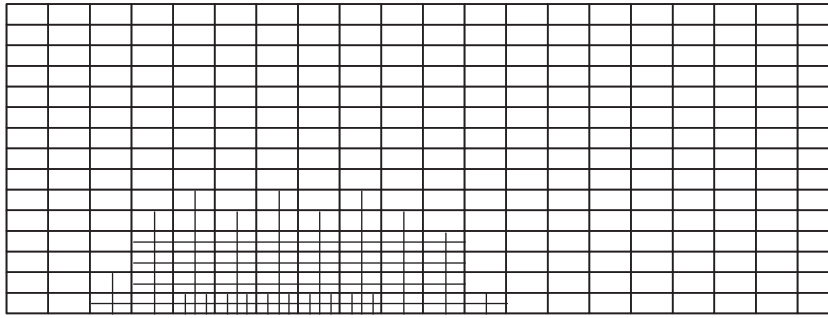


FIG. 4.15 An embedded Cartesian mesh without matching cell faces near the bottom boundary.

major fluid flow action or whether the real flow action is far away from the intended significant flow activity to be resolved by the generated stretched grid region that is not known a priori.

In the event where specific interest on the finer details of the local flow physics are required to be predicted, the use of embedded meshes can also be adopted. Here, such meshes do not necessarily have to be constrained to have matching cell faces. Fig. 4.15 illustrates an example of embedded Cartesian mesh without matching cell faces near the bottom boundary for the rectangular-type geometry. We can view this type of mesh as a special case of a local mesh refinement strategy. It is noted that the locally refined region in Fig. 4.15 could also have been achieved through the use of other types of elements such as triangular or polyhedral elements or a combination of different types of elements.

4.5 OVERLAPPING MESH TECHNIQUES

Instead of block-structured mesh where the attachment of a number of adjacent blocks is realized at block boundaries, the use of overlapping grids to cover the irregular flow domains further presents another grid generation approach in handling complex geometries. Here, rectangular, cylindrical, spherical, or non-orthogonal grids can be combined with the parent Cartesian grids in the solution domain. An example of an overlapping grid for a cylinder in a channel with inlet–outlet mappings is shown in Fig. 4.16. This approach is attractive because the structured mesh blocks can be placed freely in the domain to fit any geometrical boundary whilst satisfying the essential resolution requirements. Information between the different grids is achieved through the interpolation process. Block-structured grids with overlapping blocks are sometimes referred as *Chimera* grids. The advantages of employing such grids are that complex domains are treated with ease and they can especially be employed to follow moving bodies in stagnant surroundings. Some examples can be found in Tu and Fuchs (1992) and Hubbard and Chen (1994, 1995). The disadvantages

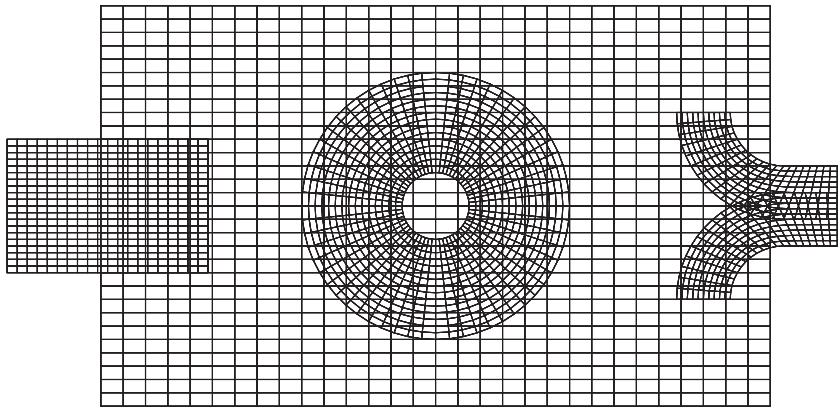


FIG. 4.16 A structured overlapping grid for a cylinder in a channel with inlet–outlet mappings.

of these grids are that conservation is usually not maintained or enforced at block boundaries, and the interpolation process may introduce errors or convergence problems if the solution exhibits strong variation near the interface.

4.6 ADAPTIVE MESH WITH SOLUTION

Solution adaptation through the use of an adaptive mesh is a grid network that automatically or dynamically clusters the grid points in regions where large gradients exist in the flow field. It therefore employs the solution of the flow properties to locate the grid points in the physical flow domain. During the course of the solution, the grid points in the physical flow domain *migrate* in such a manner as to *adapt* to the evolution of the large flow gradients or discontinuities. Hence, the actual grid points are constantly in motion during the solution of the flow field and become stationary when the flow solution approaches some quasi steady-state condition. An adaptive mesh is therefore intimately linked to the flow-field solution and alters as the flow field develops unlike the stretched grid described in the previous section where the grid generation is completely separate from the flow-field solution. For this purpose, unstructured meshes are well suited especially in automating the generation of elements such as triangular or tetrahedral meshes of various sizes to solve the critical flow regions. If a solution method can be applied on an unstructured mesh with cells of varying topology, the adaptive mesh is thus subjected to fewer constraints

Adaptive gridding techniques can generally be categorized into two broad classes: adaptive mesh redistribution and adaptive mesh refinement. Techniques for adaptive mesh redistribution continuously reposition a fixed number of cells so that they improve the resolution in particular locations of the fluid flow domain. Techniques for adaptive mesh refinement add new cells as required and delete other cells that are no longer required. A sample illustration

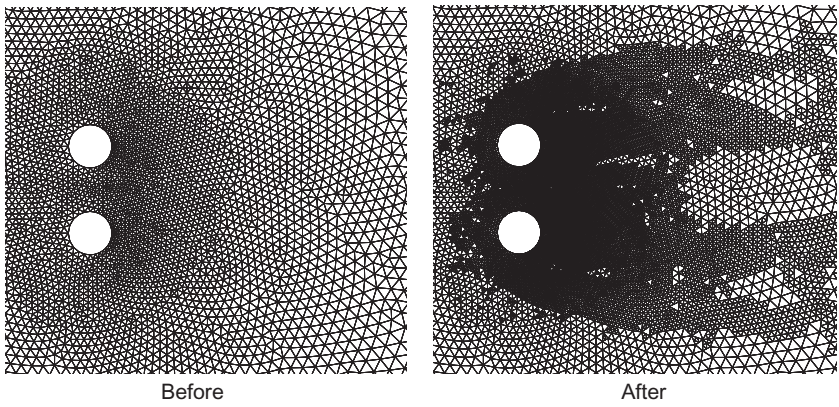


FIG. 4.17 A demonstration of solution adaptation through the use of triangular meshes for the fluid flowing over two cylinders.

of solution adaptation via adaptive mesh refinement for the fluid flowing over two cylinders investigated in Chapter 2 is given in Fig. 4.17. For this particular flow problem, the wake region has been further resolved to capture the essential formation and shedding of vortices behind the two cylinders using triangular elements. Adaptive mesh refinement by further subdividing the cells into smaller ones can also be made possible whereby a nonrefined neighbouring cell, although it retains its original shape, becomes a *polyhedron* since its cell face is now replaced by a set of subfaces. An adaptive mesh with *polyhedral* elements certainly offers many challenges and potential prospects in CFD. Most commercial codes nowadays offer some form of automated techniques for solution adaptation.

4.7 MOVING MESHES

The solution adaption via adaptive mesh redistribution is described herein. In the context of finite volumes and fixed number of grid points, this particular solution adaption is alternatively known as moving meshes. A requirement of this solution adaption approach is to generate a suitable mapping from a regular domain in computational space whereby the discretized equations are solved to predict the physical processes occurring in an irregularly shaped domain in physical space. Three key ingredients are described in the following.

The first ingredient is the use of mesh equations. Principally, they determine a one-to-one mapping from a regular domain in the computational space to an irregularly shaped domain in the physical space. By connecting points in the physical space corresponding to discrete points in the computational space, the physical domain can be overlaid with a suitable computational mesh for the solution of the discretized equations via the finite-volume method. Selecting

suitable mesh equations and solving them efficiently are crucial for the effectiveness of solution adaption via moving meshes.

The second ingredient is the consideration of a mesh density function that is also known as monitor function to guide the mesh redistribution. This monitor function is usually restricted both to redistribute the point movement and to find a mesh relaxation in the search of its redistributed state. The choice of a monitor function may depend on the arc length of the solution in one-dimensional problems, in the solution curvature, and in errors calculated a posteriori. Most importantly, the monitor function must be based on both physical and geometrical considerations that account for the distance or the area between the interfaces, and the new mesh being adapted is as close as possible to the reference (old) mesh. Once the monitor function is determined, the mesh is redistributed in some way and should be verified. The redistribution problem by itself is an algebraic nonlinear problem. In practice, some smoothing or spatial and time relaxation is necessary to improve the mesh quality, thereby decreasing the distortion of the elements.

The third ingredient is the requirement to introduce interpolations. If the mesh equations are time-dependent and are solved simultaneously with the given differential governing equations, then interpolation of dependent variables from the old mesh to the new mesh is unnecessary. Such interpolation-free moving meshes allow problems with large solution gradients or discontinuities for steep wave fronts and moving boundaries to be handled easily unlike static meshes where some kind of interpolation is required to pass the solution information on the newly generated mesh from the old mesh. They can also assist in reducing time variation to allow larger time step to be employed.

An example on the application of moving meshes for the movement of a limb swinging backward and forward is illustrated in Fig. 4.18. During the remeshing process, constraints on the cell and face skewness are imposed to control the size distribution as the limb undergoes its swinging motion. Adjacent cells and faces around the limb are also allowed to move with the limb rather than being deformed in order to properly resolve the boundary layer fluid flow.

Despite the ability to resolve large solution variations occurring within the physical domain, the limitation of moving meshes is manifested by the difficulty of proper definition of an adequate time interval due to the fact that the grid points vary their position with time, increasing the stiffness of the system, which requires implicit time integration to work efficiently. The applicability of moving meshes is also limited to the fixed number of degrees of freedom and to a constant connectivity to the mesh polygons. More importantly, extra attentions have to be paid to guarantee that the important properties for the physical solutions will not be lost after moving the grid points. One of the main difficulties in developing a scheme for moving meshes is how mass conservation of the flow field can be properly maintained throughout the course of the numerical calculations. The reader should bear in mind that grid quality (skewness and/

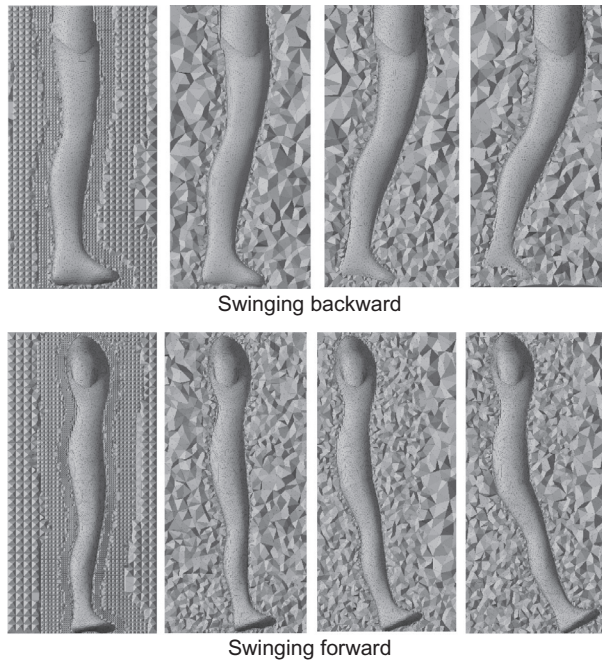


FIG. 4.18 A demonstration of moving meshes for a swinging limb.

or aspect ratio) might suffer or not improve as a consequence of adaptive gridding techniques. Adaptive meshes are still progressively being enhanced in CFD. The concept of solution adaptation described in this section and in the previous section is by no means exhaustive. We strongly encourage the reader to consult the literature for more in-depth understanding on this extensive subject.

4.8 GUIDELINES FOR MESH QUALITY AND MESH DESIGN

As aforementioned, grid generation is by no means a trivial exercise. The mesh for each class of problem is usually unique to the specific CFD geometry, thereby demanding a more measured consideration during the grid generation process.

Firstly, adopting the mindset of applying a coarse mesh topology for a particular CFD problem at the initial step is one of the recommended strategies as part of grid design as it offers the opportunity to evaluate the specific computer code's storage and running time. More importantly, the utilization of a suitable coarse mesh allows a number of 'test runs' to be carried out with the aim of better assessing the convergence or divergence behaviour of the numerical calculations. When a solution is found to be converging, mesh refinement in the flow domain can then be undertaken to achieve the eventual CFD solution.

For a diverging solution, the user needs to negotiate and investigate the problems and causes arising during the numerical calculations. We note that 'test runs' performed on such a mesh also provides the means of rectifying possible sources of solution errors such as *physical modelling* and *human* errors that may be present during the course of the numerical simulations.

Evidently, 'test runs' are not recommended on a fine mesh since this could take hours or days to examine the numerical solutions. Care should also be taken in hastily applying a fine mesh at the first instance because of the plausible diverging tendency that may occur during the iterative procedure. Let us elucidate this point by examining the convective (first-order gradients) and diffusive (second-order gradients) terms along the Cartesian x and y directions in the governing transport equation that can be approximated according to the following discretizations:

$$u\frac{\partial\phi}{\partial x}\approx u\frac{\Delta\phi}{\Delta x},\ v\frac{\partial\phi}{\partial y}\approx v\frac{\Delta\phi}{\Delta y}\ \text{ and }\ \frac{\partial^2\phi}{\partial x^2}\approx\frac{\Delta^2\phi}{\Delta x^2},\ \frac{\partial^2\phi}{\partial y^2}\approx\frac{\Delta^2\phi}{\Delta y^2} \tag{4.9}$$

On a fine mesh, the mesh spacing of Δx and Δy may be very small resulting in

$$\frac{\Delta^2\phi}{\Delta x^2},\ \frac{\Delta^2\phi}{\Delta y^2}>>u\frac{\Delta\phi}{\Delta x},\ v\frac{\Delta\phi}{\Delta y} \tag{4.10}$$

When the above Eq. (4.10) is coupled with poor initial conditions for the transport variable ϕ during the first iteration, we observe that the values of the second-order gradients can become extremely large because of the step change of ϕ being small. This can cause the flow solver to misbehave and the iterative procedure to subsequently diverge in due process. One practical way to overcome the poor initial guesses or unresolved steep gradients in the flow field is through the use of *underrelaxation factors*, as will be discussed in Section 5.4.3, to curtail the iterative advancement of the numerical calculations. The other strategy that is worthwhile noting and is available in many commercial codes is to initially solve the problem in a coarse mesh. The solution of this mesh is later interpolated onto a fine mesh in the subsequent calculations to aid convergence and promote numerical stability and efficiency.

Secondly, we address the grid quality of a generated mesh that depends on the consideration of the cell shape: aspect ratio, skewness, warp angle, or included angle of adjacent faces.

Fig. 4.19 illustrates a quadrilateral cell having mesh spacing of Δx and Δy and an angle of θ between the grid lines of the cell. Accordingly, we can define the grid *aspect ratio* of the cell as $AR=\Delta y/\Delta x$. One pertinent guideline to bear in mind during the course of grid generation is that large aspect ratios should always be avoided in important regions inside the interior flow domain as they can degrade the solution accuracy and may result in possible poor iterative convergence (or divergence) depending on the flow solver during the numerical computations. Whenever possible, it is recommended that AR is maintained

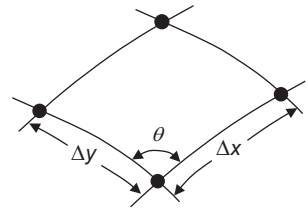


FIG. 4.19 A quadrilateral cell having mesh spacing of Δx and Δy and an angle of θ between the grid lines of the cell.

within the range of $0.2 < AR < 5$ within the interior region. For near-wall boundaries, the condition for AR can, however, be relaxed. If the fluid flow is in the y direction, the need to appropriately choose small Δx mesh spacing in the x direction will generally yield $AR > 5$. In such a case, the approximated first- and second-order gradients are now only biased in the y direction mimicking more of a one-dimensional flow behaviour along this direction since

$$\frac{\Delta^2\phi}{\Delta x^2} << \frac{\Delta^2\phi}{\Delta y^2} \quad \text{and} \quad \frac{\Delta\phi}{\Delta x} << \frac{\Delta\phi}{\Delta y} \tag{4.11}$$

This behaviour is also exemplified where $AR < 0.2$ if the fluid flow is in the x direction. Eq. (4.11) can assist in possibly alleviating convergence difficulties and enhancing the solution accuracy especially in appropriately resolving the wall boundary layers where the rapid solution change exists along the perpendicular direction of the fluid flow.

The next aspect concerning the cell shape deals with grid *distortion* or *skewness*, which relates to the angle θ between the grid lines as indicated in Fig. 4.19. It is normally desirable that the grid lines should be optimized in such a way that the angle θ is approximately 90° (orthogonal). If the angle $\theta < 45°$ or $\theta > 135°$, the mesh contains these highly skewed cells and often exhibits a deterioration of the computational results or leads to numerical instabilities. A typical example of highly skewed cells can be seen in Fig. 4.11 for the structured non-orthogonal body-fitted grid filling the interior circular cylinder. For some complicated geometries, there is a high probability where the generated mesh may contain cells that are just bordering the *skewness* angle limits. The convergence behaviour of such a mesh may be hampered due to the significant influence of additional terms in the discretized form of the transformed equations. Such a case may be remedied through the use of *underrelaxation factors* to increase the diagonal dominance in the matrix solver, thereby gradually improving the solution between iterations. It is also necessary to avoid nonorthogonal cells near the geometry walls. The angle between the grid lines and the boundary of the computational domain (especially the wall, inlet or outlet boundaries) should maintain as close as possible to 90°. The reader should pay special attention to this requirement and it is stronger than the requirement given for the grid lines in the flow field far away from the domain boundaries.

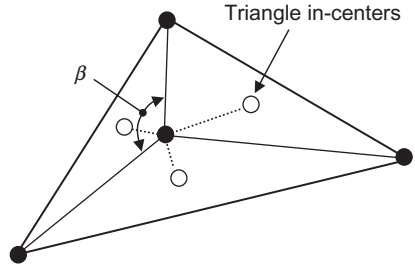


FIG. 4.20 A triangular cell having an angle of β between the surfaces normal to the triangular parts of the faces connected to two adjacent triangles.

If an unstructured mesh is adopted, special care needs to be taken to ensure that the *warp angles* measuring between the surfaces normal to the triangular parts of the faces are not greater than 75° as indicated by the angle β in Fig. 4.20. Cells with large deviations from the coplanar faces can lead to serious convergence problems and deterioration in the computational results. In many grid generation packages, the problem can be overcome by a grid smoothing algorithm to improve the element *warp angles*. Whenever possible, the use of tetrahedral elements should be avoided in wall boundary layers. Prismatic or hexahedral cells are preferred because of their regular shape and their ability to adjust in accordance with the near-wall turbulence model requirements, which will be further discussed at a later section.

Thirdly, special grid design features such as the H-grid, O-grid, or C-grid and careful consideration to locate block interfaces in a sensible manner can assist *en masse* to improve the overall quality of a block-structured mesh. The presence of arbitrary mesh coupling, nonmatching cell faces, or extended changes of element types at block interfaces should always be avoided in critical regions of high flow gradients or high shear. Wherever possible, finer and more regular mesh in these critical regions that may also include significant changes in the geometry or where suggested by error estimates, should be employed. In all cases, it is recommended that the CFD user checks the assumptions made when setting up the grid with regards to the critical regions of high flow gradients and large changes agreeing with the result of the computation, and proceed to rearrange the grid nodal points if found to be necessary.

Finally, it is desirable that a grid independent study is performed to analyze the suitability of the mesh and to yield an estimate of the numerical errors in the simulation for each class of problem. Ideally, at least three significant different grid resolutions should be employed. Strictly speaking, *grid independency* could be examined by doubling the grid twice in each direction and then making sure later by applying the Richardson extrapolation (Roache, 1997). If this is not feasible, selective local refinement of the grid in critical flow regions of the domain can be applied. Otherwise, the reader may attempt to compare different

order of spatial discretizations on the same mesh, which will be further expounded in Section 6.5.

4.9 SUMMARY

Most engineering flows involve complex geometries. In principal, the mesh being considered is subject to constraints imposed by the *discretization* method. For a regular geometry, designing a mesh system is relatively simple since it is evident that the grid lines usually follow the coordinate directions. The use of structured and to a certain extent the curvilinear meshes complies with this requirement. For an irregular geometry, the choice of a mesh system conforming to the complicated shape is however not entirely trivial. The application of unstructured meshes that allows the natural filling of cells of general shapes such as quadrilaterals or triangles in two dimensions or hexahedra or tetrahedral in three dimensions provides the ease and flexibility of meshing such geometry. The meshing of complicated geometry using polyhedral cells has also attracted much attention and becoming rather popular in recent times.

In spite of the different types of cells that could be realized either via structured, curvilinear, or unstructured mesh to fill the specific geometry of the CFD problem, the resolution of specific flow features requires particular attention. Some practical guidelines are summarized here. The use of local refinement via stretched or embedded meshes could assist in the propensity of better resolving the flow gradients that exist for wall bounded flows. Solution adaption via adaptive mesh redistribution or refinement allows the flexibility of adding or concentrating cells to better capture the presence of large flow discontinuities. The use of overlapping meshes permits the handling of moving bodies in stagnant fluids to be treated by resolving the fluid flow around the objects. Nevertheless, these practical guidelines that have been provided are by no means exhaustive. In essence, this chapter has been particularly written with the primary aim of exposing the reader to some basic understating of different mesh structures and to recommend some specific guidelines for flow problems that are frequently encountered in the context of CFD.

The means of obtaining a solution to the governing equations are discussed in the next chapter. We will present some of the basic computational techniques that can be employed to solve such partial differential equations. The many discretization procedures predicting the fluid motion and heat-transfer processes will also be further discussed and elaborated.

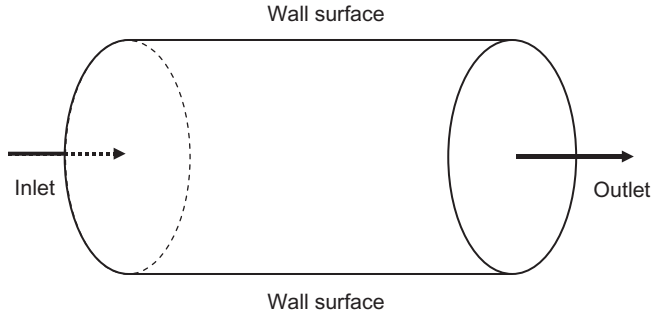
REVIEW QUESTIONS

4.1 What are some of the benefits of a well-designed grid?
4.2 What are some of the advantages of a structured mesh?
4.3 Why is it difficult to write CFD programmes that involve a structured mesh for complex geometries?

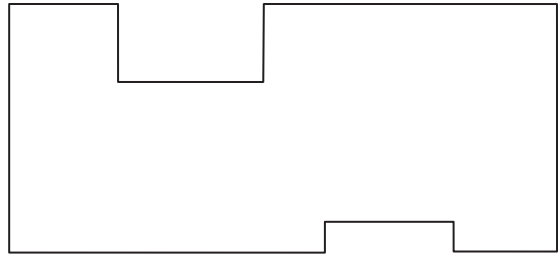
4.4 Discuss some of the advantages of an unstructured grid.

4.5 What are some of the difficulties that arise regarding programming of CFD problems for an unstructured mesh?

4.6 What conditions and constraints apply if you had to use a structured mesh for the geometry below? What about for an unstructured mesh? Discuss the advantages and disadvantages for this case.

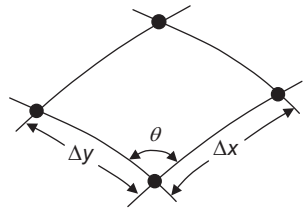


4.7 For the geometry below, discuss how using a block-structured mesh has advantages over a single-structured or unstructured mesh.



4.8 Why is it more favourable to start off with a coarse mesh when solving a CFD problem?

4.9 What is the aspect ratio of a mesh element? Why should a large aspect ratio be avoided, especially in important regions within the flow field? (See diagram below.)

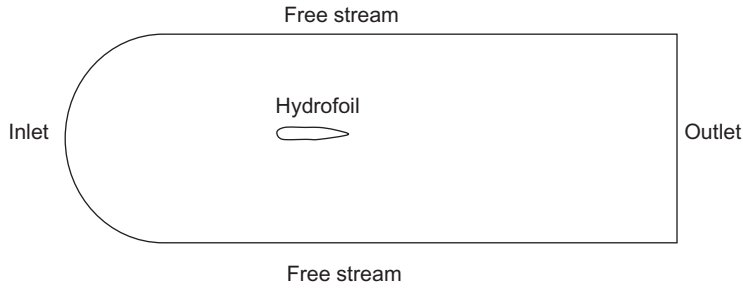


4.10 What is the skewness of a mesh element? Why is it best to avoid highly skewed elements?

4.11 Discuss why tetrahedral elements are a poor choice for meshing near walls and boundaries.

4.12 What techniques can be used in the solver when highly skewed and high aspect ratio elements exist within the mesh?

4.13 A computational domain with different boundary types for the flow around a hydrofoil is shown below. Show where a fine mesh should be appropriately located.



4.14 The stretched grid technique is an example of a local refinement technique. What is one problem associated by the application of this technique?

4.15 Describe how solution adaptation uses an adaptive or moving mesh for grid refinement.

Chapter 5

CFD Techniques: The Basics

5.1 INTRODUCTION

Some of the basic computational techniques that are required to solve the governing equations of fluid dynamics are examined in this chapter. Here, the authors will endeavour to demonstrate how these techniques are employed to obtain an approximate solution for the governing equations of flow problems with appropriate boundary conditions applied for the specific problem considered.

The process of obtaining the computational solution consists of two stages. The *first stage* involves the conversion of the partial differential equations and auxiliary (boundary and initial) conditions into a system of discrete algebraic equations. This *first stage* is commonly known as the *discretization* stage.

In Chapter 3, some analytical solutions have been derived for the partial differential equations of the Navier-Stokes to some simple one-dimensional flow problems. There, the closed-form expressions of u, v, w, p, etc., as functions of one of the spatial locations x, y, and z, were used to provide the desired values of the flow-field variables. However, real fluid flows are generally three-dimensional in nature; analytical relationships are not easily attainable. Even for a simplified three-dimensional flow to a two-dimensional problem, this can be difficult. We have seen in Chapter 2 how CFD can be employed to solve a simple two-dimensional channel flow problem. Instead of closed-form expressions, the respective values of u, v, w, p, etc. were obtained at the discrete locations within the flow domain by the CFD solver, and the original Navier-Stokes equations were approximated by algebraic derivatives. The partial differential equations, totally replaced by a system of algebraic equations, solved the discrete values of the flow-field variables. For such a solution, the original partial differential equations were considered to be discretized in order to yield the values at the discrete locations.

All numerical methods in the mainstream of CFD to solve the fluid flow equations require some form of *discretization*.

Firstly, the *finite-difference* method is regarded as the oldest method within the CFD community that uses Taylor series expansions to generate appropriate finite-difference expressions to approximate the partial derivatives of the governing equations. These derivatives are replaced by finite-difference approximations to yield an algebraic equation for the flow solution at each grid

Computational Fluid Dynamics. https://doi.org/10.1016/B978-0-08-101127-0.00005-2
© 2018 Elsevier Ltd. All rights reserved.

point. Because of the need to have a high degree of regularity, such a method is more suited for structured meshes.

Secondly, the *finite-element* method requires the application of simple piecewise polynomial functions that are employed on local elements to describe the variations of the unknown flow-field variables. The concept of weighted residuals is introduced to measure the errors associated with the approximate functions, which are minimized with successive solution iterations, up to the limits of accuracy achievable by the level of geometrical *discretization*. A set of nonlinear algebraic equations for the unknown terms of the approximating functions is solved and hence yield a flow solution. The attraction of the *finite-element* method over *finite-difference* method is the ability to handle complicated geometries (and boundaries) with relative ease. Whilst *finite-difference* method is restricted to handle predominantly rectangular shapes and simple variations, the handling of geometries in *finite-element* method is theoretically straightforward. Nevertheless, such a method tends to require greater computational resources and computer processing power. One well-known method to solve the Navier-Stokes equations is the discontinuous Galerkin method proposed by Bassi and Rebay (2000). This method combines features of both *finite-element* and *finite-volume* methods, and the solution is represented within each element as a polynomial approximation (*finite-element* method), whilst the interelement advection terms are resolved with appropriate approximation of the fluxes (*finite-volume* method). The discontinuous Galerkin method is used to simulate a wide range of flow regimes and has been adapted for use with compressible and incompressible, steady and unsteady, and laminar and turbulent flows. Further description of the *finite-element* method is given in Section 5.2.3.

Thirdly, *spectral* method employs the same general approach as the *finite-difference* and *finite-element* methods where the unknowns of the governing equations are replaced with a truncated series. The difference is that, where the previous two methods employ local approximations, the *spectral method* uses global approximation that is either by means of a truncated Fourier series or a series of Chebyshev polynomials for the entire flow domain. The discrepancy between the exact solution and the approximation is dealt with by using a weighted residual concept similar to the *finite-element* method. As a variant to the *finite-element* method, the *spectral element* method is a formulation of the *finite-element* method that utilizes high-degree piecewise polynomials. The *spectral element* method as described in Patera (1984) employs high-degree piecewise polynomials based on orthogonal Chebyshev polynomials or very-high-order Legendre polynomials over nonuniformly spaced nodes. However, a significant disadvantage of *spectral element* method is its inherent difficulty in modelling complex geometries when compared with the flexibility of *finite-element* method. Further description of the *spectral* method is provided in Section 5.2.4.

Fourthly, *finite-volume* method like the *finite-element* method has the capacity of handling arbitrary geometries with ease. It can be applied to structured,

body-fitted and unstructured meshes. More importantly, this method bears many similarities with the *finite-difference* method; it is thus simple to apply. Because of the many advantages, one of which being consistent with the concept of the control volume approach, the most common form of *discretization* in use today for finite-volume applications will be thus emphasized.

The overview process of the computational solution procedure is illustrated in Fig. 5.1. Two main headings that are *finite-difference* and *finite-volume* methods constitute the most popular *discretization* approaches in CFD, which will be further elaborated in Section 5.2. The authors will concentrate in detail on the basic derivations of the *finite-difference* and *finite-volume* methods within this book. The *finite-difference* method is illustrated because of its simplicity in formulating the algebraic equations and it also forms the foundation of comprehending the essential basic features of *discretization*. The *finite-volume* method is employed in the majority of all commercial CFD codes today. We believe that the reader should familiarize themselves with this approach because of its ability to be applied to not only *structured* mesh but also *unstructured* mesh that is gaining in popularity and usage in handling arbitrary geometrical shapes. *Structured* mesh is usually designated as a mesh containing cells having

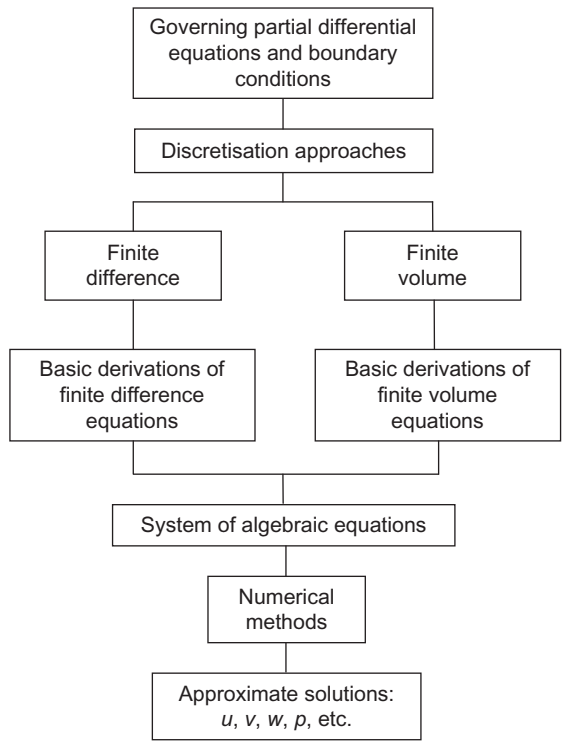


FIG. 5.1 Overview process of the computational solution procedure.

either a regular-shape element with four nodal corner points in two dimensions or a hexahedral-shape element with eight-nodal corner points in three dimensions. *Unstructured* mesh commonly refers however to a mesh overlaying with cells that are in the form of either a triangle-shape element in two dimensions or a tetrahedron-shape element in three dimensions.

The *second stage* of the solution process involves the implementation of numerical methods to provide a solution to the system of algebraic equations. Appropriate methods for obtaining the numerical solution for the system of algebraic equations are discussed in Section 5.3.

Throughout this chapter, we will concentrate more towards considering only systems of algebraic equations typically arising from the solution of steady-state flow problems. These governing equations contain only spatial derivatives that can be discretized by employing either the *finite-difference* or *finite-volume* method. Nevertheless, some basic approximations to the time derivatives for unsteady flow problems, which in practice are exclusively discretized using the *finite-difference* method, are briefly described in Section 5.2.1.

5.2 DISCRETIZATION OF GOVERNING EQUATIONS

5.2.1 Finite Difference Method

The finite-difference method is the oldest of the methods for the numerical solution of partial differential equations. It is believed to have been developed by Euler in 1768 that was used to obtain numerical solutions to differential equations by hand calculation. At each nodal point of the grid used to describe the fluid flow domain, the Taylor series expansions are used to generate finite-difference approximations to the partial derivatives of the governing equations. These derivatives, replaced by finite-difference approximations, yield an algebraic equation for the flow solution at each grid point. In principle, finite difference can be applied to any type of grid system. However, the method is more commonly applied to structured grids since it requires a mesh having a high degree of regularity. The grid spacing between the nodal points need not be uniform, but there are limits on the amount of grid stretching or distortion that can be imposed, to maintain accuracy. Topologically, these finite-difference structured grids must conform to the constraints of general coordinate systems such as Cartesian grids composed of six-sided computational domains. However, the use of an intermediate coordinate mapping such as the body-fitted coordinate system allows this major geometrical constraint to be relaxed, such that complex shapes can be modelled.

Finite difference allows the incorporation of higher-order differencing approximations on regular grids that provide a higher degree of accuracy in the solution. However, the main disadvantage is that the conservation property is not usually enforced unless special care is taken.

The first step towards obtaining a numerical solution involves the discretization of the geometrical domain, that is, a numerical grid must be defined. In the finite-difference method, the grid is usually taken to be locally structured, which means that each grid node may be considered the origin of a local coordinate system, whose axes coincide with the grid lines. These two grid lines also imply that they do not intersect elsewhere and that any pair of grid lines belonging to the different families intersects only once at the grid point. In three dimensions, three grid lines intersect at each node; none of these lines intersect each other at any other grid nodal point. Fig. 5.2 illustrates examples of one-dimensional and two-dimensional uniformly distributed Cartesian grids commonly used in the finite-difference method. Within these two grid systems, each node is uniquely identified by a set of indices, which are indices of the grid lines that intersect at (i, j) in two dimensions and (i, j, k) in three dimensions. The neighbouring nodes are defined by increasing or reducing one of the indices by unity.

Analytical solutions of partial differential equations involve closed-form expressions that provide the variation of the flow-field variables continuously throughout the domain. This is in contrast to numerical solutions where they provide answers only at discrete points in the geometrical domain, for example, at the grid points (open symbols) shown in Fig. 5.2. To illustrate the finite-difference method, let us conveniently assume that the spacing of

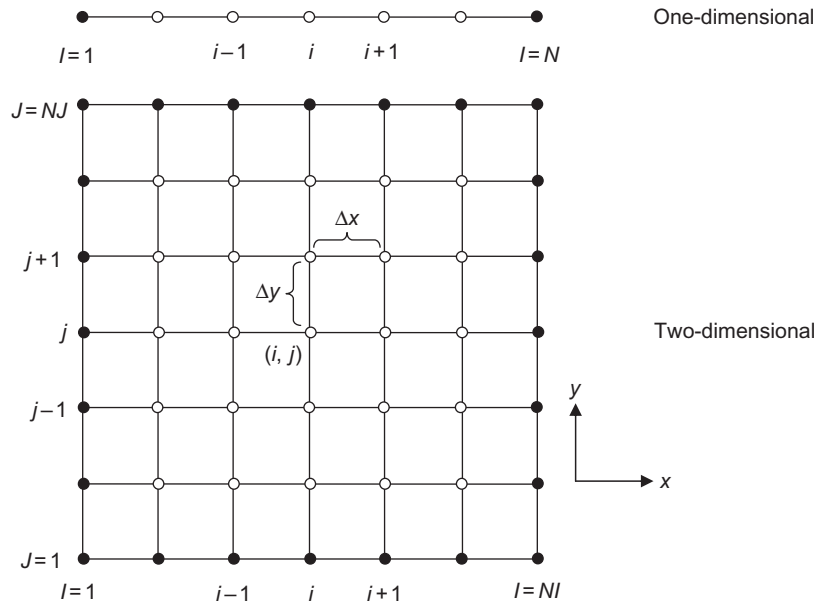


FIG. 5.2 A representation of a one-dimensional and two-dimensional uniformly distributed Cartesian grid for the finite-difference method (full symbols denote boundary nodes, and open symbols denote computational nodes).

the grid points in the x direction is uniform and given by Δx and that the spacing of the points in the y direction is also uniform and given by Δy. The spacing of Δx or Δy need not necessarily be uniform. We could have easily dealt with totally unequal spacing in both directions. This uniform spacing does not have to correspond in the physical x–y space. As is frequently handled in CFD, the numerical calculations can be performed in a transformed computational space that has uniform spacing in the transformed independent variables but still corresponds to a nonuniform spacing in the physical space. In any event, we assume uniform spacing in each of the coordinate directions in describing the basic techniques of the finite-difference method.

The starting point to the representation of the partial derivatives in the governing equations is the Taylor series expansion. We have encountered the use of the Taylor series expansion in formulating the conservation equations in Chapter 3. Here, we are interested in replacing the partial derivative with a suitable algebraic difference quotient—a finite difference. For example, referring to Fig. 5.2, if at the indices (i, j) there exists a generic flow-field variable ϕ, then the variable at point $(i+1, j)$ can be expressed in terms of a Taylor series expanded about the point (i, j) as

$$\phi_{i+1,j} = \phi_{i,j} + \left(\frac{\partial \phi}{\partial x}\right)_{i,j} \Delta x + \left(\frac{\partial^2 \phi}{\partial x^2}\right)_{i,j} \frac{\Delta x^2}{2} + \left(\frac{\partial^3 \phi}{\partial x^3}\right)_{i,j} \frac{\Delta x^3}{6} + \cdots \tag{5.1}$$

Similarly, the variable at point $(i-1, j)$ can also be expressed in terms of Taylor series about points (i, j) as

$$\phi_{i-1,j} = \phi_{i,j} - \left(\frac{\partial \phi}{\partial x}\right)_{i,j} \Delta x + \left(\frac{\partial^2 \phi}{\partial x^2}\right)_{i,j} \frac{\Delta x^2}{2} - \left(\frac{\partial^3 \phi}{\partial x^3}\right)_{i,j} \frac{\Delta x^3}{6} + \cdots \tag{5.2}$$

Eqs (5.1) and (5.2) are mathematically exact expressions for the respective variables $\phi_{i+1,j}$ and $\phi_{i-1,j}$ if the number of terms is infinite and the series converges and/or $\Delta x \to 0$. By subtracting these two equations, we obtain the approximation for the first-order derivative of ϕ:

$$\left(\frac{\partial \phi}{\partial x}\right) = \frac{\phi_{i+1,j} - \phi_{i-1,j} - (\Delta x^3/3)\left(\partial^3 \phi / \partial x^3\right)}{2\Delta x} + \cdots$$

or

$$\left(\frac{\partial \phi}{\partial x}\right) = \frac{\phi_{i+1,j} - \phi_{i-1,j}}{2\Delta x} + \underbrace{O\left(\Delta x^2\right)}_{\textit{Truncation error}} \quad \text{Central difference} \tag{5.3}$$

The term $O(\Delta x^n)$ signifies the truncation error of the finite-difference approximation, which measures the accuracy of the approximation and determines the rate at which the error decreases as the spacing between points is reduced. Eq. (5.3) is taken to be second-order accurate because the truncation error is of order 2. This is a major simplification, and its validity depends on the

size of Δx. The smaller Δx is, the better the agreement. This equation is called *central difference* since it depends equally on values to both sides of the node at x. It is also possible to form other expressions for the first-order derivative by invoking Eqs (5.1) and (5.2). These are

$$\left(\frac{\partial \phi}{\partial x}\right) = \frac{\phi_{i+1,j} - \phi_{i,j}}{\Delta x} + \underbrace{O(\Delta x)}_{\text{Truncation error}} \qquad \text{Forward difference} \qquad (5.4)$$

and

$$\left(\frac{\partial \phi}{\partial x}\right) = \frac{\phi_{i,j} - \phi_{i-1,j}}{\Delta x} + \underbrace{O(\Delta x)}_{\text{Truncation error}} \qquad \text{Backward difference} \qquad (5.5)$$

The above two equations are termed the *forward* and *backward differences*. They reflect their respective biases, and both of these finite-difference approximations are only first-order accurate. It is expected that they will be less accurate in comparison with the central difference for a given value of Δx.

We further explore the idea behind finite-difference approximations that is borrowed directly from the definition of derivatives. A geometrical interpretation of Eqs (5.3), (5.4), and (5.5) is provided in Fig. 5.3. The first-order derivative $\partial\phi/\partial x$ at the point i in the direction of x is the slope of tangent to the curve $\phi(x)$ at that point and is the line marked *exact* in the figure. Its slope can be approximated by the slope of a line passing through the neighbouring points $-\ i+1$ and $i-1$ on the curve. The forward difference is evaluated by the slope B C between the points i and $i+1$, whilst the backward difference is achieved by the slope AB between the points $i-1$ and i. The line labelled central represents the approximation by a central

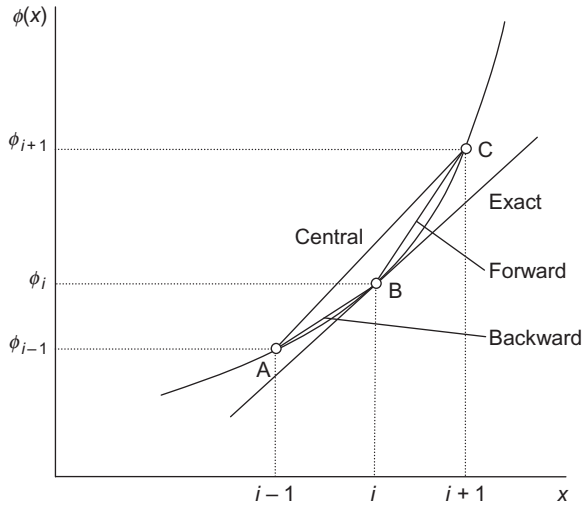


FIG. 5.3 Finite-difference representation of the first-order derivative for $\partial\phi/\partial x$.

difference that evaluates the slope AC. From the figure, it can be seen that some approximations are better than others. The line for the central difference, indicated by the slope AC, appears to be closer to the slope of the exact line; if the function $\phi(x)$ were a second-order polynomial and the points equally spaced in the x direction, the slopes would match exactly. It also appears that the quality of approximation improves when additional points are made closer to point, that is, as the grid is refined, the approximation improves.

Differences for the y derivatives are obtained in exactly the same fashion. The results are directly analogous to the previous equations for the x derivatives. They are given by

$$\left(\frac{\partial \phi}{\partial y}\right) = \frac{\phi_{i,j+1} - \phi_{i,j}}{\Delta y} + \underbrace{O(\Delta y)}_{\textit{Truncation error}} \quad \text{Forward difference} \tag{5.6}$$

$$\left(\frac{\partial \phi}{\partial y}\right) = \frac{\phi_{i,j} - \phi_{i,j-1}}{\Delta y} + \underbrace{O(\Delta y)}_{\textit{Truncation error}} \quad \text{Backward difference} \tag{5.7}$$

$$\left(\frac{\partial \phi}{\partial y}\right) = \frac{\phi_{i,j+1} - \phi_{i,j-1}}{2\Delta y} + \underbrace{O(\Delta y^2)}_{\textit{Truncation error}} \quad \text{Central difference} \tag{5.8}$$

The second-order derivative can also be obtained through the Taylor series expansion as have been applied to approximate the first-order derivative. By summing Eqs (5.1) and (5.2), we have

$$\left(\frac{\partial^2 \phi}{\partial x^2}\right) = \frac{\phi_{i+1,j} - 2\phi_{i,j} + \phi_{i-1,j}}{\Delta x^2} + \underbrace{O(\Delta x^2)}_{\textit{Truncation error}} \tag{5.9}$$

This equation represents the central finite difference for the second-order derivative with respect to x evaluated at the point (i, j). The approximation is second-order accurate. An analogous expression can easily be obtained for the second-order derivative with respect to y, which results in

$$\left(\frac{\partial^2 \phi}{\partial y^2}\right) = \frac{\phi_{i,j+1} - 2\phi_{i,j} + \phi_{i,j-1}}{\Delta y^2} + \underbrace{O(\Delta y^2)}_{\textit{Truncation error}} \tag{5.10}$$

The Taylor series expansion for time derivatives can also be obtained similar to those of the Taylor series expansion for space, Eq. (5.1). Since the numerical solution is more likely to be marched continuously in discrete time interval of Δt, the finite approximation derived for the first-order spatial derivatives applies equally for the first-order time derivative. For a forward difference approximation in time,

$$\left(\frac{\partial \phi}{\partial t}\right) = \frac{\phi_{i,j}^{n+1} - \phi_{i,j}^{n}}{\Delta t} + \underbrace{O(\Delta t)}_{\textit{Truncation error}} \quad \text{Forward difference} \tag{5.11}$$

The above equation introduces a truncation error of $O(\Delta t)$. More accurate approximations to the time derivative can be obtained through the consideration of additional discrete values of $\phi_{i,j}$ in time.

5.2.2 Finite Volume Method

The finite-volume method discretizes the integral form of the conservation equations directly in the physical space. It was initially introduced by researchers such as McDonald (1971) and MacCormak and Paullay (1972) for the solution of two-dimensional time-dependent Euler equations and was later extended to three-dimensional flows by Rizzi and Inuoye (1973). The computational domain is subdivided into a finite number of contiguous control volumes, where the resulting statements express the exact conservation of relevant properties for each of the control volumes. At the centroid of each of the control volumes, the variable values are calculated. Interpolation is used to express variable values at the control volume surface in terms of the centre values, and suitable quadrature formulae are applied to approximate the surface and volume integrals. An algebraic equation for each of the control volumes can be obtained, in which a number of the neighbouring nodal values appear.

As the finite-volume method works with control volumes and not the grid intersection points, it has the capacity to accommodate any type of grid. Here, instead of structured grids, unstructured grids can be employed that allow a large number of options for the definition of the shape and location of the control volumes. Since the grid defines only the control volume boundaries, the method is conservative so long as the surface integrals that are applied at these boundaries are the same as the control volumes sharing the boundary. One disadvantage of this method compared with the finite-difference schemes is that higher-order differencing approximations greater than the second order are more difficult to develop in three dimensions. This is because of the requirement for two levels of approximation, which are interpolation and integration. However, the finite-volume method has more advantages than disadvantages. One important feature of the method is that a 'finite-element'-type mesh can be used, which the mesh can be formed by the combination of triangles or quadrilaterals in the case of two dimensions or tetrahedra and hexahedra in three dimensions. This type of unstructured mesh offers greater flexibility for handling complex geometries. Another attractive feature is the method requires no transformation of the equations in terms of body-fitted coordinate system as is required in finite-difference method.

As with the finite-difference method, a numerical grid must be initially defined to discretize the physical flow domain of interest. For the finite-volume method, we now have the flexibility of representing the grid by either structured or unstructured mesh. For illustration purposes of the finite-volume method, we consider a typical representation of structured (quadrilateral) and unstructured (triangle) finite-volume elements in two dimensions shown in Fig. 5.4 for the

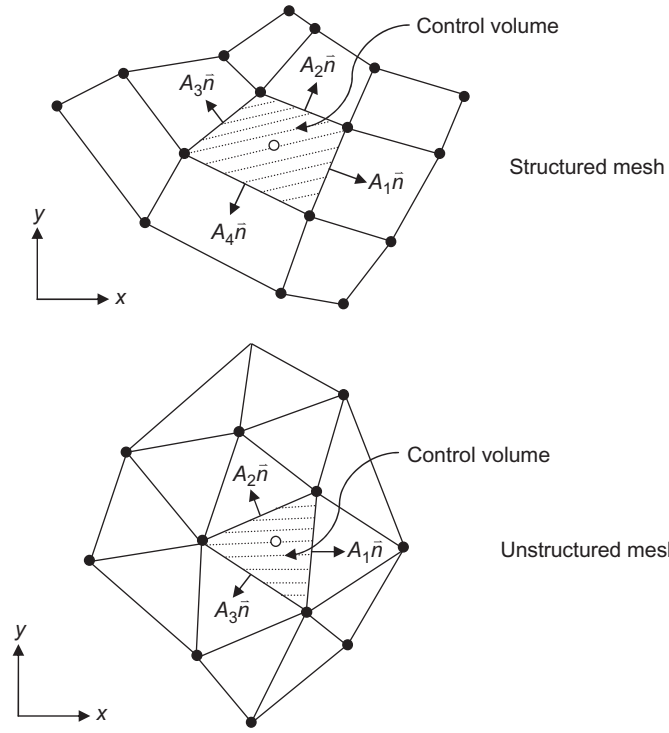


FIG. 5.4 A representation of structured and unstructured mesh for the finite-volume method (full symbols denote element vertices, and open symbols at the centre of the control volumes denote computational nodes).

discretization of the partial differential equations. The cornerstone of the finite-volume method is the *control volume integration*. In a control volume, the bounding surface areas of the element are directly linked to the discretization of the first- and second-order derivatives for ϕ (the generic flow-field variable). Here, the surface areas in the normal direction $(\vec{n})$ to the volume surfaces as indicated in Fig. 5.4 are resolved with respect to the Cartesian coordinate directions to yield the projected areas A_i^x and A_i^y in the x and y directions, respectively. The projected areas are positive if their outward normal vectors from the volume surfaces are directed in the same directions of the Cartesian coordinate system; otherwise, they are negative.

By applying Gauss's divergence theorem to the volume integral, the first-order derivative of ϕ in two dimensions, for example, the term along the x direction represented in Eq. (3.13), can be approximated by

$$\left(\frac{\partial \phi}{\partial x}\right) = \frac{1}{\Delta V}\int_V \frac{\partial \phi}{\partial x} dV = \frac{1}{\Delta V}\int_A \phi dA^x \approx \frac{1}{\Delta V}\sum_{i=1}^{N} \phi_i A_i^x \tag{5.12}$$

where ϕ_i are the variable values at the elemental surfaces and N denotes the number of bounding surfaces on the elemental volume. Eq. (5.12) applies for any type of finite-volume element that can be represented within the numerical grid. For a quadrilateral element in two dimensions for the structured mesh as seen in Fig. 5.4, N has the value of four since there are four bounding surfaces of the element. In three dimensions, for a hexagonal element, N becomes six. Similarly, the first-order derivative for ϕ in the y direction is obtained in exactly the same fashion, which can be written as

$$\left(\frac{\partial \phi}{\partial y}\right) = \frac{1}{\Delta V}\int_{\Delta V}\frac{\partial \phi}{\partial y}dV = \frac{1}{\Delta V}\int_{A}\phi dA^{y} \approx \frac{1}{\Delta V}\sum_{i=1}^{N}\phi_i A_i^{y} \tag{5.13}$$

Example 5.1

Consider the conservation of mass as described in Chapter 3. Determine the discretized form of the two-dimensional continuity equation $\frac{\partial u}{\partial x} + \frac{\partial v}{\partial y} = 0$ by the finite-volume method in a structured uniform grid arrangement.

Solution: An elemental control volume of the two-dimensional structured grid is shown in Fig. 5.1.1. The centroid of the control volume is indicated by the point P, which is surrounded by the adjacent control volumes having their respective centroids indicated by the following points: east, E; west, W; north, N; and south, S. The control volume face between points P and E is denoted by the area A_e^x. Subsequently, the rest of the control volume faces are, respectively, A_w^x, A_n^y, and A_s^y.

We begin the analysis by introducing the control volume integration, which forms the key step of the finite-volume method. Applying Eqs (5.12) and (5.13) yields the following expressions that are applicable to both structured and unstructured grids:

$$\frac{1}{\Delta V}\int_{V}\frac{\partial u}{\partial x}dV = \frac{1}{\Delta V}\int_{A}udA^{x} \approx \frac{1}{\Delta V}\sum_{i=1}^{4}u_i A_i^{x} = \frac{1}{\Delta V}\left(u_e A_e^{x} - u_w A_w^{x} + u_n \cancelto{0}{A_n^{x}} - u_s \cancelto{0}{A_s^{x}}\right)$$

$$\frac{1}{\Delta V}\int_{V}\frac{\partial v}{\partial y}dV = \frac{1}{\Delta V}\int_{A}v\,dA^{y} \approx \frac{1}{\Delta V}\sum_{i=1}^{4}v_i A_i^{y} = \frac{1}{\Delta V}\left(v_e \cancelto{0}{A_e^{y}} - v_w \cancelto{0}{A_w^{y}} + v_n A_n^{y} - v_s A_s^{y}\right)$$

For the structured uniform grid arrangement, the projection areas A_n^x and A_s^x in the x direction and the projection areas A_e^y and A_w^y in the y direction are zero. One important aspect demonstrated here by the finite-volume method is that it allows direct discretization in the physical domain (or in a body-fitted conformal grid) without the need of transforming the continuity equation from the physical domain to a computational domain.

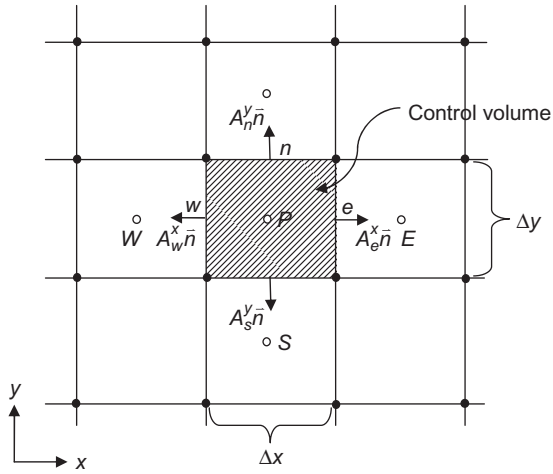


FIG. 5.1.1 Control volume for the two-dimensional continuity equation problem.

Since the grid has been taken to be uniform, the face velocities u_e, u_w, v_n, and v_s are located midway between each of the control volume centroids, which allows us to determine the face velocities from the values located at the centroids of the control volumes. Thus,

$$u_e = \frac{u_P + u_E}{2};\quad u_w = \frac{u_P + u_W}{2};\quad v_n = \frac{v_P + v_N}{2};\quad v_s = \frac{v_P + v_S}{2}$$

By substituting the above expressions to the discretized form of the velocity first-order derivatives, the final form of the discretized continuity equation becomes

$$\left(\frac{u_P + u_E}{2}\right)A_e^x - \left(\frac{u_P + u_W}{2}\right)A_w^x + \left(\frac{v_P + v_N}{2}\right)A_n^y - \left(\frac{v_P + v_S}{2}\right)A_s^y = 0$$

From Fig. 5.1.1, $A_e^x = A_w^x = \Delta y$ and $A_n^y = A_s^y = \Delta x$, the above equation can then be expressed by

$$\left(\frac{u_P + u_E}{2}\right)\Delta y - \left(\frac{u_P + u_W}{2}\right)\Delta y + \left(\frac{v_P + v_N}{2}\right)\Delta x - \left(\frac{v_P + v_S}{2}\right)\Delta x = 0$$

and reduced to

$$\left(\frac{u_E - u_W}{2}\right)\Delta y + \left(\frac{v_N - v_S}{2}\right)\Delta x = 0$$

or in another form

$$\frac{u_E - u_W}{2\Delta x} + \frac{v_N - v_S}{2\Delta y} = 0$$

For a uniform grid arrangement, the distances between P and E and W and P are equivalent to Δx. Similarly, the distances between P and N and S and P are

given by Δy. If the finite-difference method is applied to discretize the continuity equation through the central difference scheme, we obtain the same discretized form of the equation at point P as compared with the form derived through the finite-volume method. The accuracy obtained is of second order as inferred from the finite-difference central difference scheme.

Discussion: The purpose of this example is to demonstrate the use of the finite-volume method to discretize the two-dimensional continuity equation and compare its form with the finite-difference approximation. We observed that the exact representation of the discretized form for the continuity equation can be obtained by applying either the finite-volume or finite-difference method for a uniform grid arrangement. Nevertheless, there are two major advantages that the finite-volume method holds over the finite-difference method. Firstly, it has good conservation properties from the physical viewpoint, and secondly, it allows the accommodation of complicated physical domains to be discretized in a simpler way rather than the need to transform the equation to generalized coordinates in the computational domain.

From the above example, the first-order derivatives that appear in the continuity equation have been discretized through the finite-volume method. The discretization of the second-order derivatives is no different from those performed on the first-order derivatives. The second-order derivative along the x direction, for example, the diffusion terms represented in Eqs (3.24) and (3.25), can be evaluated by

$$\left(\frac{\partial^2\phi}{\partial x^2}\right) = \frac{1}{\Delta V}\int_{\Delta V}\frac{\partial^2\phi}{\partial x^2}dV = \frac{1}{\Delta V}\int_A \frac{\partial\phi}{\partial x}dA^x \approx \frac{1}{\Delta V}\sum_{i=1}^{N}\left(\frac{\partial\phi}{\partial x}\right)_i A_i^x \tag{5.14}$$

An analogous expression can be also easily obtained for the second-order derivative with respect to y, which is given by

$$\left(\frac{\partial^2\phi}{\partial y^2}\right) = \frac{1}{\Delta V}\int_{\Delta V}\frac{\partial^2\phi}{\partial y^2}dV = \frac{1}{\Delta V}\int_A \frac{\partial\phi}{\partial y}dA^y \approx \frac{1}{\Delta V}\sum_{i=1}^{N}\left(\frac{\partial\phi}{\partial y}\right)_i A_i^y \tag{5.15}$$

From Eqs (5.14) and (5.15), it can be seen that in order to approximate the second-order derivatives, the respective first-order derivatives of $(\partial\phi/\partial x)_i$ and $(\partial\phi/\partial y)_i$ appearing in the equations are required to be evaluated at the elemental surfaces of the control volume.

The approximation of the first-order derivatives at the control volume faces is usually determined from the discrete ϕ values of the surrounding elements. For example, in a structured mesh arrangement as shown in Fig. 5.5 where the central control volume (shaded) is surrounded by only one adjacent control volume at each face, the first-order derivatives could be approximated by a piecewise linear gradient profile between the central and adjacent nodes. If needed, higher-order quadratic profiles could also be employed to attain higher accuracy for the numerical solution, which require more surrounding elemental volumes within the mesh system.

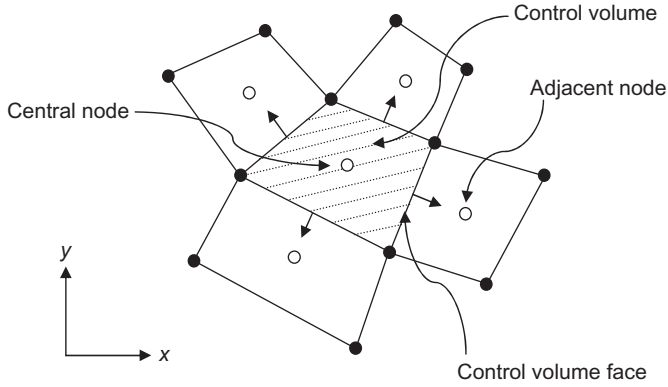


FIG. 5.5 A representation of a structured mesh arrangement (open symbols at the centre of the control volumes denote computational nodes) for the evaluation of the face first-order derivatives.

5.2.3 Finite Element Method

In many aspects, the finite-element method, which was developed initially as an ad hoc engineering procedure for determining the stress and strain displacement solutions in structural analysis, is similar to the finite-volume method. Both the finite-element and finite-volume methods are suitable for irregular computational domains, meaning that they can accommodate complex geometries.

Nevertheless, one distinguishing feature of the finite-element method is that the governing equations are first approximated by multiplication with the so-called shape functions before they are integrated over the entire computational domain. For the domain that is divided into a set of finite elements, the generic variable ϕ can be approximated by

$$\phi = \sum_{j=1}^{n} \phi_j \psi_j(x, y, z) \tag{5.16}$$

where n represents the number of discrete nodal unknowns ϕ_j and $\psi_j(x, y, z)$ are the shape functions. For the consideration of linear shape functions, they can be constructed simply from the values at the corners of the elements. As a general guide, the use of linear shape functions generates solutions of about the same accuracy as those of second-order finite-difference method. This approximation is then substituted into the integral of the weighted residual over the computation domain that is taken to be equal to zero,

$$\iiint W_m(x, y, z) R \, dx dy dz = 0 \tag{5.17}$$

in order to generate a system of algebraic equations for ϕ_j, which can be normally solved via numerical methods. In Eq. (5.17), R is referred to as the equation residual, whilst W_m represents the weight functions. Different choices of W_m give rise to different methods. For example, if the Galerkin method is

adopted, the weight functions are chosen to be the same as the shape functions. More details on the application of finite-element method to fluid mechanics can be found in Thomasset (1981), Baker (1983), and Fletcher (1984).

5.2.4 Spectral Method

The finite-difference, finite-volume, and finite-element methods are generally considered as *local* methods. Consequently, these methods can be identified in terms of the discrete nodal unknowns. In contrast, spectral method is a *global* method, which makes it more difficult to implement in practice. Nevertheless, the method allows approximate solutions of high degree of accuracy; the number of grid points required to achieve the desired precision can therefore be very low.

The spectral method is actually built on the same principal ideas as the finite-element method discussed in the previous section. One main difference between these two methods is that the spectral method approximates the solution with linear combination of continuous functions that are generally nonzero throughout the whole domain (Fourier series, Legendre polynomials, and Chebyshev polynomials) whilst the finite-element method approximates the solution of piecewise functions that are nonzero on localized subdomains. Thus, spectral method works best when the solution is smooth.

Like the finite-element method, the starting point for the spectral method is the introduction of the approximate solution of ϕ that can be assumed to be

$$\phi = \sum_{j=1}^{n} a_j(t)\varphi_j(x, y, z) \tag{5.18}$$

where $a_j(t)$ are the unknown coefficients and $\varphi_j(x, y, z)$ are the trial functions. The choice of trail functions is dependent on the particular consideration of the flow problem being solved. Fourier series are particularly suited for periodic boundary conditions, whilst Chebyshev polynomials are more appropriate for nonperiodic boundary conditions. Substitution of Eq. (5.18) into the transport equation yields the residual of the equation. The unknown coefficients are now determined via the integration of the vanishing weighted residual over the computational domain, that is, applying Eq. (5.17). Here again, if the Galerkin method is adopted, the weight functions are automatically chosen from the same family as the trial functions. More details on the application of spectral method to fluid mechanics can be found in Fletcher (1984) and Canuto et al. (1987).

5.3 CONVERTING GOVERNING EQUATIONS TO ALGEBRAIC EQUATION SYSTEM

The basic derivations of the finite-difference and finite-volume methods and some basic descriptions of the finite-element and spectral methods have been provided. Primarily concentrating on the finite-difference and finite-volume

methods, the next task is to consider the appropriate application of these various discretization techniques to numerically solve the governing partial differential equations. A numerical method is developed by considering the three transport processes associated with it: (1) pure diffusion in steady state, (2) steady convection-diffusion, and (3) unsteady convection-diffusion. We further simplify the problem by systematically working through a one-dimensional equation in order to demonstrate the application of the discretization techniques to finally attain the algebraic form of the governing equation. It can be seen later that this discretized form of equation is easily extended and accommodated for two- and three-dimensional diffusion problems.

Pure diffusion process: Let us consider the steady-state diffusion of the generic variable ϕ in a one-dimensional domain. The equation that governs such a process is given by

$$\frac{\partial}{\partial x}\left(\Gamma\frac{\partial \phi}{\partial x}\right)+S_\phi=0 \tag{5.19}$$

where Γ is the diffusion coefficient and S_ϕ is the source term. This equation is typical of a one-dimensional heat conduction process, which we will further investigate in detail through worked examples. For this problem, the applications of the finite-difference and finite-volume methods to discretize the equation are illustrated.

5.3.1 Finite Difference Method

The use of the finite-difference method is explored here. The first step in developing a numerical solution for this method involves dividing the geometrical domain into discrete nodal points. Let us consider a general nodal point P and its surrounding neighbouring nodal points to the west and east, W and E, for the one-dimensional geometry as demonstrated in Fig. 5.6. A uniform grid spanning the three nodal points W, P, and E is produced.

The next step in the discretization process is to discretize equation (5.19) around the nodal point P. To derive a suitable expression for the finite-difference method, Eq. (5.19) is required to be expanded into its nonconservative form, which is given by

$$\frac{\partial \Gamma}{\partial x}\frac{\partial \phi}{\partial x}+\Gamma\frac{\partial^2 \phi}{\partial x^2}+S_\phi=0 \tag{5.20}$$

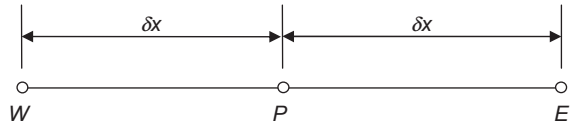


FIG. 5.6 A schematic representation of the uniform grid spacing along the x direction for the one-dimensional geometry.

By applying the central differencing of the first-order derivative equation (5.8) and second-order derivative equation (5.9), the discretized form of Eq. (5.20) is obtained as

$$\frac{(\Gamma_E-\Gamma_W)}{2\delta x}\frac{(\phi_E-\phi_W)}{2\delta x}+\Gamma_P\frac{(\phi_E-2\phi_P+\phi_W)}{\delta x^2}+S_\phi=0 \tag{5.21}$$

After some rearrangement, Eq. (5.21) can be alternatively expressed as

$$\frac{2\Gamma_P}{\delta x^2}\phi_P=\left[\frac{(\Gamma_E-\Gamma_W)}{4\delta x^2}+\frac{\Gamma_P}{\delta x^2}\right]\phi_E+\left[-\frac{(\Gamma_E-\Gamma_W)}{4\delta x^2}+\frac{\Gamma_P}{\delta x^2}\right]\phi_W+S_\phi \tag{5.22}$$

Identifying the coefficients of ϕ_E and ϕ_W in Eq. (5.19) as a_E and a_W and the coefficient of ϕ_P as a_P, the equation can be written in a simple form

$$a_P\phi_P=a_E\phi_E+a_W\phi_W+b \tag{5.23}$$

where

$$a_E=\frac{(\Gamma_E-\Gamma_W)}{4\delta x^2}+\frac{\Gamma_P}{\delta x^2};\quad a_W=-\frac{(\Gamma_E-\Gamma_W)}{4\delta x^2}+\frac{\Gamma_P}{\delta x^2};\quad a_P=\frac{2\Gamma_P}{\delta x^2};\quad b=S_\phi$$

5.3.2 Finite Volume Method

When the finite-volume method is applied, we have to consider the physical domain as being divided into finite control volumes surrounding the nodal points W, P, and E. Fig. 5.7 shows a control volume surrounding the nodal point P. The distances between the nodes W and P and between nodes P and E are identified by the respective notations δx_W and δx_E. For this one-dimensional case, the control volume width surrounding the nodal point P is Δx since Δy and Δz have dimensions of unit length.

To apply the finite-volume discretization, the gradient term in Eq. (5.19) can be approximated by the use of Eq. (5.12). This gives

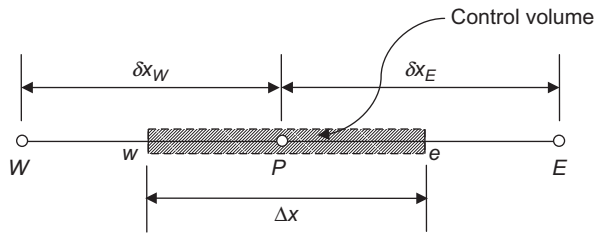


FIG. 5.7 A schematic representation of a control volume around a node P in a one-dimensional domain using the finite-volume method.

$$\frac{\partial}{\partial x}\left(\Gamma\frac{\partial\phi}{\partial x}\right)=\frac{1}{\Delta V}\int_{\Delta V}\frac{\partial}{\partial x}\left(\Gamma\frac{\partial\phi}{\partial x}\right)dV=\frac{1}{\Delta V}\int_{A}\left(\Gamma\frac{\partial\phi}{\partial x}\right)dA^{x}\approx\frac{1}{\Delta V}\sum_{i=1}^{2}\left(\Gamma\frac{\partial\phi}{\partial x}\right)_{i}A_{i}^{x} \tag{5.24}$$

Here, the projected areas A_i^x for the one-dimensional case are given by $A_1^x=-A_W$ and $A_2^x=A_E$. Eq. (5.24) can thus be written as

$$\left(\Gamma\frac{\partial\phi}{\partial x}\right)_{e}A_E-\left(\Gamma\frac{\partial\phi}{\partial x}\right)_{w}A_w \tag{5.25}$$

For the remaining term in the equation, the source term is approximated as

$$\frac{1}{\Delta V}\int_{\Delta V}S_\phi dV=S_\phi \tag{5.26}$$

where S_ϕ is assumed to be constant within ΔV, which is the finite control volume. The final form of the discretized equation becomes

$$\frac{1}{\Delta V}\left(\Gamma\frac{\partial\phi}{\partial x}\right)_{e}A_E-\frac{1}{\Delta V}\left(\Gamma\frac{\partial\phi}{\partial x}\right)_{w}A_w+S_\phi=0 \tag{5.27}$$

To express an algebraic form for Eq. (5.27) with the nodal points W, E, and P, approximations to the gradients $\partial\phi/\partial x$ at the west ('w') and east ('e') faces of the control volume are required. We will assume the piecewise linear gradient profiles spanning the nodal points between W and P and between P and E to sufficiently approximate the first-order derivatives at 'w' and 'e'; the diffusive fluxes are evaluated as

$$\left(\Gamma\frac{\partial\phi}{\partial x}\right)_{e}A_E=\Gamma_eA_E\left(\frac{\phi_E-\phi_P}{\delta x_E}\right) \tag{5.28}$$

$$\left(\Gamma\frac{\partial\phi}{\partial x}\right)_{w}A_W=\Gamma_wA_W\left(\frac{\phi_P-\phi_W}{\delta x_W}\right) \tag{5.29}$$

Substitution of Eqs (5.28) and (5.29) into Eq. (5.27) gives

$$\frac{\Gamma_eA_E}{\Delta V}\left(\frac{\phi_E-\phi_P}{\delta x_E}\right)-\frac{\Gamma_wA_W}{\Delta V}\left(\frac{\phi_P-\phi_W}{\delta x_W}\right)+S_\phi=0 \tag{5.30}$$

Eq. (5.30) presents a very attractive feature of the finite-volume method. This discretized equation possesses a clear physical interpretation. It states that the difference between the diffusive fluxes of ϕ at the east and west faces of the control volume equals to the generation of ϕ and constitutes a balance equation for ϕ over the control volume. Eq. (5.30) can be rearranged as

$$\frac{1}{\Delta V}\left(\frac{\Gamma_eA_E}{\delta x_E}+\frac{\Gamma_wA_W}{\delta x_W}\right)\phi_P=\frac{1}{\Delta V}\left(\frac{\Gamma_eA_E}{\delta x_E}\right)\phi_E+\frac{1}{\Delta V}\left(\frac{\Gamma_wA_W}{\delta x_W}\right)\phi_W+S_\phi \tag{5.31}$$

As above, by identifying the coefficients of ϕ_E and ϕ_W in Eq. (5.31) as a_E and a_W and the coefficient of ϕ_P as a_P, the algebraic form can be written as

$$a_P\varphi_P = a_E\phi_E + a_W\phi_W + b \tag{5.32}$$

where

$$a_E = \frac{\Gamma_e A_E}{\Delta V \delta x_E};\quad a_W = \frac{\Gamma_w A_W}{\Delta V \delta x_W};\quad a_P = a_E + a_W;\quad b = S_\phi$$

Eq. (5.32) represents the discretized form through the finite-volume method for Eq. (5.19). For the one-dimensional problem considered here, the face areas A_E and A_W are unity since Δy and Δz have dimensions of unit length; the finite control volume ΔV is therefore the width Δx.

5.3.3 Comparison of the Finite Difference and Finite Volume Discretizations

Although the same algebraic form of equation for the steady-state one-dimensional diffusion process is obtained, different expressions for the coefficients of a_E, a_W, and a_P are derived as seen in Eq. (5.23) for the finite-difference method and Eq. (5.32) for the finite-volume method. Nevertheless, let us consider for a special case where the diffusion coefficient is spatially invariant and the mesh is uniformly distributed. The coefficients in the algebraic equation (5.23) for the finite-difference method reduce to

$$a_E = \frac{\Gamma}{\delta x^2};\quad a_W = \frac{\Gamma}{\delta x^2};\quad a_P = a_E + a_W;\quad b = S_\phi$$

whilst for the finite-volume method, the coefficients in Eq. (5.32) become

$$a_E = \frac{\Gamma}{\delta x^2};\quad a_W = \frac{\Gamma}{\delta x^2};\quad a_P = a_E + a_W;\quad b = S_\phi$$

where the control volume is $\Delta x = \delta x$ (uniform grid and Δy, Δz is unity). From the example above for the discretization of the continuity equation, the resultant algebraic equations are again exactly the same whether adopting either the finite-difference or the finite-volume discretization.

It should be noted that the finite-difference method generally requires a uniformly distributed mesh in order to apply the first- and second-order derivative approximations to the governing equation. For a nonuniform grid distribution, some mathematical manipulation (e.g. transformation functions) is required to transform Eq. (5.20), into a computational domain in generalized coordinates before applying the finite-difference approximations. This requirement is however not a prerequisite for the finite-volume method. Because of the availability of having different control volume sizes, any nonuniform grid could therefore be easily accommodated.

In comparison with the finite-difference method that is mathematically derived from the Taylor series, the finite-volume method ensures that the property is conserved and it retains this physical significance throughout the discretization process. Almost all commercial CFD codes adopt the finite-volume discretization of the Navier-Stokes equation to obtain numerical solutions for complex fluid flow problems as the mesh is not restricted to structured-type elements but can include a variety of unstructured-type elements of different shapes and sizes.

Example 5.2

Consider the problem of a steady heat conduction problem in a large brick plate with a uniform heat generation. The faces A and B as shown in Fig. 5.2.1 below are maintained at constant temperatures. The governing equation is of the generic form presented in Eq. (5.15). The diffusion coefficient Γ governing the heat conduction problem becomes the thermal conductivity k of the material. For a given thickness $L = 2$ cm with constant thermal conductivity $k = 5$ W/m^2 K, determine the steady-state distribution in the plate. Temperatures at T_A and T_B are, respectively, 100 and 400°C, and heat generation q is 500 kW/m^3.

Solution: Assuming that the dimensions in the y direction and z direction are so large that the temperature gradients are only significant in the x direction, we can reduce the problem to a one-dimensional analysis. We apply the finite-volume method to obtain the solution of this simple heat conduction problem.

Let us divide the domain into four control volumes (see Fig. 5.2.2) giving $\delta x = 0.005$ m. There are four nodal points, each representing the central location for the four control volumes. For illustration purposes, a unit area is considered in the y–z plane.

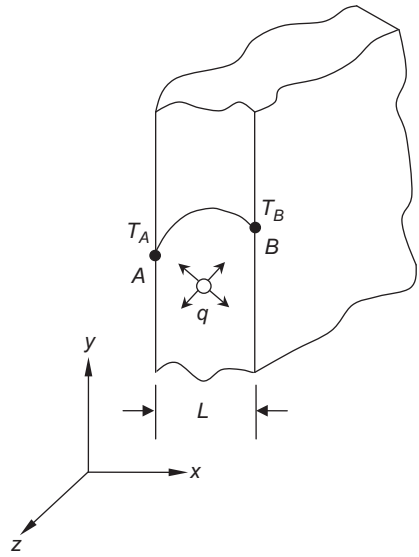


FIG. 5.2.1 Schematic representation of the large brick plate with heat generation.

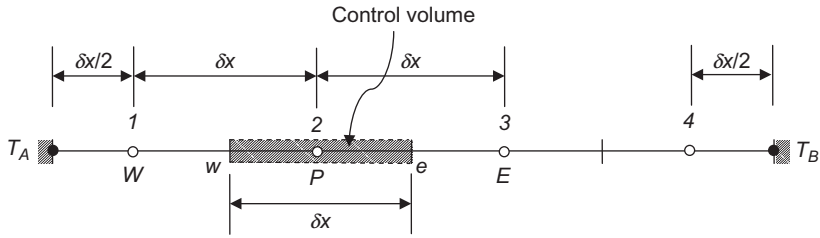


FIG. 5.2.2 Finite-volume discretization of the large brick plate domain.

Since the thermal conductivity is constant, we can define $k = k_e = k_w$ and the volumetric source term S_ϕ equal to q; the general discretized form of the equation at point P (node 2), as from Eq. 5.29, is given as

$$a_P T_P = a_E T_E + a_W T_W + b$$

where the coefficients are

$$a_E = \frac{kA}{\delta x^2};\quad a_W = \frac{kA}{\delta x^2};\quad a_P = a_E + a_W;\quad b = q$$

This algebraic equation is also valid for the control volume of node 3.

For the control volumes of nodes 1 and 4, we apply a linear approximation for the temperatures between the boundary points and its adjacent nodal point of the control volume. At the west face of the control volume at the fixed end, the temperature is known by T_A. We begin by revisiting Eq. (5.24).

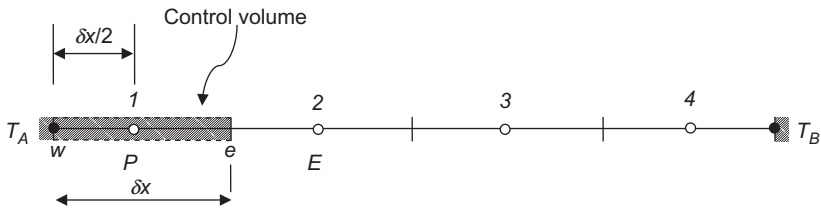


FIG. 5.2.3 Finite-volume discretization of the large brick plate domain, showing the first control volume.

For a constant thermal conductivity and uniform heat generation, the equation becomes

$$k\left(\frac{\partial T}{\partial x}\right)_e - k\left(\frac{\partial T}{\partial x}\right)_w + q\delta x = 0$$

Introducing linear approximations to the gradients at the east and west faces of the control volume 1 gives

$$kA\left(\frac{T_E - T_P}{\delta x}\right) - kA\left(\frac{T_P - T_A}{\delta x/2}\right) + q\delta x = 0$$

The above equation can be rearranged to yield the discretized equation for node 1:

$$a_P T_P = a_E T_E + a_W T_W + b$$

where the coefficients are

$$a_E = \frac{kA}{\delta x};\ \ a_W = 0;\ \ a_P = a_E + a_W + \frac{2kA}{\delta x};\ \ b = q\delta x + \frac{2kA}{\delta x} T_A$$

The area $a_W = 0$, since it is a fixed end. At node 4, the temperature of the east face of the control volume is known. The node is similarly treated, and we obtain

$$k\left(\frac{\partial T}{\partial x}\right)_e - k\left(\frac{\partial T}{\partial x}\right)_w + q\delta x = 0$$

and

$$kA\left(\frac{T_B - T_P}{\delta x/2}\right) - kA\left(\frac{T_P - T_W}{\delta x}\right) + q\delta x = 0$$

with the discretized equation for node 4 given as

$$a_P T_P = a_E T_E + a_W T_W + b$$

where

$$a_E = 0;\ \ a_W = \frac{kA}{\delta x};\ \ a_P = a_E + a_W + \frac{2kA}{\delta x};\ \ b = q\delta x + \frac{2kA}{\delta x} T_B$$

Substitution of numerical values for the thermal conductivity $k = 5$ W/m^2 K, heat generation $q = 500$ kW/m^3, $\delta x = 0.005$ m, and unit area $A = 1$ m^2 throughout provides the coefficients of the discretized equation summarized in Table 5.2.1.

TABLE 5.2.1 The Coefficients at Each Node of the Control Volumes

Node	a_E	a_W	a_P	b
1	1000	0	3000	$2500 + 2000T_A$
2	1000	1000	2000	2500
3	1000	1000	2000	2500
4	0	1000	3000	$2500 + 2000T_B$

The resulting set of algebraic equations for this example is

$$\begin{aligned} 3000T_1 &= 1000T_2 + 2000T_A + 2500 \\ 2000T_2 &= 1000T_1 + 1000T_3 + 2500 \\ 2000T_3 &= 1000T_2 + 1000T_4 + 2500 \\ 3000T_4 &= 1000T_3 + 2000T_B + 2500 \end{aligned}$$

This set of equation can be rearranged in matrix form as

$$\begin{bmatrix} 3000 & -1000 & 0 & 0 \\ -1000 & 2000 & -1000 & 0 \\ 0 & -1000 & 2000 & -1000 \\ 0 & 0 & -1000 & 3000 \end{bmatrix} \begin{bmatrix} T_1 \\ T_2 \\ T_3 \\ T_4 \end{bmatrix} = \begin{bmatrix} 2000T_A + 2500 \\ 2500 \\ 2500 \\ 2000T_B + 2500 \end{bmatrix}$$

The above set of equations yields the steady-state temperature distribution for the given situation.

Discussion: For a one-dimensional steady heat conduction process we obtained the algebraic equations in matrix form. Because the problem only involves a small number of nodes, the matrix can be solved directly with a software package such as MATLAB (*The Student Edition of MATLAB*, The Math Works Inc., 1992). Analytically, the matrix can be solved by methods such as Gaussian elimination. This matrix algorithm will be discussed in the next section.

In most CFD problems, however, the complexity and size of a set of equations depends on the dimensionality of the problem and the number of grid nodes, where the system can consist of up to 100,000 or 1 million equations. For such problems, the available computer resources set a powerful constraint, and the Gaussian elimination may not be the most economical way in obtaining the solution of the discretized equations. We will further explore other algorithms that are currently available to efficiently obtain the solution to the algebraic equations in Section 5.3.

Steady convection-diffusion process: In the absence of sources, the equation governing the steady convection and diffusion process of a property ϕ in a given one-dimensional flow field u from Eq. (3.53) simplifies to

$$\frac{\partial}{\partial x}(\rho u \phi) = \frac{\partial}{\partial x}\left(\Gamma \frac{\partial \phi}{\partial x}\right) \tag{5.33}$$

The mass conservation for the one-dimensional convection–diffusion process is enforced through

$$\frac{\partial(\rho u)}{\partial x} = 0 \tag{5.34}$$

By applying the finite-volume method based on the elemental volume described in Fig. 5.7, the algebraic form of Eq. (5.33) can be expressed as

$$(\rho u \phi)_e A_E - (\rho u \phi)_w A_W = \left(\Gamma \frac{\partial \phi}{\partial x}\right)_e A_E - \left(\Gamma \frac{\partial \phi}{\partial x}\right)_w A_W \tag{5.35}$$

Assuming piecewise linear gradient profiles spanning the nodal points between W and P and between P and E, the first-order derivatives at 'w' and 'e' of the diffusive fluxes can be similarly approximated using the expressions formulated in Eqs (5.28) and (5.29) to yield

$$(\rho u \phi)_e A_E - (\rho u \phi)_w A_W = \Gamma_e A_E \left(\frac{\phi_E - \phi_P}{\delta x_E}\right) - \Gamma_w A_W \left(\frac{\phi_P - \phi_W}{\delta x_W}\right) \tag{5.36}$$

In hindsight, it seems rather sensible for the convective term to be approximated in a similar fashion. Using the Taylor series expansion, the interface values ϕ_w and ϕ_e at the respective cell faces w and e can be obtained via linear interpolation between the neighbouring points as

$$\phi_w = \frac{1}{2}(\phi_W + \phi_P) \tag{5.37}$$

$$\phi_e = \frac{1}{2}(\phi_P + \phi_E) \tag{5.38}$$

The above approximation is second-order accurate, and the scheme does not exhibit any bias on the flow direction. Using these relationships, Eq. (5.36) thus becomes

$$\begin{aligned}(\rho u)_e A_E \frac{1}{2}(\phi_P + \phi_E) - (\rho u)_w A_W \frac{1}{2}(\phi_W + \phi_P) \\ = \Gamma_e A_E \left(\frac{\phi_E - \phi_P}{\delta x_E}\right) - \Gamma_w A_W \left(\frac{\phi_P - \phi_W}{\delta x_W}\right)\end{aligned} \tag{5.39}$$

Eq. (5.39) can be rearranged as

$$\begin{aligned}&\left(\frac{\Gamma_e A_E}{\delta x_E} + \frac{(\rho u)_e A_E}{2} + \frac{\Gamma_w A_W}{\delta x_W} - \frac{(\rho u)_w A_W}{2}\right)\phi_P \\ &= \left(\frac{\Gamma_e A_E}{\delta x_E} - \frac{(\rho u)_e A_E}{2}\right)\phi_E + \left(\frac{\Gamma_w A_W}{\delta x_W} + \frac{(\rho u)_w A_W}{2}\right)\phi_W\end{aligned} \tag{5.40}$$

By identifying the coefficients of ϕ_E and ϕ_W in Eq. (5.40) as a_E and a_W and the coefficient of ϕ_P as a_P, the algebraic form can be written as

$$a_P \phi_P = a_E \phi_E + a_W \phi_W \tag{5.41}$$

where

$$a_E = \frac{\Gamma_e A_E}{\delta x_E} - \frac{(\rho u)_e A_E}{2}; \quad a_W = \frac{\Gamma_w A_W}{\delta x_W} + \frac{(\rho u)_w A_W}{2};$$
$$a_P = a_E + a_W + (\rho u)_e A_E - (\rho u)_w A_w$$

One renowned inadequacy of the central differencing schemes in a strongly convective flow is its inability to identify the flow direction. It is well recognized that the above treatment usually results in large 'undershoots' and 'overshoots', eventually causing the numerical procedure to diverge. Increasing the mesh resolution for the flow domain with very small grid spacing could probably overcome the problem, but such an approach usually precludes practical flow calculations to be carried out robustly and effectively in practice.

Consider for a moment the flow moving from the upstream point W (left) to the downstream point E (right). Through the central differencing approximation, the interface values of ϕ are always assumed to be equally weighted by the influence of the available variables at the neighbouring grid nodal points.

This implies that the downstream values of ϕ_P and ϕ_E are prevailing during the evaluation of ϕ_w and ϕ_e. In the majority of flow cases, these values are not known *a priori*; the remedy is therefore to design a numerical solution to recognize the direction of the flow by exerting an unequal weighting influence based on the available variables located at the surrounding grid nodal points to appropriately determine the interface values. This is essentially the hallmark of the *upwind* or *donor-cell* concept. The first-order upwind scheme is described herein. With reference to Fig. 5.7, if the interface velocities $u_w > 0$ and $u_e > 0$, respectively, the interface values ϕ_w and ϕ_e according to the *donor-cell* concept are now approximated according to their upstream neighbouring counterparts as

$$\phi_w = \phi_W \tag{5.42}$$

$$\phi_e = \phi_P \tag{5.43}$$

Using the above relationships, Eq. (5.36) can be expressed as

$$(\rho u)_e A_E \phi_P - (\rho u)_w A_W \phi_W = \Gamma_e A_E \left(\frac{\phi_E - \phi_P}{\delta x_E}\right) - \Gamma_w A_W \left(\frac{\phi_P - \phi_W}{\delta x_W}\right) \tag{5.44}$$

and the coefficients a_E, a_W, and a_P as described by Eq. (5.41) are given by

$$a_E = \frac{\Gamma_e A_E}{\delta x_E};\quad a_W = \frac{\Gamma_w A_W}{\delta x_W} + (\rho u)_w A_W;\quad a_P = a_E + a_W + (\rho u)_e A_E - (\rho u)_w A_w$$

Similarly, if the interface velocities $u_w < 0$ and $u_e < 0$, respectively, the interface values ϕ_w and ϕ_e are conversely evaluated by

$$\phi_w = \phi_P \tag{5.45}$$

$$\phi_e = \phi_E \tag{5.46}$$

Using the above relationships, Eq. (5.38) can be written as

$$(\rho u)_e A_E \phi_E - (\rho u)_w A_W \phi_P = \Gamma_e A_E \left(\frac{\phi_E - \phi_P}{\delta x_E}\right) - \Gamma_w A_W \left(\frac{\phi_P - \phi_W}{\delta x_W}\right) \tag{5.47}$$

and the coefficients a_E, a_W, and a_P are now given by

$$a_E = \frac{\Gamma_e A_E}{\delta x_E} - (\rho u)_e A_E;\quad a_W = \frac{\Gamma_w A_W}{\delta x_W};\quad a_P = a_E + a_W + (\rho u)_e A_E - (\rho u)_w A_w$$

A more in-depth look at the different discretization schemes based on upwind and central differencing schemes can be described by three fundamental properties: *transportiveness*, *boundedness*, and *conservativeness*.

Transportiveness concerns the direction of the flow. Central differencing scheme introduces the influence at node P from all directions from its neighbouring nodes to calculate the convective and diffusive fluxes. Hence, this particular scheme does not recognize the direction or the strength of the convection relative to diffusion and does not possess the transportiveness property. Nevertheless, the upwind differencing scheme accounts for the flow direction

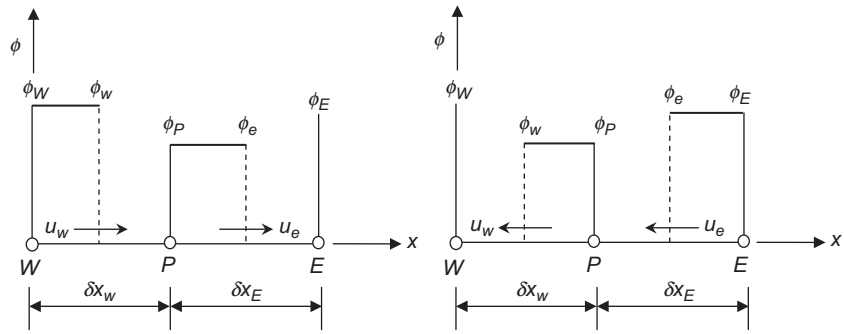


FIG. 5.8 A schematic representation of the upwind differencing scheme.

and satisfies the transportiveness property. Fig. 5.8 illustrates the preferential direction of the flow moving across three control volumes from the upstream node W (left) to the downstream node E (right) for interface velocities $u_w > 0$ and $u_e > 0$ and in the opposite direction from upstream node E (right) to downstream node W (left) for interface velocities $u_w < 0$ and $u_e < 0$, respectively.

Boundedness concerns the condition whereby the resulting matrix of the coefficients is diagonally dominant to ensure numerical convergence. It can be demonstrated that the matrix coefficients for central differencing can become negative that greatly violates the requirement of boundedness and may lead to unphysical solutions. For coefficients a_W and a_E, it is highly possible that they can become negative if advection dominates. For a_W and a_E to be positive, they must satisfy the following conditions:

$$\frac{(\rho u)_w}{\Gamma_w/\delta x_W} = Pe_w < 2 \quad \text{and} \quad \frac{(\rho u)_e}{\Gamma_e/\delta x_E} = Pe_e < 2 \tag{5.48}$$

If the local Peclet numbers Pe_w and Pe_e are greater than 2, a_W and a_E become negative, and these coefficients violate the requirement of boundedness and may result in physically impossible solution. However, all coefficients in the upwind differencing scheme are positive, and the coefficient matrix is diagonally dominant that satisfy the requirement of boundedness.

In addition, Spalding (1972) developed a scheme that combines the central and upwind differencing schemes by employing piecewise formulae based on the Peclet number. This so-called *hybrid differencing* retains a second-order accuracy for small Peclet numbers due to central differencing but reverts to the upwind differencing for large Peclet numbers. For the case where the interface velocities are positive, $u_w > 0$ and $u_e > 0$, the interface values ϕ_w and ϕ_e according to the hybrid differencing formulae are given by

$$\phi_w = \frac{1}{2}(\phi_W + \phi_P); \quad \phi_e = \frac{1}{2}(\phi_P + \phi_E) \quad \text{for } Pe_w, Pe_e < 2 \tag{5.49}$$

$$\phi_w = \phi_W; \quad \phi_e = \phi_P \quad \text{for } Pe_w, Pe_e \geq 2 \tag{5.50}$$

where

$$Pe_w = \frac{(\rho u)_w}{\Gamma_w/\delta x_W} \quad \text{and} \quad Pe_e = \frac{(\rho u)_e}{\Gamma_e/\delta x_E}$$

Similar considerations can be obtained for the respective interface values of ϕ_w and ϕ_e when the interface velocities u_w and u_e are in the opposite direction or negative. Like upwind differencing, this scheme is highly stable, satisfies transportiveness, and produces physically realistic solutions.

Another popular scheme that is considered to yield better results than the hybrid scheme is the *power-law differencing scheme* of Patankar (1980). Here, the upwind differencing becomes effective only when $Pe > 10$. For example, the interface values ϕ_w and ϕ_e according to the power-law differencing formulae for the respective interface velocities $u_w > 0$ and $u_e > 0$ can be determined as

$$\phi_w = (1-\chi_w)\phi_W + \chi_w\phi_P; \quad \phi_e = (1-\chi_e)\phi_P + \chi_e\phi_E \quad \text{for} \quad 0 < Pe_w, Pe_e < 10 \tag{5.51}$$

where $\chi_w = (1-0.1Pe_w)^5/Pe_w$ and $\chi_e = (1-0.1Pe_e)^5/Pe_e$

$$\phi_w = \phi_W; \quad \phi_e = \phi_P \quad \text{for } Pe_w, Pe_e \geq 10 \tag{5.52}$$

The power-law differencing scheme possesses similar properties to the hybrid scheme. It has also enjoyed much extensive usage in practical flow calculations and can be used as an alternative to the hybrid scheme.

Conservativeness concerns the fluxes being represented in a reliable manner. The upwind and central differencing schemes use consistent expressions to evaluate the convective and diffusive fluxes at the control volume faces. This meant that fluxes cancel out when summed and overall conservation is satisfied.

It should be noted that despite the favourable properties of the upwind differencing scheme in satisfying the above fundamental properties and promoting numerical stability, it is widely known that it generally causes unwanted numerical diffusion in space. In order to reduce these numerical errors, high-order approximations such as the second-order upwind and third-order QUICK scheme that are widely applied in many CFD problems have been proposed. The formulation of these schemes is further described in Appendix B.

Unsteady convection-diffusion process: The equation governing the unsteady convection and diffusion process of a property ϕ in a given one-dimensional flow field u is given by

$$\frac{\partial(\rho\phi)}{\partial t} + \frac{\partial}{\partial x}(\rho u\phi) = \frac{\partial}{\partial x}\left(\Gamma\frac{\partial\phi}{\partial x}\right) + S_\phi \tag{5.53}$$

For the purpose of illustration, let us assume that the fluid is incompressible, (i.e. density is constant) and Eq. (5.53) can be rearranged as

$$\frac{\partial\phi}{\partial t} + \frac{\partial}{\partial x}(u\phi) = \frac{1}{\rho}\frac{\partial}{\partial x}\left(\Gamma\frac{\partial\phi}{\partial x}\right) + \frac{S_\phi}{\rho} \tag{5.54}$$

The mass conservation becomes

$$\frac{\partial u}{\partial x}=0 \tag{5.55}$$

Assuming central differencing for the convective and diffusive terms, the partial algebraic form of Eq. (5.53) via the finite-volume method is given by

$$\begin{aligned}&\frac{\partial \phi}{\partial t}+u_e A_E\frac{1}{2}(\phi_W+\phi_P)-u_w A_W\frac{1}{2}(\phi_P+\phi_E)\\&=\Gamma_e A_E\frac{1}{\rho}\left(\frac{\phi_E-\phi_P}{\delta x_E}\right)-\Gamma_w A_W\frac{1}{\rho}\left(\frac{\phi_P-\phi_W}{\delta x_W}\right)+\frac{S_\phi}{\rho}\Delta V\end{aligned} \tag{5.56}$$

In the majority of cases, the time derivative can be approximated by applying the first-order forward difference scheme as above:

$$\frac{\partial \phi}{\partial t}=\frac{\phi^{n+1}-\phi^n}{\Delta t}=\frac{\phi_P^{n+1}-\phi_P^n}{\Delta t} \tag{5.57}$$

where Δt is the incremental time step and the superscripts n and $n+1$ denote the previous and current time levels, respectively. It should be apparently clear from above that a suitable time-marching procedure needs to appropriately update the property ϕ at the central point P and the neighbouring points through time. Let us first examine the implication due to an *explicit* approach. For this approach, Eq. (5.56) can be written as

$$\begin{aligned}&\frac{\phi_P^{n+1}-\phi_P^n}{\Delta t}+u_e^n A_E\frac{1}{2}\left(\phi_W^n+\phi_P^{n+1}\right)-u_w^n A_W\frac{1}{2}\left(\phi_P^{n+1}+\phi_E^n\right)\\&=\Gamma_e^n A_E\frac{1}{\rho}\left(\frac{\phi_E^n-\phi_P^{n+1}}{\delta x_E}\right)-\Gamma_w^n A_W\frac{1}{\rho}\left(\frac{\phi_P^{n+1}-\phi_W^n}{\delta x_W}\right)+\frac{S_\phi^n}{\rho}\Delta V\end{aligned} \tag{5.58}$$

Here again, by identifying the coefficients of ϕ_E and ϕ_W in Eq. (5.58) as a_E and a_W and the coefficient of ϕ_P as a_P, the algebraic form can be written as

$$a_P\phi_P^{n+1}=a_E\phi_E^n+a_W\phi_W^n+b \tag{5.59}$$

where

$$a_E=\frac{\Gamma_e^n A_E}{\rho\delta x_E}-\frac{u_e^n A_E}{2};\quad a_W=\frac{\Gamma_w^n A_W}{\rho\delta x_W}+\frac{u_w^n A_W}{2};$$

$$a_P=a_E+a_W+u_e^n A_E-u_w^n A_W+\frac{1}{\Delta t};\quad b=\frac{S_\phi}{\rho}\Delta V+\frac{1}{\Delta t}\phi_P^n$$

Casting our attention to Eq. (5.58) and the sketch in Fig. 5.9, we see a straightforward mechanism of evaluating the unknown ϕ_P^{n+1} (indicated by the square at time level $n+1$) that is calculated directly from all the values obtained from the indicated circles of the property ϕ at the previous time level n. By definition, in an *explicit* approach, each difference equation contains only one unknown and therefore can be solved *explicitly* for this unknown in a simple manner.

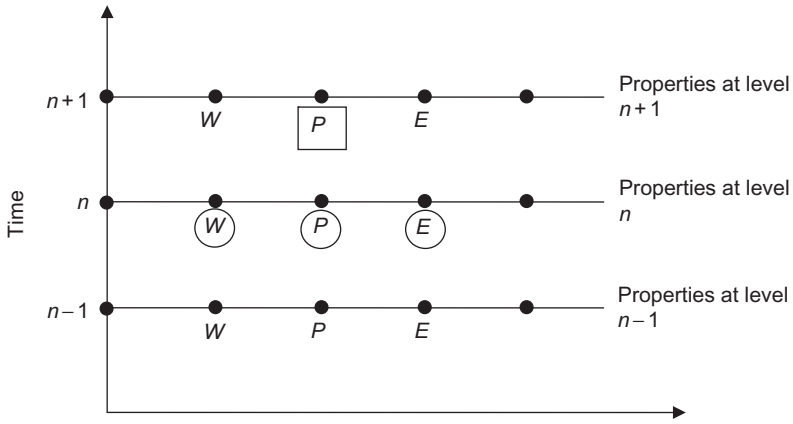


FIG. 5.9 Illustration of an explicit method.

On the other hand, let us consider a time-marching procedure that requires the solution for all the variables at the time level $n+1$. Eq. (5.58) can be rewritten as

$$\frac{\phi_P^{n+1}-\phi_P^n}{\Delta t}+u_e^{n+1}A_E\frac{1}{2}\left(\phi_W^{n+1}+\phi_P^{n+1}\right)-u_w^{n+1}A_W\frac{1}{2}\left(\phi_P^{n+1}+\phi_E^{n+1}\right)$$
$$=\Gamma_e^{n+1}A_E\frac{1}{\rho}\left(\frac{\phi_E^{n+1}-\phi_P^{n+1}}{\delta x_E}\right)-\Gamma_w^{n+1}A_W\frac{1}{\rho}\left(\frac{\phi_P^{n+1}-\phi_W^{n+1}}{\delta x_W}\right)+\frac{S_\phi^{n+1}}{\rho}\Delta V \quad (5.60)$$

In its algebraic form, Eq. (5.60) can be recast as

$$a_P\phi_P^{n+1}=a_E\phi_E^{n+1}+a_W\phi_W^{n+1}+b \quad (5.61)$$

where

$$a_E=\frac{\Gamma_e^{n+1}A_E}{\rho\delta x_E}-\frac{u_e^{n+1}A_E}{2};\quad a_W=\frac{\Gamma_w^{n+1}A_W}{\rho\delta x_W}+\frac{u_w^{n+1}A_W}{2};$$
$$a_P=a_E+a_W+u_e^{n+1}A_E-u_w^{n+1}A_W+\frac{1}{\Delta t};\quad b=\frac{S_\phi}{\rho}\Delta V+\frac{1}{\Delta t}\phi_P^n$$

As sketched in Fig. 5.10, the property ϕ at the central point P and the properties at the neighbouring points are required to be solved simultaneously and possibly coupling with other flow variables such as pressure and temperature appearing in the source term S_ϕ at the current time level within the same difference equation. This is another example of the *fully implicit* approach. By definition, an *implicit* approach is one where the unknowns must be obtained by means of a simultaneous solution of the difference equations applied at *all* grid nodal points at a given time level. Implicit methods usually involve the manipulation of large matrices because of the need to solve large systems of algebraic equations.

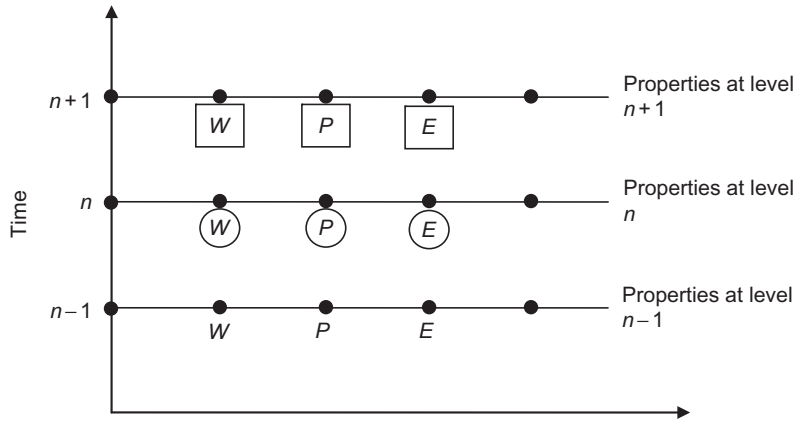


FIG. 5.10 Illustration of an implicit method.

The above explicit and implicit schemes are generally considered as methods having first order in time. Similar to the first order in space, these methods may also cause unwanted numerical diffusion in time. In order to reduce these numerical errors, second-order approximations such as the explicit Adams-Bashforth and semi-implicit Crank-Nicolson schemes have been proposed. The formulation of these schemes is further described in Appendix C.

5.4 NUMERICAL SOLUTIONS TO ALGEBRAIC EQUATIONS

The various discretization methods for the partial differential equations have been described. Through this process, we obtain a system of linear or nonlinear algebraic equations that needs to be solved by some numerical methods. The complexity and size of this set of equations depends on the dimensionality and geometry of the physical problem. Whether the equations are linear or nonlinear, efficient and robust numerical methods are required to solve the system of algebraic equations. There are essentially two families of numerical methods: *direct methods* and *iterative methods*.

Previously, we have highlighted a direct method such as the Gaussian elimination, which can be used to solve the resultant matrix form of a simple one-dimensional steady heat conduction process. It is noted that there are other direct methods that may be employed, such as Cramer's rule for matrix inversion and the Thomas algorithm (tridiagonal matrix algorithm). For finite-difference or finite-volume discretization on structured mesh, the resultant matrix of the algebraic equations is typically sparse; most of the elements are zero, and the nonzero terms are close to the diagonal. For one-dimensional situations, the Thomas algorithm or tridiagonal matrix algorithm is actually a direct method that takes advantage of this particular matrix structure. It is computationally inexpensive and requires a minimum amount of storage in the core

memory and as a result is extensively used in CFD programmes. The Thomas algorithm is further described in the next section.

Iterative methods are, however, based on the repeated applications of an algorithm leading to its eventual convergence after a number of repetitions. They are generally much more economical, and only nonzero terms of the algebraic equations are required to be stored in the core memory. For nonlinear problems, they are used out of necessity but are just as valuable for sparse linear systems. Well-known point-by-point methods such as Jacobi and Gauss-Seidel are described in Section 5.3.2 in order to provide the reader some basic understanding of iterative methods. Other variants from these two iterative methods will also be described particularly those algorithms that are used in solving CFD problems.

5.4.1 Direct Methods

One of the most basic methods for solving linear systems of algebraic equations is the *Gaussian elimination*. The algorithm derives from the basis of systematic reduction of large systems of equations to smaller ones. Let us suppose that the systems of equations can be written in the form

$$A\phi = B \tag{5.62}$$

where ϕ is the unknown nodal variables. Matrix A contains nonzero coefficients of the algebraic equations as illustrated below:

$$A = \begin{bmatrix} A_{11} & A_{12} & A_{13} & \cdots & A_{1n} \\ A_{21} & A_{22} & A_{23} & \cdots & A_{2n} \\ A_{31} & A_{32} & A_{33} & \cdots & A_{3n} \\ \vdots & \vdots & \vdots & \ddots & \vdots \\ A_{n1} & A_{n2} & A_{n3} & \cdots & A_{nn} \end{bmatrix} \tag{5.63}$$

whilst B is composed of known values of ϕ, for example, that are given by the boundary conditions or source/sink terms.

It can be observed that the diagonal coefficients of the matrix A are represented by the entries of $A_{11}, A_{22}, \ldots, A_{nn}$. The heart of the algorithm is to eliminate the entries below the diagonal to yield a lower triangle of zeros. This means eliminating the elements of $A_{21}, A_{31}, A_{32}, \ldots, A_{nn-1}$ by replacing them with zeros. We begin the elimination process by considering the first column elements of $A_{21}, A_{31}, \ldots, A_{n1}$ in the matrix A. By multiplying the first row of the matrix by A_{21}/A_{11} and subtracting these values from the second row, all the elements in the second row are subsequently modified, which includes the terms in B on the right-hand side of the equations. The other elements $A_{31}, A_{41}, \ldots, A_{n1}$ in the first column of matrix A are treated similarly, and by repeating this process down the first column, all the elements below A_{11} are reduced to zero. The same procedure is then applied for the second column

(for all elements below A_{22}) and so forth until the process reaches the $n-1$ column.

After this process is complete, the original matrix A becomes an *upper triangular matrix* that is given by

$$U = \begin{bmatrix} A_{11} & A_{12} & A_{13} & \cdots & A_{1n} \\ 0 & A_{22} & A_{23} & \cdots & A_{2n} \\ 0 & 0 & A_{33} & \cdots & A_{3n} \\ \vdots & \vdots & \vdots & \ddots & \vdots \\ 0 & 0 & 0 & \cdots & A_{nn} \end{bmatrix} \tag{5.64}$$

All the elements in the matrix U except the first row differ from those in the original matrix A. It is therefore more efficient to store the modified elements in place of the original ones. This process is called the *forward elimination* process. The upper triangular system of equations can now be solved by the *back substitution* process. It is observed that the entry of the matrix U contains only one variable, ϕ_n, and is solved as

$$\phi_n = \frac{B_n}{U_{nn}} \tag{5.65}$$

The entry in matrix U just above Eq. (5.65) contains only ϕ_{n-1} and ϕ_n, and once ϕ_n is known, it can be solved for ϕ_{n-1}. By proceeding in an upward fashion, each of the variables ϕ_i is solved in turn. The general form of equation for ϕ_i can be expressed as

$$\phi_i = \frac{B_i - \sum_{j=i+1}^{n} A_{ij}\phi_j}{A_{ii}} \tag{5.66}$$

It is not difficult to see that the bulk of the computational effort is in the *forward elimination* process; the back substitution process requires less arithmetic operations and is thus much less costly. Gaussian elimination can be expensive especially for a full matrix containing a large number of unknown variables to be solved, but it is as good as any other methods that are currently available.

As observed in Example 5.2, we obtained a matrix of the form typically found from the application of the finite-difference or finite-volume method. This special form of matrix can be solved by the Thomas algorithm. We observed that the nonzero elements (neighbouring entries) lie close to the main diagonal entries; it is useful to consider variants of Gaussian elimination that take advantage of this particular banded structure of the matrix (tridiagonal) to maximize computational resources and reduce the arithmetic operations. Let us consider the tridiagonal form of a system of algebraic equations as

$$\begin{bmatrix} A_{11} & A_{12} & & & & & & \\ A_{21} & A_{22} & A_{23} & & & & & \\ & \cdots\cdots & \cdots\cdots & \cdots\cdots & & & & \\ & & A_{ii-1} & A_{ii} & A_{ii+1} & & & \\ & & & \cdots\cdots & \cdots\cdots & \cdots\cdots & & \\ & & & & A_{nn-2} & A_{n-1n-1} & A_{n-1n} & \\ & & & & & A_{nn-1} & A_{nn} & \end{bmatrix} \begin{bmatrix} \phi_1 \\ \phi_2 \\ \cdots\cdots \\ \phi_i \\ \cdots\cdots \\ \phi_{n-1} \\ \phi_n \end{bmatrix} = \begin{bmatrix} B_1 \\ B_2 \\ \cdots\cdots \\ B_i \\ \cdots\cdots \\ B_{n-1} \\ B_n \end{bmatrix} \tag{5.67}$$

The *Thomas algorithm* like the Gaussian elimination solves the system of equations above in two parts: *forward elimination* and *back substitution*. For the *forward elimination* process, the neighbouring banded entries are eliminated below the diagonal to yield zero entries. This means replacing the elements of $A_{21}, A_{32}, A_{43}, \ldots, A_{nn-1}$ with zeros. For the first row, the diagonal entry A_{11} is normalized to unity, and the neighbouring entry A_{12} and matrix B term B_1 are modified according to

$$A'_{12} = \frac{A_{12}}{A_{11}}, \quad B'_1 = \frac{B_1}{A_{11}} \tag{5.68}$$

Like the Gaussian elimination, by multiplying the first row of the matrix by A_{21} and subtracting it from the second row, all the elements in the second row are subsequently modified, which also include the terms in B on the right-hand side of the equations. Applying the same procedure to the rest of the rows of the matrix, the neighbouring element entries and the matrix B terms in general form are

$$A'_{ii+1} = \frac{A_{ii+1}}{A_{ii} - A_{ii-1}A'_{i-1i}}, \quad B'_i = \frac{B_i - A_{ii-1}B'_{i-1}}{A_{ii} - A_{ii-1}A'_{i-1i}} \tag{5.69}$$

The matrix containing the nonzero coefficients is therefore manipulated into

$$\begin{bmatrix} 1 & A'_{12} & & & & & & \\ & 1 & A'_{23} & & & & & \\ & & \cdots\cdots & \cdots\cdots & & & & \\ & & & 1 & A'_{ii+1} & & & \\ & & & & \cdots\cdots & \cdots\cdots & & \\ & & & & & 1 & A'_{n-1n} & \\ & & & & & & 1 & \end{bmatrix} \begin{bmatrix} \phi_1 \\ \phi_2 \\ \cdots\cdots \\ \phi_i \\ \cdots\cdots \\ \phi_{n-1} \\ \phi_n \end{bmatrix} = \begin{bmatrix} B'_1 \\ B'_2 \\ \cdots\cdots \\ \boldsymbol{B'_i} \\ \cdots\cdots \\ B'_{n-1} \\ B'_n \end{bmatrix} \tag{5.70}$$

The second stage simply involves the *back substitution* process, which involves evaluating

$$\phi_n = B'_n \quad \text{and} \quad \phi_i = B'_i - \phi_{i+1}A'_{ii+1} \tag{5.71}$$

It can be seen that the Thomas algorithm is more economical than the Gaussian elimination because of the absence of arithmetic operations (multiplication and divisions) in obtaining ϕ_i during back substitution. Nevertheless, in order

to prevent ill-conditioning (and hence round-off error) for the two direct methods, it is necessary that

$$|A_{ii}| > |A_{ii-1}| + |A_{ii+1}| \tag{5.72}$$

This means that the diagonal coefficients are required to be much larger than the sum of the neighbouring coefficients.

Example 5.3

A steady heat conduction problem in a large brick plate with a uniform heat generation is presented in Example 5.2. With the boundary temperatures of T_A and T_B given, respectively, by 100 and 400°C, determine the discrete nodal temperatures across the brick plate using the Thomas algorithm.

Solution: In this worked example, we will illustrate the arithmetic operations of the Thomas algorithm to solve the resultant system of equations for the one-dimensional steady heat conduction process. The system of equations in matrix form that was previously derived is given as

$$\begin{bmatrix} 3000 & -1000 & 0 & 0 \\ -1000 & 2000 & -1000 & 0 \\ 0 & -1000 & 2000 & -1000 \\ 0 & 0 & -1000 & 3000 \end{bmatrix} \begin{bmatrix} T_1 \\ T_2 \\ T_3 \\ T_4 \end{bmatrix} = \begin{bmatrix} 2000T_A + 2500 \\ 2500 \\ 2500 \\ 2000T_B + 2500 \end{bmatrix}$$

Substituting the temperatures of $T_A = 100$°C and $T_B = 400$°C into the right-hand side of the forcing terms, we have

$$\begin{bmatrix} 3000 & -1000 & 0 & 0 \\ -1000 & 2000 & -1000 & 0 \\ 0 & -1000 & 2000 & -1000 \\ 0 & 0 & -1000 & 3000 \end{bmatrix} \begin{bmatrix} T_1 \\ T_2 \\ T_3 \\ T_4 \end{bmatrix} = \begin{bmatrix} 202{,}500 \\ 2500 \\ 2500 \\ 802{,}500 \end{bmatrix}$$

In the Thomas algorithm, the first step of the *forward elimination* process involves eliminating the lower triangular coefficients below the diagonal coefficients to yield zero entries. By applying Eqs (5.68) and (5.69), the matrix is reduced to

$$\begin{bmatrix} 1 & -0.333 & 0 & 0 \\ 0 & 1 & -0.6 & 0 \\ 0 & 0 & 1 & -0.714 \\ 0 & 0 & 0 & 1 \end{bmatrix} \begin{bmatrix} T_1 \\ T_2 \\ T_3 \\ T_4 \end{bmatrix} = \begin{bmatrix} 67.5 \\ 42.0 \\ 31.8 \\ 365.0 \end{bmatrix}$$

The second stage of the Thomas algorithm simply involves the *back substitution* process. Using Eq. (5.71), the solution to the above system is

$$\begin{bmatrix} T_1 \\ T_2 \\ T_3 \\ T_4 \end{bmatrix} = \begin{bmatrix} 140.0 \\ 217.4 \\ 292.4 \\ 365.0 \end{bmatrix}$$

Discussion: For this simple problem, we could have obtained the solution using the Gaussian elimination instead of the Thomas algorithm. For such a small matrix, the additional arithmetic operations required for the Gaussian elimination to perform on the zero entries may not be as significant compared with the Thomas algorithm. Nevertheless, this is not true when a number of grid points are used to better predict the temperature distribution across the plate. This is because of the additional and more cumbersome numerical computations (multiplication and divisions) that have to be performed on the matrix entries. The algorithm degenerates and becomes inefficient once the order of the matrix becomes higher (>10).

5.4.2 Iterative Methods

Direct method such as Gaussian elimination can be employed to solve any system of equations. Unfortunately, in most CFD problems that usually result in a large system of nonlinear equations, the cost of using this method is generally quite high. It has been demonstrated through the worked example in the previous section that the Thomas algorithm is particularly economical in obtaining the solution for a one-dimensional steady-state heat conduction problem because of the inherent banded matrix structure (tridiagonal). For multidimensional situations, the nature of the solver, however, cannot be readily extended to solve such problems.

This therefore leaves the option of employing iterative methods. In an iterative method, one guesses the solution and uses the equation to systematically improve the solution until it reaches some level of convergence. If the number of iterations is small in achieving convergence, an iterative solver may cost less to use than a direct method. This is usually the case for CFD problems.

Jacobi and Gauss-Seidel methods: The simplest method from the various classes of iterative methods is the Jacobi method. Let us revisit the system of equations, $A\phi = B$, as described in the previous section; the general form of the algebraic equation for each unknown nodal variables of ϕ can be written as

$$\sum_{j=1}^{i-1} A_{ij}\phi_j + A_{ii}\phi_i + \sum_{j=i+1}^{n} A_{ij}\phi_j = B_i \tag{5.73}$$

In Eq. (5.73), the Jacobi method requires that the nodal variables ϕ_j (non-diagonal matrix elements) are assumed to be known at iteration step k and the nodal variables ϕ_i are treated as unknown at iteration step $k+1$. Solving for ϕ_i, we have

$$\phi_i^{(k+1)} = \frac{B_i}{A_{ii}} - \sum_{j=1}^{i-1} \frac{A_{ij}}{A_{ii}}\phi_j^{(k)} - \sum_{j=i+1}^{n} \frac{A_{ij}}{A_{ii}}\phi_j^{(k)} \tag{5.74}$$

The iteration process begins by an initial guess of the nodal variables ϕ_j ($k=0$). After repeated application of Eq. (5.74) to all the n unknowns, the first iteration, $k=1$, is completed. We proceed to the next iteration step, $k=2$, by

substituting the iterated values at $k=1$ into Eq. (5.74) to estimate the new values at the next iteration step. This process is continuously repeated for as many iterations as required to converge to the desired solution.

A more immediate improvement to the Jacobi method is provided by the Gauss-Seidel method in which the updated nodal variables $\phi_j^{(k+1)}$ are immediately used on the right-hand side of Eq. (5.74) as soon as they are available. In such a case, the previous values of $\phi_j^{(k)}$ that appear in the second term of the right-hand side of Eq. (5.74) are replaced by the current values of $\phi_j^{(k)}$, which the equivalent of Eq. (5.74) becomes

$$\phi_i^{(k+1)} = \frac{B_i}{A_{ii}} - \sum_{j=1}^{i-1} \frac{A_{ij}}{A_{ii}} \phi_j^{(k+1)} - \sum_{j=i+1}^{n} \frac{A_{ij}}{A_{ii}} \phi_j^{(k)} \tag{5.75}$$

Comparing the above two iterative procedures, the Gauss-Seidel iteration is typically twice as fast as the Jacobi iteration. After repeated applications of Eqs (5.74) and (5.75), convergence can be gauged in a number of ways. One convenient condition to terminate the iteration process is to ensure that the maximum difference $\phi_j^{(k+1)} - \phi_j^{(k)}$ falls below some predetermined value of acceptable error. The smaller the acceptable error, the more accurate the solution will be but it is noted that this is achieved at the expense of more number of iterations.

Example 5.4

Based on the same worked example of the steady heat conduction problem in a large brick plate with a uniform heat generation, as previously presented in Example 5.2, determine the discrete nodal temperatures across the brick plate using the following:

(a) The Jacobi method
(b) The Gauss-Seidel method

Solution: (a)To illustrate the *Jacobi method*, the resulting set of algebraic equations as previously derived in Example 5.2 is rewritten:

$$\begin{aligned}
3000\,T_1 + 1000\,T_2 + 0 \times T_3 + 0 \times T_4 &= 2500 + 2000\,T_A \\
1000\,T_1 + 2000\,T_2 + 1000\,T_3 + 0 \times T_4 &= 2500 \\
0 \times T_1 + 1000\,T_2 + 2000\,T_3 + 1000\,T_4 &= 2500 \\
0 \times T_1 + 0 \times T_2 + 1000\,T_3 + 3000\,T_4 &= 2500 + 2000\,T_B
\end{aligned}$$

Substituting the boundary temperatures of $T_A = 100°C$ and $T_B = 400°C$, we have

$$\begin{aligned}
3000\,T_1 + 1000\,T_2 + 0 \times T_3 + 0 \times T_4 &= 202{,}500 \\
1000\,T_1 + 2000\,T_2 + 1000\,T_3 + 0 \times T_4 &= 2500 \\
0 \times T_1 + 1000\,T_2 + 2000\,T_3 + 1000\,T_4 &= 2500 \\
0 \times T_1 + 0 \times T_2 + 1000\,T_3 + 3000\,T_4 &= 802{,}500
\end{aligned}$$

The above set of equations can be reorganized so that the required variable is on the left-hand side of the equation:

$$T_1 = 0.333\,T_2 + 0 \times T_3 + 0 \times T_4 + 67.5$$
$$T_2 = 0.5\,T_1 + 0.5\,T_3 + 0 \times T_4 + 1.25$$
$$T_3 = 0 \times T_1 + 0.5\,T_2 + 0.5\,T_4 + + 1.25$$
$$T_4 = 0 \times T_1 + 0 \times T_2 + 0.333\,T_3 + 267.5$$

By employing initial guesses $T_1^{(0)} = T_2^{(0)} = T_3^{(0)} = T_4^{(0)} = 100$, the nodal temperatures for the first iteration are determined as

$$T_1^{(1)} = 0.333(100) + 67.5 = 100.8$$
$$T_2^{(1)} = 0.5(100) + 0.5(100) + 1.25 = 101.25$$
$$T_3^{(1)} = 0.5(100) + 0.5(100) + 1.25 = 101.25$$
$$T_4^{(1)} = 0.333(100) + 267.5 = 300.8$$

The above first iteration values of $T_1^{(1)} = 100.8$, $T_2^{(1)} = 101.25$, $T_3^{(1)} = 101.25$, and $T_4^{(1)} = 300.8$ are substituted back into the system of the equations; the second iteration yields

$$T_1^{(2)} = 0.333(101.25) + 67.5 = 101.2$$
$$T_2^{(2)} = 0.5(100.8) + 0.5(101.25) + 1.25 = 102.3$$
$$T_3^{(2)} = 0.5(101.25) + 0.5(300.8) + 1.25 = 202.3$$
$$T_4^{(2)} = 0.333(101.25) + 267.5 = 301.2$$

After repeated applications of the iterative process up to 10 and 20 iterations, the nodal temperatures have advanced to

$$\begin{bmatrix} T_1^{(10)} \\ T_2^{(10)} \\ T_3^{(10)} \\ T_4^{(10)} \end{bmatrix} = \begin{bmatrix} 135.2 \\ 207.9 \\ 282.2 \\ 360.5 \end{bmatrix} \quad \text{and} \quad \begin{bmatrix} T_1^{(20)} \\ T_2^{(20)} \\ T_3^{(20)} \\ T_4^{(20)} \end{bmatrix} = \begin{bmatrix} 139.7 \\ 217.1 \\ 292.0 \\ 364.7 \end{bmatrix}$$

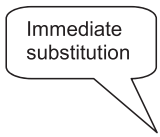
From the previous Example 5.3, we obtained the exact direct solution by the Thomas algorithm, which are

$$\begin{bmatrix} T_1^{exact} \\ T_2^{exact} \\ T_3^{exact} \\ T_4^{exact} \end{bmatrix} = \begin{bmatrix} 140.0 \\ 217.4 \\ 292.4 \\ 365.0 \end{bmatrix}$$

It is observed that the nodal temperatures after 20 iterations are edging closer towards the exact nodal temperature values.

(b) Let us now employ the iterative *Gauss-Seidel method* to the system of algebraic equations. We begin as in the Jacobi method with the set of equations:

$$T_1 = 0.333\,T_2 + 67.5$$
$$T_2 = 0.5\,T_1 + 0.5\,T_3 + 1.25$$
$$T_3 = 0.5\,T_2 + 0.5\,T_4 + + 1.25$$
$$T_4 = 0.333\,T_3 + 267.5$$



Employing the same initial guesses, the first iteration yields

$$T_1^{(1)} = 0.333(100) + 67.5 = 100.8$$

$$T_2^{(1)} = 0.5T_1^{(1)} + 0.5(100) + 1.25 = 0.5(100.8) + 0.5(100) + 1.25 = 101.7$$

$$T_3^{(1)} = 0.5T_2^{(1)} + 0.5(100) + 1.25 = 0.5(101.7) + 0.5(100) + 1.25 = 102.1$$

$$T_4^{(1)} = 0.5T_3^{(1)} + 267.5 = 0.333(102.1) + 267.5 = 301.5$$

After performing 10 iterations, the nodal temperatures have advanced to

$$\begin{bmatrix} T_1^{(10)} \\ T_2^{(10)} \\ T_3^{(10)} \\ T_4^{(10)} \end{bmatrix} = \begin{bmatrix} 139.4 \\ 216.7 \\ 291.9 \\ 364.7 \end{bmatrix}$$

The temperature values obtained through the Gauss-Seidel method at this present stage are comparable with the values obtained by the Jacobi method at 20 iterations.

Discussion: We can infer from this example that the Gauss-Seidel iteration is twice as fast as the Jacobi iteration. Convergence is achieved quicker by the Gauss-Seidel method because of the *immediate substitution* of the temperatures to the right-hand side of the equations whenever they are made available. Thus far, we have not discussed the issue of terminating the iteration process for this particular problem. The degree to which you wish convergence to be achieved is entirely up to you. If the absolute maximum difference $\left|\phi_j^{(k+1)} - \phi_j^{(k)}\right|$ is chosen as the condition for the termination process, the accuracy of the solution depends on the targeted number of significant figures you wish to obtain for the temperatures. The smaller the acceptable error, the higher the number of iterations, but this will achieve greater accuracy.

Sometimes, the convergence to a solution can be enhanced by utilizing the numerical technique called the *successive overrelaxation*. The basic idea behind this technique is an extrapolation procedure where the intermediate nodal variables $\phi_j^{(k+1)}$ are further advanced by a weighted average of the current values of $\phi_j^{(k+1)}$ with the previous values of $\phi_j^{(k)}$. The extrapolated values for $\phi_j^{(k+1)}$ are obtained as $\overline{\phi}_i^{(k+1)} = (1-\lambda)\phi_i^{(k)} + \lambda\phi_i^{(k+1)}$.

These extrapolated values are continuously used in the system of equations as the iteration process progresses. In the above equation, λ is a relaxation factor whose value is usually found by trial-and-error experimentation for a given problem. Generally, the value of λ is bounded between $0 < \lambda < 2$ in order to ensure convergence. If the *successive overrelaxation* is used in conjunction with

the Gauss-Seidel method, for a value λ between $1 < \lambda < 2$, a significant improvement to the nodal temperatures obtained at each iteration step is realized, and hence, convergence is achieved at a faster rate.

Right up to this moment, we have only discussed the application of the iterative methods on one-dimensional problems. For multidimensional problems, with a larger number of grid points, thus a larger number of equations to be solved, the Jacobi and Gauss-Seidel methods, despite their simplicity, may prove rather expensive especially since they generally require a large number of iterations to reach convergence. Successive overrelaxation described above though provides a way of accelerating the iteration process; however, the difficulty in determining the optimum values of λ precludes its wide application in tackling CFD problems. Nevertheless, the primary aim of this section is to introduce the reader to some basic understanding of iterative methods and demonstrate with some worked examples their numerical computations.

Other methods: A practice often applied to multidimensional problems is the use of iterative matrices that correspond to lower-dimensional problems. One commonly used method is the alternating direction implicit (ADI), introduced by Peaceman et al. (1955), which is used to reduce multidimensional problems, whether they are two-dimensional or three-dimensional, to a sequence of a one-dimensional problem. The resulting matrix is of a tridiagonal form of which the Thomas algorithm is applied in each of the coordinate directions; this procedure solves the nodal variables for the lines in one direction and repeats for the lines in other directions. Another iterative method for solving multidimensional discretization equations, particularly for structured mesh, is the strongly implicit procedure (SIP) proposed by Stone (1968). The basic idea of this method involves approximating the matrix A, Eq. (5.31), by an incomplete lower-upper (LU) factorization to yield an iteration matrix M. Unlike other methods, SIP is a good iterative technique in its own right. It has been used in some commercial CFD codes as the standard solver for nonlinear equations. It also provides a good basis for acceleration techniques such as the conjugate gradient methods and multigrid methods.

5.5 PRESSURE–VELOCITY COUPLING—SIMPLE SCHEME

The incompressible forms of the conservation equations governing the fluid flow are derived in Chapter 3 and summarized in Section 3.6. Because of the incompressible assumption, solution to the governing equations is complicated by the lack of an independent equation for pressure. In each of the momentum equations, the fluid flow is driven by the contribution of the pressure gradients. With the additional equation provided by the continuity equation, this system of equations is self-contained; there are four equations for four dependents u, v, w, and p but no independent transport equation for pressure. The implication here is that the continuity and momentum equations are all required to solve for the velocity and pressure fields in an incompressible flow. For such a flow, the continuity equation is a kinematic constraint on the velocity field rather than a

dynamic equation. In order to link the pressure with the velocity for an incompressible flow, one possible way is to construct the pressure field so as to guarantee the conservation of the continuity equation.

Within this section, we describe the basic philosophy behind one of the most popular schemes of pressure-velocity coupling for an incompressible flow. It belongs to the class of iterative methods, which is embodied in a scheme called SIMPLE where the acronym stands for semi-implicit method for pressure-linkage equations. This scheme was developed for practical engineering solutions by Patankar and Spalding (1972). Ever since the pioneering work by them, it has found widespread application in the majority of commercial CFD codes. In this scheme, a guessed pressure field is used to solve the momentum equations. A pressure-correction equation, deduced from the continuity equation, is then solved to obtain a pressure-correction field, which in turn is used to update the velocity and pressure fields. These guessed fields are progressively improved through the iteration process until convergence is achieved for the velocity and pressure fields. The salient features of the SIMPLE scheme and the assembly of the complete iterative procedure will be discussed later.

Variable arrangement on the grid: Before describing the SIMPLE scheme, the choice of arrangement on the grid requires some consideration. Amongst the many arrangements, the two most popular that have gained wide acceptance are the *staggered* and *collocated* grid arrangements.

The aim of having a *staggered* grid arrangement for CFD computations is to evaluate the velocity components at the control volume faces, whilst the rest of the variables governing the flow field, such as the pressure, temperature, and turbulent quantities, are stored at the central node of the control volumes. A typical arrangement is depicted in Fig. 5.11 on a structured finite-volume grid, and it can be demonstrated that the discrete values of the velocity component, u, from the x-momentum equation are evaluated and stored at the east, e, and west, w, faces of the control volume. By evaluating the other velocity components using the y-momentum and z-momentum equations on the rest of the control volume faces, these velocities allow a straightforward evaluation of the mass fluxes that are used in the pressure-correction equation. This arrangement therefore provides a strong coupling between the velocities and pressure, which helps to avoid some types of convergence problems and oscillations in the pressure and velocity fields. Historically, staggered grid arrangement enjoyed its dominance within the CFD framework between the 1960s and 1980s. However, as the use of nonorthogonal grids became a commonplace because of the need to handle complex geometries, alternative grid arrangements had to be explored because of some inherent difficulties in the staggered approach. In particular, if the staggered approach is used in generalized coordinates, curvature terms are required to be introduced into the equations that are usually difficult to treat numerically and may create nonconservative errors when the grid is not smooth.

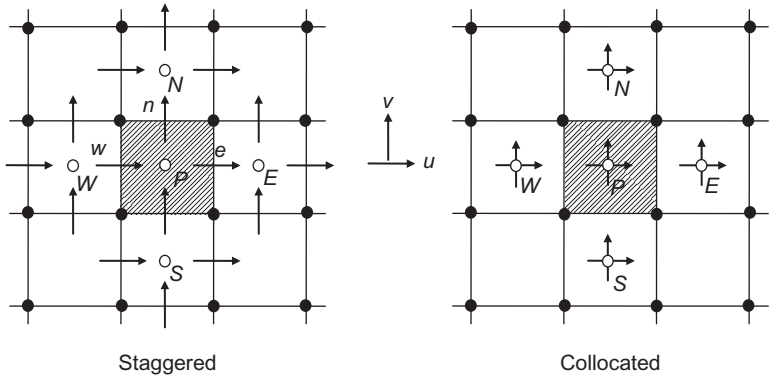


FIG. 5.11 Staggered and collocated arrangements of velocity components on a finite-volume grid (full symbols denote element vertices, and open symbols at the centre of the control volumes denote computational nodes for the storage of other governing variables).

Nowadays, the alternative grid arrangement that is frequently adopted in many commercial CFD codes is the *collocated* grid arrangement. Here, all the flow-field variables including the velocities are stored at the same set of nodal points. For the finite-volume grid as shown in Fig. 5.12, they are stored at the central node of the control volumes (open symbols). The collocated arrangement offers significant advantages in complicated domains especially the capability of accommodating slope discontinuities or boundary conditions that may be discontinuous. Furthermore, if multigrid methods are used, the collocated arrangement allows the ease of transfer of information between various grid levels for all the variables. This grid arrangement was out of favour for incompressible flow computation for a substantial period because of the

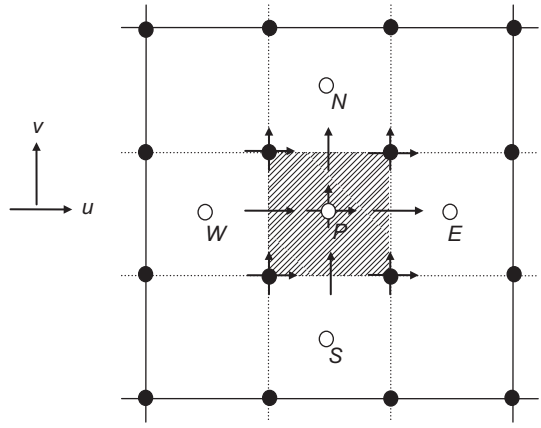


FIG. 5.12 Arrangement of velocity components on a control volume element of a structured grid at the central node, element faces, and element vertices.

difficulties faced in coupling the pressure with the velocity and the occurrence of oscillations in the pressure. Nevertheless, the widespread use of the collocated grid arrangement became prominent once again through the significant developments of the pressure-velocity coupling algorithms such as the well-known Rhie and Chow (1983) interpolation scheme. This scheme that has provided physically sensible solutions on structured collocated meshes generated much interest for unstructured meshing applications. For the vast majority of general flows, this treatment ties together the pressure fields to yield smooth solutions whilst only minimally affecting the mass fluxes. More details of this interpolation scheme are left to the interested reader.

Pressure-correction equation and its solution: The SIMPLE scheme is essentially a guess-and-correct procedure for the calculation of pressure through the solution of a pressure-correction equation. The method is illustrated by considering a two-dimensional steady laminar flow problem in a structured grid as shown in Fig. 5.11.

The SIMPLE scheme provides a robust method of calculating the pressure and velocities for an incompressible flow. When coupled with other governing variables such as temperature and turbulent quantities, the calculation needs to be performed sequentially since it is an iterative process. The sequence of operations in a typical CFD iterative process that embodies the SIMPLE scheme is given in Fig. 5.13 with more details of each of the iterative steps elaborated below:

Step 1. The iterative SIMPLE calculation process begins by guessing the pressure field, p^*. During the iterative process, the discretized momentum equations are solved using the guessed pressure field. Applying the finite-volume method, the equations for the x-momentum and y-momentum that yield the velocity components, u^* and v^*, can be expressed in the same algebraic form as previously derived in Eq. (5.30), which can be recast into

$$a_P^u u_P^* = \sum a_{nb}^u u_{nb}^* - \frac{\partial p^*}{\partial x}\Delta V + b' \tag{5.76}$$

$$a_p^v v_P^* = \sum a_{nb}^v v_{nb}^* - \frac{\partial p^*}{\partial y}\Delta V + b' \tag{5.77}$$

where ΔV is the finite control volume. Here, we simplify the above expressions by introducing a_{nb} to represent the presence of the neighbouring coefficients and $u_{nb}{}^*$ and $v_{nb}{}^*$ to denote the neighbouring nodal velocity components. The pressure gradient terms appearing in the above two equations are taken out from the original source term b of the momentum equations, whilst the other terms governing the fluid flow are left in the source term b'.

Step 2. If we define the correction p' as the difference between the correct pressure field and the guessed pressure field p^*, we get

$$p = p^* + p' \tag{5.78}$$

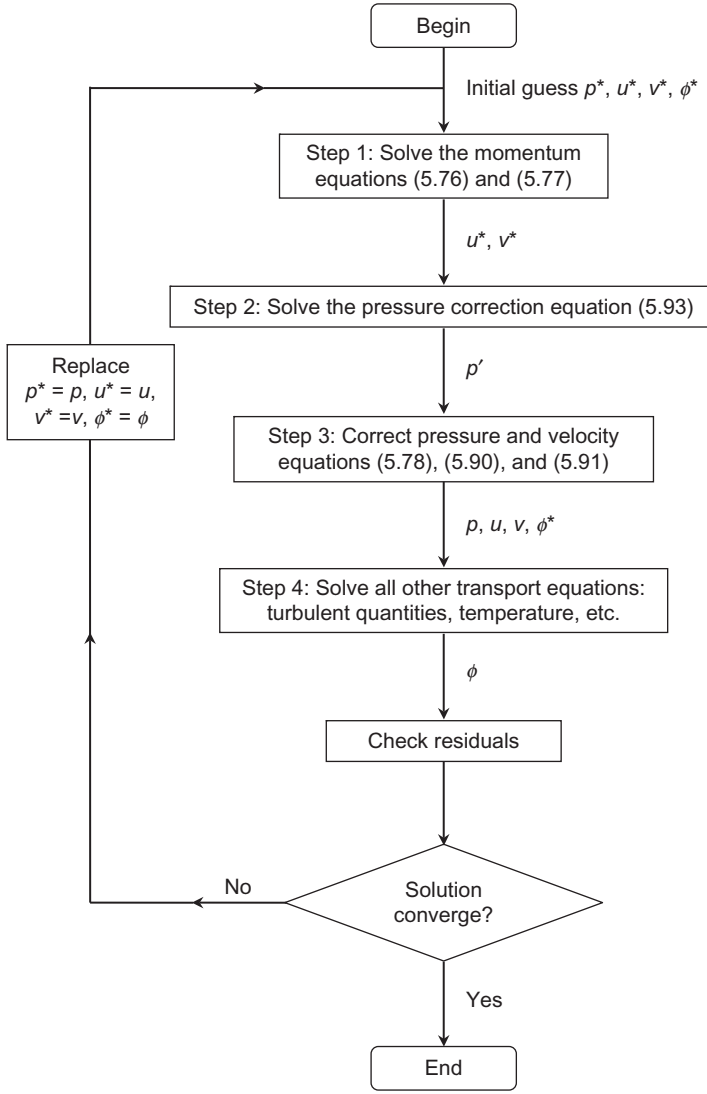


FIG. 5.13 The SIMPLE scheme.

Similarly, we can also define the corrections u' and v' to relate the correct velocities u and v to the guessed velocities u^* and v^*:

$$u = u^* + u' \tag{5.79}$$

$$v = v^* + v' \tag{5.80}$$

The algebraic form of the correct velocities u and v can also be similarly expressed as presented in Eqs (5.76) and (5.77), so that

$$a_P^u u_p = \sum a_{nb}^u u_{nb} - \frac{\partial p}{\partial x}\Delta V + b' \tag{5.81}$$

$$a_p^v v_p = \sum a_{nb}^v v_{nb} - \frac{\partial p}{\partial y}\Delta V + b' \tag{5.82}$$

Subtracting Eqs (5.81) and (5.82) from Eqs (5.76) and (5.77), we obtain

$$a_P^u \left(u_p - u_p^*\right) = \sum a_{nb}^u \left(u_{nb} - u_{nb}^*\right) - \frac{\partial (p - p^*)}{\partial x}\Delta V \tag{5.83}$$

$$a_P^u \left(v_p - v_p^*\right) = \sum a_{nb}^u \left(v_{nb} - v_{nb}^*\right) - \frac{\partial (p - p^*)}{\partial y}\Delta V \tag{5.84}$$

Using the correction formulae (5.78)–(5.80), the above equations may be rewritten as follows:

$$a_P^u u_p' = \sum a_{nb}^u u_{nb}' - \frac{\partial p'}{\partial x}\Delta V \tag{5.85}$$

$$a_P^v v_p' = \sum a_{nb}^v v_{nb}' - \frac{\partial p'}{\partial y}\Delta V \tag{5.86}$$

The SIMPLE scheme approximates the above two Eqs (5.85) and (5.86) by the omission of the terms $\sum a_{nb}^u u_{nb}'$ and $\sum a_{nb}^v v_{nb}'$. It is reminded that this scheme is an iterative approach, and there is no reason why the formula designed to predict p' needs to be physically correct. Hence, we are allowed to construct a formula for p' that is simply a numerical artifice with the aim to expedite the convergence of the velocity field to a solution that satisfies the continuity equation. This is the essence of the algorithm. Once the pressure-correction field is known, the correct velocities u and v can be obtained through the guessed velocities u^* and v^* from the simplified equations of (5.85) and (5.86):

$$u_p = u_P^* - D^u \frac{\partial p'}{\partial x} \tag{5.87}$$

$$v_p = v_P^* - D^v \frac{\partial p'}{\partial y} \tag{5.88}$$

where

$$D^u = \frac{\Delta V}{a_p^u} \quad \text{and} \quad D^v = \frac{\Delta V}{a_p^v} \tag{5.89}$$

Although the above Eqs (5.87)–(5.89) have been developed to correct the velocities from the guessed velocities at the central node of the control volume, these correction formulae can also be generally

applied to any location where the velocity components reside within the computational grid (as shown in Fig. 5.9, the velocities may be located at central node P, or at the control volume faces, or at the vertices of the control volume). The general form of the velocity-correction formulae, by removing the subscript P, can be expressed as

$$u = u^* - D^u \frac{\partial p'}{\partial x} \tag{5.90}$$

$$v = v^* - D^v \frac{\partial p'}{\partial y} \tag{5.91}$$

The derivation of a pressure-correction equation utilizes the above two equations. By differentiating equation (5.90) by the Cartesian direction x and Eq. (5.91) by the Cartesian direction y and summing them together yields

$$-\frac{\partial}{\partial x}\left(D^u \frac{\partial p'}{\partial x}\right) - \frac{\partial}{\partial y}\left(D^v \frac{\partial p'}{\partial y}\right) + \underbrace{\frac{\partial u^*}{\partial x} + \frac{\partial v^*}{\partial y}}_{\text{guessed velocity gradients}} = \underbrace{\frac{\partial u}{\partial x} + \frac{\partial v}{\partial y}}_{\text{correct velocity gradients}} \quad (= 0) \tag{5.92}$$

By invoking the continuity equation, it is shown that the term represented by the source term of the right-hand side for Eq. (5.84) is zero and Eq. (5.84) can be rearranged as

$$\frac{\partial}{\partial x}\left(D^u \frac{\partial p'}{\partial x}\right) + \frac{\partial}{\partial y}\left(D^v \frac{\partial p'}{\partial y}\right) = \underbrace{\left(\frac{\partial u^*}{\partial x} + \frac{\partial v^*}{\partial y}\right)}_{\text{mass residual}} \tag{5.93}$$

Interestingly, Eq. (5.93) behaves like a steady-state diffusion process in a two-dimensional domain. It is a Poisson's equation—one of the well-known equations from classical physics and mathematics. The solution to this Poisson's equation can be achieved through some efficient numerical solvers (conjugate gradient and multigrid methods) as previously discussed above to accelerate its convergence.

Step 3. Once the pressure-correction p' field is obtained, the pressure and velocity components are subsequently updated through the correction formulae of Eqs (5.78), (5.90), and (5.91), respectively. If the solution only concerns a laminar CFD flow problem, the iteration process proceeds directly to check the convergence of the solution. If the solution is not converged, the process is repeated by returning to step 1. The source term appearing in the pressure-correction equation (5.93), commonly known as the *mass residual*, is normally used in CFD computations as a criteria to terminate the iteration procedure. As the mass residual continues to diminish, the pressure correction p' will be zero, thereby yielding a converged solution of $p^* = p$, $u^* = u$, and $v^* = v$.

Step 4. This step is executed if the CFD flow problem is turbulent or it may involve the transfer of heat or mass exchanges between different flow phases. Additional transport equations governing such a flow system need to be solved before convergence is checked. If the solution is not converged, the iterative process returns to step 1, and repetitive calculations are carried out until convergence is reached.

The application of this SIMPLE scheme can be best illustrated by solving Chapter 2 CFD problem of a steady two-dimensional incompressible laminar flow in a channel, which is described by the worked example below.

Example 5.5

Consider the case for a steady two-dimensional incompressible, laminar flow between two stationary parallel plates as in Chapter 2. By obtaining the solution from a CFD code using finite-volume method, track the progress of the intermediate values of u, v, p, p' and the mass residual during the iterative process at a computational nodal point at the centre of the channel.

Solution: The problem is described as follows:

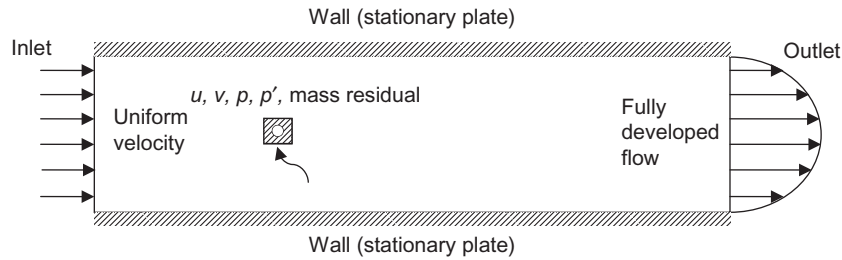


FIG. 5.5.1 Two-dimensional laminar flow in a channel with a monitoring point located at the centre of the channel.

To demonstrate the robustness of the SIMPLE scheme, the iterative process begins by employing the initial guesses: $p^* = 0$, $u^* = 0$, and $v^* = 0$. The discretized equations governing the momentum and pressure correction are solved using the default iterative solvers provided in the commercial CFD code. The inlet, outlet, and wall conditions remain the same as applied in Chapter 2.

Based on Eqs (5.63), (5.64), (5.65), (5.77), (5.78), and (5.80), the calculated values of the pressure p, pressure correction p', velocities u and v, and mass residual for the first iteration at the *monitoring point* are

$$\begin{bmatrix} p^{(1)}_{monitor} \\ p'^{(1)}_{monitor} \\ u^{(1)}_{monitor} \\ v^{(1)}_{monitor} \end{bmatrix} = \begin{bmatrix} 0.02043 \\ 0.06812 \\ 0.01033 \\ -0.1246\times10^{-4} \end{bmatrix} \quad \boxed{\begin{matrix} mass\ residual \Rightarrow \\ 1.2\times10^{-4}\ \mathrm{kg/s} \end{matrix}}$$

The solution of the first iteration from above is subsequently used as intermediate values for the next iteration step; the second iteration yields

$$\begin{bmatrix} p^{(2)}_{monitor} \\ p'^{(2)}_{monitor} \\ u^{(2)}_{monitor} \\ v^{(2)}_{monitor} \end{bmatrix} = \begin{bmatrix} 4.774\times10^{-3} \\ -0.0522 \\ 0.01181 \\ 1.104\times10^{-5} \end{bmatrix} \quad \boxed{\begin{array}{l} mass\ residual \Rightarrow \\ 2.0494\times10^{-4}\ \text{kg/s} \end{array}}$$

After repeated applications of the iterative process, the respective values for the pressure p, pressure correction p', velocities u and v, and mass residual after 10 and 20 iterations are

$$\begin{bmatrix} p^{(10)}_{monitor} \\ p'^{(10)}_{monitor} \\ u^{(10)}_{monitor} \\ v^{(10)}_{monitor} \end{bmatrix} = \begin{bmatrix} 6.83\times10^{-4} \\ -4.949\times10^{-4} \\ 0.01419 \\ -2.963\times10^{-6} \end{bmatrix} \quad \boxed{\begin{array}{l} mass\ residual \Rightarrow \\ 1.8639\times10^{-5}\ \text{kg/s} \end{array}}$$

and

$$\begin{bmatrix} p^{(20)}_{monitor} \\ p'^{(20)}_{monitor} \\ u^{(20)}_{monitor} \\ v^{(20)}_{monitor} \end{bmatrix} = \begin{bmatrix} 6.626\times10^{-4} \\ 3.793\times10^{-6} \\ 0.01482 \\ 2.444\times10^{-7} \end{bmatrix} \quad \boxed{\begin{array}{l} mass\ residual \Rightarrow \\ 5.061\times10^{-7}\ \text{kg/s} \end{array}}$$

From a theoretical viewpoint, the vertical velocity v is zero at the monitoring point, and the iterative process confirms the trend of the prediction towards the zero value. It is seen during the iterative process that the intermediate values of this velocity are much smaller than the rest of the other governing variables; the convergence history plot of this velocity component is therefore omitted since no quantitative comparison can be realized against the other variable convergence histories. The convergence histories for the rest of the governing variables that include the pressure p, pressure correction p', horizontal velocity u, and mass residual are illustrated below:

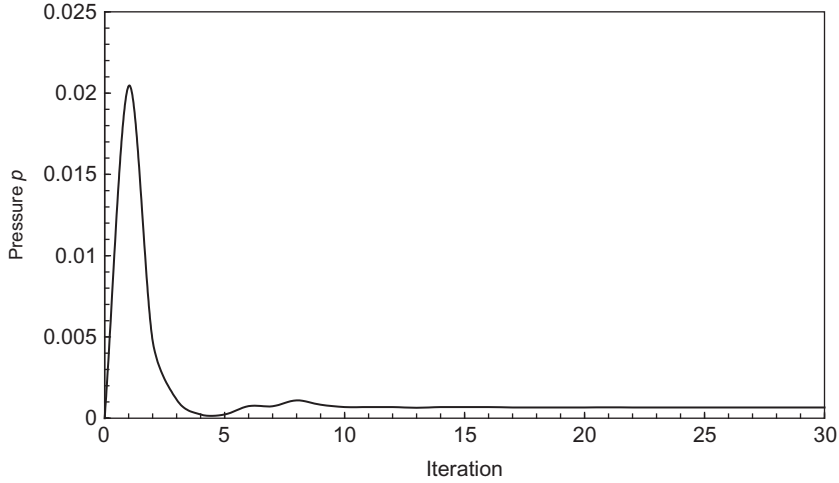


FIG. 5.5.2 Convergence history of the pressure p.

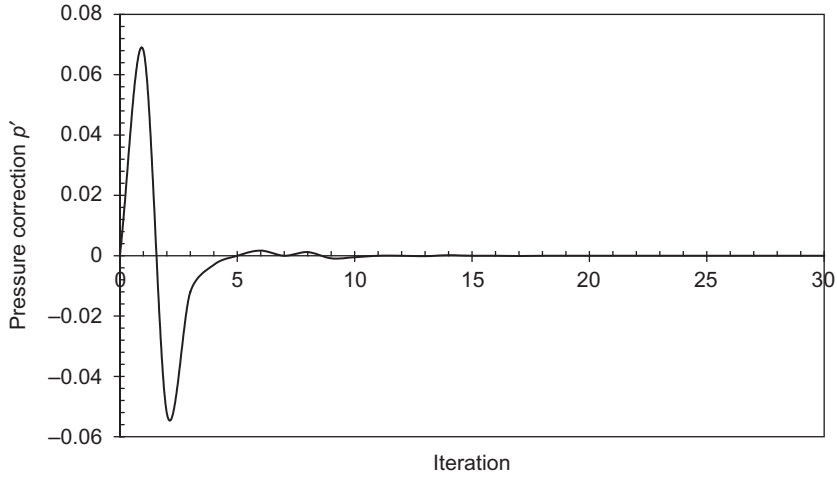


FIG. 5.5.3 Convergence history of the pressure correction p'.

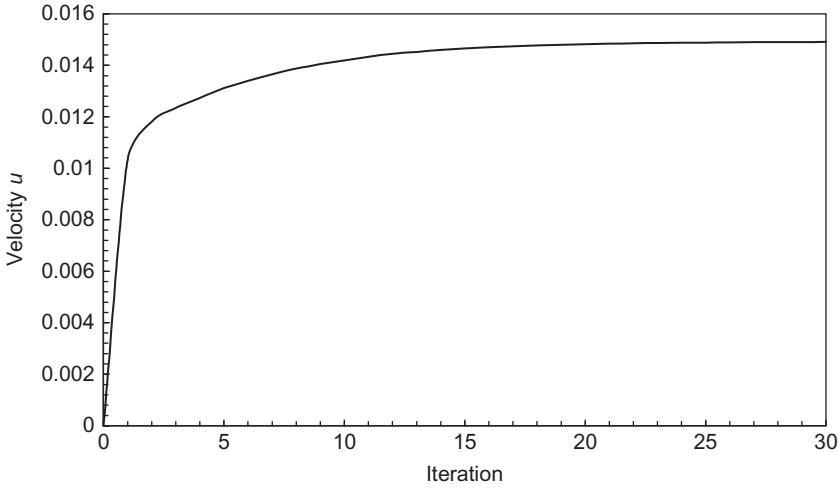


FIG. 5.5.4 Convergence history of the horizontal velocity u.

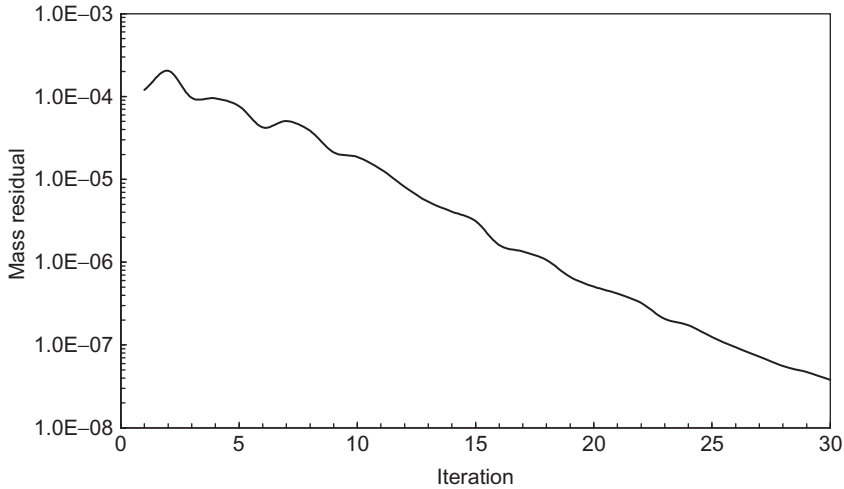


FIG. 5.5.5 Convergence history of the mass residual.

Discussion: From this worked example of a channel flow, the SIMPLE scheme provides an efficient iterative procedure in obtaining the velocity and pressure fields for an incompressible flow. The SIMPLE scheme is a robust method that produces rapid stabilization of the velocity and pressure as seen by their respective convergence histories after five iterations. The mass residual that appears as a source term in the pressure-correction equation (5.80) continues to diminish during the iteration process, thus reaffirming conservation in the continuity equation. Subsequently, the pressure correction p' is seen to be approaching zero. Hence, the corrections that are required to update the velocity field are also approaching zero. The trend of the convergence histories favours the likelihood of a converged steady-state solution.

The reader should be aware of other types of pressure-velocity coupling algorithms that employ a similar philosophy to the SIMPLE algorithm that are employed by CFD users or adopted in commercial CFD codes. These variant SIMPLE algorithms have been formulated with the aims of better improving the robustness and convergence rate of the iterative process. We do not intend to provide the reader with all the details of the available algorithms but to briefly indicate and describe the modifications made to the original SIMPLE algorithm.

The SIMPLE-consistent (SIMPLEC) algorithm by Van Doormal and Raithby (1984) follows the same iterative steps as in the SIMPLE algorithm. The main difference between the SIMPLEC and SIMPLE is that the discretized momentum equations are manipulated so that the SIMPLEC velocity-correction formulae omit terms that are less significant than those omitted in SIMPLE. Another pressure-correction procedure that is also commonly employed is the pressure implicit with splitting of operators (PISO) algorithm proposed by Issa (1986).

This pressure-velocity calculation procedure was originally developed for noniterative computation of unsteady compressible flows. Nevertheless, it has been adapted successfully for the iterative solution of steady-state problems. PISO is simply recognized as an extension of SIMPLE with an additional corrector step that involves an additional pressure-correction equation to enhance the convergence. The SIMPLE-revised (SIMPLER) algorithm developed by Patankar (1980) also falls within the framework of two corrector steps like in PISO. Here, a discretized equation for the pressure provides the intermediate pressure field before the discretized momentum equations are solved. A pressure correction is later solved where the velocities are corrected through the correction formulae as similarly derived in the SIMPLE algorithm.

There are other SIMPLE-like algorithms such as SIMPLE-ShorTened (SIMPLEST) of Spalding (1980), SIMPLEX of Van Doormal and Raithby (1985), or SIMPLE-modified (SIMPLEM) of Acharya and Moukalled (1989) that share the same essence in their derivations. More details of all the above pressure-velocity coupling algorithms are left to keen and interested readers.

5.6 MULTIGRID METHOD

For the multigrid method, it can be categorized into two types: geometrical and algebraic. The former, also known as the full approximation scheme (FAS) multigrid, involves a hierarchy of meshes (cycling between fine and coarse grids), and the discretized equations are evaluated on every level, whilst in the latter, the coarse-level equations are generated without any geometry or rediscretization on the coarse levels—a feature that makes algebraic multigrid particularly attractive for the use on unstructured meshes.

Multigrid method is ideal for solving the Poisson-like pressure or pressure-correction equation such as the SIMPLE method, which will be further discussed in the next section. Conceptually, the multigrid method can be described in the following. Focusing on the system of equations, $A\phi = B$, intermediate solutions of ψ are obtained if this system is solved with an iterative method after some unspecified number of iterations. The residuals R can be defined as

$$A\psi = B - R \tag{5.94}$$

By also defining the errors as the difference between the true and intermediate solutions

$$E = \phi - \psi \tag{5.95}$$

and subtracting Eq. (5.95) from Eq. (5.94), the following relationship between the errors and residuals is

$$AE = R \tag{5.96}$$

During the multigrid cycle, the matrix of coefficients of A and the residuals as described by Eq. (5.70) are transferred from a finer grid to a coarser grid

through volume-weighted *restrictions*. After obtaining the converged solutions of the errors, *prolongations* of computed corrections on the coarse grids are transferred to the next fine grids through trilinear interpolations. The simplest choice of a multigrid cycle can be described by the typical V-cycle with five different grid levels described as shown in Fig. 5.14 (see further details in Section 8.2.4 and references given within). Another strategy, for example, a W-cycle such as depicted in Fig. 5.15, may also be used for cycling between coarse and fine grids. Efficiency may be improved by the decision to switch

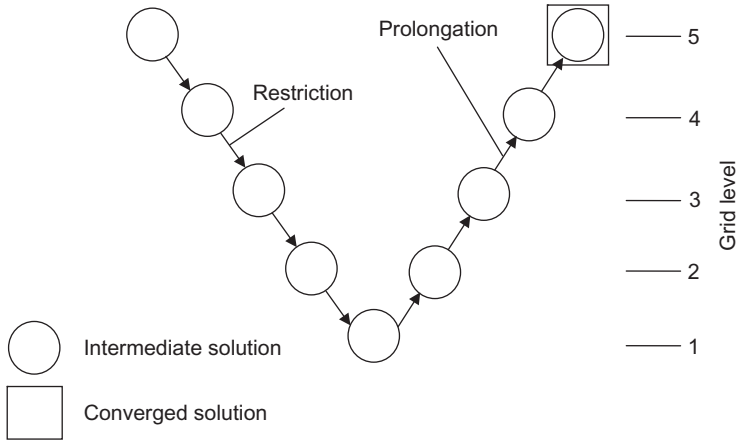


FIG. 5.14 Schematic representation of a multigrid method using a V-cycle.

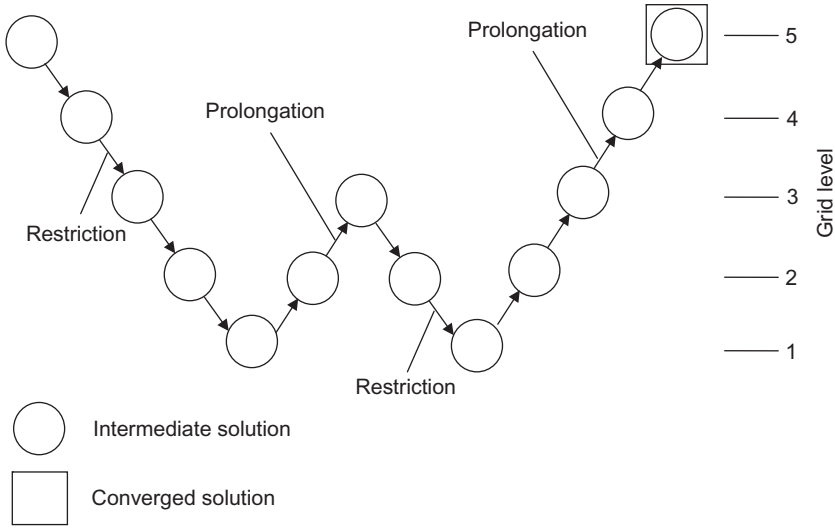


FIG. 5.15 Schematic representation of a multigrid method using a W-cycle.

from one grid to another on the rate of convergence through the combination of V-W cycles or other possible combinations. The optimum choice of parameters is problem-dependent, but their effect on performance is not as dramatic as for the single-grid method.

In theory, the advantage of geometrical multigrid over algebraic multigrid is that the former should perform better for nonlinear problems since nonlinear properties in the system are propagated down to the coarse levels through rediscretization whilst for the latter, once linearization is performed on the system of equations, the nonlinear properties are not 'felt' by the solver until the fine level operator is updated. Multigrid approach is more a strategy than a particular method. More details of these acceleration techniques are left to the interested reader.

5.7 SUMMARY

Let us review some of the basic computational techniques that have been examined in this chapter to solve the governing equations of fluid dynamics.

The first stage of obtaining the computational solution involves the conversion of the governing equations into a system of algebraic equations. This is usually known as the *discretization stage*. We have discussed some of the *discretization tools* such as the finite-difference and finite-volume methods, which form the foundation of understanding the basic features of *discretization*. Both of these methods are abound in many CFD applications.

The second stage involves numerically solving the system of algebraic equations, which can be achieved by either the *direct methods* or the *iterative methods*. Basic direct methods such as the Gaussian elimination and the Thomas algorithm have been described of which the latter is exceedingly economical for a tridiagonal matrix system and is a standard algorithm for the solution of fluid flow equations in a structured mesh. Simple iterative methods such as the point-by-point Jacobi and Gauss-Seidel methods are also described. Nevertheless, CFD problems are generally multidimensional and composed of a large system of equations to be solved. Efficient iterative methods such as the ADI or Stone's SIP are often applied to solve such a system of equations. To further enhance the convergence of the computational solution, precondition conjugate gradient methods or multigrid methods are employed to accelerate the iteration process.

The reader may return to Fig. 5.1 to view how these two stages fit within the overview process of the computational solution procedure. Within the block that is composed of numerical methods, an iterative algorithm for the calculation of pressure and velocity fields based on the SIMPLE scheme is presented for an incompressible flow. The basic philosophy behind this popular scheme is to initially guess a pressure field in the discretized momentum equations to yield the intermediate velocities. The continuity equation in the form of a pressure correction is subsequently solved, which is then used to correct the velocity

and pressure fields. These guessed fields are continuously improved until convergence is reached. The reader may refer back to Fig. 5.13 for a more exhaustive description of the iterative steps that are involved within the SIMPLE scheme.

Finally, we have not discussed in depth the assessment of *convergence*. In practice, the algebraic equations that result from the discretization process yield the flow solution at each nodal point on a finite grid layout. It is expected that, from the truncation errors given in Section 5.2.1, more accurate solutions can be obtained through refining the grid. For an unsteady problem, this can be achieved by employing smaller time intervals. However, for a given required *solution accuracy*, it may be more economical to solve higher-order approximations of the first- and second-order derivative equations governing the fluid flow on a coarse grid rather than using a low-order approximation on a finer grid. This leads to the concept of *computational efficiency*. Other issues such as the *solution consistency* and *stability* of the numerical procedure are also important considerations for the *convergence* of the computational solution. All of these will be investigated in the next chapter.

REVIEW QUESTIONS

5.1 What are the differences between solving a fluid flow problem analytically compared with solving numerically? What are the advantages and disadvantages of each method?

5.2 What are the main advantages and disadvantages of discretization of the governing equations through the finite-difference method?

5.3 Is finite difference more suited for structured or unstructured mesh geometries? Why?

5.4 Consider the following finite-difference formulation for a simplified flow: $\frac{\phi_{i-1}-2\phi_i+\phi_{i+1}}{\Delta x^2}=0$. Is the flow steady or transient? Is it one-, two-, or three-dimensional? Is the nodal spacing constant or variable?

5.5 Using finite difference, show that the steady one-dimensional heat conduction equation $k\frac{\partial^2 T}{\partial x^2}=0$ can be expressed as $\frac{T_{i-1}-2T_i+T_{i+1}}{\Delta x^2}=0$.

5.6 What is the second term in the central difference approximation for a first-order derivative (given below) called, and what does it measure? $\left(\frac{\partial \phi}{\partial x}\right)=\frac{\phi_{i+1,j}-\phi_{i-1,j}}{2\Delta x}+O(\Delta x^2)$

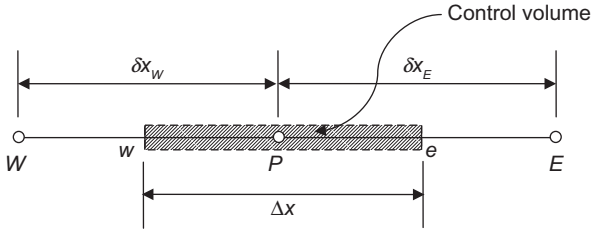
5.7 Which of the following, *forward difference*, *backward difference*, and *central difference*, is most accurate and why?

5.8 What are the main advantages and disadvantages of discretization of the governing equations through the finite-volume method?

5.9 Is finite-volume method more suited for structured or unstructured mesh geometries? Why?

5.10 What is the significance of the integration of the governing equations over a control volume during the finite-volume discretization?

5.11 For the control volume below, show how the one-dimensional steady-state diffusion term $\frac{\partial}{\partial x}\left(\Gamma\frac{\partial\phi}{\partial x}\right)$ is discretized to obtain its discretized equation $\left(\Gamma\frac{\partial\phi}{\partial x}\right)_e A_E - \left(\Gamma\frac{\partial\phi}{\partial x}\right)_w A_w$ for central grid nodal point P.



5.12 In a finite-difference scheme, data are resolved at nodal points. How is this different from the finite-volume scheme?

5.13 How is a steady convective-diffusion process different from a pure diffusion process?

5.14 Why are upwind schemes important for strongly convective flow?

5.15 Why are higher-order upwind schemes more favourable than the first-order upwind scheme?

5.16 For the unsteady convection-diffusion process, what is the difference between *explicit* and *implicit* time-marching approaches?

5.17 What is the difference between using a direct method and an iterative method to solve the discretized equations?

5.18 Is the direct method or iterative method more suitable in solving for a large system of nonlinear equations?

5.19 Why does the Gauss-Seidel iterative method converge to a solution quicker than the Jacobi method?

5.20 What is the technique associated with the *successive overrelaxation*, and why is it used?

5.21 Where are the flow-field variables located in collocated grids? How is this different to the locations in a staggered grid?

5.22 Write down the formulation of central difference scheme for u velocity in the x direction. What is its truncation error in terms of Δx? And state the order of this discretization scheme.

5.23 What is the purpose of the SIMPLE scheme? Does it give us a direct solution or depend on the iterative concept?

5.24 What is the Gaussian elimination method based on? Can this method be used to solve a system of nonlinear algebraic equations?

5.25 Solve the following set of equations by Gaussian elimination:

$$\begin{bmatrix} 100 & 100 & 0 \\ 200 & 100 & - \\ 300 & - & - \\ - & 200 & 300 \end{bmatrix} \begin{bmatrix} T_1 \\ T_2 \\ T_3 \end{bmatrix} = \begin{bmatrix} 400 \\ 100 \\ -300 \\ 400 \end{bmatrix}$$

5.26 Solve the following set of equations by the Thomas Algorithm:

$$\begin{bmatrix} 100 & - & 200 & - \\ 200 & - & 300 & - \\ 100 & 100 & 100 & 0 \\ 100 & - & 400 & 300 \end{bmatrix} \begin{bmatrix} T_1 \\ T_2 \\ T_3 \\ T_4 \end{bmatrix} = \begin{bmatrix} 800 \\ -2000 \\ -200 \\ 400 \end{bmatrix}$$

5.27 Solve the following set of equations using the Gauss-Seidel method:

$$\begin{bmatrix} -1000 & -100 & 200 \\ -100 & -1100 & -100 \\ 200 & -100 & 1000 \\ 0 & 300 & -100 \end{bmatrix} \begin{bmatrix} T_1 \\ T_2 \\ T_3 \end{bmatrix} = \begin{bmatrix} 600 \\ -2500 \\ 1100 \\ 1500 \end{bmatrix}$$

5.28 For the same matrix given in Question 5.27, use the Jacobi method to solve the set of equations. Compare the number of iterations for convergence between the Jacobi method and the Gauss-Seidel method.

5.29 Solve the following set of equations using the Gauss-Seidel method:

(a)

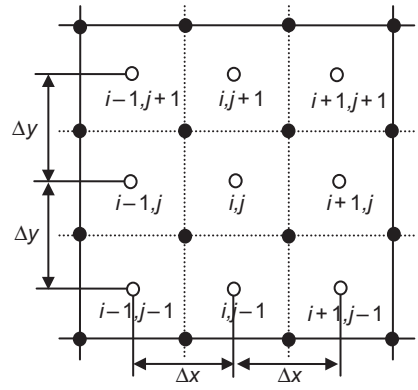
$$\begin{array}{llllllll} 3x_1 & - & x_2 & + & 3x_3 & = & 0 \\ -x_1 & + & 2x_2 & + & x_3 & = & 3 \\ 2x_1 & - & x_2 & - & x_3 & = & 2 \end{array}$$

(b)

$$\begin{array}{llllllllll} 10x_1 & - & x_2 & + & 2x_3 & & & = & 6 \\ -x_1 & + & 11x_2 & - & x_3 & + & 3x_4 & = & 25 \\ 2x_1 & - & x_2 & - & 10x_3 & - & x_4 & = & -11 \\ & & 3x_2 & - & x_3 & + & 8x_4 & = & 15 \end{array}$$

5.30 Following the grid arrangement below, derive the following expression:

$$\left(\frac{\partial^2 u}{\partial x \partial y}\right)_{i,j} = \frac{u_{i+1,j+1} - u_{i+1,j-1} - u_{i-1,j+1} + u_{i-1,j-1}}{4\Delta x \Delta y}$$


i−1,j+1
i,j+1
i+1,j+1
Δy
i−1,j
i,j
i+1,j
Δy
i−1,j−1
i,j−1
i+1,j−1
Δx
Δx

Chapter 6

CFD Solution Analysis: Essentials

6.1 INTRODUCTION

Analysing a *computational solution* represents an integral part in the use of CFD. In Chapter 5, some basic discretization techniques are introduced to allow the reader to familiarize with common methodologies of converting the governing partial differential equations into a system of algebraic equations. This system of algebraic equations is subsequently solved through numerical methods to provide *approximate solutions* to the governing equations. It is these *approximate solutions* that we can interchangeably refer to as *computational solutions*.

In the context of CFD, some of the primary concerns regarding the *computational solutions* are whether the solution can be guaranteed to approach the exact solution of the partial differential equations and if so under what circumstances. This can be (superficially) achieved by forcing the computational solution to converge to an exact solution as the finite quantities shrink to zero. We recall from Chapter 5 that the finite quantities, in time Δt and in space Δx, Δy, and Δz, are prevalent in the system of algebraic equations as a result from the discretization of the partial differential equations. Nevertheless, *convergence* can be neither straightforward nor directly established. Indirect considerations of convergence need, however, to be implicated from aspects such as *consistency* and *stability*. Firstly, it is required that the formulation of the system of algebraic equations through the discretization process should be consistent with the original partial differential equations. The implication of *consistency* here is the recovery of the governing equations by reversing the discretization process through a Taylor series expansion. Secondly, for any chosen numerical algorithm adopted to solve the algebraic equations, *stability* shares a part of the platform and with the *consistency* criteria ensures *convergence*.

The *accuracy* of the *computational solutions* can be affected by errors and uncertainties in the numerical calculations. These errors and uncertainties can be generated either in the conceptual modelling or during the computational design phase, which need to be measured or bounded. The credibility of the *computational solutions* is strongly dependent on whether the errors and uncertainties are identified and qualified, irrespective of their sources. Systematic reduction of errors and uncertainties leads to better representation of real physical flow problems and thus increases the confidence in the use of the CFD simulation code. We will provide a pragmatic approach for estimating

Computational Fluid Dynamics. https://doi.org/10.1016/B978-0-08-101127-0.00006-4
© 2018 Elsevier Ltd. All rights reserved.

these errors and uncertainties in CFD through the *verification* and *validation* procedures.

To close this chapter, indicative case studies are selected to demonstrate the relevance and credibility of the computational solutions by addressing the essentials of *consistency*, *stability*, *convergence*, and *accuracy* that concern a CFD solution analysis. Through discussing these essentials, the reader may take upon himself/herself to realize and appreciate various numerical aspects that are involved in solving the particular flow problems. Each of these embraces its own physical significance; it is assumed that the reader already possesses some basic knowledge of the fluid flow and heat-transfer processes in order to better understand the physical considerations of the numerical simulations.

6.2 CONSISTENCY

The property of *consistency* appears rather rhetorical at hindsight. Nevertheless, it is an important property and concerns the discretization of the partial differential equations where the approximation performed should diminish or become exact if the finite quantities, such as the time step Δt and mesh spacing Δx, Δy, and Δz, tend to zero. In Section 5.2.1 of the finite-difference method, the concept of *truncation error* measures the discrete approximation obtained through a Taylor series expansion about a single nodal point. Essentially, the *truncation error* represents the difference between the discretized equation and the exact one. As a result, the original partial differential equation is recovered by the addition of a remainder, the *truncation error*. This error basically measures the accuracy of the approximation and determines the rate at which the error decreases as the time step and/or mesh spacing is reduced.

For any numerical method to be *consistent*, the *truncation error* must become zero when the time step $\Delta t \to 0$ and/or mesh spacing Δx, Δy, and $\Delta z \to 0$. This error is usually proportional to a power of nth for the finite quantities. If the most important term is proportional to $(\Delta t)^n$ or $(\Delta x_i)^n$, the numerical method results in an nth-order approximation for $n > 0$. Ideally, all terms in the governing equations should be discretized with the approximation of the same order of accuracy. However, in practice, some terms (e.g. advection terms for high Reynolds number flows) may be particularly dominant, and a high-order approximation may be required to treat them with more accuracy than others.

Some basic ideas of *consistency* are further elucidated through the illustrative worked examples below.

Example 6.1

Consider the discretized form of the incompressible steady-state two-dimensional continuity equation $\frac{\partial u}{\partial x} + \frac{\partial v}{\partial y} = 0$ in a structured uniform grid arrangement as in Example 5.1. Discuss the remainder or truncation error associated with the original form of the partial differential equation.

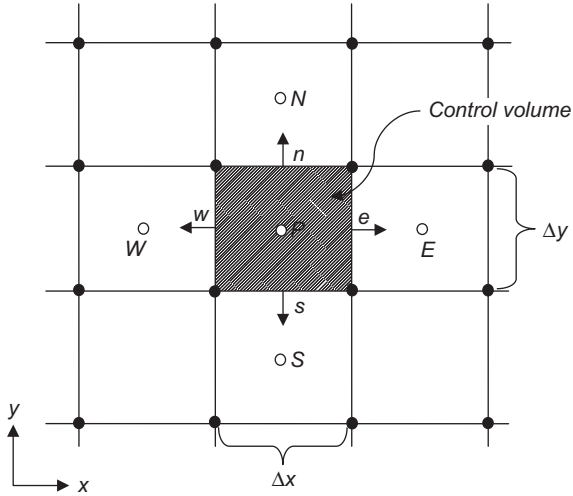


FIG. 6.1.1 Control volume for the two-dimensional continuity equation problem.

Solution: An elemental control volume of the two-dimensional structured grid is shown in Fig. 6.1.1. The centroid of the control volume is indicated by the point P, which is surrounded by adjacent control volumes having their respective centroids indicated by the following points: east, E; west, W; north, N; and south, S. The control volume having its centroid at P has respective faces indicated by east, e; west, w; north, n; and south, s.

The discretized form obtained through the finite-volume method is expressed by

$$\frac{u_e - u_w}{\Delta x} + \frac{v_n - v_s}{\Delta y} = 0$$

The face velocities u_e, u_w, v_n, and v_s are located midway between each of the control volume centroids, which allows us to determine the face velocities through the interpolation of the centroid values. Thus,

$$u_e = \frac{u_P + u_E}{2};\quad u_w = \frac{u_P + u_W}{2};\quad v_n = \frac{v_P + v_N}{2};\quad v_s = \frac{v_P + v_S}{2}$$

By substituting the above expressions to the discretized form of the velocity first-order derivatives, we get

$$\frac{u_E - u_W}{2\Delta x} + \frac{v_N - v_S}{2\Delta y} = 0$$

To recover the original form of the partial differential equation, the above equation can be rewritten in terms of the truncation errors obtained through Taylor series expansion described in Section 5.2.1 of Eqs (5.3) and (5.8) as

$$\frac{u_E - u_W}{2\Delta x} + \frac{v_N - v_S}{2\Delta y} + \left[\underbrace{O\left(\Delta x^2, \Delta y^2\right)}_{Truncation\ error}\right]_P = 0$$

The numerical method results in an nth-order approximation of 2. The approximation is therefore second order accurate at the grid nodal point P.

Discussion: The original partial differential equation is recovered (satisfying *consistency*) from the discretized equation that includes the truncation error, as the mesh spacing Δx and $\Delta y \to 0$. For the above second-order scheme, halving the mesh spacing results in a reduction in the truncation errors by a factor of four.

Example 6.2

Consider the discretized form of the one-dimensional transient diffusion equation. Assuming that the thermal diffusivity α $(=k/\rho C_p)$ is constant, discuss the remainder or truncation error associated with the DuFort–Frankel (DuFort and Frankel, 1953) differencing of the transient heat conduction equation.

Solution: The one-dimensional transient diffusion equation can be expressed as

$$\frac{\partial \phi}{\partial t} - \alpha \frac{\partial^2 \phi}{\partial x^2} = 0 \tag{6.2A}$$

Applying the DuFort and Frankel differencing to the above equation yields

$$\frac{\phi_i^{n+1} - \phi_i^{n-1}}{2\Delta t} - \frac{\alpha}{\Delta x^2}\left(\phi_{i+1}^n - \phi_i^{n+1} - \phi_i^{n-1} + \phi_{i-1}^n\right) = 0$$

The left-hand-side term of Eq. (6.2A) that represents the time derivative about the ith node is analogous to the truncation error of the second-order central differencing in space, namely,

$$\frac{\partial \phi}{\partial t} = \frac{\phi_i^{n+1} - \phi_i^{n-1}}{2\Delta t} + \underbrace{O\left(\Delta t^2\right)_i}_{Truncation\ error}$$

The right-hand-side term of Eq. (6.2A) can be represented according to the second-order derivative in space of Eq. (5.9) yielding the following truncation error:

$$\alpha \frac{\partial^2 \phi}{\partial x^2} = \frac{\alpha}{\Delta x^2}\left(\phi_{i+1}^n - \phi_i^{n+1} - \phi_i^{n-1} + \phi_{i-1}^n\right) + \underbrace{O\left(\Delta x^2\right)_i}_{Truncation\ error}$$

A Taylor series expansion of the exact solution substituted into the one-dimensional transient heat conduction equation, neglecting higher-order terms, is thus given by

$$\left[\frac{\partial\phi}{\partial t}-\alpha\frac{\partial^2\phi}{\partial x^2}+\alpha\left(\frac{\Delta t}{\Delta x}\right)^2\frac{\partial^2\phi}{\partial t^2}\right]_i+\left[\underbrace{O\left(\Delta t^2,\Delta x^2\right)}_{Truncation\ \ error}\right]_i=0$$

Discussion: As demonstrated in Fletcher (1991), $\Delta t/\Delta x$ must $\rightarrow 0$ at the same rate as Δt, $\Delta x \rightarrow 0$ to achieve *consistency*. It is also required that $\Delta t \ll \Delta x$ for *consistency* or else the scheme becomes inaccurate (i.e. if $(\Delta t/\Delta x)^2$ is large). From a practical viewpoint, there is effectively a restriction on the size of Δt when using the DuFort and Frankel scheme. Consider the Dirichlet boundary conditions set at the opposite ends as $\phi\ (t, x=0)=1$ and $\phi\ (t, x=1)=0$. With a constant thermal diffusivity of $\alpha=0.5$ and $\Delta x=1/10$, the steady-state solutions to Eq. (6.2A) subjected to time step $\Delta t=1/10$ (blue) and time step $\Delta t=50$ (red) are shown in Fig. 6.2.1. The exact solution is given in Fig. 6.2.2. It is clearly seen that the solution for large $(\Delta t/\Delta x)$ is inconsistent with the exact solution when compared with the result obtained for a smaller $(\Delta t/\Delta x)$.

From the worked examples above, it is clear that the property of *consistency* is necessary if the approximate solution is to converge to the solution of the partial differential equation. Nevertheless, this property alone is not a sufficient condition. Even though the discretized equations might be equivalent to the partial differential equation as the finite quantities shrink to zero, it may not necessarily mean that the solution of the discretized equations follows the exact solution of the partial differential equation. The latter is evidenced by the inaccurate solution as a result of large $(\Delta t/\Delta x)$ in Example 6.2.

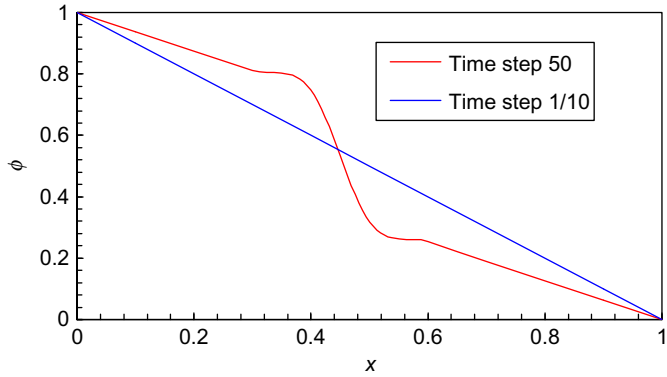


FIG. 6.2.1 Steady-state solution for $\Delta t=1/10$ and $\Delta t=50$ with a fixed grid step size $\Delta x=1/10$.

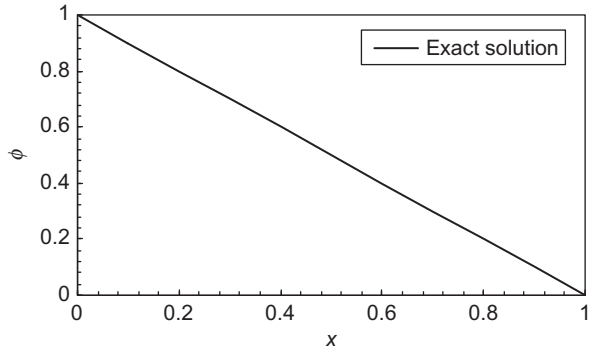


FIG. 6.2.2 The exact solution for Eq. (6.2A).

6.3 STABILITY

In addition to *consistency*, another property that also strongly governs the numerical solution method is *stability*. This property concerns the growth or decay of errors introduced at any stage during the computation. It is noted that the errors being referred here are not those produced by incorrect logic but those that occur because of rounding off at every step of computation due to the finite number of significant figures the computer hardware can accommodate as well as poor initial guess. A numerical solution method is therefore considered to be stable if it does not magnify the errors that appear in the course of the numerical solution process. *Stability* in temporal problems guarantees that the method yields a bounded solution whenever the exact solution is bounded. *Stability* in the context of iterative methods ensures that the solution does not diverge.

The property of *stability* can be rather difficult to investigate. The problem is further exacerbated when boundary conditions and nonlinearities are present. For this reason, the *stability* aspect for a numerical method is commonly investigated with constant coefficients without boundary conditions. The results obtained in this way can often be applied to more complicated problems albeit with some notable exceptions. However, when solving complex, nonlinear and coupled equations with complex boundary conditions, there are few stability studies we can infer. In this circumstance, we have to rely on experience and intuition to ensure *stability* of the numerical procedure. A number of solution schemes require that the time step is set below a certain limit or promote underrelaxation in the system of algebraic equations. We shall discuss these issues and provide guidelines for the appropriate selection of time step size and suitable underrelaxation factors in Section 6.4.3.

For linear problems, the two most common methods of stability analysis are the matrix method and the von Neumann method. Both methods are based on predicting whether there will be a growth of error between the true solution of the numerical method and the actual computed solution, which also includes the round-off contamination. A worked example will be demonstrated on the

application of the von Neumann stability method on a convection-type equation. Other related stability issues will also be demonstrated by additional numerical examples below.

Example 6.3

Consider the one-dimensional convection-type equation: $\frac{\partial \phi}{\partial t} + u\frac{\partial \phi}{\partial x} = 0$. Demonstrate the use of the von Neumann stability method to analyse the stability properties of the linear partial differential equation.

Solution: The exact form of the stability criterion depends on the particular differencing approximation applied to the equation. Using the finite-difference method, let us approximate the time and spatial derivatives with forward and central differences, where the discretized form of the convection-type equation becomes

$$\frac{\phi_i^{n+1} - \phi_i^n}{\Delta t} + u\frac{\phi_{i+1}^n - \phi_{i-1}^n}{2\Delta x} = 0 \tag{6.3A}$$

where u is the velocity. To analyse the stability of the above equation, consider the errors introduced at every grid point as

$$\xi_i^n = \phi_i^n - {}^*\phi_i^n \tag{6.3B}$$

where ϕ_i^n is the true solution of the numerical method and ${}^*\phi_i^n$ is the actually computed solution. For the discretized equation, we are actually calculating

$$\frac{{}^*\phi_i^{n+1} - {}^*\phi_i^n}{\Delta t} + u\frac{{}^*\phi_{i+1}^n - {}^*\phi_{i-1}^n}{2\Delta x} = 0$$

Substituting Eq. (6.3B) into the above followed by the application of Eq. (6.3A) yields

$$\frac{\xi_i^{n+1} - \xi_i^n}{\Delta t} + u\frac{\xi_{i+1}^n - \xi_{i-1}^n}{2\Delta x} = 0 \tag{6.3C}$$

For a linear computational algorithm, the error ξ_i^n in the majority of textbooks (Fletcher, 1991; Anderson, 1995) deals with just one term of the finite complex Fourier series, which is given as

$$\xi_i^n = e^{at}e^{ik_m x} \tag{6.3D}$$

where a is a constant and k_m is the wave number. Substituting the above into Eq. (6.3C), we obtain

$$\frac{e^{a(t+\Delta t)}e^{ik_m x} - e^{at}e^{ik_m x}}{\Delta t} + u\frac{e^{at}e^{ik_m(x+\Delta x)} - e^{at}e^{ik_m(x-\Delta x)}}{2\Delta x} = 0$$

After some arithmetic manipulation and applying trigonometric identities, the above equation reduces to

$$e^{a\Delta t} = 1 - iC\sin(k_m \Delta x)$$

where $C = u\Delta t/\Delta x$. For von Neumann stability, the following requirement needs to be satisfied for the amplification factor $\left|e^{a\Delta t}\right| \leq 1$; therefore, the criterion for C is $C^2 \leq 2\Gamma$ (diffusion coefficient). Based on the latter criterion, the discretized equation (6.3A) since being inviscid ($\Gamma = 0$) will lead to an unstable solution no matter what values of Δt in the parameter C. It is therefore classified as *unconditionally unstable*.

Alternatively, let us replace the time variable ϕ_i^n in Eq. (6.3A) as an average value between grid points $i+1$ and $i-1$, that is

$$\phi_i^n = \frac{1}{2}\left(\phi_{i-1}^n + \phi_{i+1}^n\right)$$

Substituting the above into Eq. (6.3A), the discretized form becomes

$$\frac{\phi_i^{n+1} - \frac{1}{2}\left(\phi_{i-1}^n + \phi_{i+1}^n\right)}{\Delta t} + u\frac{\phi_{i+1}^n - \phi_{i-1}^n}{2\Delta x} = 0 \tag{6.3E}$$

We get a similar error equation in the form of Eq. (6.3C) as

$$\xi_i^{n+1} = \frac{\xi_{i-1}^n + \xi_{i+1}^n}{2} - C\frac{\xi_{i+1}^n - \xi_{i-1}^n}{2}$$

By substituting Eq. (6.3D) into the above and after some arithmetic manipulation, the amplification factor becomes

$$e^{a\Delta t} = \cos\left(k_m\Delta x\right) - iC\sin\left(k_m\Delta x\right)$$

Here, the von Neumann stability requirement of $\left|e^{a\Delta t}\right| \leq 1$ is met as long as the parameter $C \leq 1$.

Discussion: The von Neumann stability analysis performed on a simple linear equation provided some fundamental insights into the application of various differencing schemes to achieve stability. The forward differencing in time employed in Eq. (6.3A) fails to satisfy the stability requirement of $\left|e^{a\Delta t}\right| \leq 1$. However, by cleverly replacing the time derivative with a first-order difference where the variable $\phi(t)$ is represented by an average value between neighbouring grid points as illustrated in Eq. (6.3E), the stability requirement of $\left|e^{a\Delta t}\right| \leq 1$ can be met for $C \leq 1$. The differencing used to represent the time derivative is called the *Lax method* named after the mathematician Peter Lax who first proposed it. The recurring parameter C in this example is commonly called the Courant number. It means that $\Delta t \leq \Delta x/u$ for the numerical solution to be stable. Moreover, it is also commonly called the *Courant-Friedrichs-Lewy* condition, generally written as the CFL condition. It is an important stability criterion for convection-type equations.

Example 6.4

Consider again the one-dimensional transient diffusion equation as described in Example 6.2. By applying the finite-difference discretization to the equation, discuss the stability of the numerical solution using the explicit Euler method at two different time step sizes of $\Delta t = 1/100{,}000$ and $\Delta t = 1/1000$ with a fixed

grid step size of $\Delta x = 1/100$. Approximate the time and spatial derivatives according to the first-order forward and second-order central differences. The initial condition is set according to $\phi\ (t=0,\ x) = 1 - x + \sin(2\pi x)$ where $0 \le x \le 1$. The Dirichlet boundary conditions are, respectively, $\phi\ (t,\ x=0) = 1$ and $\phi\ (t,\ x=1) = 0$. The thermal diffusivity α is also assumed constant with a value of 0.5.

Solution: The finite-difference discretized form of the diffusion equation (6.2A) using the explicit Euler method in this example can be expressed as

$$\varphi_i^{n+1} = \varphi_i^n + \alpha \frac{\Delta t}{\Delta x^2} \left(\varphi_{i+1}^n - 2\varphi_i^n + \varphi_{i-1}^n \right)$$

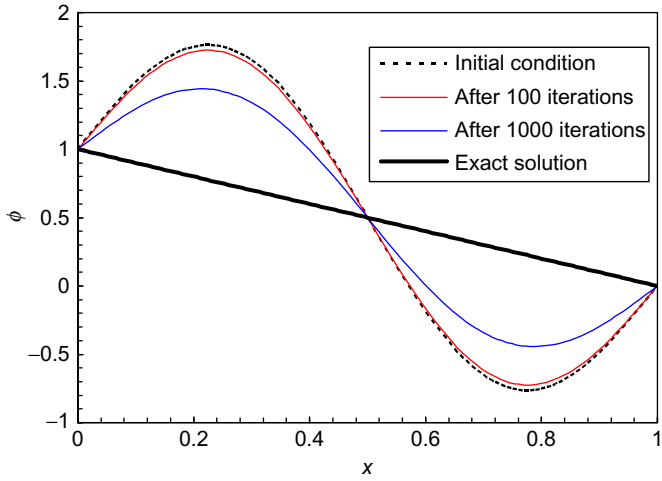


FIG. 6.4.1 Time advancement with $\Delta t = 1/100{,}000$ and $\Delta x = 1/100$.

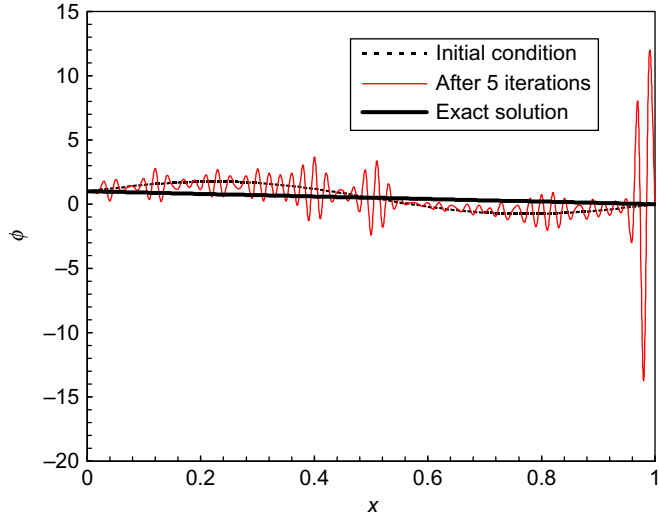


FIG. 6.4.2 Time advancement with $\Delta t = 1/1000$ and $\Delta x = 1/100$.

The transient results for ϕ are as follows:

Discussion: The sensitivity of the time step Δt to the time-advancement procedure is demonstrated for the explicit Euler method of a diffusion-type equation. For this particular example, the condition for stability is given by $\Delta t \leq \Delta x^2$. In Fig. 6.4.1 where the time step Δt, which is much smaller than the grid size Δx, the numerical procedure marches in a stable fashion and shows signs of convergence tendencies. After 1000 iterations, the intermediate result is gradually approaching towards the exact solution profile. Nevertheless, for larger time step such as employed for the case in Fig. 6.4.2 (note the difference in scale along the vertical axis for ϕ), when the time step Δt is much greater than the grid size Δx, the numerical procedure strongly exhibits strong signs of instability. This is evidenced even after five iterations.

Example 6.5

Consider again the convection-type equation as described in Example 6.3. Using the finite-difference method to discretize the equation, discuss the stability of the numerical solution using the explicit Euler method with a fixed time step size of $\Delta t = 1$ at two different grid step sizes of $\Delta x = 1$ and $\Delta x = 1/2$. Approximate the time and spatial derivatives according to the first-order forward and backward differences. The initial condition is set according to a Gaussian profile (similar to the initial value proposed in Hu et al., 1996):

$$\phi(t=0,x) = \exp\left[-\ln(2)\left(\frac{x-50}{3}\right)^2\right]$$

with the Dirichlet boundary condition of $\phi\ (t,\ x=0)=0$.

Solution: The finite-difference discretization of the convection-type equation using the explicit Euler method is given by

$$\phi_i^{n+1} = \phi_i^n - u\frac{\Delta t}{\Delta x}\left(\phi_i^n - \phi_{i-1}^n\right)$$

For stability, the CFL number must be less or equal to unity, that is $C \leq 1$. Assuming a constant CFL number of unity, $\Delta t \leq \Delta x/u$. If the velocity u is taken to be 1 m/s, the approximation is stable when $\Delta t \leq \Delta x$. The transient results for ϕ are as follows:

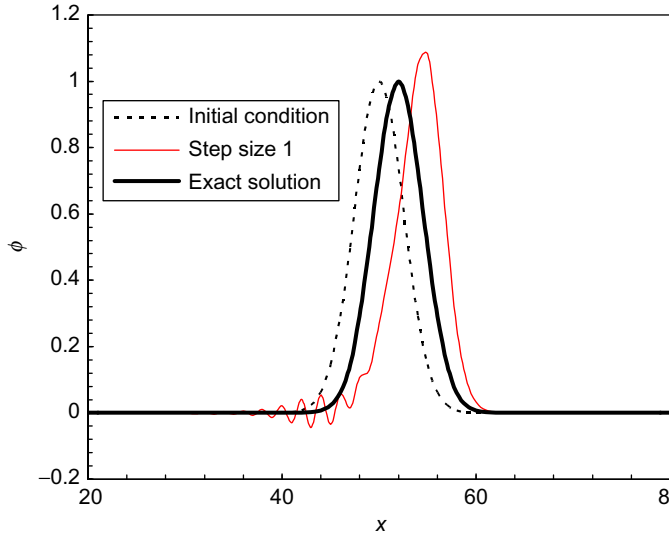


FIG. 6.5.1 Time advancement with $\Delta t = 1$ and $\Delta x = 1$.

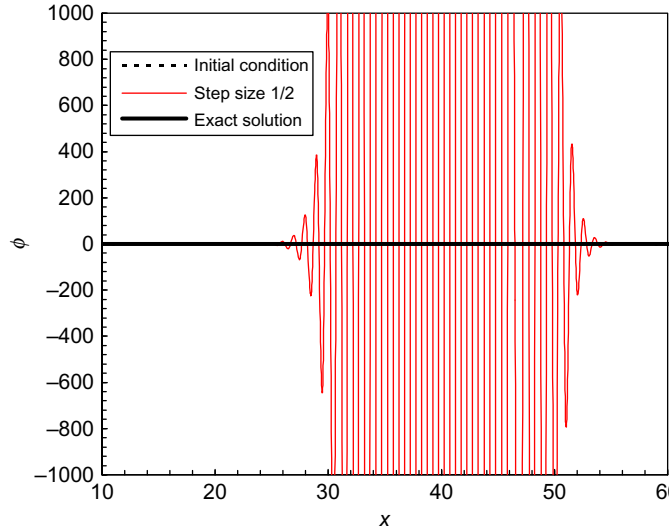


FIG. 6.5.2 Time advancement with $\Delta t = 1$ and $\Delta x = 1/2$.

Discussion: The sensitivity of the grid size Δx to the time-advancement procedure, whilst maintaining a fixed time step Δt, is demonstrated for the explicit Euler method for a convection-type equation. This example illustrates the influence of the important CFL number to the stability of the numerically explicit marching procedure. For the case in Fig. 6.5.1 where the condition is $\Delta t = \Delta x$, the numerical procedure is relatively stable though some unfavourable wiggles are attained during the numerical computations. The removal of these unwanted wiggles can be overcome by marching with smaller time step sizes. However, when $\Delta t > \Delta x$ as for the case depicted in Fig. 6.5.2 (note again the difference in scale along the vertical axis for ϕ), the time-advancing numerical procedure is evidently unstable. The case that is solved in Fig. 6.5.2 clearly accentuates the violation of the CFL number for explicit time-marching methods.

We have thus far discussed *stability* by predominantly focusing on explicit types of numerical procedures in the worked examples above. Explicit-type procedures can be considered as *conditionally stable* since they are strongly influenced by the temporal resolution. For implicit-type procedures, they are usually *unconditionally stable*. This is because allowance is provided for the variable to be continuously updated within the time step instead of calculating from the previous time step values. The majority of commercial CFD codes employ implicit-type procedures due to the inherent stability they possess. Nevertheless, instability that arises in these codes does not depend on the temporal resolution but rather the adoption of the segregated approach where the calculations of the transport variables are performed sequentially in the iterative process. In order to ensure *convergence*, the use of underrelaxation factors can assist in promoting *stability* of the segregated iterative computations. These will be further discussed and explored in the next section.

6.4 CONVERGENCE

6.4.1 What is Convergence

If a numerical method can satisfy the two important properties of *consistency* and *stability*, we generally find that the numerical procedure is convergent. *Convergence* of a numerical process can therefore be stated as the solution of the system of algebraic equations approaching the true solution of the partial differential equations having the same initial and boundary conditions as the refined grid system (*grid convergence*). For initial value (marching) problems governed by the finite-difference approximations of linear partial differential equations, Lax's equivalence theorem is given here without proof. It states that 'given a property initial valued problem and a finite-difference approximation *consistency* and *stability* are necessary and sufficient conditions that need to be satisfied for *convergence*', that is *consistency* + *stability* = *convergence*. We might add that most computational work for nonlinear partial differential equations, as used in CFD, proceeds as though this theorem applies, although it has not been proven directly for this general category of equations.

In the majority of commercial CFD codes, the system of algebraic equations is usually solved iteratively. When dealing with these codes, there are three important aspects to abide by for *iterative convergence*. Firstly, all the discretized equations (momentum, energy, etc.) are deemed to be converged when they reach a specified tolerance at every nodal location. Secondly, the numerical solution no longer changes with additional iterations. Thirdly, overall mass, momentum, energy, and scalar balances are obtained. During the numerical procedure, the imbalances (errors) of the discretized equations are monitored, and these defects are commonly referred to as the *residuals* of the system of algebraic equations, that is they measure the extent of imbalances arising from these equations and terminate the numerical process when a specified tolerance is reached. For satisfactory convergence, the *residuals* should diminish as the numerical process progresses. In the likelihood that the imbalances grow, as reflected by increasing residual values, the numerical solution is thus classified as being unstable (divergent). It is noted that *iterative convergence* is not the same as *grid convergence*. *Grid convergence* seeks a grid-independent solution, which means approaching the exact solution. We will further discuss this later. Additionally, in Section 6.4.2, the concepts of *residuals* and *convergence tolerance* are discussed in the context of attaining a numerical solution.

Example 6.6

Based on the explicit Euler method as previously described in Example 6.4 for the one-dimensional transient diffusion equation with a time step size of $\Delta t = 1/100{,}000$ and a grid step size of $\Delta x = 1/100$, discuss the aspect of convergence for the numerical solution attained with identical initial and boundary conditions. The thermal diffusivity α is also assumed constant with a value of 0.5.

Solution: The computational results showing the transient development for the variable ϕ are given by the following:

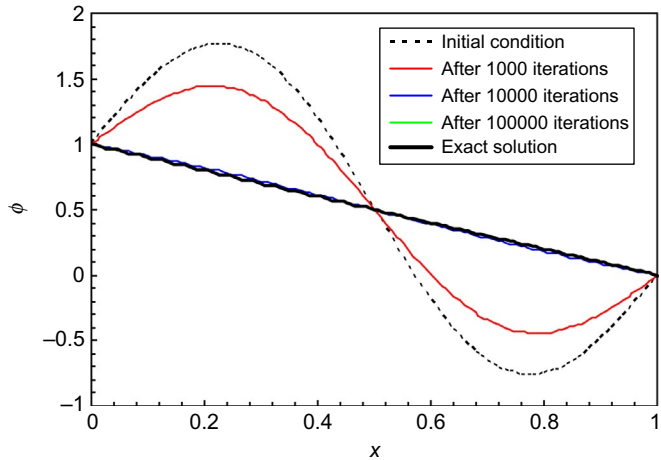


FIG. 6.6.1 Transient development of the variable ϕ with $\Delta t = 1/100{,}000$ and $\Delta x = 1/100$.

Discussion: The purpose of this simple example is to illustrate the condition of *consistency + stability = convergence*. The first aspect concerns *stability*; it is observed that no signs of instability are experienced during the course of the numerical calculations. The second aspect concerns *convergence*; after 100,000 cycles, the numerical result converges and collapses to the exact solution profile. Since the difference between the discretized equation and the exact one is negligible and thus the remainder or truncation error diminishes, *consistency* prevails.

6.4.2 Residuals and Convergence Tolerance

For any transport variable ϕ, the discretized form of the partial differential can be specifically written as

$$a_P\phi_p = \sum a_{nb}\phi_{nb} + b_P \tag{6.1}$$

In Eq. (6.1), the central coefficient a_P and neighbouring coefficients a_{nb} normally depend on the solution of other flow-field variables including the time- and spatial-varying fluid flow properties. These coefficients are updated consecutively during the iterative procedure. At the start of each iteration step, the equality in Eq. (6.1) will not hold. We can therefore rewrite the above equation by introducing an imbalance variable called residual R_p where Eq. (6.1) can be re-expressed as

$$R_P = \sum a_{nb}\phi_{nb} + b_P - a_P\phi_p \tag{6.2}$$

From the above equation, we introduce the concept of *residuals* as applied for each discretized equation of the system of transport equations. For a well-posed formulation, the *residuals* become *negligible* with increasing iterations. In CFD, *residuals* are employed to monitor the behaviour of the numerical process. Importantly, they implicate whether the solution shows a trend of convergence or divergence. It is noted that the concept of *mass residual* introduced in Section 4.3.3 and used in Example 5.5 is different from the concept of *residuals* defined herein. The former is a source term appearing in the pressure-correction Eq. (4.80), whilst the latter pertains to the imbalances in Eq. (6.2) during the iterative procedure.

The residual that arises in Eq. (6.2) actually depicts the imbalance (error) at the nodal point P for one cell volume. For practical purposes, a *global* residual R, taken as the sum of each *local* residual R_p over all the grid nodal points, is monitored:

$$R = \sum_{grid\ points} |R_P| \tag{6.3}$$

Convergence is deemed to be achieved for the discretized equation (6.1) so long as the global residual R satisfies a specified tolerance, that is $R \leq \varepsilon$ or $\sum_{grid\ points} |R_P| \leq \varepsilon$. The variable ε is usually referred to as the *convergence tolerance* for the system of algebraic equations. There is some practical guidance in selecting appropriate values for the *convergence tolerance*. It is noted that specifying appreciably small tolerance values will incur a large number of iteration steps in reaching convergence. On the other hand, large tolerance values constitute an early termination of the iteration process for which the numerical solution of the algebraic equations is considered to be rather coarse or not sufficiently converged. By default, the monitored residuals are usually scaled. Generally, a decrease of the residual by three orders of magnitude during the iteration process indicates at least *qualitative convergence*. Here, the major flow features are considered to be sufficiently established. Nevertheless, stricter convergence consideration is required for transport variables like energy and scalar species. It is recommended that the scaled energy residual decreases to a recommended convergence tolerance of 10^{-6} whilst the scaled scalar species may need to only decrease to a convergence tolerance of 10^{-5} to achieve energy and species balance, respectively. For *quantitative convergence*, changes are monitored for all considered flow-field variables. During the monitoring of these residuals, the reader is also advised to ensure that property conservation is satisfied.

Example 6.7

Consider the two-dimensional CFD case of the incompressible laminar flow between two stationary parallel plates with the dimensions of height $H = 0.1$ m and length $L = 0.5$ m. Demonstrate the convergence behaviour through monitoring the residuals of the transport variables u and v in their algebraic form represented in Eq. (6.2) and the pressure correction p' from Eq. (4.80) where air (density $\rho = 1.2$ kg/m^3 and viscosity 4×10^{-5} kg/m s) is the working fluid. The inlet velocity is fixed at $u_{in} = 0.01$ m/s. The outlet and wall conditions remain the same as applied in Chapter 2.

Solution: The schematic diagram of the channel flow is identical to the one that is used in Example 4.5. Here, the discretized equations governing the momentum and pressure correction are solved using default iterative solvers as provided from an in-house research CFD code.

Convergence histories of the velocities u and v and pressure correction p' are depicted in Fig. 6.7.1 below. The residuals for each of the transport variable are not scaled, and the convergence tolerance ε has been set at 10^{-7} to terminate the numerical simulation.

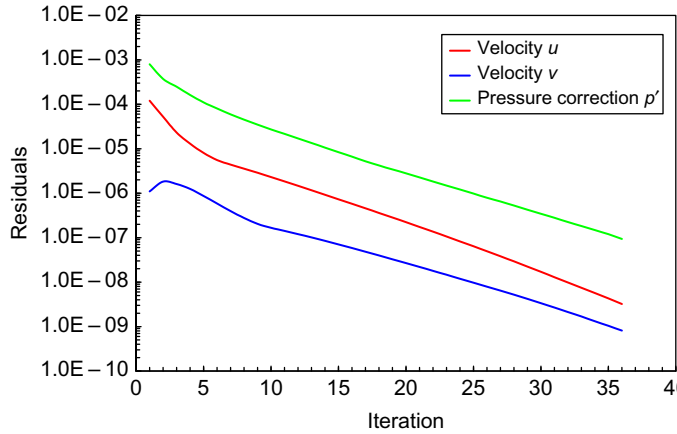


FIG. 6.7.1 Convergence histories of the horizontal velocity u, vertical velocity v, and pressure correction p'.

Discussion: In the previous Example 6.6, convergence is demonstrated and ascertained for an *explicit* methodology. Here, convergence is illustrated for an *implicit* methodology. The well-posed behaviour of the numerical solution is evident by the diminishing values for the residuals of the velocities u and v and pressure correction p'. Convergence is achieved, thereby satisfying the condition of Eq. (6.3) when all the residuals fall below the convergence tolerance of $\varepsilon = 1 \times 10^{-7}$. Nevertheless, there are circumstances where divergence can occur during the simulation of a channel flow problem. Such behaviour is typically exhibited by the ascending trend of the residuals leading to large catastrophic values during the iterative process as shown in Fig. 6.7.2. This ill-posed (opposite to well-posed) numerical solution that is particularly designed for the purpose of illustration is due to the incorrect usage of the underrelaxation factors to control the numerical calculations. More discussions on the importance of underrelaxation factors generally required for implicit methods are elaborated in the next section.

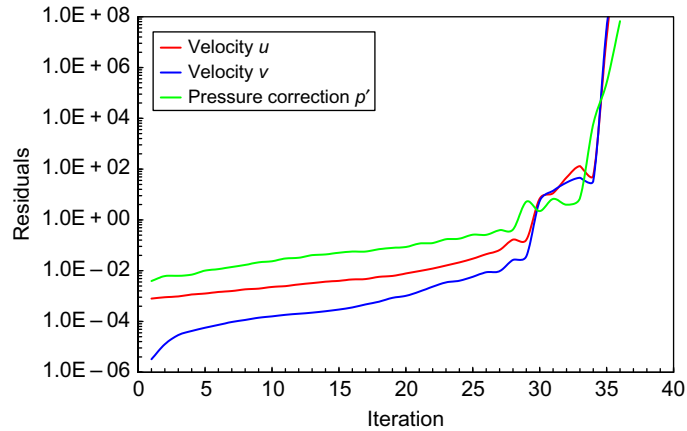


FIG. 6.7.2 Divergence histories of the horizontal velocity u, vertical velocity v, and pressure correction p'.

6.4.3 Convergence Difficulty and Using Under-Relaxation

In consideration of the channel flow example discussed in the previous chapters and herein, the residuals for the continuity (pressure correction) and velocity components represent useful indicators that can be progressively evaluated to ascertain the convergence trend of the numerical calculations. Whether these residuals are being tracked locally at some grid nodal point within the flow system or globally through the sum of the local residuals, a convergence trend showing a diminishing residual value ensures the satisfaction of the conservation laws of mass and momentum (see above Example 6.7). Since these laws are the physical statements of fluid dynamics, the removal of any imbalances is imperative. In some flow cases, the local solution may be known, and the converged solution can be gauged and assessed by directly comparing the computed results with the available solution values. There are also practical considerations during the numerical calculations where convergence can be assessed through the evaluation of some physical variables. For example the calculation of the drag or lift coefficients for a flow of air over an aerofoil are useful indicators for determining convergence of the flow system and thus determining when to terminate the numerical procedure.

In any numerical calculation, numerical instabilities can occur whilst solving the discretized equations. Poorly constructed mesh, improper solver settings, nonphysical boundary conditions, and selection of inappropriate models are typically some of the apparent factors that may cause the ill-convergence of the numerical calculations. These are usually exhibited and amplified by the increasing (diverging) or 'plateau' residual values throughout the iteration process (as seen from above in Example 6.7). Diverging residuals clearly imply the increasing of imbalances in the conservation equations, and thus, the physical laws of the fluid flow are vigorously violated. Computational results that are not converged are misleading.

There are, however, some practical corrective steps that can be undertaken to overcome the difficulties in achieving convergence. For a poor-quality mesh, the flow region can be remeshed by increasing the number of grid nodal points. Such a strategy is particularly adopted to avoid the grid from having large aspect ratios or highly skewed cells. In cases where high-order approximations are required, it may be sensible to initially compute the solution using low-order approximations. The diffusive nature of the low-order approximations allows large imbalances to dissipate quickly and promote stability of the numerical procedure. Once the flow is established, greater accuracy of the numerical solution can be attained by switching to the high-order approximations.

Another strategy to promote convergence is through the use of *underrelaxation factors*. Poor initial guesses or unresolved steep gradients in the flow field may cause divergence in the iterative process. The incorporation of underrelaxation factors into the system of algebraic equations can significantly moderate the iteration process by limiting the change in each of the transport variables

from one step to the next. By introducing an underrelaxation factor β, the change in the value of the transport variable ϕ at the central node of the cell volume between subsequent iteration steps can be expressed as

$$\phi_P^{New} = \phi_P^{Old} + \beta\left(\phi_p^{New} - \phi_p^{Old}\right) \tag{6.4}$$

In CFD, underrelaxation is often introduced to stabilize the numerical calculations of the governing equations that are generally nonlinear and where the equation of one transport variable is dependent on the others, for example temperature affecting the velocities in buoyancy flows. The underrelaxation factor β in Eq. (6.4) controls the advancement of the transport variable ϕ_P during the iteration process. For a specified underrelaxation factor of 0.5, a restriction of 50% change is implied for ϕ_P from the value determined at the previous iteration to the current iteration step. The advancement for ϕ_P through the iteration process will therefore be increasingly impeded as smaller underrelaxation factors are employed. For the numerical solution in Example 6.7, the advancement of pressure has been underrelaxed by a factor of 0.3, which is typically employed when applying the SIMPLE scheme (Ferziger and Perić, 1999), to ensure stability and convergence of the iterative process.

In the majority of commercial CFD codes, the default settings of the underrelaxation factors are generally applicable to a wide range of problems. It is usually recommended to employ default factors in beginning the numerical calculations. Nevertheless, a more aggressive approach may be warranted by tightening the transport variable advancement through smaller underrelaxation factors to aid convergence. CFD users still constantly face many challenges in ascertaining optimal underrelaxation factors, usually not known a priori, to solve CFD problems. Settings of appropriate underrelaxation factors remain best learned from practical experience and application of CFD methodologies.

6.4.4 Accelerating Convergence

Some practical guidelines to attain quicker convergence of the computational solution are explored. In the majority of cases handling flow problems, the supply of good initial or starting conditions is insurmountable, which leads to beneficial consequences in the iteration process. This can be achieved either by knowledge of similar physical conditions that can be imposed or by beginning the iteration from a previously converged solution. Inappropriate initial conditions generally lead to slower convergence but may result in some untenable situations that promote divergence tendencies. Good initial or starting conditions promote computational efficiency and reduce computational efforts and resources. In the previous section, the use of underrelaxation factors was employed to promote stability during the iteration process. Default settings of the underrelaxation factors or Courant number in commercial CFD codes

are generally applicable to a wide range of flow problems. Nevertheless, there are special circumstances where depending on the flow problem, the underrelaxation factors or Courant number can be plausibly increased to accelerate the convergence. However, excessively high underrelaxation values can lead to unwanted instabilities. The reader may wish to adopt a strategy whereby to store intermediate solutions through incrementally increasing the underrelaxation factors. This can be carried out periodically before carrying out subsequent calculations. Such procedure allows computations to be kept at a minimum but more importantly eliminating the need to recompute the problem from the initial state. In Chapter 4, a number of accelerating techniques that are gaining prominence in solving CFD problems were described. In many commercial CFD codes, multigrid solvers—a procedure to solve the algebraic equations by employing a combination of iterative solvers such as Jacobi, Gauss-Seidel, or SIP and direct solver cycling through different levels of grid densities (see Sections 5.5 and 9.2.4 for more detailed description)—are offered as the default solvers in accelerating the convergence for the iteration process. In this case, provisions are given for users to change, at their discretion, the settings of the multigrid solver. More often than not, the default settings provided are sufficiently robust, and they do not necessarily need to be altered.

6.5 ACCURACY

The previous discussion of *convergence*, *consistency*, and *stability* has been primarily concerned with the solution behaviour where the finite quantities, such as the time step Δt and mesh spacing Δx, Δy, and Δz, diminish. Since the discretized forms of the transport equations governing the flow and energy transfer are always solved numerically on a finite grid layout and the effects of turbulence are generally modelled through approximate theories, the solution obtained is always approximate. The corresponding issue of *accuracy* therefore becomes another important consideration.

In Section 6.2, the determination of consistency produces an explicit expression for the truncation error. As aforementioned, the truncation error represents the difference between the discretized equation and the exact one, and it provides a means of evaluating the *accuracy* of the solution for the partial differential equations. The order of the truncation error coincides with the order of the solution error if the grid spacings are sufficiently small and if the initial and auxiliary boundary conditions are sufficiently smooth. It is commonly implied that an improvement in accuracy (from the truncation error) of high-order approximations can be achieved for a sufficiently fine grid. Refining the grid will often produce a superior accuracy for high-order approximations over low-order approximations. However, at an absolute accuracy level, justification for more expensive computations may not demonstrate the desired superior accuracy due to limited computing capacity.

One method where accuracy can be assessed for a particular algorithm on a finite grid is to apply it to a related but simplified problem that possesses an exact solution. However, accuracy is usually problem-dependent; an algorithm that is accurate for one model problem may not necessarily be as accurate as for another more complicated problem. Another probable way for assessing accuracy is to obtain solutions on successively refined grids (*grid convergence*) and to check that, with successive refinements, the solution is not changing satisfying some predetermined accuracy. This technique assumes that the approximate solutions will converge to the exact solution as the finite quantities diminish and then the approximate solution on the finest grid can be used in place of the exact solution; grid independence solution is thus achieved. Assuming that the *accuracy* of this approximate solution can be assessed, it is important to consider the related question of how accuracy may be improved. At a specific level, the use of high-order approximation or grid refinement would be expected to produce more accurate solutions. Nevertheless, such choices are only meaningful if they are considered in conjunction with execution time and computational efficiency.

It is important that the reader be aware that *a converged solution does not necessarily mean an accurate solution*. Some possible sources of solution errors resulting from the numerical calculations of the algebraic equations require analysis, and this will be discussed in the next section. If these errors are to be minimized, some systematic steps to perform numerical analysis such as grid independence and verification and validation of numerical models are necessary.

6.5.1 Source of Solution Errors

Not only should the reader be aware of the existence of errors in *computational solutions*, but also more importantly, the reader must attempt to distinguish one from another. This section serves to address the possible sources of errors that the reader is likely to encounter applying CFD methodologies. Errors are introduced because the numerical solutions of the fluid flow and heat-transfer problems are only *approximate solutions*. Some prevalent source of errors dealing with numerical solutions includes the following classification:

- *Discretization error*
- *Round-off error*
- *Iteration or convergence error*
- *Physical modelling error*
- *Human error*

Before we elaborate the source of these errors in CFD, we would like to establish a clear and logical distinction between *error* and *uncertainty* that is based on the publication of AIAA guide for the verification and validation of

computational fluid dynamics simulations (AIAA, 1998). Error can be defined as *a recognizable deficiency that is not due to the lack of knowledge*, whilst uncertainty can be *defined as a potential deficiency that is due to the lack of knowledge*. Although these definitions appear to be rather philosophical, they will become clearer as the origin of these errors in CFD is further explored below.

Discretisation Error

These errors are due to the difference between the exact solution of the modelled equations and a numerical solution with a limited time and space resolution. They arise because an exact solution to the equation being solved is not obtained but numerically approximated. For a consistent discretization of the algebraic equations, the computed results are expected to become closer to the exact solution of the modelled equations as the number of grid cells is increased. However, the results are strongly affected by the density of the mesh and distribution of the grid nodal points.

We identify two types of discretization errors: local and global (or accumulated). To have an idea about the *local error* and *global error*, consider the finite-difference formulation of the derivatives for the transport variable ϕ in space and time at a specified grid nodal point expressed through the Taylor series expansion:

$$\left(\frac{\partial \phi}{\partial x}\right) = \frac{\phi_{i+1,j} - \phi_{i,j}}{\Delta x} + \underbrace{O(\Delta x)}_{Truncation\ error} \qquad Spatial\ derivative \tag{6.5}$$

$$\left(\frac{\partial \phi}{\partial t}\right) = \frac{\phi_{i,j}^{n+1} - \phi_{i,j}^{n}}{\Delta t} + \underbrace{O(\Delta t)}_{Truncateion\ error} \qquad Time\ derivative \tag{6.6}$$

Termination of the Taylor series expansion in Eqs (6.5) and (6.6) results in the so-called truncation errors involved in the approximation.

The *local error* is the formulation associated with a single step and provides an idea about the accuracy of the method used. For this error, the accuracy of the numerical solution concerns mainly on the approximation of the spatial derivative. The solution accuracy for a transient problem, however, focuses on the advancement of the transport variable ϕ through time usually characterized by the *global error*. The representations of the *local error* and *global error* are best illustrated in Fig. 6.1. We can observe that the smaller the mesh size or time step in transient problems, the smaller the error, and thus the more accurate the approximation.

We shall illustrate the significance of the discretization error through a worked example below.

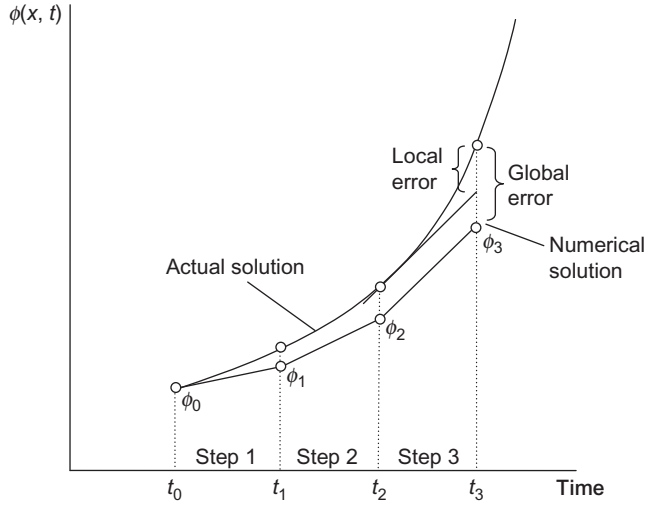


FIG. 6.1 The local and global discretization errors resulting from the finite-difference method at a specified grid nodal point.

Example 6.8

Consider the transient one-dimensional convection-type equation to further illustrate the aspect of discretization error. A fourth-order central difference is employed for the spatial derivative to attain higher accuracy. Using the Euler explicit method, demonstrate the discretization error that is associated with the numerical solution obtained through the first- and second-order approximations to the time derivative at a fixed time step size of $\Delta t = 1/128$ accompanied by the variation of two different grid step sizes of $\Delta x = 1$ and $\Delta x = 1/2$.

Solution: Through the consideration of additional grid nodal points along the spatial direction x and applying the Taylor series expansion, the fourth-order finite-difference approximation can be obtained as

$$\left(\frac{\partial \phi}{\partial x}\right) = \frac{-\phi_{i+2} + 8\phi_{i+1} - 8\phi_{i-1} + \phi_{i-2}}{12\Delta x} + \underbrace{O(\Delta x^4)}_{\textit{Truncation error}}$$

Substituting the above approximation along with the first-order forward difference to the time derivative yields the following algebraic equation:

$$\frac{\phi_i^{n+1} - \phi_i^n}{\Delta t} - u\left(\frac{-\phi_{i+2} + 8\phi_{i+1} - 8\phi_{i-1} + \phi_{i-2}}{12\Delta x}\right) = 0$$

For the second-order approximation of the time derivative, the central difference is employed, in other words,

$$\frac{\phi_i^{n+1}-\phi_i^{n-1}}{2\Delta t}-u\left(\frac{-\phi_{i+2}+8\phi_{i+1}-8\phi_{i-1}+\phi_{i-2}}{12\Delta x}\right)=0$$

This newly developed formula is similar to the well-known *leapfrog* method.

The computed results compared with the exact solution for the first-order and second-order time approximations against two different grid sizes are illustrated in Figs 6.8.1 and 6.8.2.

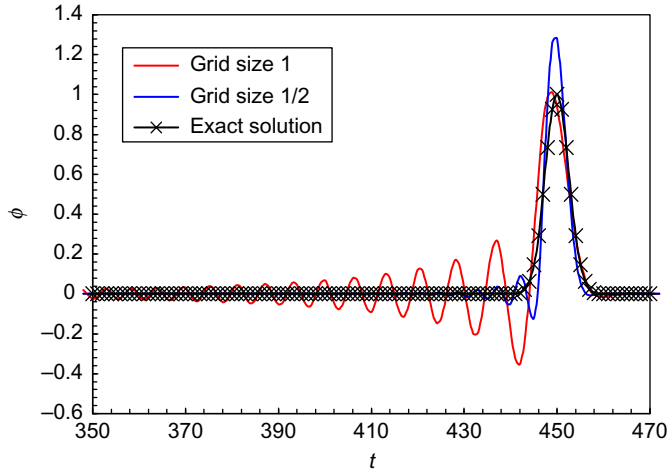


FIG. 6.8.1 Fourth order grid and first order time approximations of convection-type equation for the variable ϕ with a fixed time step of $\Delta t = 1/128$ and two grid sizes of $\Delta x = 1$ and $\Delta x = 1/2$.

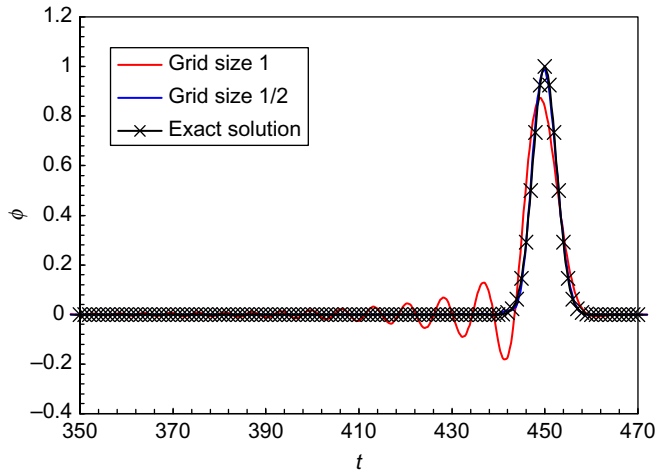


FIG. 6.8.2 Fourth order grid and second order time approximations of convection-type equation for the variable ϕ with a fixed time step of $\Delta t = 1/128$ and two grid sizes of $\Delta x = 1$ and $\Delta x = 1/2$.

Discussion: By increasing the approximation of the time derivative from first order to second order, the numerical simulation for the higher-order time approximation at a grid size of $\Delta x = 1$ is shown to be less sensitive to the time step changes with the suppression of wiggles through time (compare the solutions between Figs 6.8.1 and 6.8.2). By halving the grid size to $\Delta x = 1/2$, the numerical simulation is stabilized. The solution for the second-order time derivatives converges to the exact solution profile, but the first-order solution retains some oscillatory wiggles around the exact solution profile and is still far from its converged state. In this example, the systematic reduction of the grid step sizes and the use of higher approximation for the time derivative characterize the diminishing contribution of the respective local and global discretization errors.

Round-Off Error

These errors exist due to the difference between the machine accuracy of a computer and the true value of a variable. Every computer represents numbers that have a finite number of significant figures. The default value of the number of significant digits for many computers is 7, and this is commonly referred to as *single precision*. However, calculations can also be performed using 15 significant figures, which is referred as *double precision*. The error due to the retaining of a limited number of computer digits available for storage of a given physical value is therefore called the round-off error. This error is naturally random, and there is no easy way of predicting it. It depends on the number of calculations, rounding-off method, rounding-off type, and even sequence of calculations.

Consider the case of a simple arithmetic operation performed with a computer in single precision. Given that $a = 8888888$, $b = -8888887$, and $c = 0.3333341$, let us evaluate the operations of $D = a + b + c$ and $E = a + c + b$. The arithmetic calculation for D proceeds as

$$\begin{aligned} D &= 8888888 - 8888887 + 0.3333341 \\ &= 1 + 0.3333341 \\ &= 1.333334 \ (\text{correct result}) \end{aligned}$$

whilst E performs the following operations:

$$\begin{aligned} E &= 8888888 + 0.3333341 - 8888887 \\ &= 8888888 - 8888887 \\ &= 1.000000 \ (\text{in error by } 25\%) \end{aligned}$$

In algebra, we learned that $a + b + c = a + c + b$, which is reasonably accepted as a mathematically proven statement. But this is not necessarily true for the calculations that will be performed in a computer, as demonstrated from above. It is noted that the sequence of calculations in single-precision mode results in a

solution error of 25% in just two operations. Imagine that thousands or even millions of such operations are to be performed sequentially; the round-off error would accumulate and lead to serious error without any prior warning signs. If computer round-off errors are suspected of being significant, one test that can be performed is to employ double precision or on a computer known to store floating-point numbers at a higher precision. An attempt to continuously refine a coarse grid solution to achieve a solution of diminishing finite quantities may be feasible; however, this may not usually be possible for more complex algorithms. Nevertheless, it is noted that round-off errors are usually not the dominant contributor to the source of solution errors when compared with discretization errors. The implication of round-off errors in a CFD problem will be expounded in the test case investigated in Section 6.7.1.

Iteration or Convergence Error

These errors occur due to the difference between a fully converged solution of a finite number of grid points and a solution that has not fully achieved convergence. The majority of commercial CFD codes solve the discretized equations iteratively for steady-state solution methodologies. For procedures requiring an accurate intermediate solution at a given time step, this is solved iteratively in transient methods. It is expected that progressively better estimates of the solution are generated as the iteration step proceeds and ideally satisfies the imposed boundary conditions and equations in each local grid cell and globally over the whole domain. However, if the iterative process is terminated prematurely, then errors arise. Convergence errors therefore can occur because of either being impatient to allow the solution algorithm to complete its progress to the final converged solution or applying too large convergence tolerances to halt the iteration process when the CFD solution may still be considerably far from its converged state.

Physical Modelling Error

These errors are those due to uncertainty in the formulation of the mathematical models and deliberate simplifications of the models. Here, we reinforce the definition of uncertainty from above where the Navier–Stokes equations can be considered to be exact and solving them is impossible for most flows of engineering interest because of the lack of sufficient knowledge to model them. The sources of uncertainty in physical models are as follows:

(1) The phenomenon is not thoroughly understood.
(2) Parameters employed in the model are known to possess some degree of uncertainty.
(3) Appropriate models are simplified; thus, uncertainty is introduced.
(4) Experimental confirmation of the models is not possible or is incomplete.

Modelling is often required for turbulence, which places huge demands on computational resources if it is to be simulated directly. Other phenomena like combustion, multiphase flow, and chemical processes are difficult to describe exactly, and they inevitably require the introduction of approximate models. Even Newton's and Fourier's laws are themselves models though they are solidly based on experimental observations for many fluids. In addition, the underlying mathematical model is nearly exact, but some fluid properties may not be exactly known. They depend strongly on temperature, species concentration, and possibly pressure; this dependence is ignored, thus introducing modelling errors (e.g. the use of Boussinesq approximation for natural convection). In some situations, a simplified model may be adopted within the CFD code for the convenience of a more efficient computation even though a physical process is known to a high level of accuracy. Physical modelling errors are examined by performing validation studies that focus on certain models. The conceptual idea and definition of validation will be expounded in Section 6.5.3.

Human Error

There are essentially two categories of errors associated with human error. Firstly, computer programming errors involve human mistakes made in programming, which are the direct responsibility of the programmers. These errors can be removed by systematically performing verification studies of subprograms of the computer code and the entire code, reviewing the details inserted into the code and performing validation studies of the code. We will review and discuss the concept of verification in Section 6.5.3. Secondly, usage errors are also due to the application of the code in a less-than-accurate or improper manner. Inexperience in handling CFD codes may result from either incorrect computational domains (such as improper geometry construction or grid generation) or inappropriate setting of boundary conditions. Selection of bad numerical schemes or computational models to simulate certain flow problems compounds the undesirable usage errors. The reader should note that the potential for usage errors increases with the increased level of options available in CFD. Nevertheless, usage errors can be minimized and controlled through proper training and analysis and the accumulation of experience. Some practical guidelines will be discussed in the next chapter.

6.5.2 Controlling the Solution Errors

It is good engineering practice that the CFD user examines any potential pitfalls when employing numerical methodologies. Numerical errors are primarily concerned with discretization and round-off errors. They have the tendency to accumulate through computational processes that may yield unphysical CFD solutions. The results that seem rather reasonable overall at hindsight may be in considerable error at certain locations within the flow domain. Controlling

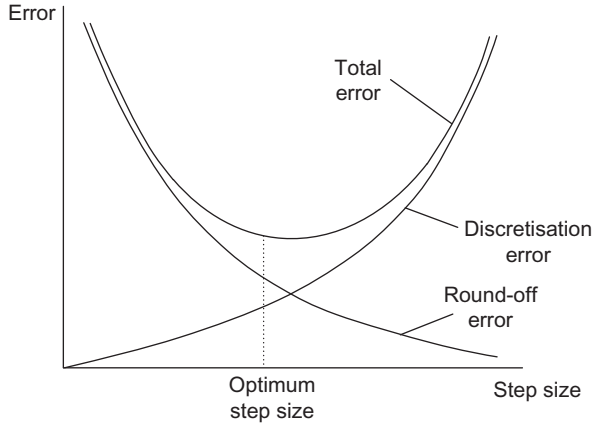


FIG. 6.2 The discretization, round-off, and total errors as a function of mesh and/or time step size.

the solution errors therefore represents a crucial step towards obtaining reliable and meaningful CFD solutions.

We begin by focusing on the contribution of the discretization and round-off errors obtained through numerical methods. As the mesh or time step size decreases, it is seen in Fig. 6.2 that the discretization error decreases with step size whilst the round-off error increases. For the total error that is taken as the sum of the discretization and round-off errors, it is evident that continually decreasing the step size does not necessarily mean that more accurate results are attained. The opposite is true at small step sizes where less accurate results are obtained because of the quicker increase in the round-off error. In order to contain this error, we should therefore avoid a large number of computations with very small numbers.

In practice, we will not be able to determine the magnitude of the error involved in the numerical method. It is seen from above that the knowledge of discretization error alone is meaningless without a true estimate of the round-off error. To better assess the accuracy of the results obtained, some practical guidelines are recommended.

Firstly, the issue of *grid independence* is explored. To address this issue, we can begin by solving the flow problem with reasonable mesh sizes of Δx, Δy, and Δz (and a time step of Δt for transient problem) based on acquired experience. The computational results may look qualitatively good, but let us assume that the problem is repeated with twice as many grid points, thus halving the mesh sizes in each direction by $\Delta x/2$, $\Delta y/2$, and $\Delta z/2$. If the results obtained do not differ significantly from the results obtained in the original grid layout, we can conclude that the discretization error is at an acceptable level. But if the values for the transport variables are quite different for this second calculation, then the solution is a function of the number of grid points. In all practical cases, the grid needs to be refined by increasing the number of grid points until a

solution is achieved where no significant changes in the results occur. This indicates that the discretization error is reduced to an acceptable error and *grid independence* is reached. This issue will be further investigated in a test case described in Section 6.7.1.

Secondly, the majority of CFD calculations are usually performed in single precision to avoid overburdening the computational resources. Nevertheless, if the round-off error is found to be significant, the flow calculations can be repeated by using double precision whilst holding the mesh sizes (and the size of the time step in transient problems) constant. If the results do not change considerably, we conclude that the round-off error is not a problem to the CFD solution. However, if the changes are larger than expected, we may attempt to reduce the total number of calculations by either increasing the mesh sizes or changing the order of computations such as adopting a higher approximation to evaluate the first-order spatial derivatives of the convective terms and/or the first-order time derivatives in the conservation equations. As seen from Fig. 6.2, discretization error increases with increasing mesh size; the reader should therefore acknowledge this important trend and seek some reasonable compromise.

Thirdly, selection of appropriate turbulence models or other approximate models can be a daunting task especially attempting to minimize the physical modelling errors. The desired level of simplification that can be accepted to adequately model the physical flow problem is not straightforward as it depends on the choice of models that govern and characterize the particular flow physics. Also, carelessness in setting up a feasible geometrical model and an improper choice of boundary conditions are some of the human errors that frequently arise in CFD. Succinct practical guidelines to eliminate such pitfalls will be discussed in the next chapter.

6.5.3 Verification and Validation

In addition to errors, uncertainties can also arise whilst performing a numerical simulation. These can be due to the improper modelling of physics such as a misunderstanding of the phenomena leading to falsifying assumptions or the incorrect computational design such as making wrong approximations and simplifications about the parameters that govern the fluid dynamics. For a CFD solution to be credible, it requires a detailed analysis to be performed, to quantify the modelling and numerical uncertainties in the simulation. Verification and validation procedures are the means by which a CFD solution can be properly assessed through quantitatively estimating the inherent errors and uncertainties.

Verification and validation have very distinct definitions. Although there is an absence of a universal agreement on the details of these definitions, there is a fairly standard and consistent agreement on their usage. In this book, we will

adopt definitions that are focused on numerical errors and uncertainties where they cannot be considered negligible or overlooked.

An important aspect to remember about verification and validation is that it is applied in two very distinct ways. We can differentiate verification and validation in the following. *Verification* can be defined *as a process for assessing the numerical simulation uncertainty and when conditions permit, estimating the sign and magnitude of the numerical simulation error and the uncertainty in that estimated error*. This procedure concerns primarily to the input parameters used for geometry, initial conditions, and boundary conditions. They are required to be carefully checked and systematically documented. It is also important that mesh and time step sensitivity studies are extensively performed to bound the errors, whether they may be insufficient spatial discretizations, too large temporal advancement, the lack of iterative convergence, or computer programming errors, which are associated with the discrete approximations employed for the partial differential equations. On the other hand, *validation* can be defined *as a process for assessing simulation model uncertainty by using benchmark experimental data and when conditions permit, estimating the sign and magnitude of the simulation modelling error itself*. This procedure simply means validating the calculations by establishing a range of physical conditions obtained from the calculations and performing comparisons of the results from the CFD code with experiments that span the range of conditions. This represents the final phase of the credibility process of the models applied and is interpreted as the stage to determine the degree to which a model corresponds to an accurate representation of the real physical flow problem that is solved.

We shall further demonstrate the use of the verification and validation procedures in the case studies described in Section 6.7.

6.6 EFFICIENCY

The rapid advancement and reduced costs of computer hardware and resources have revolutionized the use of CFD. Current users have nowadays the luxury of accessing many commercial or shareware computer codes. More complex engineering systems and applications can be solved because of the feasibility of constructing high-quality grids to resolve the physical flow structures. Such flow problems usually require a substantial amount of grid points to envelope the whole physical domain to achieve adequate resolution. If the mesh requires further refinement, almost all iterative solution methods suffer from slower convergence on the finer grids. The rate of convergence depends on the particular numerical method; the number of iterations for many methods is linearly proportional to the number of grid nodal points in one coordinate direction. This behaviour is related to the fact that, for iterative procedures, information has to travel back and forth across the domain several times.

To overcome the convergence problem, applications of conjugate gradient and multigrid methods have received unprecedented attention to enhance the

efficiency of a CFD procedure. The former is essentially a method that seeks the minimum of a function that belongs to the class of *steepest descent methods*. The basic method in itself converges rather slowly and is not very useful, but when it is used in conjunction with some *preconditioning* of the original matrix, major enhancements in its speed of convergence have been recorded. This preconditioning technique is achieved by either applying the *incomplete Cholesky* factorization for symmetric matrices or applying *biconjugate gradients* for asymmetric matrices. The latter such has been discussed in Chapter 4 employs a hierarchy of meshes. In the simplest case, the coarse ones are just the subsets of the fine ones. Efficiency may be improved by the decision to switch from one grid to another on the rate of convergence through the V-cycle, W-cycle, combination of V–W cycles, or other possible strategies. Additional details of the multigrid method can be further referred in Section 9.2.4. The conjugate gradient and multigrid methods are ideal for solving the Poisson-like pressure or pressure-correction equation such as the SIMPLE method.

Another approach to achieve computational *efficiency* is parallel computing. The increase in the capability of single-processor computers has almost reached their peak performances. It now appears that further increases in speed will require multiple processors—parallel computers. One of the advantages of parallel computers over classical vector supercomputers is scalability. Parallel computers employ standard processing chips and are therefore cheaper to produce and to attain. Commercially available parallel computers may have thousands of processors, gigabytes of memory, and computing power measured in gigaflops. The basic idea of parallel computing involves the subdivision of the solution domain into subdomains and assigns each subdomain to one processor. In such a case, the same computer code runs all processors. Since each processor needs data that reside in other subdomains, exchange of data between processors and storage overlap is necessary. This demonstrates that parallel computing environments require redesign of algorithms. Good parallelization therefore needs modification of the solution algorithm.

Explicit marching methods are relatively easy to parallelize since all operators are performed on data from preceding time steps. It is only necessary to ensure that data are exchanged at the interface regions between neighbouring subdomains after each step is completed. The sequence of operations and the results are identical on one and many processors. Or course, the problem remains handling the solution of the Poisson-like pressure equation. Implicit methods are more difficult to parallelize because the iterative solvers that are efficient in serial computations are not suited when performed in parallel. Some solvers can be parallelized and perform the same sequence of operations on multiprocessors as on a single one. However, these arithmetic operations are inefficient, and the communication overhead is extremely large.

One possible way to achieve parallelization for implicit methods is by data parallelism or domain decomposition. For steady flow problems, the concept of spatial domain decomposition is to divide the solution domain into a number of

subdomains with the objective to maximize efficiency, thus distributing the same amount of work on each processor. The usual approach is to split the global matrix coefficients that are composed of the central coefficient a_P and neighbouring coefficients a_{nb} into a system of diagonal blocks. Each of these blocks is assigned to one processor, and data are then transferred on two levels of communications. Local communication takes place between processors operating on neighbouring blocks, whilst global communication gathers information from all blocks in a 'master' processor whilst broadcasting some information back to the other processors. For transient flow problems, domain decomposition in space can also be equally applied in time. More details of parallel computations (see Section 9.2.5 and references given within) are left to the interested reader.

Recent advances in graphics processing units (GPUs) have also gained significant traction within the CFD community for parallel computing due to their considerably lower cost than supercomputers or workstation clusters. In essence, GPU computing has the ability of accelerating parallel computer codes for high-performance computing and has demonstrated remarkable performance and enhanced computational precisions. Typically, GPUs are employed to drive the display of a computer that requires many threads and are thus very suitable because of their inherent feature to run many threads all at once. This inherent multithreading ability of GPU makes it ideal for general-purpose computing. In comparison with the central processing units (CPUs), GPUs have an intelligent throughput architecture that executes many concurrent threads slowly, rather than executing a single thread rapidly. Massive multithreading in hardware aims to overcome latencies that derive from the communication of data in the device. GPU programming has been greatly facilitated with the release of the CUDA device. The use of compute unified device architecture (CUDA)—a parallel computing developed by NVIDIA—has provided developers with direct access to virtual instruction set and memory of the parallel computational elements. For CFD, GPUs have shown the propensity of accelerating arithmetic operations with impressive speedups and significant reduction in runtimes. More descriptions of GPUs and CUDA environment (see Section 9.2.6 and references given within) are left to the interested reader.

6.7 CASE STUDIES

A selection of case studies is presented to demonstrate the relevance of the computational solutions in *consistency*, *stability*, *convergence*, and *accuracy*. These cases will individually show two or three of the following effects: discretization error (*truncation error*), iteration or convergence error (*grid convergence*), and physical modelling error (application uncertainty of boundary conditions, geometry, and CFD models, e.g. turbulence model). They will also include comparisons with an analytical solution (*verification*) and with experimental data (*validation*). It is important to note that the presence of the test case from

a particular code is not intended to provide any endorsement or the acceptance of the code for this particular purpose. Likewise, the absence of a test case from any particular code does not provide a statement on the unsuitability of the code for this particular application.

6.7.1 Test Case A: Channel Flow

This test case was calculated using an in-house finite-volume CFD computer code.

Model description: The geometry of the test problem is a two-dimensional laminar flow between two parallel plates as used in previous worked examples. For this test problem, the channel has dimensions of height $H = 0.1$ m and length $L = 1.0$ m with air taken as the working fluid.

Grid: The governing equations are discretized on a collocated grid arrangement. Velocity and pressure are collocated (cell-centred) such as described in Fig. 4.8. A uniform mesh is generated spanning the height and length of the channel. *Grid convergence* (*independency*) is performed with meshes of 5×10, 10×20, and 20×40 control volumes.

Features of the simulation: The numerical technique is based on the finite-volume discretization. The algorithm for the solution of the Navier–Stokes equations relies on the implicit segregated velocity-pressure formulation such as the SIMPLE scheme. This leads to a Poisson's equation for the pressure correction that is solved through a default iterative solver within the in-house CFD code. To avoid nonphysical oscillations of the pressure field and the associated difficulties in obtaining a converged solution, the Rhie and Chow (1983) interpolation scheme is employed.

The fluid is incompressible, and its density and viscosity have values of 1.2 kg/m^3 and 4×10^{-5} kg/m s, respectively. With the inlet velocity specified at 0.01 m/s, the corresponding Reynolds number (see Eq. 3.26 in Chapter 3) based on this inlet velocity and height of the channel is 30.

Results: As demonstrated in Example 6.7, a stable and converged solution is evidenced by diminishing residuals as the number of iterations increases. The decreasing trends of the residuals for a coarse grid distribution of 5×10, medium grid distribution of 10×20, and a fine grid distribution of 20×40 control volumes also exhibit the desirable aspects of *stability* and *convergence*. Since the diminishing nature of the residuals is represented in all three respective grid distributions, only indicative residuals obtained from the fine grid distribution are illustrated, as shown in Fig. 6.4. The numerical calculations are terminated for all three different meshes when all velocities, pressure correction, and mass residuals fall below the convergence tolerance of $\varepsilon = 1 \times 10^{-7}$. It is noted that the pressure-correction residual is the same as the mass residual; only this mass residual is presented in Fig. 6.3.

The numerical solution is verified against the analytical solution developed in Example 3.4. Recalling the relationship of Eq. (3.4A) in Chapter 3, which has been developed for $-H/2 \leq y \leq H/2$, the horizontal velocity u can be determined as

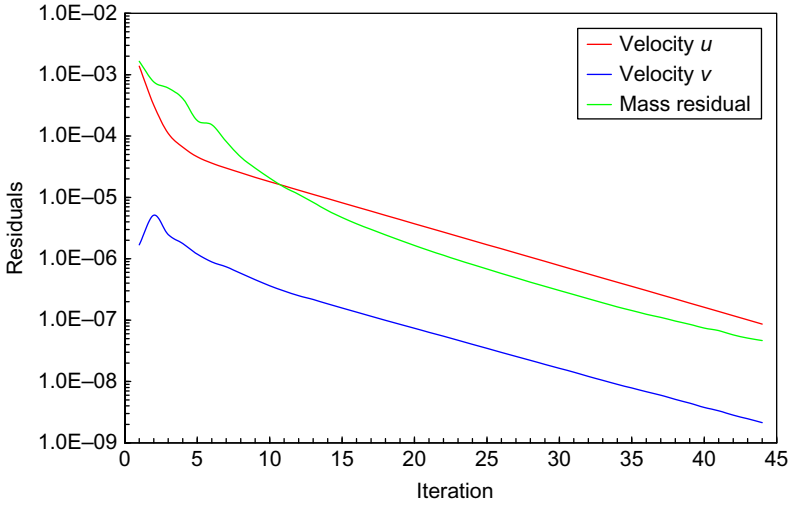


FIG. 6.3 Convergence histories of the horizontal velocity u, vertical velocity v, and mass residual for the fine grid distribution.

$$u(y) = \frac{3}{2}U_m\left[1 - \frac{y^2}{(H/2)^2}\right]$$

where the average velocity U_m in this test problem corresponds to the uniform inlet velocity $u_{in} = 0.01$ m/s. Fig. 6.4 compares the numerical solutions for the three meshes with the analytical solution in the fully developed flow region.

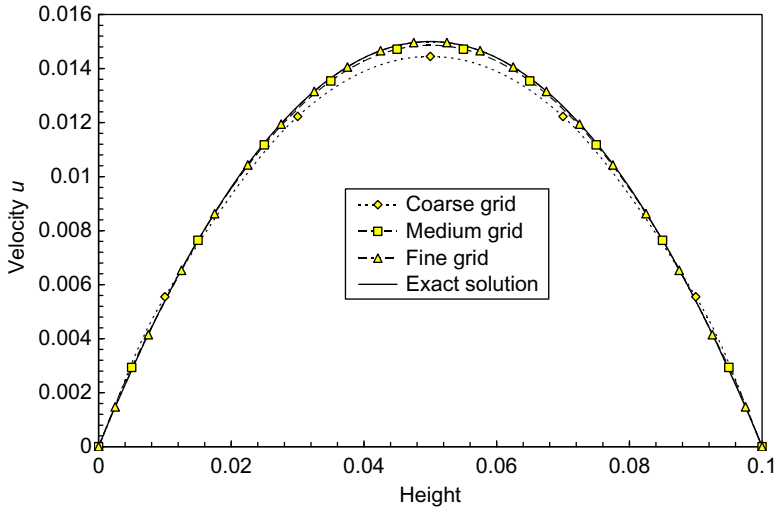


FIG. 6.4 Velocity profiles in the fully developed region for the computational results of three different grid distributions and analytical solution.

TABLE 6.1 Solution Errors Between the Predicted and Analytical Maximum Velocities for the Three Different Grid Distributions

Mesh	Predicted Max Velocity u	Analytical Max Velocity u	Error = $(u_{analytical} - u_{predicted})/u_{analytical} \times 100\%$
5×10	0.01444	0.015	3.73
10×20	0.01472	0.015	1.87
20×40	0.01496	0.015	0.27
40×80	0.01496	0.015	0.27

Controlling the solution error due to spatial discretization is fundamentally addressed through this parametric study. As the mesh is refined, the approximate solution approaches the exact solution. Herein, *consistency* is achieved since the truncation error diminishes with an increasing mesh resolution. Table 6.1 presents the solution error evaluated for the maximum magnitude of the horizontal velocity u between the analytical value and predicted results for four different meshes. The results demonstrate that *accuracy* is attained for the numerical solution on grid distributions of 20×40 and 40×80 control volumes. With the additional refinement made to the channel geometry consisting of 40×80 control volumes, *grid independency* is thus achieved since this approximate solution is the same as the results obtained for the grid distribution of 20×40 control volumes.

As shown in Table 6.1, the solution error appears to be levelling off even though the mesh is further refined from a grid distribution of 20×40 to 40×80 control volumes. Here, the solution error registers below 1%, which could not be totally eliminated due to the presence of round-off error during the numerical computations. This round-off error is due to the *single-precision* setting during the numerical calculations. As shown in Fig. 6.2, further refinement of the mesh may lead to an increase of the round-off error. One possible way of significantly reducing this round-off error is to extend the number of significant figures during the iterative procedure to *double precision*. Bear in mind that the *double-precision* setting tends to incur additional computational burden. In practice, some trade-off of the solution *accuracy* to achieve a quicker turnaround of the numerical computations is generally required especially for fluid flows that are complex.

Conclusion: In this test case, the various aspects concerning *consistency*, *stability*, *convergence*, and *accuracy* are succinctly illustrated for a two-dimensional channel flow problem. The error contribution to the numerical solution is investigated on the basis of evaluating the discretization or truncation

error. The increasing mesh resolution demonstrates two important outcomes. Firstly, as the spatial discretization error becomes smaller, a grid-independent solution is achieved. Secondly, the excellent agreement between the approximate and analytical solutions verifies the numerical algorithm that is adopted and provides credibility of the computational solution.

6.7.2 Test Case B: Flow over a 90° Bend

This test case was calculated using a commercial finite-volume CFD computer code ANSYS FLUENT, version 6.1.

Model description: The geometry of the test problem is a three-dimensional turbulent flow over a 90° bend. The schematic view of the experimental setup comprising an open-circuit suction wind-tunnel system for the 90° duct bend is shown in Fig. 6.5, which comprises a 3.5 m long horizontal duct, a 90° bend with a radius ratio of 1.5, and a 1.8 m long vertical straight duct. Air flows through a 10 mm thick Perspex square test section with the bulk gas velocity U_b adjusted through the aid of a variable frequency controller. Experimental

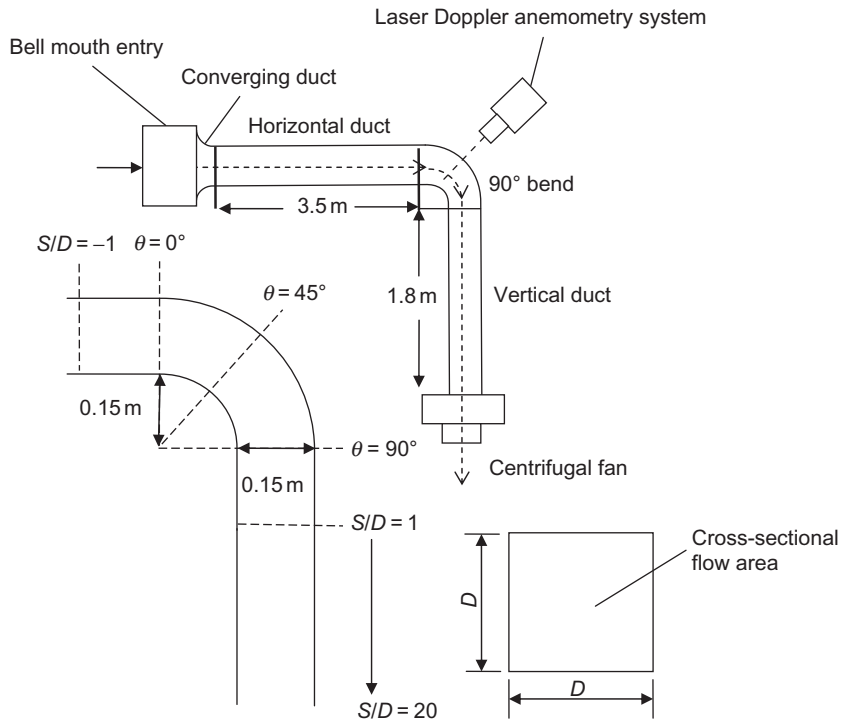


FIG. 6.5 Schematic view of the experimental rig of the 90° bend.

data are obtained on this experimental setup using flow visualization and laser Doppler anemometry (LDA) system.

Grid: For the 90° square-section bend, the computational domain begins at a distance of 2D upstream from the bend entrance and extends to 20D downstream from the bend exit. A structured mesh of $325 \times 43 \times 41$ control volumes in the respective directions along the streamwise, width, and height is generated for the whole computational domain.

Features of the simulation: This test case illustrates the importance of evaluating the choice of the turbulence models, standard k–ε (Launder and Spalding, 1974), and Reynolds stress (Launder et al., 1975; Launder, 1989), for computing the flow separation around the 90° bend and validating the computational solutions against experimental data.

The algorithm for the solution of the Navier–Stokes equations relies on the implicit segregated velocity-pressure formulation such as the SIMPLE scheme. This leads to a Poisson's equation for the pressure correction that is solved through the default iterative solver, normally the multigrid solver in the ANSYS FLUENT computer code. Finite-volume discretization is employed to approximate the governing equations. To avoid nonphysical oscillations of the pressure field and the associated difficulties in obtaining a converged solution on a collocated grid arrangement, the Rhie and Chow (1983) interpolation scheme is employed.

The working fluid, air, is taken to be incompressible, and the default initial conditions implemented in the computer code are used for the simulations.

Boundary conditions: At the inlet, Dirichlet conditions are used for all variables. The bulk velocity U_b was taken as constant with a value of 10 m/s. With the density and viscosity of air having the values of 1.2 kg/m^3 and 2×10^{-5} kg/m s, respectively, the corresponding Reynolds number based on this inlet velocity and height of the channel is 90,000. The turbulent kinetic energy k and dissipation ε are determined from the measured turbulence intensity I of about 1% at the centre of the duct cross-section. For the Reynolds stresses, the diagonal components are taken to be equal to 2/3 k, whereas the extra-diagonal components are set to zero (assuming isotropic turbulence). At the outlet, Neumann boundary conditions are applied for all the transported variables. The nonequilibrium wall function (as will be described in the next chapter) is employed for the airflow at solid walls because of its capability in better handling complex flows where the mean flow and turbulence are subjected to severe pressure gradients and rapid change, such as flow separation, reattachment, and impingement.

Results: The comparison between the measured and calculated longitudinal mean velocities normalized by the bulk velocity U_b at the bend exit ($\theta = 90°$) and 0.5D after the bend exit is illustrated in Fig. 6.6. The prediction of the streamwise velocities using the Reynolds stress model is observed to yield better agreement in contrast to the standard k–ε model, which is due to the capability of the Reynolds stress model capturing the anisotropy behaviour of the flow separation region around the 90° bend.

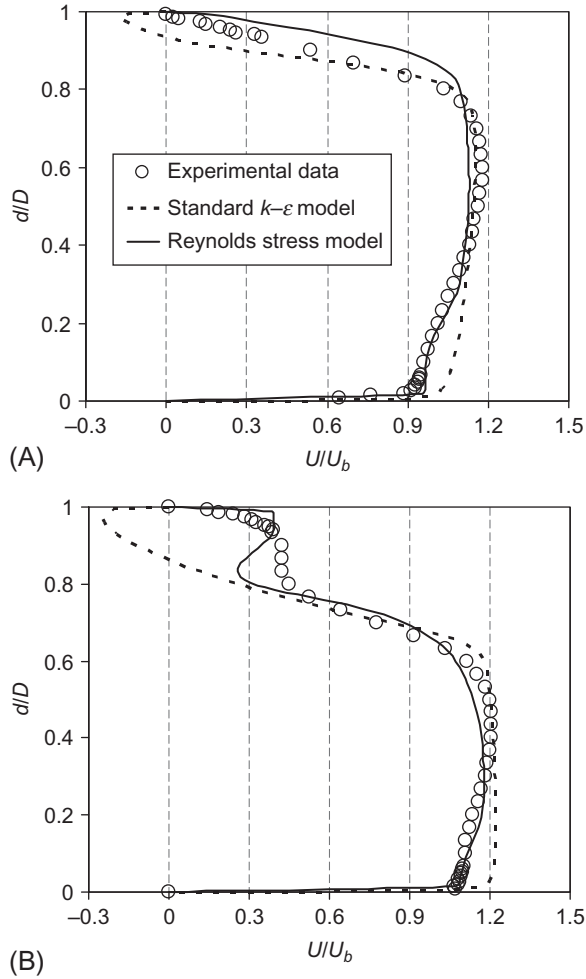


FIG. 6.6 Comparison between measured and calculated longitudinal mean velocities normalized by the bulk velocity U_b: (A) streamwise velocity at bend exit ($\theta = 90°$) and (B) streamwise velocity at 0.5D after the bend exit (see figure for more description).

The predicted longitudinal mean velocity normalized by the bulk velocity U_b using the Reynolds stress model is further compared with the measure data at different locations in the duct centre plane, as represented in Fig. 6.7. At the bend entrance ($\theta = 0°$), the turbulence model successfully predicts the acceleration of the airflow near the inner wall. The fluid deceleration caused by the unfavourable pressure gradient is also captured near the outer wall. More importantly, the turbulence model adequately reproduces the distorted longitudinal velocity profiles at the angles of $\theta = 30°$, $\theta = 45°$, and $\theta = 60°$ after the bend entrance.

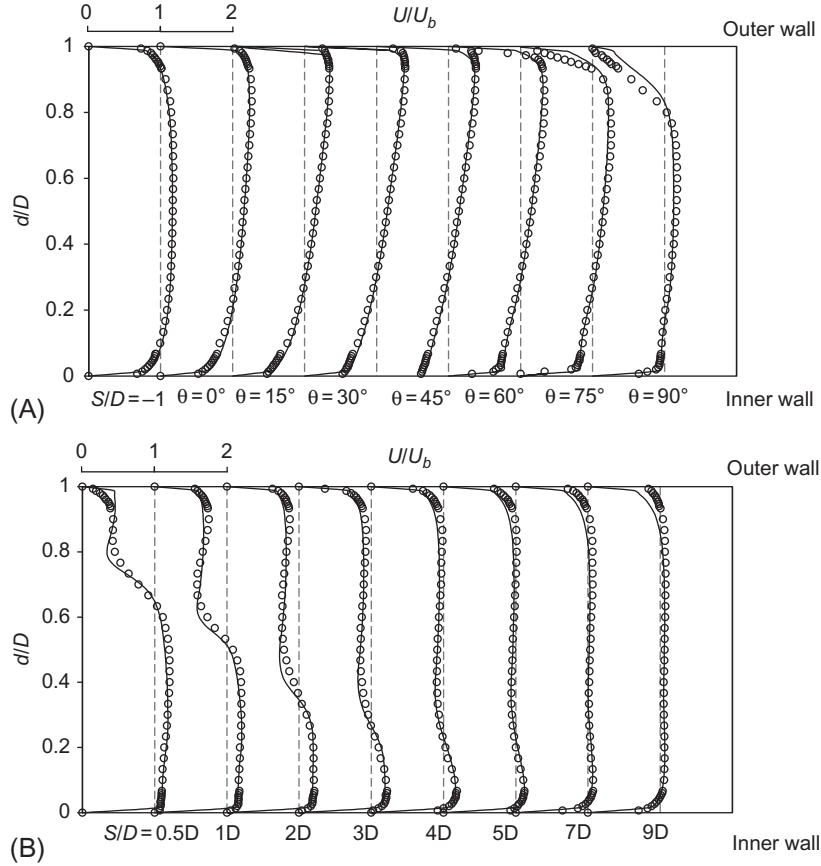


FIG. 6.7 Comparison between measured and calculated longitudinal mean velocities normalized by the bulk velocity U_b at different locations in the duct centre plane: (A) between bend entrance and exit and (B) downstream of bend exit (see again Fig. 6.6 for more description).

To better understand the flow characteristics around the 90° bend, Fig. 6.8 presents the calculated velocity vectors and pressure distribution of the airflow obtained through the Reynolds stress model at different cross-sections of the duct flow. Fig. 6.8A and B shows the calculated air velocity vector and pressure distribution at the cross-sectional middle plane of the duct flow. Favourable (positive) and unfavourable (negative) longitudinal pressure gradients persist near the inner and outer walls of the bend entrance. The presence of the favourable and unfavourable pressure gradients is caused by the balance of centrifugal force and radial pressure gradient in the bend (Humphrey et al., 1981). This physical phenomenon is typical of curved duct flows. Secondary flows are developed due to the direct consequence of the cross stream pressure gradient. The predicted secondary flow vectors are clearly depicted by the three square

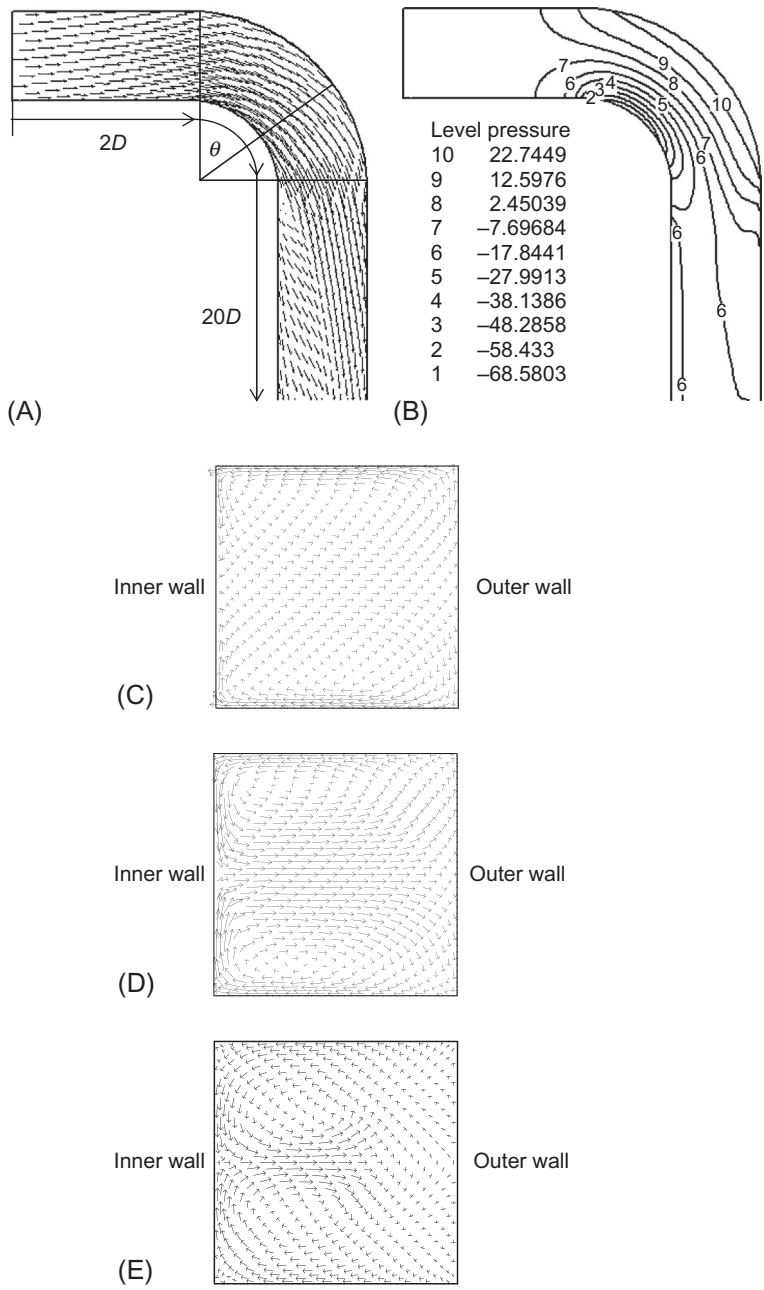


FIG. 6.8 Calculated flow field: (A) airflow in the duct middle plane, (B) static pressure distribution in the duct middle plane, (C) secondary flow at a cross-sectional flow area of location $\theta = 45°$, (D) secondary flow at a cross-sectional flow area of location $\theta = 90°$ (bend exit), and (E) secondary flow at cross-sectional flow area of location $S/D = 3$D after the bend exit.

cross-sectional flow areas at angles of $\theta = 45°$ and $\theta = 90°$ and distance of 3D after the bend exit ($S/D = 3$) in Fig. 6.8C–E, respectively.

Conclusion: This test case focuses on the use of approximate models such as the turbulence models to predict the physical characteristics of the turbulent flow around a 90° bend. Owing to the absence of analytical solutions, *validation* of the computational solutions is performed by comparing the predictions with the experimental data in order to address the simulation model uncertainty and the degree to which models correspond to an accurate representation of the real physical flow. The flow around a 90° bend though geometrically simple exhibits complex flow structures due to the existence of secondary flows in the vicinity of the bend region, which are generally anisotropic in nature. The results from the more sophisticated Reynolds stress model are shown to better capture the anisotropy behaviour of the flow in contrast to the standard k–ε model that assumes isotropy in its original model formulation.

6.8 SUMMARY

The credibility of a computational solution is analysed and assessed in this chapter through the consideration of the various aspects of *consistency*, *stability*, *convergence*, and *accuracy*. It is usually possible to demonstrate whether a discretized form of the governing fluid flow equations is consistent and also if the algebraic form of these equations is stable. Convergence requires, however, implications from *consistency* and *stability*, that is *consistency* + *stability* = *convergence*. In any numerical calculations, errors and uncertainties affect the accuracy of the computational solution. It is imperative that the errors and uncertainties are systematically reduced so that the computational solution better represents the real physical flow problem that is being solved. The conceptual framework linking the various aspects of *consistency*, *stability*, *convergence*, and *accuracy* beginning from the governing partial differential equations as considered in Chapter 3 and arriving at the approximate solution of the algebraic equations as described in Chapter 4 can be seen in Fig. 6.9.

The application of a Taylor series expansion to the discrete approximation of the governing equations results in an explicit expression for the truncation error (Section 6.2). This error measures the accuracy of the finite-difference or finite-volume approximation and determines the rate at which the error decreases as the finite quantities, time step and/or mesh spacing, diminish. It is noted that because of the close correlation between truncation error and solution error (Section 6.5.1), reducing the truncation error has beneficial consequences in the likelihood of also reducing the solution error.

Numerous worked examples and test cases presented throughout this chapter have aimed to better illustrate the conceptual properties of *consistency*, *stability*, *convergence*, and *accuracy* whilst solving the discretized form of the partial differential equations. In addition, it is important that the computational solution should be subjected to the rigorous process of *verification* and

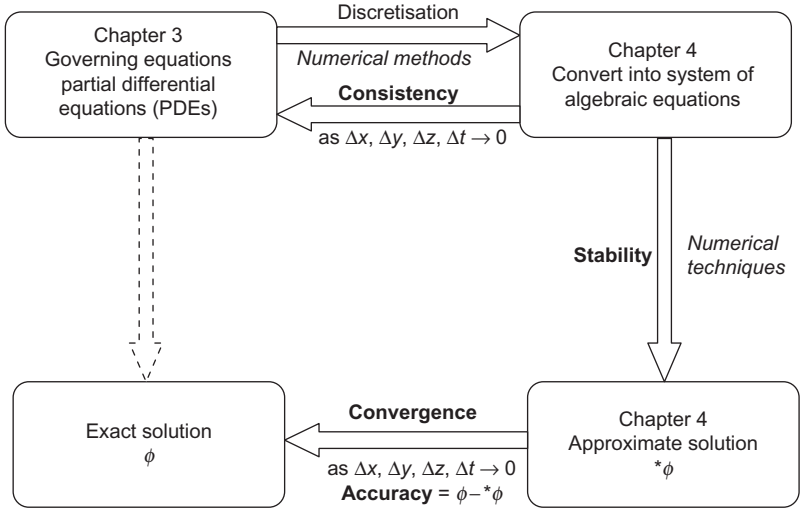


FIG. 6.9 A conceptual framework linking the various aspects of consistency, stability, convergence, and accuracy in arriving at a solution for the transport equations.

validation, which was demonstrated through two test cases. For a simple two-dimensional channel flow problem in test case A, it is feasible to verify the computational solution against an analytical relationship. However, for a more complicated flow problem that employs a computational solution in a three-dimensional domain, the absence of an analytical solution requires the dependency of benchmark and/or experimental data to validate the computational solution. This is evidenced by test case B for a three-dimensional airflow around a 90° bend. In this example, we demonstrated the use of appropriate turbulence models to better capture the physical flow behaviour in a 90° bend. This aspect highlights the uncertainty that arises through the use of approximate models for solving turbulent flow that will be further investigated in the next chapter. More practical guidelines will be further discussed in this chapter in better equipping the reader in handling and solving a range of CFD problems.

REVIEW QUESTIONS

6.1 Why do the results obtained through numerical methods differ from the exact solutions solved analytically? What are some of the causes for this difference?

6.2 In the analysis of CFD results, what does consistency imply?

6.3 What are the key aspects of consistency?

6.4 If a system of algebraic equations is equivalent to the partial differential equation as the grid spacing tends to zero, does this also mean the solution

of the system of algebraic equations will approach the exact solution of the partial differential equation? Why?

6.5 Explain why the following Taylor series expansion of the one-dimensional transient diffusion equation $\left[\frac{\partial \phi}{\partial t} - \alpha\frac{\partial^2 \phi}{\partial x^2} + \alpha\left(\frac{\Delta t}{\Delta x}\right)^2 \frac{\partial^2 \phi}{\partial t^2}\right]_i = 0$ does not show consistent properties.

6.6 Describe the concept of stability.

6.7 What is the stability criteria produced by the von Neumann analysis?

6.8 What is the Courant number, and what is its function?

6.9 Consider the following discretized equation, locate the Courant number, and discuss the *Courant-Friedrichs-Lewy* condition for stability in this case:

$$\phi_i^{n+1} = \phi_i^n + \alpha\frac{\Delta t}{\Delta x^2}\left(\phi_{i+1}^n - 2\phi_i^n + \phi_{i-1}^n\right)$$

6.10 Provide a definition on the concept of convergence.

6.11 State *Lax's equivalence theorem* for convergence. Does it apply to non-linear problems?

6.12 What are the three important rules when considering *iterative convergence*?

6.13 How is the concept of residual applied to describe the discretized equation of the system of transport equations?

6.14 Differentiate between a local residual and a global residual.

6.15 What is implied when the residuals become negligible with increasing iterations?

6.16 What is the usual recommended residual tolerance level?

6.17 Define underrelaxation factor. State its advantages and disadvantages when using a small value.

6.18 Discuss ways in which convergence can be accelerated.

6.19 Is a converged solution also an accurate solution? Why?

6.20 Discuss some types of errors that can cause a solution to be inaccurate.

6.21 What are discretization errors? What is the difference between a global error and a local error?

6.22 Which methods can be used to minimize discretization errors?

6.23 What are round-off errors, and what kinds of calculations are most affected by them?

6.24 Which method can be used to minimize round-off errors?

6.25 What does it mean to perform a grid convergence (independency) test?

6.26 What is the difference between verification and validation? Why are these two steps important in analysing results?

6.27 Discuss briefly how multigrid methods are employed to increase the computational efficiency of solving CFD problems.

6.28 Discuss briefly how parallel or GPU computing is used to achieve computational efficiency.

6.29 Consider the following algebraic equation: $a_p\Phi_p = \sum a_{nb}\Phi_{nb} + b$ as described in Chapter 4. In matrix form, a_p represents the diagonal element, whilst a_{nb} is the neighbouring element. The condition for convergence stipulates that $\sum |a_{nb}| // a_P \leq 1$, which simply means that the sum of the neighbouring elements divided by the diagonal elements must be less than unity, at all grid nodal points. Analyse the condition for convergence given the system of equations below:

Case 1
$\Phi_1 = 0.5\Phi_2 + 1.5$ (1)
$\Phi_2 = \Phi_1 + 2$ (2)

by rearranging the above equations, we have

Case 2
$\Phi_1 = \Phi_2 - 2$ (2)
$\Phi_2 = 2\Phi_1 - 3$ (1)

Chapter 7

Practical Guidelines for CFD Simulation and Analysis

7.1 INTRODUCTION

The necessity to understand the physics of a flow problem in hand, the basis of the numerical methods employed to solve the governing equations, and the means to obtain the most accurate and consistent results given the available computing resource are some of the common challenges faced by the CFD user. This chapter is particularly written to address these common aspects of CFD, and the aim is to provide some practical guidelines in carrying out a CFD simulation, solution assessment, and analysis.

In Chapter 2, grid generation was viewed as one of the key important considerations during the preprocess stage following the definition of computational domain geometry. The generation of a mesh such has been described in Chapter 4 is an important numerical issue where the type of mesh chosen for a given flow problem can determine the *success* or *failure* in attaining a computational solution. Because of this, grid generation has become an entity by itself in CFD. As a guide to grid generation, the mesh must be sufficiently fine to provide an adequate resolution of the important flow features and geometrical structures. For flows with bounded walls, it is recommended that recirculation vortices or steep flow gradients within the viscous boundary layers are properly resolved through locally refining or clustering the mesh in the vicinity of wall boundaries. Mesh concentration may also be required for fluid flows having high shear and/or high-temperature gradients. Furthermore, the quality of the mesh has significant implications on the convergence and stability of the numerical simulation and accuracy of the computational result obtained. All of these grid generation issues will be examined in the next section.

Also in Chapter 2, special attention was given to specifying a range of boundary conditions commonly applied for a given CFD problem. The physical meanings of the various boundary conditions that were employed to close the fluid flow system were later illustrated in Chapter 3. Boundary conditions have serious implications on the CFD solution. This further reinforces the requirement to define suitable boundary conditions that appropriately mimic the real physical representation of the fluid flow. In many real applications, there is always great difficulty in defining in detail some of the boundary conditions

Computational Fluid Dynamics. https://doi.org/10.1016/B978-0-08-101127-0.00007-6
© 2018 Elsevier Ltd. All rights reserved.

at the inlet and outlet of a flow domain that is required for an accurate solution. A typical example is the specification of turbulence properties (turbulent intensity and length scale) at the inlet flow boundary, as these are arbitrary in many CFD problems. Nevertheless, by carrying out an uncertainty analysis, the reader can develop a good feel of the appropriateness and inappropriateness of the boundary conditions that are being imposed within the physical context of the CFD problem being solved. Some useful guidelines on the specification of inlet, outlet, wall, and other types of boundary conditions for different classes of problems will be examined and discussed.

Since most flows of engineering significance are turbulent in nature, the classical two-equation modelling approach of handling turbulence was briefly introduced in Chapter 3 where the basic formulation of the standard k–ε model was described. Nonetheless, we demonstrated in the test case of a flow over a 90° bend of Chapter 6 that the use of a more sophisticated turbulence model, the Reynolds stress model, was deemed necessary to better capture the anisotropy behaviour of the flow separation around the bend region. A turbulence model is a computational procedure to instinctively close the system of mean-flow governing equations. Nowadays, the two-equation and Reynolds stress models form the basis of turbulence calculations in numerous commercial, shareware, and in-house CFD codes. On the other hand, due to some inherent limitations of the standard k–ε model, development of other dedicated models for limited categories of flows has led to the formulation of many variants to the standard model. A CFD user is therefore confronted with the pressing choice of selecting a suitable turbulence model. The provision of appropriate guidelines is therefore insurmountable. Although many industrial problems fall within the limited class of flow that can be resolved by the standard k–ε model, the only probable way to validate more specific flow problems is to conduct a case-by-case examination to determine the optimum turbulence model. Pertinent turbulence modelling issues are explored later in this chapter.

As we continue to unravel the mysteries of CFD, this chapter by and large assembles all the essential knowledge gathered in the previous chapters, thereby bringing to fruition the realization of CFD simulation and analysis. We begin by focusing on some practical guidelines required for handling grid generation.

7.2 GUIDELINES FOR BOUNDARY CONDITIONS

7.2.1 Overview of Setting Boundary Conditions

The pursuit of setting proper physical boundary conditions like in the section of local refinement and solution adaptation also governs the computational stability and the numerical convergence of the CFD problem. In many real applications, there is always great difficulty in prescribing some of the boundary conditions at the inlet and outlet of the computational domain. Boundary conditions for fluid flow are generally more complex due to the coupling of velocity

fields with the pressure distribution. In the context of CFD, defining suitable boundary conditions generally encompasses the specification of two types of boundary conditions: the *Dirichlet* and *Neumann* boundary conditions. The physical meanings of these boundary conditions have been described in Section 3.7. For brevity, the *Dirichlet* boundary condition can be simply defined for the transport property ϕ as the requirement of specifying the physical quantity over the boundary, such as the following:

$$\phi = f(\text{analytic}) \tag{7.1}$$

The *Neumann* boundary condition involves, however, the prescription of its derivative at the boundary given by

$$\frac{\partial \phi}{\partial n} = 0 \tag{7.2}$$

A practice that is widely adopted for inflow boundaries is to set the transported quantities of either a uniform or some predetermined profile over the boundary surface (*Dirichlet*). For outflow boundaries, the convective derivative normal to the boundary face is set equal to zero; the transported quantities at the boundaries are extrapolated along the stream-wise direction of the fluid flow (*Neumann*). However, the use of such an approach is not as straightforward in some selected applications. Some difficulties may arise during the implementation of such boundary conditions. For example, *non-physical* reflection of outgoing information back into the calculation domain (Giles, 1990) such as the fluid that may inadvertently re-enter the domain through these outflow boundaries and in the regions of possible high swirl, large curvatures or pressure gradients may significantly affect the convergence behaviour of the iterative procedure. In addressing some of these difficulties, the specification of radial equilibrium of a pressure field is deemed to be more preferable than the usual constant static pressure for swirling flows at an outlet. Also, when strong pressure gradients are present, special nonreflecting boundary conditions are sometimes required for the inflow and outflow boundaries (Giles, 1990).

Some other difficulties that are also important to note include the specification of suitable inlet turbulence intensity, length scales, turbulence kinetic energy, and dissipation for a turbulent flow entering the flow domain; the correct description of the boundary-layer velocity profile on the walls and at the inlet; and also the precise distribution of scalar or species concentrations at the inflow boundary. It is therefore not surprising that as a CFD user, he/she must be fully aware of these problems and needs to develop a good feel for the certainty or uncertainty of the boundary conditions that are being imposed.

In ensuring consistency of the boundary conditions imposed with the CFD models, it is vital that the boundary conditions strongly reflect the application that is being calculated. Some general guidelines are provided. Whenever possible, it is useful to examine the potential of modifying the computational domain by moving the domain boundaries to a position where the boundary

conditions are more readily identifiable where they can be more precisely specified. It is also important to be mindful of upstream or downstream obstacles such as bends, contractions, diffusers, and blade rows outside of the flow domain, which may significantly affect the flow distribution. Often, information on these components upstream and downstream of the domain is lacking or not available; it may be required to incorporate these pertinent components in the calculations so that appropriate flow predictions are obtained. In handling a wide range of different CFD applications, it may be beneficial to carry out a sensitivity analysis in which the boundary conditions are systematically altered within certain limits to detect any significant variation of the computational results. Should any of these variations prove to greatly influence the simulated results and lead to large changes in the simulation, it is then necessary to obtain more accurate data of the boundary conditions that are being specified. When commercial codes are used, default settings of the boundary conditions for the domain boundaries are given and the user is usually not required to specify any boundary conditions. Nonetheless, he/she still needs to ensure that appropriate boundary conditions are applied for the application that is being solved. We proceed to concentrate on more specific guidelines for the inlet, outlet, wall, and symmetry and periodicity boundary conditions, which are subsequently discussed below.

7.2.2 Guidelines for Inlet Boundary Conditions

Since flows inside a CFD domain are driven by boundary conditions, carrying out a sensitivity analysis by systematically changing the inlet boundary conditions within allowable limits is highly recommended. The aim of this practical guideline is to ensure that appropriate boundary conditions are applied at the inflow boundaries. Depending on the flow problem, certain key parameters can be scrutinized to ascertain the suitability of the inlet boundary conditions that are being specified. Some useful parameters that can be examined are the following:

- Inlet flow direction and the magnitude of the flow velocity
- A uniform distribution of a parameter or a profile specification, for example, either a uniform inlet velocity or some predetermined inlet velocity profile
- Variation of physical properties
- Variation of turbulence properties at inlet

The reader should also take note that an inlet boundary represents a potential *mass source* for the fluid flow. It is thereby imperative that an outlet boundary is imposed within the flow domain to characterize the *mass sink* of the fluid flow. Without an outlet boundary, the mass is not conserved. Not surprisingly, the CFD calculations in this circumstance will tend to 'blow up' rather swiftly.

By revisiting the case for the fluid flowing between two stationary parallel plates, the various combinations of the inlet and outlet boundary conditions can

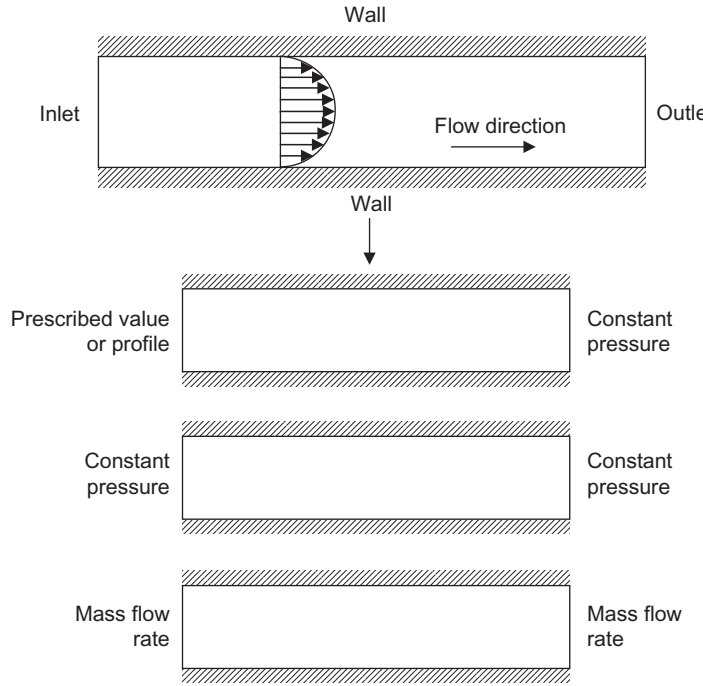


FIG. 7.1 Configurations for a simple flow between two stationary parallel plates.

be appropriately demonstrated. The various configurations that are typically adopted are illustrated in Fig. 7.1. The first configuration that involves the specification of a prescribed velocity profile at the inlet and a constant pressure at the outlet is commonly employed in many CFD calculations. For rapid convergence and computational robustness, most commercial codes generally recommend the implementation of this type of configuration. Nonetheless, other highlighted configurations may be equally applicable if proper initial conditions are accommodated prior to the CFD calculations. At steady state, the CFD solution for all the configurations should yield identical velocity profiles especially at the fully developed region situated near the channel exit.

For certain types of geometries, the specification of inlet boundary conditions for the upstream flow may require special attention. At the predesignated inlet location, the exact distribution may be unknown. The possibility of moving the inlet boundary to a position where the fluid flow is allowed to develop through some distance inside the domain should therefore always be examined. Let us consider a typical flow problem of the backward-facing step geometry. For high accuracy, it is necessary to demonstrate that the interior solution is unaffected by the choice of location of the inlet by carrying out a sensitivity study for the effect of different upstream distances from the flow expansion region as indicated in Fig. 7.2. If the inlet is too close, the velocity profile

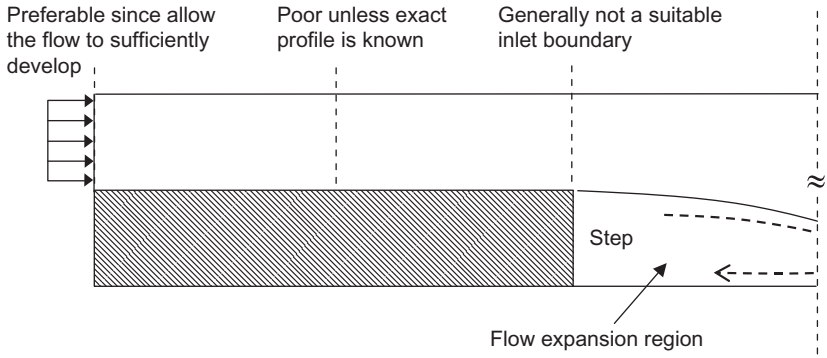


FIG. 7.2 Inlet locations for the backward-facing step flow problem.

will be changing in the flow direction before the flow expansion region that significantly affects the recirculation vortex and subsequently the reattachment length. Such a solution, of course, cannot be fully trusted and a re-examination of the inlet location is required.

7.2.3 Guidelines for Outlet Boundary Conditions

It is vital that the boundary condition imposed at the outlet is always selected on the basis that it has a weak influence on the upstream flow. The most suitable outflow conditions, as demonstrated in Fig. 7.1, are weak formulations involving the specification of a constant pressure such as static pressure at the outlet plane. Whenever possible, the outlet boundary must be placed as far away as possible from the region of interest and should be avoided in regions of strong geometrical changes or in wake regions with recirculation. Let us illustrate the potential hazards of the latter by revisiting the backward-facing step geometry flow problem.

Fig. 7.3 shows typical velocity profiles downstream from the step and the appropriate choice for the location of the outlet boundary. As aforementioned, a common practice that is adopted for outflow boundaries in many CFD calculations is to apply the *Neumann* boundary condition where the convective derivative normal to the boundary face is enforced to zero, and the boundary value is later evaluated based on the stream-wise extrapolation of the transported quantities. If the outlet is located at *Position 1*, a plane in this position cuts across the wake region of recirculation (Fig. 7.3). Not only is the assumed boundary condition not valid, but also the problem is exacerbated by the apparent area of reverse flow where the fluid enters the domain. Further downstream at *Position 2*, there may not be any reverse flow, but the zero-gradient condition still does not hold since the velocity profile is changing in the flow direction. As a practical guideline, the outlet boundary should be placed much further downstream by at least 10 step heights ($>10h$) to give accurate results—*Position 3*. It is also

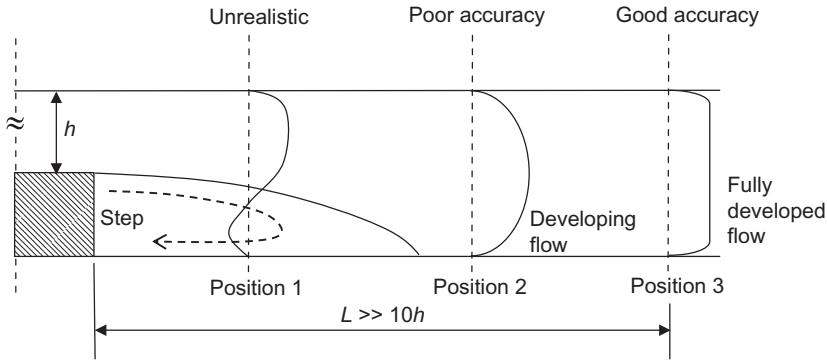


FIG. 7.3 Outlet locations for the backward-facing step flow problem.

necessary to ensure and demonstrate that the interior solution is not affected by the location of the outlet boundary. It is imperative that the downstream distance between the step and outlet boundary is extended until no significant change to the interior solution is observed.

For some CFD problems where the outlet boundaries may not be feasibly relocated in the domain, care should be exercised that the possibility of fluid flow entering through the outflow boundaries does not lead to progressive instability of the numerical procedure or to the extent of attaining an incorrect solution. In such an event, some reconfiguration of the model geometry may be required, and the flow area at these outlets is restricted, provided that the outlet boundaries are situated at a location substantially far away from the region of interest. Nonetheless, if the outflow boundary condition permits flow to re-enter the domain, then appropriate *Dirichlet* boundary conditions should be imposed for all transported quantities.

7.2.4 Guidelines for Wall Boundary Conditions

Wall boundary conditions are generally employed for solid walls bounding the flow domain. Here, care should always be taken to ensure that the boundary conditions imposed on these types of walls are consistent with both the numerical model used and the actual physical features of the flow geometry. For the fluid flowing between two stationary parallel plates in Fig. 7.1, wall boundary conditions are enforced for the channel walls. Nonetheless, these boundary conditions are also often used to bound fluid and solid regions such as applied for the presence of the step within the flow domain or the two cylinders inside the open surrounding flow environment.

For stationary walls, the default consideration is to assume that the no-slip condition applies, which simply means that the velocities are taken to be zero at the solid boundaries. This condition implies that the fluid flow comes to rest at the solid walls. We may also explore the possibility of modelling the boundary

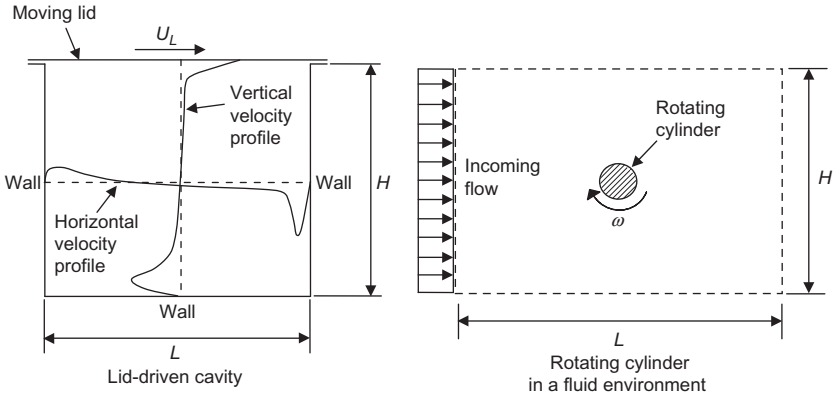


FIG. 7.4 Illustrative fluid flow examples with moving or rotating walls.

conditions on the solid walls as a free-slip condition, which assumes that the flow is parallel to the wall at this point. This condition corresponds to the absence of viscous effects in the continuum equations and is applied to the problem where the continuum approach breaks down as the fluid approaches the wall in viscous flow. For a general fluid flow case where the transport of heat takes precedence within the domain, great care must be taken to specify boundary conditions (e.g. adiabatic walls or local heat fluxes) on the solid boundaries of the numerical model that properly represent the heat-transfer characteristics of the solid walls in the actual physical model.

In flow cases with moving or rotating walls, it is important that the boundary conditions that need to be specified are consistent with the motion of the solid walls. A lid-driven cavity and a rotating cylinder in a fluid environment as shown in Fig. 7.4 are some typical examples exemplifying the moving boundary problems in CFD. These types of problems allow a positive or negative tangential velocity to be imposed at the top boundary of the lid-driven cavity or a clockwise or anticlockwise rotational speed to be specified on the circumferential surface of the rotating cylinder. Other more complex CFD problems may require the need to employ sliding or moving meshes to better emulate the motion of a rotating impeller stirring the fluid in a tank or the sea waves hitting the ship's hull. The use of sliding or moving meshes is beyond the scope of this introductory book. Interested readers are advised to consult literatures for more information (see e.g. Ferziger and Perić, 1999).

7.2.5 Guidelines on Symmetry and Periodic Boundary Conditions

These boundary conditions are generally used when the flow geometry possesses some symmetry or periodic properties that allow the flow problem to be simplified by solving only a fraction of the domain.

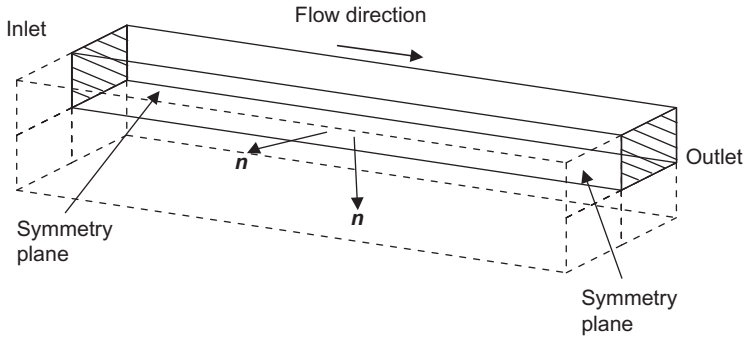


FIG. 7.5 Application of symmetry boundary conditions for the airflow through a square duct.

For symmetry boundary conditions, they are applied when the physical geometry and the flow field has a mirror symmetry. At the symmetry plane, the following requirements must be satisfied:

- The normal velocity is zero.
- The normal gradients for all transported properties are zero.

Consider the flow problem where air is flowing through a square duct as described in Fig. 7.5. The application of symmetry planes can significantly reduce the computational effort since only a quarter of the flow domain needs to be modelled. Care should always be exercised especially in prescribing the mass flow rates at the inlet and outlet boundaries. For this simplified flow geometry, the correct mass flow rates to be imposed at these boundaries are only a quarter of the actual mass flow rates.

To apply the periodic boundary conditions, it is imperative that the periodic planes come in pairs. The key requirement in employing these boundary conditions is that not only they have to be physically identical but also the mesh distribution in the respective planes must also be identical. In CFD applications, this condition implies that the flow leaving one of the periodic planes is equal to the flow entering in the other. For wall-bounded flows such as the fluid flowing between two stationary parallel plates or air flowing through a square duct, the inlet and outlet boundaries can otherwise be prescribed as periodic planes where now the flow field leaving the outlet boundary is taken to be the same entering the inlet boundary. Fig. 7.6 further illustrates the application of periodic boundary conditions for the fluid flow in a mixing tank and across an in-line arrangement of heat-exchanger tubes. For the former, the flow field is known as rotationally or cyclically periodic where the flow field leaving 'Boundary 2' is enforced as inlet flow condition at 'Boundary 1'. For the latter, the flow field is, however, considered as translationally periodic. As before, the flow field leaving 'Boundary 2' is used as inlet flow field at 'Boundary 1'. It is worthwhile noting that this flow case is particularly similar to the aforementioned wall-bounded flows.

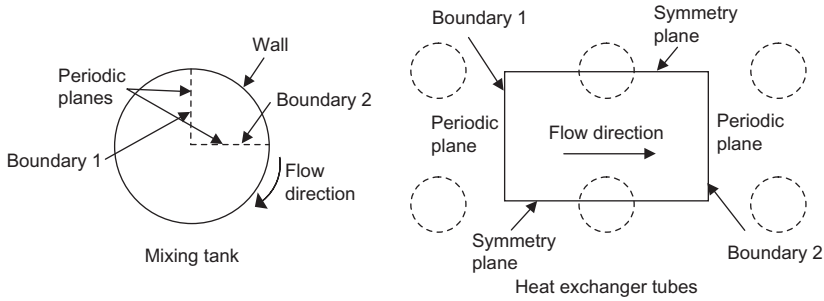


FIG. 7.6 Some illustrative examples on the application of periodic boundary conditions.

7.3 GUIDELINES FOR TURBULENCE MODELING

7.3.1 Overview of Turbulence Modeling Approaches

Some pertinent properties characterizing flows that are turbulent have been discussed and described in Chapter 3. The reader may wish to momentarily revisit Section 3.5.1 and recapitulate the various aspects detailed therein. In brief, turbulent flows can be classified as being highly unsteady and random. They are also known to contain large coherent structures responsible for the mixing or stirring processes. Nonetheless, the fluctuating property across a broad range of length and timescales particularly from the modelling standpoint makes the direct numerical simulation of these types of flows very difficult. Turbulent flows are constantly encountered in many engineering systems. They tend to demand more computational resources compared with flows that are laminar. For research and design purposes, CFD analysts and engineers are expected to understand and predict the effects produced by turbulence. In this section, we review many state-of-the-art turbulence modelling approaches that have been developed and applied to date.

7.3.1.1 Advanced Techniques

The most accurate approach to turbulence simulation is to solve directly the governing transport equations without undertaking any averaging or approximation other than the numerical discretizations performed on them. Through such simulations, all of the fluid motions contained in the flow are considered to be resolved. This approach is commonly known as the direct numerical simulation or by its more well-established acronym, DNS. Since DNS requires all significant turbulent structures to be adequately captured (i.e. the domain of which the computation is carried out needs to accommodate for the smallest and largest turbulent eddy), it can be very expensive to be employed. Alternatively, we can consider another approach where the structure of turbulent flow can be viewed as the distinct transport of large- and small-scale motions.

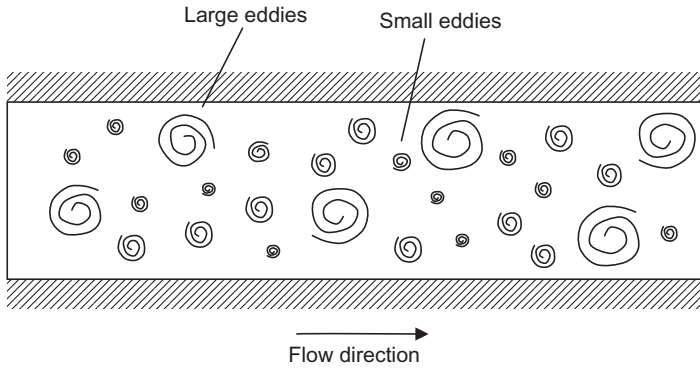


FIG. 7.7 Schematic representation of a turbulent motion.

Fig. 7.7 presents a schematic illustration of such flow. Since the large-scale motions are generally much more energetic and by far the most effective transporters of the conserved properties than the small ones, a simulation that treats the *large eddies* exactly but approximates the *small eddies* makes rather perfect sense. Such an approach is recognized as the large-eddy simulation or by its more widespread acronym, LES. It is still expensive but much less costly than DNS. In general though, DNS is the preferred method because it is more accurate. LES is, however, the preferred method for flows in which the Reynolds number is too high or the geometry is too complex to allow application of DNS.

The results of a DNS or LES simulation contain very detailed information about the flow, producing an accurate realization of the flow whilst encapsulating the broad range of length and timescales. For design purposes, it is far more information than any engineer needs. DNS and LES approaches usually require high usage of computational resources and often cannot be used as a viable *design tool* because of the enormity of the numerical calculations and the large number of grid nodal points. A question therefore arises of their usefulness and what role they can play in CFD. Because of the wealth of information, DNS and LES taken as a *research tool* can provide a qualitative understanding of the flow physics and also can construct a quantitative model allowing other, similar, flows to be computed. More importantly, they can assist in some cases to improve the performance of currently applied turbulence models in practice. We shall demonstrate the use of DNS as a research tool in some sample aerodynamic investigations in Section 8.4.5.

7.3.1.2 Practical Techniques

For most engineering purposes, it is unnecessary to resolve the details of the turbulent fluctuations such as the DNS and LES approaches. In general, the effects of the turbulence on the mean flow are usually sufficient to quantify

the turbulent flow characteristics. For a turbulence model to be practical and useful in a general-purpose CFD code, it must have wide applicability and be simple, accurate, robust, and economical.

In Chapter 3, the Reynolds-averaged approaches to turbulence result in the formulation of the two-equation turbulence model—the *standard k–ε model* proposed by Launder and Spalding (1974). This model is well established and widely validated and gives rather sensible solutions to most industrially relevant flows. Nonetheless, numerous limitations are also identified especially for flows with large, rapid, extra strains (e.g. highly curved boundary layers and diverging passages) since the model generally fails to fully describe the subtle effects of the streamline curvature on turbulence. This weakness has been exemplified in Chapter 6 through the worked example in Section 6.7.2. The test case results revealed that the *Reynolds stress model* works better because of the ability of the model to accommodate the *anisotropic* turbulent stresses occurring around the 90° bend. The *standard k–ε model* that is a consequence of the eddy viscosity concept assumes that the turbulent stresses are linearly related to the rate of strain by a scalar turbulent viscosity, and the principal strain directions are aligned to the principal stress directions—*isotropic*. Owing to the deficiencies of the treatment of the normal stresses, secondary flows that exist in the 90° bend, which are driven by *anisotropic* normal Reynolds stresses, could not be properly predicted.

The *Reynolds stress model*, also called the second-moment closure model, dispenses the notion of turbulent viscosity and determines the turbulent stresses directly by solving a transport equation for each stress component. This requires the solution of six additional equations ($\overline{u_1'2}$, $\overline{u_2'2}$, $\overline{u_3'2}$, $\overline{u_1'u_2'}$, $\overline{u_1'u_3'}$, and $\overline{u_2'u_3'}$), which are solved accordingly in the form of Eq. (3.53) in Chapter 3 in order to account for the directional effects of the Reynolds stress field. An additional equation for ε is also solved to provide a length scale determining quantity. For a comprehensive explanation of this particular type of turbulence model, interested readers can consult to relevant reference texts by Launder (1989) and Rodi (1993). In a similar manner, the turbulent heat fluxes can be determined directly by solving three additional equations, one for each flux component, thereby removing the notion of a turbulent Prandtl number. There is no doubt that *Reynolds stress model* has a greater potential to represent the turbulent flow phenomena more correctly than the *standard k–ε model*. This type of model can handle rather complex strain and, in principle, can cope with nonequilibrium flows. The shortcoming of this model is the very large computing costs that may be incurred because of the extra governing equations. Also, the model success thus far has been rather moderate, specifically for axisymmetric and unconfined recirculating flows where they have been shown to perform as poorly as the *standard k–ε model*.

A lot of research is still being performed in this field, and new models are constantly being proposed. The turbulent states that can be encountered across

the whole range of industrially relevant flows are rich, complex, and varied. It is now accepted that no single turbulence model can span these states since none is expected to be universally valid for all flows. Accordingly, Bradshaw (1994) refers to turbulence as *the invention of the devil on the seventh day of creation, when the Good Lord wasn't looking*. Because of its difficult nature, we will attempt to propose some useful strategies for selecting appropriate turbulence models in handling turbulent fluid engineering problems in the proceeding section.

7.3.2 Strategy for Selecting Turbulence Models

In CFD, different types of turbulent flows require different applications of turbulence models. In the event that insufficient knowledge precludes the selection of an appropriate model, we strongly encourage the use of the two-equation model such as the *standard k–ε model* as a starting point for turbulent analysis. This model offers the simplest level of closure since it has no dependence on the geometry or flow regime input. As a first step to turbulence model selection, the *standard k–ε model* is robust and stable and is as good as any other more sophisticated turbulence models in some applications. The majority of in-house and commercial codes generally set this model as the default modelling option for handling flows that are turbulent. It is not entirely surprising because it has been a de facto standard in industrial applications and still remains the workhorse of industrial computations.

Nevertheless, the *standard k–ε model* as aforementioned is not without any weaknesses. It is therefore imperative that the major weaknesses associated with this model are catalogued in some fashion so as to instigate palliative actions that might be fruitfully considered for improving the numerical predictions. These advisory actions, that will be given shortly, should not be viewed as definitive cures but rather recommendations whereby possible alternatives to the *standard k–ε model* can be systematically investigated. There is also no guarantee the specific advice will yield significantly improved results. The necessary task of carrying out careful *validation* and *verification* remains the defining step in order to fully justify the application of turbulence models for the particular CFD problem being solved.

7.3.2.1 Guideline on a Particular Weakness of the Standard k–ε Model

Historically, the five adjustable constants C_μ, σ_k, σ_ε, $C_{1\varepsilon}$, and $C_{2\varepsilon}$ in the *standard k–ε model* have been calibrated against comprehensive data for a wide range of turbulent flows but of simple geometrical flow origins. This has been evidenced by its remarkable successes in handling thin-shear-layer, recirculating, and confined flows. Deviation from such flow behaviours has, however, resulted in the

standard k–ε model performing rather poorly especially in important flow cases having the following:

- Flow separation (Baldwin and Lomax, 1978)
- Flow reattachment (Kato and Launder, 1993)
- Flow recovery (Ince and Launder, 1995)
- Some unconfined flows (e.g. free-shear jet) (Apsley et al., 1997)
- Secondary flows in complex geometrical configurations (flow around a poppet valve in Ferziger and Perić, 1999)

Let us demonstrate a specific palliative technique for the weakness under consideration for the *standard k–ε model* of a worked example represented by the backward-facing step flow problem described earlier. It is well known that the reattachment length l_r (Fig. 7.8) is generally poorly predicted by this model under turbulent flow because of the overprediction of the turbulent kinetic energy. The high turbulence levels predicted upstream following the flow expansion at the step are transported downstream, and the real boundary-layer development is subsequently swamped by this effect. For illustration purposes, we investigate the use of other more sophisticated turbulence models such as the *RNG k–ε model* and *realizable k–ε model*, respectively, proposed by Yakhot et al. (1992) and Shih et al. (1995) to exemplify the improvements that can be achieved in the numerical predictions.

For this flow problem, the CFD commercial code, ANSYS FLUENT, version 6.1, is utilized to predict the continuum gas phase under steady-state conditions through solutions of the conservation of mass and momentum in two dimensions. A computational domain with a size of $12h$ (length) $\times$ $1h$ (height) before the step and $50h$ (length) $\times$ $2h$ (width) after the step is considered. The Reynolds number based on the free-stream velocity u_∞ of 40 m/s and step height h for this investigation is evaluated as 64,000.

Some pertinent differences are worthwhile mentioning with regards to each of the turbulence models before proceeding to discuss the numerical

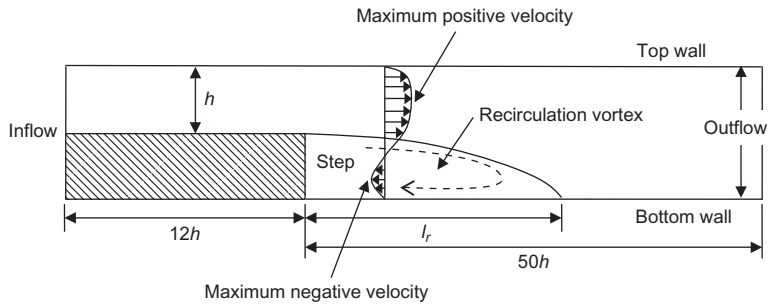


FIG. 7.8 A schematic illustration of the reattachment length location and respective dimensions for the regions before and after the step for the backward-facing step geometry.

results. The *RNG k–ε model* includes a modification to the transport ε-equation where the source term is solved as

$$S_\varepsilon = \frac{\varepsilon}{k}(C_{\varepsilon 1}P - C_{\varepsilon 2}D) - R \tag{7.3}$$

In the *standard k–ε model*, the rate of strain term R in the above equation is absent (compared with Eq. (3.57) in Chapter 3). The presence of this R term is formulated in the form of

$$R = \frac{C_\mu \eta^3 (1 - \eta/\eta_o)}{1 + \beta\eta^3}\frac{\varepsilon^2}{k} \tag{7.4}$$

where β and η_o are constants with values of 0.015 and 4.38. The significance of the inclusion of this term is its responsiveness towards the effects of rapid rate of strain and streamline curvature, which cannot be properly represented by the *standard k–ε model*. According to the renormalization group theory (Yakhot and Orszag, 1986), the constants in the turbulent transport equations are given by

$$C_\mu = 0.0845, \quad \sigma_k = 0.718, \quad \sigma_\varepsilon = 0.718, \quad C_{\varepsilon 1} = 1.42, \quad C_{\varepsilon 2} = 1.68.$$

For the *realizable k–ε model*, the term *realizable* means that the model satisfies certain mathematical constraints on the normal stresses, consistent with the physics of turbulent flows. In this model, the development involved the formulation of a new eddy-viscosity formula involving the variable C_μ in the turbulent viscosity relationship. It also differs in the changes imposed to the transport ε-equation (based on the dynamic equation of the mean-square vorticity fluctuation) where the source term is now solved according to

$$S_\varepsilon = C_1\rho\left(2S_{ij}^2\right)^{1/2}\varepsilon - C_2\rho\frac{\varepsilon^2}{k + \sqrt{\nu_T\varepsilon}}, \quad S_{ij} = \frac{1}{2}\left(\frac{\partial u_i}{\partial x_j} + \frac{\partial u_j}{\partial x_i}\right) \tag{7.5}$$

and the variable constant C_1 is expressed as

$$C_1 = \max\left[\frac{\eta}{\eta + 5}\right], \quad \eta = \frac{k}{\varepsilon}\left(2S_{ij}^2\right)^{1/2}$$

The variable C_μ, no longer a constant, is evaluated from

$$C_\mu = \frac{1}{A_o + A_s\dfrac{kU^*}{\varepsilon}} \tag{7.6}$$

Consequently, model constants A_o and A_s are determined as

$$A_o = 4.04, \quad A_s = \sqrt{6}\cos\varphi, \quad \varphi = \frac{1}{3}\cos^{-1}\left(\sqrt{6}W\right), \quad W = \frac{S_{ij}S_{jk}S_{ki}}{\widetilde{S}^3}, \quad \widetilde{S} = \sqrt{S_{ij}^2}$$

whilst the parameter U^* is given by

$$U^* \equiv \sqrt{S_{ij}^2 + \widetilde{\Omega}_{ij}^2}, \quad \widetilde{\Omega}_{ij} = \Omega_{ij} - 2\varepsilon_{ijk}\omega_k, \quad \Omega_{ij} = \widetilde{\Omega}_{ij} - \varepsilon_{ijk}\omega_k$$

Other constants in the turbulent transport equations for this model are $C_2 = 1.9$, $\sigma_\kappa = 1.0$, and $\sigma_\varepsilon = 1.2$, respectively. The k-equation in both the *RNG k–ε model* and *realizable k–ε model* is the same as that in the *standard k–ε model* except for the model constants.

The computed velocity profiles normalized by the free-stream velocity u_∞ at locations of $x/H = 0$, 1, 3, 5, 7, and 9 behind the step, predicted through each turbulence model for the backward-facing step geometry, are illustrated in Fig. 7.9. In order to validate the numerical predictions, the results are compared with measurements of Ryck and Makiola (1988). We can observe that the flow velocities are better predicted by the *RNG k–ε model* and *realizable k–ε model* and that significant deviations from the experimental data are evident for the *standard k–ε model* at downstream locations of $x/H = 5$, 7, and 9.

Under the same flow condition, the maximum negative velocity profiles of the flow in the recirculation zone are shown in Fig. 7.10. Much lower values of the maximum negative velocities are predicted by all the three turbulence models in comparison with the experimental value. Amongst these three turbulence models, the reattachment length of the *realizable k–ε model* comes closest to the measurement (a predicted value of $x/H = 8.2$ compared with the measured value of $x/H = 8.1$). Note the reattachment length l_r as described in Fig. 6.27. The *RNG k–ε model* marginally overpredicts the reattachment length with a value of $x/H = 8.5$. The *standard k–ε model* claims the last spot as it severely

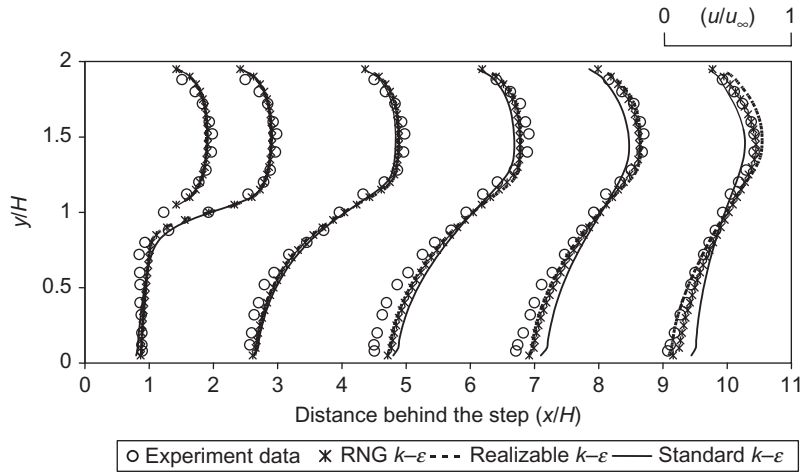


FIG. 7.9 Measured and predicted normalized velocity profiles at locations of $x/H = 0$, 1, 3, 5, 7, and 9 behind the step for the backward-facing step geometry.

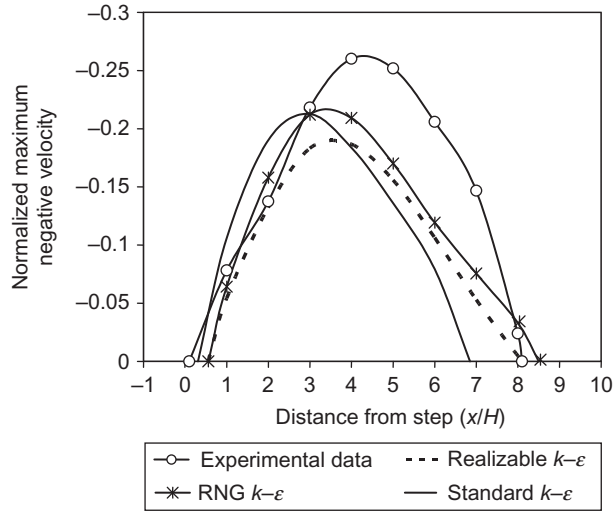


FIG. 7.10 Maximum measured and predicted negative velocity profiles of the flow in the recirculation zone.

underpredicts the reattachment length by a substantial margin yielding a value of $x/H = 6.9$.

As aforementioned, the *standard k–ε model* generally overpredicts the gas turbulence kinetic energy k in the recirculation region, which leads to the evaluation of a higher turbulent viscosity ν_T $(= C_\mu k^2/\varepsilon)$. Fig. 7.11A demonstrates the normalized profiles of the turbulent kinetic energy k at location of $x/H = 5$, whilst Fig. 7.11B provides the normalized profiles of the turbulent dissipation rate ε at the same location determined by the respective three turbulence models. It is evident that the *standard k–ε model* predicts higher

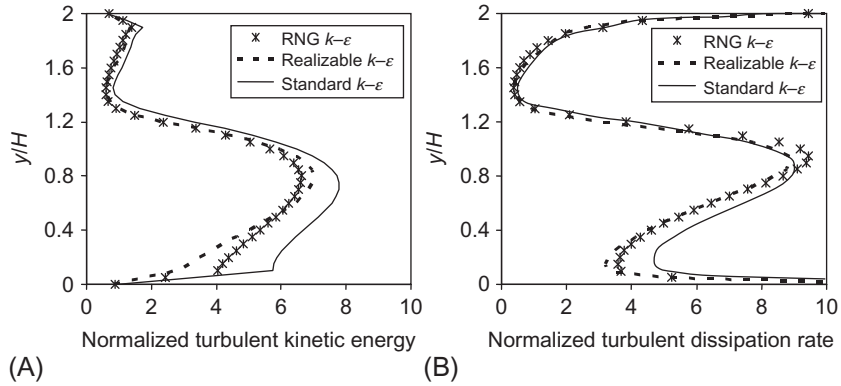


FIG. 7.11 Normalized profiles at location of $x/H = 5$ (recirculation region): (A) turbulent kinetic energy and (B) turbulent dissipation rate.

turbulent kinetic energy in the recirculation zone. This therefore results in the production of excessive mixing in the *standard k–ε model*, which significantly reduces the intensity of this zone (as also confirmed through Murakami, 1993). Another possible cause is the ε-transport equation of the *standard k–ε model*. The modifications in the ε-transport equation of the *RNG k–ε model* and *realizable k–ε model* accommodate the possibility of handling large rates of flow deformation. Both the rate of production of k and rate of destruction of ε can be reduced to yield smaller eddy viscosity. We note that even though the turbulence dissipation rate ε is predicted lower by the *RNG k–ε model* and *realizable k–ε model* in Fig. 7.11B, the turbulent viscosities predicted through these two models are still much lower because of the apparent k^2 evaluation in the turbulent viscosity relationship, which is dominated by the higher turbulent kinetic energy k predicted by the *standard k–ε model*.

7.3.2.2 Other Useful Guidelines

It is noted that for wall-attached boundary layers such as that found within a simple flow between two stationary parallel plates or the backward-facing step geometry, turbulent fluctuations are suppressed adjacent to the wall and the viscous effects become prominent in this region known as the *viscous sublayer*. This modified turbulent structure generally precludes the application of the two-equation models such as *standard k–ε model*, *RNG k–ε model*, and *realizable k–ε model* or even the *Reynolds stress model* at the near-wall region, which thereby requires special near-wall modelling procedures. Selecting an appropriate near-wall model represents another important strategy in the context of turbulence modelling. Here, the reader has to decide whether he/she adopts the so-called wall-function method, in which the near-wall region is bridged with *wall functions*, or a *low-Reynolds-number turbulence model*, in which the flow structure in the *viscous sublayer* is totally resolved. This decision will certainly depend on the availability of computational resources and the accuracy requirements for resolution of the boundary layer. Some useful guidance on the application of relevant low Reynolds number models that can be employed all the way through the wall is provided herein. More discussions and practical guidelines will also be given for near-wall treatments using the wall-function method in the next section below.

The *k–ω model* developed by Wilcox (1998), where ω is a frequency of the large eddies, has been shown to perform splendidly close to walls in boundary-layer flows. Such a model is common in the majority of commercial codes, and it works exceptionally well particularly under strong adverse pressure gradients hence its popularity in aerospace applications. Like the *standard k–ε model*, a modelled transport equation is solved for ω to determine its local distribution within the fluid flow. Nonetheless, the model is very sensitive to the free-stream value of ω, and unless great care is taken in prescribing this value, spurious results are obtained in both boundary-layer flows and free-shear flows. In

general, the *standard k–ε model* is less sensitive to the free-stream values but is often inadequate under adverse pressure gradients. To overcome such problems, Menter (1994a,b) proposed to combine both the *standard k–ε model* and *k–ω model*, which retains the properties of *k–ω* close to the wall and gradually blends into the *standard k–ε model* away from the wall. This *Menter's model* has shown to eliminate the free-stream sensitivity problem without sacrificing the *k–ω* near-wall performance.

To account for strong nonequilibrium effects, the shear-stress transport (SST) variation of *Menter's model* (1993, 1996) leads to a significant improvement in handling nonequilibrium boundary-layer regions such as those found behind shocks and close to separation. It is therefore highly recommended for flow separation since the real flow is more likely to be much closer to separation (or more separated) than the calculations from the *standard k–ε model* suggest. Bear in mind that SST should not be viewed as a universal cure for turbulence modelling because it still inherits noticeable weaknesses. SST, for example, is less able to cope with flow recovery following flow reattachment. For this, a promising possibility is the use of a length-scale limiting device as proposed by Ince and Launder (1995). Interested readers may also wish to refer to Patel et al. (1985) for the applications of other various low Reynolds number versions of the *standard k–ε model* and the *Reynolds stress model* where modifications to the governing transport equations are used to deal with near-wall effects allowing these models to be deployed directly through to the wall. Alternatively, the *standard k–ε model* and the *Reynolds stress model* can be employed in the interior of the flow and coupled to the one-equation *k-L model* (Wolfshtein, 1969) that is dedicated to resolve mainly the wall region (see the review by Rodi, 1991), a so-called two-layer model. It is imperative that whatever low Reynolds number models are adopted, sufficient number of grid nodal points must be placed into a very narrow region adjacent to the wall to adequately capture the rapid variation in the flow variables.

7.3.3 Near Wall Treatments

It is inevitable that appropriate near-wall models are required for handling wall-bounded turbulent flow problems. In addition to turbulent models that can be applied all the way through the wall, another modelling procedure commonly adopted is *wall functions*. The use of these functions is prevalent in industrial practice and can be found practically in every CFD commercial and in-house computer codes. Through this approach, the difficult near-wall region is not explicitly resolved within the numerical model but rather is bridged using such functions (Launder and Spalding, 1974; Wilcox, 1998). To illustrate the modelling procedure, attention will be primarily directed towards the consideration of the flow domain having smooth walls; the alternative treatment of rough walls will be subsequently mentioned as a special case.

To construct these functions, it is usual that the region close to the wall is characterized in terms of dimensionless variables with respect to the local conditions at the wall. If we let y be the normal distance from the wall and U be the time-averaged velocity parallel to the wall, then the dimensionless velocity U^+ and wall distance y^+ can be appropriately described in the form as U/u_τ and $y\rho u_\tau/\mu$, respectively. Within these dimensionless parameters, the wall friction velocity u_τ is defined with respect to the wall shear stress τ_w, as $\sqrt{\tau_w/\rho}$. If the flow close to the wall is solely determined by the conditions at the wall then to some limiting value of dimensionless wall distance y^+, the dimensionless velocity U^+ can be expected to be a *universal* (wall) function as

$$U^+ = f(y^+) \tag{7.7}$$

For wall distance of $y^+ < 5$, the layer is dominated by viscous forces that produce the no-slip condition and is subsequently called the *viscous sublayer*. We may assume that the shear stress is approximately *constant* and equivalent to the wall shear stress τ_w. A linear relationship between the time-averaged velocity and the distance from the wall can thus be obtained, and making use of the definitions of U^+ and y^+ leads to

$$U^+ = y^+ \tag{7.8}$$

Outside the *viscous sublayer*, turbulent diffusion effects are felt, and a logarithmic relationship is usually employed to account for this. The profile is

$$U^+ = \frac{1}{\kappa} \ln(Ey^+) \tag{7.9}$$

The above relationship is often called the *log-law*, and the layer where the wall distance y^+ lies between the range of $30 < y^+ < 500$ is known as the *log-law layer*. Fig. 7.12 illustrates the validity of Eqs (7.8) and (7.9) inside the turbulent boundary layer. The values for κ ($\sim$0.4) and E ($\sim$9.8) are universal constants valid for all turbulent flows past smooth walls at high Reynolds numbers. For rough surfaces, the constant E in Eq. (7.9) is usually reduced. Additionally, the law of the wall must also be modified by scaling the normal wall distance y on the equivalent roughness height, h_o (i.e. y^+ is replaced by y/h_o), and appropriate values must be selected from data or literature. A similar universal, non-dimensional function can also be constructed to the heat and scalar fluxes. This can be used to bridge the near-wall region when solving the energy and scalar equations.

The reader should be aware that the universal profiles presented above have been derived based on an attached two-dimensional Couette flow configuration with the assumptions of *small pressure gradients*, *local equilibrium of turbulence* (production rate of k equals to its dissipation rate), and *a constant near-wall stress layer*. Therefore, it is imperative that care is always exercised to check the validity of wall functions to the CFD problem that is being solved. The calculated flow must be consistent or nearly consistent with the specific

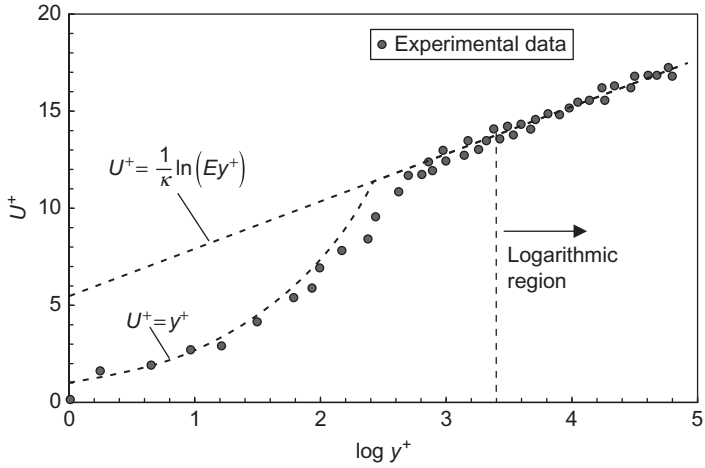


FIG. 7.12 The turbulent boundary layer: respective dimensionless velocity profile as a function of the wall distance in comparison with experimental data.

assumptions made, in arriving at the wall-function relationships. Applying the wall functions outside this application range will lead to significant inaccuracies attained in the CFD solution.

To remove some of the limitations imposed by the above standard wall functions, a two-layer-based, nonequilibrium wall function is also available. A more in-depth discussion regarding the formulation of such a wall function can be found in Kim and Choudbury (1995). Briefly, the key elements are (1) the *log-law* that is now sensitized to pressure gradient effects and (2) the two-layer-based concept that is adopted to calculate the cell-averaged turbulence kinetic energy production and dissipation in wall-adjacent cells. Based on the latter, the turbulence kinetic energy budget for the wall-adjacent cells is sensitized to the proportions of the *viscous sublayer* and the *fully turbulent layer*, which can significantly vary from cell to cell in highly nonequilibrium flows. This effectively relaxes the *local equilibrium of turbulence* that is adopted by the standard wall functions. Because of its capability to partly account for the effects of pressure gradients and departure from equilibrium, the nonequilibrium wall functions are recommended for complex flows that may involve flow separation, flow reattachment, and flow impingement. In such flows, improvements are obtained in the CFD solution, particularly in the prediction of wall shear and heat transfer. We note that the nonequilibrium wall functions were employed for the results obtained through the worked example of the backward-facing step turbulent flow problem considered in the preceding Section 7.4.2.

Another useful near-wall modelling method worth considering is the enhanced wall treatment that combines a two-layer model with enhanced wall

functions. The main thrust of this approach is to achieve the goal of implementing the standard two-layer approach for fine meshes whilst not significantly reducing the accuracy for coarse meshes. By formulating the law of the wall as a single wall law for the entire wall region, the enhanced wall function extends its applicability throughout the near-wall region. This can be achieved by blending the linear and logarithmic laws of the wall as

$$U^+ = e^{\Gamma} U^+_{lam} + e^{1/\Gamma} U^+_{turb} \tag{7.10}$$

where Γ is a blending function. Similarly, the general equation for $\partial U^+/\partial y^+$ can also be expressed by

$$\frac{\partial U^+}{\partial y^+} = e^{\Gamma} \frac{\partial U^+_{lam}}{\partial y^+} + e^{1/\Gamma} \frac{\partial U^+_{turb}}{\partial y^+} \tag{7.11}$$

The above equation allows the turbulent law to be easily modified and extended to account for effects such as pressure gradients or variable properties. It also guarantees the correct asymptotic behaviour for large and small values of the wall distance y^+ and reasonable representation of the velocity profiles in cases where y^+ lies inside the wall buffer region ($3 < y^+ < 10$). More details of this approach can be referred in Kader (1993).

7.3.3.1 Near-Wall Meshing Guidelines on Wall Functions

Since the use of wall functions is to relate the flow variables to the first computational mesh point, thereby removing the requirement to resolve the structure in between, the lower limit of y^+ at this point must be carefully placed so that it does not fall into the *viscous sublayer*. In such a case, the meshing should be arranged so that the values of y^+ at all the wall-adjacent integration points are considered only slightly above the recommended limit, typically between 20 and 30. This procedure offers the best opportunity to resolve the turbulent portion of the boundary layer. Besides checking the lower limit of y^+, it is important that the upper limit of y^+ is also investigated during the computational calculation. For example, a flow with moderate Reynolds number has a boundary layer that extends up to y^+ between 300 and 500. If the first integration point placed at a value of $y^+ = 100$ then this will certainly yield an impaired solution due to insufficient resolution for the region. Adequate boundary-layer resolution generally requires at least 8–10 grid nodal points in the layer, and it is recommended that a postanalysis of the CFD solution is undertaken to determine whether the degree of resolution is achieved or the flow calculation is subsequently performed with a finer mesh. This can be achieved by plotting the ratio between the turbulent diffusion to the molecular diffusion (due to molecular viscosity) that is generally high inside the boundary layer.

7.3.3.2 Near-Wall Meshing Guidelines With Low-Reynolds-Number Turbulence Models

A universal near-wall behaviour over a practical range of y^+ may not be realizable everywhere in a flow such as that found for low-Reynolds-number flows. Under such circumstances, the wall-function concept breaks down, and its use will lead to significant errors. The alternative is to fully resolve the flow through the wall, which can be achieved by low Reynolds number turbulence models as aforementioned, but it should be noted that the cost of the solution is around an order of magnitude greater than when wall functions are used because of the additional grid nodal points involved. With the intention of resolving the viscous sublayer inside the turbulent boundary layer, y^+ at the first node adjacent to the wall should be set preferably close to unity (i.e. $y^+ = 1$). Nevertheless, a higher y^+ is acceptable so long as it is still well within the *viscous sublayer* ($y^+ = 4$ or 5). Depending on the Reynolds number, the reader should ensure that there are between 5 and 10 grid nodal points between the wall and the location where y^+ equals to 20 that is within the viscosity-affected near-wall region in order to resolve the mean velocity and turbulent quantities. This most likely will result in 30–60 grid nodal points inside the boundary layer to achieve adequate boundary-layer resolution.

7.3.4 Setting Boundary Conditions

Specifying appropriate boundary conditions is particularly important in turbulence modelling. In this section, we survey the various approaches in handling the various types of boundaries within the flow domain and provide some useful guidelines in setting proper boundary conditions for turbulence.

In many practical CFD problems, specification of the turbulence quantities at the inlet can be rather difficult, and some sensible engineering judgment usually needs to be exercised. This is because the magnitude of turbulent kinetic energy k and dissipation ε can have a significant influence on the CFD solution. In most cases, readily accessible measurements of k and ε are rare in practice. In exploratory design computations, the problem is compounded by the inexistence of any available boundary condition information to operate the turbulence models. Preferably, experimentally verified quantities should always be applied as inlet boundary conditions for k and ε. Nonetheless, if they are unavailable, then the values need to be prescribed using sensible engineering assumptions, and the influence of the choice taken must be examined against sensitivity tests with different simulations. For the specification of the turbulent kinetic energy k, appropriate values can be specified through a turbulence intensity I that is defined by the ratio of the fluctuating component of the velocity to the mean velocity. In general, the inlet turbulence is a function of the upstream flow conditions. Approximate values for k can be determined according to the following relationship:

$$k_{inlet} = \frac{3}{2}(U_{inlet} I)^2 \tag{7.12}$$

In external aerodynamic flows over airfoils, the turbulence intensity level is typically 0.3%. For atmospheric boundary-layer flows, the level can be as high as two orders of magnitude, that is 30%. In internal flows, the turbulence level between 5% and 10% is deemed to be appropriate. Similarly, the specification of the dissipation ε can be approximated by the following assumed form:

$$\varepsilon_{inlet} = C_\mu^{3/4} \frac{k^{3/2}}{L} \tag{7.13}$$

where L appearing in Eq. (7.13) is the characteristic length scale. If the *k–ω model* is employed, ω can be approximated by

$$\omega_{inlet} = \frac{k^{1/2}}{C_\mu^{1/4} L} \tag{7.14}$$

For external flows remote from the boundary layers, a value determined from the assumption that the ratio of turbulent and molecular viscosity between 1 and 10 is a reasonable guess. For internal flows, a constant value of length scale derived from a characteristic geometrical feature can be employed such as 1%–10% of the inlet hydraulic diameter. If the *Reynolds stress model* is applied, all stress components ($\overline{u_1'2}$, $\overline{u_2'2}$, $\overline{u_3'2}$, $\overline{u_1'u_2'}$, $\overline{u_1'u_3'}$, and $\overline{u_2'u_3'}$) are required to be properly specified. If these are unavailable, as often the case, the diagonal components ($\overline{u_1'2}$, $\overline{u_2'2}$, and $\overline{u_3'2}$) are taken to be equal to two-thirds k, whereas the extradiagonal components ($\overline{u_1'u_2'}$, $\overline{u_1'u_3'}$, and $\overline{u_2'u_3'}$) are set to zero (assuming isotropic turbulence). In cases where problems arise in specifying appropriate turbulence quantities, the inflow boundary should be moved sufficiently far away from the region of interest so that the inlet boundary layer and subsequently the turbulence are allowed to be developed naturally.

For solid walls, boundary conditions for k and ε or ω are substantially different depending on whether low Reynolds number turbulence models or the wall-function method is employed. For the former, it is appropriate to set $k = 0$ at the wall, but the dissipation ε is determined through either

$$\frac{\partial \varepsilon}{\partial n} = 0 \quad \text{or} \quad \varepsilon = \left(\frac{\partial v_t}{\partial n}\right)^2 \tag{7.15}$$

where v_t is the velocity component tangential to the wall. For the *k–ω model*, the rough-wall method by Wilcox (1998) can be adopted. The surface value for ω can be written as follows:

$$\omega_{wall} = \frac{u_\tau}{\nu_{wall}} S_R \tag{7.16}$$

The variable ν_{wall} is the kinematic viscosity on the wall, whilst S_R is a non-dimensional function determining the degree of surface roughness of the wall. However, when the law-of-the-wall type boundary conditions are employed instead, the diffusive flux of k through the wall is usually taken to be zero, thus yielding

$$\frac{\partial k}{\partial n} = 0 \tag{7.17}$$

The dissipation ε is, however, derived from the *local equilibrium of turbulence* assumption. It is noted that ε is not applied at the wall but rather is calculated at the first computational mesh point. For the finite-volume method, ε_P is evaluated at the control volume centre and is given by

$$\varepsilon_P = \frac{C_\mu^{3/4} k_P^{3/2}}{\kappa n_P} \tag{7.18}$$

where n_P denotes the first computational mesh point normal to the wall. In cases where the nonequilibrium wall function is used instead, ε_P is now calculated according to

$$\varepsilon_P = \frac{1}{2n_P}\left[\frac{2\mu}{\rho y_v} + \frac{C_\mu^{3/4} k_P}{\kappa} \ln\left(\frac{2n_p}{y_v}\right)\right] k_P \tag{7.19}$$

where y_v is the physical viscous sublayer thickness computed from $y^* \mu/\rho C_\mu^{1/4} k_P^{1/2}$ and y^* is set at 11.225. More details considering the formulation of Eq. (7.19) can be referred to in Kim and Choudbury (1995).

At the outlet or symmetry boundaries, the *Neumann* boundary conditions are applicable, namely,

$$\frac{\partial k}{\partial n} = 0; \quad \frac{\partial \varepsilon}{\partial n} = 0; \quad \frac{\partial \overline{u_i' u_j'}}{\partial n} = 0 \tag{7.20}$$

In the free-stream flow where the computational boundaries are far away from the region of interest, the following boundary conditions can be used:

$$k \asymp 0; \quad \varepsilon \asymp 0; \quad \overline{u_i' u_j'} \asymp 0 \tag{7.21}$$

which results in the turbulent viscosity $\mu_T \asymp 0$.

7.3.5 Test Case: Assessment of Two-Equation Turbulence Modeling for Hydrofoil Flows

This test case was calculated using a commercial finite-volume CFD computer code ANSYS FLUENT, version 6.1.

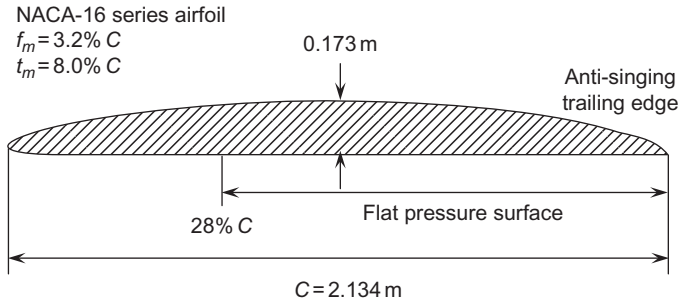


FIG. 7.13 Schematic view of the two-dimensional hydrofoil geometry.

7.3.5.1 Model Description

The geometry is a two-dimensional hydrofoil, spanning the test section with a distance of 3.05 m and a chord length (C) of 2.134 m. The cross-section profile is represented by a generic naval propeller of moderate thickness (t) and camber (f), utilizing a NACA-16 airfoil profile ($t/C = 8\%$ and $f/C = 3.2\%$) with two modifications. A detailed diagram of the hydrofoil geometry is illustrated in Fig. 7.13, whilst the anti-singing trailing edge geometry is detailed in Bourgoyne et al. (2000). Experiments performed on this test hydrofoil were conducted in the world's largest water tunnel, the William B. Morgan Large Cavitation Channel (LCC) in Memphis, Tennessee, the United States.

7.3.5.2 Grid

For the hydrofoil geometry, the computational domain extends $1.5 \times C$ upstream of the leading edge, $1.5 \times C$ above and below the pressure surface and $3 \times C$ downstream from the trailing edge. A mesh overlay of quadrilateral elements is constructed for the flow domain. Particular attention of the mesh generation is directed towards an offset *inner region* encompassing the hydrofoil. Within this region, a considerable fine O-type mesh is applied to sufficiently resolve the hydrofoil surface and the boundary-layer region. For the *wake region* (downstream from the trailing edge of the inner region), a considerably fine H-type mesh is, however, applied to accurately resolve the near- and far-wake flow behaviour. The remaining *outer region* of the domain is subsequently filled with a coarser H-type mesh. A total number of 208,416 grid nodal points is generated for the whole computational domain with an average distribution of y^+ at 2.31 and a minimum and maximum y^+ at 0.09 and 4.06, respectively. The computational grid is shown in Fig. 7.14.

7.3.5.3 Features of the Simulation

This test case illustrates the importance of not only evaluating the choice of various turbulence models described above but also more importantly assessing the

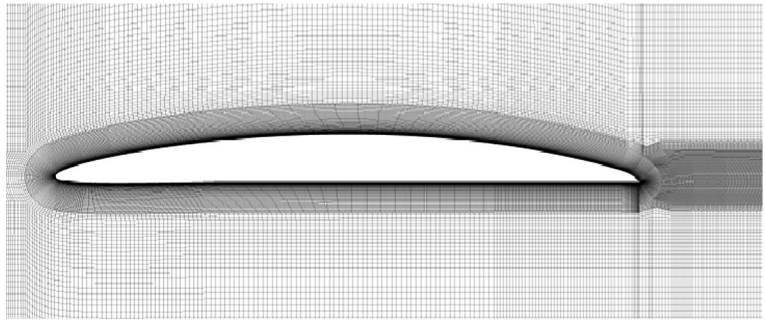


FIG. 7.14 Close-up view of the computational grid around the foil.

wall functions employed to model the near-wall region of the hydrofoil at high Reynolds numbers. Three wall treatments—standard logarithmic wall function, nonequilibrium wall function, and enhanced wall treatment—are investigated.

The algorithm for the solution of the Navier-Stokes equations utilized an implicit segregated velocity-pressure formulation such as the SIMPLE scheme. This lead to a Poisson equation for the pressure correction and was solved through the default iterative solver, normally the multigrid solver, of the ANSYS Fluent computer code. Finite-volume discretization was employed to approximate the governing equations. To avoid non-physical oscillations of the pressure field and the associated difficulties in obtaining a converged solution on a collocated grid arrangement, the Rhie and Chow (1983) interpolation scheme was employed. A second-order upwind scheme was used for the convection, whilst the central-differencing scheme was used for the diffusion terms.

The working fluid, water, was taken to be incompressible, and default initial conditions implemented in the computer code were used for the simulations.

7.3.5.4 Boundary Conditions

At the inlet, Dirichlet conditions were used for all variables. The inlet velocity based on the free-stream velocity U_{ref} was taken as constants with values of 3 and 6 m/s. With the density and viscosity of water having values of 995.1 kg/m^3 and 7.69×10^{-4} kg/m s, the corresponding Reynolds numbers based on the inlet velocities and the chord length are 8.284×10^6 and 1.657×10^7, respectively. At the free-stream field, the inlet velocity was also applied to the computational domain walls above and below the hydrofoil. The turbulent kinetic energy k and dissipation ε were determined from the measured turbulence intensity I of about 0.1%. At the outlet, zero-gradient conditions were applied for all the transported variables. No-slip wall boundary conditions were applied to the pressure and suction surfaces of the hydrofoil.

7.3.5.5 Results

The comparison between the measured and calculated coefficients of pressure distribution at the surface of the hydrofoil using different wall treatments is illustrated in Fig. 7.15. In this figure, the realizable k–ε model is adopted in conjunction with the three wall treatments to predict the coefficients of pressure distribution. It is apparent that the use of different wall treatment approaches impacts the solution behaviour. For strong adverse pressure gradients and boundary-layer separation flows, the enhanced wall treatment produces the most accurate distribution. The prediction by the standard logarithmic wall function is slightly less accurate but still performs rather well at the leading and trailing edges. Nevertheless, the use of nonequilibrium wall function produces questionable results, particularly at the leading edge where the coefficient of pressure distributions at the suction and pressure surfaces cross each other.

Fig. 7.16 represents the experimental and predicted pressure-surface boundary-layer velocity profiles at 93% C at a free-stream velocity of 3 m/s. The realizable k–ε model is also employed here in conjunction with the three wall treatments to predict the pressure-surface boundary-layer velocity profiles. As expected in the near-wall region, the use of different wall treatment procedures results in different predictions of the velocity profiles. Amongst these three different wall treatments, good agreement is achieved between the measurements and the enhanced wall treatment approach. The use of the standard logarithmic wall function produces a boundary-layer velocity profile similar to that produced by the enhance wall treatment except having a larger boundary-layer thickness. An even greater boundary-layer thickness is predicted for the nonequilibrium wall function.

Figs 7.17 and 7.18 demonstrate the measured and predicted pressure-surface boundary-layer velocity profiles applying different turbulent models at 93% C

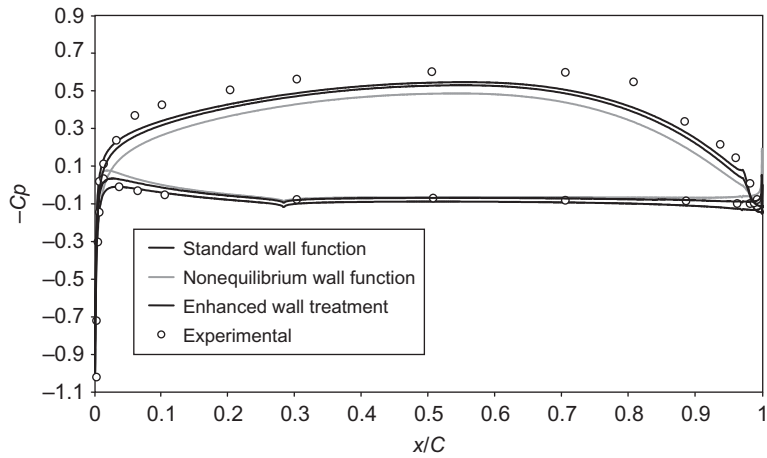


FIG. 7.15 Wall treatment analysis: pressure coefficient (C_p) distribution at the surface of the hydrofoil ($U_b = 3$ m/s).

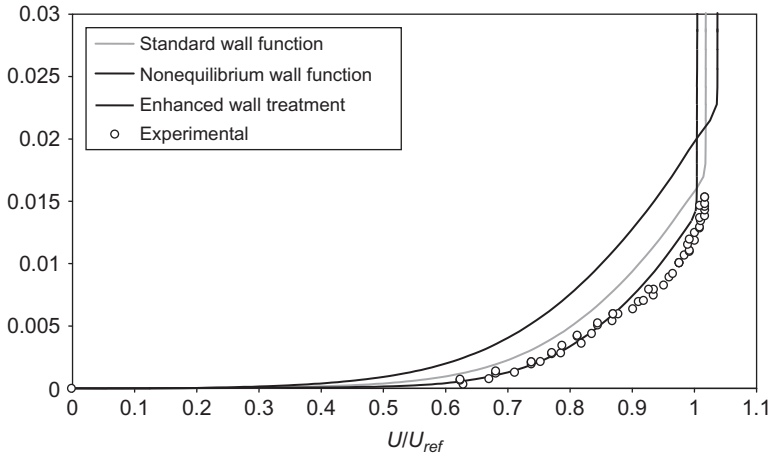


FIG. 7.16 Wall treatment analysis: pressure-surface boundary-layer normalized mean velocity profile at 93% C ($U_{ref}=3$ m/s).

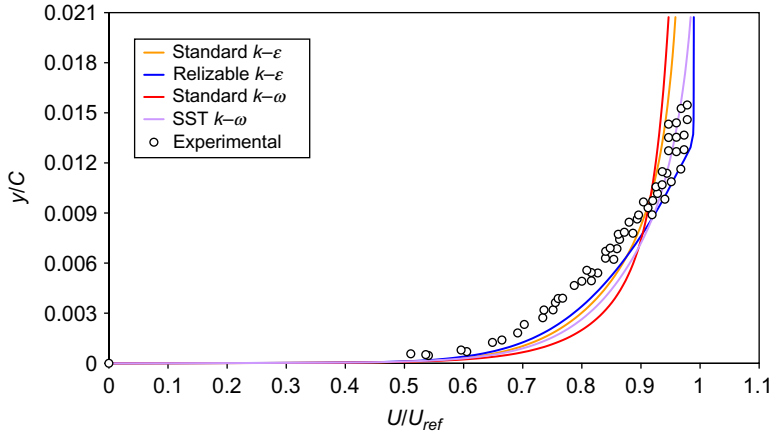


FIG. 7.17 Turbulence model performance: pressure-surface boundary-layer normalized mean velocity profile at 93% C ($U_{ref}=3$ m/s).

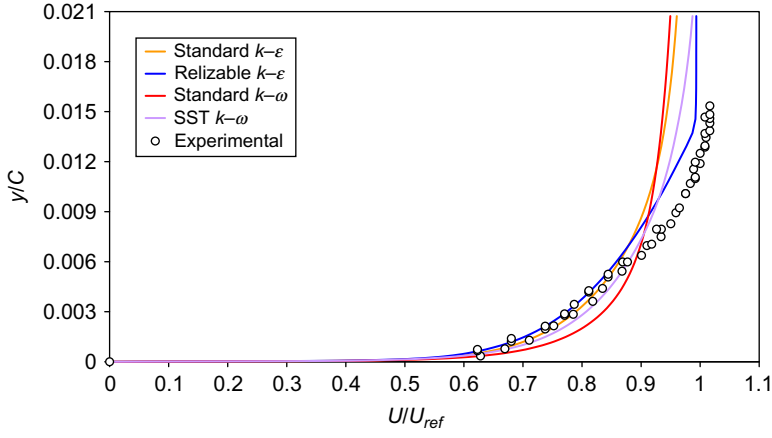


FIG. 7.18 Turbulence model performance: pressure-surface boundary-layer normalized mean velocity profile at 93% C ($U_{ref}=6$ m/s).

for free-stream velocities of 3 and 6 m/s, respectively. It is observed that the three turbulent models of standard k–ε, standard k–ω (Wilcox's), and SST k–ω (Menter's) generally overpredict the boundary-layer thickness when compared with the experimental result. Realizable k–ε appears, however, to be the only turbulence model to accurately predict the boundary-layer velocity profile. Close to the surface ($y/C < 0.5\%$), this model predicts the boundary-layer exceptionally well and continues to maintain a high degree of correlation further from the surface. Unlike the other models, realizable k–ε model produces a definable gradient change where the velocity profile becomes rather blunt.

7.3.5.6 Conclusion

This test case focused on the evaluation of turbulence model applications based on the standard k–ε, standard k–ω (Wilcox's), SST k–ω (Menter's), and realizable k–ε in conjunction with three wall treatment approaches—standard logarithmic wall function, nonequilibrium wall function, and enhanced wall treatment—for a turbulent boundary-layer flow over a hydrofoil at high Reynolds numbers. As for the test case presented in Chapter 6, *validation* of the computational solutions is performed by comparing the predictions with experimental data to address the simulation model uncertainty and the degree to which models correspond to an accurate representation of the real physical flow in the absence of analytical solutions. The realizable k–ε model is found to accurately predict the pressure coefficient distribution at the surface of the hydrofoil leading to good overall predictions of the pressure-derived lift and drag coefficients. It also resolves the velocity profile and correctly predicts the thinning of the boundary layer, the commencement of boundary-layer separation, and the full separation point of the turbulent boundary layer moving rearwards with increasing Reynolds number. For flows with adverse pressure gradients and boundary-layer separation, the enhanced wall treatment is considered to be a good candidate to handle such near-wall flow complexities. It is nevertheless noted that the numerical results obtained pertained to only the above test case and they may well be different for other types of flow problems considered.

7.4 OTHER PRACTICAL GUIDELINES FOR CFD USERS

7.4.1 Guidelines on Problem Definition

CFD users should always give careful thought at the outset of defining the CFD problem to be solved. The questions and issues that are worth considering especially for problem definition include the following:

- What are the local or global information required for the intended CFD simulation?

- What are the important flow physics to be solved? For example, laminar, turbulent, transitional, steady, unsteady, compressible single phase or multiphase, heat transfer, internal flow, and external flow.
- What is the area of primary interest or domain of the flow calculation? Any simplifications that can be imposed through the specifications of the boundary conditions at inlets or outlets or the use of symmetry or periodic boundaries?
- What level of validation is necessary for the CFD problem? For a routine application where validation and calibration of models has been performed on similar flow fields, only relatively small changed can be expected from earlier similar simulations. For a nonroutine application where little earlier validation work has been carried out, the assessment should be based in assessing the flow physics and conditions of the applied models.
- What sensitivity tests that are be performed to assess the simulation accuracy? For example, mesh refinement on the prediction of the coefficient of drag, lift or pressure or the local distribution of flow quantities.
- What results are meaningful for reporting for the CFD problem?

7.4.2 Guidelines on Solution Strategy and Global Solution Algorithm

Translating the problem definition into adopting a suitable solution strategy and global solution algorithm forms another important part in attaining the intended results of the CFD problem. The following recommendations include:

- The adequacy of the solution procedure must always be checked with respect to the physical properties of the fluid flow. For example, compressible or incompressible flow.
- For CFD users employing existing commercial computer codes, it is always preferable as a first step to employ the default mathematical and physical models, numerical schemes, and pressure- or density-based solution method to begin with.
- If it is necessary to alter the parameters within the existing commercial computer codes to aid convergence, a step-by-step change of the relaxation factors or time-step sizes would allow CFD users to keep track of the parameters that will influence the convergence of the flow calculations. Rectifying the specification of boundary conditions, decreasing relaxation factors or time-step sizes or performing more number of iterations could alleviate the divergence problem.
- Convergence of the numerical solution should not be assessed purely in terms of the achievement of a particular level of residual error. The numerical solution should be evaluated on the convergence on global balances (conservation of mass, momentum, and energy) where possible.
- A systematic one-by-one testing of the models, schemes, and solution methods should always be enforced in order to keep track of the models,

schemes, and solution methods that have been employed for the CFD problem. For example, the use of more sophisticated turbulence models with different mesh densities is carried out to assess the accuracy of the numerical solutions.

- Time development of the flow quantities in the locations of interest will allow CFD users to examine whether the flow has reached its steady-state condition even though a solution has been computed. Using the steady solution as the initial condition, an unsteady simulation, preferably with a small perturbation, can be carried out to determine whether the fluid flow has achieved its steady-state condition.

7.4.3 Guidelines on Validation

In assessing the CFD results, the following guidelines on validation of models may be adopted. They include the following:

- The experimental data set to be employed should be independent of any data set for the construction of the CFD model. They should be carefully checked for quality and accuracy and should include measurements targeted for the purpose of CFD validation. These intended data sets should also be checked in order that they are consistent with initial and boundary conditions for CFD simulation.
- The CFD model should be validated against the data set of an application with similar flow structures and flow physics. For a design application where accurate performance and flow-field data are required, the CFD model would require more detailed validation than just the preliminary investigation of a fluid flow. The CFD results attained should always be checked against the prominent and relevant flow features.
- For complex fluid flows, the taxonomy of the flow should be considered, and it is recommended that the CFD model is validated against relevant simpler flows. Simple test cases would allow the assessment of different mesh densities so that the results of calculations at typical mesh resolution expected in the application can be investigated.
- The fluid flow should always be examined against a well-understood and well-tested baseline design application comprising the same important flow features as means of calibrating the expected accuracy. Reliability of a new design can subsequently be assessed by taking into account of the calibration with the baseline design.

7.5 SUMMARY

Practical guidelines specifying appropriate boundary conditions within the CFD context and turbulence modelling and other useful guidelines on problem definition, solution strategy, and global solution algorithm and validation have been discussed in this chapter. The guidelines provided thus far

are by no means exhaustive, but they should put the reader in an advantageous position to understand how an appropriate CFD solution can be attained that is physically valid and meaningful through the above guidelines. It was also shown in this chapter that CFD simulation and analysis are more than a mechanically driven oriented exercise. They actually encapsulate, at one hand, an understanding of the application of the essential fundamental theory of conservation equations and numerical methods to solve the CFD problem whilst, on the other hand, an appreciation of setting a viable mesh, defining suitable boundary conditions and models to arrive at a proper CFD solution.

Although not expounded within this chapter, the reader may well benefit in considering the use of either the steady-state or transient approach to achieve a steady-state solution. Generally, a steady-state calculation yields a solution in a shorter execution time in comparison with a transient calculation. However, there may be some underlying circumstances where convergence and/or stability cannot be guaranteed through the steady-state approach and a transient calculation may be required to march the numerical procedure towards the steady-state condition. Other issues concerning the aspects of *computational accuracy* and *efficiency* can also have a strong influence on the CFD solution. Subject to the availability of computational resources, it is nearly always inevitable that some compromise has to be reached for solving complex CFD problems. By increasing the number of cells, that is with decreasing mesh spacing, in the computational domain geometry, the *accuracy* of the computational solution is usually enhanced. There is, however, a trade off that needs to be considered between increased computer storage and running time. One possible way that comparable *accuracies* can be obtained on a coarser mesh whilst maintaining *computational efficiency* is to employ higher-order discretization schemes to solve such problems. More sophisticated CFD approaches such as DNS and LES techniques for pertinent applications can yield solutions of high *computational accuracy* due to the application of fine meshes but are still subject to stringent *computational efficiency* due to computer hardware requirements. In practice, DNS and LES techniques should only be employed as a last resort when nothing else succeeds or to check the validity of a particular turbulence model being applied. Hence, it is still beneficial to explore other practical turbulence models to solve a number of real engineering flows. As demonstrated in the above test case, a more advanced turbulence model based on the realizable k–ε with enhanced wall treatment can be applied to successfully resolve flows with adverse pressure gradients and boundary-layer separation especially such as those experienced on hydrofoil or even aerofoil geometries.

In the next chapter, we will apply the CFD techniques to a variety of practical problems of various degrees of complexities. The culmination of theory and practice will be demonstrated through these worked examples.

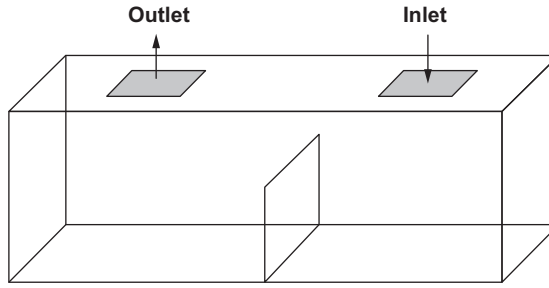
REVIEW QUESTIONS

7.1 What are the problems/difficulties in setting up correct boundary conditions?

7.2 What types of conditions may be applied for an inlet boundary, and why do you need a corresponding outlet condition?

7.3 What is the *Neumann* boundary condition? Explain how it is used as an outlet boundary condition.

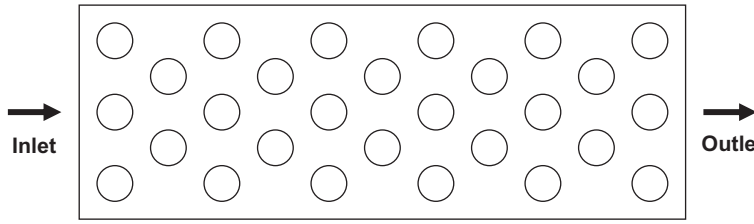
7.4 The geometry for an air-conditioning problem in two rooms separated by a partitioned wall is shown below. Label the boundaries that have to be defined and discuss what types of conditions may be applied.



7.5 What requirements must be satisfied for a symmetry boundary condition, and what are the benefits in using this condition?

7.6 Discuss the main difference between a symmetry boundary condition and a periodic boundary condition.

7.7 The geometry of staggered tube-bank heat exchanger in two dimensions is shown below. Show, by a sketch, how you would define a computational domain for this geometry, by making use of the periodicity or the symmetry boundary condition.



7.8 In general, describe how large-eddy simulation (LES) solves a turbulent flow. How does this differ from direct number simulation (DNS)?

7.9 Why do engineers prefer the Reynolds-averaged-based turbulence models such as the k–ε model over the complex LES model?

7.10 What are some of the major problems experienced with the k–ε model?

7.11 The standard k–ε turbulence model overpredicts the turbulent kinetic energy k when compared with the *realizable* and *RNG* turbulence models in the recirculation zones. For the backward-facing step case given below, provide an explanation on your final predictions of the reattachment length L_R for these turbulence models in comparison with the experimental result (L_E is the actual length). In modelling turbulent flow, we effectively solve the following equations:

$$u\frac{\partial \phi}{\partial x} + v\frac{\partial \phi}{\partial y} = \mu_t\left[\frac{\partial^2 \phi}{\partial x^2} + \frac{\partial^2 \phi}{\partial y^2}\right] + S_\phi$$

(a) Use the relationship between $\mu_t = \rho C_\mu k^2/\varepsilon$ and k to discuss the flow prediction.

(b) Which area within the domain requires fine mesh, and where can coarse mesh be used?

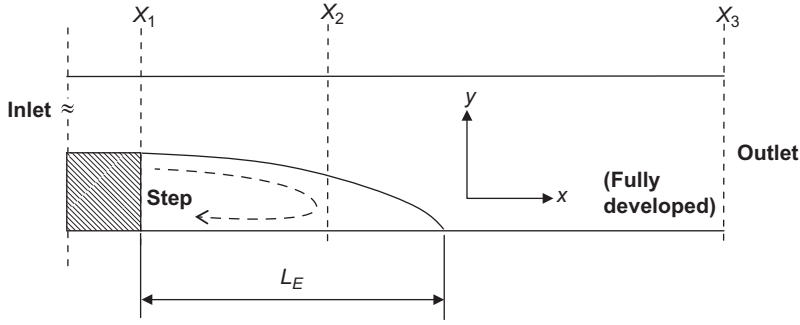
(c) What kinds of boundary conditions do we impose for the inlet, outlet, and at the wall?

(d) How should the flow pattern at the outlet be described?

(e) What are the values of the horizontal u velocity (positive or negative) before, after, and at the reattachment point?

(f) Sketch to show the development of the velocity profile throughout the flow from the inlet to the outlet at X_1, X_2, and X_3.

(g) Keeping the inlet velocity the same, what would be the L_E if the working fluid is changed from air to water?



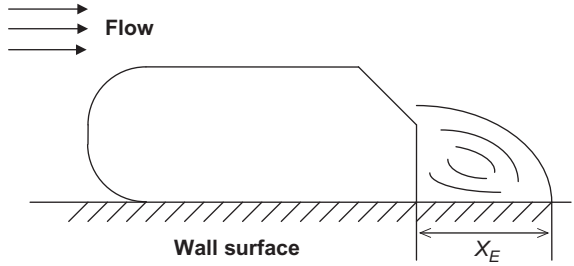
7.12 What is y^+, and why is it important in context of near-wall turbulent modelling?

7.13 What should a typically recommended y^+ value for the first adjacent node next to the wall in order to account for the viscous sublayer?

7.14 Without experimental data for turbulent inlet profiles, what is the recommended method to consider turbulence effects?

7.15 **(a)** For the modelling of flow around a simplified car model given below, state and justify the values of y^+ to be used around the car, if 'enhanced wall function' model is employed.

(b) If C_d, (coefficient of drag) is used for testing mesh independency, on what basis would you think of achieving it? Substantiate your answer with an X–Y plot?



Chapter 8

Some Applications of CFD With Examples

8.1 INTRODUCTION

The increasing demand of CFD in resolving numerous fluid flow problems is growing within the scientific community. Needless to say, such an accomplishment could only have been made possible through the meticulous developments by persistent researchers and, more recently, the extension to industrial usage by dedicated code developers that have resulted in the availability of a number of commercial CFD packages. The cornerstone of any CFD analysis lies in the heart of transport equations and the building blocks of efficient numerical techniques. Throughout this book, the authors have continually stressed the importance of grasping the essential conservation equations as described in Chapter 3 and the basic understanding of numerical approximations considered in Chapters 4 and 5. In Chapter 6, the authors further provided useful guidelines of handling practical flow problems such as the requirement of suitable turbulence models to resolve real fluid flow processes, which incidentally exemplifies the range of computed results presented in Chapter 1.

We should be thoroughly aware that CFD is not confined to predict only the fluid flow behaviour. Consideration of adequate physical models that may appropriately handle chemical reactions (e.g. combustion), multiphase flows (e.g. transport of gas–liquid, gas–solid, liquid–solid, or even gas–liquid–solid mixtures), or phase changes (e.g. solidification or boiling) is increasingly being incorporated within the CFD framework to tackle some of these complex and challenging industrial processes. Obtaining real engineering solutions through CFD is now a very realizable prospect due to not only the evolution of computer hardware but also the mature development in numerical methods.

Having worked through the many important aspects of CFD in previous chapters, it is therefore fitting that this chapter culminates the knowledge gathered by aptly describing the application of theory into practice. From a practical viewpoint, it is envisaged that the selected examples that are illustrated in the subsequent sections ranging from rudimentary to complex flow physics and simple to complicated geometrical domains will assist in establishing some concrete steps towards undertaking any CFD problems that are exemplified through

Computational Fluid Dynamics. https://doi.org/10.1016/B978-0-08-101127-0.00008-8
© 2018 Elsevier Ltd. All rights reserved.

a wide range of engineering disciplines. The important aims of this chapter are thus

- to illustrate the basic steps required for the reader to solve a practical flow problem,
- to guide the reader on how to appropriately apply the knowledge gained within this book and any additional knowledge that may be required to solve other complex flow problems,
- to demonstrate how CFD can be adopted as a research tool in better comprehending particular flow behaviours,
- to demonstrate how CFD can be employed as a design tool in enhancing performance through better understanding of the flow systems.

8.2 TO ASSIST IN DESIGN PROCESS—AS A DESIGN TOOL

As previously described in Chapter 1, CFD is progressively being adopted to better optimize existing equipments and/or predicting the performance of new designs even whilst in their conceptual stage of development. To illustrate how CFD can function as a design tool, a specific flow system is solved in the subsequent section—for example, a three-dimensional airflow in an office room layout. In practice, this flow problem is very prevalent in the design of ventilation systems.

The flow process within these systems is generally turbulent in nature, and the suitability of which turbulence models (Chapters 3 and 6) to be applied characterized by low-Reynolds-number (LRN) turbulence will be assessed and discussed in the first half of this example. CFD is also increasingly being considered as the preferred approach in the ventilation design process since scale-up experimental room measurements can be rather difficult to perform due to the expensive costs of instrumentation. The use of CFD as a design tool in enhancing the diffuser outlet design of a room ventilation system will be demonstrated in the second half of this example.

8.2.1 Indoor Airflow Distribution

Understanding the airflow distribution in enclosed environments is integral to indoor air quality control. It is well known that this is usually a function of the building's ventilation systems. With the availability of CFD computer codes, building engineers are increasingly embracing this methodology as an attractive alternative tool to predict the airflow distribution instead of employing scale modelling methods.

Despite many encouraging success, some uncertainties still remain particularly in the application of turbulence models for ventilation design. An important aspect with regards to modelling indoor airflows is the characterization of LRN turbulence. The improper handling of LRN turbulence can contribute to

inaccurate calculations since the airflow is strongly affected by the air phase velocity and turbulent fluctuations. Before CFD can be confidently applied for assisting engineers in ventilation system design, it is imperative to evaluate and validate the range of available turbulence models.

In this specific example (Tian et al., 2006), the application of three turbulence models, standard k–ε, RNG k–ε, and RNG-based LES models, is investigated for an indoor airflow environment. The calculated airflow velocities are evaluated and validated against experimental data obtained by Posner et al. (2003) in a ventilated model room.

Model description: The geometrical structure of the model room for the purpose of this investigative study is illustrated in Fig. 8.1. The width, depth, and height of the room are, respectively, 91.4, 45.7, and 30.5 cm. Within this model room, a partition with a height of 15 cm is located in the middle of the room. Air is allowed to enter the room through one ceiling vent and leave through the other as indicated by the outlet vent shown in Fig. 8.1.

Grid: For the room geometry, a structured mesh with rectilinear elements, distributed uniformly, is allocated for the whole physical domain yielding an elemental volume size of $0.8 \times 0.8 \times 0.8$ cm. The computational mesh is shown in Fig. 8.2, which results in a total number of 246,924 finite volumes generated for the whole computational domain. In any CFD calculation, it is recommended that grid independency (Chapter 5) is performed to assess the numerical errors generated by the computed results. For this flow problem, the mesh is further refined to an elemental volume size of $0.5 \times 0.5 \times 0.5$ cm. The difference in the air phase velocity predicted by the turbulence RNG k–ε model for the original mesh and the refined mesh is found to be less than 1%. For computational efficiency, the following results presented below are obtained with a mesh with an elemental volume size of $0.8 \times 0.8 \times 0.8$ cm.

Features of the simulation: The vertical inlet velocity (U_{inlet}) of 0.235 m/s and a characteristic length of 0.1 m provide a flow Reynolds number of 1500. All computations are performed in transient state in which the time-dependent

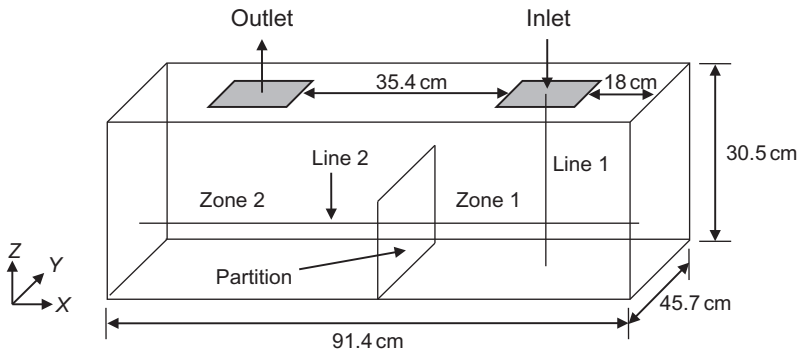


FIG. 8.1 Schematic view of the ventilation inside model room geometry.

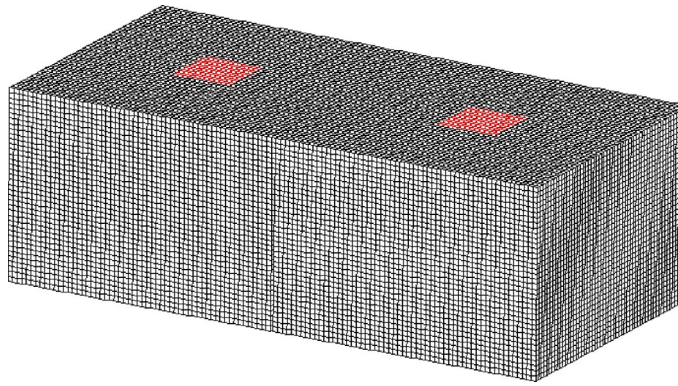


FIG. 8.2 Computational mesh for the model room geometry.

terms appearing in the transport equations are handled through an implicit second-order backward differencing in time. A nondimensional time step of 0.035 is used. This time step has been defined by $t' = U_{inlet}\, t/H$, where U_{inlet} is the inlet air velocity as given above, t is the physical time step with a value of 0.05 seconds, and H is the room height. The transport equations are discretized using the finite-volume method (Chapter 4). For the RANS approach employing the standard k–ε and RNG k–ε models (see Chapters 3 and 6 again for more detailed description), a third-order interpolation scheme such as the *QUICK* scheme (see Appendix B) is used to approximate the convective terms at the faces of the control volumes. In LES, energetic eddies that exist near the cutoff wave number can significantly influence the spatial discretization errors (Park et al., 2004). The contribution of the LES subgrid-scale force may be overwhelmed by the use of *upwind-* and *upwind-biased* schemes (Mittal and Moin, 1997), and hence, the use of a central difference scheme is thus adopted for the LES calculations. For the pressure–velocity coupling, the SIMPLE algorithm is employed (Chapter 4). As the airflow in near-wall meshes can be at very low Reynolds number ($y^+ \approx 1$), this study employs an enhanced wall treatment, a near-wall modelling method that combines a two-layer model with enhanced wall functions, for the k–ε models (Chapter 6). For the LES model, a very fine mesh is required to resolve the wall layer that is very computationally expensive especially for engineering applications. Therefore, a wall model, like the RANS approach, is used to bridge the wall with the adjacent turbulent airflow. Convergence for the airflow governing variables (velocities, pressure, k, and ε) is assumed to have been reached when the iteration residuals are reduced by five orders of magnitude (e.g. 1×10^{-5}).

Model validation against experimental data: The case of the ventilated model room as investigated by Posner et al. (2003) is used to evaluate the turbulent indoor airflow through the standard k–ε, RNG k–ε, and RNG-based LES models. The initial condition of the flow field in room is assumed to have a

randomly perturbed velocity about the magnitude of the mean velocity U_{inlet}. To ensure that the solution for the LES computations achieve sufficient statistical independence from the initial state, time-averaged results are obtained from the instantaneous transient values after the airflow simulation is marched for 2000 nondimensional time steps, which represents 100 seconds in physical time. After this time, the instantaneous values such as the airflow velocities are averaged over 10000 nondimensional time steps (500 seconds in physical time). The simulated vertical air velocity component along the vertical inlet jet axis (line 1 in Fig. 8.1) and the vertical air velocity component along the horizontal line at midpartition height (line 2 in Fig. 8.1) are validated against the measured results.

Fig. 8.3 shows the comparison between the predicted and measured vertical air velocity component along the horizontal line at the midpartition height. Between the location of $x = 0$ m and the partition position, all three turbulence models yield almost similar results. Here again, the RNG-based LES model provides a slightly better prediction in the region between $x = 0.2$ m and the partition position. In the near-wall regions about the locations $x = 0.46$ m and $x = 0.9$ m, the RNG-based LES model successfully captures the highest positive vertical velocities, whilst the two k–ε models significantly underpredict the velocities. From these results, it is apparent that better prediction is achieved through the RNG-based LES model as demonstrated through the excellent agreement with the experimental results in the region from the partition position to the horizontal location of $x = 0.6$ m. Considerable underprediction of the negative vertical velocity by the k–ε models, found in the region immediately beneath the inlet, may well be attributed by the excessive diffusion caused by the eddy-viscosity modelling. Marginal discrepancy between the measured data and the simulation results found in the region about the location $x = 0.85$ m shows that the k–ε models' results are slightly better than the RNG-based LES

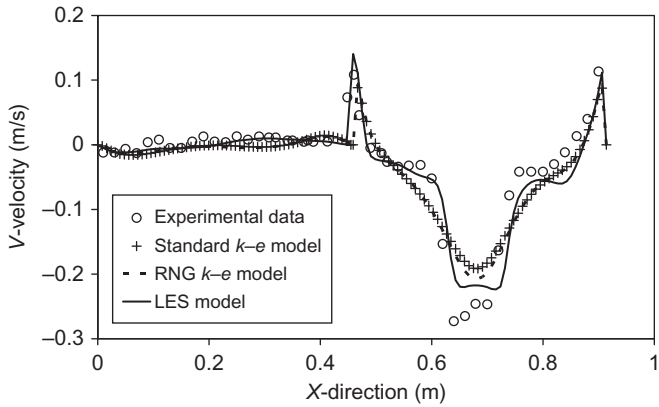


FIG. 8.3 Comparison between predicted and measured results of the vertical velocity component along the horizontal line at midpartition height.

model. Overall, all three turbulence models perform rather well; good agreement is achieved between the predictions and measured data, and the flow trends are successfully captured. One significant aspect in this study is that the RNG-based LES model has shown to provide significantly better results especially in zone 2 because of the model's inherent ability to better capture the fluid flow characteristic within a confined space. Despite this important discovery, we observe that the predicted velocities by the two k–ε models are still within reasonable limits of the measurements. Practically, these models can still be applied with some degree of confidence and are generally quite sufficient for the majority of engineering applications.

Design of a room ventilation system: The practical use of CFD is illustrated herein. As a design tool, CFD can be systematically employed to parametrically investigate a number of ventilation design system features. Let us investigate the scenario of a ventilated compartment as depicted in Fig. 8.4. In this example, cold air is supplied through the top plenum duct. A portion of this main air supply diverts into the diffuser grills at the ceiling and consequently exhausts at the bottom of the diffuser outlet into an open space inside the enclosure. The diffuser grill is connected to the top plenum duct by an adjoining duct at a length H. Two design features—design A and design B—in the vicinity of the diffuser outlet are shown in Fig. 8.5. From a ventilation perspective, design A generally results in a distortion of the air distribution as it exits through the diffuser grill. In order to achieve a more symmetrical diffusion pattern, guiding vanes near the adjoining duct are introduced as part of the improved design feature to better redistribute the airflow before reaching the diffuser outlet.

CFD simulations of design A and design B with the adjoining duct of length H are presented in Fig. 8.6. The colour spectrum of the velocity vectors exemplifies the velocity magnitude whereby the lowest speed is designated by the colour blue whilst the highest speed is indicated by red. As observed, the proposed design change with the guiding vanes being positioned upstream of the adjoining duct in design B has a dramatic impact on the air distribution at the

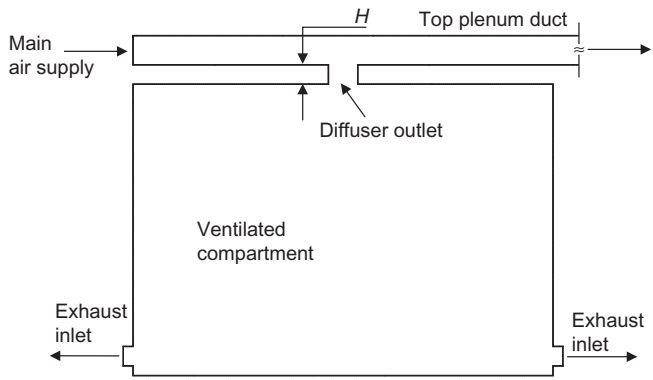


FIG. 8.4 Schematic scenario of a ventilated compartment.

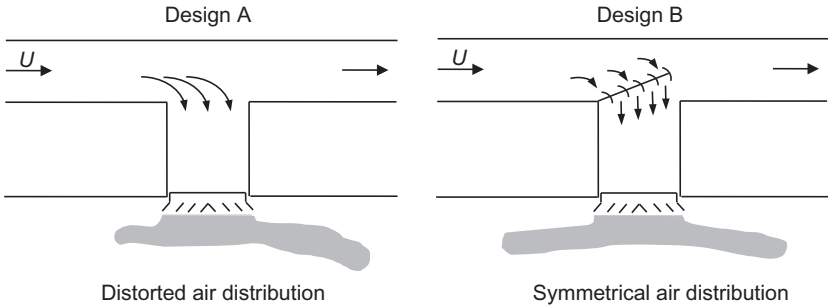


FIG. 8.5 Distorted and symmetrical air diffusion through diffuser grill.

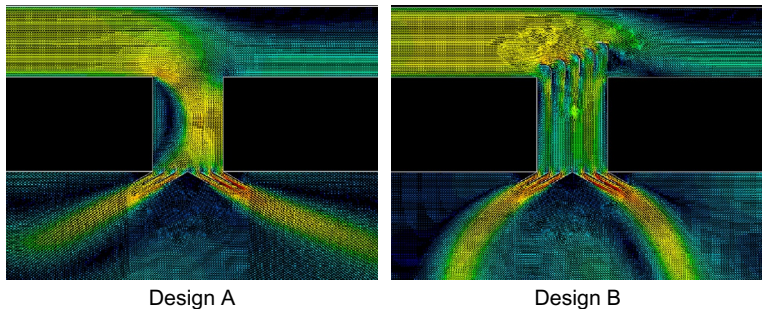


FIG. 8.6 Comparison between design A and design B for the predicted air distribution in the vicinity of the diffuser outlet with an adjoining duct of length *H*.

diffuser exit. The airflow appears to be more uniformly distributed before reaching the diffuser grill. A symmetrical flow pattern is obtained. This is not, however, the case that is seen in design A. A stagnant flow region persists, and the airflow beyond the diffuser grill behaves more like a jet stream being injected into the ventilated compartment.

Conclusion: Two key points are demonstrated through this example. Firstly, the mature development achieved in turbulence modelling demonstrates the feasibility of employing such models for engineering applications with some degree of confidence. Secondly, it exemplifies the possible use of CFD in assisting the design process where multiple parametric investigations can be performed at low costs and hence providing engineers with the opportunity to better assess numerous design options towards the eventual selection of a viable system.

Before we proceed towards how CFD can be used nowadays as a research tool to enhance understanding of some challenging complex flows, the authors would like to elude towards an important aspect regarding application of turbulence models. Despite the significant advances achieved in the area of turbulence even to the point where LES models nowadays can be feasibly applied

with current computational resources, the standard k–ε still remains the workhorse model that can provide reliable predictions for many engineering flow problems. In practice, the standard k–ε model should be advocated for carrying out initial exploratory design calculations. The results obtained may well be adequate within the acceptable limits of engineering solutions, but in the event that the model fails to capture the essential flow physics or crystallize any viable solutions, more advanced turbulence models can be applied as the next step of the design process to improve the CFD results.

8.3 TO ENHANCE UNDERSTANDING—AS A RESEARCH TOOL

In retrospect, CFD had been established more as a research tool rather than a design tool to comprehend the many important physical aspects of a flow field. We have briefly observed in Chapter 1 whereby CFD can be applied nowadays to elucidate some interesting flow structures over cylindrical obstacles. In spite of the many significant advances and the maturity achieved in CFD research of single-phase flow problems, the use of this methodology is currently being realized in two-phase flow investigations. To further demonstrate the versatility of this tool, we further concentrate on another challenging area in CFD that is the numerical study of gas-particle flow.

Gas-particle flows are frequently encountered in numerous important processes such as in the minerals, petroleum, chemical, metallurgical, and energy industries and environmental engineering industries. Scaled-up experiments involving such flows are usually rather difficult to be performed mainly due to the inherent complexity of the flow phenomena (e.g. clusters appearing within the gas-particle flows) that require high-precision instrumentation. Fig. 8.7 illustrates an experimental flow visualization of solid particles (glass

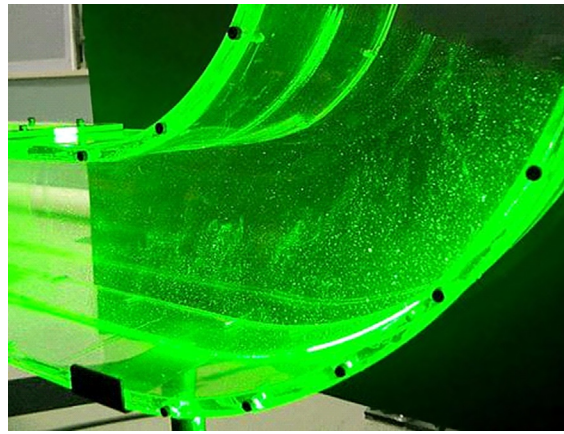


FIG. 8.7 Flow visualization of solid particles suspended in a gas flow.

beads with a mean diameter of 66 μm) suspended in the gas flow through a 90 degrees bend.

During the last decade, significant research efforts have been made in both academic and industrial research to better understand the dispersed two-phase flows using CFD techniques. Note that this next CFD example should only be construed as merely to provide a brief overview of the additional modelling effort that is required in modelling dispersed two-phase flows. Handling such flows generally requires the consideration of additional conservation equations and appropriate models where the gas phase is usually regarded as a carrier and the particle phase is taken to be dispersed within the gas flow. Firstly, the Lagrangian approach can be adopted by treating the gas phase as a continuum fluid with discrete particles in the fluid space. Secondly, both the gas and particle phases can alternatively be assumed to be continuum fluids, which is the essence of the Eulerian approach. Transport equations (mathematical models) describing the gas-particle flow according to the two different approaches will be discussed in the next section.

8.3.1 Gas-Particle Flow in a 90 degrees Bend

Two different CFD computer codes, an in-house research code (Tu, 1997) and a commercial CFD code ANSYS FLUENT, version 6.1, are employed to simulate the gas-particle flow. The discrete approach described by the Lagrangian model is handled by the ANSYS FLUENT code, whilst the continuum approach that is essentially the Eulerian model is solved through the in-house research code. The simulated results are validated against the experimental data of Kliafas and Holt (1987).

Model description: The geometry of this example is a three-dimensional turbulent airflow with particles travelling around a 90 degrees duct bend as exemplified in Fig. 8.10. The schematic view of the experimental setup for this geometry is similar to Fig. 5.6 of the test case B in Chapter 5, which comprises a 1.2 m long horizontal duct, a 90 degrees bend with a radius ratio of 1.76 (bend radius to bend hydraulic diameter), and a 1 m long vertical straight duct. Air enters the square test section with a bulk gas velocity U_b adjusted through the aid of a variable frequency controller. Experimental data for both the gas and particle fields are obtained through the laser Doppler anemometry (LDA) system.

Grid: For the 90 degrees square-section bend, the computational domain begins at 1 m (10D) upstream from the bend entrance and extends to 1.2 m (12D) downstream from the bend exit. A structured mesh overlaying with hexahedral elements is generated for the in-house computer code. On the other hand, an unstructured mesh comprising of tetrahedral elements fills the whole 90 degrees bend geometry as illustrated in Fig. 8.8 for the ANSYS FLUENT computer code.

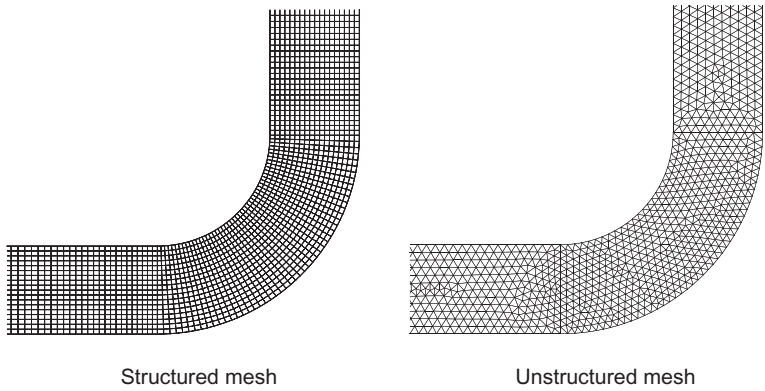


FIG. 8.8 Computational meshes for the 90 degrees square-section bend.

Physics and mathematical models: For both approaches, the governing equations for the gas phase are the same as described by equation 3.53 (Chapter 3), which can be rewritten as

$$\frac{\partial \phi}{\partial t}+\frac{\partial (u\phi)}{\partial x}+\frac{\partial (v\phi)}{\partial y}+\frac{\partial (w\phi)}{\partial z}=\frac{\partial}{\partial x}\left[\Gamma_\phi \frac{\partial \phi}{\partial x}\right]+\frac{\partial}{\partial y}\left[\Gamma_\phi \frac{\partial \phi}{\partial y}\right]+\frac{\partial}{\partial z}\left[\Gamma_\phi \frac{\partial \phi}{\partial z}\right]+S_\phi \tag{8.1}$$

By setting the transport property ϕ equivalent to 1, u_g, v_g, w_g, k_g, and ε_g and selecting appropriate values for the diffusion coefficient Γ_ϕ and source terms S_ϕ, we obtain the set of transport equations as presented in Table 3.2 (see Chapter 3) for each partial differential equations describing the conservation of mass, the momentum, and the turbulent quantities of the gas phase.

8.3.1.1 Governing Equations of Particle Phase Using the Lagrangian Approach

This approach calculates the trajectory of each individual discrete particle by integrating Newton's second law, written in a Lagrangian reference frame (Chiesa et al., 2005). Appropriate forces such as the drag and gravitational forces can be incorporated into the equation of motion. The equation can thus be written as

$$\frac{du_p}{dt}=F_D\left(u_g-u_p\right)+\frac{g\left(\rho_p-\rho_g\right)}{\rho_p} \tag{8.2}$$

where $F_D\left(u_g-u_p\right)$ is the drag force per unit particle mass and F_D is given by

$$F_D=\frac{18\mu_g}{\rho_p d_p^2}\frac{C_D Re_p}{24} \tag{8.3}$$

The relative Reynolds number Re_p is defined as

$$Re_p = \frac{\rho_p d_p |u_p - u_g|}{\mu_g} \tag{8.4}$$

whilst the drag coefficient C_D is determined from

$$C_D = a_1 + \frac{a_2}{Re_p} + \frac{a_3}{Re_p^2} \tag{8.5}$$

In Eq. (8.5), the coefficients denoted by a_1, a_2, and a_3 are empirical constants for smooth spherical particles over several ranges of particle Reynolds number (Morsi and Alexander, 1972). The *eddy-lifetime* model is used to account for the effect of gas-phase turbulence on the particle phase. More details regarding this model can be found in Tian et al. (2005).

8.3.1.2 Governing Equations of Particle Phase Using the Eulerian Approach

For this approach, the governing equations for the particle phase can also be expressed in the form of Eq. (8.1) described above. The set of transport equations can be similarly obtained by setting the transport property ϕ_p equivalent to 1, u_p, v_p, w_p, k_{gp}, k_p, and ε_{gp} and selecting appropriate values for the diffusion coefficient $\Gamma_{\phi p}$ and source terms $S_{\phi p}$; the special forms tabulated in Table 8.1 describe the partial differential equations for the conservation of mass, the momentum, and the turbulent quantities of the particle phase. Details on the derivations of these equations can be found in Tu (1997).

Features of the simulation: The governing transport equations are discretized using a finite-volume approach with a nonstaggered grid system

TABLE 8.1 General Form of Governing Equations for the Particle Flow in an Eulerian Reference Frame

ϕ_p	$\Gamma_{\phi p}$	$S_{\phi p}$
ρ_p	0	0
u	ν_{pT}	$F_D^u + F_G^u + F_{WM}^u$
v	ν_{pT}	$F_D^v + F_G^v + F_{WM}^v$
w	ν_{pT}	$F_D^w + F_G^w + F_{WM}^w$
k_{gp}	$\frac{\nu_{pT}}{Pr_T}$	$P_{kgp} - \overline{\rho}_p \varepsilon_{gp} - II_{gp}$
k_p	$\frac{\nu_{pT}}{\sigma_k}$	$P_{kp} - I_{gp}$
ε_{gp}	$\frac{\nu_{pT}}{\sigma_\varepsilon}$	$\frac{\varepsilon_g}{k_g}\left(C_{\varepsilon 1} P_g - C_{\varepsilon 2} D_g\right)$

(see Chapter 4 for more explanation). A third-order *QUICK* scheme (Appendix B) is used to approximate the convective terms, whilst second-order accurate central difference scheme is adopted for the diffusion terms. The velocity-pressure linkage is realized through the SIMPLE algorithm (Chapter 4). In order to mimic the experimental conditions, a uniform velocity ($U_b = 52.19$ m/s) for both gas and particle phases is imposed at the top inlet 1 m away from the bend entrance, which corresponds to a Reynolds number of 3.47×10^5. The inlet turbulence intensity is prescribed at 1%, whereas the particles are taken to be glass spheres of density $\rho_s = 2{,}990$ kg/m^3 and size 50 μm. The corresponding particulate loading and volumetric ratios are 1.5×10^{-4} and 6×10^{-8}, respectively, for which the particle suspension is considered to be very dilute. At the outflow, the normal gradient for all dependent variables are set to zero. A nonslip boundary condition is employed along the wall for the gas phase and the particulate phase at the wall. Appropriate boundary conditions also need to be specified to represent the particle-wall momentum transfer for the Eulerian approach of which more details can be found in Tu and Fletcher (1995).

For the Lagrangian model, the particle transport using a discrete random walk (DRW) model is computed from the converged solution of the gas flow. For the DRW model, 20,000 individually tracked particles are released from 10 uniformly distributed points across the inlet. The independence of statistical particle phase predictions is tested using 10,000, 20,000, and 50,000 particles. The difference in the maximum positive velocities of 20,000 and 50,000 particles is found to be less than 1%.

In the Eulerian approach, the numerical method for the solution of governing equations of the particle phase is similar to the method for scalar transport variables such as temperature for the gas phase. This is due to the fact that there is no pressure term in the particle momentum equations based on an assumption of no collisions amongst particles in a diluted gas-particle flow. All the governing equations for both gas and particle phases are solved sequentially at each iteration step. They are iteratively solved via the strongly implicit procedure (SIP) solver. The above solution process is marched towards steady state until convergence is attained.

The CPU time for the Lagrangian approach is generally much greater than the Eulerian approach. It is thus not surprising since significantly more computations are required to determine each individual particle trajectory in the Lagrangian approach when compared with the much reduced computational effort in only calculating the particle phase as one entity in the Eulerian approach.

Model validation against experimental data: The mean quantities of both gas and particle phases employing the two different numerical approaches are compared with the well-established experimental results of Kliafas and Holt (1987). In this example, an important dimensionless parameter particularly for gas-particle flow is the Stokes number, which is defined as the ratio between the particle relaxation time to a characteristic time of the fluid motion, in other

words, $St = t_p/t_s$. This dimensionless number determines the kinetic equilibrium of the particles with the surrounding gas. The system relaxation time, t_s, in the Stokes number can usually be derived from the characteristic length (L_s) and the characteristic velocity of the system under investigation. In this example, it is the free-stream velocity (U_b); hence, $t_s = L_s/U_b$. A small Stokes number ($St \ll 1$) signifies that the particles are in near velocity equilibrium with the carrier fluid. For larger Stokes number ($St \gg 1$), particles are no longer in equilibrium with the surrounding fluid phase; they divert rather substantially from the fluid stream path.

Mean quantities are of utmost interest in engineering applications. For the gas and particle phases, the mean velocity, concentration, and fluctuation distributions along the bend are compared with measurements at the midplane along the spanwise direction of the duct geometry. All the values reported here (unless otherwise stated) are normalized using the inlet bulk velocity (U_b). Fig. 8.9 shows the comparison of the numerical results against the experimental data for the mean streamwise gas velocity (the case for $St < 0.1$) along various sections of the bend. There appears to be qualitative agreement for both of the numerical models against the data reported by Kliafas and Holt (1987).

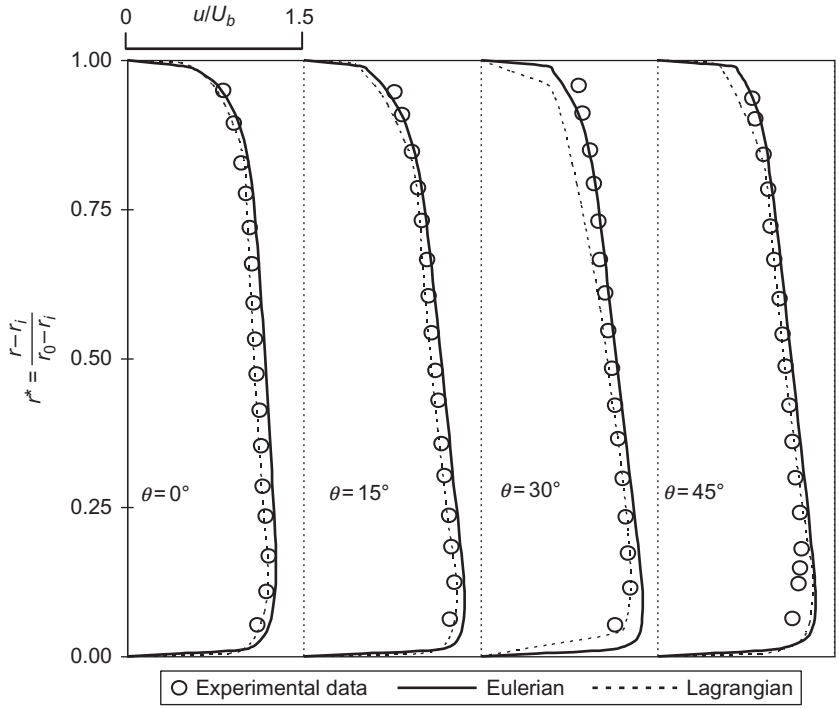


FIG. 8.9 Mean streamwise particle velocities along the bend for Stokes number $St = 0.01$.

Enhance understanding through research: As a research tool, CFD can further enhance our understanding of particle behaviour around the carrier gas phase by carrying out *numerical experiments* for the gas-particle flow. The following results demonstrate the use of this important tool.

To better understand the particle paths along the bend of different Stokes number, Fig. 8.10 depicts the paths using Lagrangian tracking for each respective case. For a Stokes number of 0.01, it is clearly evident that the particles have a tendency to act as 'gas tracers'. In such a flow scenario, they are generally considered to be in equilibrium with the carrier phase. However, this phenomenon is less pronounced as the Stokes number is increased. A positive slip velocity between the particulate and gas phase at the outer walls exists alongside with the gas velocities at the inner walls due to the presence of a favourable pressure gradient. These 'gas-tracing' phenomena of the particles become less pronounced as they approach towards the bend exit since the flow regains the energy it lost due to slip. It is observed that for flows with $St \geq 1$, the positive slip velocity between the particle and gas velocity decreases along with the bend radius and reverts to negative slip velocity at the bend exit where the particles now lag the gas. They are unable to keep pace with the gas due to its own inertia and the energy lost through particle-wall collisions. As the Stokes number increases, the particles show a greater tendency in migrating towards the outer bend.

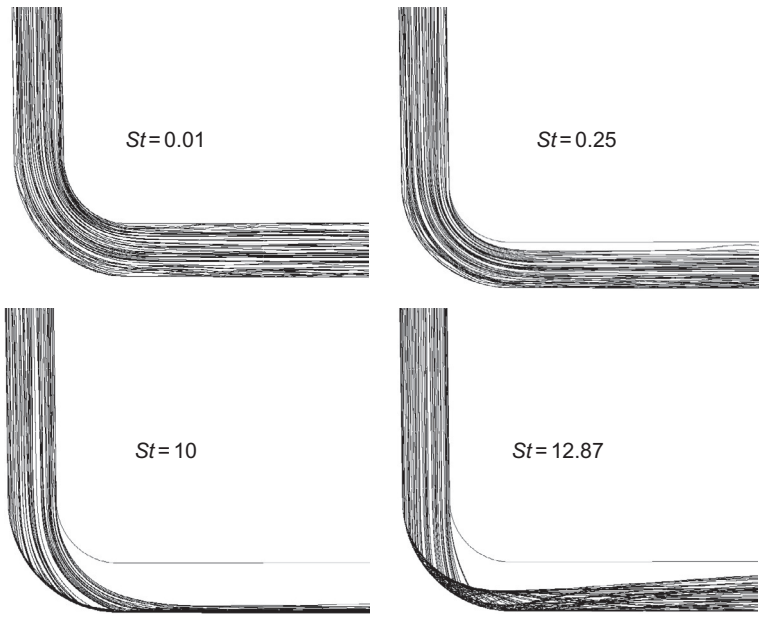


FIG. 8.10 Lagrangian particle paths for varying Stokes number.

Conclusion: With the increasing computing power and availability of a viable discrete approach described by the Lagrangian model or a continuum approach by the Eulerian framework that entails the consideration of additional conservation equations, many complex multiphase flow problems are increasingly being tackled through CFD. The feasibility of attaining qualitative and quantitative numerical results in this example represents not only the many rich physical insights that can be gained through the CFD methodology but also a testimonial feat of the rigorous advancements that have been made to the state-of-the-art multiphase flow research.

8.4 OTHER IMPORTANT APPLICATIONS

8.4.1 Heat Transfer Coupled With Fluid Flow

There are other applications within the CFD framework whereby heat transfer significantly influences the fluid flow behaviour. To properly handle such flows, two examples are presented below to further elucidate pertinent features associated with modelling and procedures of obtaining meaningful practical solutions associated with these types of CFD problems.

8.4.1.1 Heat Exchanger

Heat exchangers are employed in numerous industries. Steam generation in a boiler, air cooling within the coil of an air conditioner, and automotive radiators represent just some of the conventional applications of this mechanical system. Of particular importance in the design of heat exchangers is the pivotal understanding of heat transfer in flow across a bank of tubes. Tube banks, as used in many heat exchangers, can be systematically arranged in an in-line or staggered manner as described in Fig. 8.11. Here, the crossflow exchanger of cooler fluid removing the heat from the warmer fluid within the tubes flowing perpendicular to the schematic drawing is shown. For design purposes, tube banks are usually characterized by a number of important dimensionless parameters such as the transverse, longitudinal, and diagonal pitches. These parameters allow engineers to assess various heat-transfer augmentation methods to specifically design special types of heat exchangers such as compact heat exchangers. According to Žukauskas and Ulinskas (1988), these types of heat exchangers (the main focus in this CFD example) are categorically considered by the dimensionless transverse and longitudinal pitches being less than 1.25. They have shown to provide a higher heat-transfer coefficient in *laminar flow* than that offered by a highly *turbulent flow*. Typically, the heat-transfer surface areas are substantially increased whilst augmenting the flow, creating various secondary flows and simultaneously destroying the hydrodynamic and thermal boundary layers created by the repetitive nature of the flow.

Clearly, the long-standing practice in designing and manufacturing of heat exchangers has been dominated by experimental methods and semiempirical

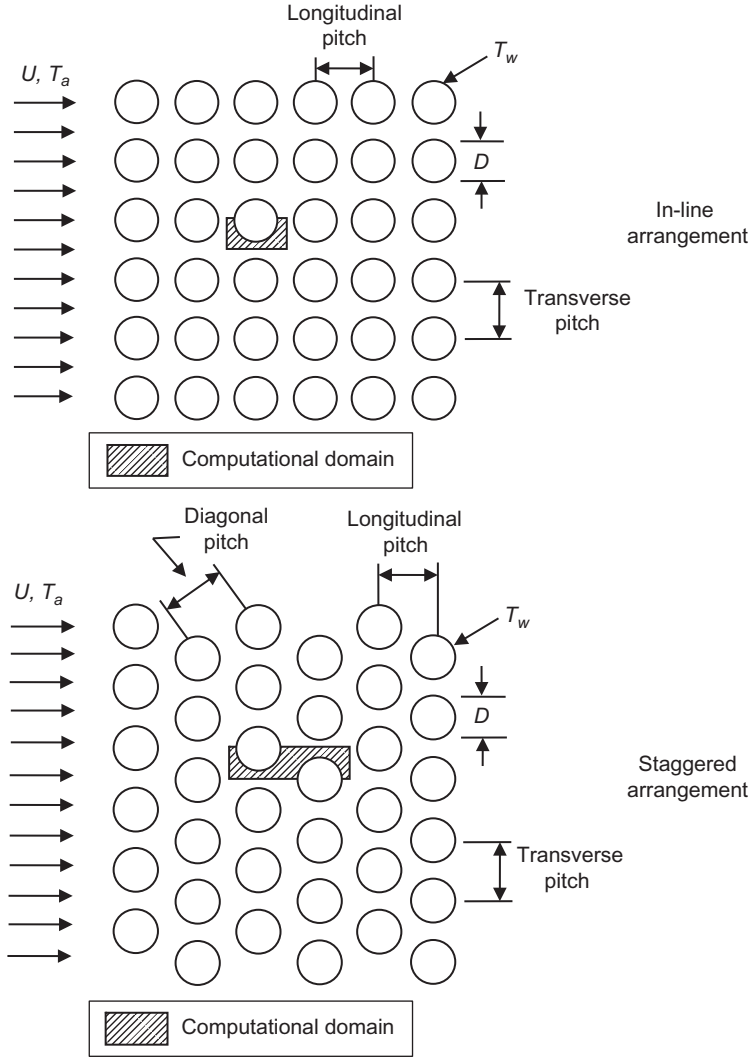


FIG. 8.11 Schematic description of in-line and staggered arrangements of tube banks.

integral approaches based on simple criteria relations for the heat-transfer coefficient. As early as the 1930s, Colburn (1933) has proposed a simple correlation for the heat transfer having flow across banks of staggered tubes, whilst others such as Aiba et al. (1982a,b) and Žukauskas and Ulinskas (1988) have reported extensive experimental heat transfer and fluid friction during viscous flow across in-line and staggered banks of tubes covering both isothermal and isoflux boundary conditions. Lately, Khan et al. (2006) provided analytical correlations

that could be used for either in-line or staggered arrangement for a wider range of parameters. With the advent of commercial CFD packages, engineers are nonetheless warming up to the immense possibility of gaining insight to processes that are not easily amenable to analysis by measurements or simple overall computations, assess both qualitatively and quantitatively their performance, and optimize design and operation parameters through CFD. There are many advantages in the use of CFD for the design of heat exchangers. Recent literatures by Witry et al. (2005), Hájek et al. (2005), and Wang et al. (2006) exemplify some of the current trends in the application of CFD to a variety of heat-exchanger systems. With the increasing usage of this methodology, it is therefore appropriate to demonstrate and provide some useful practical guidelines of how CFD can be applied in solving the flow- and heat-transfer characteristics for compact heat exchangers.

Problem considered: For the in-line and staggered arrangements of tube banks illustrated in Fig. 8.17, fluid at a prescribed mass flow rate or velocity U and an inlet ambient temperature T_a much lower than the wall temperature T_w enters the tube banks from the left and exits at the right. By taking the advantage of special geometrical features such as the inherent repetitive nature of the flow behaviour, the computational fluid domain allows the possible exploitation of *symmetric* and *cyclic* (*periodic*) boundary conditions (as described in Chapters 2 and 6) in speeding up the computations and in turn enhancing the computational accuracy of the simplified geometries. The use of these boundary conditions that are important features in practical CFD applications will be demonstrated through this example.

Cyclic (*periodic*) boundary conditions can be suitably prescribed to ensure that the characteristics of the fluid leaving and entering the domain are identical. They are usually imposed on walls *perpendicular* to the flow direction. The rationale behind *symmetric* boundary conditions is however to replicate the fluid flow within the solution region to adjacent regions containing the same flow structures. They are commonly applied on walls *along* the flow direction. The solution regions of the two configurations are depicted by the shaded areas as shown in Fig. 8.11. Specification of the relevant boundary conditions and the computational meshes that have been generated is described in Fig. 8.12. A hybrid mesh (structured and unstructured elements) is generated for each of the computational domains. For both cases, a boundary-layer stretched mesh of rectangular elements (structured) is concentrated near the tube walls, whilst the rest of the internal flow domain is filled by triangular elements (unstructured).

CFD simulation: The governing equations for the two-dimensional laminar flow within the simplified computational domains can be written as

$$\frac{\partial(\rho u\phi)}{\partial x}+\frac{\partial(\rho v\phi)}{\partial y}=\frac{\partial}{\partial x}\left[\Gamma_\phi\frac{\partial\phi}{\partial x}\right]+\frac{\partial}{\partial y}\left[\Gamma_\phi\frac{\partial\phi}{\partial y}\right]+S_\phi \tag{8.6}$$

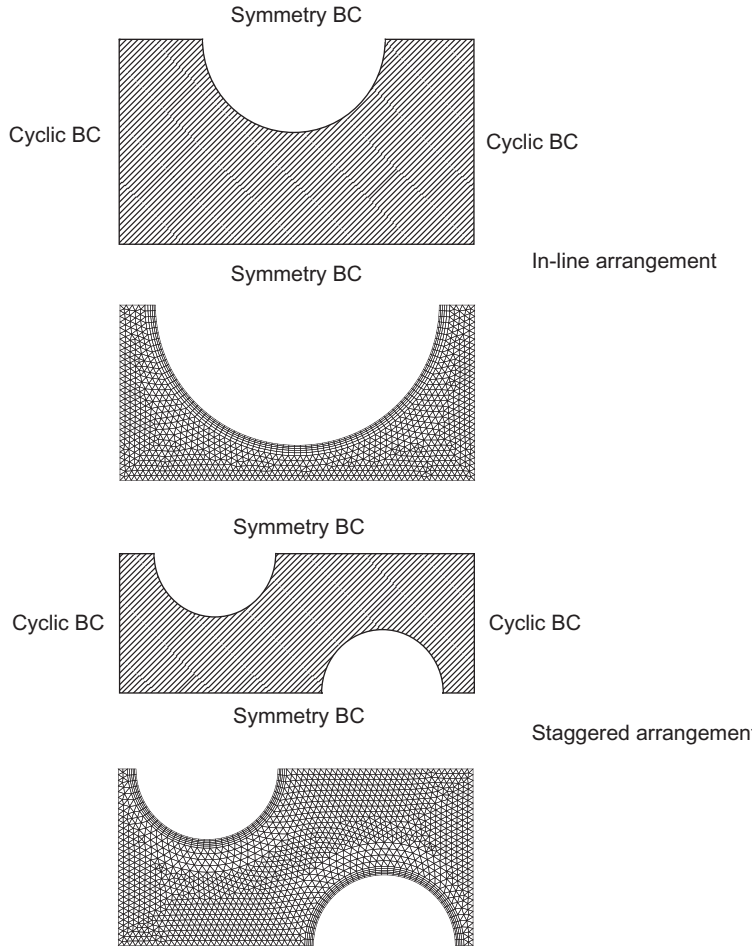


FIG. 8.12 Specification of boundary conditions and computational meshes for the solution regions associated with the in-line and staggered arrangements.

By setting the transport property ϕ equal to 1, u, v, and H ($=C_pT$ where C_p is the specific heat of constant pressure) and selecting appropriate values for the diffusion coefficient Γ_ϕ and source terms S_ϕ, we obtain the special forms presented in Table 8.2 for each of the partial differential equations for the conservation of mass, momentum, and energy. The solution is marched towards steady state where convergence is deemed to have been reached when the iteration residual of enthalpy is reduced by six orders of magnitude (e.g. 1×10^{-6}).

A hybrid mesh (structured and unstructured elements) is generated for each of the computational domains represented in Fig. 8.12. For both cases, a boundary-layer stretched mesh of rectangular elements (structured) is

TABLE 8.2 Conservation Equations Governing the Fluid Flow Within the In-Line and Staggered Arrangements

ϕ	Γ_ϕ	S_ϕ
ρ	0	0
u	μ	$-\frac{\partial p}{\partial x}+\frac{\partial}{\partial x}\left[\mu\frac{\partial u}{\partial x}\right]+\frac{\partial}{\partial y}\left[\mu\frac{\partial v}{\partial x}\right]$
v	μ	$-\frac{\partial p}{\partial y}+\frac{\partial}{\partial x}\left[\mu\frac{\partial u}{\partial y}\right]+\frac{\partial}{\partial y}\left[\mu\frac{\partial v}{\partial y}\right]$
H	$\frac{\mu}{Pr}$	0

concentrated near the tube walls, whilst the rest of the internal flow domain is filled by triangular elements (unstructured).

CFD results: This example is calculated using a commercial finite-volume CFD computer code ANSYS FLUENT, version 6.1.22. The relevant data employed for the CFD calculations of the in-line and staggered arrangements are provided in Table 8.3. The working fluid is taken to be water. Fluid properties of water at reference temperature of 25°C are also given in the table below. Based on these properties, the dimensionless Prandtl number Pr can be evaluated; a value of 7.0 is thus obtained. For the computed results presented

TABLE 8.3 Data Used for the In-Line and Staggered Tube Bank Arrangements

Quantity	Dimension
Tube diameter D, mm	10.0
Longitudinal pitch, mm	12.5
Transverse pitch, mm	12.5
Tube wall temperature T_w, °C	70
Mass flow rate, kg/s	0.01–0.4
Water properties	
Thermal conductivity k, W/m K	0.6
Density ρ, kg/m^3	998.2
Specific heat C_p, J/kg K	4182
Kinematic viscosity ν, m^2/s	1×10^{-6}
Prandtl number Pr	7.0

henceforth, it shall be assumed that there is negligible effect of change in temperature on the fluid properties.

In Chapter 2, the nondimensional Reynolds number has been shown to be a useful parameter in characterizing the fluid flow. Another important dimensionless parameter that is commonly associated with heat transfer is the Nusselt number (Nu) after Wilhelm Nusselt, which may be obtained by multiplying the convective heat-transfer coefficient h with the ratio L/k where L is the characteristic length scale and k is the thermal conductivity, namely,

$$Nu = \frac{hL}{k} \tag{8.7}$$

A large Nu essentially signifies that the *convection heat transfer* is superseding the *conduction heat transfer* in the bulk fluid flow. For the design of heat exchangers, the diameter of the tube is usually taken as the characteristic length in the definition of Nusselt and Reynolds numbers. These numbers can be defined as $Nu_D = D\ h/k$ and $Re_D = D\ U_{max}/\nu$. Instead of the usual inlet velocity being used as the reference velocity, the definition of Reynolds number here differs by employing U_{max} that is the maximum velocity in minimum flow area to be determined directly from the CFD solution. It is noted that the dimensions given for the longitudinal and transverse pitches in Table 8.3 correspond to the configuration of compact heat exchangers where the dimensionless longitudinal and transverse pitches are 1.25 (12.5/10 mm).

Fig. 8.13 illustrates the streamlines at different Reynolds numbers for the in-line arrangement. There appears to be two distinct flow regimes within the spaces separating the tubes along the longitudinal and transverse distances at low Reynolds number flows. In between the spacing of the top and bottom

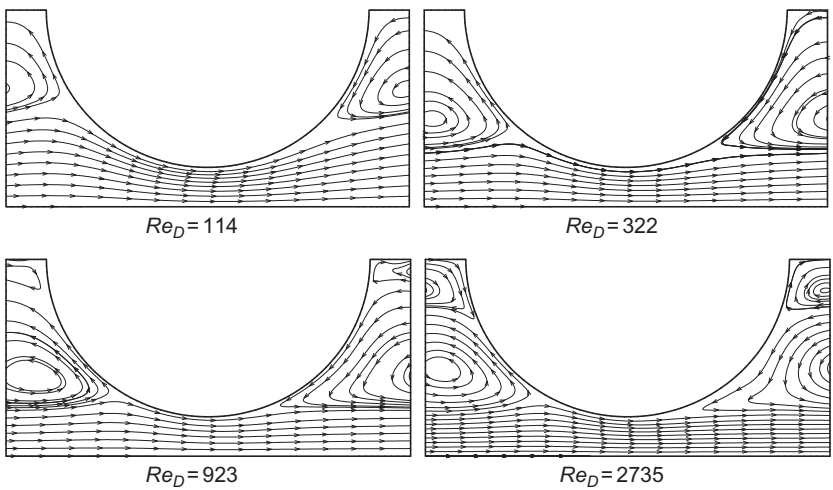


FIG. 8.13 Streamlines of in-line arrangement at different Reynolds numbers.

tubes lies the primary fluid flow of the system of which represents the multiple horizontal layers of fluid flowing along the longitudinal direction of the entire in-line tube bank. Sandwiched between these layers are the presence of two secondary recirculation vortices in between the spacing of the front and rear tubes. At sufficiently high Reynolds number flows, the breakdown of these larger secondary cells results in the formation of two smaller cells, further adding to the complexity of the fluid flow and heat-transfer processes.

Fig. 8.14 nonetheless shows the streamlines predicted for the staggered arrangement with boundary-layer separation prevailing at downstream of the fluid flow (indicated by points 'S' in the figure). Here, the flow patterns resemble more like a snake weaving around the tubes. Further increase of Reynolds numbers tends to elongate and intensify the fixed recirculation eddies, which clearly show the flow breaking away from the tube at high Reynolds numbers. Such observation shares many similarities to the classical vortex-shedding phenomenon, which represents an important aspect from the viewpoint of ensuring structural integrity. The shedding of these vortices gives rise to a lateral force acting on the tube. Since these forces are generally periodic following the frequency of vortex shedding, the tubes may be subjected to forced vibration, sometimes called self-induced vibration. As also observed in Fig. 8.14, the mainstream of these wavy flow layers in between the staggered spacing of the top and bottom tubes envelops the secondary elongated recirculation eddies residing in between the spacing of the front and rear tubes.

Higher heat-transfer rates being experienced in staggered arrangement over in-line arrangement of tube banks in compact heat exchangers are further confirmed by the plot of average Nusselt number against Reynolds number for the

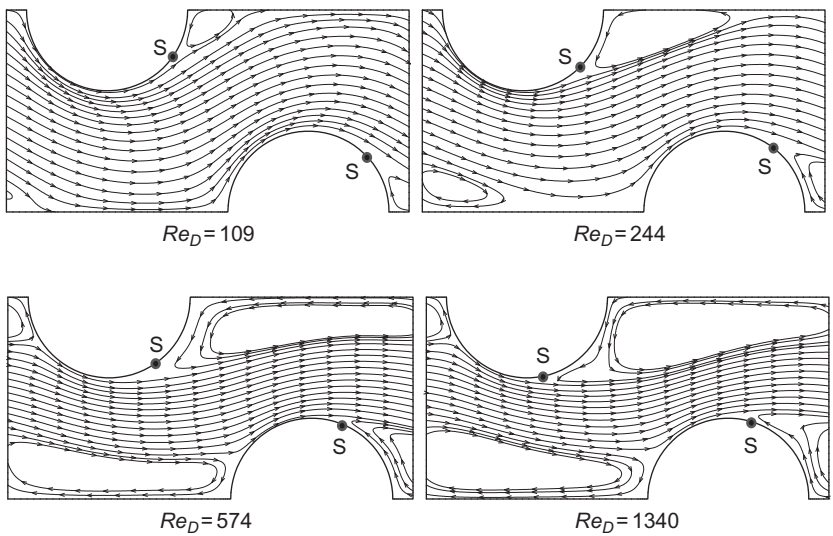


FIG. 8.14 Streamlines of staggered arrangement at different Reynolds numbers.

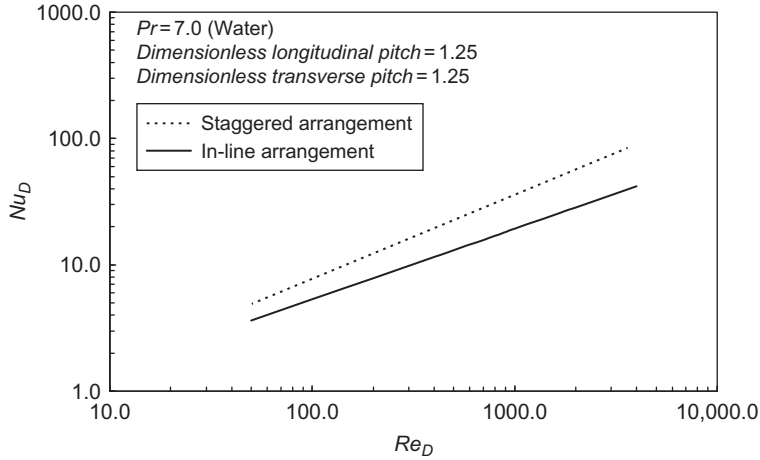


FIG. 8.15 Average heat transfer for the in-line and staggered arrangement of tube banks.

same dimensionless pitches in Fig. 8.15. From thermal-hydraulic considerations, one plausible explanation is that in a staggered bank, the path of the main flow is deemed to be more tortuous and extends a greater coverage over the surface areas of downstream tubes and thereby results in more efficiently removing the heat that are contained within the internal tubes of this compact heat-exchanger system. Nevertheless, this is quite the opposite for the in-line arrangement where evidently from the flow structures observed above the main flow path appears to only glide over the tips of the top and bottom tube surfaces, which in retrospect may explain the reduced effectives experienced in in-line arrangement .

8.4.1.2 Conjugate and Radiation Heat Transfer[1]

Safety concerns and integrity issues strongly govern the removal of a single plate-type molybdenum target (consisting of a composite mixture of uranium and aluminium) from water into air after being irradiated for some considerable period in the open-pool Australian light-water (OPAL) research reactor. Owing to the bombardment of neutrons, heat is generated internally within the plate as a result of nuclear fission. After some considerable period of allowing the plate to be sufficiently cooled in the water, the plate experiences a decay power output due to residual fission heating. At low power levels, the plate is unloaded, placed into a holder, and subsequently cooled in air by natural convection; process handling to extract molybdenum for nuclear medicine purposes proceeds

1. The materials in this section were provided by my colleagues David Wassink and Mark Ho working at the Australian Nuclear Science Technology Organization (ANSTO). The authors are indebted to their time in kindly preparing the materials and their useful input to the writing of this section in the spirit of the rest of the book.

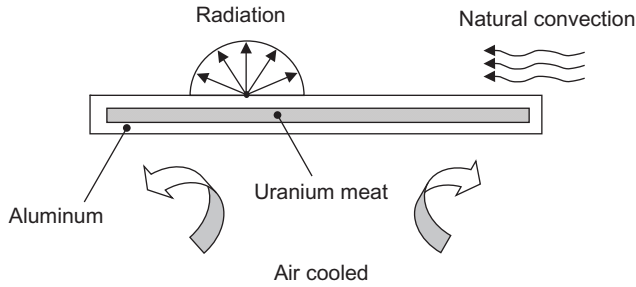


FIG. 8.16 Schematic representation of a single plate-type molybdenum target radiating heat and cooled by natural convective currents of air.

thereafter. The schematic representation of the configuration of a typical plate layered with uranium and aluminium is shown in Fig. 8.16. From thermal-hydraulic considerations, the key objectives are to ascertain at which power level the temperature inside the plate remains below the blistering temperature of 600°C (melting temperature of aluminium) in the air environment and ensure that the structural integrity of the plate is not breached or compromised.

From a modelling viewpoint, this particular CFD example exposes a number of challenging aspects. Firstly, heat being conducted out from the solid plate is radiated to the surrounding and taken away by the natural convective air currents. This highlights the importance of the need to consider the heat-transfer processes between both solid and gas regions, which require *conservation of energy equations to be solved for each region*, in order to accurately predict the solid-gas interface and internal temperatures of the solid plate (*conjugate heat transfer*). Secondly, the modelling of buoyant flow in air generally requires additional considerations particularly in the governing equations for the momentum and turbulence. Formulation of appropriate source terms is required to capture this essential flow characteristic. Thirdly, this example demonstrates the requirement of employing suitable turbulence model and imposing appropriate boundary conditions in order to sensibly attain numerical results that closely mimic the actual flow behaviour as observed during experiments.

Problem considered: Experimental target plate designed at the ANSTO water tunnel laboratory was constructed by carefully clamping two aluminium plates together to form a single plate with a thickness of 5 mm as shown in Fig. 8.17. In between the plates, matched grooves were machined into both matching faces of the plates to accommodate the heater wire and thermocouples. Electrical insulation of the heater wire to the target plate was achieved by anodizing the plates prior to assembly. The aluminium plates were held together with small screws, and heat-transfer compound was applied to the mating faces to ensure good thermal contact between the heater wire and thermocouples.

The case where the target plate suspended horizontally in air was considered. Fig. 8.18 depicts the experimental setup for the target plate being centrally supported in a box having open sides. During experiments, the outer boundaries

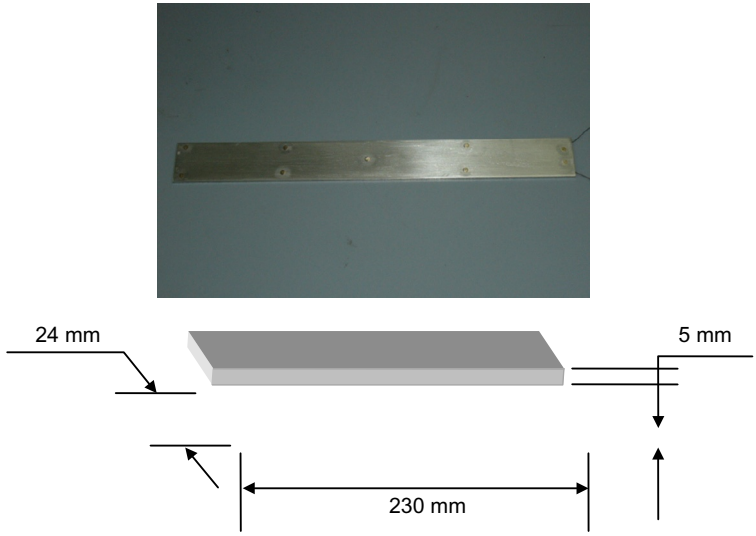


FIG. 8.17 Experimental assembled target plate.

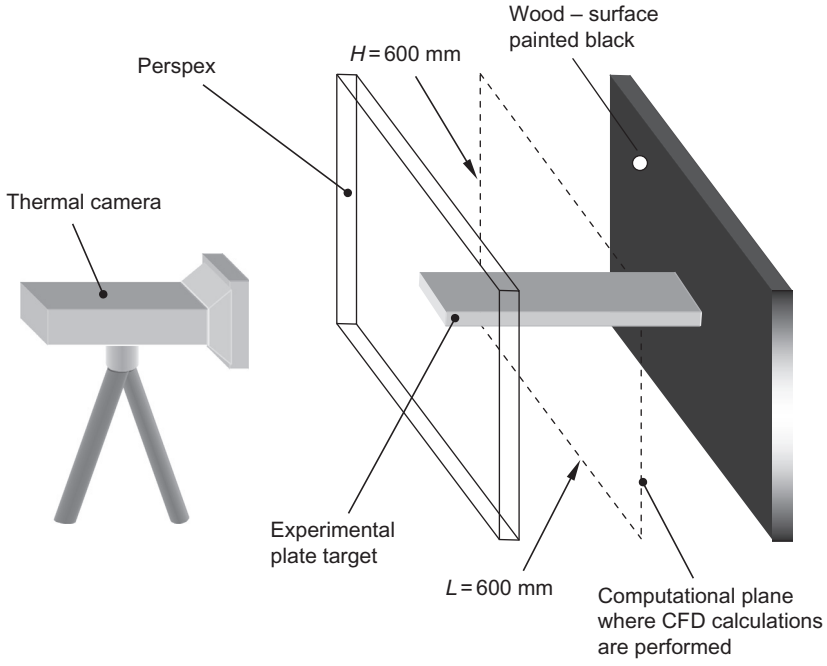


FIG. 8.18 Experimental setup of assembled target plate in an open box.

of the box were closed to permit flow visualization on the convective airflow. Smoke seeding was used, and the resultant flow streamlines were recorded by measuring the velocities at various points around the target plate through imaging and laser Doppler velocimetry (LDV) techniques. Internal temperatures in the solid plate were measured via thermocouples connected to the LabView data acquisition system. The plate power was manually controlled with the power level determined as a product of the *voltage* and *current* applied to the plate; losses in transmission were allowed to ensure accuracy of the specific plate power measured. In order to determine the effect of emissivity on the power radiated as heat from the plate—radiation heat transfer, data were obtained from the plate using different surface finishes. They were (i) black anodized; (ii) anodizing removed, surface burnished using 800 grit carborundum paper; and (iii) after development of an oxide layer by immersion in heated water. Images of the target plate using a thermal camera were obtained in order to enable the emissivity value to be estimated for CFD calculations.

CFD simulation: The two-dimensional 'suspended' experimental target plate is modelled according to the computational domain shown in Fig. 8.19 (see also in Fig. 8.18 where the computational plane—an area of 600 mm^2—is considered for CFD calculations) and solved using ANSYS-CFX, version 10, commercial code. An orthogonal mesh totalling 280,000 elements covering the solid plate and surrounding air is generated for the computational domain. Fine mesh resolution around and inside the solid plate as shown by the exploded

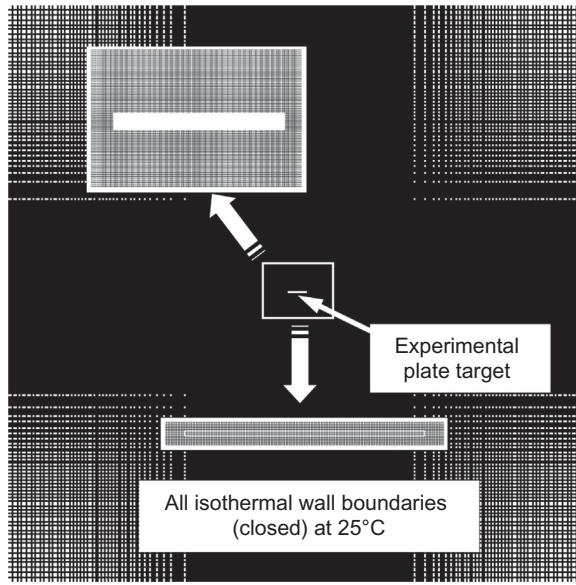


FIG. 8.19 Computational model for the experimental assembled target plate in a closed environment.

view within Fig. 8.19 is aimed to resolve the formation of complex boundary layers due to the natural convective flow and internal heat conduction through the composite materials. To replicate the boundary conditions that enclose the physical experiment, all boundaries are simulated as wall boundaries at a uniform temperature of 25°C. The working fluid is taken to have the properties of air at a reference temperature of 25°C.

As abovementioned, buoyant airflow requires additional modelling effort. Here, the momentum equation should now include the body force resulting from buoyancy. For this particular example, the gravity acts in the y direction; hence, the additional source term due to buoyancy needs to be incorporated in the *y-momentum* equation. The two-dimensional form of the *y-momentum* equation becomes

$$\frac{\partial(\rho v)}{\partial t}+\frac{\partial(\rho uv)}{\partial x}+\frac{\partial(\rho vv)}{\partial y}=\frac{\partial \tau_{xy}}{\partial x}+\frac{\partial \sigma_{yy}}{\partial y}-g(\rho-\rho_0) \tag{8.8}$$

For completeness, the *x-momentum* and *continuity* equations can be expressed as

$$\frac{\partial(\rho u)}{\partial t}+\frac{\partial(\rho uu)}{\partial x}+\frac{\partial(\rho vu)}{\partial y}=\frac{\partial \sigma_{xx}}{\partial x}+\frac{\partial \tau_{yx}}{\partial y} \tag{8.9}$$

$$\frac{\partial \rho}{\partial t}+\frac{\partial(\rho u)}{\partial x}+\frac{\partial(\rho v)}{\partial y}=0 \tag{8.10}$$

where the normal stresses σ_{xx} and σ_{yy} due to the combination of pressure p and normal viscous stress components τ_{xx} and τ_{yy} acting perpendicular to the control volume and the tangential viscous stress component $\tau_{xy}=\tau_{yx}$ that are formulated considering a Newtonian fluid can be found in Appendix A. The additional source term $-g(\rho-\rho_0)$ in Eq. (8.8) represents the buoyancy term with the reference density denoted by the variable ρ_0. In addition, appropriate modifications to the two-equation k–ε turbulence model are also required besides the buoyancy term incorporated within the *y-momentum* equation. Like the production (P) and destruction (D) of turbulence in the two equations as described in Chapter 3, the inclusion of buoyancy into the model also follows similar considerations. For example, the k-equation now takes the form of

$$\frac{\partial(\rho k)}{\partial t}+\frac{\partial(\rho uk)}{\partial x}+\frac{\partial(\rho vk)}{\partial y}=\frac{\partial}{\partial x}\left[\frac{\mu_T}{\sigma_k}\frac{\partial \phi}{\partial x}\right]+\frac{\partial}{\partial y}\left[\frac{\mu_T}{\sigma_k}\frac{\partial \phi}{\partial y}\right]$$
$$+\underbrace{\left\{2\mu_T\left[\left(\frac{\partial u}{\partial x}\right)^2+\left(\frac{\partial v}{\partial y}\right)^2\right]+\mu_T\left(\frac{\partial u}{\partial y}+\frac{\partial v}{\partial x}\right)^2\right\}}_{P}-\underbrace{\rho\varepsilon}_{D}+G_{buoy} \tag{8.11}$$

where the generation term G_{buoy} relating to the buoyancy along the y direction can be formulated as

$$G_{buoy}=g\frac{\mu_T}{\sigma_T}\frac{1}{\rho}\frac{\partial \rho}{\partial y} \tag{8.12}$$

For the dissipation of turbulence kinetic energy ε, the modelled transport equation accounting buoyancy is given by

$$\frac{\partial(\rho\varepsilon)}{\partial t}+\frac{\partial(\rho u\varepsilon)}{\partial x}+\frac{\partial(\rho v\varepsilon)}{\partial y}=\frac{\partial}{\partial x}\left[\frac{\mu_T}{\sigma_k}\frac{\partial\varepsilon}{\partial x}\right]+\frac{\partial}{\partial y}\left[\frac{\mu_T}{\sigma_k}\frac{\partial\varepsilon}{\partial y}\right]+\frac{\varepsilon}{k}(C_{\varepsilon 1}P-C_{\varepsilon 2}D)+\frac{\varepsilon}{k}C_{\varepsilon 1}C_{\varepsilon 3}\max\left(G_{buoy},0\right) \tag{8.13}$$

From Eqs (8.11) and (8.12), the adjustable constants σ_T and $C_{\varepsilon 3}$ are usually specified as having values of 0.9 and 1.0, respectively.

To account for the heat transfer in the solid plate and air, the appropriate conservation equations for the solid and gas phases are solved. For the solid plate, the heat-conduction equation in two dimensions can be expressed as

$$\rho_s C_{ps}\frac{\partial T_s}{\partial t}=\frac{\partial}{\partial x}\left[k_s\frac{\partial T_s}{\partial x}\right]+\frac{\partial}{\partial y}\left[k_s\frac{\partial T_s}{\partial y}\right]+\dot{S} \tag{8.14}$$

where T_s is the solid-phase temperature and $\dot{S}$ is the internal volumetric heat source. The variables ρ_s, C_{ps}, and k_s are the thermophysical properties of the solid plate. For the gas phase, it is generally more preferable to solve the heat transfer through the thermal energy H. The two-dimensional governing equation for the enthalpy is given by

$$\frac{\partial(\rho H)}{\partial t}+\frac{\partial(\rho uH)}{\partial x}+\frac{\partial(\rho vH)}{\partial y}=\frac{\partial}{\partial x}\left[\left(\frac{\mu}{Pr}+\frac{\mu_T}{Pr_T}\right)\frac{\partial H}{\partial x}\right]+\frac{\partial}{\partial y}\left[\left(\frac{\mu}{Pr}+\frac{\mu_T}{Pr_T}\right)\frac{\partial H}{\partial y}\right] \tag{8.15}$$

Here, μ and Pr are the laminar viscosity and Prandtl number, whilst μ_T and Pr_T are the turbulent counterparts with values given as 0.7 and 0.9, respectively. The gas-phase temperature can be determined as a result of the solution obtained from the enthalpy equation (8.15). At the solid plate surface interfacing with the air, energy balance is invoked to obtain the surface or wall temperature, which entails

$$\underbrace{-k_s\left.\frac{\partial T}{\partial n}\right|_s}_{\text{solid phase heat flux}}=\underbrace{-k_g\left.\frac{\partial T}{\partial n}\right|_g}_{\text{gas phase heat flux}}+\underbrace{e\sigma\left(T_g^4-T_w^4\right)}_{\text{radiation heat flux}} \tag{8.16}$$

where σ is the Stefan-Boltzmann constant. The appropriate values for the emissivity e are required to evaluate Eq. (8.16); they are determined through experimental recordings of the thermal camera.

Because of the fine resolution imposed around the solid plate, the shear-stress transport (SST) turbulence model is utilized ahead of other many available turbulent models to resolve especially the low turbulent flow near the solid surface. This model actually represents a better alternative in bridging the wall with the bulk airflow when compared with the default usage of the logarithmic

wall function coupled with the standard k–ε model. Another important consideration of this flow problem is the need to incorporate the *radiation heat transfer* between the different viewing orientations of the solid boundaries and outer walls of the computational domain. Here, the Monte Carlo radiation model is applied to account for the radiation rays transmitted, primarily from wall to wall, within the domain.

CFD results: One important input parameter that is required for the present CFD calculations is the surface characteristic of the sold plate that is the surface emissivity. During the experiments, a plate model at a low emissivity of 0.1 was exposed to water at a power of 25 W over 3 days. The growth in the aluminium oxide layer resulted in an increased emissivity to a range of 0.3–0.5 as measured by the pyrometer. As a conservative approximation, an emissivity of 0.3 is adopted in the CFD simulations. Based on the power of 25 W, the internal volumetric heat source $\dot{S}$ appearing in Eq. (8.15), considering the region encompassing the heating elements inside the solid plate that comprises a rectangular prism with a volume of 2.76×10^{-5} m^3 (0.005 (thickness) $\times$ 0.024 (width) $\times$ 0.23 m (length)), can be evaluated to yield a power density of 9.058×10^{-6} W/m^3 (25 W/2.76×10^{-5} m^3). A transient simulation is performed, and convergence is deemed to have been reached within each time step when the normalized residuals fall below the criteria of 1×10^{-5}.

The experimental streamline of smoke traces observed during experiments is depicted by the photograph in Fig. 8.20. To determine the velocities, smoke seeding used to permit visualization of the convection flow allowed velocities to be measured at the specific locations around the plate using imaging and LDV techniques as indicated in Fig. 8.28. Table 8.4 shows the comparison between these measured velocities and predictions made by the computational model. The close agreement between the measured and predicted velocities validates

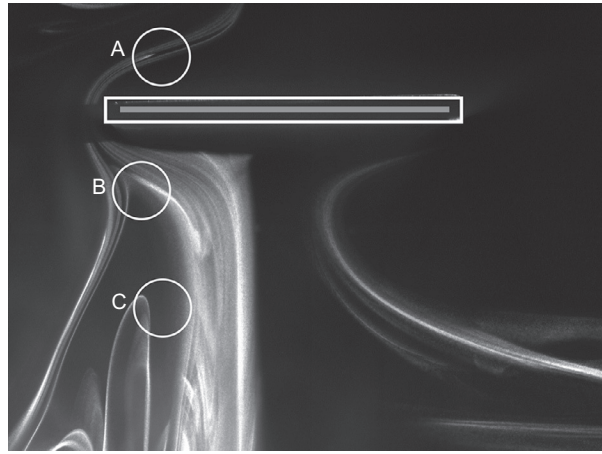


FIG. 8.20 Experimental streamline of smoke traces.

TABLE 8.4 Comparison Between Predicted and Measured Velocities at the Specific Locations Highlighted in Fig. 8.20

Location	Measurement	Prediction
A	100 mm/s	108.4 mm/s
B	35 mm/s	32.4 mm/s
C	15 mm/s	12.2 mm/s

and verifies the numerical models to aptly resolve this flow problem. The adopted models also provide confidence in the usage of CFD methodology to tackle the complex processes associated with conjugate and radiation heat transfer.

Fig. 8.21 illustrates the temperature contours predicted inside the solid plate and the surrounding air enveloping the solid plate accompanied by the velocity vectors around the solid plate. For the latter, the predicted flow pattern shows remarkable resemblance with the observed streamline in Fig. 8.20 where the flow appears to be biased towards the left of the solid plate. Cool air is seen being entrained from some distance away onto the solid plate and is heated whilst flowing around the solid plate. A strong upward buoyant thermal plume is generated as confirmed by the temperature contours and velocity vectors. Since aluminium is a very good conductor, there is essentially no appreciable difference of temperatures that can be found within the solid plate and on the solid walls. For the current CFD simulation, a uniform temperature of 164.5°C is predicted for the entire solid region as indicated by the red colour temperature contour. The blue colour temperature contour depicts the surrounding temperature at 25°C.

Calculations without the additional consideration of radiation heat transfer were also performed to ascertain whether it has a significant influence on the

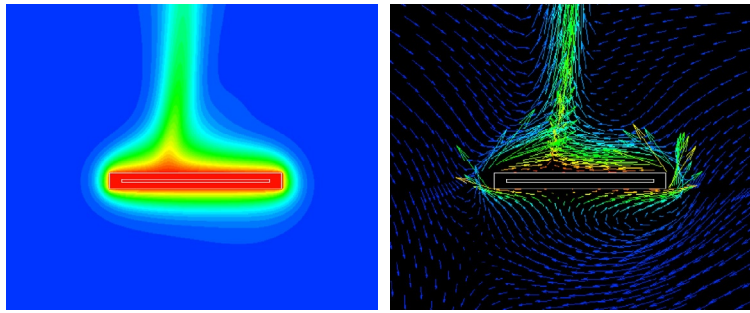


FIG. 8.21 Temperature contours showing the surrounding and internal temperatures and velocity vectors around the solid plate.

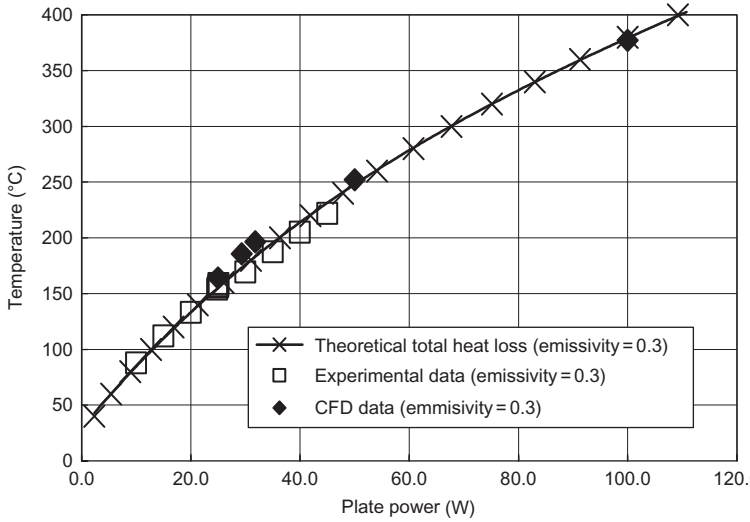


FIG. 8.22 Distribution of temperature inside and around the solid plate.

numerical solution. The simulation revealed a solid temperature of around 300°C, which is considerably higher from the case with radiation heat transfer. *Which of these two temperatures are the correctly predicted values*, *and most importantly*, *which of them actually reflect reality*? Let us ponder the implication of these two computational results. During experiments, rigorous measurements have repetitively found erring towards a lower temperature of approximately 159°C. Through this, it is clear that the need to accommodate additional sophistication to the CFD modelling by accounting radiation heat transfer is essential to yield CFD results corresponding to the actual physical flow processes. Also, radiation heat loss measured during experiments accounts for almost 40% of the total heat emission from the solid plate, which further fuels the need to aptly incorporate the effect of radiation heat transfer into the CFD modelling.

Additional CFD calculations on different power settings ranging as high as 100 W with the same emissivity value of 0.3 are illustrated in Fig. 8.22. The close agreement of the predicted temperatures against the experimentally measured data and the analytical total heat loss expression based on Incropera and DeWitt (1985) further confirms the application of models to adequately resolve the flow- and heat-transfer characteristics of this particular flow problem.

8.4.2 A Buoyant Free-Standing Fire

As evidenced through experiments performed by McCaffrey (1979), Cox and Chitty (1980), buoyant fires can be distinguished into three distinct regions:

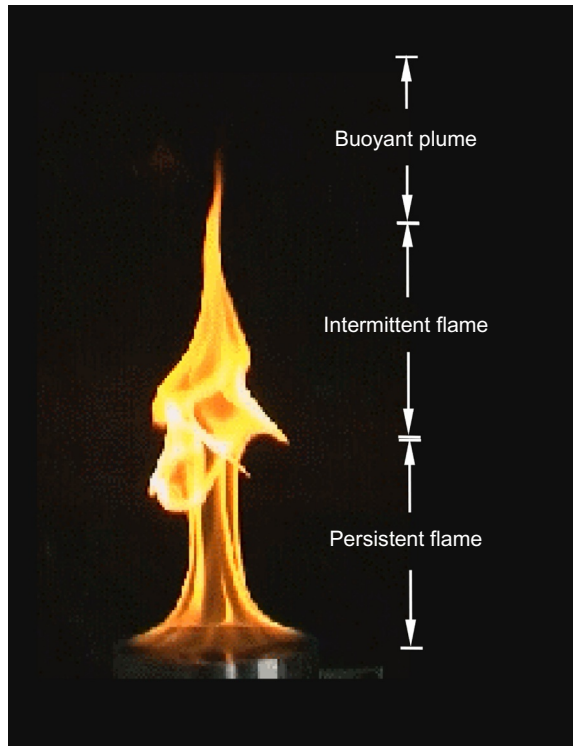


FIG. 8.23 A photographic image of a buoyant fire.

a persistent flame, *an intermittent flame*, and *a buoyant plume*. Fig. 8.23 exemplifies a typical three-zone flame structure for a buoyant fire (Cheung et al., 2007).

Buoyant fires are generally characterized by a very low initial momentum, and they are strongly governed by buoyancy effects. It is also recognized that such fires exhibit an oscillatory behaviour. The occurrence of this oscillation, generally known as the 'puffing' effect, stems from the presence of coherent structures above a fire plume. These structures are a consequence of the developing buoyancy-driven instabilities, which subsequently leads to vortex shedding especially through the formation of large flaming vortices that rise up until they burn out at the top of the flame. The pulsating characteristics of such fires are strongly governed by the rate of air entrainment into the flame, flame height, combustion efficiency, and radiation heat output of the flames. Simulating such fires can be rather challenging.

According to McCaffrey (1983), the 'puffing' mechanism can be described as follows. The initial momentum and buoyancy of combustion gases in stagnant air sets a large toroidal vortical structure. The entrainment of air is assisted into the reaction zone that causes the combustion gases to accelerate, creating the

characteristic 'necking'. As the vortex propagates upwards, it leaves an area of low pressure that is immediately filled by the combustion gases, creating a 'bulge'. This bulge rises resulting in the formation of another toroidal vortex at the base of the fuel source. The vortex below the bulge shifts the plume surface outward in the radial direction, whilst the bulge above drags the plume surface inwards. Hence, the bulge structure is maintained. The rotational motion in the upper vortex causes the plume to be stretched in the axial direction. This periodic oscillation is usually referred to in the literature as the pulsation frequency of the flame-flickering phenomenon. Pulsation frequencies for buoyant diffusion flames have been reported by many researchers (Portscht, 1975; Zukoski et al., 1984) with Malalasekera et al. (1996) providing an excellent review.

CFD simulation: The turbulent buoyant fire is solved using an in-house large-eddy simulation (LES) computer code to examine the coupled turbulence, combustion, soot chemistry, and radiation effects. The three-dimensional, Favre-filtered, compressible mass, momentum, energy and mixture fraction and its scalar variant conservation equations are closed using the LES Smagorinsky subgrid-scale (SGS) turbulence model. The numerical method is based on a two-stage predictor-corrector approach for low-Mach-number compressible flows to account for the strong coupling between the density and fluid flow equations. The infinitely fast chemistry approach is adopted as the combustion model. A combination of a presumed beta-filtered density function and a conservation equation for the scalar variance is used to account for the SGS mixture fraction and scalar dissipation fluctuations on the filtered composition and local heat release rate. A soot model incorporating nucleation and surface growth agglomeration is considered. The radiation heat transfer has been accommodated through the discrete ordinates model. More details regarding this model can be found in Cheung et al. (2007).

A three-dimensional computation is performed on a designated $3 \times 3 \times 3$ m domain. The gaseous fuel is injected through a porous square burner on the floor level with dimensions of 0.3×0.3 m. A structured mesh totalling $96 \times 96 \times 96$ cells is generated for the computational domain. Transient analysis is performed with about 27500 time steps. To ensure that the analysis achieves stability and a pseudo-steady-state status, a simulation of 35 s in real time is used, which by employing a Pentium IV PC with a speed of 3.0 GHz and 2.0 GB RAM, the CPU time for a real 35 s simulation are of the order of 400 h in order to ensure that it achieves stable and pseudo-steady-state status.

CFD results: Fig. 8.24 illustrates a series of frames capturing a flickering period comparing the macroscopic predictions using the LES approach against the photographic images obtained from McCaffrey (1979) experiments. The naturally flickering behaviour demonstrates the flow undergoing a phase shift along the axial direction. Numerically predicted images in Fig. 8.25 correspond to three isometric surfaces of temperatures at 800 (visible flame), 450, and 310 K (cold smoke). Two distinct regions of the flame that comprise the upper flame separated from the lower persistent flame depicted in frames 1 and 8 by

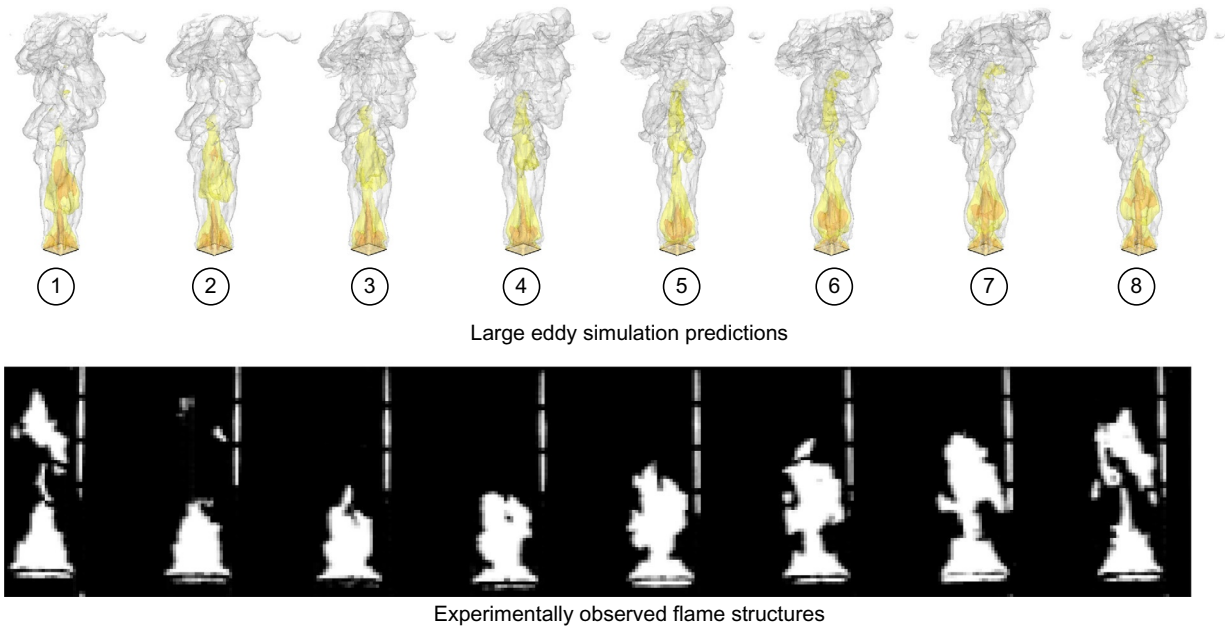


FIG. 8.24 Demonstration of the puffing effect during one flickering cycle.

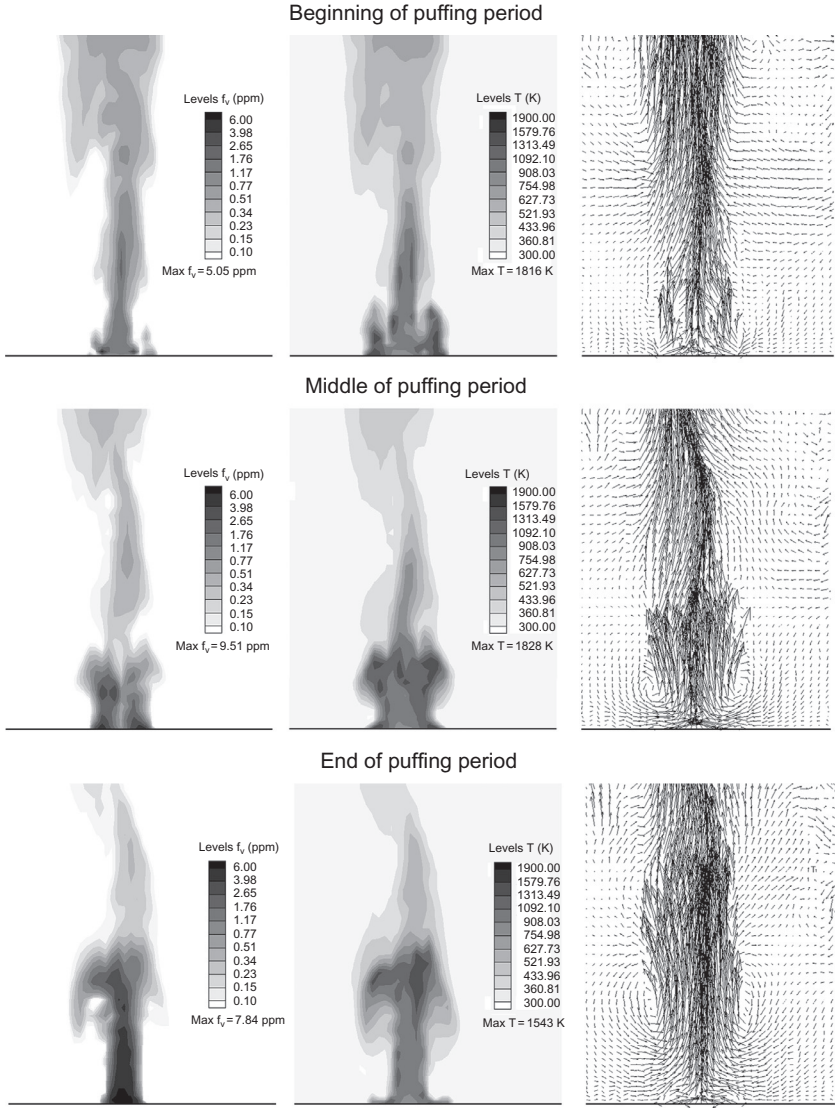


FIG. 8.25 Distribution of instantaneous soot distribution accompanied by the temperature contours and velocity vectors during one puffing period.

the numerical model show remarkable resemblance to the associated frames of the photographic images. The surging upward flame structures in frames 6 and 7 before flame separation in frame 8 are also adequately captured by the model when compared with the corresponding images of the developing fire observed during experiments.

The radiative cooling due to soot is demonstrated through the instantaneous soot distribution accompanied by the temperature contours and velocity vectors shown in Fig. 8.25. Buoyant diffusion flame behaves rather differently from jet diffusion flame. At the beginning of the puffing period, soot is formed at the outer fringes of the fire bed where the meeting of the fuel and air is ideal. Owing to the self-excited toroidal vortex motion above these fringes, the soot being formed is found to be entrained in the continuous flame region, which is then carried upwards during the middle and end of the puffing periods. The peak soot content is located predominantly in the middle portion of the continuous flame region for the buoyant fire; the temperature is thus subsequently lowered due to soot radiation.

8.4.3 Flow Over Vehicle Platoon

In order to meet the surging consumer's demand and to reduce cost and time to market, automobile manufacturers are progressively aiming to develop more economical, safer, and comfortable vehicles at an increasingly rapid pace. Traditional wind-tunnel testing can be expensive to build, and road-testing techniques may take long development cycle times. To overcome these difficulties and to maintain a competitive market edge, automotive manufacturers need to focus on computational techniques such as the emergence of computational fluid dynamics. Nowadays, CFD and model scale tests are often used in car development with full-size wind tunnels used for validation and refinement for global simulation of the entire flow field rather than for extensive parametrical studies as found in the current industrial practice (Hucho, 1996).

As the human population continues to grow, the need for more practical and efficient methods of transportation becomes evermore vital. The primary aim of the future generation intelligent transport system (FGITS) is to establish a platoon of vehicles with significantly reduced intervehicle spacing on the highway. By this system, it is expected that the aerodynamic efficiencies of the individual vehicles will be improved since their drag coefficients are expected to be reduced with close vehicle spacing. Overall, fuel efficiencies of vehicles in platoon can also be realized with reduced emission levels and added safety. Vehicles would be equipped with intelligent transport systems (ITS) such as distance sensors, antilock breaking system (ABS), global positioning systems (GPS), and other ITS systems that would enable the vehicles to travel close together *safely* (e.g. less than one car length), closely resembling a convoy of train carriages. However, before such systems can be implemented, a detailed understanding of how these vehicles would behave aerodynamically when in close proximity to one another is required. CFD can play an important role in conducting significant aerodynamic research associated with various forms of vehicle-to-vehicle interference.

Problem considered: The Ahmed model geometry as shown in Fig. 8.26 is a generic automotive bluff body with the backlight (slant) region configurable

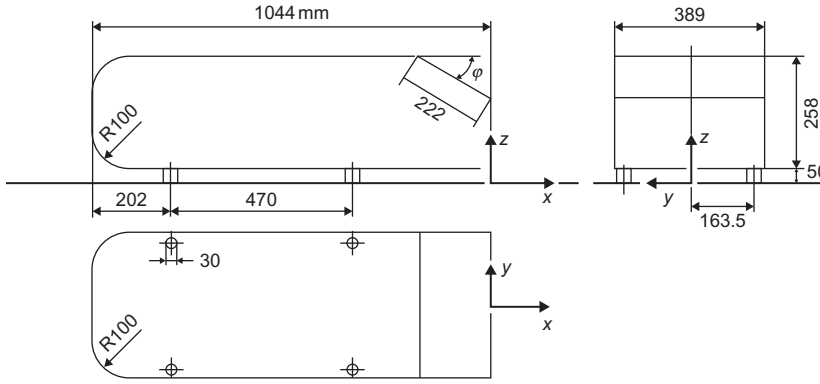


FIG. 8.26 The Ahmed car geometry.

through various angles. Despite the relatively simple geometry, the model is capable of replicating dominant flow structures pertinent to those generated about the C-pillar of a practical road car.

The experiment representation of two vehicles in tandem considered in this example is illustrated in Fig. 8.27. They are placed inside a closed-jet, fixed ground wind-tunnel facility, having a test section of 2 m high, 3 m wide, and 9 m long. Two Ahmed models, a lead model (75% scale model) and a trailing model (100% scale model) with 30° rear slant angles, are positioned at different intervehicle spacing, which is varied according to the length of the 100% scale model ($L = 1.044$ m). The intervehicle spacing is varied between 0.25 and 2 L. The free-stream velocity is set at 30 m/s corresponding to a Reynolds number of 1.55×10^6 based on 75% of the scale Ahmed model length. Free-stream turbulence intensity is maintained at 1.8%; the blockage ratio is less than 2%, which is not corrected for in the study.

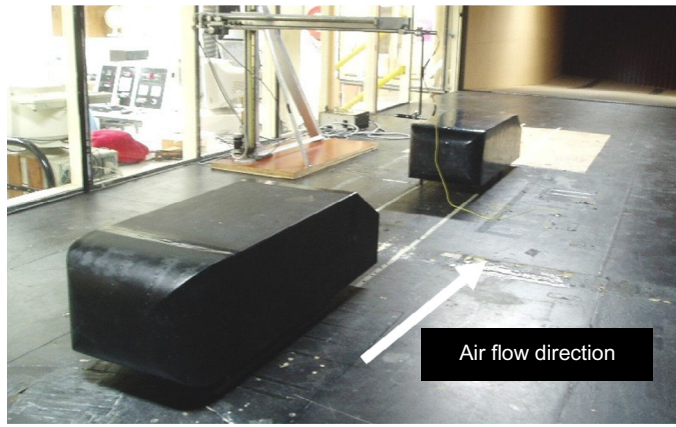


FIG. 8.27 Two Ahmed vehicles in tandem inside a wind-tunnel facility.

To obtain the correlation between the flow structure and forces exerted on the trailing model, time-averaged lift and drag measurements are taken at each model position. This is achieved through a JR3 six-component force balance sensor that has been mounted inside the lead (75% scale) test model. The arrangement is shown in Fig. 8.28. More details on the experimental setup and the CFD model to be discussed below can be found in Rajamani (2006).

CFD simulation: The computational domain that comprises a section of the wind-tunnel configuration is shown in Fig. 8.29. Within this figure, the enlarged view illustrates the lead and trailing Ahmed model vehicles. The total length of

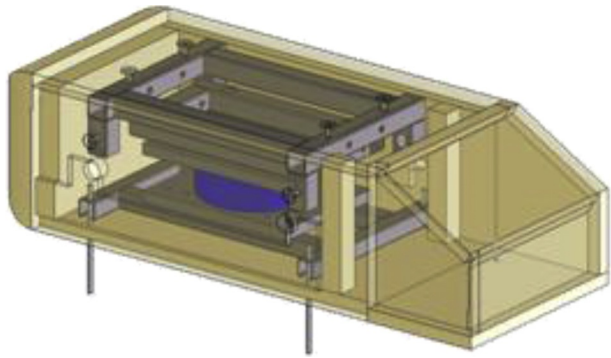


FIG. 8.28 Internally mounted force balance arrangement for the lead model.

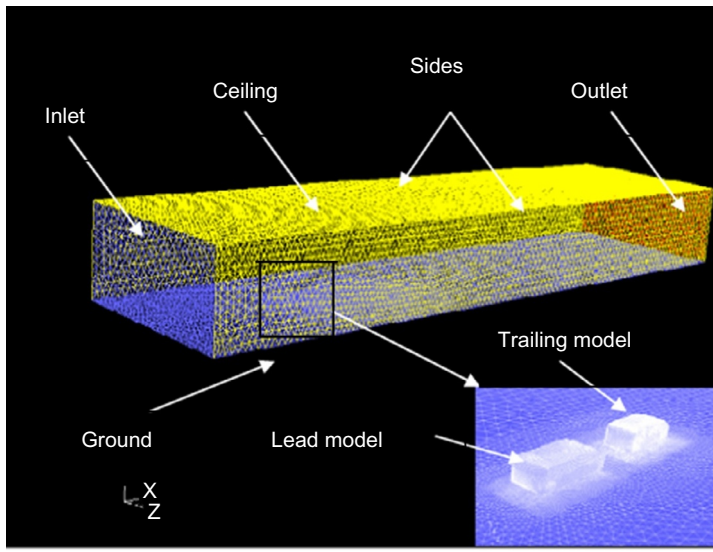


FIG. 8.29 Computational domain comprising of the lead and trailing Ahmed vehicles models inside a section of the wind tunnel.

the test domain is 13 L. The inlet is positioned 4 L from the front of the lead model. The outlet was positioned 8 L from the rear of the trailing model. The sides were 2 L on either side from the full-scale model, whilst the ceiling is 2.5 L from the top of the full-scale model. The lead model is located 0.0375 m from the ground, and the trailing model was positioned 0.05 m from the ground in both the experimental and computational investigations.

An unstructured mesh consisting of tetrahedral elements totalling over 1.8 million cells is generated to accommodate all the necessary geometrically intricate details. The simulation of the turbulent flow is handled through the commercial CFD code ANSYS FLUENT, version 6.1.22. Realizable k–ε model is chosen as the preferred turbulence model for this particular flow problem. To satisfy mass conservation, the SIMPLE algorithm is adopted to establish the linkage between the velocity and pressure, whilst a multigrid solver is employed to accelerate the numerical calculations towards the steady-state solution. Convergence is deemed to have been reached when the residual mass falls below a value of 1.0×10^{-5}.

CFD results: The case for the critical rear slant angle of 30 degrees, after Ahmed et al. (1984), is used to validate the CFD results for the case of an isolated model. For the two models in tandem, however, this case has been compared with the experimental data of Vino et al. (2004). The predicted drag coefficient for the isolated Ahmed model as shown in Fig. 8.30 is seen to agree rather well against experimental measurements of Ahmed et al. (1984) and Vino et al. (2004). Despite some discrepancies between the predicted and measured drafting effects on the coefficient of drag especially at low intervehicle spacing

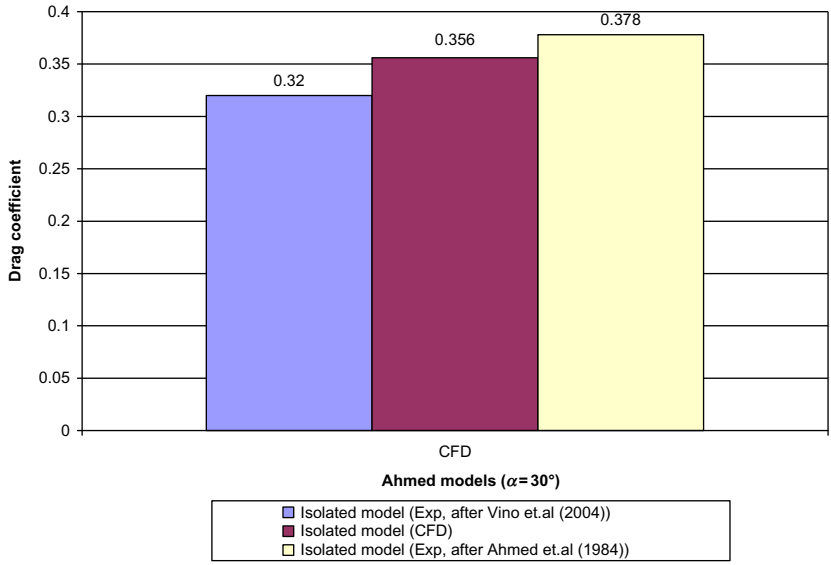


FIG. 8.30 Comparison of drag coefficients for an isolated Ahmed model.

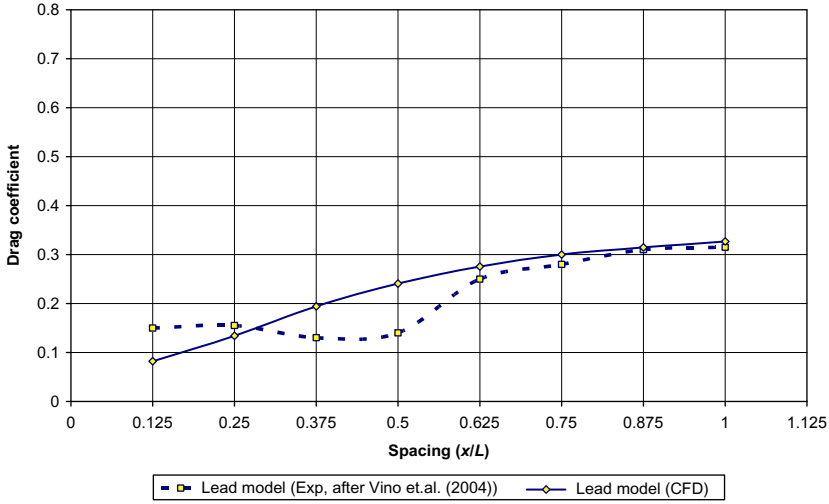


FIG. 8.31 Effects of intervehicle spacing on the lead model.

for the case of two vehicles in tandem as illustrated in Fig. 8.31, the predicted values are nonetheless still in close agreement with experiments.

The 30 degrees rear slant angle of the Ahmed model is often considered as the most critical angle (Ahmed et al., 1984), since any slight decrease or increase in the angle would considerably reduce the drag coefficients. In this particular configuration, the separation bubble, which is caused by flow separation at the slant side, reaches its maximum size at this critical angle—one of the main reasons for its high drag coefficient. This high drag regime is mainly characterized by the presence of strong counter-rotating C-pillar vortices that are rich in kinetic energy as shown in Fig. 8.32 where the colour spectrum indicates the highest value with red and the lowest value with blue.

At very close intervehicle spacing as demonstrated by the case of $x/L = 0.25$ in Fig. 8.33, the drag coefficient of the lead model is considerably lower when compared with that of the trailing model. This effect is caused by the apparent presence of another model in its wake. The mere presence of this trailing model increases the base pressure of the lead model, which subsequently reduces the

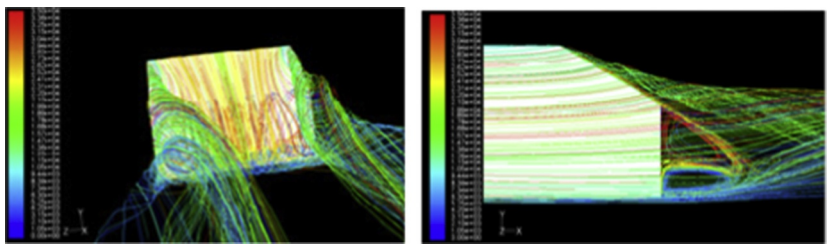


FIG. 8.32 High drag configuration—critical angle of 30 degrees.

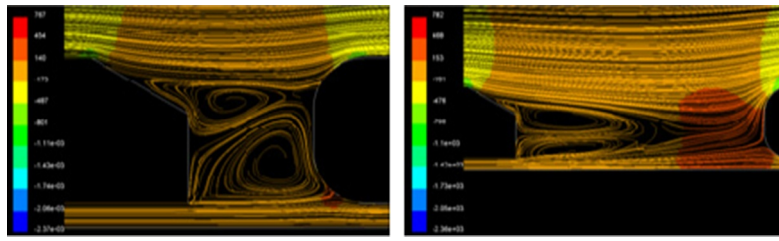
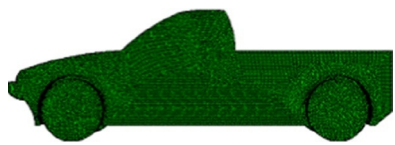


FIG. 8.33 Pressure pathlines between intervehicle spacing.

drag of the lead model. The flow that separates from the leading edge of the rear slant of the lead model also creates a flow impingement on the front portion of the trailing model. This effect increases the drag coefficient of the rear model, which can be observed from the pathlines of pressure in Fig. 8.33. At an intervehicle spacing of $x/L = 1$ (see also in the same figure), the trailing model's drag coefficient reaches its peak value; the increase in drag is caused by the very high flow impingement.

CFD is also well suited to analyse a wide range of shape options. These simulations are particularly useful in predicting trends of considering different design configurations that can affect the flow-field features of vehicles. A CFD simulation also permits investigations that at some circumstances cannot be realistically duplicated in a wind tunnel. Let us consider the 25% scaled model of Ford Falcon EXT 2003 model with model dimensions given in Fig. 8.34. The model is considered to be a bluff model that produces the basic flow structures of a pickup truck. Information on the side rear-view mirrors, bull bars, engine components, and underbody information is not included. The test velocity is 40 m/s with a model-length-based Reynolds number of 3.3×10^6.

The effects on the drag coefficient are analysed. The rear tub is left opened for this current case. A drag coefficient of 0.44 is predicted, which shows an immediate increase from a value of 0.38 if the rear tub is closed. With the rear tub exposed, the formation of a large recirculation flow region behind the cab is evident as illustrated in Fig. 8.35. The flow pathlines are coloured according to the static pressure where the highest pressure is depicted in red and lowest by blue. Along the symmetry plane as represented in the same figure, the pressure drop is comparatively high in the vicinity of the cab-tub region.



Model information

Length = 1.2 m
Height = 0.12 m
Width = 0.432 m
Ground clearance = 0.06 m

FIG. 8.34 Pickup truck model information.

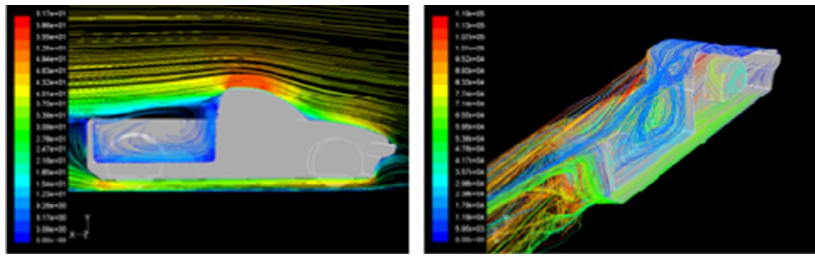


FIG. 8.35 Recirculation region of open tub configuration of pickup truck.

8.4.4 Air/Particle Flow in the Human Nasal Cavity

An alternative to oral and injection routes of delivering systemic drugs for a variety of diseases is through nasal drug delivery. The many advantages associated with such delivery are well documented and one of which is a viable treatment for respiratory ailments such as congestion and allergies. One aspect that still concerns the prescription of such treatment is the availability of useful particle deposition information within the nasal cavity that can significantly improve the effectiveness of a nasal sprayer device to deliver the drug to specific targeted sites within the human nasal cavity.

Current in vivo and nasal cavity replica methods are usually rather limited in the scope of more intensive studies because of their intrusiveness and being very time-consuming and expensive in implementation. Nevertheless, the accessibility of rapid computers to perform numerous numerical analyses such as the repeatability and accuracy of a nasal spray injection released from the same location with quick turnaround times, and possibly extending a wider range of investigations, has certainly revolutionized how medical research can be carried out nowadays. Advanced application of CFD is certainly gaining enormous interest as evidenced in Keyhani et al. (1995), Yu et al. (1998), and Hörschler et al. (2003). With the aid of graphical representations of the local particle deposition sites, particle and airflow paths, velocity contours, and vectors at any location, detailed critical assessments can be obtained on the effectiveness of delivery for a particular nasal sprayer device being tested.

Spray particle deposition can be ascertained through several parameters:

(1) Gas-phase flow field such as velocity and turbulence effects
(2) Deposition mechanisms involving the interaction between particles and its continuum
(3) Material properties of the particle and initial spray conditions such as particle density, size, and spray cone angle.

Knowledge of the fluid flow field allows prediction of the particle dispersion and deposition. The construction of the complex nasal cavity geometry needs to be appropriately managed for CFD simulations before calculations can proceed. This has been addressed in detail by Inthavong et al. (2006), and some

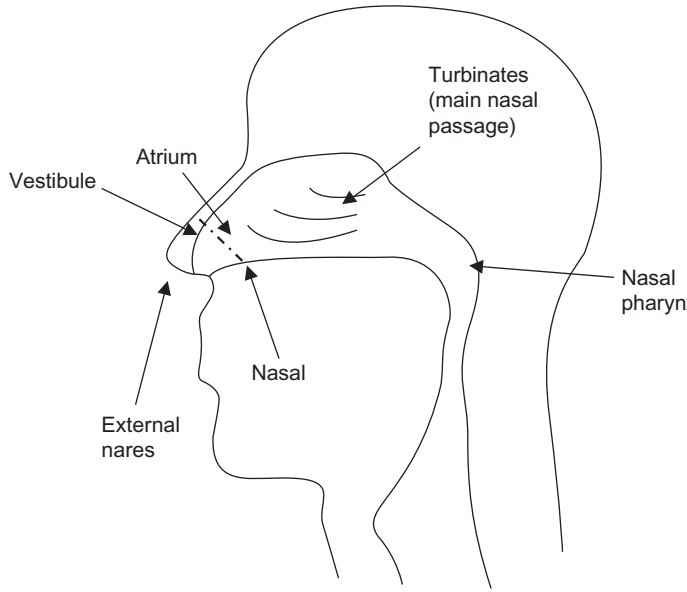


FIG. 8.36 Schematic drawing of the human nasal cavity.

pertinent practical aspects concerning the geometry construction are discussed below.

Problem considered: The schematic drawing of the human nasal cavity is illustrated in Fig. 8.36. Constructing the complex geometrical model of a human nasal cavity is a very challenging task. Slices of three-dimensional CT scan image are taken at various positions from the entrance of the nasal cavity to the anterior of the larynx. The image analysis data obtained consist of *xyz* coordinates of the airway perimeters for cross-sections spaced at intervals of 1–5 mm apart depending on the topography of the anatomy.

Through the solid modelling tool GAMBIT—the preprocessor facility of the CFD commercial code ANSYS FLUENT, version 6.1.22—a computational mesh as illustrated in Fig. 8.37 is generated enveloping the entire anatomical geometry. The reader should take note that the mesh generation step presents the most labour-intensive component of the entire simulation process because of the requirement to appropriately mesh the intricate surface topology of the airway geometry. A denser mesh distribution is concentrated near the surface boundaries to better resolve the large velocity gradients of the airflow.

A preliminary model is created with a total mesh cell of 82,000. This coarse mesh provides a basis whereby enhancements are further performed to address grid quality criteria such as cell skewness, resolution in the vicinity of the cavity wall, and cell-to-cell volume change. Three further meshes are generated—286,000, 586,000, and 822,000 cells—to check for grid independency. The reader should be well aware that accuracy of computed results increases with

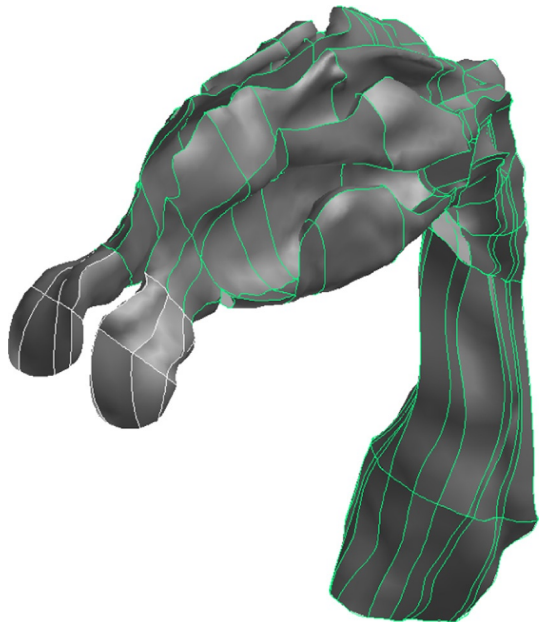


FIG. 8.37 Construction of surface topology of the human nasal cavity through CT scan.

finer mesh but at higher computational costs. Carrying out a grid independence test allows an optimum mesh grid size to be ascertained. The Navier-Stokes equations for the gas phase are solved at a flow rate of 20 L/min. Fig. 8.38 shows the velocity profiles for different mesh densities. It is observed that a mesh of 586,000 cells exhibits no further improvement from a much denser mesh of 822,000 cells. The nasal cavity model with 586,000 cells is thus accepted to be sufficient for current simulation purposes and is used for generating the results below.

CFD simulation: The solution of the flow field representing the continuum gas phase under steady-state conditions is achieved by solving the full Navier-Stokes equations. These equations are discretized using the finite-volume approach. The *QUICK* scheme is used to approximate the momentum equation, whilst the pressure–velocity coupling is realized through the SIMPLE method. According to Tu et al. (2004a,b), the flow velocity inside the human nasal cavity can reach as high as 22 m/s. This suggests that the flow is turbulent, which is also confirmed by Keyhani et al. (1995) and Yu et al. (1998) where the k–ε turbulence model has been used for flows around 200–300 mL/s. This two-equation approach is the most commonly used turbulence model, based on the assumption of isotropic turbulence and a single eddy viscosity for all three components of the velocity vector. This can nonetheless cause inaccuracies for flows with high swirling action where the turbulence is apparently anisotropic.

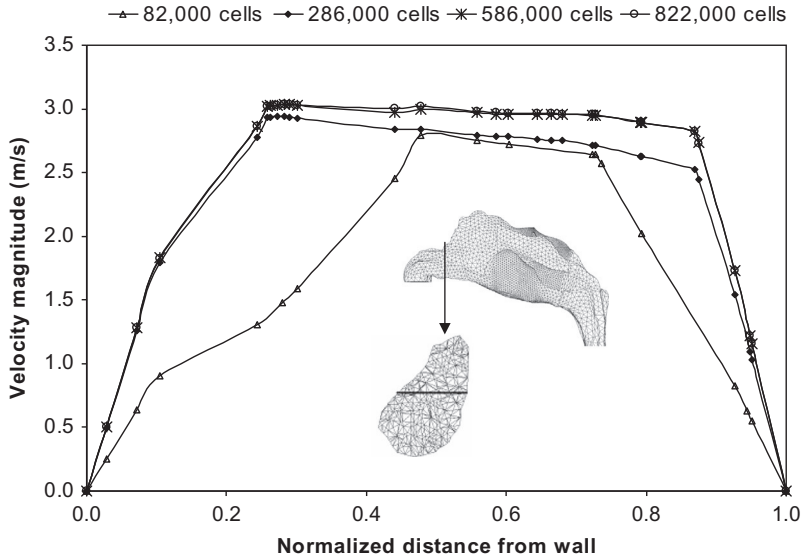


FIG. 8.38 Velocity profiles of a coronal section near the nasal valve region for the four different nasal cavity models.

For flows in the nasal cavity that exhibit low levels of swirl, the k–ε approximation should be deemed to be sufficient given the low computational costs compared with more sophisticated approaches such as large-eddy simulations and Reynolds stress model. In this example, the realizable k–ε model proposed by Shih et al. (1995) is adopted. For the particle dispersion, a Lagrangian particle tracking method is used to track the migration of particles within the nasal cavity.

The human nasal cavity is subjected to constant airflow rates of 20–40 L/min. The internal walls are modelled using an enhanced wall treatment function to consider the nonslip condition on the airflow. The particles are assumed to be spherical water droplets since most drug formulations can be considered as diluted with water. Initial particle conditions are taken from analytical methods due to the lack of experimental data. The conditions for the release of particles into the constant flow rate differed for the parameter under investigation and will be elucidated upon later. The internal walls of the nasal cavity are set according to a 'trap' condition meaning that particles that touch a wall deposit at that location.

Appropriate boundary conditions for the particles are specifically chosen to simulate a number of realistic situations. Physically speaking, the initial particle velocity can be controlled in many ways such as changing the nozzle diameter and the actuation mechanism. The full spray cone angle, β, characterizes the internal atomizer type of the spray device. A small β generally refers to a narrow spray that is typical of plain orifice atomizers. However, a larger β depicts a

wider spray that belongs to the family of pressure-swirl atomizers. This angle is analysed to simulate the dispersion of particles exiting from the nozzle tip from a nasal spray device to observe the physical differences with changing β. Monodispersed particles are released, and the average deposition within the left and right nasal cavity is recorded. Particles are released at 10 m/s from an internally fixed location with a diameter of 0.8 mm and a range of β between 20 and 80 degrees.

CFD results: The airflow characteristic within the human nasal cavity with a total airflow rate of 20 L/min through both nostrils is illustrated in Fig. 8.39A and B. Noting that the colour red indicates the highest speed and the colour blue for the lowest speed, the airflow increases at the nasal valve where the cross-sectional area is known to be smallest and reaches a maximum area-averaged velocity of 2.28 m/s from an initial uniform inlet velocity $u_{in} = 2.1$ m/s. The velocity subsequently decreases as the nasal cavity expands. It can be observed that the bulk of the airflow remains within the middle and lower regions of the nasal cavity, close to the septum walls, rather than diverging outwards. A region

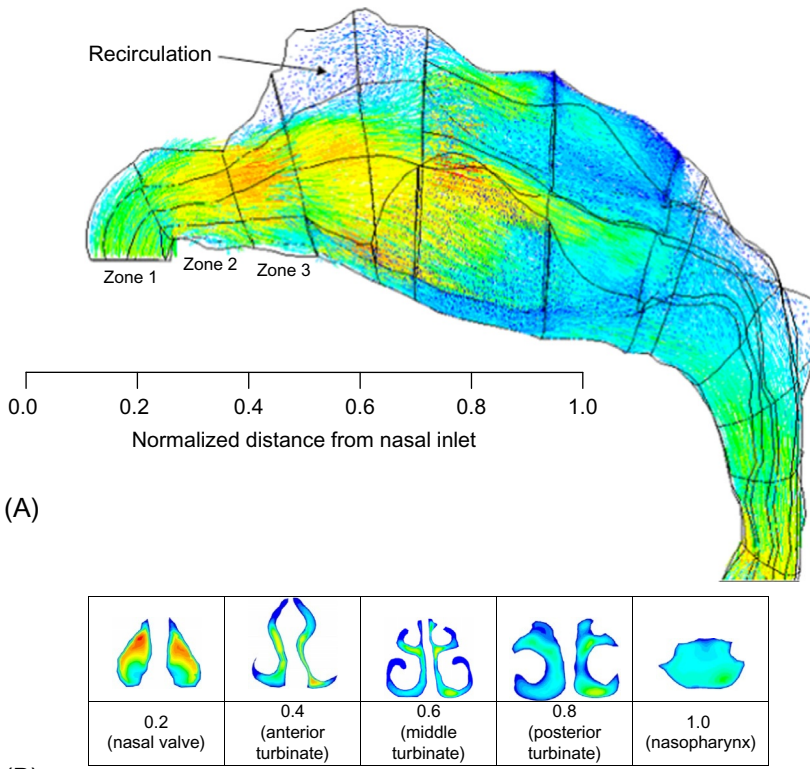


FIG. 8.39 Velocity distribution within the human nasal cavity—(A) vector field in the horizontal plane and (B) velocity contours at different cross-sections.

of recirculation appears in the expanding region near the top of the olfactory region. At the nasal pharynx, the velocity increases due to the smaller flow area. Such complex flow patterns for the single-phase airflow have been confirmed through a number of prominent numerical studies as evidenced in Zwartz and Guilmette (2001) and Hörschler et al. (2003). The reader may wish to refer to these important works to supplement his/her understanding.

For the study on the different full spray cone angle β affecting the particle distribution, the smaller ranged particles that follow the gas-phase velocity more readily are optimized when released with a narrow β than a wider β as the latter gives rise to a larger range of dispersion of particles due to the nature of a 360 degrees spray cone. The larger dispersion creates a low ratio of favourably dispersed particles (those pointing with the flow) to those being dispersed away from the curvature (i.e. in the opposite direction) of the gas flow. The effect becomes more apparent as the particle size increases. Fig. 8.40 shows the flow for 15 μm being centralized when $\beta = 20$ degrees and the increase in deviation from the centre when $\beta = 80$ degrees. Deposition for $\beta = 20$ degrees remains along the roof of the nasal cavity and near the septum walls with

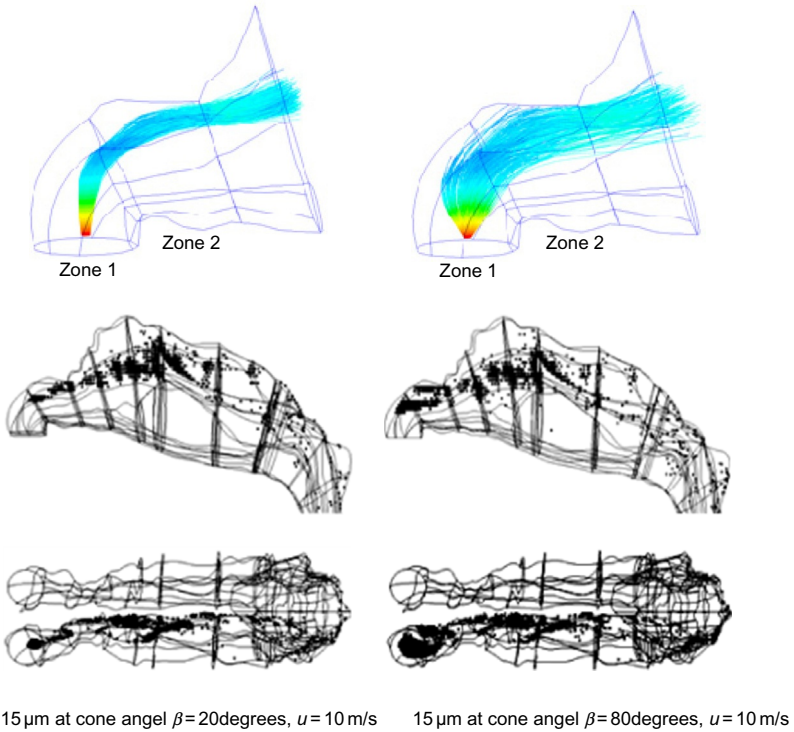


FIG. 8.40 Deposition patterns for 15 μm particles released at 10 m/s from a small internal diameter at 20 and 80 degrees spray cone angles.

28% deposit in the first two zones. At $\beta = 80$ degrees, deposition in the two frontal zones has increased to 47%. Note that the colour spectrum in Fig. 8.40 and in Fig. 8.41 of the particle flow trajectories indicates the velocity magnitude.

Fig. 8.41 compares the two deposition patterns for particles of 20 μm at $\beta = 20$ degrees and $\beta = 80$ degrees. A number of parametric investigations have revealed that 20 μm size particles result in almost 100% deposition in the front two zones. By increasing β, more particles are dispersed favourably by projecting the particles into the already curved streamlines, thereby allowing them to travel further downstream along the nasal cavity. At $\beta = 20$ degrees, impaction occurs at the roof of the vestibule directly above the injection release point in a concentrated area. When $\beta = 80$ degrees, a wider area of deposition is observed in the frontal zones where these particles projected favourably towards the nasal valve are able to travel beyond the 90 degrees bend. However, deposition eventually occurs within the middle sections of the nasal cavity due to the higher particle inertia.

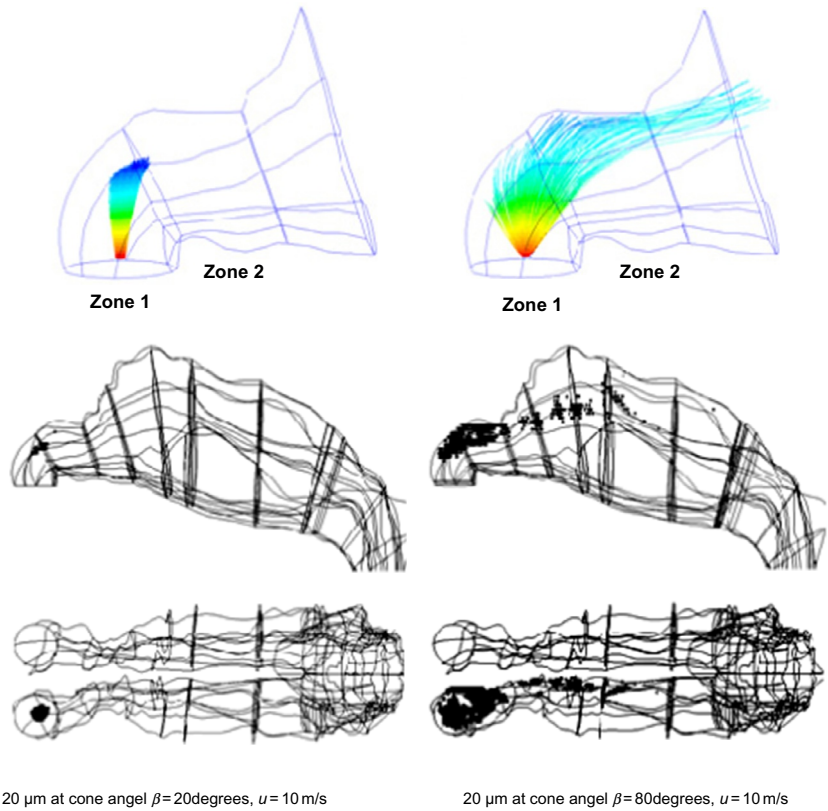


FIG. 8.41 Deposition patterns for 20 μm particles released at 10 m/s from a small internal diameter at 20 and 80 degrees spray cone angles.

8.4.5 High Speed Flows

All the examples demonstrated above have thus far concentrated where the application of CFD pertains only to *subsonic* flows—flows below the velocity of sound. The velocity of sound or sonic velocity is an important consideration in fluid mechanics. At *subsonic* velocities, small pressure waves can be propagated from both upstream and downstream. Nevertheless, when the velocity of fluid exceeds the sonic velocity, the fluid flow becomes *supersonic*, and small pressure waves cannot be propagated upstream. Many numerical investigations in the aerodynamic and aerospace fields, the genesis of most CFD methods and techniques, involve *supersonic* fluid flows. The ratio of the fluid velocity to the sonic velocity is generally known as the dimensionless Mach number (*Ma*). If Mach number > 1, flow is *supersonic*; if Mach number < 1, flow is *subsonic*.

With the aim of providing the same genre of guidelines as for the examples of *subsonic* flows above, two examples of *supersonic* flows over a simple flat-plate geometry and complex NACA0012 wing configuration are demonstrated within this section. Salient aspects particularly in obtaining practical solutions for high-speed flows are described below.

8.4.5.1 Supersonic Flow Over a Flat Plate

Supersonic flow over a flat plate is a classical *boundary-layer* fluid dynamics problem. Despite its simplicity, an exact analytical solution remains *absent* for the fluid flow over this simple geometry. Consider the supersonic flow over a thin sharp flat plate at zero incidence and of length L as sketched in Fig. 8.42. As the free-stream fluid approaches the flat plate, a boundary layer develops at the leading edge of the flat plate. It is noted that the boundary layer is taken as the region of fluid close to the surface immersed in the flowing fluid. Away from the leading edge, the free-stream fluid no longer 'views' the sharp flat plate, but rather, a fictitious curvature is formed due to the presence of the viscous boundary layer. If the Reynolds numbers are based on the distance from the leading edge of the plate, it can be appreciated that, initially, the value is low so that fluid flow close to the surface may be categorized as *laminar*. However, as the distance from the leading edge increases, so does the Reynolds number until a point must be reached where the flow regime becomes *turbulent*. In practice, the transition does not occur at one well-defined point, but rather, a transition zone is established between the laminar and turbulent flow regimes as shown in Fig. 8.42. As also illustrated in the same schematic illustration, a curved induced shock wave is generated at the leading edge, and the *shock layer* encapsulates the inviscid and viscous flows. In addition, *viscous dissipation* (dissipation of kinetic energy within the viscous flow) can cause high flow-field temperatures; high heat-transfer rates are thus attained within the boundary layer.

Problem considered: In this particular example, the reader will gain an understanding of the flow physics through solving the complete Navier-Stokes equations. The flow over a flat plate is arguably the easiest application, and it is packed with interesting fluid phenomenon. This example consists of two parts.

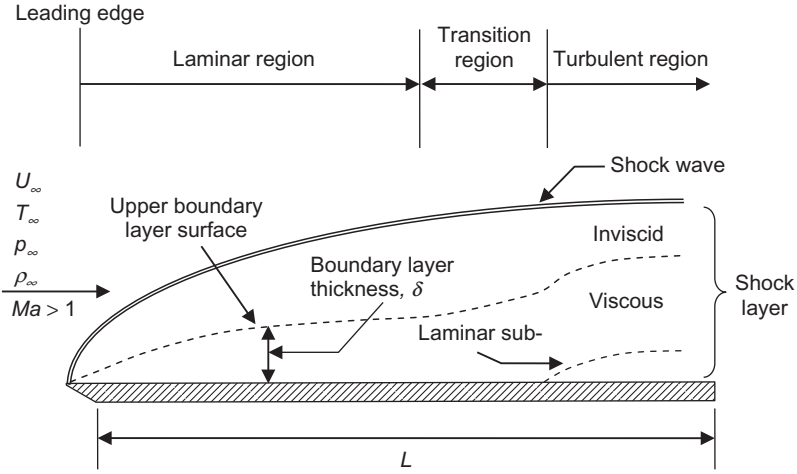


FIG. 8.42 Illustration of supersonic flow over a sharp leading-edge flat plate at zero incidence and development of boundary layer along the plate.

Firstly, we will start from the very beginning by simply solving a laminar flow in two dimensions. This, of course, means that the length of the plate needs to be extremely small for the Reynolds number to be low. More importantly, the main aim of this problem is to demonstrate the practicability usage of a commercial computer code to sufficiently capture the desired flow physics. Fig. 8.43 depicts the size of the computational domain for the numerical calculations of $Ma = 3$ over the flat plate. The length of the plate has been chosen to be $L = 2.85 \times 10^{-5}$ m, which yields a Reynolds number of around 2000 based on the gas properties at reference sea-level values. A uniform structure mesh of rectangular elements totalling 80×80 cells overlays the computational

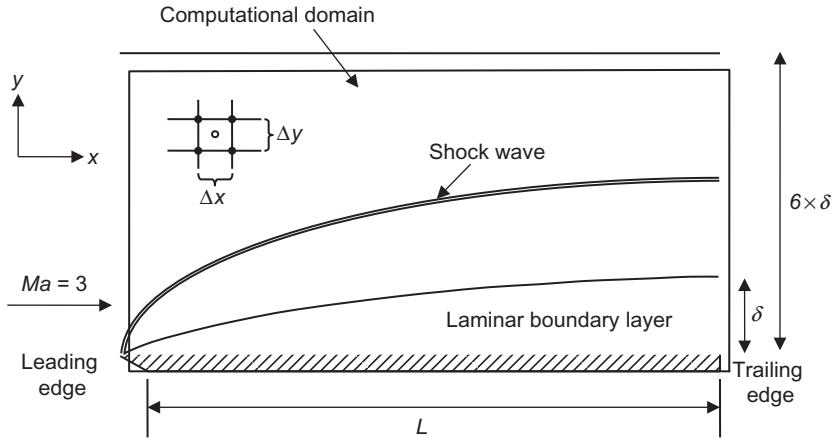


FIG. 8.43 Illustration of two-dimensional computational domain.

domain. The step size in the x direction (Δx) is 3.5625×10^{-7} m (0.000285/80). In the y direction, it is imperative that the height of the domain must encapsulate the shock wave in order to obtain an accurate description of the fluid flow. As predicted by a Blasius calculation at the trailing edge, it is reasonable to assume that the computational domain is at least six times the height of the boundary layer δ, where δ is given by

$$\delta = \frac{5L}{\sqrt{Re_L}} = 3.186 \times 10^{-6} \text{ m} \tag{8.17}$$

The step size in the y direction (Δy) is thus 2.3898×10^{-7} m ($6 \times 3.186 \times 10^{-6}/80$). As a consequence of the stronger gradients in the direction normal to the plate, it makes rather perfect sense that the step size in the y direction is smaller than the x direction in order to better capture the flow field especially near the flat-plate surface.

Secondly, with the current availability of computational speeds and resources such as the advent of computer clusters, the feasibility of employing direct numerical simulation techniques (see Chapter 6) is within reach to predict the onset of transition to turbulence for the fluid flow over this simple geometry. Here, the supersonic flow at $Ma = 4.5$ is solved. A solution to the three-dimensional complete Navier-Stokes equations is solved instead to fully describe the laminar-turbulent transition of the supersonic boundary layer as shown by the schematic drawing in Fig. 8.44. Based on the local boundary-layer length scale $l_s = 3.0486 \times 10^{-4}$ m, the nondimensional dimensions of the computational domain are $L_x/l_s = 3259$, $L_y/l_s = 65.6$, and $L_z/l_s = 438$–587. Owing to

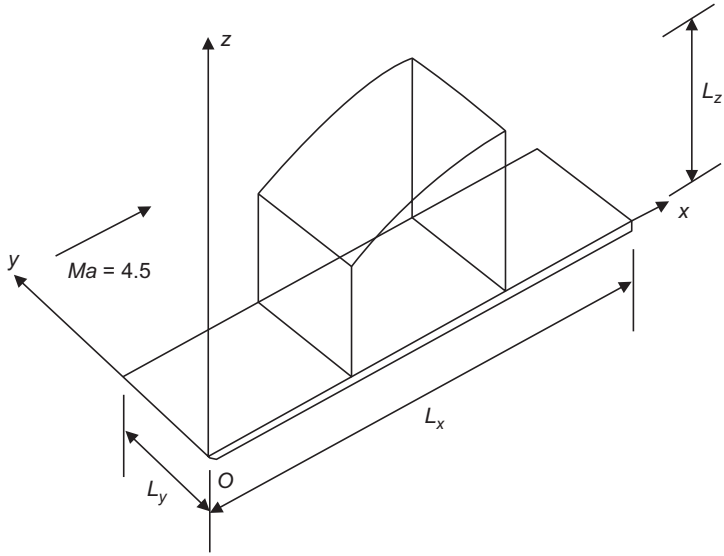


FIG. 8.44 Illustration of three-dimensional computational domain.

the increasing local resolution requirements for the streamwise evolution of the nonlinear instability wave, the direct numerical simulation is performed in multiple stages involving overlapping subdomains or boxes (see details in Table 8.4) to better manage the highly demanding computational resources (note the requirement for the increasing number of grid nodal points to resolve the wave propagation characteristics in the last column at high Reynolds numbers). The last box contains approximately a total of 65 million grid nodal points, a resolution that is deemed to be sufficient in capturing the structure of a fully developed turbulent flow. More details on the simulations carried out for the flow on this particular geometry can be found in Jiang et al. (2006) (Table 8.5).

CFD simulation: The advantage of employing the complete Navier-Stokes equations extends not only to investigations that can be carried out on a wide range of flight conditions and geometries but also in the process; the location of the shock wave and the physical characteristics of the shock layer can be precisely determined. The Navier-Stokes equations for *compressible flows* have been described in Chapter 3. Note that for the energy conservation of *supersonic* flows, the specific energy E is solved instead of the usual thermal energy H applied in *subsonic* flow problems. In other words,

$$E = \underbrace{e}_{\text{internal energy}} + \underbrace{\frac{1}{2}\left(u^2 + v^2 + w^2\right)}_{\text{kinetic energy}} \tag{8.18}$$

It is evident from above that the kinetic energy term contributes greatly to the conservation of energy because of the high velocities that can be attained for flows where $Ma > 1$.

TABLE 8.5 Parameters Employed for Each Computational Box

Box No.	*Re*	$N_x \times N_y \times N_z$	Points/Wavelength
1	400–1800	$864 \times 16 \times 132$	60
2	1600–2146	$864 \times 32 \times 132$	90
	1400–2099	$1024 \times 32 \times 160$	96
3 (Transition)	1968–2540	$1080 \times 48 \times 160$	96
	1968–2649	$1590 \times 102 \times 160$	112
	1968–2649	$1590 \times 256 \times 160$	112

Note: The range of Reynolds numbers evaluated above is based on the local boundary-layer length scale ls. *Nx*, *Ny*, and *Nz* represent the total number of grid nodal points along the *x*, *y*, and *z* directions.

The solution to supersonic flows requires nonetheless additional equations to close the fluid flow system. Firstly, the equation of state on the assumption of a perfect gas is employed, that is

$$p=\rho RT$$

where R is the gas constant. Secondly, assuming that the air is calorically perfect, the following relation holds for the internal energy:

$$e = C_v T$$

where C_v is the specific heat of constant volume. Thirdly, if the Prandtl number is assumed constant of which is approximately 0.71 for calorically perfect air, the thermal conductivity can be evaluated by the following:

$$k = \frac{\mu C_p}{Pr}$$

Sutherland's law is typically used to evaluate the viscosity μ, which is provided by

$$\mu = \mu_0 \left(\frac{T}{T_0}\right)^{1.5} \frac{T_0 + 120}{T + 120} \tag{8.19}$$

where μ_0 and T_0 are reference values at standard sea-level conditions.

Fig. 8.45 illustrates the boundary conditions for the high-speed laminar fluid flow in two dimensions. At the left-hand side and upper boundaries of the computational domain, *Dirichlet* boundary conditions on the velocity, pressure, and temperature are imposed at their respective free-stream values. At the right-hand side, it is imperative to note that the outflow condition in *supersonic* flows is not influenced by downstream conditions and thus differs from the usual

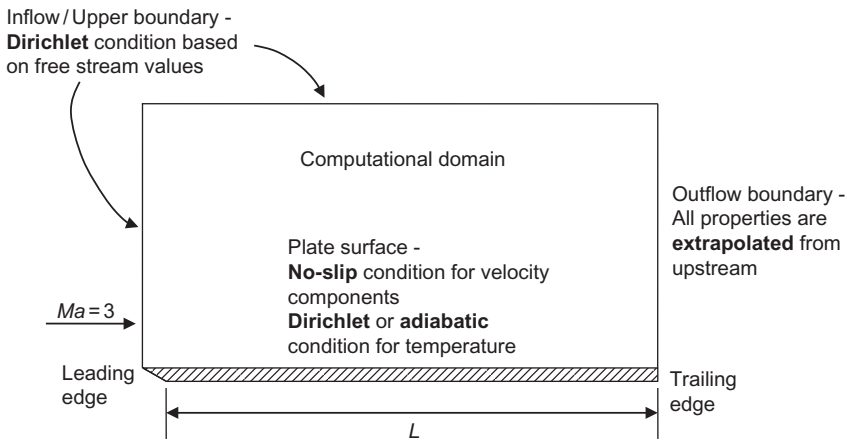


FIG. 8.45 Application of boundary condition for the two-dimensional laminar supersonic flow.

Neumann boundary condition in *subsonic* flows whereby all properties are now calculated based on an extrapolation from upstream in contrast to imposing the *zero*-normal-gradient constraint. Finally, the *no-slip* condition is prescribed for the for all the velocity components ($u = v = 0$). One of the most significant advantages of CFD is the ability to conduct numerical experiments in order to gain an understanding of the implications of changing a flow parameter. The impact between a constant wall temperature and an adiabatic wall will be assessed in the numerical calculations. For the constant-temperature wall boundary condition, it is assumed that the temperature is prescribed at the free-stream value.

One of the many challenging aspects of direct numerical simulation is the requirement to impose appropriate flow conditions at the inflow boundary. To represent the actual characteristic of the flow through this boundary, *different single pair of oblique first-mode disturbances* has been introduced to parametrically study the sensitivity of the chaotic inflow conditions entering the computational domain influencing the internal flow. For the outflow boundary, all properties are extrapolated as considered for the two-dimensional case. For the side boundaries encasing the flow along the spanwise y direction (see Fig. 8.44), *periodic* boundary conditions such as those exemplified for the compact heat-exchanger problem above are employed. At the upper boundary, the *free-slip* condition is imposed, whilst the usual no-slip condition is prescribed with an adiabatic condition for the temperature at the surface of the plate.

CFD results: The relevant data such as the free-stream conditions and several thermodynamic constants for the laminar boundary-layer simulation are detailed in Table 8.6. For the particular case considered, the commercial code ANSYS-CFX, version 10, is used to obtain all the numerical results of the laminar flow condition.

Fig. 8.46 shows the steady-state temperature contours and velocity vectors for the supersonic flow over the flat plate. Note that the range of colours depicted by the velocity vectors has been chosen to correspond to the temperature distribution. For both the adiabatic and constant-wall-temperature cases, the distinctive regions occupied by the inviscid and viscous flows are clearly identified within the shock layer by the CFD methodology. The profile of the curved induced shock wave separating the silent zone (upstream free stream) from the shock layer is also well established. An adiabatic wall is seen to increase the boundary-layer temperature by a substantial margin above the constant wall. This is primarily due to the result of a relatively lower density that leads to a thicker boundary layer and consequently a broader shock layer as illustrated in Fig. 8.46.

The normalized temperature and u component velocity profiles at the trailing edge are plotted in Figs. 8.47 and 8.48 to further confirm the aforementioned observation. In plotting the profiles, the normalized y distance is adopted as suggested by Van Driest (1956) that is $\overline{y} = y\sqrt{Re}/x$. The normalized temperature (T/T_∞) profiles adequately capture the leading-edge shock wave and the

TABLE 8.6 Data Used for the Laminar Flow Case

Quantity	Dimension
Plate length L, m	0.0000285
Free-stream air properties at sea level	
Speed of sound U_∞, m/s	340.28
Pressure p_∞, N/m^2	101,325.0
Temperature T_∞, K	288.16
Density ρ_∞, kg/m^3	1.225
Dynamic viscosity μ, kg/m s	1.7894×10^{-5}
Specific gas constant R, J/kg K	287.0
Specific heat C_p, J/kg K	1005.4
Prandtl number	0.71
Ratio of specific heats γ (C_p/C_v)	1.4

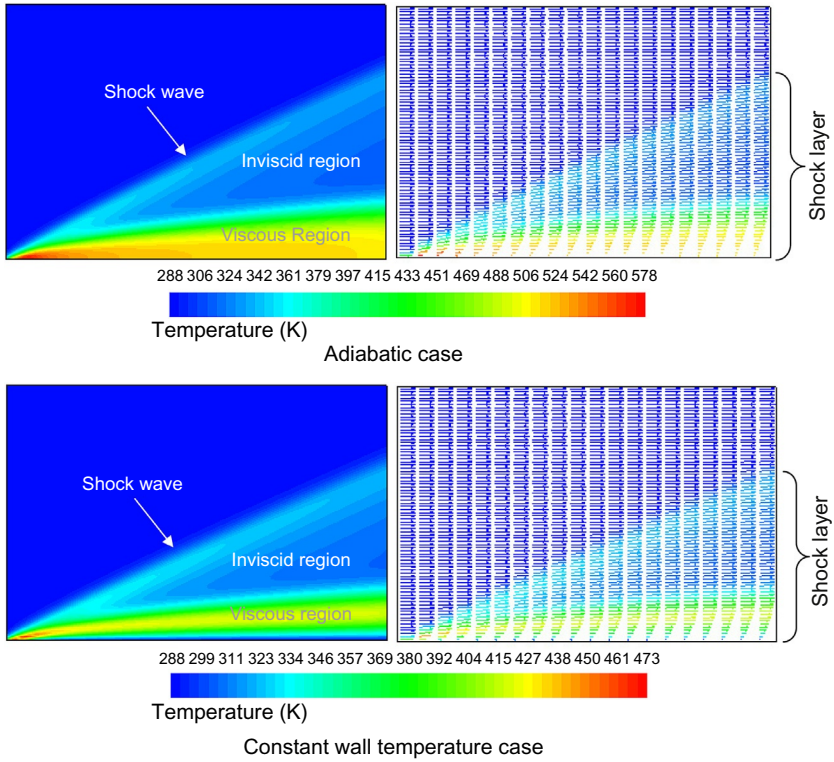


FIG. 8.46 Temperature contours and velocity vectors describing the distinct regions of the inviscid and viscous flows within the shock layer for the adiabatic and constant-wall-temperature conditions for $Ma = 3$.

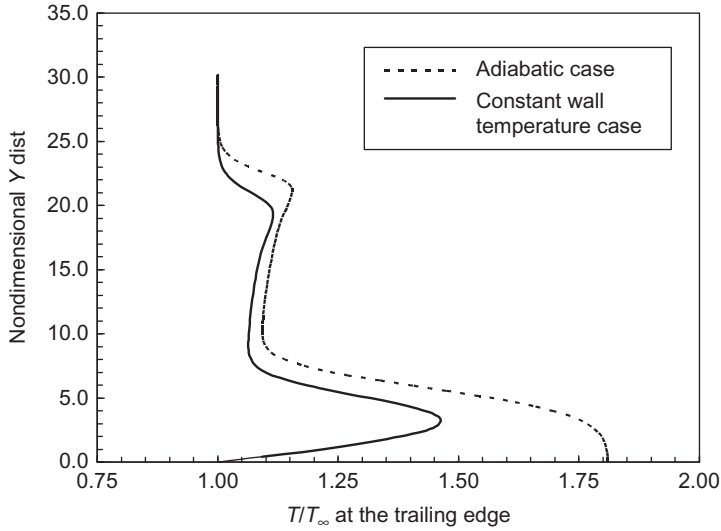


FIG. 8.47 Normalized temperature profiles for the adiabatic and constant-wall-temperature conditions for $Ma = 3$ at the trailing edge.

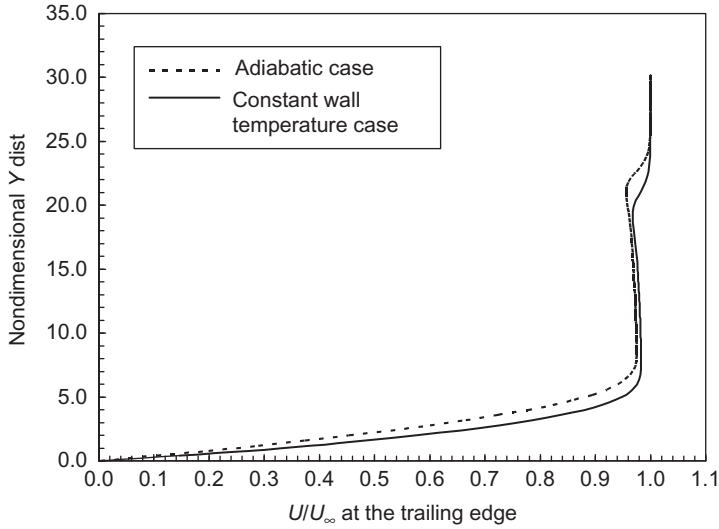


FIG. 8.48 Normalized u component velocity profiles for the adiabatic and constant-wall-temperature conditions for $Ma = 3$ at the trailing edge.

classical boundary-layer behaviour near the plate surface. Since the temperature gradient is zero at the wall for the adiabatic case, temperatures within the thermal layer are expectedly to be higher than those of the constant-wall-temperature case. Essentially, a colder wall temperature suppresses the boundary-layer flow. Similarly, a closer examination on the normalized velocity (U/U_∞) profiles near the surface as exemplified in Fig. 8.48 also shows a thicker boundary layer for the adiabatic case. The local Mach number at the trailing edge is graphically presented in Fig. 8.49 of which the relative strength of the two leading-edge shock waves clearly illustrates a stronger shock wave migrating across the flat plate when the adiabatic condition is imposed at the surface of the plate.

Nowadays, the increasing computational capabilities offer immense possibilities of actually revisiting a number of classical CFD problems such as the current boundary-layer problem typified in this example through the use of direct numerical solution (DNS) techniques. Particularly, the laminar investigation as described above can be further extended to study the onset of flow instability and better understand the transition from laminar flow to turbulent flow. For this flow problem, an in-house DNS computer code developed at University of Texas at Arlington is employed to particularly predict the nonlinear evolution of instability waves and onset of breakdown to turbulence in a Mach 4.5 flat-plate boundary-layer flow after the occurrence of shock. To verify the DNS predictions, they are also subjected to intense scrutiny against the parabolic

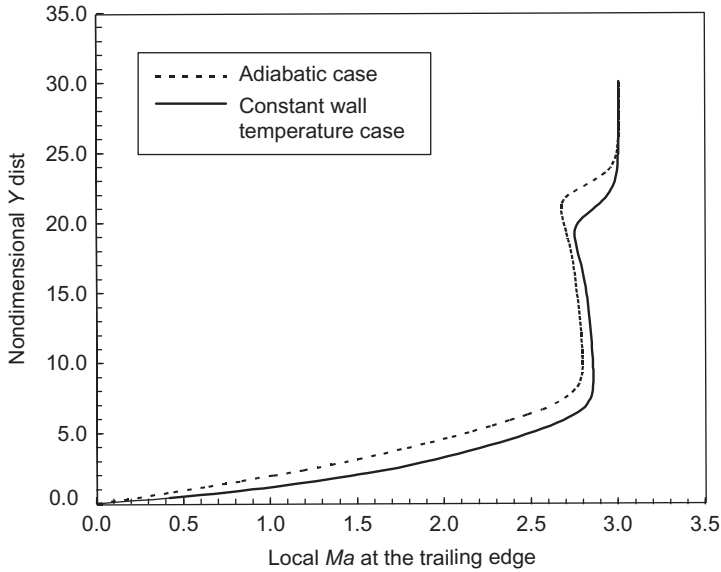


FIG. 8.49 Local Mach number profiles for the adiabatic and constant-wall-temperature conditions for $Ma = 3$ at the trailing edge.

stability equation (PSE) calculations of NASA Langley of which this work is based on the investigation performed by Jiang et al. (2006). For the remainder of the section, some results extracted from the work on the laminar-turbulent transition investigation are presented and discussed below.

One of the many challenges in DNS is to prescribe suitable inflow boundary conditions. Since DNS is a fully deterministic approach where all spatial and temporal scales are required to be computed, the specification of appropriate inflow conditions is of paramount importance. The comparison of wave propagation characteristics prior to the onset of transition based on various disturbance modes predicted by DNS is illustrated in Fig. 8.50. In Fig. 8.50, the DNS modal profiles of the fluctuating velocity components and temperature subject to different disturbance modes as a function of the local scaled wall-normal coordinate are shown to be in excellent agreement with the results determined through the PSE calculations. For each of the disturbance modes affecting the numerical calculations, a successful cross validation of the DNS solutions for the linear and early nonlinear stage of disturbance growth is clearly demonstrated, which greatly suggests the independent influence of the initial boundary conditions on the onset of laminar-turbulent transition.

It is noted that the prediction of the onset of breakdown to turbulence after the nonlinear interaction is beyond the capability of PSE. However, since DNS solves the full unsteady Navier-Stokes equations without any *ad hoc* assumptions, the present methodology is able to provide solutions across a broadband of fluid dynamics ranging from laminar state to the early and later stages of transition and even to capture the manifestation of chaotic structures in a fully developed turbulent flow. To gain an insight of the complex flow structures occurring along the flat plate, the evolution of the contours for the density fluctuation and wall-normal vorticity along the increasing distance along the flat

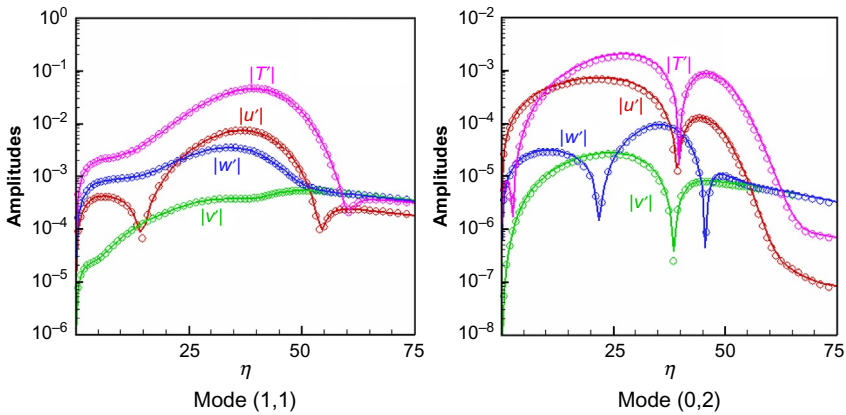


FIG. 8.50 Modal profiles at $Re = 1500$ as a function of η (the local scaled wall-normal coordinate) subjected to two disturbance modes.

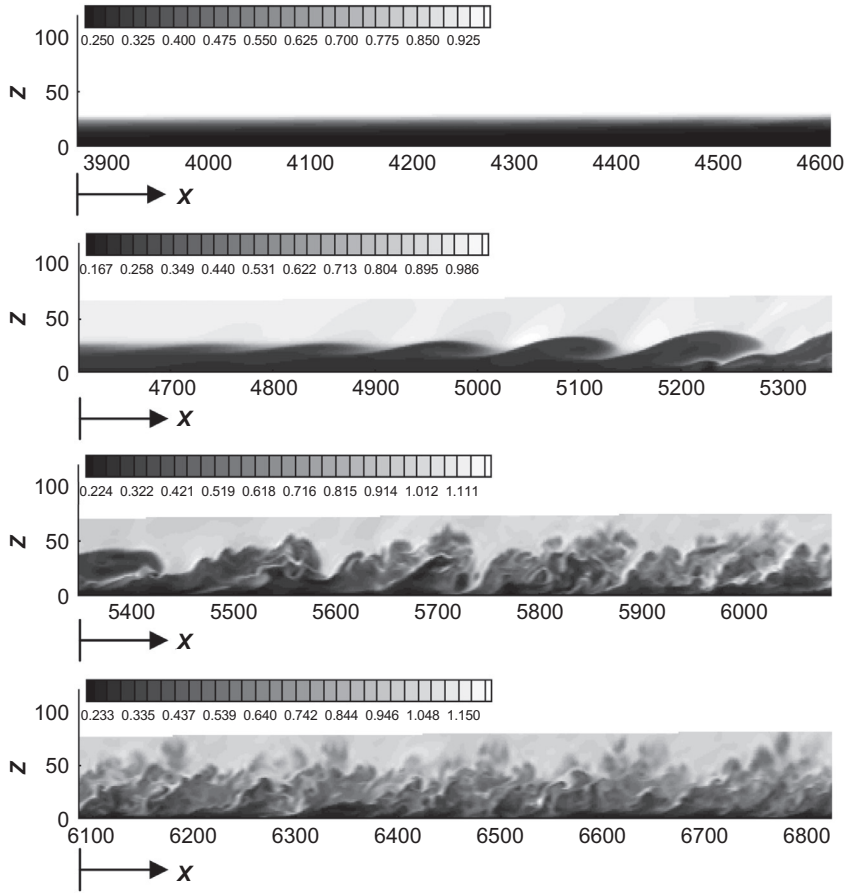


FIG. 8.51 Contours of density fluctuation in the x–z plane midway along the spanwise direction.

plate is illustrated in Figs. 8.51 and 8.52. As observed from these two figures, the flow remains quite laminar for $x < 4600$. Flow instability or transition nonetheless begins to creep in at about $x = 4800$ with the increasing undulation persisting over the flow patterns after this point. Shortly after some distance downstream at $x = 5400$, the onset of breakdown of the flow to turbulence subsequently prevails, and the fluid flow remains rather turbulent thereafter by the establishment of substantial density fluctuations within the fluid and vigorous coherent structures of wall-normal vorticities at $x = 6800$.

8.4.5.2 Subsonic and Supersonic Flows Over a Wing

An aerofoil can be defined as a streamlined body designed specifically to produce lift. It will also experience the counteracting influence of drag whilst placed in a fluid stream. The primary purpose for the construction of the aerofoil

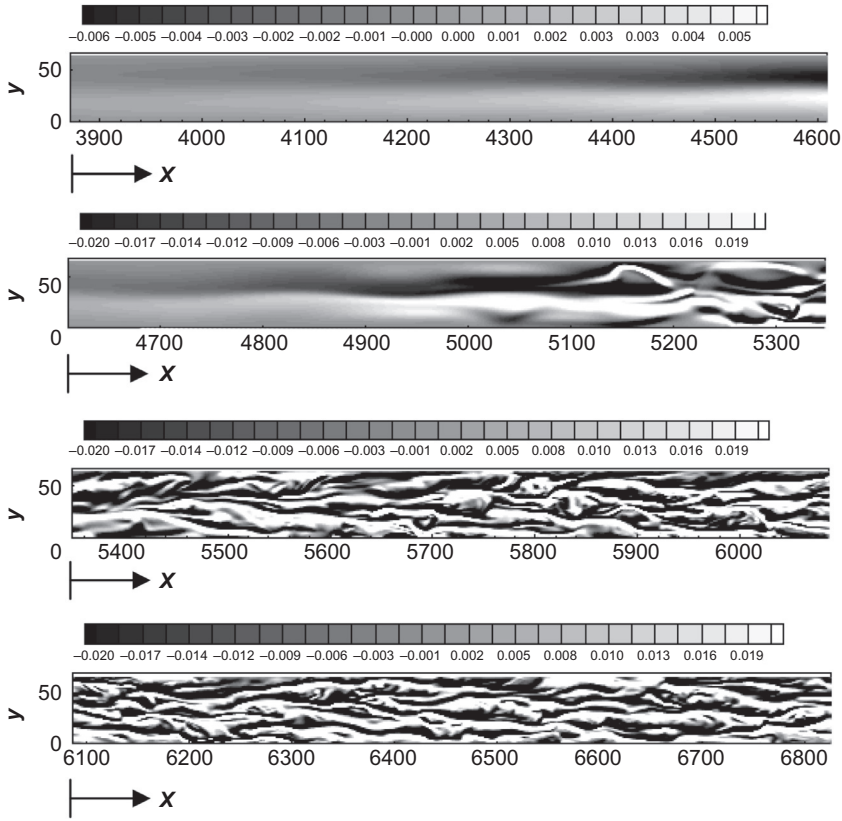


FIG. 8.52 Contours of wall-normal vorticity in the x-y plane at a vertical nondimensional distance of $z^+ = 12.21$.

to be streamlined is to minimize the drag imposed on the body. As a measure of its usefulness, for example, as a wing section of an aircraft, the ratio of lift to drag must be sufficiently large in order that it is capable of producing high lift at a small penalty of the drag. For an aircraft to remain in the airspace, the creation of lift on the wing surface is of paramount importance. Nevertheless, what is necessary to propel the craft's forward motion is the drag that absorbs the engine power.

Problem considered: In order to illustrate another CFD application example for high-speed flows, the fluid flowing past an NACA0012 aerofoil is considered herein. This particular geometry has been specifically chosen because of the numerous aerodynamic investigative studies that have been carried out in research and design practices. There are a number of accepted terminologies concerning an aerofoil; it is best that familiarization with them is necessary in order to understand the discussion of the flow past such geometry.

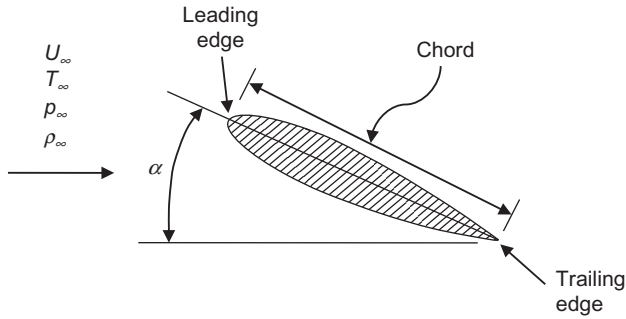


FIG. 8.53 Schematic drawing of an aerofoil.

Fig. 8.53 illustrates the schematic drawing of the aerofoil geometry, and some of the pertinent terms relating to an aerofoil cross-section that will be constantly referred are the following:

- *Leading edge*—the front or upstream edge, facing the direction of flow
- *Trailing edge*—the rear or downstream edge
- *Chord line*—a straight line linking the centres of curvature of the leading and trailing edges
- *Chord*, c—the length of chord line between the leading and trailing edges
- *Span*, b—the length of the aerofoil in the direction perpendicular to the cross-section of the wing
- *Angle of attack* (*incidence*), α—the angle between the direction of the relative motion and the chord line

The CFD example in this section considers the subsonic and supersonic flows past an infinitely long aerofoil. The Reynolds-averaged Navier-Stokes (RANS) equations are solved alongside with the shear-stress transport (SST) turbulence model for the supersonic flow ($Ma = 2.5$) over the wing geometry. As only time-averaged results are of primary interest especially in RANS simulation and since the length b is infinite, such conditions or assumptions mean that the flow is truly two-dimensional; there is negligible spanwise variation of flow patterns and forces for a constant chord aerofoil. Numerical calculations are thus carried out in a two-dimensional fluid domain, which also include parametric investigations on the influence of different angles of attack affecting the expanding shock layers as the fluid travels past the aerofoil. This investigation forms the first part of this example. At flows that are just below the speed of sound ($Ma = 0.2$ is considered for the present problem), currently available computational hardware permits the feasibility use of DNS techniques to fundamentally study the onset of flow instability and subsequent transition to turbulence subject to different inlet conditions. Here, the complete three-dimensional Navier-Stokes equations are solved to accommodate the spectrum of varying length scales that exist within the complicated fluid phenomenon spanning along

the streamwise (x), spanwise (y), and vertical (z) directions. This study shapes the second part of this example.

CFD simulation: One challenging aspect of the present CFD example of the fluid flowing over the aerofoil involves the generation of appropriate meshes surrounding the geometry. Two different types of grid topologies that could be specifically used to solve the problem are illustrated in Figs. 8.54 and 8.55. One approach that can be suitably considered especially for RANS simulations is the block structured or multiblock mesh (see Chapter 6) as shown in Fig. 8.54. The entire fluid region is now subdivided into six contiguous blocks. This approach offers immense flexibility in generating different grids in each block particularly the increased mesh densities in blocks 2 and 5 capturing the developing boundary layer along the chord line between the leading and trailing edges and expanding shock layers along the aerofoil. From the viewpoint of practicality and general application, the attractiveness of multiblock meshing allows the ease of porting the mesh information into any commercial computer packages. Alternatively, it is also possible to employ a single-block mesh to fit the entire fluid domain. The three-dimensional structured C-grid type encapsulating the aerofoil as seen in Fig. 8.55 typifies such grid topology, and it has been purposefully employed for the DNS calculations. Numerical solutions are obtained in a mesh totalling 22,000 rectangular elements for the two-dimensional case and 1200 (streamwise) $\times$ 32 (spanwise) $\times$ 180 (vertical) hexahedral elements for the three-dimensional case. For the latter, the large overlay of elemental volumes ensures that the mesh distribution based on the nondimensional spacing along the streamwise, spanwise, and vertical directions are below $\Delta x^+ < 13$, $\Delta y^+ < 15$, and $\Delta z^+ < 1$.

The *full compressible* Navier-Stokes equations are applicable for the consideration of both the subsonic and supersonic flows in this CFD example. Note

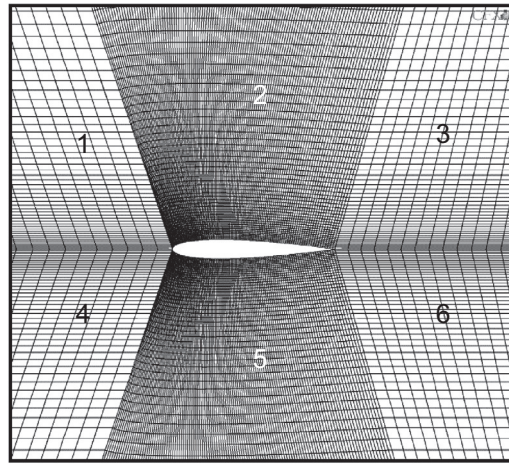


FIG. 8.54 A multiblock approach for the mesh surrounding the aerofoil for RANS calculations.

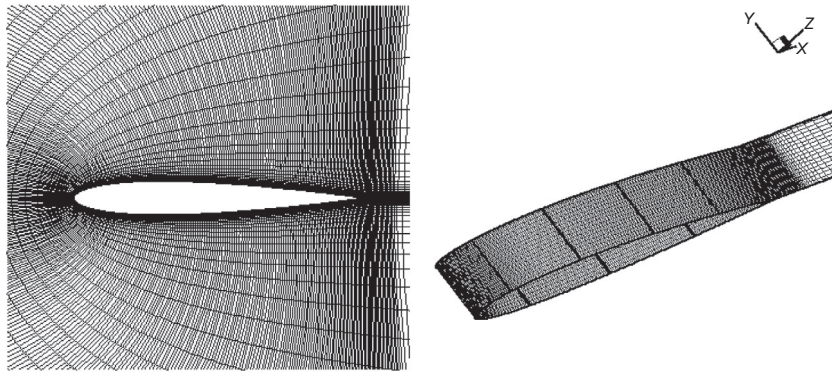


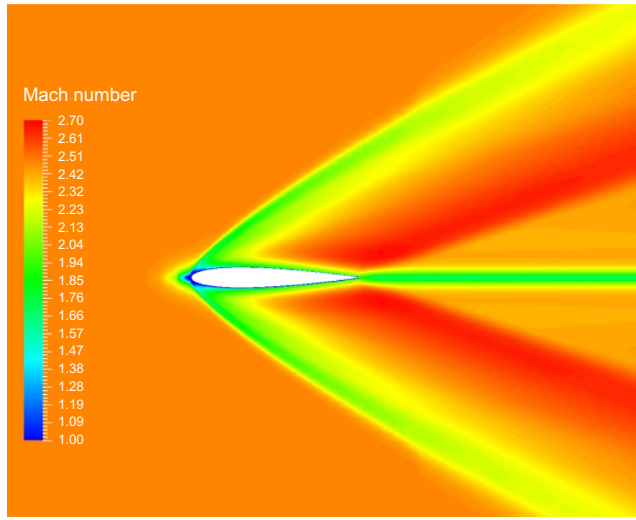
FIG. 8.55 A C-type mesh scheme adopted for DNS.

again that the two-dimensional forms are obtained by simplifying the three-dimensional governing equations, which involve the omission of the component variables in one of the coordinate directions. Boundary conditions as described by the boundary-layer flow over the sharp-edged flat plate in the previous example can also be similarly employed to the present CFD example. In other words, *no-slip* condition for the velocity components on the wing surface, *free-slip* condition on the upper and lower boundaries, *Dirichlet* condition based on the free-stream values at the inlet boundary, and *extrapolation* of the upstream values at the outlet boundary. With regard to DNS, *periodic* boundary conditions are employed for the side boundaries encasing the three-dimensional flow along the spanwise y direction. For all the numerical results attained, *adiabaticity* is assumed for the wing surface.

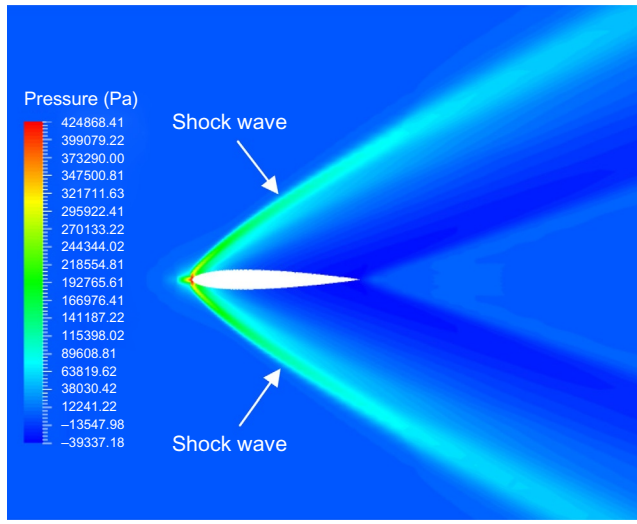
CFD results: For the RANS simulations, the commercial CFD code ANSYS-CFX, version 10, is utilized to obtain all the numerical results of the supersonic flow condition. The relevant input data such as the free-stream conditions and several thermodynamic constants are the same as those tabulated in Table 8.4.

Fig. 8.56 illustrates the contours of the local Mach number and pressure for the fluid flow past the wing geometry based of a free-stream $Ma = 2$ subject to 0 and 5 degrees angles of attack. From these results, the formation of shock waves above and below the wing surface is clearly identifiable as the fluid travels downstream from the leading edge to the trailing edge of the aerofoil. Because of complete flow symmetry, it is not entirely surprising for the case of the 0 degrees angle of attack that the growth of the boundary layer is identical at the top and bottom surfaces; one would not expect any pressure gradient to be developed, and hence, the flow vorticities should be of equal strength and opposite rotation. However, at the 5 degrees angle of attack, it is seen that the fluid flowing over the bottom surface of the aerofoil is slowed down as evidenced by the local Mach number contours. The pressure is significantly

increased from the case of the 0 degrees angle of attack at the same flow region, which means that the pressure gradient is favourable, the boundary-layer thickness is small, and, hence, the vorticity in it is also small. The opposite however prevails over the top surface whereby the boundary layer is thicker, the pressure gradient is adverse, and the vorticity in it is larger. This pressure difference



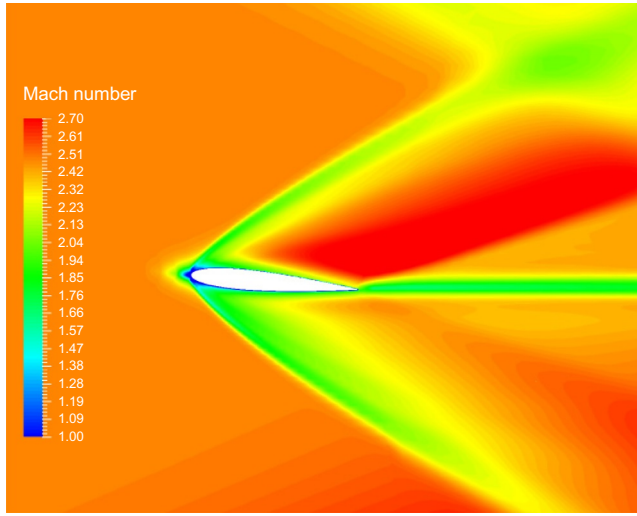
Angle of attack – 0 degree



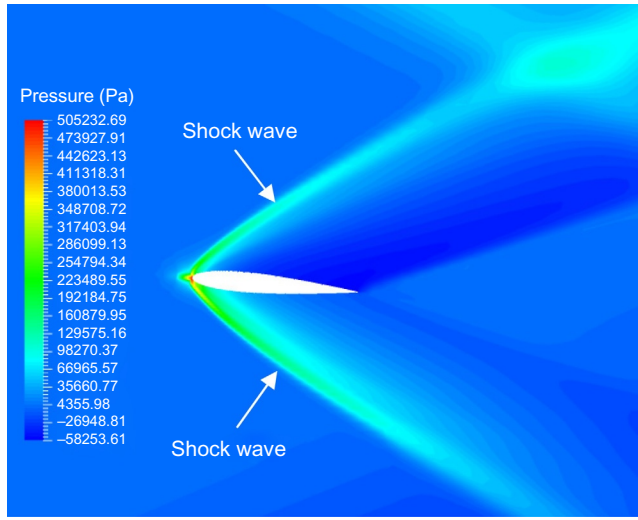
Angle of attack – 0 degree

FIG. 8.56 Local Mach number and pressure contours for the supersonic flow based on the free-stream $Ma = 2.5$ subject to 0 and 5 degrees angles of attack past the wing geometry.

(Continued)



Angle of attack – 5 degrees



Angle of attack – 5 degrees

FIG. 8.56, CONT'D

gives rise to an upward resultant force, namely, lift, which is of primary importance for an aerofoil when placed in a fluid stream.

The foregoing discussion indicates a strong dependence of lift upon the incidence angle. Well-documented observations have shown that there is also a compelling linkage between the creation of lift and the flow characteristic surrounding the aerofoil. Fig. 8.57 shows the velocity vectors for the two cases of the 0 and 5 degrees angles of attack with the spectrum of colours associated with

the pressure distribution. For these *small* angles of attack, there appears to be no separation of the boundary layer near the trailing edges. Nevertheless, a threshold limit exists whereby any further increase of incidence no longer produces an increase of lift. At this instance, significant flow separation occurs at the top surface and subsequently widens the wake behind the trailing edge of the

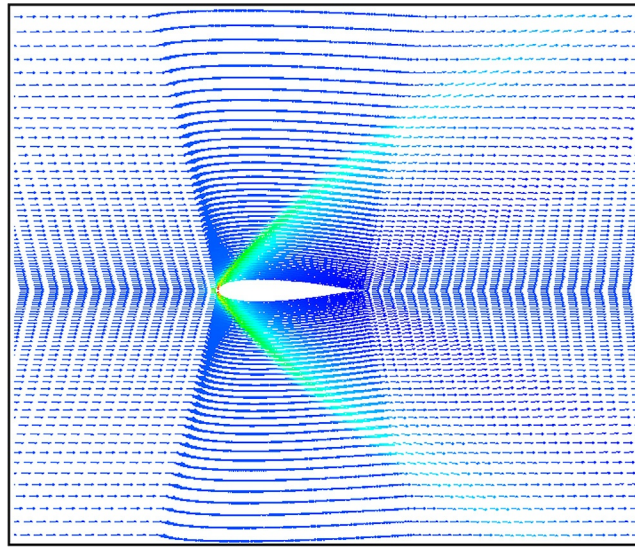
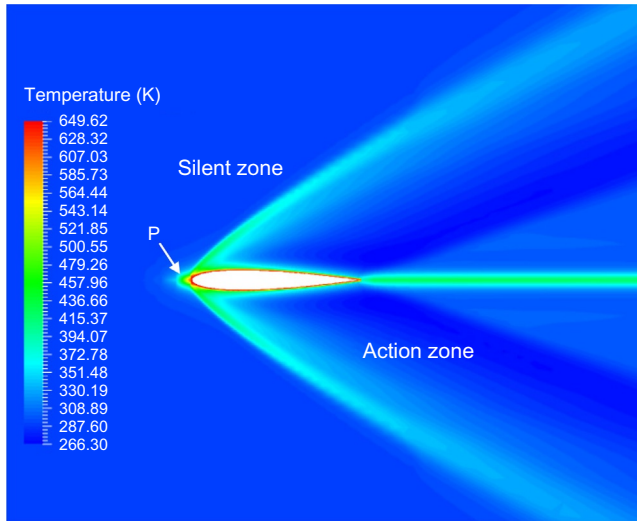


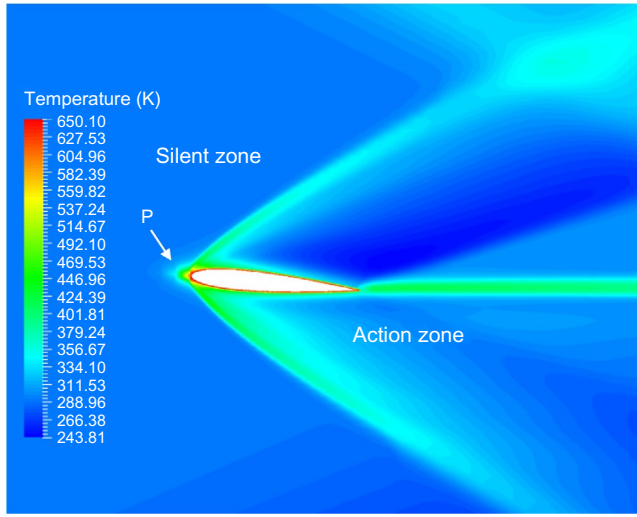
FIG. 8.57 Velocity vectors of the supersonic flow based on the free-stream $Ma = 2.5$ subject to 0 and 5 degrees angles of attack past the wing geometry.

aerofoil. This is known as the *stall* position, and it constitutes a critical angle of attack for aerodynamic design since the lift drops rapidly thereafter.

At upstream, the flow away from the leading edge or stagnation point as indicted by 'P' on the temperature contours in Fig. 8.58 is usually designated as the *silent zone*. Because the flow is supersonic, the disturbance generated



Angle of attack – 0 degree



Angle of attack – 5 degrees

FIG. 8.58 Temperature contours of the supersonic flow based on the free-stream $Ma = 2.5$ subject to 0 and 5 degrees angles of attack past the wing geometry.

at 'P' is thus not communicated to any part of the zone. Further downstream, the zone depicting the significant changes of the fluid within the shock layer is sometimes known as the *action zone*. Here again, the upper and lower temperature distributions are identical at the top and bottom of the wing surface for the case of 0 degrees angle of attack because of complete symmetry. For the case where the angle of attack increases to 5 degrees, the symmetry is broken registering a temperature gradient across the *action zone*. Temperatures are significantly higher over the bottom wing surface, whilst lower than expected temperatures are recorded over the top wing surface when compared with the case of 0 degrees angle of attack.

For the remainder of this section, the nonlinear evolution of instability waves and onset of breakdown to turbulence for the subsonic flow over the aerofoil based on the investigation performed by Shan et al. (2005) and Deng et al. (2007) through DNS techniques are presented below. The boundary conditions for the inflow and outflow are nonreflecting conditions based on the analysis of one-dimensional characteristic equations on the time-dependent Euler equations. These boundary conditions are different from the boundary conditions specified for the DNS of supersonic boundary-layer flow over the flat plate in the previous section.

Fig. 8.59 shows a snapshot of segments representing instantaneous spanwise vorticity developing in the middle of the x–z plane at different times for the fluid flow over the aerofoil at $Ma = 0.2$ with an angle of attack of 4 degrees investigated by Shan et al. (2005). As shown by the instantaneous spanwise vorticity at $t = 0.8794$, the presence of instability waves propagating downstream above the wing surface clearly establishes the onset of flow transition. As time progresses,

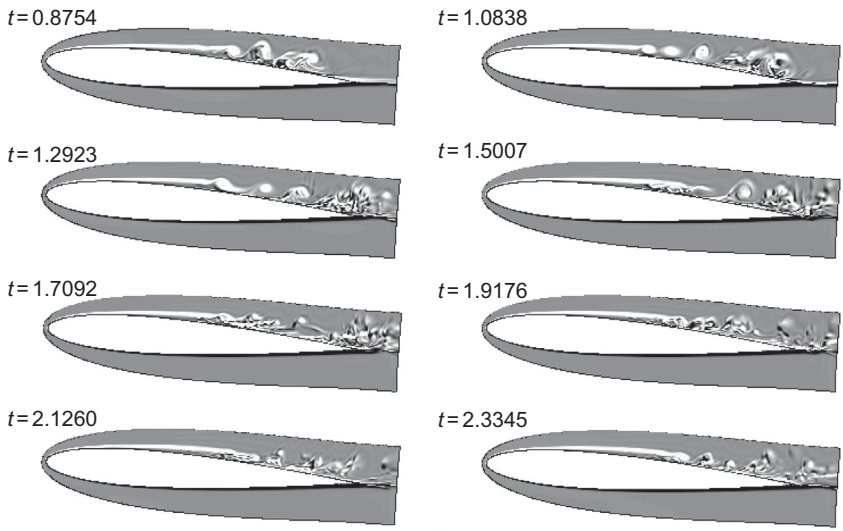


FIG. 8.59 Instantaneous spanwise vorticity at different times (t is nondimensionalized by c/U_∞).

these waves that are three-dimensional in nature continue to grow in the shear layer, and they subsequently cause the vortex to break down near the trailing edge as indicated by the chaotic three-dimensional fluid flow at the later stages of the DNS calculations. In its fully turbulent state, the presence of vortex shedding behind the trailing edge is associated with the rapid growth of the strong nonlinear interactions of velocity fluctuations within the wake region.

Isosurfaces of instantaneous vorticity along the x, y, and z directions are further illustrated in Fig. 8.60 to gain a better understanding of the flow transition.

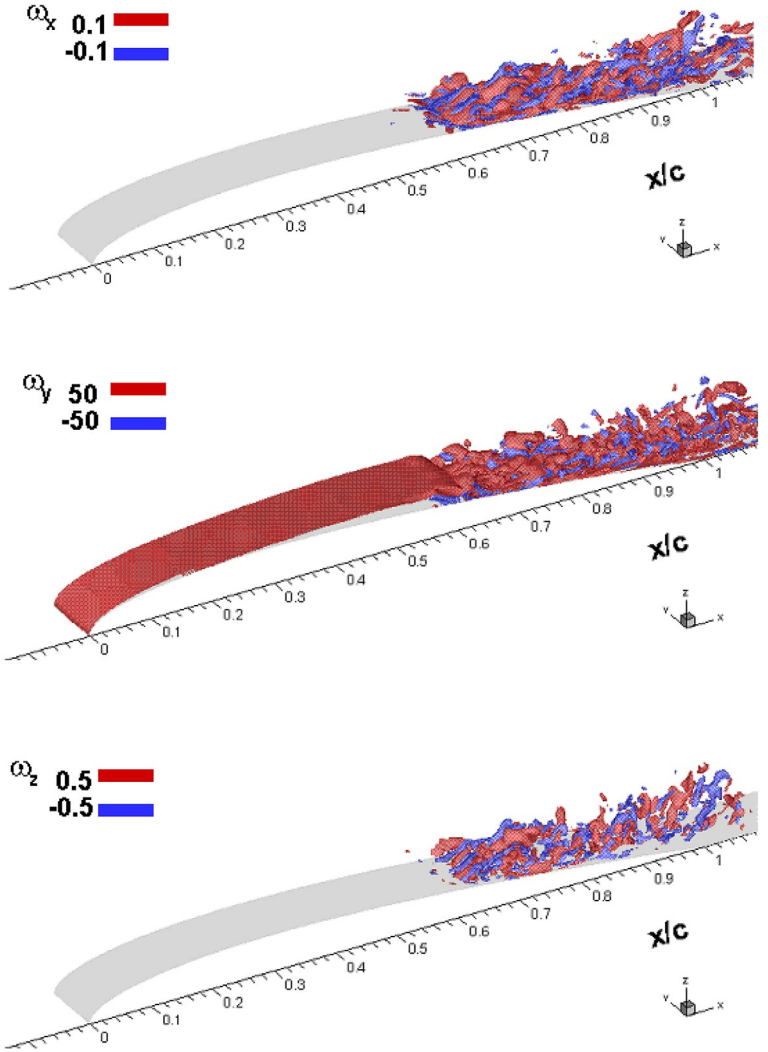


FIG. 8.60 Isosurfaces of instantaneous vorticity components (from top to bottom—streamwise, spanwise, and vertical components).

The appearance of undulated vorticity generated along the spanwise direction suggests that the fluid flow is three-dimensional and also depicts the propagation instability waves along the top surface of the aerofoil. In general, the results clearly show the simultaneous breakdown of the rolled-up shear layer along the chord line, and the vortices are shed from the separated shear layer and become distorted whilst travelling downstream. More specifically, this shedding vortex that is quickly deformed and stretched actually conforms to a negative vortex being induced by the prime vortex that is situated alongside with this negative vortex, and eventually, the prime vortex breaks down into smaller fragments corresponding to the flow transitioning to turbulence. The interaction between the streamwise and spanwise vortices leads to the development of a λ-shaped vortex, which then rolls up and breaks down. The boundary layer becomes fully turbulent after reattachment of the flow behind the trailing edge.

Recent results on the DNS performed by Deng et al. (2007) of flow separation control subject to pulsed blowing jets over the aerofoil at the same angle of attack are presented below as a comparison case to the above. Here again, a snapshot of the instantaneous spanwise vorticity being developed in the middle of the x–z plane at different times is similarly illustrated in Fig. 8.61. The unsteady blowing enforced before the separation point with the creation of a large vortex shedding prevailing close to the leading edge of the aerofoil triggers the early transition of the boundary layer. Isosurfaces of vorticity along the respective Cartesian directions in Fig. 8.62 further exemplify the breakdown of

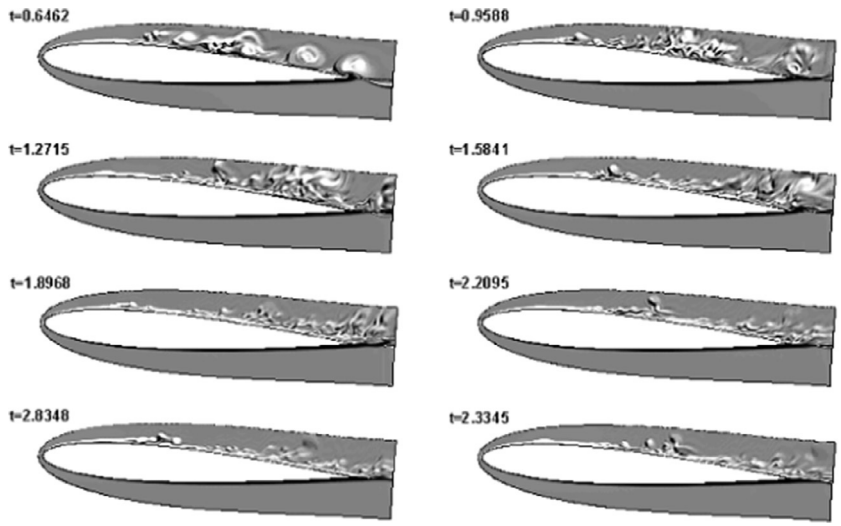


FIG. 8.61 Instantaneous spanwise vorticity at different times with pulsed blowing jets (t is nondimensionalized by c/U_∞).

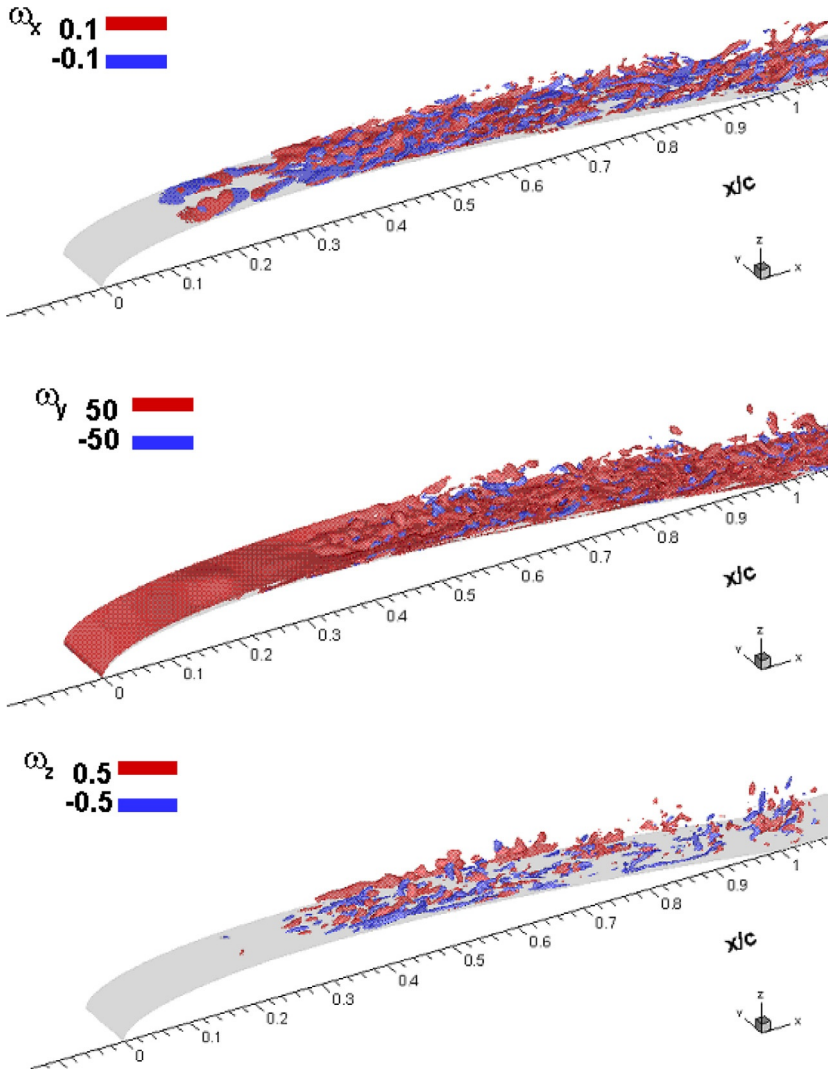


FIG. 8.62 Isosurfaces of instantaneous vorticity components with pulsed blowing jets (from top to bottom—streamwise, spanwise, and vertical components).

the separated shear layer and the development of the vortex structure. The fluid phenomenon reveals a number of interesting features. From the results obtained, it is clear that the pulsed blowing jets imposed at the inlet significantly affect the reattachment of the boundary layer shortly after separation. A shorter separation zone is developed resulting in also a much reduced separation bubble as evidenced by the vortical structures plotted in Fig. 8.62.

8.5 SUMMARY

The examples in this chapter have been purposefully selected to demonstrate the feasible application of the CFD methodology across a wide range of engineering disciplines and to provide some useful guidelines in handling some of these challenging flow problems in practice.

In the first example, detailed investigation on the appropriate turbulence models for ventilation design systems exemplifies how these models can be put to good use as a *design tool* in building design such as areas of architecture science and civil or construction engineering.

The ongoing relevance of CFD as a *research tool* is considered in the second example. For gas-particle flows, particles can be treated either as another continuum medium through additional conservations equations by the Eulerian approach or an ensemble of discrete solid particulates tracked by the Lagrangian approach within the parent-phase fluid conservation equations. These approaches represent the currently adopted state-of-the-art methods in handling such flows. The reader should take note that this so-called multiphase models with appropriate constitutive closure relationships are not only restricted to gas-particle or gas-solid flows. They can also be readily applied to resolve the transport of gas–liquid, liquid–solid, or even gas–liquid–solid mixtures.

By the consideration of additional equation for the conservation of energy coupled with appropriate source terms in the momentum and turbulence equations, fluid flows coupled with *heat transfer* are illustrated through two practical examples in this chapter. The wealth of information obtained from the fluid flow within the in-line or staggered arrangement of compact heat exchanger through CFD allows mechanical engineers to determine the required improvements in better augmenting the performance of the mechanical system. More importantly, CFD plays an important role in assisting nuclear engineers to address important radiation safety and structure integrity issues pertaining to the exposure of a searing molybdenum plate due to residual nuclear fission heating in an open-air environment (*conjugate heat transfer and radiation heat transfer*).

The fifth example presents the practicality of adopting LES over the usual RANS in resolving the combustion and radiation processes associated with a free-standing fire. Capturing the fluctuating characteristics of a buoyant fire through LES signifies the advances of knowledge benefiting fire engineers and researchers from a combustion and science background particularly on the environmental consequences that could result from accidental large-scale fires in oil fields.

Flow over a vehicle platoon, the sixth example, further establishes CFD as another effective design tool in improving the aerodynamic efficiencies of automobiles. The potential of this methodology also presents automotive designers and engineers with other improvement strategies to work towards the construction of more environmental friendly vehicles that will consequently have very low fuel consumption with significant reduction of emission levels.

Mature development of CFD meshing and numerical models as demonstrated in the seventh example represents the current state of the art to probe the many associated complex flows inside a real human nasal cavity. CFD is increasingly being considered as a viable tool in the field of biomedical engineering, and the application of this methodology is steadily growing especially the enormous interest in studying the deformation of vessel walls affecting the arterial blood flow inside a human vascular system.

Despite the long-standing application of traditional theoretical boundary-layer-solution technique in aircraft designs in the aerodynamic industries, *supersonic* flows over varying aircraft geometries and flight conditions can now be handled through efficient CFD methods and models. For the last two fluid dynamics examples shown for this engineering discipline, complete two- and three-dimensional solutions through the full Navier-Stokes equations under *supersonic* conditions can be viably obtained nowadays through the commercial CFD computer packages. From a research-oriented investigation, application of DNS to predict the onset of flow instability and transition to turbulence depicts the future direction of CFD in enhancing the understanding of basic fluid dynamics and in all classical physics especially on the prediction of turbulence.

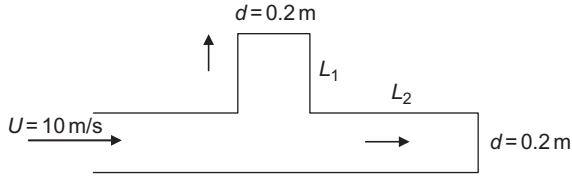
The windows of opportunity for CFD are indeed plentiful. CFD is aptly being considered as the critical technology for fluid flow investigation in the 21st century. Relishing the many successful applications of CFD achieved thus far at this present time, the reader should also be well informed of some emerging new and innovative techniques that will continue to revolutionize the current CFD methodology. These will be further discussed in the next chapter.

REVIEW QUESTIONS

8.1 Why do engineers prefer to initially use the standard k–ε turbulence model as a starting point in solving their design problems, instead of using more complex models such as the LES approach? When would an LES approach be used?

8.2 For the internal pipe flow geometry shown below, formulate appropriate answers to the following questions:

- **(a)** Define and state all the boundary conditions for this problem.
- **(b)** What would be an approximately suitable length for L_1 and L_2 to achieve a fully developed flow at the outlets ($d = 0.2$ m) for this case?
- **(c)** Show where a fine mesh should be needed.
- **(d)** From your understanding of fluid mechanics, sketch roughly what the flow streamlines will look like for this flow problem.
- **(e)** Discuss what design ideas may be used to reduce the head loss in this pipe flow and how this can be implemented using CFD.



8.3 Explain the *Lagrangian* description of a fluid motion.

8.4 What is the *Eulerian* description of a fluid motion? How does it differ from the *Lagrangian* description?

8.5 A streak of dye is released into an internal flow, and its motion is tracked and recorded. Is this a *Lagrangia*n or *Eulerian* measurement?

8.6 A stationary pitot tube is placed in a fluid flow to measure pressure. Is this a *Lagrangian* or *Eulerian* measurement?

8.7 The flow in a 90 degrees bend is shown below, formulate appropriate answers to the following questions:

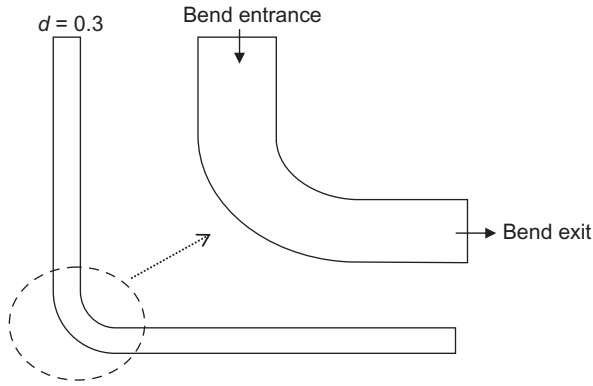
(a) Would a structured or unstructured mesh be better for this geometry? Describe how you would create the mesh?

(b) From your knowledge of the conservation equations of motion, sketch the expected flow streamlines for a flow that has a Reynolds number of 100 and a flow that has a Reynolds number of 10,000.

(c) If a particle with a Stokes number of 0.1 is released in a passive manner from the inlet under laminar conditions, sketch what would is the expected particle trajectory throughout the pipe? How would the trajectory be different if the flow is turbulent?

(d) What would the expected particle trajectory if the particle Stokes number was instead equivalent to 20 for a laminar flow and a turbulent flow?

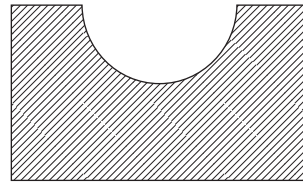
(e) If you solved this problem in the *Eulerian* reference, what kind of measurements can be made?



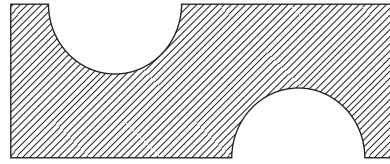
8.8 For heat transfer coupled with fluid flow, formulate appropriate answers to the following questions:

(a) Why is compact heat exchanger different from conventional heat exchanger?

(b) Symmetric and cyclic boundary conditions can usually be employed to simplify the flow geometry of a compact heat exchanger. Indicate the boundary conditions for the in-line and staggered arrangements shown below.



In-line arrangement



Staggered arrangement

(c) The Nusselt number is a ratio of two fluid properties. What are they?

(d) Explain why higher heat-transfer rates are experienced in staggered arrangement over in-line arrangement.

(e) What is *conjugate heat transfer*?

(f) Why is it important to incorporate the buoyancy effect in natural convection? What additional modelling effort is required for the transport equations?

(g) What is *radiation heat transfer*? How does it affect the surface solid temperature (see Section 8.4.1.2)?

8.9 The Ahmed model is often used to model bluff car bodies. The schematic for one model is shown along with two cars travelling in line together with the mesh geometry shown below. Analyse this problem by answering the following questions:

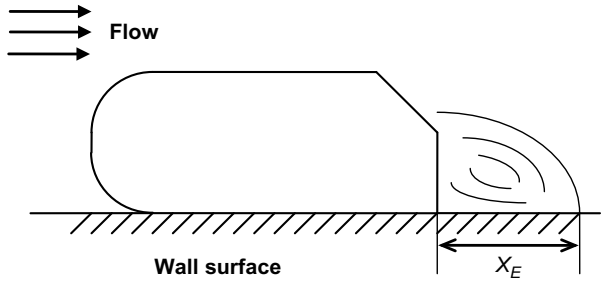
(a) Explain why there is a fine mesh surrounding the near regions of each car body.

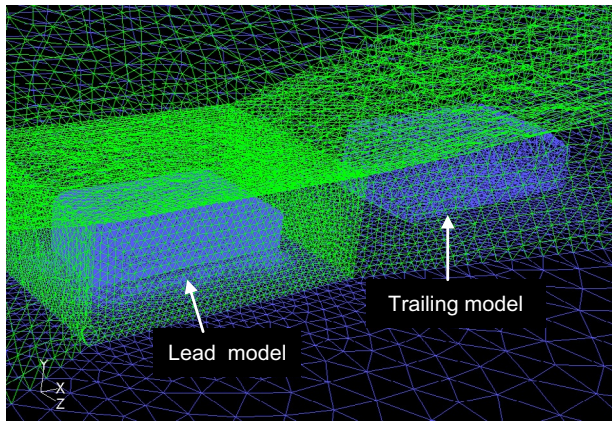
(b) Indicate the regions of high and low pressure encountered around the car bodies.

(c) What is the general effect that the lead car model has on the drag coefficient of the trailing model?

(d) What happens to the drag and lift coefficients if the distance between the two models is in close proximity (i.e. $x/L \approx 0.25$ where x is the distance and L is the length of the models)?

(e) Whilst using two different k–ε turbulence models, which one model overpredicts turbulent kinetic energy k whilst the other underpredicts it, explain the difference of the flow behaviour when using these two models against the accurate experimental value X_E, shown in the figure.



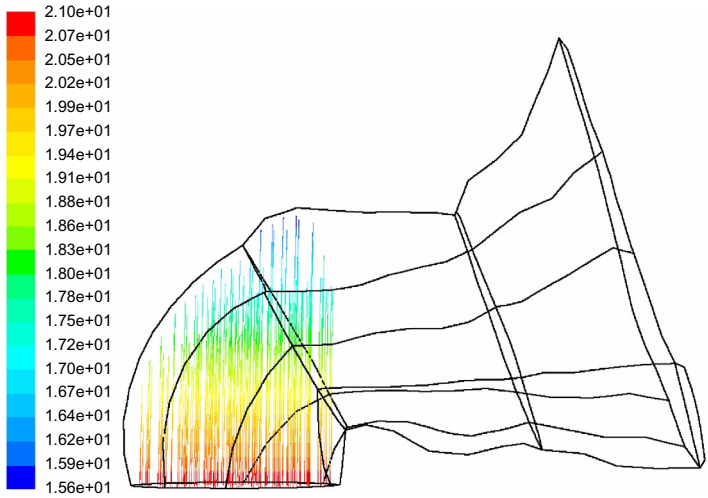


8.10 Two particle trajectory profiles are shown below for monosized particles released from the bottom inlet. The trajectories are coloured by the particle velocity magnitude, where red represents the highest value and blue the lowest value. The initial particle velocity is a factor of 10 of the airflow velocity, that is, $U^* = 10 = U_{particle}/U_{airflow}$.

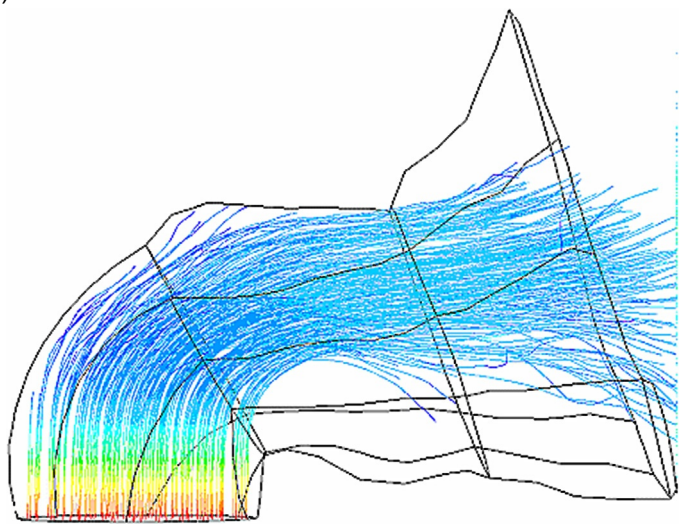
(a) What would be the approximate particle Stokes number for the flow path in *a* and for the flow path in *b* shown in the figures below?

(b) What are the velocities of the particles in flow path *a* when they impact onto the upper walls? Compare this with the velocities of particles in flow path *b* at the same location.

(c) Explain the difference between particle trajectories obtained for flow path *a* (straight) and for flow path *b* (curve) (hint, compare the velocity profiles).



(A)



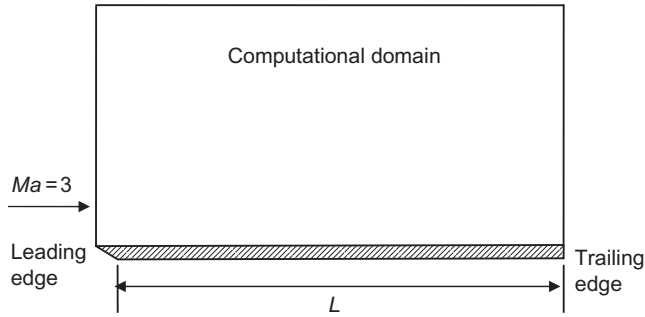
(B)

8.11 Formulate appropriate answers to the following questions for high-speed flows:

(a) Why is the DNS technique very useful for studying *supersonic* flows?

(b) How does the outflow condition in *supersonic* flows differ from the usual *Neumann* boundary condition in *subsonic* flows?

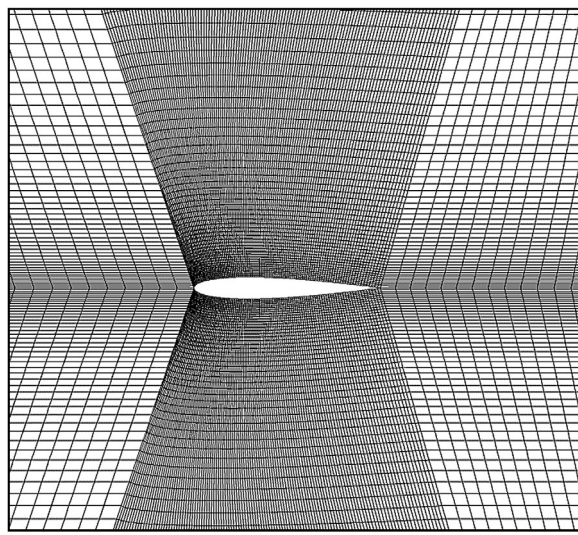
(c) For the following supersonic flow over a flat plate, discuss what types of boundary conditions are suitable to capture the flow features.



(d) Discuss the effects of using a constant wall temperature instead of an adiabatic wall in terms of the boundary-layer development and its effect on the temperature profile in *supersonic* flows.

(e) Discuss the advantages and disadvantages of using DNS methods over theoretical approaches such as the parabolic stability equation (PSE) calculations.

(f) For the following flow over an aerofoil, discuss why the following grid is necessary.



(g) When the angle of attack of the NACA0012 aerofoil is at 5 degrees, what happens to the pressure over the bottom surface, and how does this affect the temperature (see Section 8.4.5.2)?

Chapter 9

Some Advanced Topics in CFD

9.1 INTRODUCTION

Over the last three decades, considerable progress has been made in the development of CFD. In many areas of applications, the field of CFD is attaining a stage of maturity where most of the basic methodologies are rather well established and many have been implemented into a number of commercially available computer packages. Despite many significant achievements, there is still an impending need to develop and advance CFD to meet the demands bolstered from various engineering industries in resolving complex flow problems and also within research communities especially in the area of aerospace research.

The materials that have been presented in this book thus far have served to present an introductory level to the use and application of CFD. For students who are keen in pursuing a research career or for those are currently involved in research and development activities, this chapter is written specifically to provide the latest development and address some of the important issues and challenges that are currently faced by many CFD researchers.

9.2 ADVANCES IN NUMERICAL METHODS AND TECHNIQUES

9.2.1 Incompressible Flows

Incompressible flow, by definition, is an *approximation* of flow where the flow speed is insignificant compared with the speed of sound of the fluid medium. In accordance to its definition, the majority of fluid and associated flow we encounter in our daily lives belongs to the incompressible category. Mathematically, the incompressible flow formulation poses unique and challenging issues not present in compressible flow equations because of the incompressibility requirement. Physically, incompressible flow is characterized by an elliptic behaviour of the pressure waves, whereby the speed in a truly incompressible flow is *infinite*, which imposes stringent requirements on computational algorithms for satisfying incompressibility. Inherently, the major difference between an incompressible and compressible Navier–Stokes formulation is in the continuity equation. The incompressible formulation can usually be viewed as a singular limit of the compressible one where the pressure field is just considered as part of the solution. The primary issue in solving the set

Computational Fluid Dynamics. https://doi.org/10.1016/B978-0-08-101127-0.00009-X
© 2018 Elsevier Ltd. All rights reserved.

of governing equations is to appropriately satisfy the mass conservation equation.

Many engineering applications dealing with the flow of air and water and flow of biofluids are generally in the incompressible flow domain. As flow devices are required for design with more sophistication, CFD techniques are being adopted at a staggering frequency to tackle such types of flows. Because of the escalating use, this book has been specifically written from a practical viewpoint to present the fundamental development of the conservation equations accompanied by suitable numerical methods. Focusing further on the advances achieved to date and possible research prospective, the authors aim to examine the challenges and level of complexities being confronted in fluid engineering for incompressible and low-speed flow as well as the current and future status of development, which are discussed herein.

Based on the approach employing primitive variables, the two most commonly adopted methodologies are (1) methods based on pressure iteration and (2) artificial compressibility method.

For the various methodologies based on pressure iteration, the marker-and-cell (MAC) method developed by Harlow and Welch (1965) represents the first primitive variable method employing a derived Poisson's equation for pressure. Through this method, the pressure is used as a mapping parameter to satisfy the continuity equation. Reviewing the Navier–Stokes mass and momentum equations with constant density (see Eqs 3.13, 3.24, and 3.25), they can be expressed in the general form as

$$\frac{\partial u_i}{\partial x_i} = 0 \tag{9.1}$$

$$\frac{\partial u_i}{\partial t} + u_i \frac{\partial u_i}{\partial x_i} = -\frac{1}{\rho}\frac{\partial p}{\partial x_i} + \nu \frac{\partial^2 u_i}{\partial x_i^2} \tag{9.2}$$

Taking the divergence of the momentum equation, the Poisson's equation for the pressure can be obtained according to

$$\frac{\partial u_i}{\partial t} + u_i \frac{\partial u_i}{\partial x_i} = -\frac{1}{\rho}\frac{\partial p}{\partial x_i} + \nu \frac{\partial^2 u_i}{\partial x_i^2} \tag{9.3}$$

where

$$h_i = \nu \frac{\partial^2 u_i}{\partial x_i^2} - u_i \frac{\partial u_i}{\partial x_i} \tag{9.4}$$

Ever since its enormity introduction, numerous variations of the MAC methods have surfaced, and successful computations have been made.

Another pressure-based method that is also commonly used is the fractional-step procedure (Chorin, 1968; Yanenko, 1971). It is usually performed in two steps: (i) The auxiliary velocity field is obtained from solving the momentum

equation in which the pressure-gradient term can be entirely excluded or computed from the pressure in the previous time step, and (ii) the pressure is computed through a Poisson's equation similar to the MAC method that maps the auxiliary velocity onto a divergence-free velocity field. The method with the exclusion of the pressure-gradient term is illustrated as follows:

$$\frac{u_i' - u_i^n}{\Delta t} = -u_i^n \frac{\partial u_i^n}{\partial x_i} + \nu \frac{\partial^2 u_i^n}{\partial x_i^2} \tag{9.5}$$

$$\frac{u_i^{n+1} - u_i'}{\Delta t} = -\frac{1}{\rho} \frac{\partial p^{n+1}}{\partial x_i} \tag{9.6}$$

where u_i^n is the velocity at the previous time level n, u_i' is the intermediate velocity, and u_i^{n+1} is the velocity at the current time level $n+1$. By taking the divergence of Eq. (9.6), the Poisson form of the pressure can be expressed as

$$\frac{1}{\rho} \frac{\partial^2 p^{n+1}}{\partial x_i^2} = \frac{1}{\Delta t} \frac{\partial u_i'}{\partial t} \tag{9.7}$$

One important aspect of the fractional-step method that the reader should heed is that care needs to be exercised in evaluating the boundary conditions for the intermediate variables (Orszag et al., 1986). A logical way in overcoming such difficulty is to employ the physical boundary conditions for the intermediate steps. This aspect has been thoroughly discussed by Rosenfeld et al. (1991).

The artificial compressibility approach involves modifying the continuity equation by adding a time derivative of the pressure term with an *artificial compressibility parameter*. In this formulation, the continuity equation is modified by adding a time derivative of the pressure term with an *artificial compressibility parameter* β in the form of

$$\frac{1}{\beta} \frac{\partial p}{\partial t} + \frac{\partial u_i}{\partial x_i} = 0 \tag{9.8}$$

Together with the unsteady momentum equations, this forms a hyperbolic-parabolic type of time-dependent system of equations. A series of preconditioning methods (Choy and Merkle, 1993; Turkel, 1999) and numerical schemes, based on the alternating-direction implicit (ADI) procedure by Briley and McDonald (1977) and upwind differencing schemes implemented by Rogers et al. (1991), have been developed in conjunction with the compressible Navier–Stokes equations to solve the incompressible flow. Artificial compressibility relaxes the strict requirement to satisfy mass conservation in each step. Nonetheless, to utilize this convenient feature effectively, it is essential that the nature of artificial compressibility both physically and mathematically is properly understood. Useful guidelines in choosing the artificial compressibility parameter can be found in Chang and Kwak (1984).

In general, it is the authors' opinion that the above methods are well established and that they have been employed rather successfully to solve a wide range of fluid flow problems. Most of these developed methods are commonplace in many daily fluid engineering problems. Many review articles and books on CFD have been written on the state-of-the-art computational methods for viscous incompressible flow. Interested readers are strongly encouraged to refer to Gunzburger and Nicolades (1993), Hafez (2002), Loner et al. (2002), Gustafsson et al. (2002), and Kiris et al. (2002) on the latest trends and advances of these methods. Extensions of these basic formulations targeting a number of specific applications have also been reported. For example, a semi-implicit scheme has been formulated by Najm et al. (1998) that relies on a zero-Mach-number formulation of the compressible conservation equations coupled with detailed chemistry that is constructed based on the predictor-corrector treatment with additive fractional-step procedures to stabilize the computations of reacting flows with large density variations.

Despite the many significant advances achieved for the incompressible CFD methodologies, one aspect the authors still believe deserves some concerted attention is the *computational efficiency*, which is directed primarily towards the solution of the Poisson's equation for pressure. The choice of the pressure solver can be a rather crucial consideration particularly to solve a large physical domain with high mesh density and/or march the solution through small time steps for a transient flow problem. In light of the computations in rectangular-type regions, one possible consideration is to employ a direct (non-iterative) fast Fourier transform (FFT)-based solver (Sweet, 1973) for the pressure equation, which is easily accessible through a computer package called CRAYFISHPAK.[1] However, the application of this direct Poisson solver for general three-dimensional coordinates is not as straightforward and normally considered as impractical; iterative solvers still remain the only feasible option to resolve such complex geometries. Traditional iterative solvers are well-known to be inefficient due to their slow convergence, which therefore requires the development of more advanced solution methods. Currently, parallel computing presents one possible way of accelerating the computations. To maximize the computing speed, iterative matrix solver such as the parallelized version of generalized residual minimal equation solver (GRMES) by Saad and Schultz (1985), which essentially belongs to the family of Krylov methods, is a viable choice to solve the pressure equation. Another avenue that is also worth exploring is the application of multigrid acceleration technique as suggested by Kwak et al. (2005).

1. CRAYFISHPAK, a vectorized form of the elliptic equation solver FISHPAK, was originally developed at the National Center for Atmospheric Research (NCAR) in Boulder, CO.

9.2.2 Compressible Flows

From a historical perspective, numerical methods for solving equations of compressible flows were developed because of the importance and relevance in aerodynamics and aerospace. For the airflow around an aircraft, enormously high speeds can be achieved as the aircraft travels through the earth's atmosphere, thus resulting in a very high Reynolds number; the turbulence effect is mainly concentrated within the thin boundary layers. Ignoring the frictional drag, the flow may be attributed to the presence of the *wave* drag due to shocks and *pressure* drag that is essentially inviscid in nature. The latter property has indeed necessitated much of the revolutionary effort and evolution effort focusing on special methodologies that have been designed specifically to obtain the solution of the inviscid Euler equations. As reviewed by Fujii (2005), CFD was first applied to simulate transonic flows in the 1970s. Embedded shock waves were adequately captured, and the design process of commercial aircraft has drastically changed ever since then. In the middle of the 1980s, CFD was employed to simulate hypersonic flows associated with the space transportation system development including reentry vehicles. Most of these can be readily solved through the inviscid Euler equations. Practical flow simulations in aerospace employing the full compressible Navier–Stokes equations first appeared in Fujii and Obayashi (1987a,b). For high-speed flows, the use of these equations to resolve the thin viscous boundary layers around aerofoils still presents enormous challenges. The fine mesh requirement is unavoidable in order to adequately predict the near-wall turbulence for flow analysis and eventual control of flows. Finely distributed mesh resolution near walls greatly limit the time-step size for computation; this in turn dramatically increases the computational burden to achieve a solution.

With regard to some specific methods for compressible flows, the earliest scheme was the method of MacCormack (1969), which is based on an *explicit* method and central differencing. It is still being used quite extensively even to this present day. To avoid the problem of oscillations especially due to the discontinuity at the shock front, the concept of artificial dissipation is introduced into the equations. A fourth-order dissipative term is the most common addition, but higher-order terms have also been successfully applied. Another effective numerical method to solve the equations for compressible flows is the *implicit* method developed by Beam and Warming (1978), which is based on the approximate factorization of the Crank-Nicolson method. Like the MacCormack method, the addition of the explicit fourth-order dissipative term into the equations is imperative due to the central-differencing consideration.

Recently, Roe (2005) in his review paper of 'CFD—retrospective and prospective' identified some key issues to the seminal developments in CFD algorithms. One of them is to overcome the deficiency that deals with the basic matter of shock capturing when the shocks are very strong. Enormous interest has been placed to develop a class of upwind schemes of greater sophistication

to produce a well-defined discontinuity without introducing an undue error into the smooth part of the solution elsewhere. In the next section, the authors aim to provide the reader a survey of the latest developments of high-resolution schemes. Instead of dwelling on the fine detail construction of these schemes herein, interested readers are strongly encouraged to refer to the literature for more in-depth understanding. Another approach that is of significant interest in capturing the unsteady moving shock front is through the use of adaptive meshing, which will also be subsequently discussed below.

9.2.2.1 High Resolution Schemes

Consider the simple illustration of the inviscid Euler equation based on the one-dimensional wave equation in the nonconservative form:

$$\frac{\partial u}{\partial t} + c\frac{\partial u}{\partial x} = 0 \tag{9.9}$$

where c is the advective velocity describing the propagation of a wave in the direction of the x-axis. There is a discontinuity in the velocity u across the wave as described in Fig. 9.1. Assuming that c is positive, properties at grid point i should depend on the upstream flow field properties at grid point $i-1$. Grid

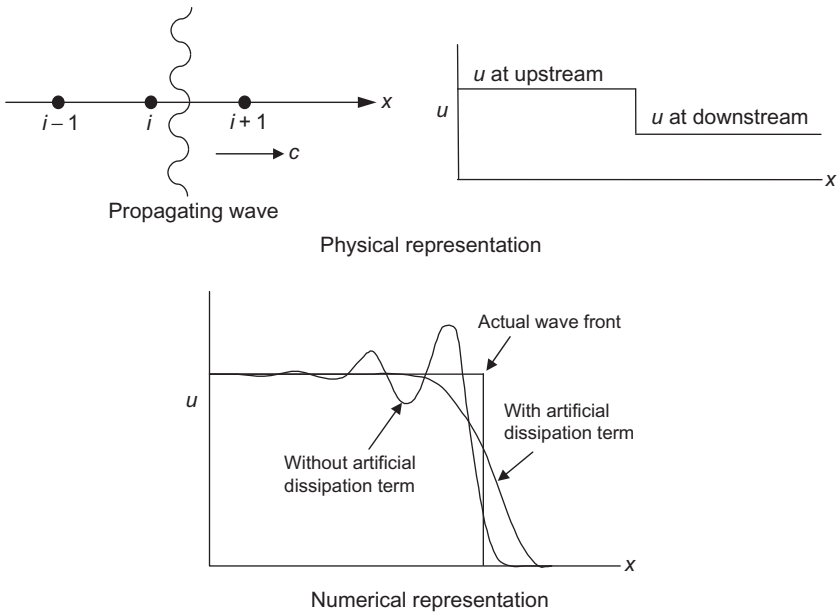


FIG. 9.1 Schematic physical representation of a propagating wave in the positive x direction accompanied by the flow field at a given instant of time and numerical representation with and without artificial dissipation term in the vicinity of the discontinuous wave interface.

point at $i+1$, on the other hand, should not physically influence the point at i; hence, the choice of numerical scheme must reflect the flow physics. If the gradient $\partial u/\partial x$ is approximated using central differencing such as the traditional approach described above for the MacCormack (1969), the velocity u profile results in an oscillatory behaviour near the discontinuous wave front. In some circumstances, the numerical procedure can lead to an unstable and chaotic solution. The common remedy as aforementioned is to introduce an artificial dissipation term. Despite the numerical result exhibiting a *monotone* variation (no oscillations), the diffusive property remains an undesirable element as illustrated for the numerical representation in Fig. 9.1.

To eliminate this undesirable property, some rather mathematically elegant algorithms have been developed during the past decade or two. These modern algorithms have include flux limiters by Sweby (1984) and Anderson et al. (1986) in the MINMOD and SUPERBEE schemes or slope limiters due to the monotone upwind scheme for conservation laws (MUSCL) family of methods that can be found in Van Leer (1974,1977a,b,1979), Godunov (1959), and approximate Riemann solvers (Toro, 1997). Amongst the many shock-capturing techniques in the literature, the total variable diminishing (TVD) algorithm is considered to be well suited for capturing shock waves. Essentially, the integrated quantity (total variation) of the gradient $\partial u/\partial x$ in Eq. (9.9) is now discretely discretized according to

$$\mathrm{TV}(u) = \sum_i |u_{i+1} - u_i| \tag{9.10}$$

To achieve the monotonic variation, the condition of $\mathrm{TV}(u^{n+1}) \leq \mathrm{TV}(u^n)$ is imposed. In general, the design of a numerical scheme that can both represent small-scale structures with minimum numerical dissipation and capturing discontinuities without spurious oscillations is a formidable task. First-order upwind scheme (Appendix B), which does not result in oscillations in the vicinity of discontinuities, can be readily shown to obey the TVD condition. Nevertheless, it still suffers the same faith like the introduction of the artificial dissipation term as being very diffusive in the vicinity of discontinuities.

The greatest challenge in the ongoing research of this area is therefore to develop schemes that are *highly accurate in smooth regions of the flow* and have *sharp nonoscillatory transitions at discontinuities*. Colella and Woodward (1984) first attempted to overcome particularly on the latter aspect by introducing a piecewise parabolic method (PPM), which is a four-point centred stencil to define the interface value; the formulation of this value is then limited to control the oscillations. Leonard (1991) later combined this limiting approach with a higher-order (up to ninth order) interface value. It is noted that the PPM can be considered as an extension of Van Leer's MUSCL scheme and MUSCL in turn is an extension of the Godunov's approach. These limiting procedures nonetheless still cause the solution accuracy to degenerate because of the first-order approximation near extrema.

Along a different line of thought, ever since the development of the third-order essentially non-oscillatory (ENO) schemes by Shu and Osher (1988, 1989) and Harten (1989), improved schemes such as the fifth-order weighted ENO (WENO) by Liu et al. (1994) and Jiang and Shu (1996) have surfaced to better define the interface value as a weighted average of the interface values from all stencils. The weights have been designed such that very high accuracy is achieved in smooth regions. The WENO schemes, however, still show a diffusive behaviour in the vicinity of discontinuities; they smear the interface front as much as the ENO schemes. Very recently, the approach by Suresh and Huynh (1997) has been developed to enlarge the TVD constraint for a better representation near extrema. The reconstructed value at the interface is limited such as to preserve both monotonicity and high-order accuracy by using local geometrical considerations to relax the monotonicity constraints near extrema. This scheme referred to as MP where MP stands for monotonicity preserving is fifth order and was developed to address the chronic problem of upwind methods, namely, the narrow stencils that cannot distinguish between shocks and extrema.

As a demonstration of the above schemes, some results extracted for the one-dimensional advection equation of Eq. (9.9) that appears in the article of Suresh and Huynh (1997) are shown in Fig. 9.2. Not surprisingly, the unfiltered approach generally exhibits unwanted oscillations—a violation of the TVD condition—near the discontinuity locations. The ENO scheme though preserving the monotone variation of the velocity u fairs however no better to the unfiltered scheme in exceeding the limiting bounds—the realizability condition. Higher-order schemes such as the fifth-order methods of WENO and MP schemes clearly satisfy not only the monotonic variation of velocity u but also the realizability condition near the extrema. The superiority of MP over WENO is succinctly demonstrated especially near the discontinuities of the velocity u profile where the latter scheme still shows some diffusion of the velocity u at these locations.

Very recently, Daru and Tenaud (2004) extended the MP schemes of Suresh and Huynh (1997) to seventh order for the solution of Euler and Navier–Stokes equations using local linearization and dimensional splitting in the multidimensional case. They commented that the schemes despite the lack of preservation of the formal high accuracy still gave very accurate results that compared well with the high-order WENO schemes at a lower cost. They also pointed out the classical drawback associated with dimensional splitting similar to the fractional method for incompressible flows, which is the treatment of boundary conditions for the intermediate step boundary for bounded viscous-flow calculations. Interested readers may wish to further investigate this pertinent aspect to improve these MP schemes.

From the brief survey conducted, it is apparent that the development of high-resolution TVD schemes for the numerical simulation of unsteady compressible flows remains an area of intense research. The current trend of research at the time of this writing appears to be the development of higher-order schemes to

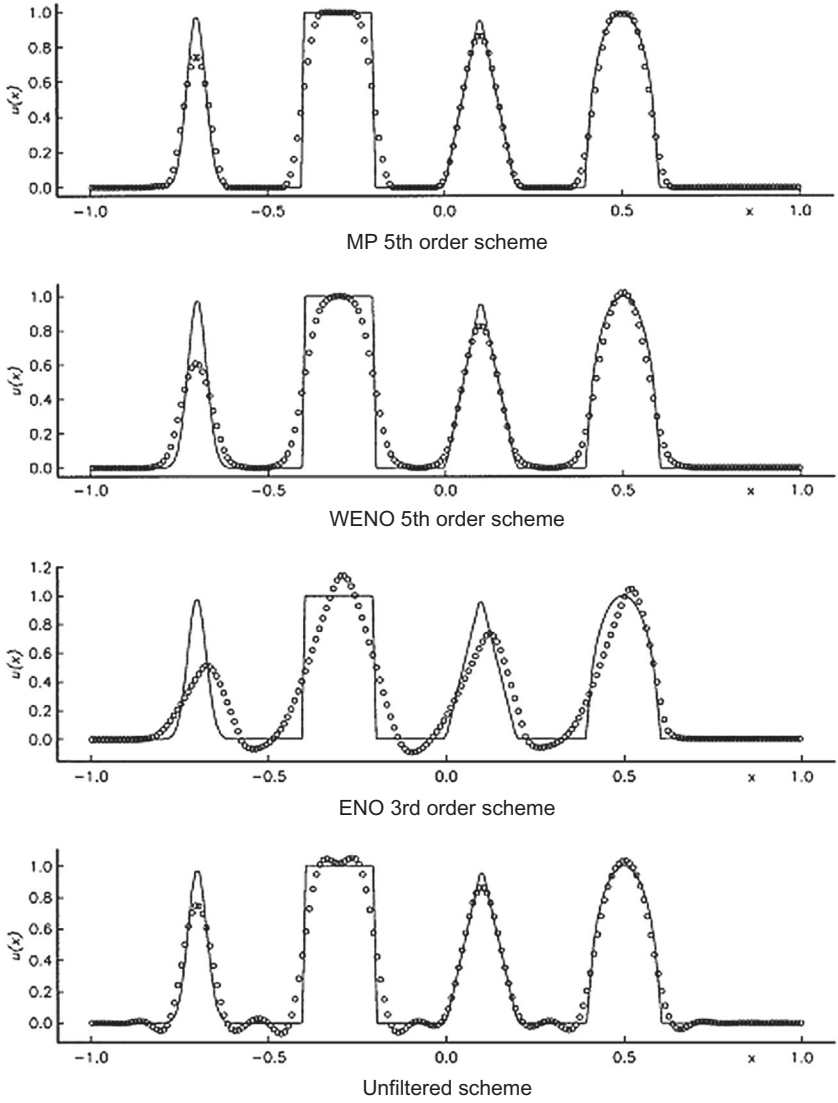


FIG. 9.2 Results extracted from Suresh and Huynh (1997) for the unsteady one-dimensional advection equation.

better capture the strong shock profiles. In the next section, the authors proceed to illustrate another cutting edge of research where the moving shock front is now progressively tracked throughout the computational domain in addition to the usual approach of resolving the shock front in a fixed-grid environment such as has been described by the present methodology discussed herein.

9.2.2.2 Adaptive Meshing

For a strong migrating shock front, dynamic grid adaptation may be required to resolve the sharp discontinuities that exist within the flow domain as the solution changes continuously through time. There are a number of adaptation categories that have recently been discussed especially in Thompson et al. (1999) and Kallinderis (2000). Interested readers are encouraged to probe deeper into the literature for a better understanding of the various state-of-the-art techniques that are being applied.

One method that has shown to perform well is the *r-refinement* technique. The basic idea is to devise an algorithm to physically relocate the original non-adapted mesh to the time-varying changes of the solution in the domain, based on some criteria for adaptation whilst maintaining the identity and data structure of the domain being solved. Many successful means are available for relocating nodes or remeshing in order to perform adaptation. However, the success of any procedure depends on the criteria used to properly guide the node location. Benson and McRae (1991) employed a gradient-based algorithm to obtain a weight function. One such measure is the local gradient (curvature) of the dependent variable for resolution evaluation. Note that there are other approaches that could also be adopted for resolution evaluation. Nevertheless, let us consider the two-dimensional multiblock dynamic adaptive algorithm developed by Ingram et al. (1993) for the purpose of illustrating shock transition. By tracking the evolution of the outer shock from right to left and observing the grid orientation, topology, cell volume, etc., the mesh clearly reflects the continuous changes of the solution process as depicted in Fig. 9.3. The sharp discontinuities are precisely captured through the concentrated mesh surrounding the shock front.

Another refinement method that is also very prevalent in the literature but not often applied to unsteady problems is the enrichment or *h-refinement* technique. The development of an adaptive remeshing scheme for application to two-dimensional triangular and three-dimensional tetrahedral meshes has been reported in Hassan and Probert (1999). Here, the cell volume and shape are changed by the *insertion* or *deletion* of mesh nodes from the data structure resulting in an overall *increase* or *decrease* of the number of cells. It is certainly a more natural technique since the algorithms used for reconnecting the nodes are the same as those used during grid generation to improve distribution or to achieve some predetermined conditions for the grid. Generally speaking, *h-refinement* is not strictly confined to only one single type of mesh structure. This rather flexible technique permits a combination use of both structured and unstructured meshes. Dynamic adaptation can also take place through a series of mesh layers fitted to the body.

Adaptive meshing is still in its infancy application in CFD. Many research issues remain outstanding and unresolved (McRae, 2000). Firstly, there is a further requirement to investigate the relationship between cell shape, size, and orientation in particular for the *r-refinement* on a structured mesh concerning

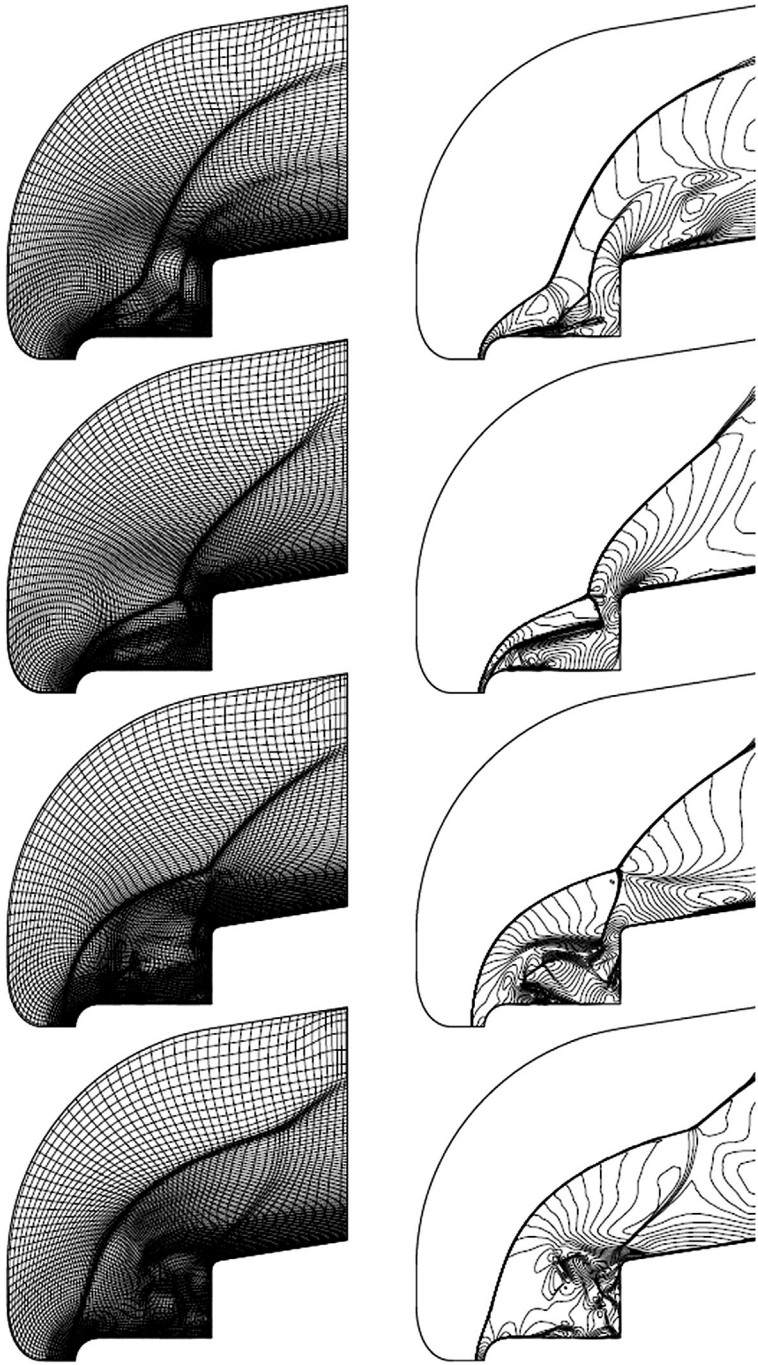


FIG. 9.3 Results extracted from Ingram et al. (1993) for the grid and density contours produced by *r-refinement* dynamic adaptation.

the grid skewness and aspect ratio in the vicinity of the shock front as illustrated by the problem in Fig. 9.3. Highly skewed cells can pose enormous problems to numerical methods; the sharp response of the flow behaviour may lead to the divergence of the solution procedure. Secondly, it must be recognized that even the best adaptive techniques with the best criteria (weight function) may not provide the same degree of resolution for all portions of the solution. In a recent article by Soni et al. (2001), it is stated in relation to the adaptive weight function that 'determination of this function is one of the challenging areas of adaptive grid generation'. Thirdly, the defining characteristic of the unstructured triangle/tetrahedral meshes for the *h-refinement* is reflected on their ability to resolve solutions based on the orientation of the cells' surfaces to the solution that can be quite random locally. This does not pose any problems in the smooth regions but can create serious resolution difficulties in regions when the solution varies rapidly.

9.2.3 Moving Grids

Moving grids exist in many engineering applications. Take for an example the simulation illustration of the flow in a diesel internal combustion engine in Chapter 1 where deforming grids have permitted the means of simulating the piston and valve motion to gain better insights into features that are present within in-cylinder flows. Another important example in Chapter 1 is the simulation of a rotating impeller that is common in gas-sparred stirred tanks. To resolve such a problem, one part of the grid can be taken to be attached to the impeller and allowed to freely move in time, whilst the other encompasses the impeller and remains stationary. It is worth noting that such an approach can also be applied to the rotor-stator interaction in turbomachinery. As suggested by Lilek et al. (1997a) and Demirdzic et al. (1997b), the moving grid is allowed to *slide* along the interface without deformation between the part of the grid that is attached to the static stator and the other part that is attached to the rotating rotor. The grids do not have to match at the interface; this allows flexibility in employing different kinds of meshes and/or achieving the desire fineness in the respective domains. Except for difficulties in ensuring exact conservation, there are essentially no limitations on the applicability of this approach. Recently, Farhat (2005) reviewed the application of CFD to the prediction of flows past flexible and/or moving deforming bodies in the aeronautical area. The driving application has centred on the nonlinear computational aeroelasticity to address problems associated with local transonic effects, limit-cycle oscillation, high-angle-of-attack flight conditions, and buffeting. Despite the achievements in the formulation and discretization of turbulence models and wall laws on dynamic meshes (Koobus et al., 2000) and successful simulations of vortex-dominated flows around manoeuvring wings over a wide range of Mach numbers (Kandil and Chung, 1988), most successes of moving-grid applications according to Farhat (2005) have concentrated so far on either *complex*

geometries with inviscid flows or *viscous flows with simple geometries*. Hence, to fill this gap, it is also with the authors' opinion as with Farhat's that further research, applied to CFD on moving grids, needs to be undertaken to perfect the robustness of mesh motion algorithms and to combine them with the possibility of automatic partial regridding.

In all the problems discussed above, the movement of the domain is predetermined by external effects. For another class of problems such as free-surface flows, the movement must be calculated as part of the solution process where the grid has to move with the boundary. In the majority of these cases, the free-surface interface can be a boundary between liquid and gas such as an ocean separated from the surrounding air atmosphere or liquid and water, for example, the freezing of water into ice. For such problems, the critical issues of this approach deal with the efficiency and stability of the numerical algorithm for the movement of the interface. As each grid point on the interface is moved through time, the surface grid may be rather irregular due to an uneven distribution and unconstrained movement. Some grid-generation algorithms that retain the curvature information of the interface are generally required to redistribute the grid points to ensure numerical integrity and stability of the solution. For illustration, some results on a numerical study of three-dimensional natural convection and freezing of water in a cubical cavity by Yeoh et al. (1990) are discussed below. The distorted ice and water domains at a particular instant of time are shown in Fig. 9.4. The ice–water interface dramatically deforms under the influence of natural convection effects that are present in the water. The appearance of two counterclockwise flow regions shown in Fig. 9.5 is distinct for freezing of water because of its density extremum at 4°C. As expected, the flow inversions around this temperature significantly influence the development of the ice-water interface. Simulating such flow problems usually requires very small time steps to advance the interface and generate a new mesh using body-fitted grids in the respective domains at each time step. Both of these steps negatively impact the simplicity, robustness, and computational cost of the solution procedure. In an article, Tezduyar (2001) indicates that the computational efficiency degenerates dramatically for cases involving large motion. Development of a more robust method is thus still required to fulfil the need in better treating this class of flow problems with moving interfaces or boundaries.

9.2.4 Multigrid Methods

In Chapter 4, the use of multigrid method to accelerate the convergence of the iterative process for large systems of nonlinear algebraic equations has been discussed, whilst in Chapter 5, the authors presented the simplest strategy for achieving computational efficiency in solving such a system of equations through the V-cycle with five different grid levels. It is by no means a comprehensive description; the authors have aimed mainly to provide the reader with a

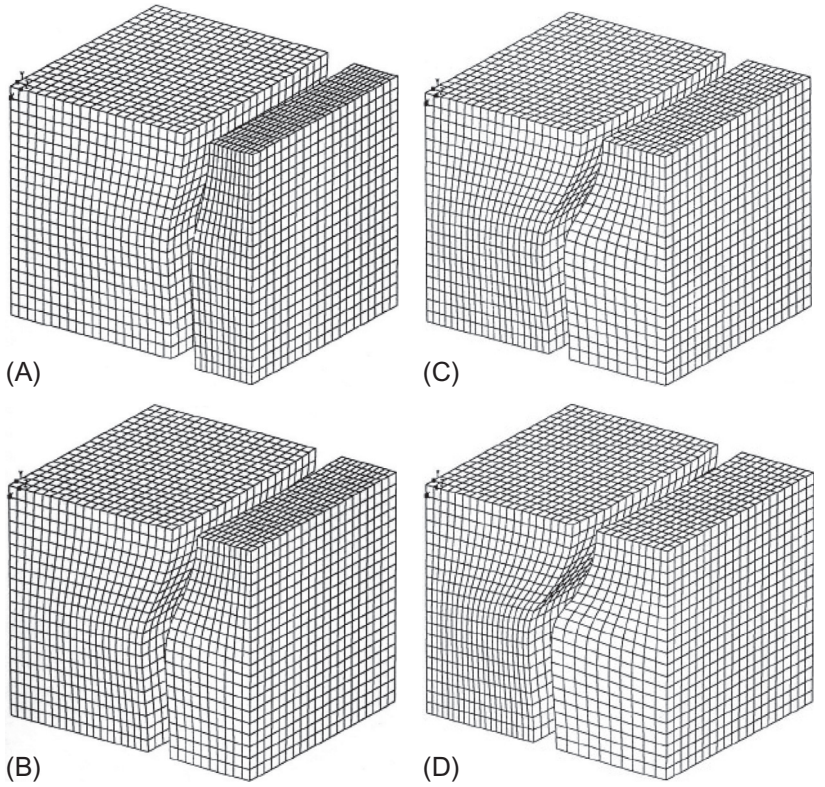


FIG. 9.4 Results extracted from Yeoh et al. (1990) for the distorted water (left) and ice (right) domains at (A) 12.7, (B) 25.5, (C) 38.2, and (D) 54.1 min.

bird's eye view of such an approach. However, recognizing its surging importance in areas of modern CFD, the basic philosophy behind this particular method is further explored within this section.

As with the V-cycle, calculations are initially carried out on a fine grid, and these results are progressively transferred downwards to a series of coarser grids; the results on the coarsest grid are obtained and transferred upwards back to the fine grid level. The process is repeated until satisfactory convergence is achieved. On a mathematical basis, the advantage of the multigrid method stems from the consideration of the enhanced damping of numerical errors through the flow field. A whole spectrum of errors can propagate throughout the numerical solution of such a flow field. For a discrete grid increment Δ_m, the *high-frequency errors* can be represented by the smallest value $\lambda_{\min} = 2\Delta_m$. The majority of iterative procedures such as the Jacobi and Gauss–Seidel (Chapter 4) are rather efficient in removing the high-frequency errors in a few iterations. It is the removal of the *low-frequency errors* that causes the slow convergence of iterative methods on a fixed grid. Nonetheless, let us imagine

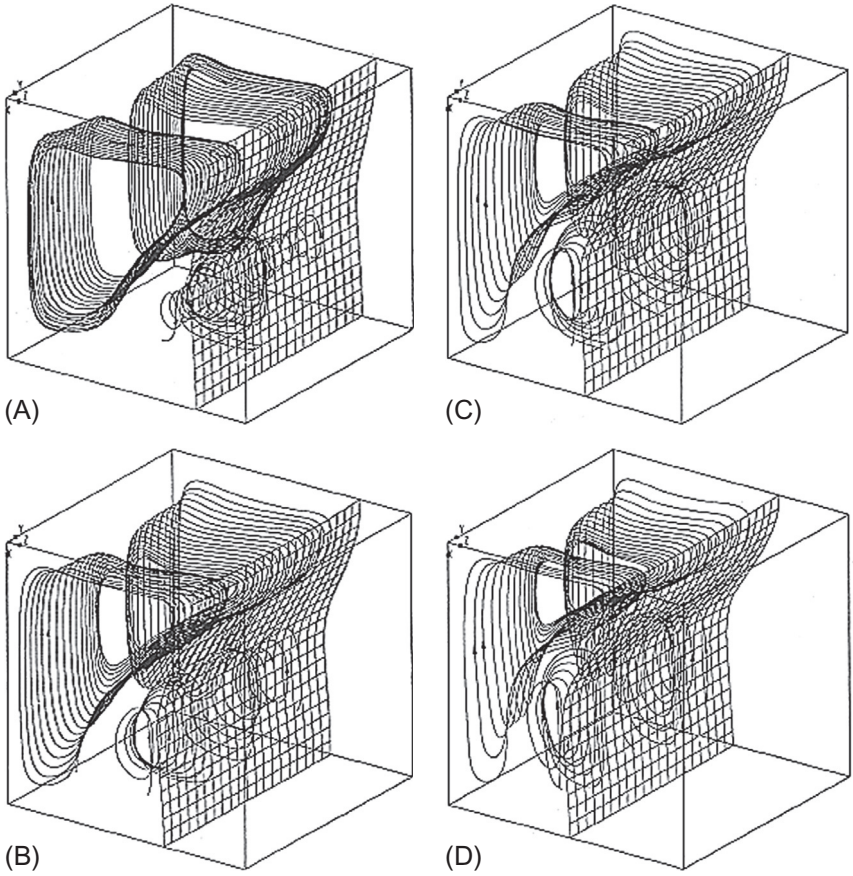


FIG. 9.5 Results extracted from Yeoh et al. (1990) for the isometric views of interface locations and particle tracks at (A) 12.7, (B) 25.5, (C) 38.2, and (D) 54.1 min.

that after carrying out a few iterations on the fine grid, the immediate results are transferred to a coarser grid. The *high-frequency errors* are now essentially lost or hidden in the coarse grid, and the solution procedure begins to damp at a more rapid rate than would have taken place in the fine grid because of the larger Δ_m. Hence, by progressively moving the intermediate results to coarser grids, the low-frequency errors are essentially damped; when these results are transferred back to the fine grid, the *low-frequency errors* are indeed much smaller than they would have been for an equal number of sweeps that are performed on the fine grid itself.

It is clear from above that the multigrid method is more of a strategy rather than applying a particular solution method to solve the algebraic equations for a given flow field. Currently, ongoing research is still being undertaken to this

very day to optimize the solution process particularly on improving the numerical methods in solving the algebraic equations at each grid level. Many challenges remain in designing the 'best' multigridding strategy whether they may be better in ascertaining suitable combination of simple or advanced iterative methods on fine grids accompanied by direct methods to obtain solutions on the coarse grids or by employing different cycling strategies using either a series combination of the V-cycle with the W-cycle or the implementation of a *full multigrid* F-cycle. Extensive efforts are also being heavily invested to extend the multigrid method to parallel computing to achieve quicker computational speed-ups in comparison with traditional single- or dual-processor computations. Interested readers can refer to Mavriplis (1988), Wesseling (1995), Timmermann (2000), and Thomas et al. (2003) for the latest trends and developments in this subject area.

9.2.5 Parallel Computing

Central processing units (CPUs) in most single- or dual-processor computers (PCs and workstations) are getting faster and more compact. At this present moment, most of these computer chips are teetering on amazing speeds. To gain any significant increase in speed, consideration for future trends in high-performance CFD computing ultimately beckons in the wake of parallel computers.

The basic idea of parallel computing stems from the simple desire to perform simultaneous operations of multiple computational tasks on a computer system. Commercially available parallel computers are generally composed of thousands of processors, gigabytes of memory, and computing power measured in megaflops or even gigaflops. The advantage of parallel computers over vector supercomputers is *scalability*. These systems usually allow the accommodation of standard computer chips and therefore are cheaper to produce. Parallel computing, particularly in CFD, is a broad field of research and development. The authors will not venture into the details regarding the taxonomy of parallel computing architectures and programming paradigms, which are beyond the scope of this introductory book. Interested readers can refer to numerous articles in journal publications such as *International Journal of High Speed Computing*, *The Journal of Supercomputing* or *Journal of Parallel Programming*, and a book by Simon (1992) for a more in-depth study particularly on the aforementioned aspects and the principal issues behind the utilization of parallel computing in CFD.

Rather, the authors would like to highlight outstanding issues that still need to be adequately addressed. For the effective utilization of parallel computing, we can first concentrate on the issues of *domain decomposition* and *load balancing*. The idea of partitioning data and computational tasks amongst multiple processors is commonly denoted as *domain decomposition*. The principal objective of *domain decomposition* is to maintain uniform computational

activities on all processors and is known as *load balancing*. In hindsight, it appears straightforward enough, but there are a number of factors that can complicate the aspect of load balancing. For example, combustion flows that involve chemical reaction rate source terms are computed only where the static temperature exceeds some threshold value. Another example is particle tracking where particles can accumulate in a particular subregion. All of these pose serious challenges in parallel computing that are in the midst of active research.

Another key concern is the impact of scaling on a given parallel computer architecture with increasingly larger numbers of processors. An important question arises: how does the *efficiency* of the computation depend on the number of processors? Generally speaking, the performance of parallel computing may be influenced by the cost of scheduling processors, communication between processors, and synchronization of time (i.e. the time required to allow processors to reach a common point following the execution of the parallel section of the code). Lastly, regarding the issue of *portability*, significant effort has been devoted to the development of standardized environments for the development of parallel computer codes. In recent years, rigorous developments of a standard computer language FORTRAN to high-performance FORTRAN (HPF) (Forum, 1993; Koelbel et al., 1994); standard heterogeneous, network-based parallel computing environments such as parallel virtual machine (PVM) (Sunderam et al., 1990; Mattson, 1995); and standard message-passing interface (MPI) (Forum, 1994) have been undertaken to expand the appeal and broaden the flexibility of parallel computing.

At the present time, many CFD researchers may still perceive parallel computing with some reservations as

(1) lacking a decisive advantage performance over conventional serial (and vector) computers in many instances,
(2) difficult to programme efficiently,
(3) grossly lacking in portability.

It appears that all these factors are likely to diminish in the not too distant future. It is also highly probable that modern parallel computers can come up to speed to equal or exceed, for example, the performance of even the largest multiprocessor Cray supercomputers. Currently, the aerospace industry has taken the lead in applying parallel computing to practical analysis and design. Other engineering areas will eventually follow in similar footsteps as the advancements of parallel computers are made more attractive for practical use and to better resolve more realistically complex fluid flow problems.

9.2.6 Graphics Processing Units and CUDA Environment

The use of graphics processing unit (GPU) platforms has been realized in a number of engineering applications especially in the field of fluid mechanics (Elsen et al., 2008; Kampolis et al., 2010), molecular dynamics (Anderson

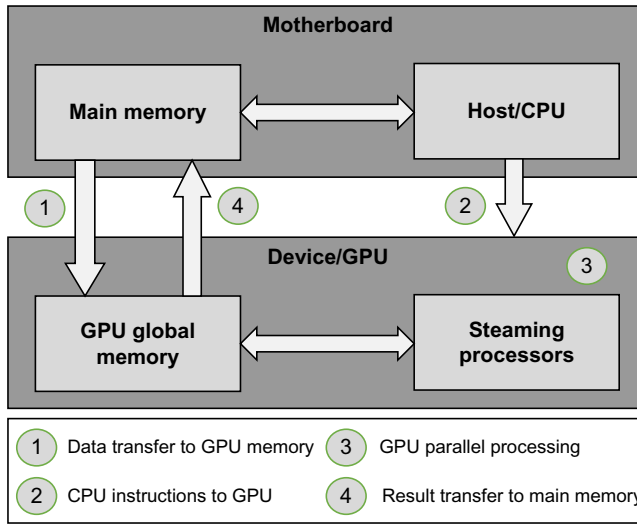


FIG. 9.6 CUDA processing flow paradigm. *(After Papadrakakis, M., Stavroulakis, G., Karatarakis, A., 2011. A new ear in scientific computing: domain decomposition methods in hybrid CPU-GPU architectures. Comput. Methods Appl. Mech. Eng. 200, 1490–1508.)*

et al, 2008; Sunarso et al., 2010), wave propagation (Komatitsch et al., 2010), and building performance simulation (Tian et al., 2016).

An illustration of the CUDA processing flow paradigm can be seen by the schematic representation in Fig. 9.6. In essence, graphics processing units (GPUs) are parallel devices of the single instruction multiple data (SIMD) that describes the devices with the handling of multiple processing elements on the operation of multiple data simultaneously. Data-level parallelism is thus exploited within the parallel devices. As data are transferred from the main memory of the motherboard to the memory of the GPU, the CPU being the host instructs the GPU to carry out the floating-point arithmetic operations that are performed in each streaming processor (SP). Since this device has a large SPs being grouped together in the streaming multiprocessors (SMPs), they can collectively have significantly more gigaflops of operations than the current high-end CPUs. Once the calculations are completed, the result is transferred back to the main memory.

As each GPU applies the same functions on a large number of data, these data-parallel functions also known as kernels generate a large number of threads to exploit data parallelism—single-instruction multiple-thread (SIMT) paradigm. A thread is considered to be the smallest unit of processing that can be scheduled by the operating system. Threads in GPUs generally take only very few clock cycles to generate and schedule due to the underlying hardware support where unlike CPUs thousands of clock cycles are required. These number of threads generated are generally organized in blocks, and a grid that is defined

by all thread generated by a kernel consists of a number of blocks being equal in size. Another form of thread grouping is warps that are units of thread scheduling in SMPs. The purpose of warps is to ensure high hardware utilization where all processes are likely to have a workload at all times in order to avoid idle processors whilst waiting for the completion of operation.

One significant feature of the CUDA device is the ability to have a variety of different memories that can be utilized to achieve high performance. The global memory that resides in the device is responsible for the interaction with the host/CPU. It is large in size and off-chip, and the constant memory allows interaction with the host to provide faster and more parallel data access paths for CUDA kernel execution. Also, other types of memories such as registers and shared memories could be assessed in a highly parallel manner in the device that cannot be assessed by the host. Registers are thread bound that can be employed for holding variables that require frequent access but do not need to be shared with other threads. Shared memories are allocated to thread blocks that allow all threads in the block to access variables in the shared memory allocated locations for that block.

Through the consideration of domain decomposition methods, a new era of computing is emerging especially through the use of hybrid CPU–GPU systems with the purpose of exploiting all available processing power and CPU memory resources. Papadrakakis et al. (2011) have shown that the processing capabilities of hybrid CPU–GPU systems in conjunction with efficient domain decomposition methods could ensure high utilization time and minimize idle time especially by exploiting the intrinsic software and hardware features of the GPUs and the numerical properties of the solution methods. Nevertheless, the difference in performance between the CPU and GPU is normally not the same when carrying out mathematical operations such as dot products, matrix–vector multiplications, or solving linear systems. Because of the difference in performance between the CPU and GPU, the arithmetic operations being executed and other parameters need to be treated carefully in order to achieve the required peak performance to solve large simulation-based applied science and engineering problems.

9.2.7 Immersed Boundary Methods

Immersed boundary methods were first introduced by Peskin (1972) to simulate cardiac mechanics and associated blood flow. One distinguishing feature of this approach is the ability to perform the entire simulation on a fixed Cartesian grid. A novel procedure was developed by directly imposing the effect of the immersed boundary on the flow; the requirement for the grids to conform to the complex geometrical structure of the heart was thus avoided. Since its inception, numerous modifications and refinements have been proposed, and a number of variants of this approach now currently exist.

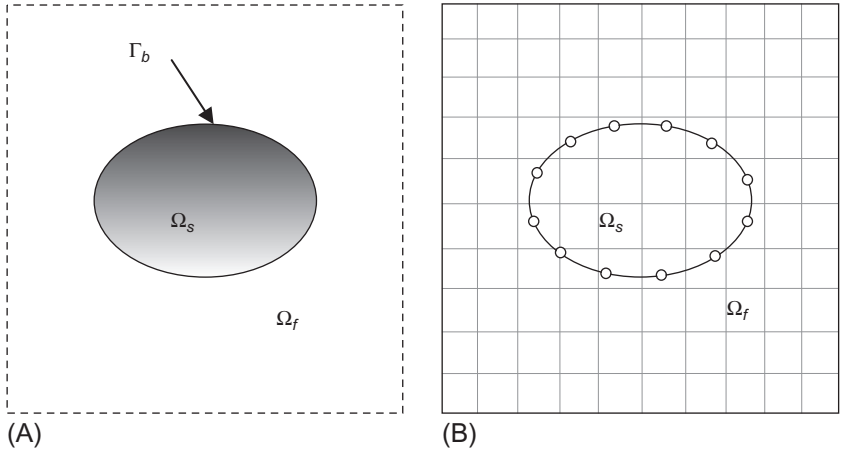


FIG. 9.7 (A) Schematic drawing showing flow past a generic body. The solid body occupies the volume Ω_s with boundary Γ_b. The volume of the fluid is denoted by Ω_f. (B) Schematic of body immersed in a Cartesian grid on which the governing equations are discretized.

Consider the schematic drawing of the simulation of flow past a solid body in Fig. 9.7A. The conventional approach would be to employ structured or unstructured grids conforming to the particular body shape. This is achieved by first defining the surface grid covering the boundary Γ_b. The internal grids encompassing the regions occupied by the fluid Ω_f and the solid Ω_s are then generated after. For the finite-difference method, the partial differential governing equations are transformed into a curvilinear coordinate system that aligns with the grid lines. They are then discretized and solved in the computational domain with relative ease. For the finite-volume method employing a structured grid, the integral form of the governing equations is discretized, and the geometrical information regarding the grid is incorporated directly into the discretization. If an unstructured grid is used instead, either the finite volume or finite element methodology can be adopted by incorporating all the relevant local cell geometry into the discretization. Both of these approaches do not have to resort to grid transformations.

On the other hand, let us consider a nonconformal body on a Cartesian grid in Fig. 9.7B. Here, the immersed boundary would still be represented through some means of the surface grid covering the boundary Γ_b, but the present Cartesian grid would be generated with no regard to this surface grid. Therefore, the solid body cuts through this Cartesian volume grid. Because the grid does not conform to the solid boundary, the immediate task is to incorporate appropriate boundary conditions by modifying the equations in the vicinity of the boundaries. The governing equations can therefore be discretized using any technique whether they may be finite difference, finite volume, or finite element, without the need to resort to coordinate transformation or complex

discretization operators. This is essentially the essence of the immersed boundary method.

Clearly, the imposition of suitable boundary conditions is not straightforward in immersed boundary methods. There are two approaches as indicated by Mittal and Iaccarino (2005) that are amenable to precisely accommodate the effects of the boundary condition on the immersed boundary. The modification can take place in the form of source terms (or forcing functions) in the governing equations in order to reproduce the effect of a boundary. In the first approach, which we can term as *the continuous forcing approach*, the forcing function is incorporated into the continuous equations applied to the entire domain before discretization, whereas for the second approach, which can be termed as *the discrete forcing approach*, the 'forcing' is introduced after the equations are discretized. The continuous forcing approach is very attractive for flows with immersed elastic boundaries. For such flows, the method has a sound physical basis and is very simple to implement. Many successful applications in biology such as sperm motility (Fauci and McDonald, 1994) and multiphase flows (Unverdi and Tryggvason, 1992) testify the viability of such an approach where elastic boundaries are abound. For the discrete forcing approach, it is however not as practical as the continuous forcing approach, but it enables a sharp representation of the immersed boundary, and this is especially desirable for high Reynolds number flows. It also allows direct control over the numerical accuracy, stability, and discrete conservations of the solver. This method has been used rather successfully for simulating compressible flow past a circular cylinder and an aerofoil (Ghias et al., 2004), flow through a rib-roughened serpentine passage (Iaccarino et al., 2003), flapping foils (Mittal et al., 2002), and objects in free fall through a fluid (Mittal et al., 2004). It is apparent that the choice of employing either the continuous or discrete forcing approaches is very problem-dependant on the particular fluid flow process. More details on the mathematical basis and numerical considerations for both of these approaches can be found in the article by Mittal and Iaccarino (2005).

As a demonstration of the application of the immersed boundary method, Fig. 9.8 illustrates the flow structures in the near wake behind a sphere. Numerical simulations performed by Yun et al. (2006) are compared with the experimental flow visualization. The large eddy simulation (LES) results are shown to be in good agreement with the experiment, thereby validating the fidelity of the immersed boundary method.

The popularity of immersed boundary methods is increasing at a tremendous rate. The few applications highlighted above do not even begin to scratch the surface of the many applications that have been simulated using these methods. In due time, concerted ongoing improvements on the issues of accuracy and efficiency and the development of innovative and creative approaches such as adaptive grid meshing with immersed boundary method (Roma et al., 1999) will see increased applications in new areas of complex turbulent flows,

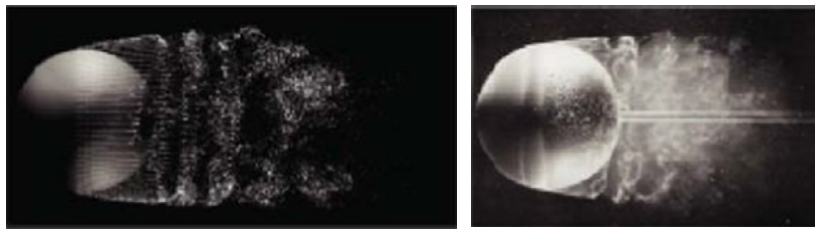


FIG. 9.8 Results extracted from Yun et al. (2006) for the flow structures in the near wake behind a sphere: (A) Reynolds number $Re = 10^4$ (immersed boundary simulation) and (B) Reynolds number $Re = 1.5 \times 10^4$ (experiment).

fluid–structure interaction, and multimaterial and multiphysics simulations and also in well-established areas such as biological and multiphase flow applications.

9.3 ADVANCES IN COMPUTATIONAL MODELS

9.3.1 Direct Numerical Simulation (DNS)

Turbulence in fluids is a nonlinear phenomenon, and it comprises a wide spectrum of spatial and temporal scales. Turbulent flow poses significant challenges to modellers as already evidenced by the range of turbulence models that have been developed and applied. Decades of active research have certainly translated some of these models as commonplace in many practical and design analyses. Lately, one significant area of activity in the modern simulation strategies for turbulent flow is the return to direct simulation of turbulence to embrace increasing realism (complexity and Reynolds numbers) in the flow as computers increase in performance.

As described in Chapter 6, direct numerical simulation (DNS) refers to computations where all relevant spatial and temporal scales are adequately resolved *for the given application*. A valid simulation must accommodate all the range of length scales including the smallest scales of which the viscosity is active. This means that it is important to capture all of the kinetic energy dissipation within the turbulent flow. Estimates for the smallest scales are available from the so-called Kolmogorov microscales. From dimensional analysis, assuming dependence only upon viscosity ν and dissipation rate of kinetic energy ε, the length microscale η can be expressed as

$$\eta = \left(\frac{\nu^3}{\varepsilon}\right)^{1/4} \tag{9.11}$$

If the integral length and velocity macroscales of the problem are, respectively, L and u and we further assume the dissipation scales in the same way as

production, that is, u^3/L, it can be shown according to Tennekes and Lumley (1976) that

$$\frac{L}{\eta} = Re_L^{3/4} \tag{9.12}$$

Here, $Re_L = uL/\nu$ is a Reynolds number based on the magnitude of the velocity fluctuations and the integral length scale. The difference between the largest and smallest length scales in turbulence thus increases as the Reynolds number increases; the number of grid points required to resolve turbulence increases as $Re_L^{9/4}$. If the time-step restriction is factored in, the computational cost scales as the cube of the Reynolds number. Clearly, flows with very high Reynolds numbers are impossible to simulate. Nevertheless, some phenomena in turbulence appear to asymptote in the range of high Reynolds numbers asymptote such as free shear-layer rates and near-wall behaviour, and so, numerical simulations that can be feasibly performed at 'high enough' Reynolds number are still required to capture these phenomena in order to enhance understanding and contribute to model development.

Some numerical issues pertaining to DNS simulations are discussed herein. The key issue that typically dictates a DNS simulation is the mesh resolution within the flow domain. Some applications, such as those requiring statistics involving higher derivatives, will definitely need greater resolution than others. Detailed grid refinement studies have shown that there are some 'rules of thumb' that can be adopted in DNS calculations. One rule of thumb that the user may adopt is that grid spacing away from the wall should be in the order of 5η, which has been found to be sufficient for most purposes in the prediction of the mean flow, second moments of turbulence, and all the terms in the kinetic energy transport equation. To suggest another rule of thumb, take for an example calculations being performed for free shear-layer flows where the ability to preserve six decades of roll-off in the energy spectrum could expect good second-moment turbulence statistics to be attained during the DNS calculations.

Another consideration for DNS is the need to implement suitable numerical methods to obtain accurate realization of a flow that contains a broad spectrum of time and length scales. DNS generally requires an accurate time history. Since small time steps are naturally adopted, *explicit* methods that are usually stable because of the strict CFL requirements have been the preferred time-advance methods in most simulations instead of *implicit* methods. There are, of course, notable exceptions especially fine meshes being concentrated near solid walls to capture the essential small-scale flow structures that may cause instability due to the explicit determination of the viscous terms in these regions. This can be easily overcome by treating these terms in an implicit manner to promote stability during transient calculations. The most commonly used time-advance methods have been the second-order Adams–Bashforth and the third- or fourth-order Runge–Kutta methods. The reader may wish to refer to Rai and Moin (1991) for a greater understanding on the use of these methods

applied to the direct simulation of turbulent flows in a channel. In practice, Runge–Kutta methods allow a larger time step for the same accuracy and thus compensate for the increased amount of computation. To treat the viscous terms, the Crank–Nicolson method (see Appendix C) is often applied in conjunction with these time-advance explicit methods.

DNS also requires appropriate *discretization* methods. Unquestionably, the prevalent method for DNS is the spectral method. However, this method places restrictions on the type of geometry and grids that can be efficiently handled. In consideration of the commonly adopted finite difference or finite volume approaches, it is imperative to reiterate the importance of employing an energy-conservative spatial differencing scheme. In many Reynolds-averaged Navier–Stokes (RANS) calculations, upwind differencing schemes are commonly advocated since the dissipations that are introduced tend to stabilize the numerical methods and bound the scalar solutions. However, when these schemes are used in DNS, the dissipation produced is often much greater due to the physical viscosity resulting in a solution that has little connection to the flow physics of the problem being solved. To overcome the issue of false diffusion, 'diffusion-free' central-differencing schemes are used instead in many DNS simulations. Accuracy ranging from second to fourth order has been applied. Nonetheless, Rai and Moin (1991) have found that the fifth-order upwind-biased scheme has proved to yield good first- and second-order statistics that agree well with experimental data. It appears that the high-order accurate upwind-biased scheme is a good candidate for direct simulations of turbulent flows with complex geometries provided that the mesh is sufficiently fine. However, the problem of false diffusion may still resurface due to the inadequate resolution of the flow domain.

Generating initial and boundary conditions for the flow domain in DNS can also be challenging. In comparison with RANS computations where only mean conditions are required, DNS must contain all the details of the three-dimensional velocity field including the complete velocity field on a plane (or surface) for the inflow conditions of a turbulent flow at each time step. Since the memory of the initial and boundary conditions may well be required through some considerable time, they can have a significant effect on the results at the later stages of the flow simulations. Certain boundary conditions that are applicable to RANS cannot be readily applied in DNS such as symmetry boundary conditions. For outflow boundaries, it is important to impose boundary conditions that do not allow the pressure waves to be reflected off these boundaries and back into the interior of the domain. Despite all attempts to prescribe the initial and boundary conditions to be as realistic as possible, a DNS simulation must take its course for some lengths of time so that the flow develops with the correct characteristics of the physical flow. The best way to ascertain the flow development is to actually monitor some flow quantity; the choice depends on the flow that is being simulated. Initially, the quantity may reveal some systematic decreasing or increasing trends, but when the flow is fully developed, the

value will show statistical fluctuations with time. At this stage, statistical averaging over time can thus be performed on the results (e.g. the mean velocity and fluctuations).

Lately, more sophisticated DNS applications such as bypass transition in which passing wakes triggering turbulence spots in a flat-plate boundary layer or vortex structure identification have been performed (Guerts, 2001). The reader should be aware that such simulations usually amount to hundreds of computational hours to arrive at a solution. It is not entirely surprising that the number of grid nodal points that can be used is limited by the processing speed and memory of computers. Nonetheless, as computers become quicker and larger memories are made available, solutions to more complex and higher Reynolds number flows are becoming more attainable. DNS allows the provision of acutely detailed information about the flow. This wealth of information covering a wide range of length and timescales can be used to attain a better understanding of the flow physics such as the mechanisms of turbulence production, energy transfer, and dissipation in turbulent flows or the effects of compressibility on turbulence. Significant insights into the physics of the flow through DNS can at times be better realized of which may not have been possible through experiments.

9.3.2 Large Eddy Simulation (LES)

Large eddy simulation (LES), also briefly described in Chapter 6, is essentially a simulation that directly solves the large-scale motion but approximates the small-scale motion. The establishment of the LES method has its roots in the prediction of atmospheric flows since the 1960s and like DNS has grown in importance as computers have increased in size and performance.

As aforementioned, LES requires a flow field where only the large-scale components are present. This can be achieved through a *filtering* process. By eliminating the small-scale eddies through localized filter functions either a Gaussian or top-hat filter, only the large- or resolved-scale field remains to be solved. The instantaneous flow variables are then decomposed into its filtered or resolvable component (essentially a local average of the complete field) and a *subgrid-scale* component that accounts for the scales not resolved by the filter width. Within the finite volume method, it is rather sensible and natural to define the filter width as an average of the grid volume. In a rough sense, the flow eddies larger than the filter width are *large eddies*, whilst eddies smaller than the filter width are *small eddies* that require modelling. When filtering is performed on the incompressible Navier–Stokes equations, a set of equations very similar to the RANS equations of momentum and energy in Chapter 3 are obtained. Similar to RANS, there are additional terms where a modelling approximation must be introduced. In the context of LES, these terms are the *subgrid-scale* turbulent stresses and heat fluxes, which require *subgrid-scale* (*SGS*) models to close the set of equations.

The most widely used *subgrid-scale* model is the one proposed by Smagorinsky (1963). Since it is prescribed through the eddy-viscosity assumption, it therefore shares many similarities to the formulation of the Reynolds stresses as obtained through the RANS approach. For the unresolved *subgrid-scale* turbulent stresses, these are modelled accordingly as

$$\tau_{ij} - \frac{\delta_{ij}}{3}\tau_{kk} = -2\nu_T^{SGS}\overline{S}_{ij},$$
$$\overline{S}_{ij} = \frac{\partial \overline{u}_i}{\partial x_j} + \frac{\partial \overline{u}_j}{\partial x_i} \tag{9.13}$$

where ν_T^{SGS} is the *subgrid-scale* kinematic viscosity and $\overline{S}_{ij}$ is the strain rate of the large- or resolved-scale field. The form of the *subgrid-scale* eddy viscosity μ_T^{SGS} noting that $\nu_T^{SGS} = \mu_T^{SGS}/\rho$ can be derived by dimensional arguments and is given by

$$\mu_T^{SGS} = C_s^2 \rho \Delta^2 \left|\overline{S}_{ij}\right|,$$
$$\left|\overline{S}_{ij}\right| = \sqrt{2\overline{S}_{ij}\overline{S}_{ij}} \tag{9.14}$$

where Δ is denoted by the grid filter width and the model constant C_s varies between 0.065 and 0.3 depending on the particular fluid flow problem. There is a difference in the way the turbulent viscosity is evaluated between LES and RANS approaches. From Eq. (9.14), LES determines the turbulent viscosity directly from the filtered velocity field. However, by referring to Eq. (3.42) in Chapter 3, RANS requires the turbulent viscosity to be evaluated through the flow field containing two additionally derived variables that are the turbulent kinetic energy k and its rate of dissipation ε values. Over the past decade, other basic subgrid-viscosity models such as the structure–function model by Métais and Lesieur (1992) and the mixed-scale model by Sagaut (2004) that exhibits a triple dependency on the vorticity of the resolved scales have also been proposed in addition to the basic Smagorinsky model. The reader should realize that all of these models have been designed assuming that the simulated flow is turbulent, fully developed, and isotropic and therefore do not incorporate any information related to an eventual departure of the simulated flow from these assumptions. To obtain an automatic adaptation of the models for inhomogeneous flows, simulations of engineering flows are more likely to be based on the dynamic formulations of the basic versions of these models, which are briefly discussed below.

One possibility for designing a self-adaptive SGS model is the dynamic procedure originally developed by Germano et al. (1991). All the basic developments rest upon the usage of the Germano et al. (1991) identity[2]:

2. This identity is also known as the Leibniz identity in classical mechanics.

$$L_{ij} = \overline{u}_i\overline{u}_j - \widetilde{\overline{u}}_i\widetilde{\overline{u}}_j = \tau_{ij}^T - \widetilde{\tau}_{ij} \tag{9.15}$$

where $\widetilde{()}$ represents a second filtering operation, called a 'test' filter, with a larger filter width than ( ) and $\overline{()}^T$ that indicates a quantity computed using the test-filtered velocity. The dynamic procedure can in principle be applied to any subgrid model. By equating L_{ij} to a term $C_s^2 M_{ij}$ where M_{ij} is given by

$$M_{ij} = -2\left(\widetilde{\Delta}^2\left|\widetilde{\overline{S}}_{ij}\right|\widetilde{\overline{S}}_{ij} - \Delta^2\left|\overline{S}_{ij}\right|\overline{S}_{ij}\right) \tag{9.16}$$

with $\widetilde{\Delta}$ as the test filter width and combining with the procedure of Lilly (1992), the model constant C_s can be obtained by minimizing the square of the error term $L_{ij} - C_s^2 M_{ij}$ to yield

$$C_s^2 = \frac{\langle L_{ij}M_{ij}\rangle}{\langle M_{ij}M_{ij}\rangle} \tag{9.17}$$

The above described procedure is the basic formulation of the dynamic Smagorinsky model. Following similar arguments, other dynamic models such as the mixed Smagorinsky-scale-similarity models developed by Zang et al. (1993) and Shah and Ferziger (1997) and the Lagrangian dynamic model of Meneveau et al. (1996) have been used with considerable success and certainly broadened the accessible applications for LES.

The numerical models and boundary conditions required for LES are essentially the same as those used in DNS. In regions close to the solid surfaces, the dynamic Smagorinsky model is well suited for such flows since it automatically decreases the model constant automatically in the correct manner near the solid wall. Nonetheless, it is also still possible to employ wall functions of the kinds used in RANS modelling whilst adopting the original Smagorinsky model or other basic SGS models in some turbulent flow problems. The van Driest (1956) wall-damping function that reduces the near-wall eddy viscosity according to the normal distance from the wall has proved to be a successful recipe. A variation to the van Driest wall-damping function such as that formulated by Piomelli et al. (1987) can also be used to suppress the near-wall eddy viscosity. Both of these models are available in the commercial code ANSYS-CFX. Another approach that is based on the renormalization group (RNG) theory by Yakhot and Orszag (1986) where the eddy viscosity reduces according to the subgrid-scale Reynolds number has also been proposed. This model is adopted in the commercial code ANSYS-FLUENT. The use of wall functions in LES has shown to work rather well for attached flow problems (Piomelli et al., 1989).

Like DNS, most LES schemes that model real flows correctly are still very computationally expensive. Owing to computational limitations, a possibly damaging aspect prevalent in most LES schemes is that the simulations are still not being performed on a fine enough grid and consequently do not capture some important dynamics at high wave numbers, which have not been filtered

or modelled. Numerical truncation errors begin to overcome the SGS model, and the original physics may be lost. Lately, a way to address some of the drawbacks has been to utilize the numerical truncation errors directly to act as a SGS model implicitly instead of the explicit models proposed above. This model is known as the monotone integrated large eddy simulation, also better recognized by the acronym MILES. The key success to this approach is how to construct a numerical method that will depict the proper SGS model, and recent investigations have shown that it is feasible to employ high-resolution shock-capturing methods (see Section 9.2.2.1). At this particular juncture, it is not the authors' intention to present the formal procedure behind the MILES type algorithm, which is beyond the knowledge at this introductory level. Interested readers are strongly encouraged to refer to Garnier et al. (1999), Sagaut (2004), and Hahn and Drikakis (2005) for a greater understanding on the background theory behind MILES and their respective applications in turbulent flow simulations.

9.3.3 RANS–LES Coupling for Turbulent Flows

The idea behind this methodology is to address the impending need to solve high Reynolds number flows especially for wall-bounded flows where the requirement of a very fine mesh near walls still precludes a full LES simulation. It is important that the near-wall turbulent structures in the viscous and buffer sublayers consisting of high-speed inrushes and low-speed ejections (often called the streak process) are properly resolved within the near-wall region. At low-to-medium Reynolds numbers, this streak process generates the major part of the turbulence production; these structures must be fully accommodated for in LES to obtain an accurate representation of the phenomena. For wall-bounded flows at high Reynolds numbers of engineering interest such as bluff bodies, the computational resource requirement of accurate LES can be prohibitively large. Because of the enormous amount of work that has been devoted to the development of RANS turbulence models for near-wall predictions, it is therefore possible to take advantage of these models, which are less expensive to capture the near-wall turbulent structures instead of the full resolution through LES. Nevertheless, it is well-known that the RANS approach is unable to account the spectrum of unsteadiness that is associated with the turbulent fluctuations away from the wall. LES, because of its explicit cutoff frequency, can choose the degree of accuracy of the description of the turbulent fluctuations; accurate results can be obtained at an affordable cost without imposing a very fine mesh resolution. Hence, the idea of combining both methods where the inner near-wall (the unsteady RANS) region is handled by the RANS approach whilst the outer region of the bulk flow is solved through LES makes rather perfect sense. In the LES region, the mesh resolution is dictated mainly by the requirement of resolving the largest turbulent scales rather than the near-wall turbulent processes.

The RANS–LES coupling of turbulent flows can be handled through a number of different approaches. For attached flow problems using LES as described in the previous section, wall law functions employed to reduce the computational cost are in some way representative of the zonal use of RANS and LES. Nonetheless, the application of these functions to simulate separated flows presents enormous problems, and they also tend to be lacking in universality when complex geometries are handled. The uses of a RANS model in the near-wall zone by adopting a reduced RANS model (e.g. of mixing-length type), solving the turbulent boundary layer equations in an embedded near-wall mesh (Balaras et al., 1996; Wang and Moin, 2002), or even applying a full RANS model designated as hybrid RANS–LES are the possible alternatives to circumvent the problems associated with wall functions. Recently, the non-linear disturbance equation (NLDE) approach initially proposed by Morris and his coworkers (1997, 1998) and recently reviewed by Labournasse and Sagaut (2004) represents another RANS–LES technique that can be applied to handle a range of complex flows. Like the hybrid RANS–LES, it solves the near-wall flow field through the RANS model and the energy and dynamics of the main unsteadiness flow in the far field through LES but with an additional subgrid model to handle the unresolved fluctuations (in the zones of interest). For the remainder of this section, the authors would like to focus on the basic concepts and advancements made to the hybrid RANS–LES models.

Hybrid RANS–LES models can be divided into two categories. The first category is the zonal decomposition into the physical space where the computational domain is divided into subdomains. Some of these subdomains are computed using a RANS approach and the other through LES. In the unsteady RANS region, two-equation models whether they may be the *standard k–ε model*, *k–ω model*, or other developed turbulent models can be employed. Davidson and Peng (2003) applied the *k–ω model* in the near-wall flow field. The transition between the domains is prescribed through a predefined switching plane, which is explicitly provided. The location of this plane or interface can be determined in many ways. It can be chosen using some blending function (sharp or smooth) (Davidson and Peng, 2003; Temmerman et al., 2005), comparing the unsteady RANS and LES turbulent scales computed from turbulence/physics requirements (Tucker and Davidson, 2004), or solving different partial differential equations to automatically locate the interface (Tucker, 2003). Although encouraging results have been obtained for selective comparative cases with the application of this zonal hybrid RANS–LES, proper treatment of the interface bridging the RANS and LES regions is crucial to the success of this model that remains an area of active research. For the second category, hybrid computations are performed without predefining a switching plane. In hindsight, this approach appears to be more preferable than the first-category models. However, the possibility that a subgrid model with a RANS is required limits this method. Similar to the NLDE where the same numerical scheme is used throughout the whole domain, instability modes such as wiggles can

appear in the RANS zone that are some of the main disadvantages of this approach; thus, no clear advantages can be found in adopting this second category over the first-category models. Examples of these models are Speziale's very large eddy simulation (VLES) (1998), detached eddy simulation (DES) (Spalart et al., 1997), and renormalization group approach (de Langhe et al., 2005a,b).

The hybrid RANS–LES coupling is an excellent candidate for massively separated flow problems. Typical successful applications that have been found in Strelets (2001) and Squires and Constantinescu (2003) are flow around a sphere or cylinder, NACA 0012 aerofoil, backward-facing step, and landing gear truck. For flow over periodic hills, overall energy and mean velocity profiles are well predicted with 20 times less grid points than that resolved using LES. Generally speaking, the mesh density in hybrid RANS–LES is comparable with those used in RANS, and it provides better results than LES on the same coarse grids. It is also superior over a full RANS simulation in predicting the energy of the main unsteadiness in the flow. The current main research issue in this methodology is turbulent synthetization. Interested readers can refer to Battan et al. (2004) for a better understanding on the required turbulent closures of this issue.

9.3.4 Multiphase Flows

In Chapter 8, we observed how CFD could enhance the understanding of physical processes associated with gas-particle flows in simple or complex geometries such as in a 90 degrees duct bend or physiological respiratory human airway system. There are nonetheless many other engineering applications that often involve multiphase flows; examples are gas bubbles in liquid or liquid droplets in gas, fluidized-bed combustion, liquid fuel injected as a spray in combustion machines, etc.

Multiphase flow investigations are certainly at the crossroads of intense research in the climate of significant advancements being achieved in computing power and performance. Two commonly adopted approaches that have been briefly described in Chapter 7 to compute two-phase flows are the Eulerian–Eulerian and Eulerian–Lagrangian methods. The Eulerian approach is usually adopted for the carrying- or continuous-phase fluid. The distinction results in the dispersed phase where it may be handled through either the discrete approach in the Lagrangian framework or the continuous Eulerian approach similar to the carrying-phase fluid. When the mass loading is small, this phase can be represented by a number of finite number of particles whose motion can subsequently be computed in a Lagrangian manner. These particles are injected into the flow domain, and their trajectories are determined from the precomputed velocity field of the background fluid. This depicts the *one-way* coupling approach. When the mass loading is substantial, the influence of particles on the fluid motion needs to be properly accounted. A *two-way* coupling requires the

computation of particle trajectories and fluid flow to be simultaneously carried out; each particle contributes to the momentum, mass, and energy of the parent fluid in each control volume cell it passes through. On the range of Eulerian–Eulerian and Eulerian–Lagrangian investigations of gas-particle flow applications, the reader may wish to refer to the current works by Tian et al. (2005, 2006).

Interaction between particles such as collision or agglomeration and between particles and walls can exist where appropriate models to account all these effects are areas of ongoing research. These subject matters are certainly complicated, and the reader can refer to the book by Crowe et al. (1998) for a broader understanding. Recently, attempts to address particle impaction particularly on curved wall boundaries have been performed, and some encouraging results are found in the articles by the present authors: Morsi et al. (2004) and Tu et al. (2004a,b). Ongoing research is still being carried out to address many of the complex issues associated with particle-wall behaviour. Robust models for practical applications remain elusive at this present stage.

For flows with large mass loadings when phase change occurs, the two-fluid model (Eulerian–Eulerian approach) is applied to both phases. Here, both phases are treated as continua with separate velocity and temperature fields. To account for interfacial effects between phases, appropriate constitutive relationships for the interphase exchange terms are required to close the system. The principles of two-fluid models have been described in detail by recent texts of Kolev (2005) and Ishii and Hibiki (2006) for the application to gas-liquid flows. In the context of a phase change multiphase flow, subcooled boiling flow presents enormous challenges in modelling and simulation. The two-fluid model that is applied to handle both continua phases occupied by the gas bubbles and liquid requires additional wall models to predict the nucleation of bubbles generated from heated walls. Based on a number of experimental observations, bubbles departing from the heated walls have been found to form bigger or smaller bubbles either through merging, shearing off, or disappearing due to condensation in the bulk subcooled liquid flow. The bubble mechanistic behaviours of coalescence and breakage handled through the *population balance approach* form an integral part in addition to the two-fluid model in determining the bubble size in the dispersed phase. The accurate determination of this bubble diameter is required because it strongly governs the drag and non-drag characteristics of the fluid flow. Much research has been performed on this particular type of multiphase flow, and the reader can refer to the latest development of models in Yeoh and Tu (2005,2006a,b). The methods required to compute these flows are similar to those described in this book except for the addition of models such as the wall and bubble mechanistic models and boundary conditions.

Lastly, it is also worth mentioning another class of multiphase flows, that is, flows with free surfaces like channel flows, flows around ships, and mould

filling including solidification or melting. The treatment of the free surface is generally treated in addition to the *interface-tracking* methods (moving grids) by another category of methods known as *interface capturing*. These methods share some similarities like the immersed boundary methods where the computation is also performed on a fixed grid; the shape of the free surface is determined by solving an additional transport equation for the void fraction of the liquid phase such as the volume of fluid (VOF), which was first introduced by Hirt and Nichols (1981) to indicate whether the control volume cell is filled by liquid and/or gas. The critical issue in this type of method is the discretization procedure for the advective term in the equation. Low-order schemes have a tendency to smear the interface and introduce artificial mixing of the two fluids. Like shocks in compressible flows, the smearing effect degrades the profile, and high-resolution schemes are generally preferred. For a sharper interface, the interface-capturing methods based on the *level-set formulation* present another alternative. Here, a stepwise variation of the fluid properties is enforced. Nevertheless, this causes problems when computing viscous flows, and the need to arbitrarily introduce some finite thickness across the interface region is necessary to promote smooth but rapid change of the properties. More details on the level-set methods can be found in Sethan (1996).

9.3.5 Combustion

The interaction between turbulence and combustion is an area of great research interest, and its complexity defies an analytic solution or even a basic understanding in most cases. This is especially true in the case of turbulent nonpremixed or diffusion flames in which turbulence and chemical reactions are strongly coupled within the thin reaction zone of the flame.

There are many difficulties associated in handling turbulent combustion flows. Firstly, there are various degrees of mixing and consequently on combustion since turbulence has a wide range of time and length scales. Secondly, the chemical reactions of combusting species are highly nonlinear; they strongly affect the flow variables such as temperature and density that can change rapidly by a factor of eight through the flame region. Thirdly, a combustion process is usually composed of a large number of species partaking in many reaction steps, which may result in having very different complicated transport properties. Fourthly, the combustion time and length scales are typically smaller than the smallest turbulent scales, making them difficult to resolve by numerical or experimental means.

Nevertheless, all types of combustion are governed by the same set of conservation laws of mass, momentum, energy, and chemical species at the fundamental level. If these laws of governing equations can be solved numerically without any approximations, then a full set of information about the flow and combustion is known. This is the basic idea behind the direct simulation of combusting flows. In most cases, the chemical scales are much smaller than

the smallest scales of turbulence, which are the Kolmogorov scales. This is why turbulent combustion presents even a bigger challenge than nonreactive turbulent flow. Conducting DNS studies on turbulent flames can be extremely difficult depending on the degree of complexity that needs to be imposed on the simulations. If detailed chemistry is to be incorporated, then the computational cost can increase dramatically, in some circumstances to epic proportions. Imagine that even for the simple combustion process of methane, more than 200 reaction steps are required to adequately represent the chemistry process. It is therefore not surprising that DNS of turbulent combustion is still restricted to small-scale laboratory flames.

To realize the feasibility of resolving complex reacting flows in practical combusting systems, simplifications to the combustion process have resulted in a number of widely applied models. A short description on some of these models for nonpremixed and premixed combustion is briefly discussed below.

By representing the combustion of fuel as a global one-step, infinitely fast, chemical reaction, the simple chemical reacting system (SCRS) assumes the oxidant reacts with the fuel to form products at stoichiometric proportions. The intermediate reactions are ignored since we are only concerned with the global nature of the combustion process. With this model, the mass fractions of the reactants and products accompanied by the inert species can be expressed as fixed algebraic state relationships in terms of a passive scalar called the mixture fraction f. As a consequence, it is only necessary to solve one extra transport equation for f rather than individual transport equations for each mass fraction. To account for the fluctuations of mass fractions due to turbulence, the average scalars of these variables can be obtained by weighting the instantaneous value with a probability density function for the mixture fraction f. Clipped Gaussian and beta functions are typical probability density functions that have been applied to provide the best results. Interested readers are encouraged to refer to Lockwood and Naguib (1975), Pope (1994), and Jones (1979) for further details.

The eddy break-up concepts introduced by Spalding (1971) and Magnussen and Hjertager (1976) present an alternative approach to the SCRS where the rate of consumption of fuel is solved as a function of local flow properties. Here, the mixing-controlled rate of reaction is expressed in terms of the turbulence timescale. The model considers the slowest rate as the reaction rate of fuel depending on the minimum dissipation rates of fuel, oxygen, and products. Within this model, it is also possible to accommodate kinetically controlled reaction terms expressed by the Arrhenius kinetic rate expression to govern the reaction rate of fuel in addition to the mixing-controlled rate of reaction. The implementation is straightforward, and it has shown to yield reasonably good predictions, but the quality of the predictions depends greatly on the turbulence models used.

In addition to the development of the SCRS and eddy break-up models, another popular combustion model is the consideration of laminar flamelets. This approach is based on the assumption that these flamelets are reaction–diffusion

layers in quasisteady state that are continuously displaced and stretched within the turbulent medium. These layers are assumed thinner than all the turbulent scales, so that their internal structures have the compositional structure of laminar flames. Like the SCRS, a transport equation for the mixture fraction is solved. However, the instantaneous species mass fractions are now deduced from the laminar state relationships, which can be taken from experimental measurements. The species fluctuations can also be accounted for through the probability density function described above to obtain the average variables. The provision of this model allows the inclusion of detailed chemistry. Application of the eddy break-up and laminar flamelet models for the predictions of velocity and temperature fields in a compartment fire has been reported in Yeoh et al. (2002); the reader may wish to refer to this article for a better understanding of simulating combusting flames in the context of fire dynamics.

Many of the traditional combustion models developed above have been derived on the basis that the flames are under near-equilibrium conditions. To predict highly nonequilibrium flame events such as ignition, lift-off, or extinction, it would be possible to modify the state relationships to include the scalar dissipation rate dependence and distinguish between the burning and extinguishing flamelets. Peters (2000) proposed a strained laminar flamelet model to accommodate such effects. Another possible approach is through the compositional probability density function transport model (Dopazo, 1993) that particularly simulates finite-rate chemical kinetic effects in turbulent reacting flows. This transport equation can be solved either through a Lagrangian approach using stochastic methods as suggested by Pope (1994) or in a Eulerian framework using stochastic fields developed by Valino (1998). It is clear that combustion modelling is still very much an area of active research. With the advancements in computer speed and parallel architectures, time-accurate LES of combusting flames is becoming ever more feasible and prevalent. The flow unsteadiness within the flame has been found to be better captured using the LES approach, and this has been succinctly demonstrated by the recent study of a free-standing buoyant flame as described by the CFD application example in Chapter 7 and investigation of a strongly radiating nonpremixed turbulent jet flame by Desjardin and Frankel (1999).

9.3.6 Fluid–Structure Interaction

Interaction between a flexible structure and the surrounding fluid promotes a variety of phenomena with applications such as stability analysis of airplane wings, design of bridges, and flow of blood through arteries (to be discussed in more detail later). In this section, the authors would like to discuss the various techniques behind the emerging area of computational aeroelasticity (CAE) for performing analyses on a range of aeroelastic applications, where the basic

approaches are equally applicable to other applications related to fluid–structure interaction problems.

Despite the many advancements in CFD methods and structural dynamic tools that have been irrespectively developed, many approaches to fluid–structure studies still seek to synthesize independent computational approaches to the fluid dynamics and structural dynamic subsystems. Such approaches are known to be fraught with complications associated with the interaction between the two simulation modules. As reviewed by Kamakoti and Shyy (2004), the task is therefore to choose appropriate models for fluid and structure based on its application and to develop an efficient interface to couple the two models. CAE can be broadly categorized into three approaches: *fully coupled*, *closely coupled*, and *loosely coupled*.

In the *fully coupled* model, the governing equations are reformulated by combining the fluid and structural equations of motion that are solved and integrated in time simultaneously. This kind of method poses severe limitations because of the need to solve the equations in two different reference systems: fluid equations as Eulerian and structural equations as Lagrangian. The stiff set of equations for the structural system makes it virtually impossible to solve the equations using monolithic computational schemes for large-scale problems. For the class of methodologies that belong to the *loosely coupled* model, unlike the *fully coupled* analysis, the structural and fluid equations are solved separately. This results in two different computational grids that may not be coincident at the interface or boundary. To establish a link between the respective regions, an interfacing technique is developed to exchange information back and forth between these modules. Fig. 9.9 illustrates a sample for the fluid and structure solvers along with selective interfacing methodologies for aeroelastic simulation. This method provides the flexibility of choosing different solvers, but the coupling procedure leads to a loss in accuracy as the modules are only updated after sufficient convergence is achieved in each of the respective regions. It is usually limited to small perturbations and problems with moderate nonlinearity. In the *closely coupled* model, the approach not only paves the way to use different solvers for the fluid and structure modules but also couples the solvers in a tight fashion through *one single module* with the exchange of information taking place at the boundary. The data exchanged here are the surface loads that are mapped from the CFD surface grid onto the structure dynamic grid and the displacement field that are mapped from the structure dynamic grid onto the CFD surface grid. This implies that a moving boundary technique is required for the CFD surface mesh so that the moving mesh algorithms such as the spring analogy and transfinite interpolation-based method by Hartwich and Agrawal (1997) or moving mesh partial differential equation by Huang and his coworkers (1994, 1999, 2001) are applied to enable remeshing of the entire CFD domain as the solution marches in time.

Based on the short description in relation to the advances achieved in fluid–structure interactions, what the authors have aimed to provide the reader is the

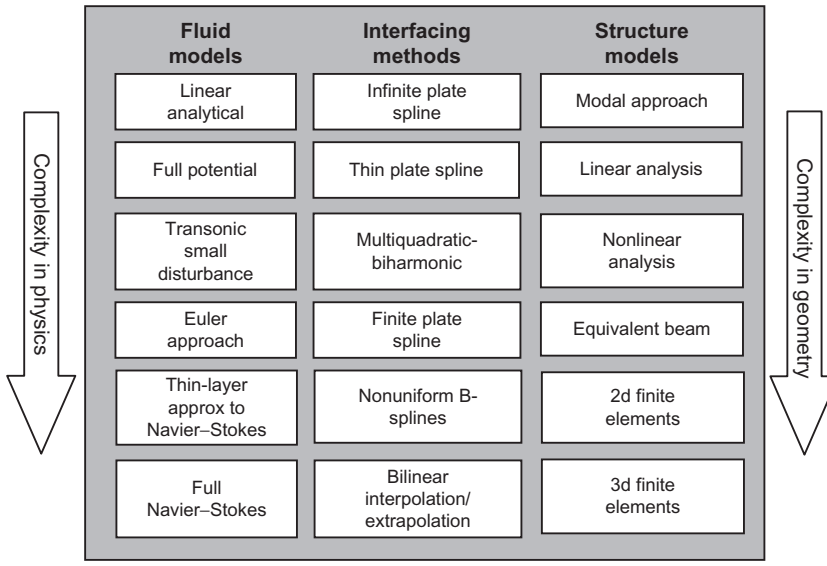


FIG. 9.9 Sample fluid and structure solvers along with select interfacing methodologies for aeroelastic simulation. *(From Kamakoti, R., Shyy, W., 2004. Fluid-structure interaction for aeroelastic applications. Prog. Aerosp. Sci. 40, 535–558.)*

culmination of some suitable solvers and interfacing methodologies for performing fluid–structure interaction calculations. The materials presented in this section are by no means exhaustive. Numerous research issues remain opened and unresolved. Particularly, future challenges lie in the development of higher-order methods to better capture the highly complex flow physics in the fluid flow and detailed structure modelling including nonlinear effects. Ultimately, the robust application of this methodology for accurately modelling large systems still lingers in the wake of more efficient procedures.

9.3.7 Physiological Fluid Dynamics

There has been an enormous interest in biomedical or biofluid engineering towards better understanding the physiological applications spanning the respiratory and cardiovascular systems in the human body. Owing to significant progress that has been made in the development and application of computational methods for modelling airflow and blood flow in the respective respiratory and cardiovascular systems, the discoveries achieved are transforming our fundamental understanding of the fluid mechanical behaviours within. When linked with medical imaging techniques such as magnetic resonance imaging (MRI), the ability to construct anatomically accurate geometric models is providing new insights to the airflow and blood flow velocities and pressure fields in normal subjects and patients. Some examples in relation to biomedical CFD have

been demonstrated in Chapters 1 and 7. Despite the wealth of data that has been attained through three-dimensional computational models, significant work still remains (Grotberg and Jensen, 2004; Taylor and Draney, 2004).

For the cardiovascular system, one prognosis for the possible cause of heart attack or stroke could be the dangerous manifestation of self-excited oscillation that arises in arterial stenoses according to Ku (1997). The resulting static and dynamic loading on the diseased arterial wall may well be sufficiently vigorous or sustained to the fracture of the stenosis' plaque cap, thereby causing fragments to be swept downstream in the arteries, a possible precursor of heart attack or stroke. In an attempt to quantify phenomena difficult to describe by in vitro techniques, computational models based on CFD methodologies have been used. Perktold et al. (1991) have adopted the finite element method to simulate the pulsatile flow of a Newtonian fluid in a model representing the carotid bifurcation using rigid wall approximations. This assumption, though justifiable for arteries where the wall motion is small (as may be expected in steady flow), may not be appropriate for arteries experiencing large deformation (e.g. pulsatile flow in younger subjects). Rappitsch and Perktold (1996) have described the transport of albumin in a stenosis model, whilst Lei et al. (1997) focused on the application of computational models to the design of end-to-end anastomoses.

Although detailed description of blood flow regions such as the complex three-dimensional flow in the event of an aneurysm can be handled by current CFD models, the future challenge remains in the development not only of closed-loop circulatory models that combine these *local* models (as described above) but also with *global* models that can accurately describe the pressure-flow relations in a vascular network composed of millions of blood vessels or pressure-volume models of the heart. Because of the availability of MRI to construct subject-specific geometric models, cardiovascular surgery planning using computational methods in predicting changes in blood flow resulting from possible therapeutic intervention for individual patients is becoming a reality (Taylor et al, 1999). Recent development of this cardiovascular surgery planning as demonstrated by Wilson (2002) has led to the creation of a plan being specifically constructed for a patient with atherosclerosis in the lower extremities. Here, three-dimensional blood flow simulations were carried out to compute the flow velocities in simulating the scenario for the clearance of a dye in the bloodstream. Such simulations have been deemed necessary as they provided useful information in identifying sites of relative flow stasis that may be prone to clot formation or thickening of the inner layer of blood vessels, where such diagnoses have provided treatment targeting specifically for patients with cardiovascular disease.

Another challenge of the cardiovascular fluid investigations is the development of models to combine molecular- and cellular-level phenomena with macroscale fluid mechanics. These models can allow the interaction between atherogenic agents and the artery wall and the response of the artery wall to hemodynamic forces from cellular to tissue scales to be studied. For such flows,

the explicit inclusion for the particle nature of matter is required through specially developed spatial-scale-multiscale models, which is discussed in the next section.

For the respiratory system, the airways can experience deformation to some degree, and flow-structure interactions underlie a number of important pulmonary conditions. Of particular significance are the expiration and inspiration flow limitations. For the latter aspect, it can lead to flow-induced instabilities that can generate snoring and upper-airway obstruction contributing to sleep apnoea. The airways of the lung also provide another source of pertinent problems where multiphase fluid mechanics has important biological applications, involving flexible tubes with a liquid lining or liquid occlusion. The consideration of how surface tension, elastic forces, and airflow acting together in controlling the configuration of a deformable airway and its internal liquid lining is critical in determining the conditions leading to airway closure; the liquid lining forms a plug occluding (and collapsing) the airway and inhibiting gas exchange, a prognosis for the possible occurrence of an asthma attack.

Many three-dimensional models have been developed to describe the three-dimensional flow-structure interaction of an internal three-dimensional Navier–Stokes flow. It has been shown that nonaxisymmetric buckling of a tube contributed to nonlinear pressure-flow relations can exhibit flow limitations through pure viscous mechanisms (Heil, 1997; Heil and Pedley, 1996). This work was extended to computations that described three-dimensional flows in nonuniformly buckled tubes at Reynolds numbers of a few hundred (Hazel and Heil, 2003). The development of models to biofluid mechanics in flexible structures is at the crossroads of intense research, and the authors have just barely scratched the surface in describing some applications to respiratory systems. Understanding the physical origin and nature of these phenomena to the vessel's biological function or dysfunction remains computationally, experimentally, and analytically challenging.

Most physiological fluid investigations have thus far concentrated on the assumption of rigid wall approximations to the geometrical model. Realistically speaking, pulsatile flows in cardiovascular system and airflow through the airways in the respiratory system require flexible wall structures to appropriately represent the actual flow characteristics. Future fluid–structure analyses will become a much required feature in carrying out investigations on the respiratory system and/or cardiovascular system.

9.4 OTHER NUMERICAL APPROACHES FOR COMPUTATION OF FLUID DYNAMICS

Unlike conventional numerical schemes based on the discretization of macroscopic continuum equations commonly used in many engineering applications, there are other alternative numerical approaches that have been developed

lately for simulating fluid flows and modelling physics in fluids. The authors would like to review three promising methods: lattice Boltzmann, Monte Carlo, and particle and discrete element methods. For particle method, an overview on the vortex methods and smooth particle hydrodynamics for the simulation of the continuum phenomena is discussed and described.

9.4.1 Lattice Boltzmann Method

Lattice Boltzmann method (LBM) is a methodology based on the microscopic particle models and mesoscopic kinetic equations. According to Kadanoff (1986), it has been found that macroscopic behaviour of a fluid system is generally not very sensitive to the underlying microscopic particle behaviour if only collective macroscopic flow behaviour is of interest. The fundamental idea behind the LBM is to construct simplified kinetic models that incorporate only the essential physics of microscopic or mesoscopic processes so that the macroscopic averaged properties obey the desired macroscopic equations. This subsequently avoids the use of the full Boltzmann equation, and one also avoids following each particle as in molecular dynamics simulations.

It is worth noting that even though LBM is based on a particle representation, the principal focus remains in the averaged macroscopic behaviour. The kinetic nature of the LBM introduces three important features that distinguish this methodology from other numerical methods. Firstly, the convection operator of the LBM in the velocity phase is linear. The inherent simple convection when combined with the collision operator allows the recovery of the nonlinear macroscopic advection through multiscale expansions. Secondly, the incompressible Navier–Stokes equations can be obtained in the nearly incompressible limit of the LBM. The pressure is calculated directly from the equation of state in contrast to satisfying Poisson's equation with velocity strains acting as sources. Thirdly, the LBM utilizes the minimum set of velocities in the phase space. Because only one or two speeds and a few moving directions are required, the transformation relating the microscopic distribution function and macroscopic quantities is greatly simplified and consists of simple arithmetic calculations.

For the LBM, the lattice Boltzmann equation (LBE) based on the lattice gas automata can be constructed via simplified, fictitious molecular dynamics in which space, time, and particle velocities are all discrete. Using the commonly adopted approach of the single-relaxation-time collision model of Bhatnagar et al. (1954), the LBE can be expressed as

$$\frac{\partial f}{\partial t} + \boldsymbol{e} \cdot \nabla f = \frac{f - f^{eq}}{\lambda} \tag{9.18}$$

where f is the particle distribution function, e is the particle velocity, λ is the relaxation time due to particle collision, and f^{eq} is the equilibrium

Boltzmann–Maxwell distribution function. It can be demonstrated that the particle velocity space e can be discretized into a small set of discrete vectors e_i such that the macroscopic conservation laws are satisfied (He and Luo, 1997). Eq. (9.18) can thus be discretized along each velocity direction e_i at each lattice by the following:

$$f_i(\boldsymbol{x}+\boldsymbol{e_i}\delta t, t+\delta t) - f_i(\boldsymbol{x}, t) = -\frac{1}{\tau}\left[f_i(\boldsymbol{x}, t) - f_i^{eq}(\boldsymbol{x}, t)\right] \tag{9.19}$$

Here, $f_i(\boldsymbol{x}, t)$ denotes the density function along velocity $\boldsymbol{e_i}$ at lattice position $\boldsymbol{x}$ and time t, $\tau = \lambda/\delta t$ represents the relaxation parameter, and δt is the time step. With the LBM, the macroscopic density ρ and flow velocity $\boldsymbol{u}$ can be defined in terms of the particle distribution function as

$$\rho = \sum_i f_i, \quad \rho\boldsymbol{u} = \sum_i f_i \boldsymbol{e_i} \tag{9.20}$$

It is shown from above that the numerical algorithm of the LBM is relatively simple when compared with conventional Navier–Stokes methods. In terms of computational effort, the LBM consists of mainly two operations: collision on the right-hand side of Eq. (9.19) and streaming on the left-hand side. The collision operation is completely local, and since streaming can be easily achieved by a simple *shift* operation that is offered as an intrinsic function by most compilers, the LBM is well suited for parallelism. Because of the availability of very fast and massively parallel machines, LBM fulfils the requirement in a straightforward manner. Eq. (9.19) can however be also interpreted as a special finite difference form of the continuous form of Eq. (9.18), which means that the time step is limited by the lattice size due to the explicit nature of the lattice. Hence, the computational efficiency of LBM remains an important issue to be evaluated particularly for steady-state flows.

Lattice Boltzmann simulations of fluid flows have been performed for flows with simple geometries including driven cavity flows, flow over a backward-facing step, flow around a circular cylinder, and flows with complex geometries. For the simulation of fluid turbulence, the development of a subgrid-scale LBE turbulent model has provided the means of possibly employing LBM for the investigation of turbulent flows in industrial applications of practical interest. LBM also provides an alternative for simulating complicated multiphase and multicomponent fluid flows. The method has proved to overcome difficulties associated with the conventional macroscopic approaches in modelling interface dynamics and important related engineering applications that include flow through porous media, boiling dynamics, and dendrite formation. Interested readers are encouraged to refer to the list of articles for the range of applicability and future innovative developments and applications of the LBM: Hou et al. (1995), Benzi et al. (1996), Hou et al. (1996), Luo (1997), He and Doolen (1997), Shan (1997), Spaid and Phelan (1997), Chen and Doolen (1998), and Yang et al. (2000), amongst others.

9.4.2 Monte Carlo Method

Lately, the direct simulation Monte Carlo (DSMC) has been proposed in addition to the LBM for the computation of fluid dynamics because of the practical scientific and engineering importance of solving high Knudsen number (Kn) flows. This dimensionless parameter Kn, by definition, generally characterizes the ratio of the molecular mean free path to the characteristic length. As the mean free path becomes comparable with or even larger than the characteristic length especially for high Kn, the particle nature of matter must be explicitly accounted since the continuum fluid approximation breaks down particularly in the area of microscale or nanoscale fluid systems. Table 9.1, as illustrated below, shows the hierarchy of mathematical models to describe the interactions of atoms, ions, and molecules. These models can range from very fundamental solutions of sets of elementary interactions of particles (such as molecular dynamics models) to approximation of systems in which the individual particles are replaced by continuum fluid elements (such as the Navier–Stokes equations). Molecular dynamics is the most fundamental level of this hierarchy; the LBM and DSMC lie somewhere in between the molecular dynamics and continuum fluid consideration.

DSMC is a direct particle simulation method based on kinetic theory. The fundamental idea behind this method is to track a large number of statistically

TABLE 9.1 Levels of Models of Many-Body Interactions

Equation	Solution Method
Newton's law $f = ma$	Molecular dynamics (deterministic, particle-based, prescribed interparticle forces)
Liouville equation $F(x_i, v_i, t)$, $i = 1, N_p$	Monte Carlo methods (statistical, particle-based methods)—DMSC
Boltzmann equation $F(x, v, t)$ Binary collision (low density)	Direct solution—LBM
Navier–Stokes equation $\rho(x, t)$, $u(x, t)$ Short mean free path	Direct solution—finite difference, finite volume, spectral methods, and so on (continuum flow methods)

From Oran, E.S., Oh, C.K., Cybyk, B.Z., 1998. Direct simulation Monte Carlo: recent advances and applications. Annu. Rev. Fluid Mech. 30, 403–441.

representative particles. The particles' motion is later used to modify their positions, velocities, or even chemical reactions in reacting flows. Conservation of mass, momentum, and energy are enforced on the requirement of the machine accuracy. The primary approximation of the DSMC method is to uncouple the molecular motions and the intermolecular collisions over small time intervals. Here, particle motions are modelled deterministically, whilst the collisions are treated statistically.

The core of the DSMC procedure consists of four primary processes. Firstly, the simulated particles are moved within a time step. Boundary conditions are enforced through modelling molecule-surface interactions, which may include physical effects such as chemical reactions, three-body collisions, and ionized flows. Secondly, indexing and cross-referencing the particles are performed in this step. This is a prerequisite for the next two steps: simulating collisions and sampling the flow field. The key to practical DSMC for large-scale processing is the accurate and fast indexing and tracking of the particles. Thirdly, the step of simulating collisions sets DSMC apart from other deterministic simulation methods such as molecular dynamics. The currently preferred model is the *no-time-counter technique* by Bird (1994), used in conjunction with the subcell technique of Bird (1986). This subcell method ensures that collisions only occur between near neighbouring particles by calculating local collision rates based on individual cells but restricts possible collision pairs to subcells. Fourthly, the sampling of the particles provides the macroscopic flow properties. The spatial coordinates and velocity components of molecules in a particular cell are used to calculate macroscopic quantities at the geometric centre of the cell. Interested readers may wish to refer to Muntz (1989), Cheng (1993), Cheng and Emmanual (1995), and Oran et al. (1998) for more details pertaining to the recent advances and developments of DSMC.

DSMC is a time-accurate explicit procedure. The method has shown to be a good candidate for unsteady flow applications in computing nonequilibrium structure of shocks and boundary layers, as well as hypersonic viscous flows and high-temperature rarefied gas dynamics. The latter application has sparked strong interest especially in the production of high-speed aerospace plane and space transportation systems. In the field of material processing, the use of DSMC in handling the growth of thin films for a variety of vapour-phase processing and plasma etch is also steadily growing. To investigate the potential of DSMC as a predictive tool, results obtained by DSMC have also been compared with experiments with Navier–Stokes calculations in the low Kn regime. Computational studies have demonstrated that DSMC solutions approach the Navier–Stokes solutions at this limit. Limitations of current computer technology though gradually diminishing may still inhibit DSMC to be extensively applied to the computation of fluid dynamics. DSMC is, however, being seriously considered to resolve more specialized flows such as flows of low speed and high Knudsen number.

9.4.3 Particle Methods

The key characteristic of particle methods especially for the simulation of the continuum phenomena though deceptively simple can be obtained through the solution of ordinary differential equations (ODEs) that determine the trajectories and the evolution of properties carried by the particles. These methods amount to the solution of a system of ODEs in the general form given by

$$\frac{d\boldsymbol{x}_p}{dt} = \boldsymbol{u}_p(\boldsymbol{x}_p, t) = \sum_{q=1}^{N} \boldsymbol{K}(\boldsymbol{x}_p, \boldsymbol{x}_q; \omega_p, \omega_q) \tag{9.21}$$

$$\frac{d\omega_p}{dt} = \sum_{q=1}^{N} \boldsymbol{F}(\boldsymbol{x}_p, \boldsymbol{x}_q; \omega_p, \omega_q) \tag{9.22}$$

where $\boldsymbol{x}_p$ and $\boldsymbol{u}_p$ denote the locations and velocities for the N particles; ω_p denotes the particle properties such as density, temperature, and vorticity; and $\boldsymbol{K}$ and $\boldsymbol{F}$ represent the dynamics governing the simulated physical system. Particles are implemented with a Lagrangian formulation, and the key common characteristic of the two popular particle methods such as vortex methods (VMs) and smooth particle hydrodynamics (SPH) involves the approximation of the Lagrangian form of the Navier–Stokes equations by replacing the derivative operators through equivalent integral operators, which are in turn discretized on the particle locations.

Particle methods are often defined as *grid-free* methods, making them an attractive alternative to *mesh-based* methods such as conventional Navier–Stokes methods that have been described rather extensively. When applied to the Lagrangian formulation of the convection-diffusion equations, particle methods enjoy an automatic adaptivity of the computational elements as dictated by the flow map. Nonetheless, truncation errors introduced in the methodology can result in the creation and evolution of spurious vortical structures through particle distortion; these methods have to be conjoined with a grid to provide consistent, efficient, and accurate simulations. The grid aims to restore regularity in the particle location via remeshing but does not detract from the inherent adaptive character of these methods.

Vortex particle methods have been employed since it was first introduced by Rosenhead (1930) to describe the evolution of vortical structures in incompressible flows. Based on the vortex-blob approximation of Krasny (1986), the field is recovered at every location of the domain by considering the collective behaviour of all computational elements. When particles do overlap, the scales of the physical quantities that are resolved are determined by the finite particle core size rather than the interparticle distance. Viscous effects are simulated using the method of particle-strength exchange (PSE) (Koumoutsakos, 2005). The kinematic boundary conditions such as no-through flow at solid boundaries are enforced by boundary integral methods, whereas viscous

boundary conditions such as nonslip are imposed by translating into a vorticity fluid boundary conditions (Cottet and Poncet, 2004) complementing the viscous part of the equations.

VMs have certainly come of age by their extensive range of engineering applications. For the DNS of flow past an impulsively started cylinder for a range of Reynolds numbers, VMs have demonstrated the capability of automatically adapting computational elements in regions of the flow where increased resolution was found to be necessary to capture the unsteady separation phenomena (Koumoutsakos and Leonard, 1995). Whereby these parts are usually not known a priori, suitable criteria need to be devised to add computational elements in these critical regions for mesh-based methods. In VMs, the computational elements are inherently linked to the flow physics they represent, and no such additional criteria are necessary. The adaptivity and robustness of VMs have also enabled simulations of reacting flows to be carried out (Knio and Ghoniem, 1992). In comparison with mesh-based methods, the capture of highly anisotropic diffusion phenomena was better attained through the Lagrangian particle methods whilst accurately transporting the scalar fields. Recently, a novel particle level set method for capturing interfaces has been proposed by Hieber and Koumoutsakos (2005). It has been well-known since the pioneering work of Krasny in the 1980s (Krasny, 1986) that particle methods are well suited for interface capturing. Comparisons on a set of benchmark problems with existing level set formulations have demonstrated the promising prospect of this proposed method in achieving superior results with a reduced number of computational elements required for interface capturing.

The method of SPH was first introduced by Lucy in the late 1970s and further developed by Monaghan (1988) for grid-free astrophysics simulations. In SPH, the interparticle distance is taken instead to identify the core size. Many simulations using SPH have been conducted by extending its application range from gas dynamics in astrophysics to Newtonian and viscoelastic flows such as that found through the important works of Monaghan (1988) and Ellero et al. (2002). Like VMs, SPH also experiences the problem of particle distortion. Several techniques have been proposed to compensate for this problem (e.g. dynamic conditions by Ellero et al., 2002). Inspired by techniques in VMs, the introduction of regularization of particle distortion in SPH via remeshing has managed to improve the method to second-order accuracy; this detracts however the characterization of the method being totally grid-free. Recently, the so-called meshless methods based on Galerkin type have been explored to increase the capabilities of SPH for flow simulations. Some works by Duarte and Oden (1996) and Belytschko et al. (1996) on the unifying methods of moving least squares, reproducing kernel particle methods, and element-free Galerkin in the context of SPH are noted. For an extended understanding of the background theory and formulation, numerical implementation and challenges, and extension of the particle methods to simulate molecular phenomena,

readers are encouraged to refer to an excellent article written by Koumoutsakos (2005) where the subject of multiscale flow simulations using particles has been thoroughly reviewed.

9.4.4 Discrete Element Method

Discrete element method (DEM) was originally developed to simulate granular flow problems such as those prevalent in rock mechanics (Cundall and Strack, 1979). Similar to particle methods, it solves the motion of each individual element by solving the linear momentum equation and the angular momentum subject to forces and torques arising both from particle interaction and those imposed on the particles by surrounding fluid. In comparison with other particle simulation methods such as molecular dynamics, dissipative particle dynamics, or Brownian dynamics, DEM differs primarily by the different particle interaction laws and by the imposition of random forcing to mimic the collisions or interaction with molecules of the surrounding fluid.

DEM can be employed for a wide range of particles sizes. While other particle simulation methods are only applicable where the particle diameters are much less than the characteristics length scale of van der Waals forces ($\sim$10 nm), DEM has the propensity of handling the collision of larger-size particles. Since it is now necessary to model the detailed mechanics by which particles interact during collision, particle contact models for DEM are therefore considerably more complex than any of the other particle simulation methods. Two different approaches are adopted to characterize the interaction of two particles during collision, which can be referred to as the hard-sphere and soft-sphere models.

The soft-sphere model considers the interparticle forces between particles, namely, the normal, tangential, damping, and sliding forces that can be modelled using springs, dashpots, and sliders. As reviewed in Kruggel-Emden et al. (2009), the treatment of the normal force acting between two particles can be considered based on the degree of overlap and displacement rate. Four main groups for the evaluation of the normal force are continuous potential models, linear viscoelastic models, nonlinear viscoelastic models, and hysteretic models. For molecular dynamics simulations on the atomic or molecular level, continuous potentials between particles are widely used such as those of the Lennard–Jones potential (Verlet, 1967). The most frequently employed models in DEM are nonetheless linear (Tsuji et al., 1993). In this model, a mean coefficient of restitution and a mean collision time are defined; the related spring stiffness and the damping coefficient are then computed. Limitations of a constant coefficient of restitution and a constant duration of contact of the linear model can be overcome by applying nonlinear spring damper models. Several force laws proposed by Kuwabara and Kono (1987), Tsuji et al. (1992), and Lee and Herrmann (1993) have been developed by extending the original approach of Hertz (1882). In order to include the effect of plasticity and to avoid

the usage of the velocity-dependent damping, the hysteretic models that may be linear or nonlinear have been proposed. Notable contributions to the development of these models are Walton and Braun (1986), Sadd et al. (1993), Thornton (1997), Vu-Quoc and Zhang (1999), and Tomas (2003). In all hysteretic models, the materials in contact result with permanent deformation.

For the evaluation of the tangential force for the soft-sphere model, a wide variety of different complex models are also available to describe the force displacement behaviour. Two main groups can be defined, linear and nonlinear models. For linear tangential models, the earliest approach that has found wide application is the model proposed by Cundall and Strack (1979). It determines the tangential force according to a linear elastic spring unless the Coulomb force is exceeded. Ever since then, several versions of linear tangential displacement models have been developed. Besides the linear models, a number of nonlinear tangential models have also been proposed especially for elastic materials following Hertz (1882) theory (Maw et al., 1976; Vu-Quoc and Zhang, 1999; Di Renzo and Di Maio, 2005). In addition to the complex models for determining the normal and tangential displacements during collisions, one important feature of the time-driven, soft-sphere model is the ability to handle problems whereby particles can remain in contact for a prolonged time period to simulate particle agglomeration.

The hard-sphere model, which is based on the proposal by Hoomans et al. (1996), assumes that interactions between particles are modelled by binary collision dynamics. Main assumptions concerning the particle shape, deformation history during collision, and nature of collisions are as follows: Particles are quasi rigid, and particle shape is retained after impact; collisions are quasi instantaneous; particle contact occurs at a point that is in contrast to the soft-sphere model where an overlap displacement is allowed; particles are in free flight in between collisions and interaction forces that are impulsive; and all other finite forces are negligible during collisions. One characteristic feature of the hard-sphere model is that a sequence of collisions is processed one collision at a time. Another important feature is that the simulations are performed with realistic values of the key parameters—restitution and friction coefficients. Particle collisions are solved using particle impulse equations. Because of the limitation of collision dynamics that has been assumed, it is not surprising that the model is much more computationally efficient than the soft-sphere model since the particle collision timescale does not need to be resolved. One characteristic feature of the soft-sphere model is the very small time required (often $<10^{-6}$ s).

Fundamentally, DEM can be employed to model simple particle systems of practical interest such as those occurring in microfluidics, particle filtration, or blood flow problems in arteries and arterioles. DEM can also be useful in the development of constitutive models for kinetic theory approach and population balance models and to better understand microstructure of large-scale system.

Owing to the exponential growth of computer power and speed and more refined collision models, applications of DEM have increased dramatically, for example, in milling processes (Mishra, 2003a,b), environmental particulate flows (Richards et al., 2004), granular mixing (Bertrand et al., 2005), and fluidized-bed processes (Deen et al., 2007). There have also been recent attempts to extend DEM for systems containing small particle sizes at submicron or even nanoscale range. Fanelli et al. (2006) have developed a model for contact forces of nanoclusters by the direct consideration of the van der Waals attractive and Born repulsive forces and applied DEM to investigate nanoparticle dispersion. Luan and Robbins (2005) have compared the predictions of contact models with molecular dynamics simulations for nanoscale particles and found that good agreement was achieved for the normal force predictions but noted that atomic-scale roughness leads to significant variation in sliding resistance force between the particles.

9.5 SUMMARY

New areas of applications in fluid mechanics have brought about the development of many novel and innovative techniques. The advanced topics presented in this chapter have thus aimed to explore these latest trends in CFD research and development. It has never been the intention of the authors from the onset to provide a critical and thorough review on each of the topics presented in this chapter but rather to provide a broad overview on the research methodologies adopted and key issues that still need to be addressed and resolved. Nevertheless, the significant advances achieved in numerical methods and computational models and successful applications of some unconventional approaches particularly the lattice Boltzmann method, direct simulation of Monte Carlo, vortex method and smooth particle hydrodynamics in simulating fluid flows, and discrete element method in simulating flows of a wide range of particles sizes should leave us in a sense of awe by the sheer enormity of CFD in the many purposeful investigations of fluid-related problems that have been covered within this chapter. Flow systems involving migration of strong shocks in transonic and hypersonic flows, complex bubble mechanistic behaviour in multiphase flow structures, or even complicated flows that exist in our human body systems that are composed of trillions of cells and billions of blood vessels capable of dramatic redistribution of blood, growth over billions of cardiac cycles, are just some of the challenging fluid dynamic problems that further accentuate the demands of CFD research. Like our predecessors, Newton, Euler, Bernoulli, Poiseuille, Young, Lighthill, and many others, the study of fluid mechanics has certainly generated decades of intense fascination. As the future unfolds, CFD methods and models will continue to remain at the forefront of intensifying research and development so long as the vast majority of fluid flows and processes remain unresolved.

REVIEW QUESTIONS

9.1 Simplify the general continuity equation below to a steady incompressible flow equation:

$$\frac{\partial \rho}{\partial t} + \frac{\partial (\rho u)}{\partial x} + \frac{\partial (\rho v)}{\partial y} + \frac{\partial (\rho w)}{\partial z} = 0$$

9.2 How is the pressure term used to satisfy the continuity equation in the marker-and-cell (MAC) method?

9.3 Discuss briefly the idea behind the fractional-step procedure.

9.4 What types of applications and situations involve compressible flows?

9.5 What difficulties arise from modelling a transient supersonic flow around an aerofoil?

9.6 What is the biggest difficulty that has to be overcome with compressible flows?

9.7 What techniques can be used to minimize oscillations that occur in compressible flow due to discontinuities at the shock front?

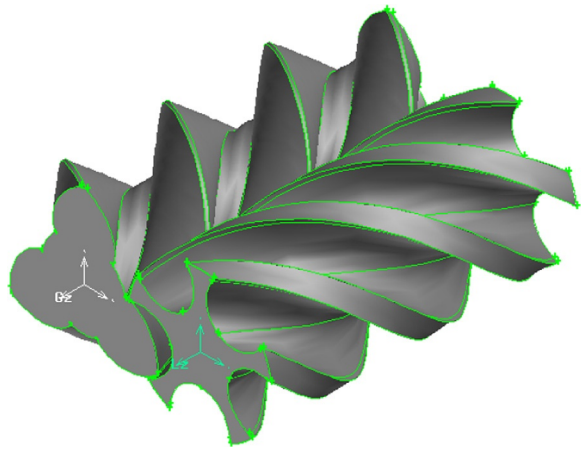
9.8 How does a higher-order scheme such as a fifth-order scheme deal with discontinuities?

9.9 Under what circumstances would adaptive meshing be used? What would happen if a fixed mesh is employed instead?

9.10 Discuss briefly the concept behind the *r-refinement* grid adaptive technique.

9.11 What kinds of applications commonly use moving grids?

9.12 Explain how a moving grid can be applied to simulate a screw supercharger shown below. What parts would need to remain stationary and what parts would be allowed to move?



9.13 What is the main advantage in the numerical solution of using multigrid methods in terms of the handling of *high-* and *low-frequency* errors?
9.14 Explain what *domain decomposition* and *load balancing* are in parallel computing.
9.15 What is the immersed boundary method, and how is this different from using a boundary-fitted grid?
9.16 What is a direct numerical simulation (DNS)? How does it differ from a Reynolds-averaged Navier–Stokes (RANS) approach in terms of its handling of turbulence?
9.17 What are the Kolmogorov microscales? How do these scales impact on the mesh design?
9.18 Why can't DNS be used to solve high Reynolds number flows at the moment?
9.19 What is the main concept behind LES in turbulent modelling?
9.20 What are the subgrid-scale (SGS) models in LES? How are they used to define small scales of turbulence?
9.21 In the RANS–LES coupling approach, in which region of the mesh would you apply the RANS model and which region would you apply the LES model?
9.22 Why would you use a RANS–LES coupling approach to model high Reynolds number turbulent flows?
9.23 What is the difference in *one-way coupling* and *two-way coupling* in multiphase flows?
9.24 Would you use an *Eulerian–Eulerian* or *Eulerian–Lagrangian* for a multiphase flow that had a high mass loading for the secondary phase (i.e. not the continuous phase)?
9.25 Combustion is a complex phenomenon to model. What types of considerations must be made in modelling combustion?
9.26 Explain fluid–structure interaction (FSI) modelling. In what applications can this be used?
9.27 What is the key requirement (and the most complex) that enables the interaction between the fluid and structure in FSI?
9.28 What advanced techniques would be required to simulate airflow through the respiratory system into the lungs? What about pulsating blood flow through veins and arteries?
9.29 Briefly discuss the concept of the lattice Boltzmann method.
9.30 Briefly discuss the concept of the Monte Carlo method.
9.31 Briefly discuss the concept of the particle method.
9.32 Briefly discuss the concept of the discrete element method.

Chapter e1

CFD Case Studies

e1.1 INTRODUCTION

With the fundamental knowledge and theories of CFD covered in the previous chapters of this book, this chapter (web chapter) demonstrates the application of knowledge and theories to various CFD problems. It is worth noting that this chapter has been specially designed to provide students who are keen to apply and practise their CFD simulation skills and explore the possibility of CFD simulations in their respective fields. Students will be introduced to step-by-step tutorials in fundamental cases by learning and practising how to set up CFD simulations and analyse the CFD results. By reviewing these cases, students will be able to expand their knowledge and build upon their acquired CFD skills to solve more advanced cases.

e1.2 FUNDAMENTAL CASE STUDIES

e1.2.1 Flow Over Cylinder—External Flow

e1.2.1.1 Introduction

The flow over a circular cylinder represents one of the most widely investigated fundamental problems of fluid mechanics. As the Reynolds number (Re) increases, the fluid exhibits a series of different flow structures (Fig. e1.1), which encompasses flow separation and vortex shedding in its wake, all contributing to drag, lift, and heat-transfer characteristics of the circular cylinder.

The flow field over the cylinder is symmetric at low Reynolds number. As the Reynolds number increases, the flow begins to separate behind the cylinder, and vortex shedding occurs. Vortex shedding is an unsteady phenomenon. Unsteady (time-dependent) simulations are needed to capture these effects. In this case study, the influence of Re on the flow characteristics and heat transfer will be investigated.

Computational Fluid Dynamics. https://doi.org/10.1016/B978-0-08-101127-0.00020-9
© 2018 Elsevier Ltd. All rights reserved.

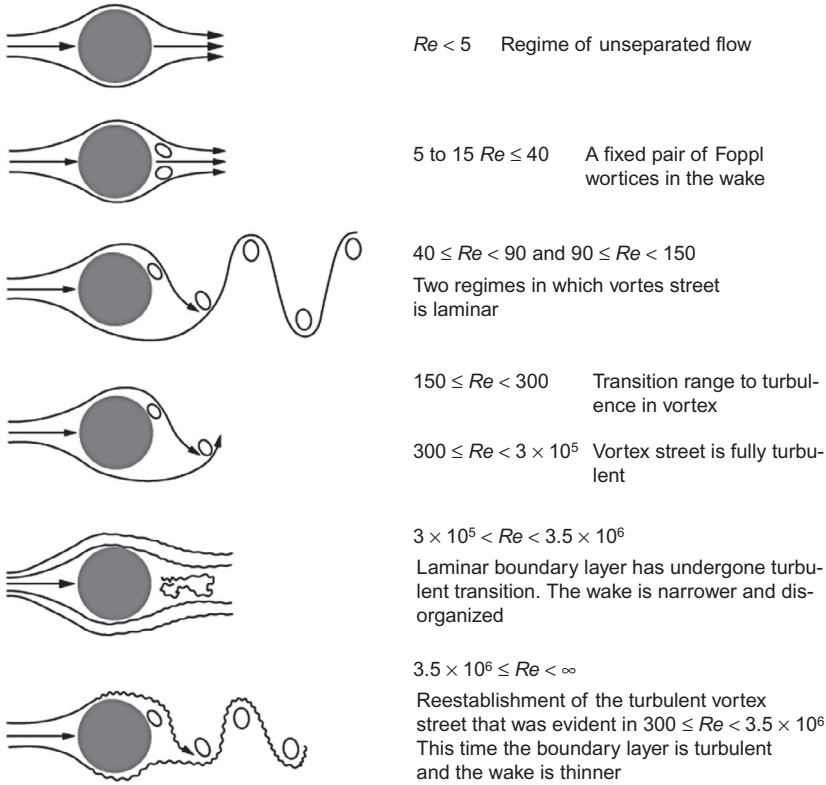


FIG. e1.1 Regimes of fluid flow across a smooth circular cylinder. *(Image from Lienhard's (1966) Synopsis of Lift, Drag, and Vortex Frequency Data for Rigid Circular Cylinders, Technical Extension Service.)*

e1.2.1.2 Simulation

❑ Case Description

An infinitely long circular cylinder of diameter $D = 0.01$ m is introduced to a uniform crossflow with velocity U, modelled in two dimensions (2-D) (see Fig. e1.2). Two boundary conditions are defined. Firstly, the flow velocity is defined at the inlet. When considering heat transfer, we have to define the temperature values at the inlet and at the cylinder wall.
The heat-transfer problem then becomes an external forced convection over a cylinder.
In this study, you are required to simulate the following cases:

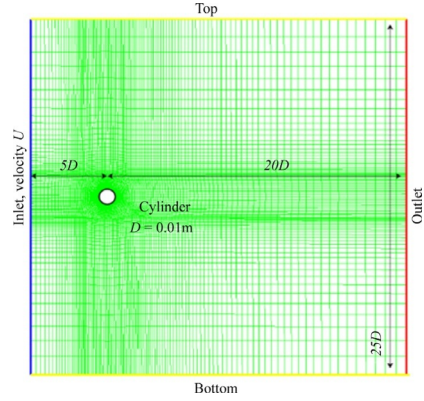


FIG. e1.2 Fluid domain.

Isothermal flows (Laminar vs Turbulent)

- ***Case 1: Re = 1, isothermal, and laminar***
- ***Case 2: Re = 100, isothermal, and laminar***
- ***Case 3: Re = 1 × 10^6, isothermal, and turbulent***

Flow with heat transfer (Laminar vs Turbulent)

- ***Case 4: Re = 20, heat transfer, and laminar***
- ***Case 5: Re = 1 × 10^6, heat transfer, and turbulent***

❑ Defining Reynolds number:

The Reynolds number is a dimensionless number that is widely used to match flow properties. This means that even if the flow conditions exhibit different material properties, velocities, and dimensions, the fluid-flow characteristics will remain the same, as long as the Reynolds number is the same. The Reynolds number is defined as

$$Re = \frac{\rho D U}{\mu}$$

where ρ is fluid density, D is pipe diameter, and μ is dynamic viscosity. The Reynolds number can be defined by changing the flow properties arbitrarily in the computational simulation to achieve a desired number. For example, for $Re = 1$, the fluid property can be defined as $\rho = 1$ kg/m^3, $D = 0.01$ m, and $\mu = 0.01$ kg/m·s, which produces

$$Re = \frac{\rho D U}{\mu} \Rightarrow 1 = \frac{1(0.01)}{0.01} U$$

This means that $U = 1$ m/s to obtain $Re = 1$ and hence gives a direct and convenient method for defining Reynolds number based on the changes in the velocity. The Reynolds number also tells us if the flow is laminar or turbulent. The settings of all cases are summarized in Table e1.1. For isothermal

TABLE e1.1 Fluid-Property Settings for All Cases

Variable	Case Unit	1	2	3	4	5
Re		1	100	1×10^6	20	1×10^6
Velocity (U)	m/s	1	1	10	0.02	10
Diameter (D)	m	0.01	0.01	0.01	0.01	0.01
Density (ρ)	kg/m^3	1	10	100	1	100
Viscosity (μ)	kg/m·s	0.01	0.001	0.00001	0.00001	0.00001
Flow condition		Laminar	Laminar	Turbulent	Laminar	Turbulent
Heat transfer		No	No	No	Yes	Yes

cases (case 1, 2, and 3), both the inlet airflow temperature and cylinder-wall temperature are *20 °C*, whilst the cylinder-wall temperature is set to *100 °C* for heat-transfer cases (case 4 and 5).

❑ Defining boundary conditions:

Instead of setting the boundary conditions one by one in Fluent, a journal file will be used for a quick setup of all cases. By using the journal file, some key parameters (air density, viscosity, velocity, etc.) are modified. An example for running $\boldsymbol{Re = 1}$ (case 1) is given below:

```
1  define/models/viscous laminar y
2  define/material/change-create/case1 case1 y constant 1 n n y constant 0.01 n n n
3  define/boundary-conditions/velocity-inlet inlet n n y y n 1 n 0 0 n 20
4  define/boundary-conditions/wall cylinder 0 n 0 n y temperature n 20 n n n 1
5  solve/initialize/compute-defaults velocity-inlet inlet
6  solve/initialize/init yes
7  report/reference-values/compute velocity-inlet inlet
8  report/surface-integrals/a-w-avg. inlet, check-re-number n
```

where

- the first line of the script describes the flow condition of the case, in which the flow is laminar for $Re = 1$ case,
- the second line of the script defines the air properties in Fluent in terms of the density (1 kg/m^3) and viscosity (0.01 kg/m·s),
- the third line of the script identifies the velocity (1 m/s) and temperature (20 °C) of the inlet air,
- the fourth line of the script defines the surface temperature (20 °C) of the cylinder.

For the rest of the other cases (case 2–5), we use the key parameters listed in Table e1.1 above (i.e. density, viscosity, and velocity) and change them in the journal file to achieve the targeted Reynolds number of each case. Load the journal file as per the boundary-condition settings in Fluent and start running the simulations. The detailed procedures of loading the case file and journal file and running the simulations are given in the next section.

e1.2.1.3 CFD Results and Discussion

❑ Tasks to be performed:

For isothermal cases (case 1, 2, and 3), you are required to

a) change the velocity, density, and viscosity in the journal file to obtain the targeted *Re*,
b) open the case file in Fluent in 2-D mode and load the journal file,
c) begin the calculation,
d) plot velocity vectors in the vicinity of the cylinder wall,

e) plot velocity and pressure contours,
f) plot XY of skin-friction and pressure coefficient over the cylinder.
For heat transfer cases (case 4 and 5), you are required to
g) plot temperature contours over the cylinder.

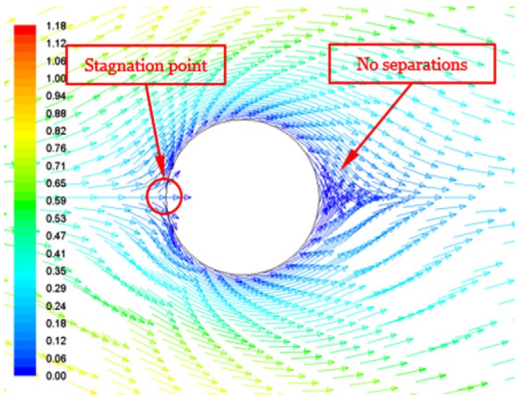
***Guides for loading and post processing of *Flow Over Cylinders* are available at Step-by-Step Tutorial. Please follow the instructions in the Appendix to generate the required results. Remember to save all the results for comparisons and discussions. ***

❑ Flow Separation for $Re = 1$, $Re = 100$ and $Re = 1 \times 10^6$

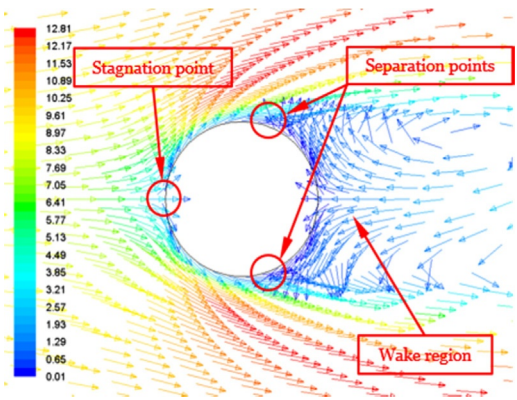
At the front of the cylinder (0 degree), the flow impacts on the cylinder at the stagnation point, in which the pressure is maximum but the velocity is zero. When the airflow develops around the cylinder surface, the stagnated airflow begins to increase from the stagnation point, and the boundary-layer pressure decreases to maintain the conservation of energy. The maximum airflow velocity occurs at roughly 90° of the cylinder, in which the pressure is minimum. With the airflow passing further across the cylinder, the pressure drops to nearly zero, and the pressure gradient changes from negative (favourable gradient) to positive (adverse gradient). The adverse pressure gradient causes the airflow to decelerate. Once the airflow velocity reduces to zero, the adverse pressure gradient causes flow separation to occur.

The wake region can be observed at the back of the cylinder at $Re = 100$ and $Re = 1 \times 10^6$. The airflow is randomly distributed inside the wake region. The size of wake region yielded by $Re = 100$ is much larger than that in $Re = 1 \times 10^6$. This is because the separation

***Re* = 1 velocity vectors**

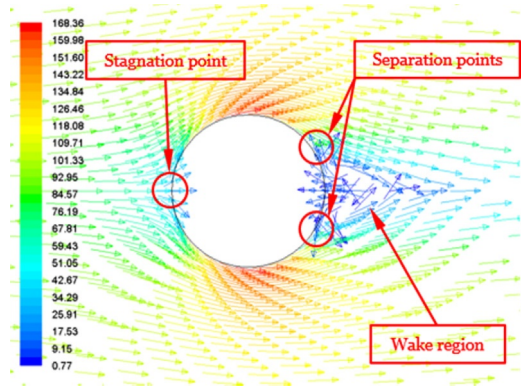


***Re* = 100 velocity vectors**



points occur much earlier in $Re = 100$ comparing with the $Re = 1 \times 10^6$ case. The late separation of the flow occurs in $Re = 1 \times 10^6$ due to the fact that the momentum induced by high Reynolds number and turbulent flow is much higher than that in the laminar flow, and thereby, it takes a longer distance for the adverse pressure to balance the momentum and subsequently the flow separation. The pressure in the rear of the cylinder, where the wake is present, is relatively low, whilst at the front of the cylinder it is high. This results in a net pressure acting on the cylinder known as pressure drag, which mainly dominates the drag for high Reynolds number.

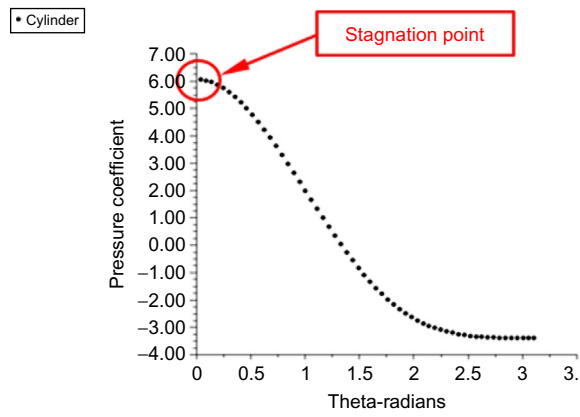
***Re* = 1,000,000 velocity vectors**



❑ Pressure coefficient comparisons among $Re = 1$, $Re = 100$ and $Re = 1 \times 10^6$

The pressure-coefficient plots illustrate how the pressure changes as the fluid moves across the surface of the cylinder. The angle represents the specific position or angle on the cylinder wall. It is evident that the pressure coefficient is at its highest across all three Reynolds numbers when the angle is 0. This is the stagnation point, in which the fluid's velocity decelerates to zero. Pressure decreases as it moves

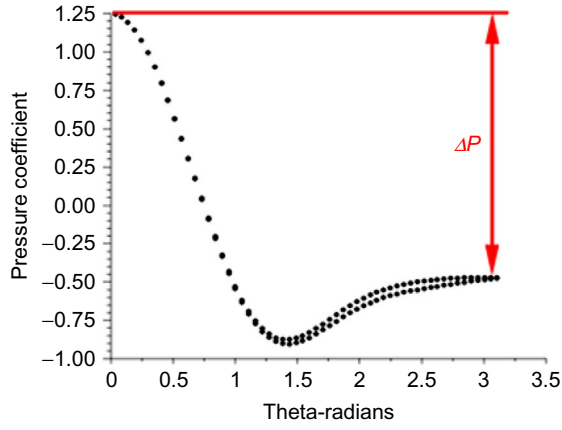
***Re* = 1 pressure-coefficient profiles**



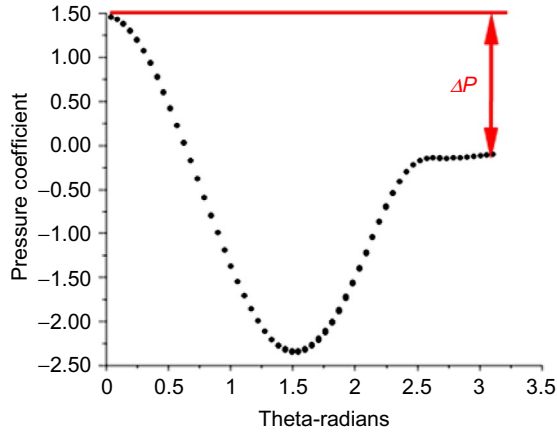
along the surface of the cylinder due to the increase of momentum. After approximately 90° (1.4 rad), the C_P begins to increase again due to the expanding area, which causes a rise of pressure in the opposite direction to the flow motion. This adverse pressure decreases the velocity of the fluid. At the back of the cylinder, the pressure-coefficient plots are fluctuating, which indicates an unsteady distribution of pressure inside the wake.

For laminar cases, the reduced C_P tends to increase a slight amount after 90°, whereas the C_P rebound is more significant in the turbulent case. This is due to the specific velocity vectors of the laminar- and turbulent-flow conditions, where the flow separations occur much later on the turbulent case. This also means that the laminar flow tends to have a larger pressure difference between the stagnation point and the back of the cylinder (wake region), which would directly result in a larger C_D

***Re* = 100 pressure-coefficient profiles**



***Re* = 1,000,000 pressure-coefficient profiles**

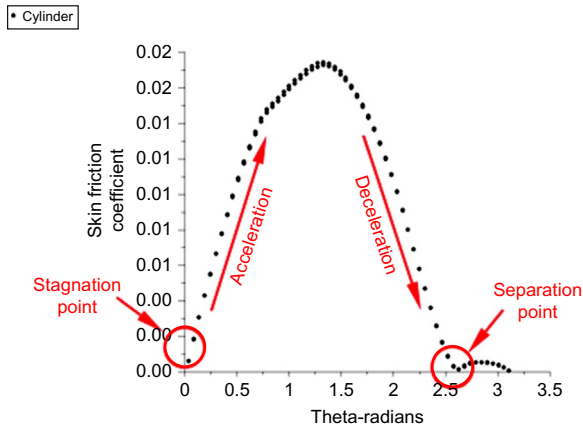


❑ Skin-friction coefficient plot for $Re = 1 \times 10^6$

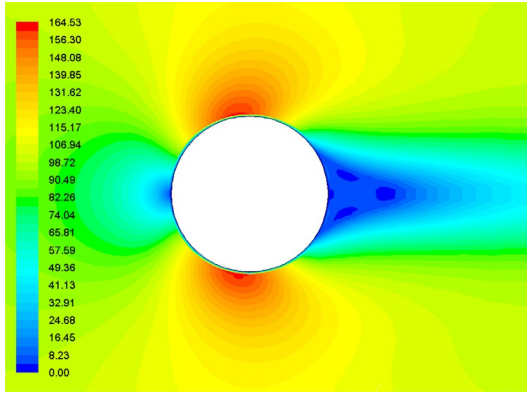
The skin-friction coefficient is representative of the wall shear-stress change over the cylinder wall. At the front of the cylinder, the friction coefficient is very close to zero in value due to the stagnation point where the velocity of the flow is stagnated. The friction coefficient increases as the flow accelerates around the cylinder surface. The maximum velocity for turbulent case of $Re = 1 \times 10^6$ occurs at approximately 85°. After the flow reaches its maximum velocity, it begins to decelerate, which is directly reflected to the decrease of skin-friction coefficient after around 1.5 rad.

When the skin-friction coefficient approaches zero, the shear stress and velocity of the flow also decrease to zero, where the flow separates from the surface of the cylinder. For $Re = 1 \times 10^6$, as the flow condition is turbulent, the C_f approaches zero fairly late at around 150° (2.6 rad). A slight increase of C_f beyond 145° can be observed in the wake region at the back of the cylinder, since the skin-friction drag still exists in the wake region due to the continuous viscous shear within the fluid inducing further drag at small magnitudes.

***Re* = 1,000,000 friction-coefficient profiles**



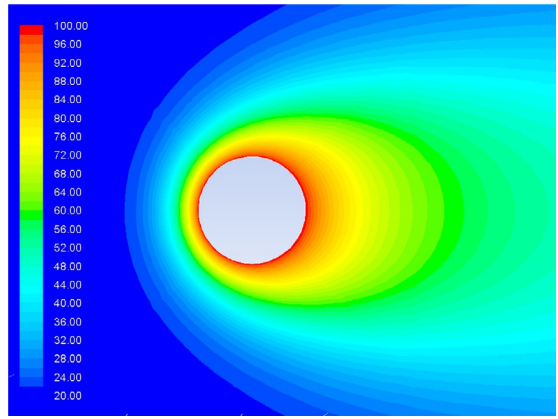
***Re* = 1,000,000 velocity contours**



❑ Heat transfer comparison between $Re = 20$ and $Re = 1 \times 10^6$

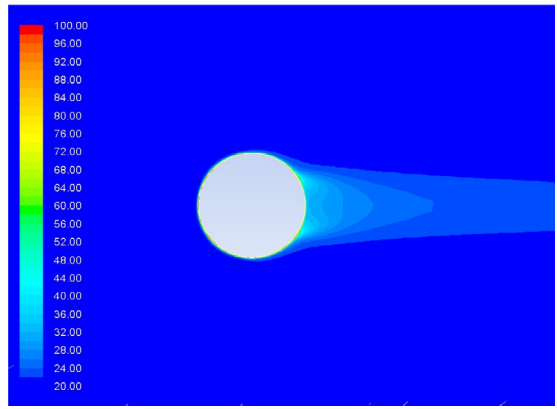
For the heat-transfer cases ($Re = 20$ and $Re = 1 \times 10^6$), the cylinder-wall surface is increased to 100 °C, whilst the incoming airflow is still 20 °C. The temperature contours show a significant difference in the heat-transfer rate between the laminar case and the turbulent case. Heat transfer occurs much quicker in $Re = 1 \times 10^6$ case as the temperature gradient is sharper. This is mainly induced by the difference of the thermal boundary layer under different Reynolds number.

Re = 20 temperature contour



For turbulent flow with $Re = 1 \times 10^6$, the thermal boundary layer around the cylinder surface is much thinner compared with the laminar case ($Re = 20$). The thin thermal boundary layer indicates a high temperature gradient in the vicinity of the cylinder wall. Therefore, since the heat disperses more quickly and effectively in the turbulent case, the heat transfer is much more effective at $Re = 1 \times 10^6$ when compared with the results from $Re = 20$. The better heat-transfer performance in $Re = 1 \times 10^6$ case is also induced by higher velocities and momentum involved in the turbulent flow, which causes intense mixing of the flow and vortices and in turn leads to the occurrence of a thinner thermal boundary layer.

Re = 1,000,000 temperature contour



Review questions:

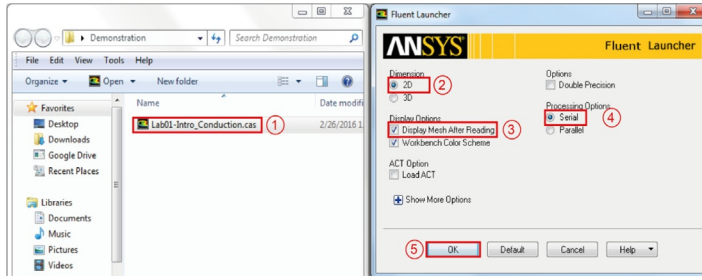
- ❑ What is the main reason causing the flow separation over the cylinder?
- ❑ At $Re = 1$, which drag is dominating the flow? Friction drag or pressure drag?
- ❑ Which case has the smallest ΔP between the front and the back of the cylinder?
- ❑ Where do the minimum and maximum C_f values occur? What happens to the flow when C_f is increasing/decreasing?
- ❑ How do you identify the position where flow separates?
- ❑ When heat transfer is involved, which case has higher heat transfer? Laminar case or turbulent case?

Exploratory questions:

- ❑ Run isothermal simulation with $Re = 20$ and compare the results with $Re = 100$. Will flow separations occur early or late at $Re = 20$ comparing with $Re = 100$?
- ❑ Run $Re = 100$ with heat transfer and compare the results with $Re = 20$. Which case has better heat transfer? What about the thermal boundary-layer thickness?
- ❑ What are the static pressure contour and total pressure contour for $Re = 1$, $Re = 100$, and $Re = 1 \times 10^6$ cases? What difference can you notice?
- ❑ Can we use Fluent to simulate all flow conditions? What are the limits?

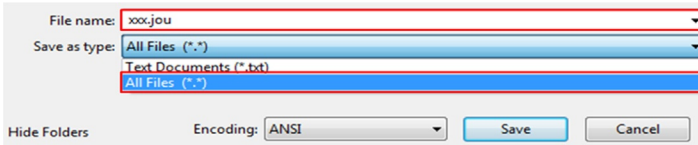
Step by Step Tutorial A: Loading files and running simulations:

- ❑ Open a new .cas file.



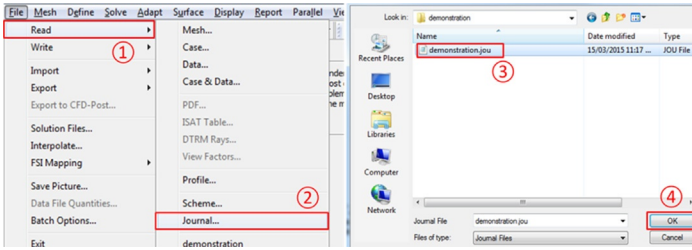
1. Double-click case file
2. 2D
3. Display Mesh After Reading
4. Serial
5. Ok

❑ Copy and paste the generated script from Excel maker to Notepad and save as .jou file.



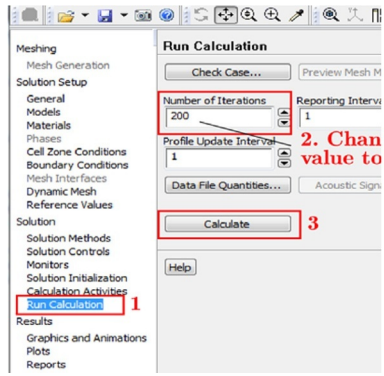
In Notepad,
1. save as. jou,
2. save as type All Files (*.*).

❑ Read the journal file in Fluent.



1. Read
2. Journal
3. Select .jou file
4. Ok

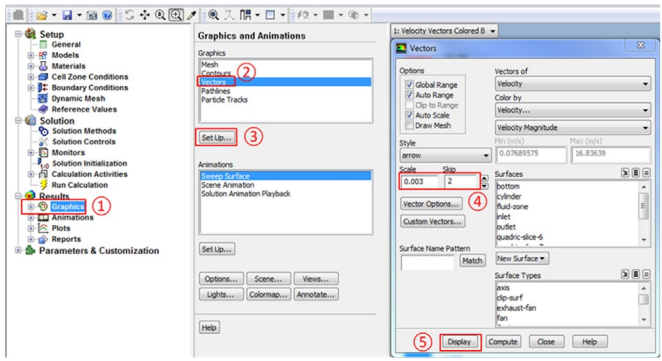
❑ Run the calculation.



1. Calculation
2. Number of iterations: *2000*
3. Calculate

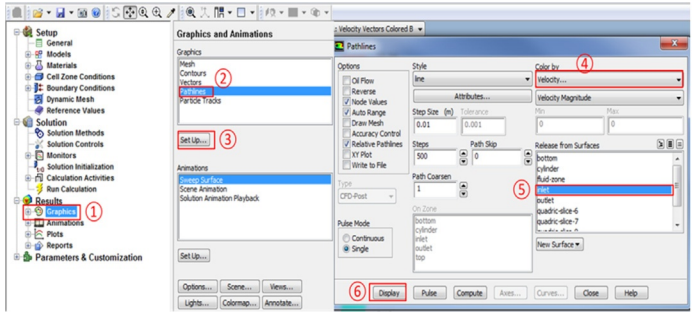
Step by Step Tutorial B: Post-processing guide

❑ Plot velocity vectors.



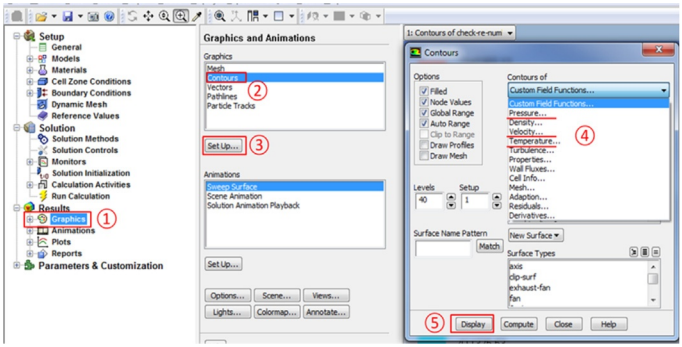
1. Graphics
2. Vectors
3. Set Up
4. ***Scale***: the size of the vector arrows (recommended range, 0.002–0.005)
Skip: to skip every n number of vectors (recommended range, 1–5)
5. Display

❑ Plot flow streamlines across the cylinder. In Fluent, these are referred as Pathlines.



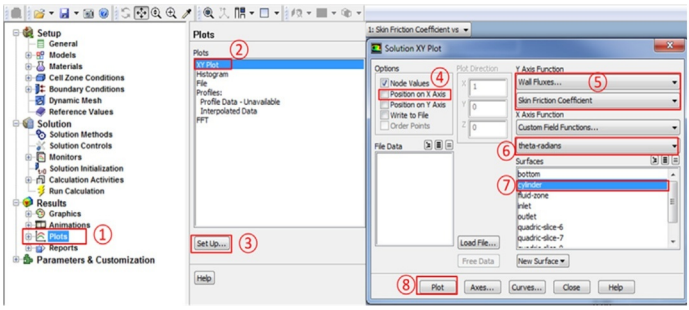
1. Graphics
2. Pathlines
3. Set Up
4. Velocity
5. Release from Surfaces: ***inlet***
6. Display

❑ Plot velocity and pressure contours.



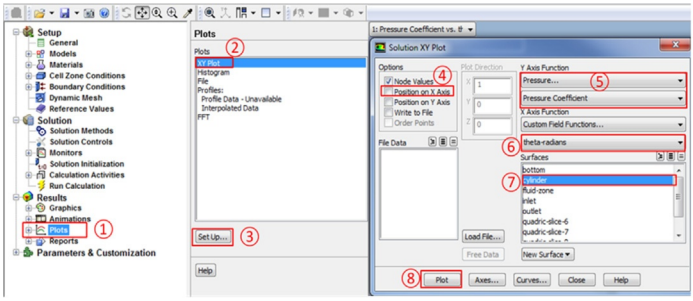
1. Graphics
2. Contours
3. Set Up
4. *Select variable* (e.g. *pressure, velocity, and temperature*)
5. Display

❑ Plot an XY plot of the skin-friction coefficient over the cylinder.



1. Plots
2. XY Plot
3. Set Up
4. *Unclick* Position on X Axis
5. Y Axis Function: Wall Fluxes → Skin Friction Coefficient
6. theta-radians
7. cylinder
8. Plot

❑ Plot an XY plot of the pressure coefficient over the cylinder.



1. Plots
2. XY Plot
3. Set Up
4. Unclick Position on X Axis
5. Y Axis Function: Pressure → Pressure Coefficient
6. theta-radians
7. cylinder
8. Plot

e1.2.2 Flow Over a Backward Facing Step—Internal Flow

e1.2.2.1 Case Introduction

A backward-facing step is commonly used as a benchmark case for the validation of numerous flow characteristics, including physical models, multiphase flows, and fundamental numerical methods. The flow physics in such a geometry is rich that includes the flow separation, flow reattachment, and recirculation zones. This problem has applications in many industries including HVAC and combustion chambers, making it an ideal case for CFD analysis for validation of the flow behaviour.

Focusing on the aspect of CFD modelling, the process of creating meshes of different quality and size for a model and applying appropriate boundary conditions and treating a model in CFD modelling software will be described, as well as the analysis of the results. The main focus of this investigation is directed towards the understanding of the flow circulation just after the step and at the point where the flow reattaches itself downstream into the expansion chamber. The reattachment point is dependent on several operating and boundary conditions, such as inlet velocity, step height, and Reynolds number. The quality of the meshed region has a substantial influence on the reattachment location; generally, the denser the mesh, the more accurate the results that are produced by the CFD simulations.

The aims of this case problem are as follows:

1. To learn the process of creating and exporting a mesh for quality CFD modelling.
2. To learn how to set boundary conditions and process a numerical model.
3. To explore the post-processing abilities of the CFD code to analyse numerical results.
4. To learn how to write concise and well-developed professional reports.

e1.2.2.2 Simulation

❑ Case description

The dimension for the geometry is assumed to be normalized based on the characteristic length of the section. In the case of the backward-facing step, it is the height of the step that is one unit high. A simplified 2-D representation of the backward-facing step problem is provided in Fig. e1.3A and B.

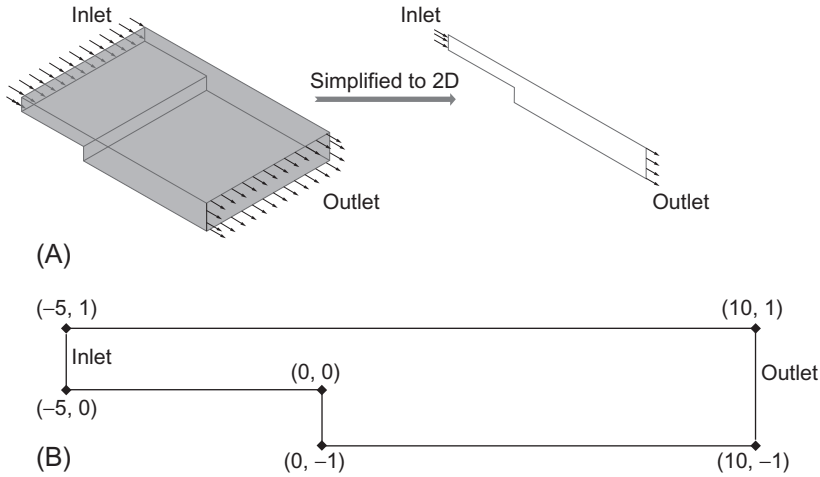


FIG. e1.3 (A) Simplifying to a 2-D problem and (B) illustration of the 2-D geometry of a backward-facing step.

The dimensions given for the geometry are dimensionless as they are normalized by a characteristic length. Bear in mind that for the case of a backward-facing step, the characteristic length is the step height (in this case 1 unit high). The fluid enters at the Inlet and exits the channel from the Outlet. The normalized inlet velocity and fluid properties that are also normalized for the characteristic length are provided as follows:

Inlet velocity:	$u_x = 1$ and $u_y = 0$
Fluid properties:	density, $\rho = 1$

Dynamic viscosity: $\mu = 1/Re$, where Re is Reynolds number.

The outlet should be defined as an outflow, and the other boundaries should be left as non-slip walls. As turbulent flow is not considered, turbulent settings are neglected. There will be no heat transfer included. The length of the 2-D geometry may have to be altered to ensure developed flow at the outlet.

❑ Numerical procedures:

1. Model creation:

Create the two-dimensional backward-facing step geometry as shown in Fig. e1.3, using **ANSYS DesignModeler** or **SpaceClaim** (Fig. e1.3A).

2. Meshing:

Use **ANSYS Mesh (CFX)** to generate a uniform mesh over the domain (Fig. e1.4). Check the mesh quality to ensure that a proper mesh quality is achieved as listed in Table e1.2.

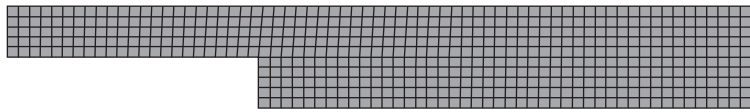


FIG. e1.4 Mesh with characteristic length of $m = 0{:}221$.

TABLE e1.2 Mesh Information

Property	Value
Characteristic length (m)	0.221
Number of nodes	1288
Number of elements	565
Mean skewness	0.0145
Skewness standard deviation	0.0158
Mean aspect ratio	22.1
Aspect ratio standard deviation	0.119

3. Defining boundary conditions:

Use **ANSYS-CFX-Pre** to define the model settings. This includes the following steps:

i. Specify the material properties of the fluid (as listed in Table e1.3) and choose the appropriate fluid-flow mode.

TABLE e1.3 Material Properties of Fluid

Dynamic Viscosity, μ (kg/ms)	Density, ρ (kg/m^3)	Molar Mass (kg/kmol)
0.01	1.00	1.00

ii. Assign the appropriate boundary conditions for the model, as shown in Fig. e1.5.

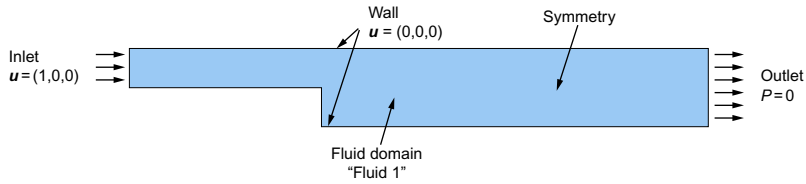


FIG. e1.5 Applied boundary conditions.

iii. Assign the initial values of the model (Table e1.4).

TABLE e1.4 Boundary Settings for the Flow Domain Named Backward Step

Name	Boundary Type	Location	Boundary Details
Inlet	Inlet	Inlet	$u = (1, 0, 0)$
Outlet	Outlet	Outlet	Average static pressure = 0 Pa
Symmetry	Symmetry	Symm 1 and Symm 2 (**Ctrl + LMB** click for the multiple selection)	
Wall	Wall	wall_top, wall_bottom, and wall_step (**Ctrl + LMB** click for the multiple selection)	

4. Running the simulations

Use **ANSYS-CFX-Solver** to run the simulation. Set the maximum iteration steps to 500 and residual target to 1×10^{-6}.

5. Post-processing the results

Use **ANSYS CFD-Post** to obtain the velocity and pressure contours and the velocity vectors. Ensure that the developed flow is present at the outlet and/or at least a close-to-developed flow is present prior to the step.

6. Results and discussions

Discuss any observed **flow characteristics** using the physical parameters.

Guides for numerical procedures of *Backward Facing Step* case are available at Step by Step Tutorial. Please follow the instructions in the Appendix to generate the required results. Remember to save all the results for comparisons and discussions..

e1.2.2.3 CFD Results and Discussion

❑ Tasks to be carried out

For Reynolds number of 100,

a. run the simulations using five different sets of mesh and obtain the location of the flow reattachment point behind to step for each case;
b. conduct mesh independence test and determine the sensitivity of the mesh fineness to the location of the reattachment point;
c. discuss this change in reattachment location with the mesh refinement, and choose the appropriate mesh for the next stage of the investigation;
d. use the selected mesh to continue and obtain the velocity and pressure contours and the velocity vectors; (Ensure that the developed flow is present at the outlet and/or at least a close-to-developed flow is present prior to the step.)
e. discuss any observed flow characteristics using the physical parameters.

For Reynolds number of 50, 150 and 200,

f. repeat the simulations for $Re = 50$, 150, and 200 using the selected mesh;
g. discuss the relationship between Reynolds numbers and reattachment points, using physical parameters to explain the phenomenon. Provide your own conclusions on this observation.

❑ Mesh quality and independence test

An efficient mesh is essential to achieve the desired accuracy within a reasonable computational time. Whilst with this simple problem, computational time is of no real concern; when larger scaled projects are confronted, some thought should be given to the mesh density as it plays an important role in the CFD analysis. DesignModeler is used to create the geometry for the backward step and then to create several meshes, each with different densities. The first two meshes considered (Fig. e1.6A and B) can be seen to be rather coarse, with an increase of mesh density from Mesh 1 to 2. The next three meshes (Fig. e1.6C–E) contain some refinement of the mesh around the flow areas of interest, mainly the step, the region of circulation behind the step, and the region around the expected reattachment location.

To determine the best mesh for the problem, the approximated reattachment length ($\boldsymbol{L_R}$) of the flow can be identified using the velocity vector, and an example is shown below in Fig. e1.7.

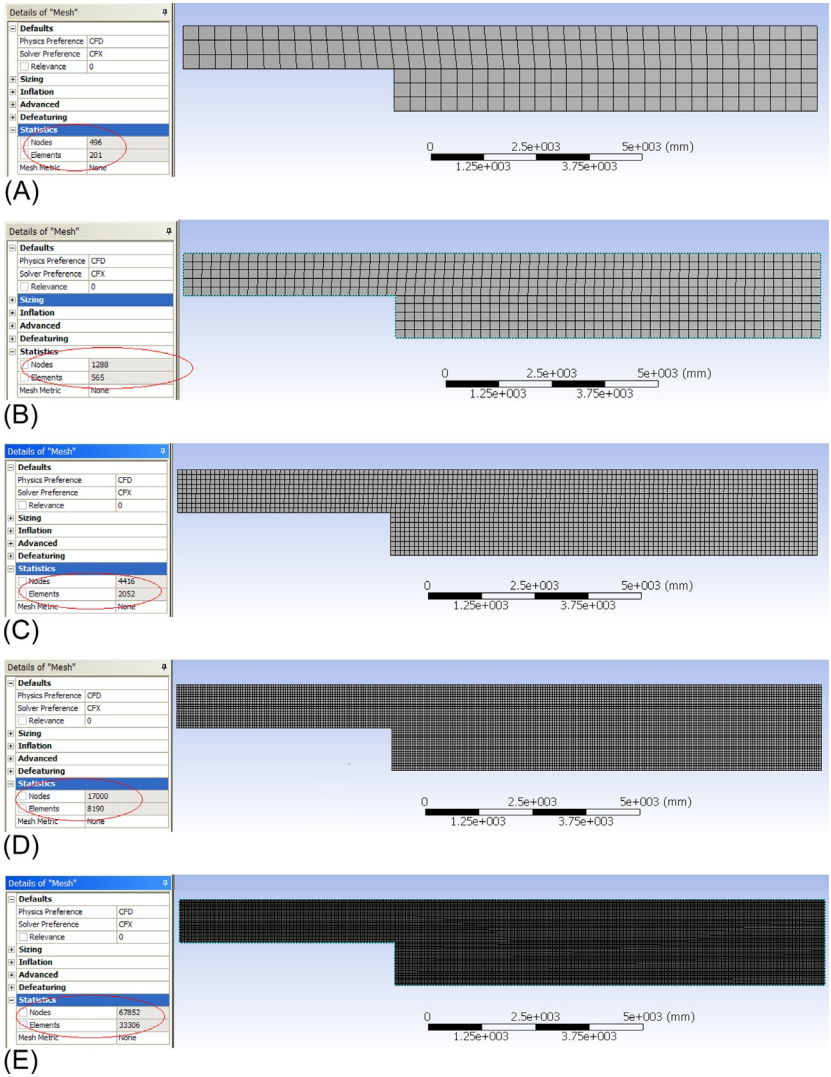


FIG. e1.6 Uniformly structured meshes with increased mesh fineness from 1(A) to 1(E). *(Note that the higher number of the mesh ID indicates the higher level of mesh refinement.)*

To identify the location of the flow reattachment, the pressure gradient along the horizontal direction (x axis) is plotted against the horizontal distance. The flow reattachment point occurs when the pressure gradient x changes from a positive value to a negative value. The simulation is conducted using CFX with a simple two-dimensional, incompressible laminar flow, with the properties and

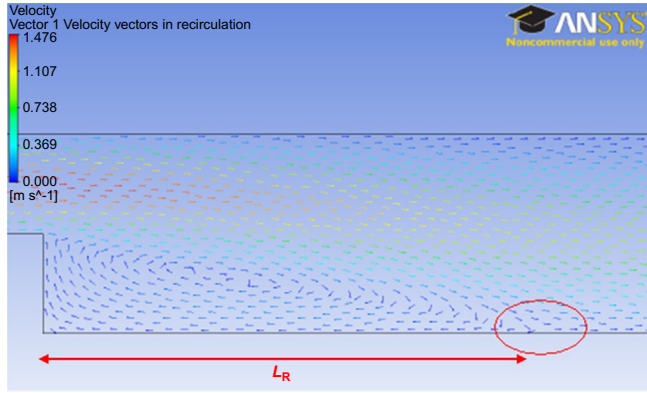


FIG. e1.7 Velocity vectors showing approximate reattachment length L_R at $Re = 100$.

boundary conditions stated earlier. Using a line just above the bottom wall, the x velocity can be plotted against distance in X, showing the point at which the flow reattaches to the bottom surface. Performing this analysis for each mesh density, the x velocities could be used to compare reattachment lengths as shown in Fig. e1.8.

The importance of mesh refinement on the reattachment length can be clearly seen on these plots (Fig. e1.8). The reattachment location increases with the growth of mesh elements in the models. When different meshes are applied (from Mesh 1 to Mesh 3), their reattachment length L_R increases. However, with

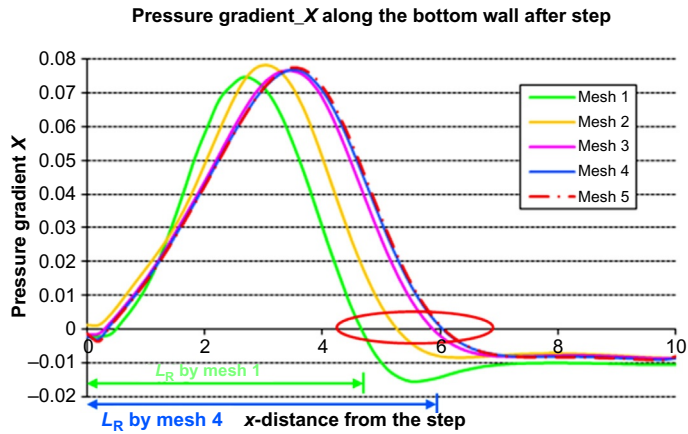


FIG. e1.8 Velocity vectors showing reattachment length L_R at $Re = 100$.

TABLE e1.5 Calculated Reattachment Length (for *Re* = 100) Using the Five Meshes

Mesh ID	1	2	3	4	5
Reattachment length	4.660908	5.271289	5.882098	6.048679	6.06816

further refinement of the mesh, the predicted reattachment lengths using Mesh 4 and 5 are not much different from each other. As further refinements do not appear to significantly improve the accuracy of the CFD simulations, Mesh 4 is thus regarded as the most efficient mesh to be adopted for the rest of the simulations and analysis of results. Detailed information regarding the reattachment length versus mesh can be seen in Table e1.5.

❑ Flow development along the backward facing step ($Re = 100$)

From the pressure contour (Fig. e1.9), the pressure tends to decrease from the inlet to a minimum value just before the step and then increases to a constant value on the rest of the region. The pressure drop after flow coming into the domain is induced by the sudden expansion of the cross-section at the step. The pressure drop rate could be directly related to the expansion ratio of the geometry and the flow condition (i.e. the Reynolds number). After the pressure drops to zero, a reversible pressure rise can be noticed near the step due to the Bernoulli effect, associated with the decrease in mean velocity due to the sudden expansion.

The velocity contours given in Fig. e1.10 demonstrate the flow distribution at different locations along the backward-facing step. The air velocity is evenly distributed at the inlet of the domain. As the flow develops inside the domain, uneven velocity gradient gradually forms with lower velocity near the wall due to the fluid viscosity and higher velocity at the centre. Since the flow distribution

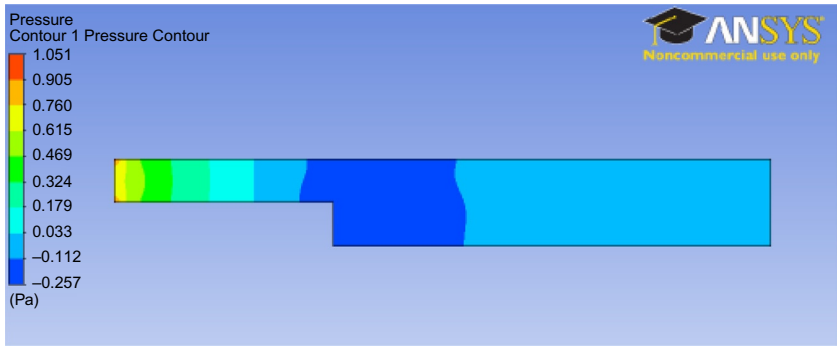


FIG. e1.9 Pressure contour.

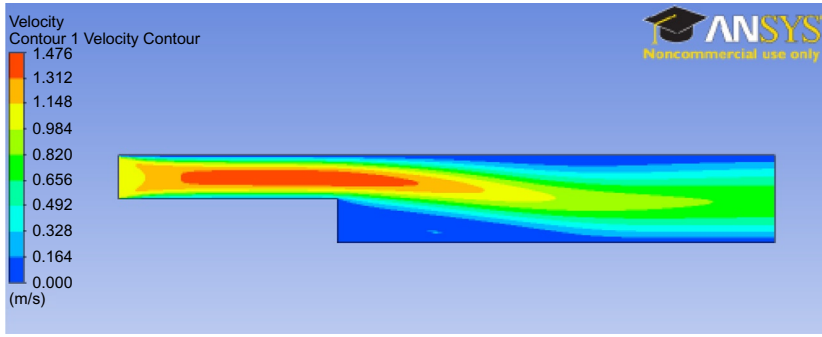


FIG. e1.10 Velocity contour.

remains unchanged at the region before the step, the flow is thus taken to be fully developed and thereby the length between the inlet and the step is deemed to be sufficient. Due to the sudden expansion of the cross-section, the flow separates at the step and continues moving forward due to inertia. The flow gradually reattaches to the bottom wall before exiting the computational domain.

As the flow separates at the step, extreme low velocities (from Fig. e1.10) are found at the bottom corner of the step; the recirculation region grows as indicated by the recirculation zone illustrated in Fig. e1.11 using the velocity streamlines.

The velocity profiles at different cross-sections before and after the step can be observed via velocity vectors. In Fig. e1.12, the velocity profile at the cross-section before the step reveals a fully parabolic shape before the step, which means that the entered flow is fully developed before entering into the expansion chamber.

The parabolic velocity profile at the outlet of the domain, as shown in Fig. e1.13, also reveals that the flow is fully developed before exiting the computational domain. The required distance to allow the flow to be fully developed would be longer with higher Reynolds number. Therefore, it is highly recommended that the computational domain is extended after the step to guarantee a fully developed flow when simulations are conducted for higher Reynolds number.

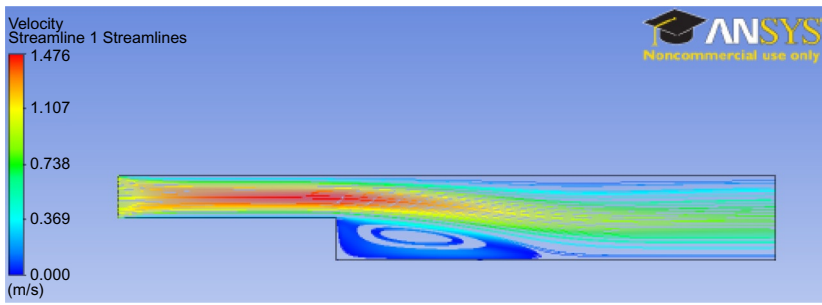


FIG. e1.11 Velocity streamlines.

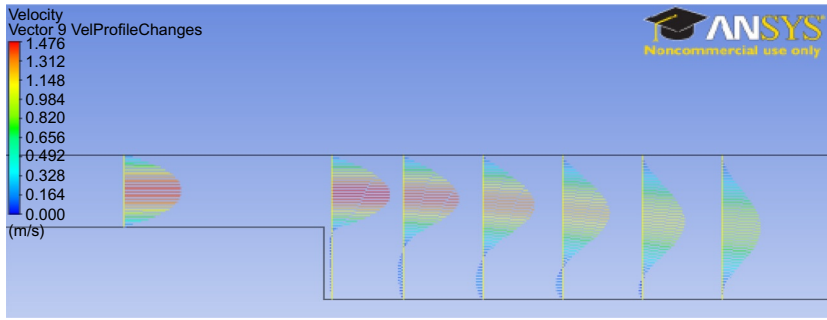


FIG. e1.12 Velocity profiles at different cross-sections before and after the step.

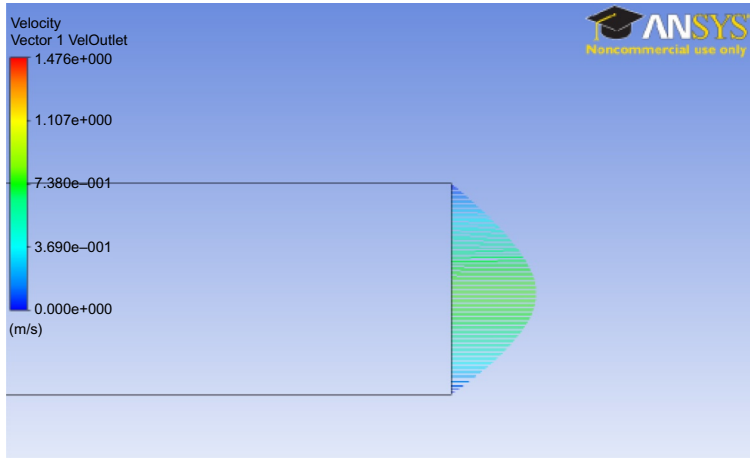


FIG. e1.13 Flow profiles at the outlet.

❑ Reattachment length versus Reynolds number

By varying the Reynolds number and keeping all other variables constant, the effect of *Re* on the flow can be determined by calculating the reattachment length. *Re* of 50, 100, 150, and 200 can be set by changing the inlet velocity. The predicted velocity streamlines of each case are compared in Fig. e1.14. In Fig. e1.14, it can be seen that the size of the recirculation zone becomes larger at higher Reynolds number, which is due to the higher inertia of the flow occurring at higher Reynolds number:

At *Re* of 200, it is noted from Fig. e1.15D that the flow is seen to be not fully developed at the outlet of the domain. To improve the CFD simulation, the computational domain therefore needs to be extended to allow the flow to be fully developed before exiting the computational domain.

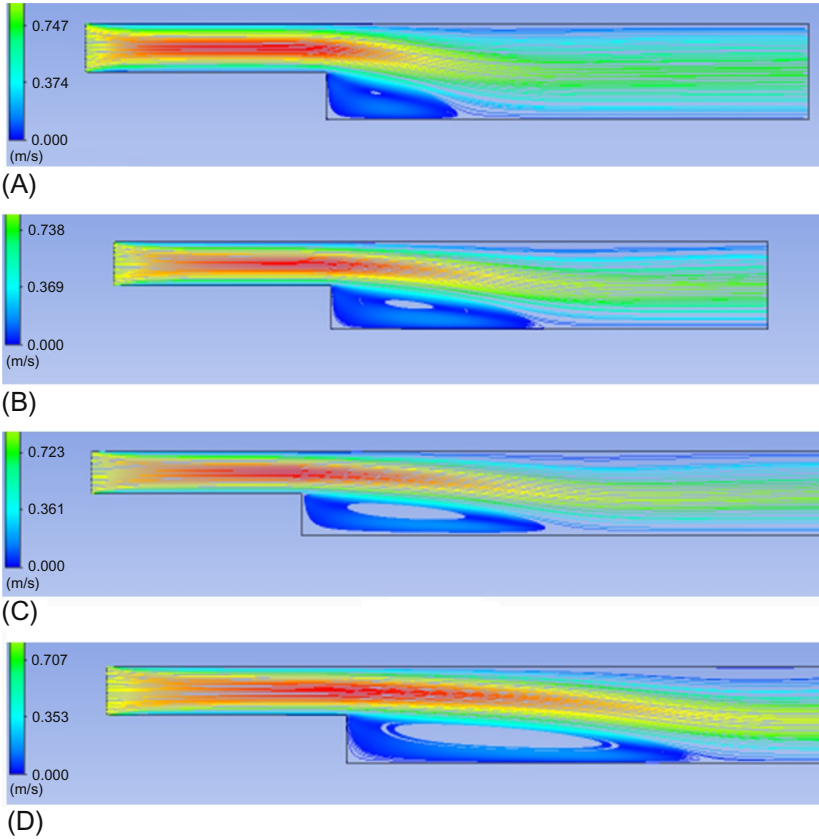


FIG. e1.14 Streamline plots for different *Re* cases. (A) $Re = 50$. (B) $Re = 100$. (C) $Re = 150$. (D) $Re = 200$.

The reattachment length (L_E) predicted by each case is summarized in Table e1.6.

The effect of Reynolds number on the stream-wise reattachment location is characterized by varying the Reynolds number for the flow and recording the data. The results are depicted in Fig. e1.16.

As can been seen in Fig. e1.16A, increasing the Reynolds number has the effect of elongating the pressure gradient and moving the flow reattachment point further towards the outlet. The movement of this reattachment point towards the outlet occurs in what appears to be a quadratic trend, depicted in Fig. e1.16B as described by the equation $y = -0.000144x^2 + 0.068517x + 0.539946$. This allows for an accurate prediction of the reattachment point for any Reynolds number within the range of data obtained. To ensure these results are accurate, the velocity curve at the outlet is analysed to ensure the flow is fully developed. In the case of $Re = 150$ and $Re = 200$, the outlet

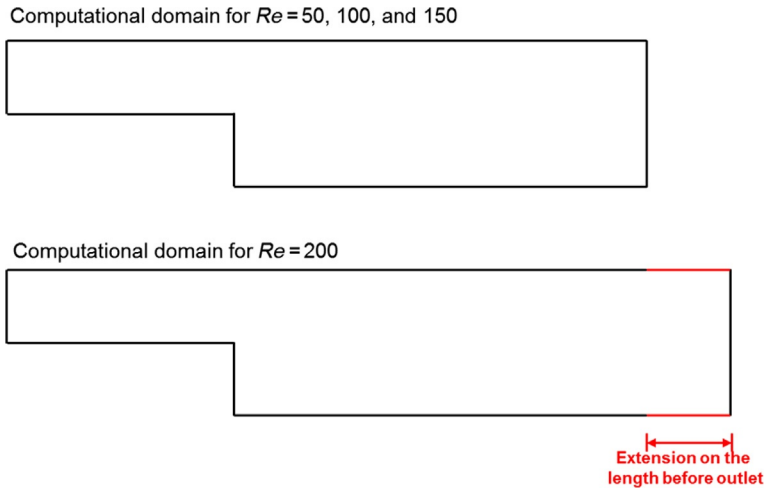


FIG. e1.15 Extension on the length before the outlet for $Re = 200$.

TABLE e1.6 The Reynolds Number Versus Reattachment Length L_E

Reynolds Number	Reattachment Length (L_E)
50	5.4
100	8.8
150	11.9
200	14.2

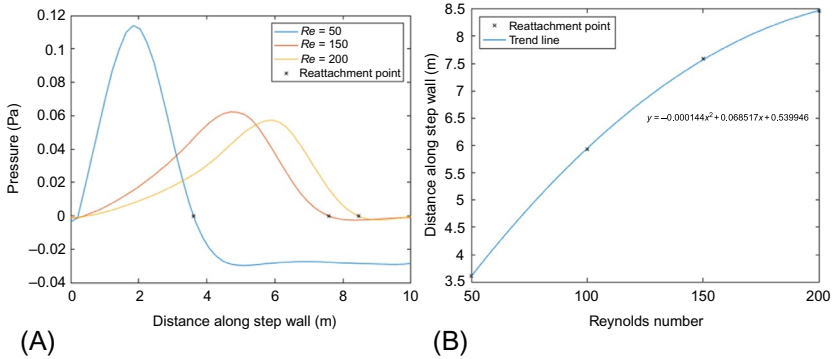


FIG. e1.16 Variation in reattachment point with change in Re. (A) Pressure gradient in the streamwise direction. (B) Variation trend.

velocity profile is not parabolic for the initial geometry, indicating that the flow has not yet reached its fully developed state. This is because the Reynolds number describes the relationship between velocity and dynamic viscosity, and density is a useful metric on how a proportional change in each of these variables has the same effect on the flow-velocity profile. In this case, the Reynolds number has been manipulated through the specification of dynamic viscosity, specifically its reduction as $1 = Re$, which reduces the friction force experienced by a particle in contact with its adjacent particles. This has the effect of elongating the velocity vectors and increasing the distance it takes for the flow to become fully developed. To rectify this, the model geometry for the case of $Re = 150$ and $Re = 200$ is lengthened to 20 m from its initial length of 10 m. The velocity vectors at the outlet of each case is predicted and shown in Fig. e1.17.

Each of the outlet flow-velocity profiles is now parabolic, indicating that the flow is fully developed. Interestingly, Fig. e1.17 shows that the outlet velocity at $Re = 100$ is faster than that at $Re = 150$ and $Re = 200$. This is interesting because the dynamic viscosity and thus friction between fluid particles at these higher Reynolds numbers are lower and indicate that there should be less resistance, more energy in the fluid, and thus higher velocity. The reason for this is likely the change in geometry. At the higher Reynolds numbers, the length for the fluid to flow has doubled, which leads to a cumulatively larger loss in energy and thus lower exit velocity.

Review questions:

- ❏ Which main criteria can be referred when checking the mesh quality?
- ❏ What governing equations are solved in this case?

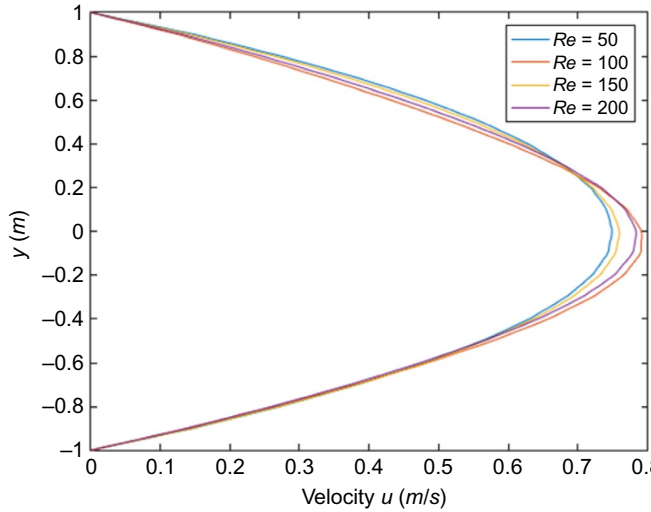


FIG. e1.17 Velocity profile at outlet for each Reynolds number.

- ❑ What is the main reason causing the flow recirculation at the step?
- ❑ How to identify the reattachment point?
- ❑ What is the reason to extend the length of the geometry under higher Re?

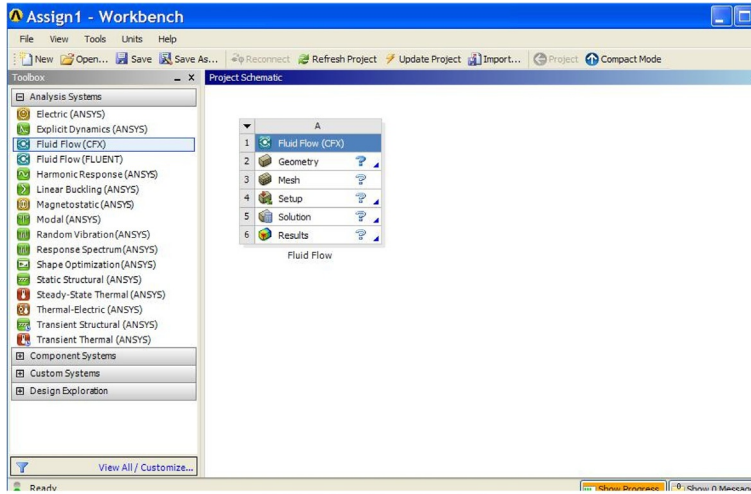
Exploratory questions:

- ❑ Change the 'Top' boundary condition from 'Non-slip' wall to 'Specified-shear' (maintaining shear stresses of X and Y components at 0 Pa) for the Reynolds number $Re = 50$ case and solve for the solution. Discuss the results obtained there in relation to the results from the previous 'Non-slip' boundary-condition model of same Reynolds number $Re = 50$ case.
- ❑ Run simulations with higher Reynolds number (turbulent flow), apply different turbulence models, and compare the results (reattachment point, reattachment length, etc.).

Step by Step Tutorial Numerical Procedures:

- ❑ **Start ANSYS Workbench**

1. From Windows Start menu, select ***ANSYS 17.2 > Workbench 17.2***.
2. When Workbench opens, select **File > Save**, and then, save the project as Assign1 into your secured folder.
3. Expand the Analysis Systems toolbox, and then, drag and drop a Fluid Flow (CFX) object into the top left area of the Project Schematic window as shown below:

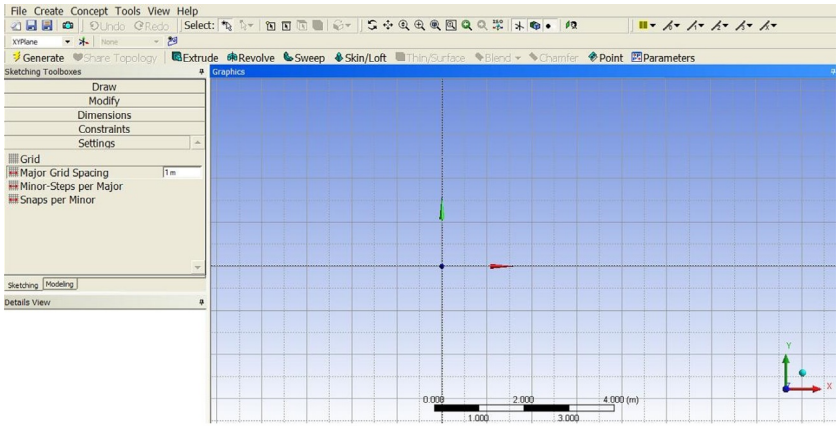


ANSYS Workbench window

❑ Stage 1 - Create the model geometry

Load the DesignModeler

1. **Right click** on the Geometry cell and select **DesignModeler**. Select ***m*** as the unit of measure for the session when prompted.
2. Under **Tree Outline**, click on *XY* Plane, and then, click on **New Sketch** icon  on the top menu. This is to insert ***Sketch 1*** in XY Plane.
3. Click on **Look At** icon  to orient the sketch plane in the normal direction.
4. Click on the Sketching tab to switch to sketch mode.
5. Sketching: *Settings* > *Grid*.
6. Toggle on **Show in 2D and Snap to Grid**.
7. Click on Major Grid Spacing and set it to *1.0 m*.
8. Click on *Minor-Steps per Major* and set it to *2*.
9. Zoom in on the model view, so that the area displayed is placed around the origin of the coordinate with 10 major steps in the positive x direction and 5 major steps in the negative x direction.



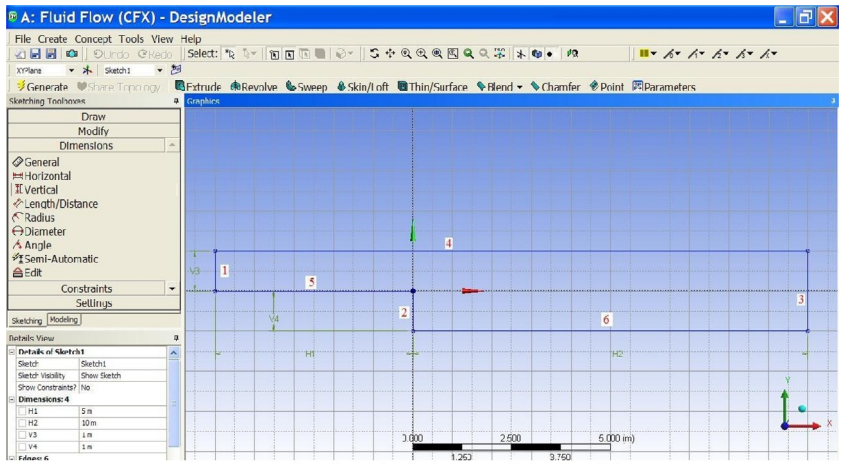
Setup the grid for creating the 2D geometry

Sketching: Draw - ≥Polyline.

Draw the outline of the 2-D backward-facing step model by **LMB** single-clicking on the points with the given coordinates sequentially, on the sketch, starting from the origin (0, 0). When you Return to the origin (0, 0), **RMB**, and then, select ***Close End*** from the pop-up menu.

The 2-D dimensions of model are defined now by drawing within the grid with the given coordinates of the model.

In the next step, we will set up the dimensions of the model. This is to parameterize the model dimensions for the possible model geometry modifications in the future.



Setup the four dimensions of the model

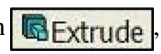
Sketching: Dimensions > Horizontal

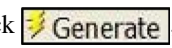
1. **LMB** single-click on the line labelled 1 to select the first line, and then, **LMB** single-click on the line labelled 2 to select the second line. A pencil will appear on the screen. Move the pencil by dragging the mouse to an appropriate location, and then, **LMB** single-click to fix the location of the dimension H1 on the drawing (note that the number on your drawing may differ due to the sequence of your setting up the dimensions).
2. Repeat the procedure by selecting the lines labelled 2 and 3 to define the dimension ***H2***.

Sketching: Dimensions > Vertical

3. **LMB** single-click on the line labelled 4 to select the first line, and then, **LMB** single-click on the line labelled 5 to select the second line. A pencil will appear on the screen. Move the pencil by dragging the mouse to an appropriate location, and then, **LMB** single-click to define the dimension ***V3*** (note that the number on your drawing may differ due to the sequence of your setting up the dimensions).
4. Repeat the same procedure by selecting the lines labelled *5* and *6* to define the dimension *V4*.

Feature Generation ≥3D Extrude

1. Click on the *Extrude* icon 

, on the top menu bar, to bring up the ***Details View*** for the 3D Extrude operation (the Tree outline will consequently switch to the *Modelling* phase).
2. In the ***Details View***, select ***Reversed*** for *Direction*, and then, enter ***0.01*** for *FD 1 Depth (> 0)***.** Then, click 

, on the top menu bar, to complete the 3D Extrude.

Details View

Details of Extrude1	
Extrude	Extrude1
Base Object	Sketch1
Operation	Add Material
Direction Vector	None (Normal)
Direction	Reversed
Extent Type	Fixed
FD1, Depth (>0)	0.01 m
As Thin/Surface?	No
Merge Topology?	Yes

3D extrude operation settings

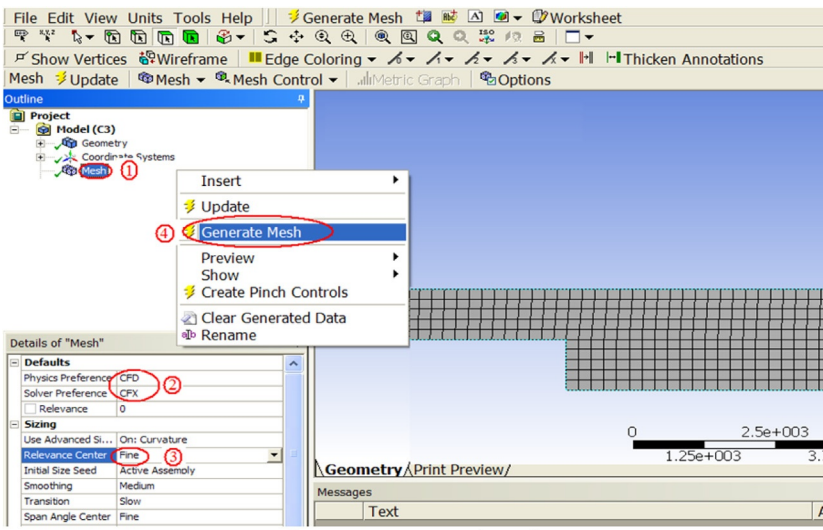
Save the Project, and exit DesignModeler to return to the **Workbench** and ready for Meshing.

❑ Stage 2 - Create the Mesh

Generate Mesh

In **ANSYS Workbench**, double-click on **Mesh** cell to bring up **ANSYS Mesh**.

1. Click on ***Mesh*** under the **Outline tree** view to bring up the ***Details of Mesh*** panel at the left bottom of the screen. In this panel,
2. set Physics Preference to **CFD**, and then, set Solver Reference **CFX**;
3. expand Sizing and set the Relevance Centre to ***Fine***;
4. In the Outline tree view, RMB click on Mesh > ***Generate Mesh*** to create the mesh.



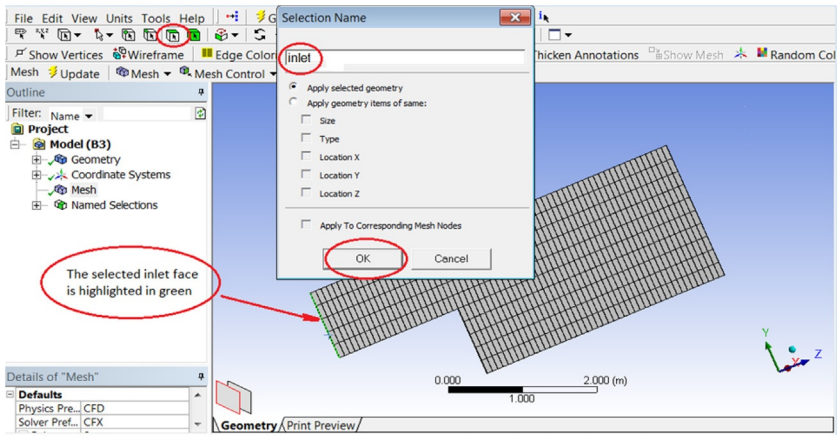
Create a structured mesh

Create boundary surfaces

Define the boundaries of the fluid domain by creating the Named Selections for all the faces that enclose the fluid domain: inlet, outlet, top wall, bottom wall, and step wall. The front and back faces of the model are also needed to be defined as the symmetry planes:

1. Define the inlet boundary through the following steps:

- Ensure that the Face Selection Filter is active; LMB single-click to select the Inlet face.
- RMB > create Named Selection.
- In the pop-up window, enter a name for the selected face, for example, inlet, then OK.



Create a named selection for the inlet face boundary

2. Repeat the same procedure to create the ***Named Selections*** for the outlet; the two symmetry planes (name them the way you like, e.G. symm 1 and symm 2); and the top, bottom, and steep walls of the channel (e.G. wall_top, wall_bottom, and wall_step).

Click ***File > Save Project***… to save the project file.

Click ***File > Close Meshing*** to exit **ANSYS Mesh** and return to the **Workbench** Project page.

In the **Workbench** Project Schematic window, there should be a green tick next to the ***Mesh*** cell. If not, **RMB** on the ***Mesh*** cell; in the pop-up menu, select **Update**. Wait until the green tick appears.

❑ Stage 3 - Specify Boundary Types, Materials, Fluid flow models and Initial values

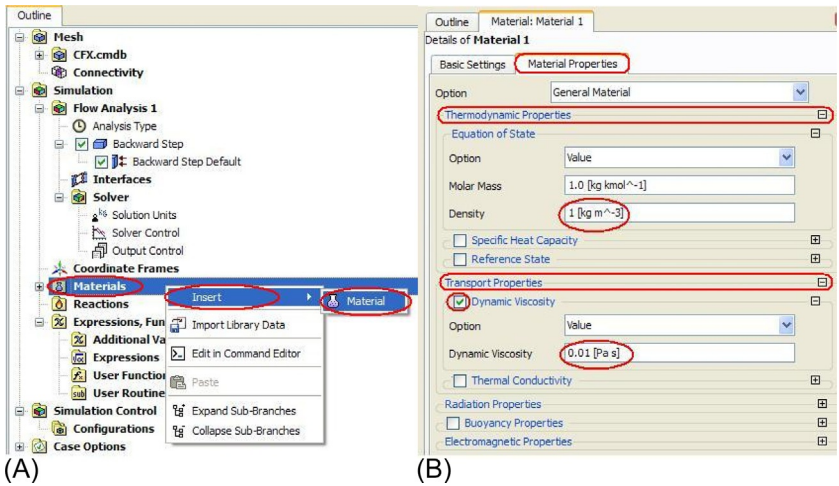
In Workbench Project Schematic window, double-click on the Setup cell to open CFX Pre.

If you wish to change the default domain name to a meaningful name, then

1. RMB on Default Domain under the Outline tree;
2. select Rename, and then, change the name to Backward Step.

Specify a new material

1. RMB on Materials > Insert > Material; in the pop-up window, click OK to accept the default material name: Material 1 (you also can change the name by replacing it to a different name).
2. In Details of Material 1, click on Material Properties tab. Under Equation of State, enter the value for Density.
3. Expand Transport Properties and tick Dynamic Viscosity, and then, enter the value for Dynamic Viscosity.
4. Click on Apply to save the change, and then, OK to exit Details of Material 1.



Specify a new fluid material property: (a) insert Material 1; (b) enter the new material property.

Under ***Flow Analysis 1***, double-click on the fluid domain renamed Backward Step to open the Details of Backward Step in **Flow Analysis 1**, which contains three tabs named Basic Settings, Fluid Models, and Initialisation. Go through each of them as follows:

1. In the ***Basic Settings*** tab, select Material 1 for the fluid material; leave other fields to the default settings.
2. Click on the ***Fluid Models*** tab, select *None* for Heat transfer; select (*None*) Laminar for Turbulence.
3. Click on *Initialisation* tab; tick the Domain Initialisation to view the default settings. Accept all the settings by clicking on **Apply** and then **OK** to exit the panel.

Specify boundary conditions.

In the Outline tree,

1. **RMB** On **backward Step > Insert > Boundary**. In the pop-up window, type inlet and then **OK**.

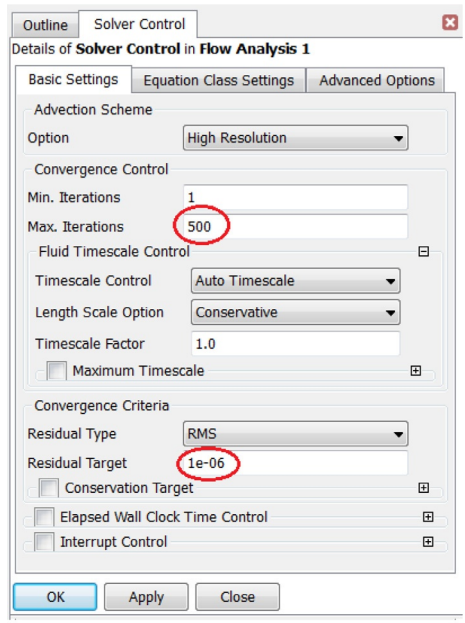
This brings up Details of inlet in ***Backward Step*** in ***Flow Analysis 1***:

(a) Select Inlet for Boundary Type; select inlet for Location.
(b) Click on ***Boundary Details*** tab, enter the value for Normal Speed, and keep other fields with the default settings.
(c) Click **Apply** to finalize the setting and then **OK** to exit the Details tab.

2. **Repeat** the same procedure to define the other boundaries of the fluid domain named ***Backward Step***. Refer to Table 1 for the corresponding settings.

Solver Control

1. Under ***Flow Analysis 1***, double-click on Solver Control to open the tab named Details of Solver ***Control in Flow Analysis 1***.
2. Under the Basic Settings tab, set
   a. Max. Iterations: 500,
   b. Residual Target: 1e − 06 (or 0.000001),
   c. **Apply** to save the change,
   d. **OK** to exit the Details tab.
3. **File > Save Project**.
4. **File > Quit** to exit **CFX—Pre** and return to the Workbench Project window.



Solver Control Tab

Solver Control tab

❑ Stage 4 - Solving for a solution

In **Workbench** Project Schematic, **LMB** double-click on Solution cell to launch the CFX Solver Manager. The **CFX Solver Manager** will start with the simulation ready to run:

1. Click on Start Run button to begin the solution process.
2. The solution process will stop when either the residual target is met or the maximum iteration number is reached, whichever comes first. Steadily decreased Residual curves indicate a convergent solution.
3. If the maximum iteration number is reached but the Residual targets have not been met, we will need to continue the iterations: LMB click on File > Define Run > Start Run, until all the Residual targets are met.

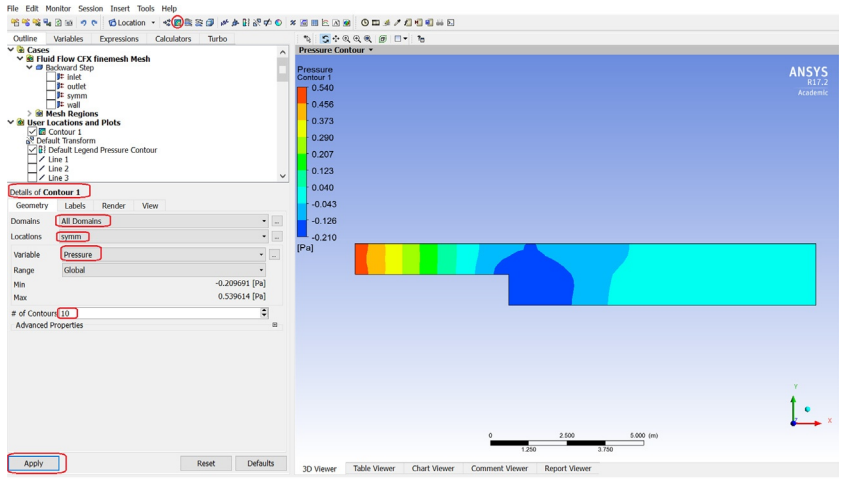
Exit **CFX Solver** Manager to return to **Workbench Project** window.

❑ Stage 5 - Post-processing the result in CFD_Post

LMB double-click the ***Result*** cell to launch the **CFD-Post**.

Create a pressure contour plot on the symmetry plane

- Click on the Contour icon from the top menu bar.
- In the pop-up window, accept the default name ***Contour 1*** by clicking on **OK**.
- In the ***Details of Contour 1***, set the Locations to *symm*.
- Set the Variable to Pressure.
- Increase the number of Contours to 10.
- Click **Apply** to generate the pressure-contour plot.



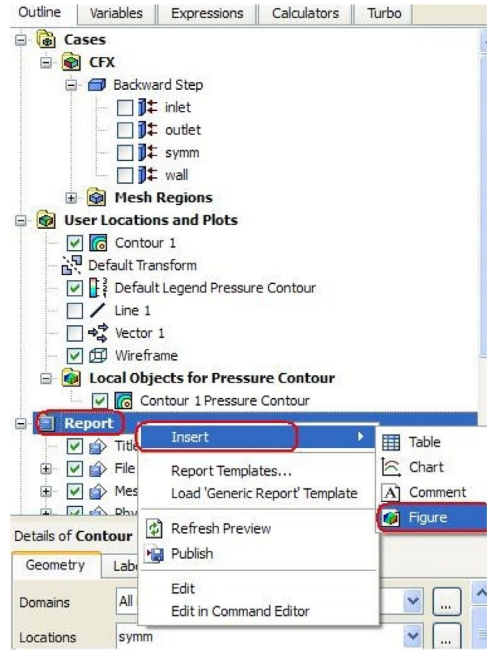
Pressure contour plot

*Study the pressure-contour plot. Has the flow reached to the fully developed stage before the step expansion? In other words, do you see roughly vertical pressure contours equally spaced certain distance before the step?

Insert the pressure contour plot into the Report:

1. Under the ***Outline*** tree, **RMB** on **Report > Insert > Figure**.
2. In the pop-up window, change the name *Fig. 1* to Pressure Contour and then **OK**.

To create another contour plot, for example, velocity contour, simply click on Contour 1 under the ***Outline*** tree, and then, change the Variable to Velocity and then **Apply** to view the plot. Similarly, we can also insert the velocity-contour plot into the Report. With the velocity-vector plot in the graphics window, **RMB** on ***Report > Insert > Figure***; then, give a name and **OK**.

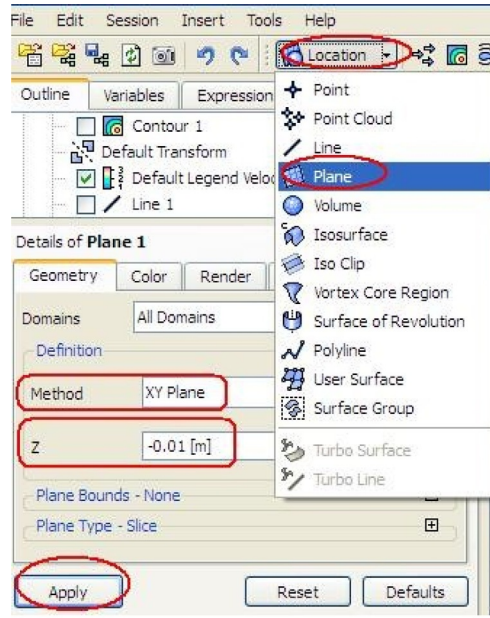


Inserting a graph

Create a plane on symmetry plane

1. In the top menu bar, click on the inverted triangle next to the **Location** icon to expand the list.
2. Select Plane in the list. In the pop-up window, click **OK** to accept the default name Plane 1.
3. *In the Details of Plane 1,*

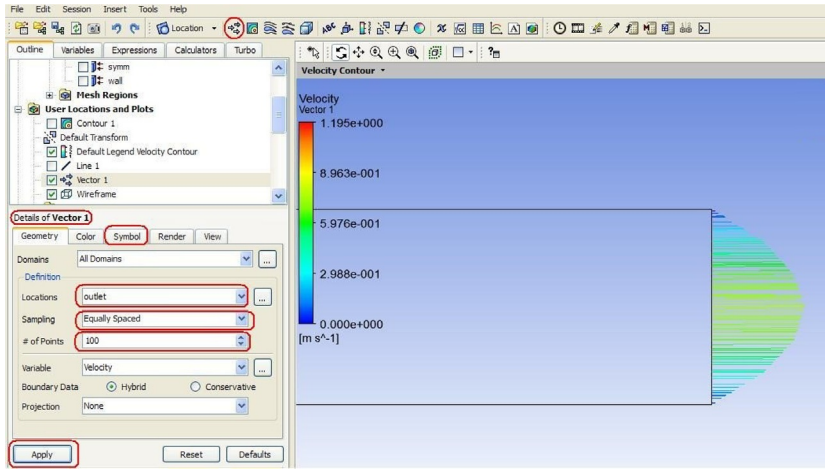
(a) *set XY Plane* for *Method,*
(b) *enter – 0.01 for Z,*
(c) *click on* ***Apply***.



Create a plane

Create a velocity vector plot on the outlet:

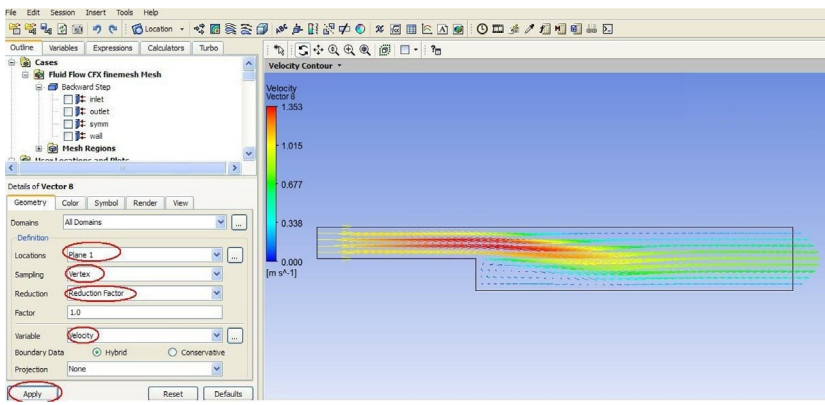
1. Click on the Vector icon from the top menu bar.
2. In the pop-up window, accept the default name Vector 1 by clicking on OK.
3. In Details of Vector 1, set the Locations to outlet.
4. Set the Variable to Velocity.
5. Click on Symbol tab, and then, enter 2 for Symbol Size.
6. Click Apply to generate the velocity-vector plot on the outlet.



Velocity vectors on outlet.

*Has the flow reached to a fully developed stage prior to the outlet?

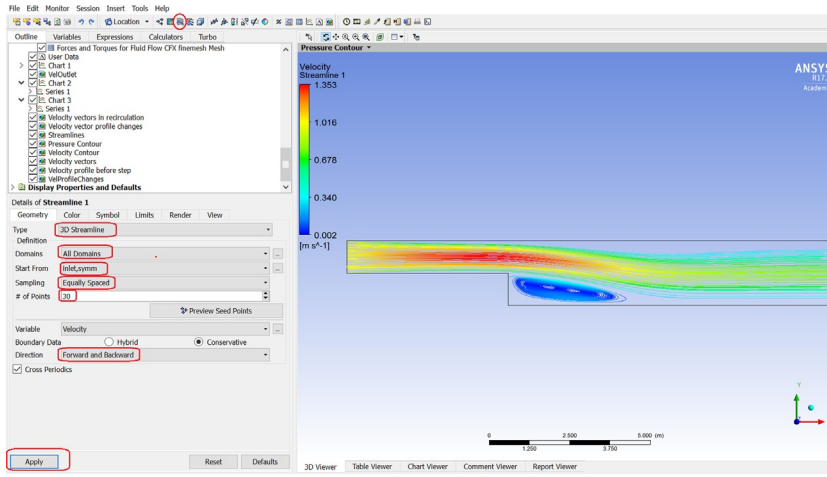
Follow the same procedure to plot the velocity vectors on Plane 1.



Velocity vectors on Plane 1.

Create a streamline plot on the symmetry plane:

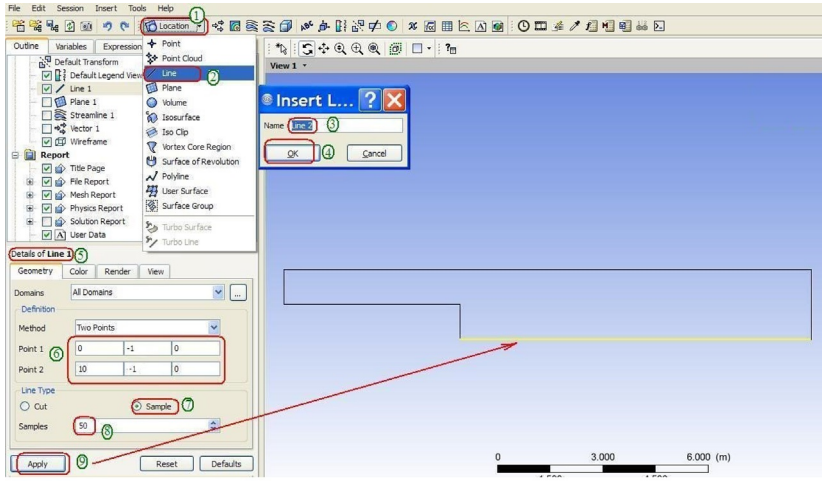
1. Click on the Streamline icon  from the top menu bar.
2. In the pop-up window, accept the default name, Streamline 1, and then **OK**.
3. In Details of Streamline 1, set
   - **a.** Type, 3D streamline;
   - **b.** Start from, *symm* and *inlet*;
   - **c.** Sampling, Equally Spaced;
   - **d.** Number of Points, 30;
   - **e.** Direction, Forward and Backward.
4. Click **Apply** to generate the streamline plot.



Procedure for creating a streamline plot

Create a line that is on the bottom wall from the step to the outlet:

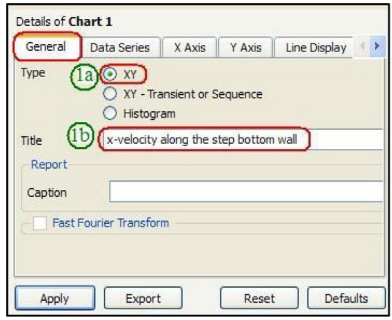
1. Expand the Location icon from the top menu bar, and then, select Line.
2. In the pop-up window, accept the default name, Line 1, and then OK.
3. In **Details of Line 1**, set
   - **a.** Domain, All Domains.
   - **b.** Enter the coordinates of Point 1 and Point 2.
   - **c.** Tick Sample for ***Line Type***.
   - **d.** Enter 30 for Samples.
   - **e.** Click **Apply** to create Line 1 (the yellow line in the Graphics window that almost overlaps with the bottom wall of the step).



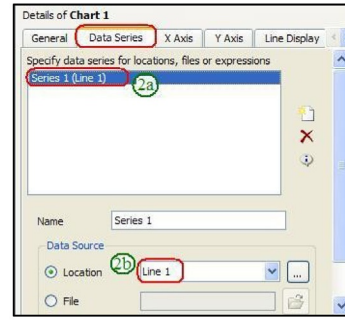
Procedure for creating Line 1 (the yellow line)

Create a chart plotting *x*-velocity along the newly created Line 1:

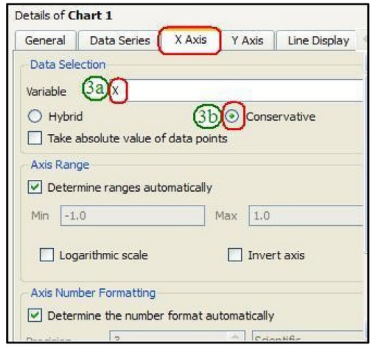
1. Click on the Insert Chart icon from the top menu bar.
2. In the pop-up window, accept the default name, Chart 1, and then **OK**.
3. In **Details of Chart 1**, there are six tabs. We need to set, at least, the first four tabs to produce the chart.
4. Under the General tab,
   (1a) for Type, select XY;
   (1b) for Title, enter the title name of your own choice, e.g. *x* velocity along the step bottom wall.
5. Click on data series tab:
   (2a) Highlight Series 1(line1).
   (2b) Tick Location, and then, select Line 1.
6. Click on X Axis tab:
   (3a) Select X for Variable.
   (3b) Tick Conservative.
7. Click on Y Axis tab:
   (4a) for Variables, select Velocity *u*.
   (4b) Tick Conservative.
   (4c) Click **Apply** to generate the Chart 1.
8. Extract the numerical data of chart 1 by clicking on export and save the data into an excel spreadsheet.



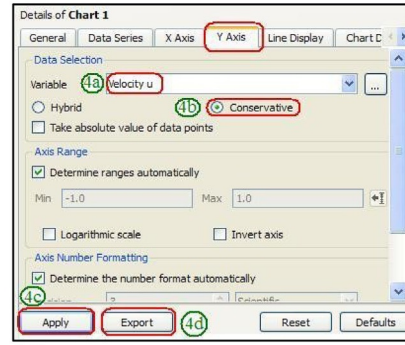
(A)



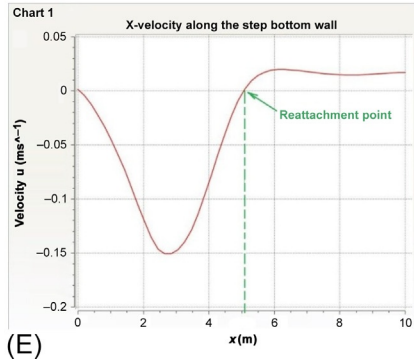
(B)



(C)



(D)



(E)

Procedure for creating the chart of *x* velocity versus Line 1: (A) General tab settings, (B) Data Series tab settings, (C) X Axis tab settings, (D) Y Axis tab settings, and (E) Chart 1 on the Graphics screen showing where the reattachment point is.

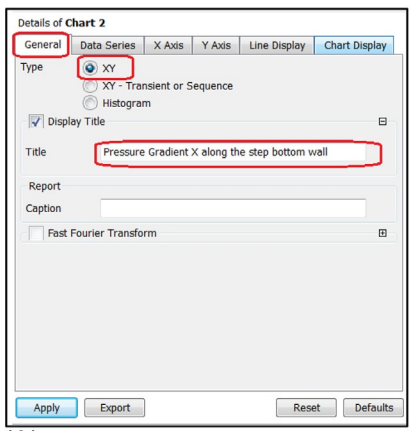
Chart 1 above shows the location of X velocity (velocity component in x direction) where it changes its direction from negative to positive. This indicates the physical phenomenon of flow reattachment, as from this point onwards the flow resumes its direction towards the outlet.

To plot the chart of the Pressure Gradient X vs. Line 1:

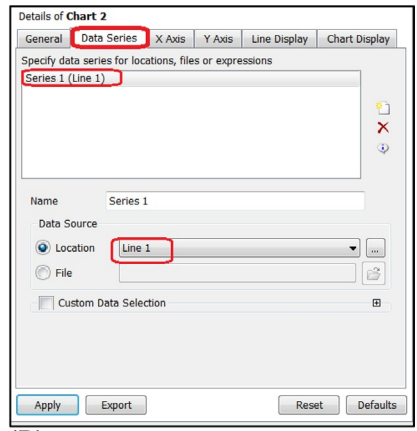
Create a chart plotting Pressure Gradient X component along the newly created Line 1:

1. Click on the Insert Chart icon  from the top menu bar.
2. In the pop-up window, accept the default name, *Chart 2*, and then **OK**.
3. In ***Details of Chart 2***, there are six tabs. We need to set, at least, the first four tabs to produce the chart.
4. Under the General tab, (1) for Type, select XY; (2) for Title, enter the title name of your own choice, e.g. Pressure Gradient_X along the inside wall versus X.
5. Click on Data Series tab: (1) for Name, select Series 1; (2) tick Location, and then, select Line 1.
6. Click on X Axis tab: (1) select X for Variable; (2) tick Conservative; (3) tick Invert axis.
7. Click on Y Axis tab: (1) select Pressure Gradient X for Variables.

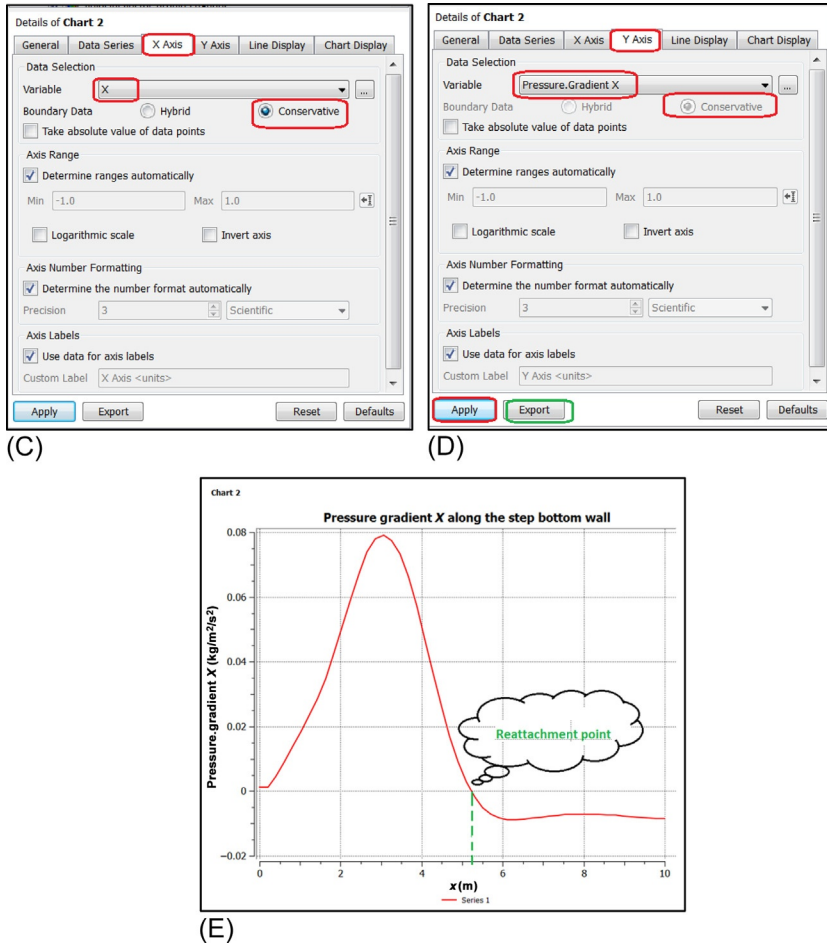
Note: Click on the  icon next to the Variable to expand the variable list, and then, choose the variable from the list; (2) tick Conservative; (3) click **Apply** to generate the Chart 2. Extract the numerical data of Chart 2 by clicking on **Export**, and then, save the data into an Excel Spreadsheet file for further calculation of the reattachment point location. We will be using the data of Pressure Gradient X to obtain the location of the reattachment point.



(A)



(B)



Procedure for creating the chart of Pressure Gradient X versus Line 1: (A) General tab settings, (B) Data Series tab settings, (C) X Axis tab settings, (D) Y Axis tab settings, and (E) Chart on the Graphics screen showing where the reattachment point is.

If you wish to include a figure in the ANSYS CFD generated report, for example, the Pressure on the symmetry plane plot, do the following:

1. Tick the **PressureOnSymm** plot under ***User Locations and Plots*** in the Outline tree.
2. **RMB** on **Report**; ***Insert > Figure***; click on **OK** in the pop-up window.

Repeat the same procedure to include other plots if needed.

Publish the report:

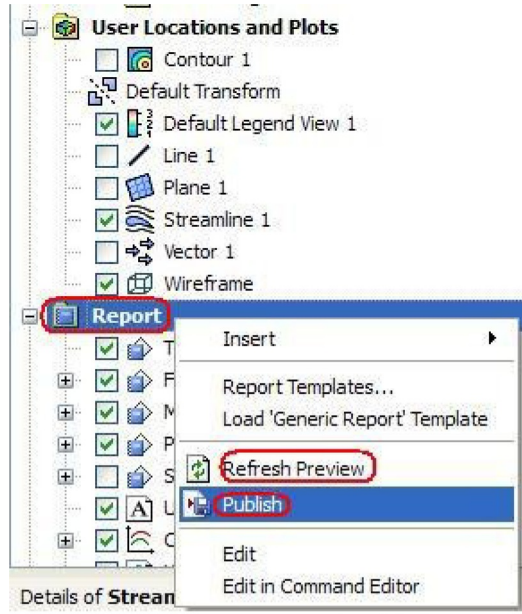
1. **RMB** on **Report**; select **Refresh Preview.**
2. **RMB** on **Report**; select **Publish.**
3. In the pop-up **Publish Report** window, note the location of the report files and then OK.

Exit CFD-Post and return to the Workbench Project page.

Save the project, and then, exit ANSYS Workbench.

File > Save.

File > Exit.



Report preview and publish

e1.3 ADVANCED CASE STUDIES

e1.3.1 Airflow Field and Contaminants Transport in an Airliner Cabin Section

Yihuan Yan
RMIT University

e1.3.1.1 Case Introduction

Whilst air travel brings convenience and efficiency, it is allowing the global spread of infectious diseases. Airline cabins are highly susceptible to the spread of communicable diseases and therefore are a great concern in the transmission of infectious diseases in medium-size airliner cabin. Fig. e1.18 shows that contaminants in the cabin environment can be generated or brought in from a wide variety of sources. When passengers are seated, disease transmission in airline cabins is predominantly controlled by the transport of airborne particles and droplets. Since the movement of airborne particles is largely controlled by the airflow field, deep understanding of the ventilation system and the main impacting factors of the airflow field inside the cabin is strongly required to minimize the exposure risks associated with the airborne particles and droplets.



FIG. e1.18 Typical cabin environment and contaminant sources.

e1.3.1.2 Problem Description

The mixing ventilation scheme has been widely employed in modern airliner cabins, which supplies air from diffusers located near the cabin ceiling or baggage compartments and exhausts waste air through outlets near the floor level. Such ventilation design was expected to suppress contaminants in a level lower than the passengers' breathing zone. However, airflow circulations still exist in some local regions, which inevitably increases the exposure risk. Also, the transport and distribution characteristics of particulate contaminants in an airline cabin could be affected by many factors including the ventilation scheme, the blockage by seats and passengers, the movement of passengers and crews, and the manikin thermal plume. Among them, the thermal buoyancy flow driven by the passenger body heat, known as the human thermal plume, could be one of the most important factors. Therefore, this case study uses Computational Fluid Dynamics (CFD) as the tool to obtain deep understanding of the airflow field inside the cabin environment and the effect of passengers' thermal plume.

It is undoubted that conducting CFD simulations under a full-scale cabin model would provide the most realistic geometries to the real conditions. However, this requires significantly high computational resources (mesh elements, computational time, etc.). It would be very challenging and time-consuming to directly conduct simulations under a full-scale cabin environment and the post-processing process. Thus, it is also necessary to reduce the computational domain using proper settings of the boundary conditions.

e1.3.1.3 Simulation

❑ Mesh settings

The CFD simulation was conducted based on the economy cabin of a Boeing 737 airliner model. The airliner cabin domain was discretized using the tetrahedral mesh in ANSYS ICEM, as illustrated in Fig. e1.19. For the purpose of achieving accurate captures of the body features and airflow field in the vicinity of the manikins, very fine meshes were built around the manikin skin. Also, 15 inflation layers were also applied in the vicinity of the manikin surface with initial layer thickness of 0.5 mm to capture the detailed gradient change of

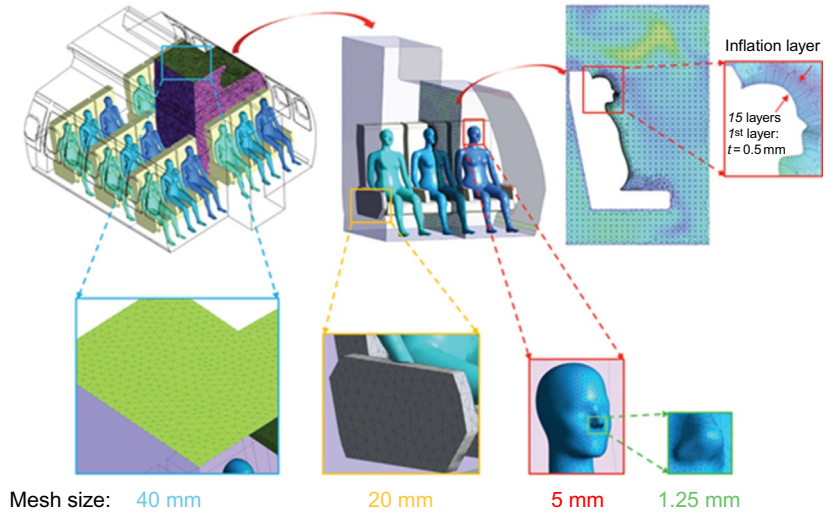


FIG. e1.19 Mesh settings using various size factors.

velocity, temperature, etc. On the other hand, relative coarse meshes were applied at less significant and regular surfaces such as the cabin walls and seats. Detailed mesh settings at some cabin and manikin surfaces (e.g. manikin head and nostril regions) are demonstrated as examples in Fig. e1.19. It is also important to conduct mesh-sensitivity study using different configurations of mesh settings and to test the quality or skewness of the mesh elements. The mesh independency was achieved at 1.5 million mesh elements in this case study.

❑ Boundary conditions

In the cabin environment, since the seat arrangements are the same on each side of the cabin, the airflow pattern is approximately symmetric across the central plane of the aisle (from left to right). Therefore, simulations can be conducted on one side of the cabin section by setting the middle plane in the aisle as the symmetrical boundary condition. This assumes that airflow information and contaminant fields are mirrored along the symmetry plane. The computational domain can be further simplified if the ventilation layout is uniform and the difference of transitional airflow pattern along the aisle (from front to back) is excluded. Based on these assumptions, translational periodicity boundaries were set up at the front and back surfaces of the cabin section. By applying periodic boundary conditions, the exact same air and particle information was specified at the front and back planes, which means that when a particle leaves the domain from one periodic boundary, the same particle enters the domain with the same velocity from the other periodic boundary. Therefore, by setting the proper boundary conditions, a half-row cabin section containing three seats and three passengers was built as the computational domain to represent the cabin environment, shown in Fig. e1.20. The detailed settings of the symmetry and periodic boundary conditions are given in Fig. e1.20.

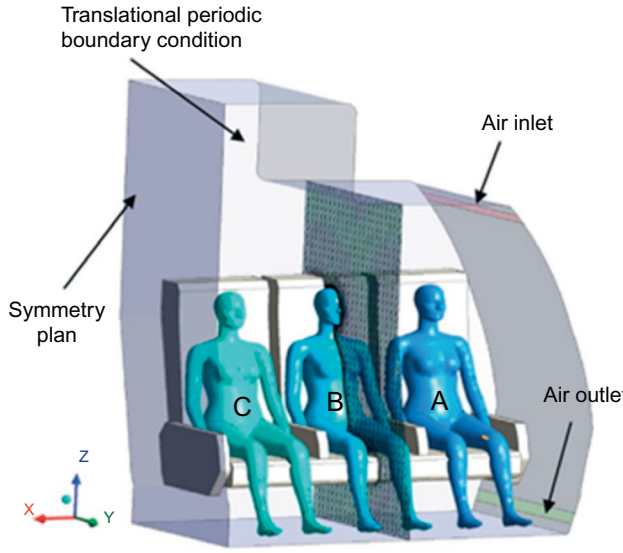
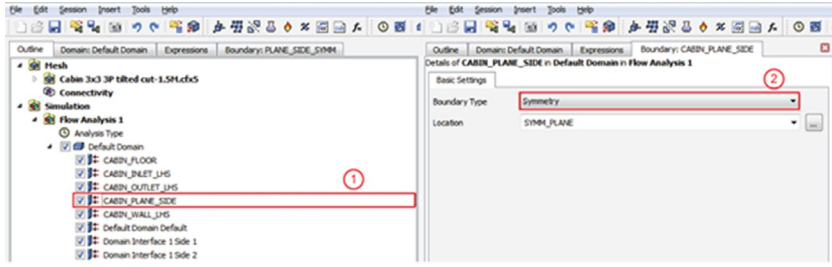
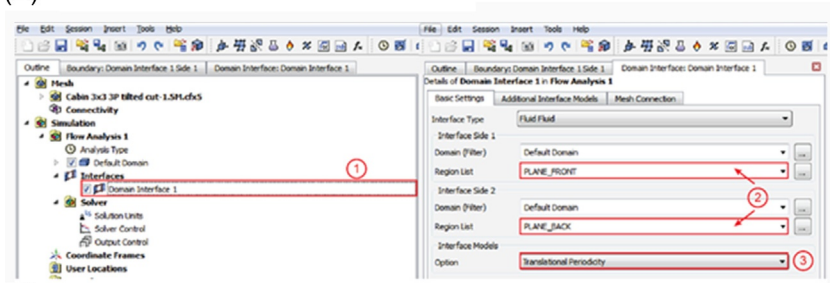


FIG. e1.20 The boundary conditions applied at the cabin to reduce computational cost.

The inlet and outlet ventilation were located at the upper and lower sides of the cabin wall, close to the baggage compartments and the floor, respectively (Fig. e1.21B). The ventilation rate was set as 0.04 kg/s at the inlet for



(A)



(B)

FIG. e1.21 Boundary-condition settings in CFX, (A) symmetry and (B) periodicity.

the three-passenger cabin section with the inlet air temperature of 25°C. To capture the realistic airflow field in the vicinity of the passengers, a 3-D-scanned female manikin model containing very detailed body features was employed as passenger model. For heat-transfer modelling, a fixed skin temperature of 31°C was applied at the manikin surface. The other solid walls, including the cabin wall, the ceiling, the floor, and the seats, were assumed to be adiabatic. Detailed boundary conditions were listed in Table e1.7.

TABLE e1.7 Boundary-Condition Settings

Name	Type	Value
Air inlet	Mass flow rate (kg/s)	0.04
	Temperature (°C)	25
Air outlet	Opening	–
Manikin	Surface temperature (°C)	31
	Heat load (W)	40
Floor	Adiabatic	–
Seats	Adiabatic	–
Side plane	Symmetry	–
Front plane	Translational periodicity	–
Back plane	Translational periodicity	–
Particles	Diameter (μm)	3.5

❑ Particle transport

Computations were conducted with particles released by each of the three passengers, respectively. The particles were tracked by using the Lagrangian approach, which continuously tracks particle movement through the domain and is possible to model transient particle transport using a steady-state simulation. Particulate contaminants were assumed to be exhaled by the passengers through coughing. Since the cabin space has a very low humidity (RH below 20%), the droplets were expected to become droplet nuclei in a very short time. Therefore, the evaporation of sputum droplets was ignored, and the droplet nuclei were treated as particles with constant diameter of 3.5 μm. Detailed particle phase settings in relation to particle size, release locations, etc. are shown below in Fig. e1.22.

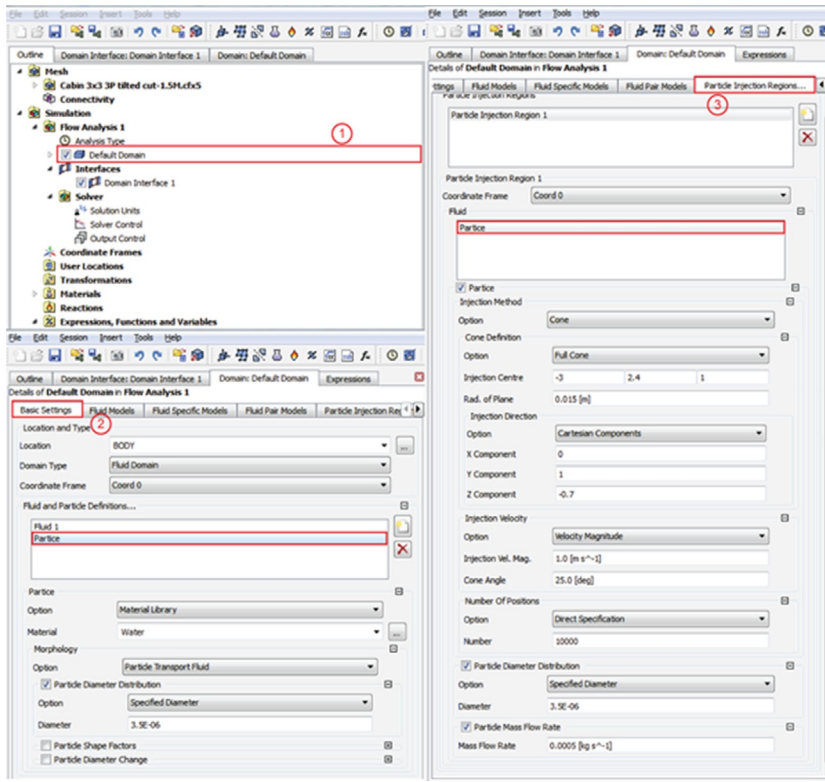


FIG. e1.22 Particle settings in CFX.

e1.3.1.4 CFD Results and Discussion

The governing equations were solved using the ANSYS-CFX. Due to its successful application in modelling indoor air, the RNG k-ε model was employed in this study for the air turbulence with a high-resolution advection scheme. Sensitivity tests were also performed for the number of representative particle trajectories tracked by the Lagrangian approach. It was found that the numerical results became stable when the number of particle trajectories increased up to 20,000. Convergence was achieved when the RMS residual of the continuity equation decreased to be lower than 1×10^{-6}. For the purpose of comparison, computations were also conducted with the isothermal condition where heat transfer was excluded from the model.

❑ Airflow analysis

Airflow fields yielded from both the isothermal and thermal conditions are presented and compared in Fig. e1.23, where Plane 1, 2, and 3 are the planes

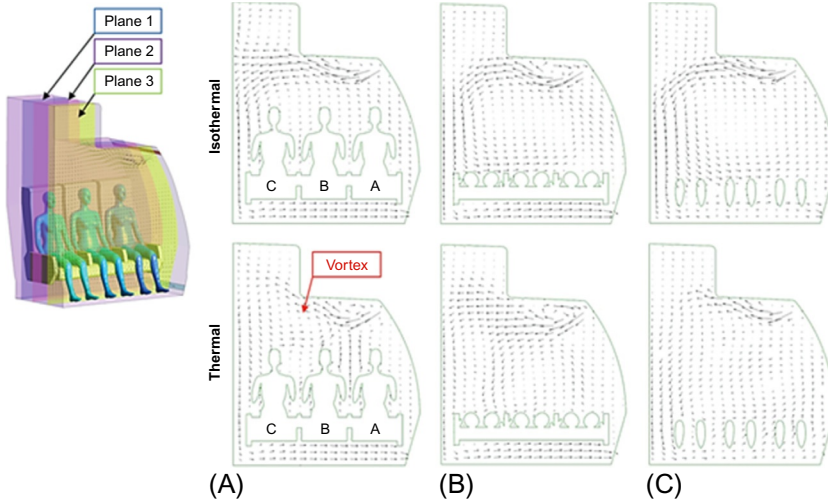


FIG. e1.23 Velocity-vector field across Y plane for isothermal and thermal case. (A) Plane 1. (B) Plane 2. (C) Plane 3.

crossing the manikin bodies, 20 mm in front of the manikin nose tips, and crossing the manikin legs, respectively. Fig. e1.23 revealed that the overall airflow in the cabin was mainly driven by the ventilation jet, whilst the thermal effect would completely change the overall airflow pattern. When heat transfer was excluded from the model, all three selected planes showed very similar airflow patterns of a large counterclockwise vortex observed in the central bulk region of each plane, whilst a small clockwise vortex appeared in the upper part of the aisle region close to the cabin roof and baggage compartments (Fig. e1.23A–C). The airflow pattern was dominated by the inlet air jet and the geometry of manikins and seats. However, with the inclusion of heat transfer into the model, the buoyancy-driven thermal plume dramatically changed the airflow pattern. At first, the size of the large vortex in the bulk region was suppressed, and the small vortex close to the cabin roof was nearly eliminated in all three selected planes. Secondly, significant rising buoyancy flows were observed above the passenger shoulders; this is especially true for the region between passenger A and B (Fig. e1.23D). However, strong prising buoyancy flow was only observed in Plane 1, which indicated that the impact of thermal effect became less significant with increased distance from the manikin torso as the heat is quickly dispersed after leaving the manikin bodies.

The local airflow field in the passengers' breathing zones is illustrated in Fig. e1.24. When heat transfer was excluded from the models, the breathing zone was completely controlled by the ventilation jet and cabin and manikin geometry. As shown in Fig. e1.24A–C, a rising airflow can be noticed in front

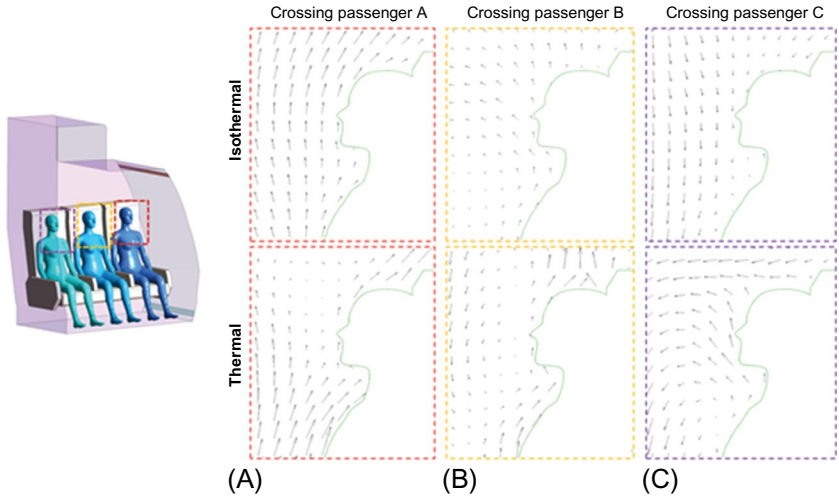


FIG. e1.24 Velocity-vector field across X plane for isothermal and thermal cases. (A) Velocity vector at BZ1 ($X = 2.0$ m). (B) Velocity vector at BZ2 ($X = 2.5$ m). (C) Velocity vector at BZ3 ($X = 3.0$ m)

of Passenger A, who was seated close to the windows. A descending airflow was observed in the breathing zone of Passenger C who was next to the aisle, whilst Passenger B was located in the middle of vortex (see Fig. e1.23B). However, when heat transfer was included in the models (Fig. e1.24D–F), significant uprising airflow appeared in the vicinity of the manikin surface. For Passengers A and B, stronger uprising airflows were observed in their breathing zones, whilst for Passenger C, the descending airflow in the breathing zone (Fig. e1.24C) was completely replaced by the uprising buoyancy flow (Fig. e1.24F).

The numerical results revealed that the airflow field in the vicinity of a manikin was highly sensitive to the position. For the purpose of quantitative analysis and comparison, the velocity profiles along the three selected vertical lines were also plotted and compared, as illustrated in Fig. e1.25. The positions of the vertical lines relative to a certain manikin were kept constant, where Line 1 (marked as Position 1 in Fig. e1.25) was located above the manikin head, Line 2 (marked as Position 2 in Fig. e1.25) was immediately in front of the manikin face, and Line 3 (marked as Position 3 in Fig. e1.25) penetrated through the middle point between the manikin knees. Fig. e1.25 revealed that the airflow field in the upper part of the cabin was significantly affected by the inlet jet. At Position 1, the velocity magnitude above Passenger A was the highest, whilst that above Passenger C was the lowest as Passenger A was seated close to the ventilation jet whilst Passenger C was farthest from the jet. The ventilation jet dispersed soon after entering the cabin. At Position

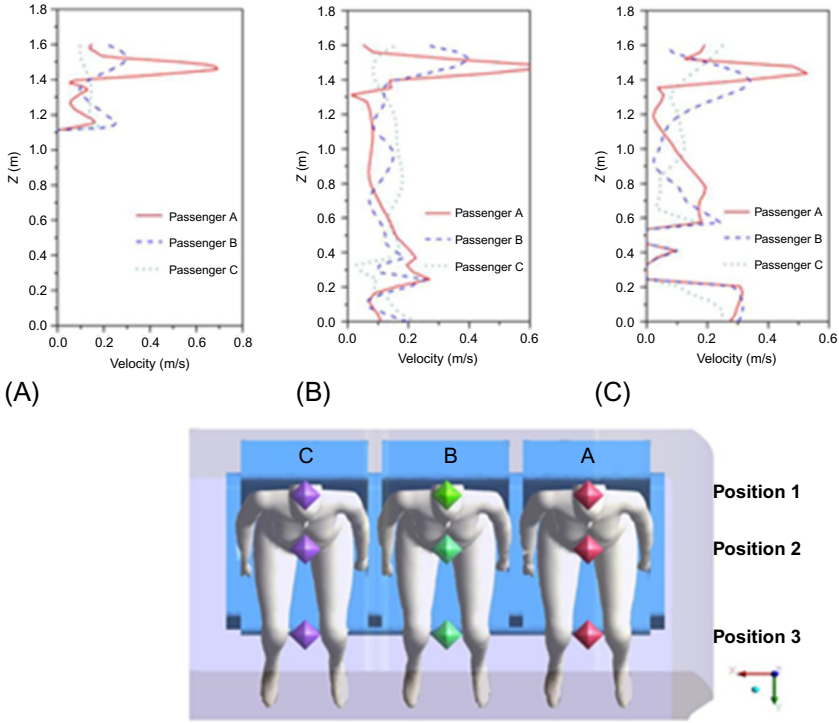


FIG. e1.25 Comparison of air velocities at selected positions. (A) Position 1. (B) Position 2. (C) Position 3.

2, the air velocity profiles in the upper part were still affected by the ventilation jet, whilst this effect was not significant in the low height. The air velocities were fluctuating in the vicinity of manikin torsos and started increasing above manikin bodies due to the buoyancy-driven thermal plume. Despite the fluctuation, the airflow velocity near the torsos was quite uniform for different passengers.

❑ Particle transport

The transport and distribution characteristics of particles generated by the coughs from the passengers were studied under both isothermal and thermal conditions. Separate computations were conducted to simulate the tracks of the particles exhaled by each of the three manikins, as illustrated in Fig. e1.26.

It is clear that the passenger body heat not only had a significant effect on the airflow field but also dramatically altered the trajectories of particle transport. Fig. e1.26 also demonstrated that the particle trajectories were jointly controlled by the ventilating airflow and the buoyancy-driven thermal plume. The particles

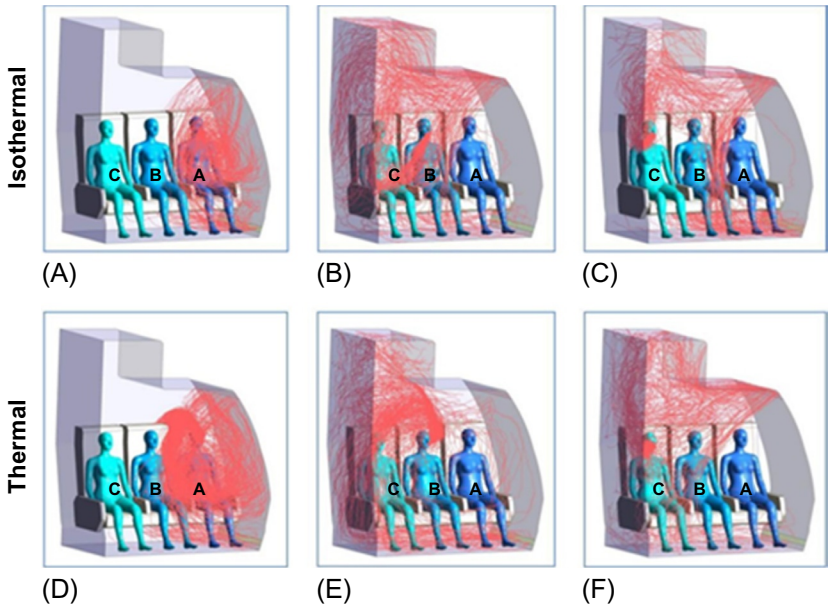


FIG. e1.26 Droplet trajectories for isothermal and thermal cases. (A) Passenger A. (B) Passenger B. (C) Passenger C. (D) Passenger A. (E) Passenger B. (F) Passenger C.

would be elevated to a higher level, descend towards the floor, or even be locked up in the breathing zone, depending on the intensity of the thermal plume.

For Passenger A (Fig. e1.26A and D) who was seated close to the windows, the exhaled particles were travelling with very limited distance rather than travelling widely through the entire cabin section. Gradually, the particles formed a lock-up circle in front of this passenger, especially at the breathing zone, in both isothermal and thermal cases. However, when heat transfer was included in the model, the particle lock-up was more intense, and the lock-up area was wider due to the balance of the uprising thermal plume against the descending ventilation airflow. Fig. e1.26B and E illustrated the trajectories of particles exhaled by passenger B who was sitting in the middle of the seats. It was noticed that when heat transfer was excluded, the model predicted that the particles exhaled by Passenger B were mainly concentrated in the bulk air above the passengers (Fig. e1.26B); thus, Passenger A was located in a region without particles. However, when heat transfer was included in the model, the particles were predicted to be distributed in a wider range (Fig. e1.26E). The transport trajectories of particles exhaled by Passenger C were illustrated in Fig. e1.26C and F. As Passenger C was located in the region affected by the inlet jet, the thermal effects of body heat were not so significantly detectable. After leaving the release point (Passenger C), the particles quickly dispersed and joined the overall flow vortex and travelled widely in the cabin.

In order to further investigate the transient characteristics of particle transport in the cabin environment under the thermal condition, the transient particle distributions at $t = 5$, 30, and 120 s were analysed, as illustrated in Fig. e1.27. It demonstrated that dispersion speed and range of particles through the air were

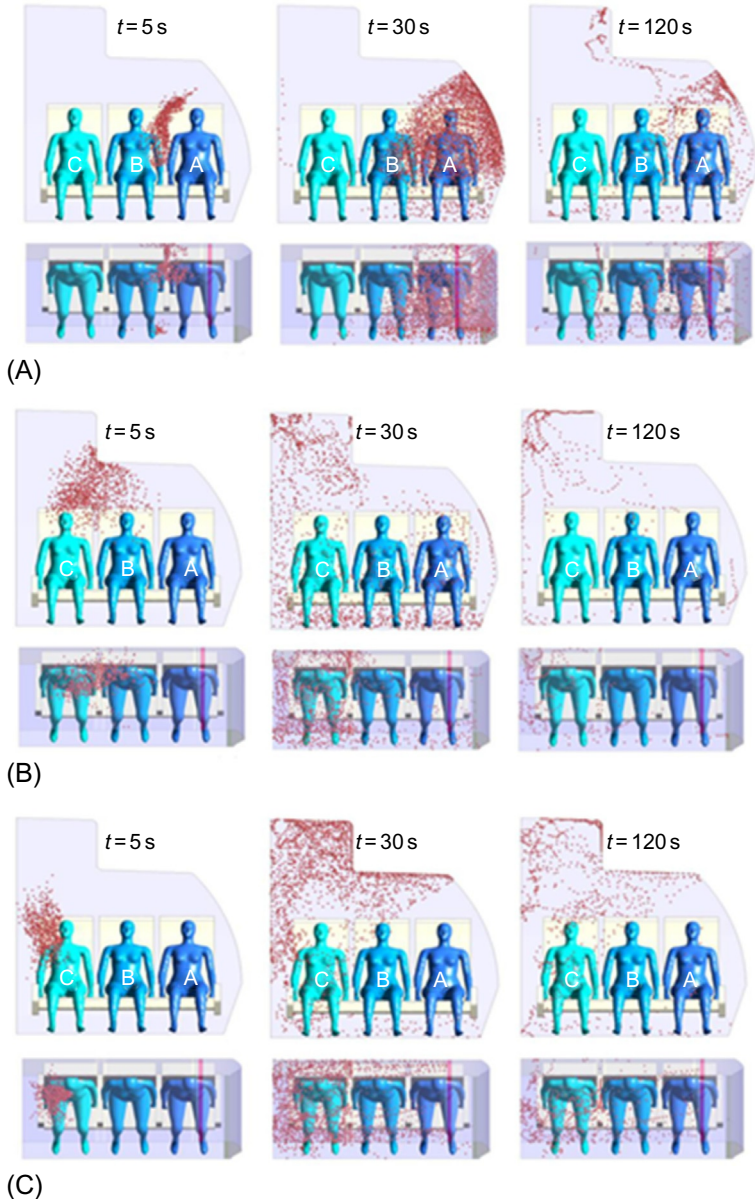


FIG. e1.27 Droplet transport and distribution at various time steps. (A) Cough by Passenger A. (B) Cough by Passenger B. (C) Cough by Passenger C.

highly sensitive to their release locations. When the particles were released by Passenger A (Fig. e1.27A), they move upwards slowly with the airflow and then suddenly changed their direction downwards when they reached the inlet jet (t = 5 s). Then, the particles were carried on by the airflow. At $t = 30$ s, the particles were fully dispersed in front of Passenger A. The vortex flow as illustrated in Fig. e1.26F then locked the particles for quite a long time. Until $t = 120$ s, there were still a number of particles presented in front of Passenger A. Comparatively, the dispersion speed of the particles released by Passenger B is much higher. At t = 5 s, the particles had been transported in the bulk region, whilst at t = 30 s, the particles were fully dispersed in the whole cabin section. At t = 120 s, there were just a few particles that remained in the breathing zone. When the particles were released by Passenger C who was affected by the ventilation jet, the exhaled particles mainly affect Passenger B and C, whilst Passenger A was not significantly affected.

Review Questions:

- What boundary conditions can be used to save the computational cost under complicated cases?
- What are the other possible approaches to save the computational resources when conducting simulations in cabin environment?
- What are some of the difficulties that arise regarding conducting simulations under densely occupied indoor spaces?
- Why large vortex of airflow field was formed in the airliner cabin?
- What are the other indoor spaces that human's body heat may have significant impact on?
- What are the possible solutions to avoid contaminants being locked in passengers' breathing zones?

Exploratory Questions:

➢ If the mass flow rate of the ventilation is doubled or halved, what will the large vortex look like?
➢ Test different sets of mesh (coarser mesh, finer mesh, etc.) and compare the results.
➢ If the mesh is overcoarsened, will the large vortex still be able to notice?
➢ Conduct simulations with different turbulence models (k-ε, SST, etc.) and compare the airflow field.

e1.3.2 Effects of Diffuser Types on Ventilation in a High-Speed Rail Cabin

Lin Yang
RMIT University

e1.3.2.1 Case Introduction

In recent years, high-speed trains (HSTs) are rapidly developed in many countries owing to their convenience and high efficiency. However, due to the fact

that HST indoor space is enclosed and occupant density in HST cabin is extremely high, the airborne disease transmission in HST cabin becomes a critical issue. In order to minimize the possibility of disease transmission whilst maintaining the ride comfort, optimizing the ventilation schemes is the most effective way raised by [16]. Research on ventilation schemes, especially diffusers, has been widely conducted both by simulation and experimentally.

Based on current studies, the diffuser is one of the crucial components in cabin ventilation system, and well-designed ventilation diffusers can effectively control the contaminant transport. Therefore, this study is aimed at investigating the effects of different types of diffusers on contaminant transport in HST cabins. Computational fluid dynamics (CFD) models for HST cabins were firstly developed in ANSYS-CFX. Four types of prevailing HST cabin diffusers were subsequently assessed in a typical HST cabin model. Also, different sizes of contaminants were investigated.

e1.3.2.2 CFD Simulation

❑ Cabin geometry and meshing setup

According to previous research, airflow pattern in HST cabin is affected by several factors including ventilation parameter,cabin geometry, seat arrangement, types of diffusers, location of exhaust vents, and seating arrangement of passengers. To maintain the comparability of types of diffusers, the other factors were assumed to be constant. A four-row CRH2 model cabin section with 2–3 seat arrangements was set up as the ventilation environment, shown in Fig. e1.28.

Based on the four-row CRH2 model cabin, four common types of diffusers were used. Details of these diffusers are explained in Fig. e1.29.

The cabin geometry model was discretized using unstructured mesh by ANSYS ICEM. To capture accurate cough flow pattern, meshes with high

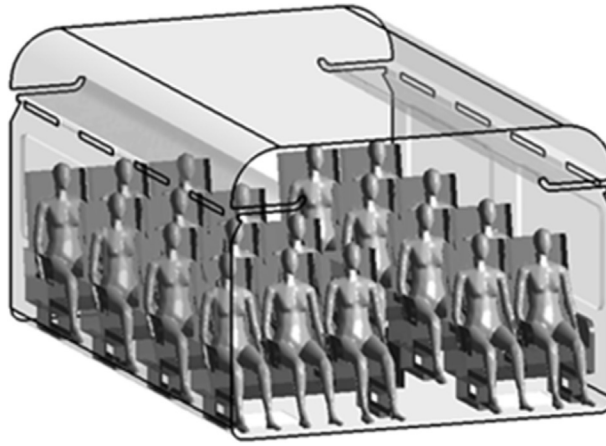


FIG. e1.28 CRH2 model simulation cabin.

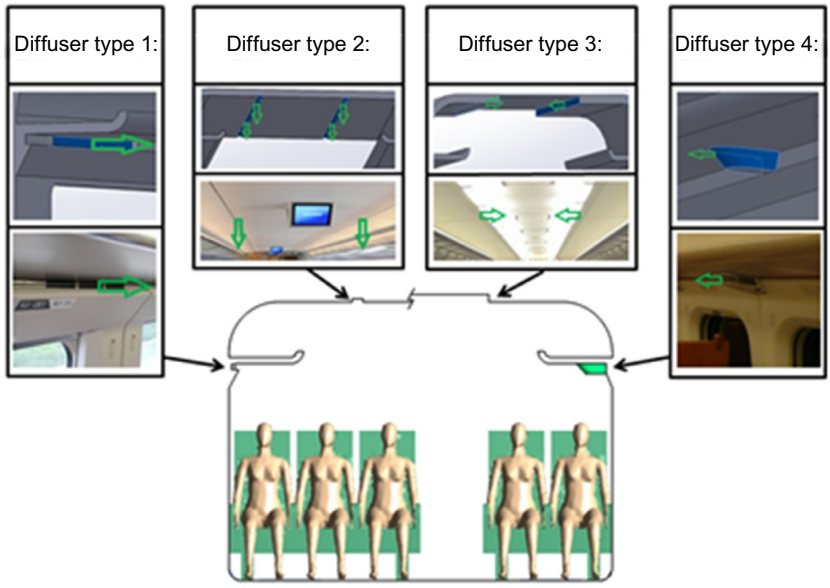


FIG. e1.29 Details of the four types of diffusers in this study.

resolution were built around diffusers and manikins, especially in the vicinity of the mouth area. Inflation layers with a grid expansion ratio were applied around the manikin surface. Prior to performing CFD simulations, grid-independency study was conducted over five grid resolutions ranging from coarse to dense. The grid-sensitivity study showed that over 4.2 million mesh elements, airflow velocity at the reference location became stable.

❑ Boundary conditions

In order to minimize disease transmission and improve ride comfort, most modern HST cabins are ventilated using an up-to-down air-conditioning scheme, as shown in Fig. e1.30. This type of ventilation design sets inlets near the cabin ceiling and outlets near the floor, creating a descending overall airflow pattern that helps retain contaminants below passengers' breathing zone. However, due to the metabolic heat released by passengers, a strong upward buoyancy flow is also created in cabins, which competes against the ventilating airflow and reduces the effectiveness of contaminant removal. Details of boundary-condition setup in ANSYS-CFX are shown in Table e1.8, and the CFX setup for simulation is shown in Fig. e1.31. In this cabin section, two translational periodicity boundaries were applied in the front and back plane. By applying periodic boundaries, the computational domain was largely trimmed down that would correspondingly increase the computational cost efficiently whilst maintaining the ventilation and contaminant transport features.

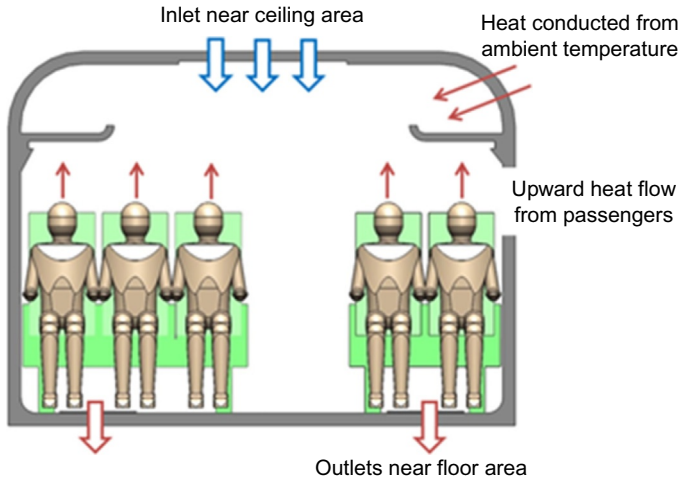


FIG. e1.30 Ventilation scheme inside the cabin.

TABLE e1.8 Boundary Conditions

Name	Boundary Type	Boundary Details	Value
Air inlet	Inlet	Mass flow rate (kg/s)	2.14
		Temperature (°C)	24
Air outlet	Opening	Relative pressure (Pa)	0
		Temperature (°C)	24
Manikin	Wall	Heat flux (W/m^2)	27.65
Floor, roof, cabin wall and windows	Wall	Outside temperature (°C)	37
		Heat-transfer coefficient	2.22
Seats	Wall	Adiabatic	–
Front and back cabin wall	Wall	Adiabatic	–

❑ Contaminants Simulation

In the simulations, the cabin was assumed to be fully occupied with very fine 3-D-scanned adult female manikin models. The mouth area of the manikin needed to be well-identified because this would serve as the cough droplet exhaust boundary in simulation. In this study, droplets were assumed to be released from the mouth of one passenger, Passenger S, who was on the seat at second row of second column. According to previous study, 2000 droplets

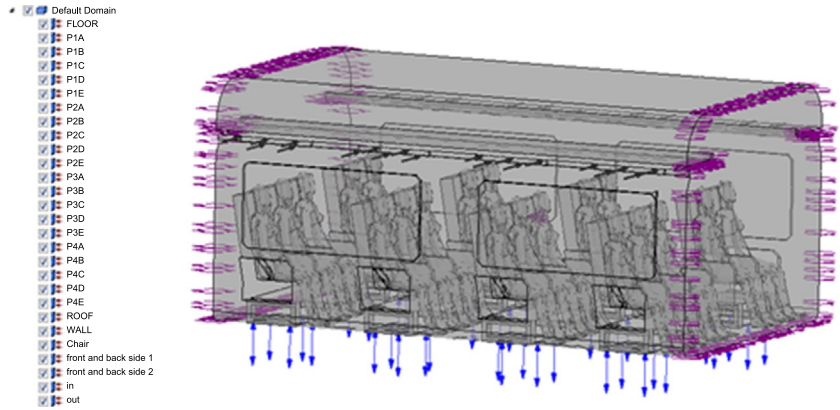


FIG. e1.31 CFX setup for simulation.

with velocity of 3 m/s have been proved to be valid in representing a single human cough. The distribution of droplet size of a single cough used in this study is plotted in Fig. e1.32. Considering the computational cost, the simulation was taken in the steady state in which the breath from all the passengers and the cough-induced airflow from Passenger S have not been modelled.

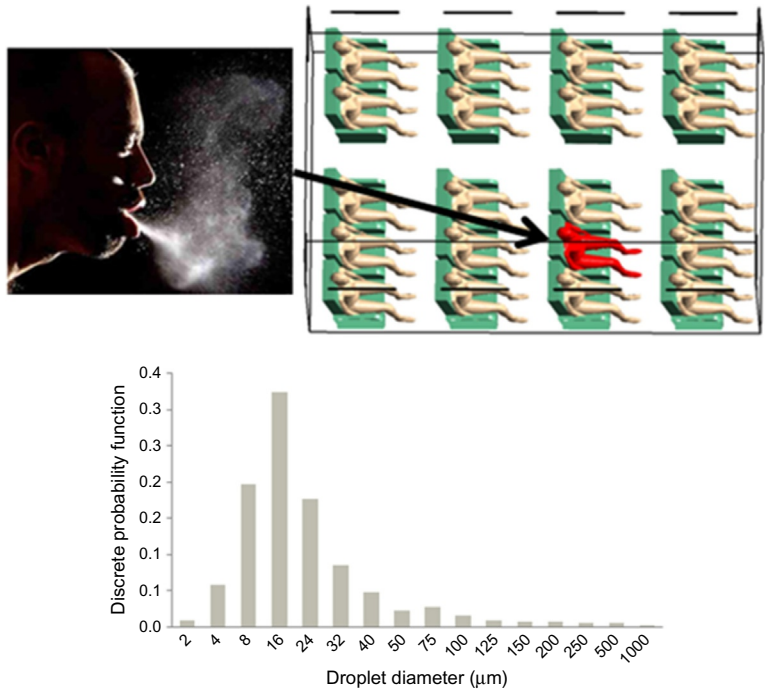


FIG. e1.32 Cough person and droplet-size distributions.

e1.3.2.3 CFD Results and Discussion

❑ Ventilation performance based on different diffuser

The planes crossing through the middle of the second-row passengers in the crosswise direction were compared to summarize the results of the ventilation performance, as shown in Fig. e1.33. The whole cabin section in Case 1 has a very good homogenous temperature field and velocity field, although the upper region has a relatively high-velocity field. Passengers in all five columns experience similar temperature and low-speed stream, which is ideal for thermal comfort. In Case 2, the velocity in the middle-upper region is relatively high because of the fresh air coming downwards from the inlet vents fitted on the cabin roof. However, due to passengers' heat-flux effect, cool flow is reduced quickly so that the airflow velocity around those passengers is small. In Case 3, a strong flow of stream exists in the middle aisle, which comes from the joint fresh air in the roof area to the aisle floor area. This strong downward airflow has an undesirable effect on the passengers in the third column as they may suffer from lower temperature and higher velocity flow compared with surrounding passengers. Different from other three cases, the lowest temperature found in Case 4 occurred around the passengers sitting near the cabin walls because fresh air blows down from the diffusers located right above them. Consequently, relatively high temperature appears around the passengers sitting near aisle. Case 4 has the overall smallest velocity field in this study, especially in the middle cabin region. Aside from the above analysis, Fig. e1.33 demonstrates that the temperature fields are mainly dependent on the velocity field.

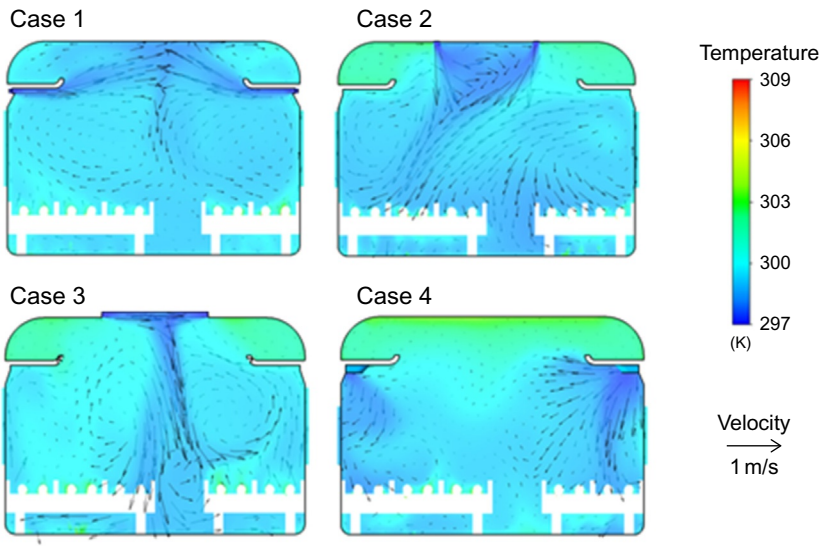


FIG. e1.33 Temperature and velocity profiles at a selected plane.

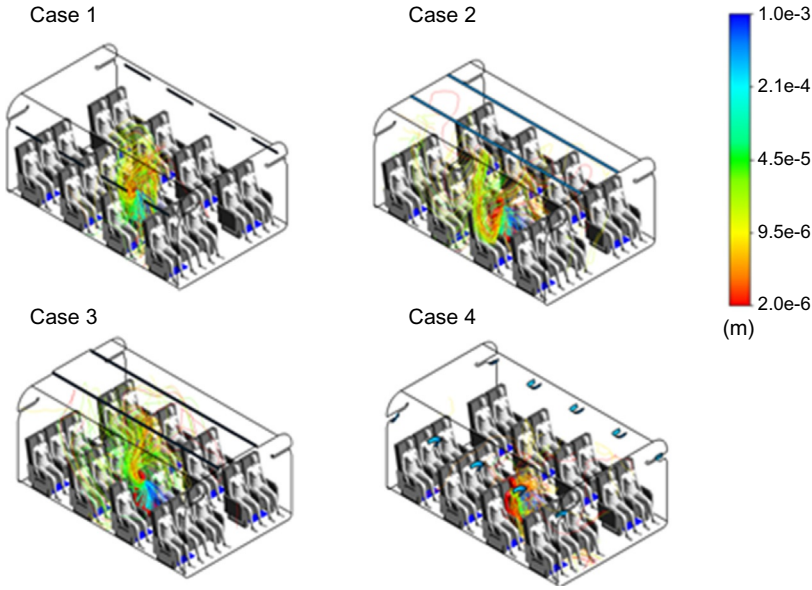


FIG. e1.34 Size-dependent droplet transport released by Passenger S.

❑ Contaminates distribution based on different diffuser

The transport and distribution characteristics of particles generated by coughs from Passenger S were studied under the conditions of different diffusers. Individual computations as shown in Fig. e1.34 were conducted to simulate the tracks of particles. The trajectories of different particle sizes were also marked in this figure using different colours.

When comparing the distribution of particles with diameter larger than 5×10^{-5} m, it can be seen that trajectories of these particles are similar in all four cases. Particles sized between 5×10^{-5} and 2×10^{-4} m fell into the leg and seat area of Passenger S following parabola trajectories, immediately after leaving the mouth. The particles with size larger than 2×10^{-4} m have similar distribution trajectories as particles with size between 5×10^{-5} and 2×10^{-4} m. However, these particles fell further to the shoe area or sunk into the back of the front seat. Therefore, a conclusion can be made that the types of diffusers have small effect on the trajectory of particle transport if the diameter of particle is larger than 5×10^{-5} m.

However, for particles with diameter smaller than 5×10^{-5} m, the types of diffusers would significantly affect the trajectories of particles. In Case 1, these particles moved towards the right side along with the airflow after being released by Passenger S and then suddenly changed their direction backwards when they reached the large flow. These small particles would eventually spread over the whole cabin. During this process, many droplets would stick

on the cabin wall beside Passenger S and the roof area above Passenger S. Case 2 model predicted that particles with size smaller than 5×10^{-5} m would mainly join the bulk air above the source passenger; thus, passengers around that area are considered to be at a relatively clean region. Then, most of these droplets would travel through the area around the passenger in the third row of third column to the outlet vent beneath the seat. Similar to Case 2, these particles quickly concentrated into the bulk airflow to the back area of Passenger S after leaving the release point. Then, they would distribute into the back cabin section and ended by sinking into the cabin wall. In Case 4, these particles travelled only limited distance rather than spreading widely through the entire cabin section. The droplets largely ended around passengers sitting near Passenger S, and the rest was taken away by the outlet vent under Passenger S.

The main reason small and large droplets travelled through significantly different trajectories can be explained by Lagrangian method. In Lagrangian approach, small droplets were dominated by the drug force caused by airflow, whilst large droplets were dominated by the inertia force caused by self-weight. Overall, the simulation results revealed that all these four types of diffusers could efficiently remove the particle contaminants within a certain time regardless of sizes, whilst small-particle distribution processes vary.

Since the potential health risks caused by the contaminant transport would be critically relevant to the amount of contaminants inhaled by passengers, a quantitative exposure-risk assessment of normalized droplet-volume fractions at each passenger's breathing zone was analysed, and it is illustrated in Fig. e1.35. As Passenger S was the source of droplets in this study, the droplet fraction at other passengers' breathing zones largely depends on their seat

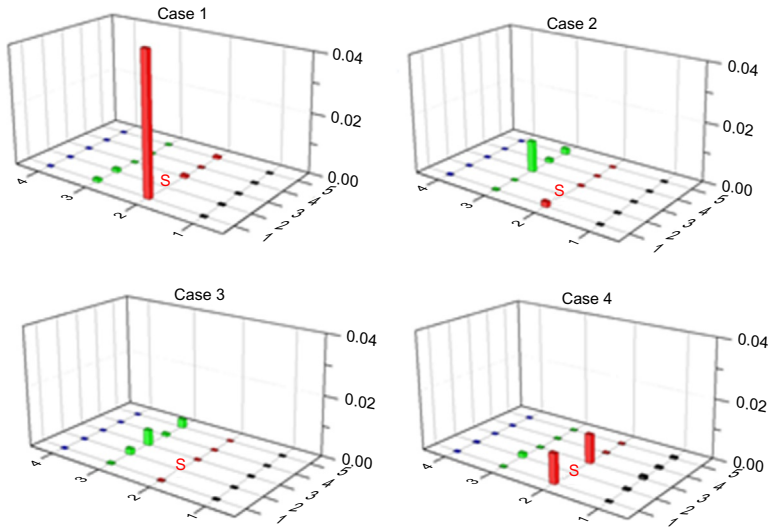


FIG. e1.35 Normalized droplet concentrations at passengers' breathing zones.

positions. The predicted results of Case 1 in Fig. e1.35 showed that the breathing zone of the passenger next to Passenger S in window side had the highest concentration of droplets. This can be illustrated from the droplet-transport trajectory in Fig. e1.33 that a strong airflow existed between them. Case 2 and Case 3 show similar situations that passengers at third row have a relatively higher concentration of droplets compared with those at other positions. This is caused by the backward airflow above Passenger S. Passengers at both sides of Passenger S in Case 4 suffered similar high concentration of droplets in their breathing zones because contaminants were highly concentrated around Passenger S for a certain period. In summary, different types of diffusers will make contaminant distributions significantly different in every passenger's breathing zone. However, all the passengers sitting under the condition of all four types of diffuser would experience contaminant concentration of only 5% of total released volume, which is an acceptable level.

Review Questions:

- Why are the four types of diffusers simulated in the same geometry HST cabin?
- If the passenger occupancy rate is changed, will the ventilation performance still be the same?
- Why do the relatively small droplets travel much longer and further away?
- Do the passengers seated near a coughing passenger suffer higher concentration of droplets?

Exploratory Questions:

➢ Conduct the simulation with larger fresh-air inlet velocity, and compare the airflow field and thermal comfortable environment.
➢ Testing the case that the train is operated in winter, will the ventilation performance be the same?
➢ What kind of droplet sizes could be ignored for reducing the computational cost?

e1.3.3 Flow Around a Submarine (Sara)

Sara Vahaji
RMIT University

e1.3.3.1 Case Introduction

Flow around underwater vehicles is of high interest in maritime engineering and has been investigated both experimentally and numerically with an extensive body of literature. Most of these studies deal with a single-phase flow. For example, the David Taylor Research Center has performed a thorough experimental investigation of turbulent single-phase flows around different submarines, including DARPA Suboff (Fig. e1.36). This geometry is adopted in the present study to run the simulations with ANSYS-CFX.



FIG. e1.36 The geometry of the DARPA Suboff model.

e1.3.3.2 Simulation

❑ Mesh Settings

For meshing the fluid domain around a submarine, different techniques are applied to capture the fluid properties. For instance, at the boundary layer around the submarine, the 'inflation-layer' technique is adopted. Also, for the locations where higher gradient of variables is expected and where geometry dictates, the 'sizing' technique is employed (please refer to Figs. e1.37–e1.39).

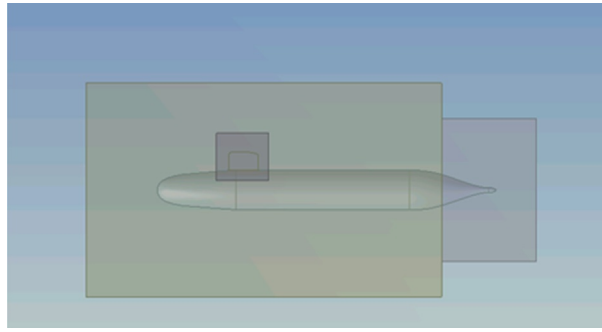


FIG. e1.37 Three bodies of influence to be used for sizing mesh technique.

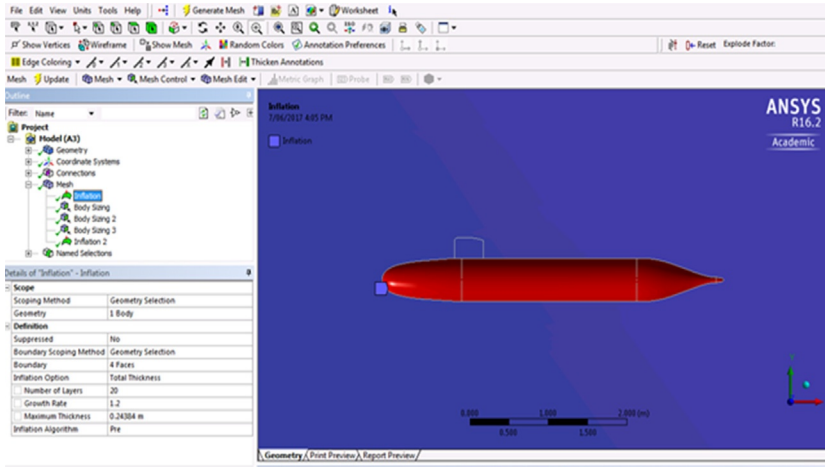


FIG. e1.38 Details of the setting for 'inflation-layer' mesh technique.

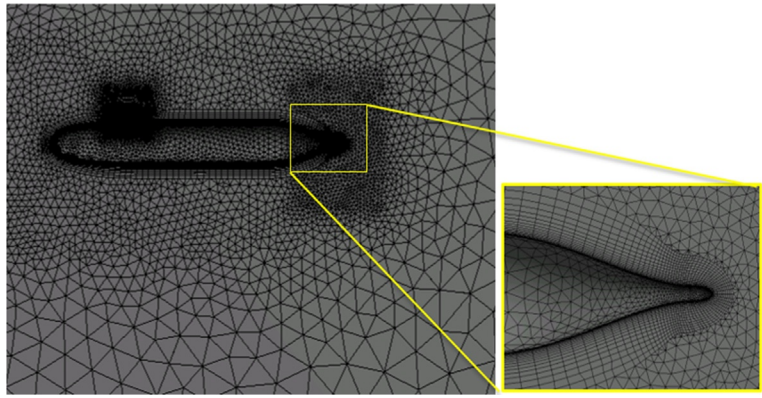


FIG. e1.39 Detailed view of inflation mesh around the submarine.

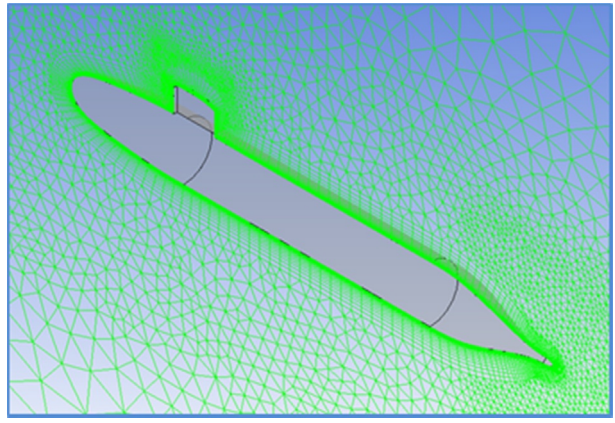


FIG. e1.40 The computational domain for half of the geometry.

❑ Boundary Conditions

For this study, since submarine has axis-symmetrical geometry, we could save computational time and cost by running the simulations for only half of the domain. This is done by applying symmetry plane as the boundary condition shown in Fig. e1.40. Other boundary conditions are inlet, outlet, opening, and wall.

The Reynolds number in this study is 12×10^6; therefore, the velocity is calculated according to the total length of the submarine (4.356 m):

$$v = \frac{Re \cdot \mu}{\rho \cdot l} = \frac{(12e+6)(8.899e-4[\mathrm{kg}/(\mathrm{m}\cdot\mathrm{s})])}{(997[\mathrm{kg}/\mathrm{m}^3])(4.356[\mathrm{m}])} = 2.459[\mathrm{m}/\mathrm{s}]$$

This velocity is set as the inlet boundary condition.

e1.3.3.3 CFD Results and Discussion

The conservation equations for mass, momentum, and energy are discretized using the finite-volume technique for a 3-D geometry. The turbulent flow is simulated based on Reynolds-averaged Navier-Stokes (RANS) equations. A two-equation model, such as either standard or shear-stress transport (SST) k-ε model, is employed. The numerical simulations are performed for flow around a moving Suboff with the diameter of 0.508 m and the length of 4.356 m, which gives a Reynolds number of 12×10^6 based on the length of the model. The dimension is chosen to match the available experiment.

❑ Validation

The validation of the numerical model is accomplished through the existing experimental data. Since the existing experimental setup had been carried out for a DARPA Suboff submarine without sail, a similar submarine model without sail is employed to perform the validation study. Fig. e1.41 demonstrates the velocity profile in both axial and radial direction at the distance 3.938 m (0.904 × 4.356 m) downstream of the head of the submarine. The numerical results and the experimental data agree well.

Fig. e1.42 depicts the comparison of computed pressure coefficient and friction coefficient along the submarine hull with the existing experimental data. In this figure, the horizontal axis is representing the normalized location along the

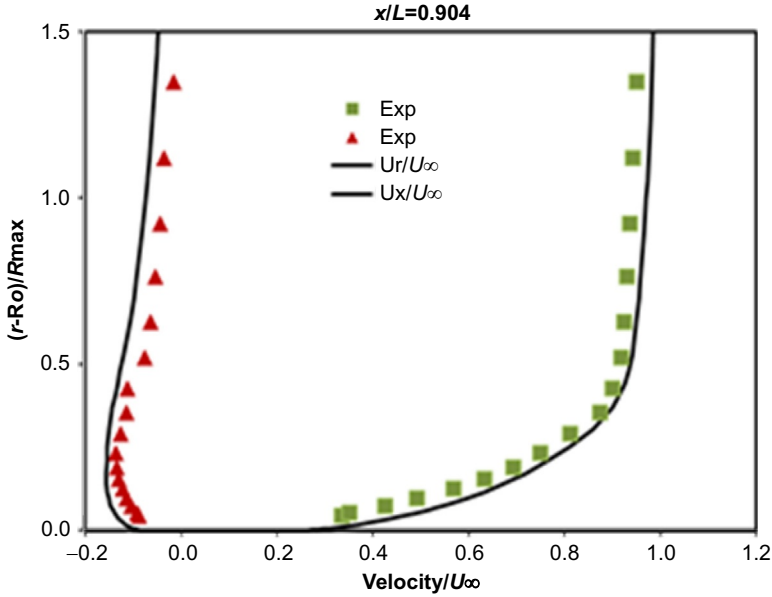


FIG. e1.41 Comparison of normalized velocity of Ur and Ux along the r direction with the existing experimental data at the line located at $x/L = 0.904$.

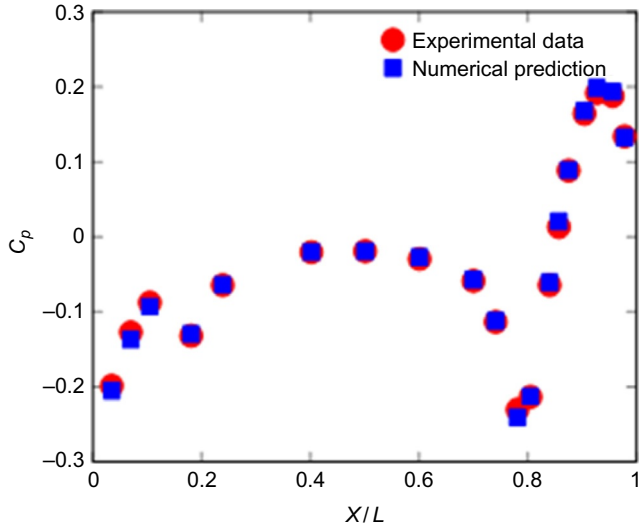


FIG. e1.42 Comparison of computed pressure coefficient with the existing experimental data.

length of the submarine where x is the axial distance measured from the nose of the submarine and L is the overall length of the submarine. At each point, the pressure coefficient is averaged at the cross-sectional area. The results show the agreement between the numerical results and the existing experimental data.

e1.3.3.4 Post Processing the Results

❏ Velocity Vector Plot

In order to visualize the velocity vector around the submarine, we need to plot the velocity vector on the symmetry plane (Fig. e1.43). In this figure, it is clear that the fluid accelerates whilst passing over the sail. The reason goes back to the geometry of the sail: When the fluid hits the sail, it stops, and stagnation

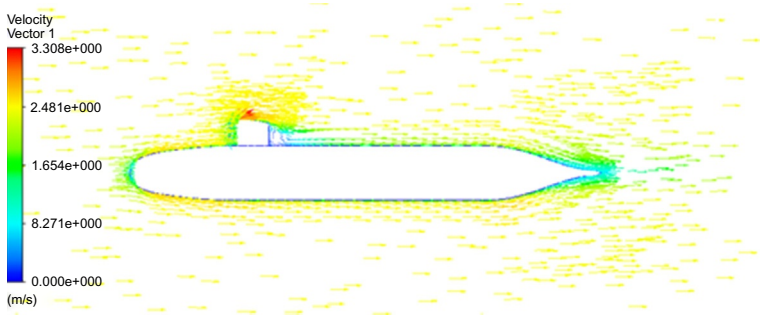


FIG. e1.43 Velocity vector around the hull of submarine.

point happens. Then, fluid moves around the sail where a small curvature exists. Due to the mass conservation, the flow accelerates until it reaches the top of the sail. After this point, the flow decelerates until it separates from the sail. At the back of the sail, the wake region exists where the energy is converted to turbulent kinetic energy. In this region, both the velocity and pressure are low.

❏ Velocity Contour Plot

The velocity-contour plot visualizes the magnitude of the velocity only (not the direction of it). Fig. e1.44 presents the velocity-vector plot around the submarine on the symmetry plane. The low-velocity regions are the stagnation points and wake areas.

❏ Pressure Contour Plot

In Fig. e1.45, the pressure distribution around the submarine's hull and sail is presented in the form of pressure contour. The regions with high pressure are referring to stagnation points where the pressure is at its maximum value and

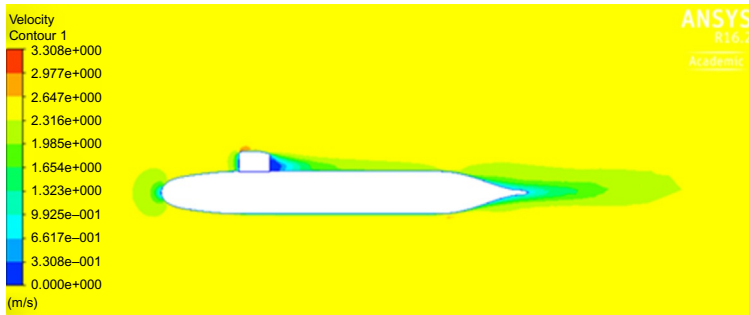


FIG. e1.44 Velocity contour around the hull of submarine.

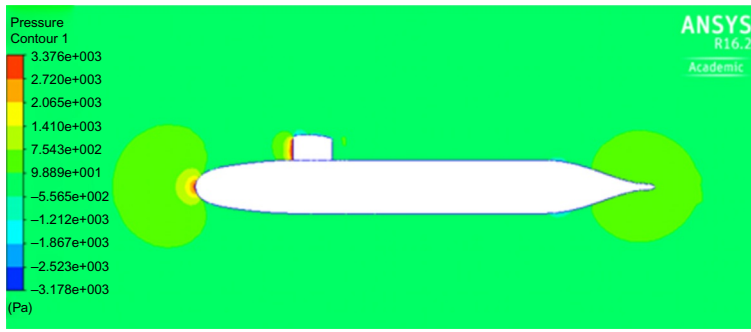


FIG. e1.45 Pressure contour around the hull of submarine.

velocity is zero. It is important to mention that this plot is showing the relative pressure with respect to the value that was assigned in the CFX—Pre.

Review Questions:

- What is the main reason causing the flow acceleration over the sail?
- Why is there a wake region after the sail?
- Why are both velocity and pressure low in the wake region?
- How many stagnation points can you identify? Explain why.
- Identify the stagnation point/s around the submarine.

Exploratory Questions:

➢ Plot the wall shear stress on the hull and sail of the submarine.
➢ Increase the Reynolds number to 18×10^6. What will be the inlet velocity?
➢ How would increasing the velocity impact on the pressure distribution around the submarine?

e1.3.4 Pollutants Dispersion in Urban Roadway Tunnels (Yao)

Yao Tao
RMIT University

e1.3.4.1 Case Introduction

Roadway tunnels are increasingly being constructed worldwide as an alternative to reduce commute time and alleviating traffic congestion. However, vehicular toxic emissions, such as CO, NOx, and smoke, can easily contaminate the air quality of the semienclosed tunnel environment and bring hazardous respiration issues to drivers and commuters, especially during severe traffic events. For short roadway tunnels, the piston effect induced by the moving vehicles can drive fresh air in and discharge vitiated air out of tunnels. Whilst for relatively long roadway tunnels, mechanical ventilation approaches such as jet fans are needed in addition to the piston effect to remove toxic gases emitted by vehicles in the tunnels and keep the vehicular toxic emissions within safety limits, especially during traffic jams. With the advantage of visualization to provide details that are hard to obtain from on-site measurement and cost less than running scaled models, CFD techniques have been widely used to study pollutant transport and distribution in the tunnel under severe traffic-jam conditions.

e1.3.4.2 Problem Description

The piston effect induced by the vehicle motion is a highly complex, three-dimensional, and unsteady process. Whether the flow patterns associated to the piston effect under low speeds could be adequate to discharge air pollutants and how it could incur risks of exposure to in-tunnel hazards remain unclear. This case aims at the influence of piston effect that resulted from the vehicle motion on the spatial distribution of pollutants inside the tunnel and outside of the exit portal. The interaction between motion-induced airflow and

mechanical ventilation was also considered. Numerical simulations using dynamic mesh method were performed on two road-tunnel traffic conditions (i.e. 10 and 40 km/h), under fan-on and fan-off conditions, respectively. CO_2 concentration was used to represent vehicular emissions under those scenarios.

e1.3.4.3 CFD Simulations

❑ Mesh Settings

The fluid domain of the numerical model consisted of a one-way tunnel, upstream and downstream open-roadway extensions, and atmosphere sections at the tunnel entry and exit where hillsides were assumed (Fig. e1.46A). The tunnel had a radius of 5 m and a length of 120 m, so as the length of each open-road extensions. The open-roadway sections were modelled as a half cylindrical shape with a radius 10 times the road tunnel's radius. The whole system was split from the midplane where symmetric flow features was assumed.

The whole computational domain consisted of moving meshes and fixed meshes that were matched with interfaces in the model. The moving part was meshed into hybrid mesh of tetrahedral volumes around moving vehicles and hexahedral control volumes at the rest portion of the moving part in order to enable the layering-mesh method for the moving meshes, which split and collapse at the boundary of hexahedral control volumes (Fig. e1.46B). The fixed part including the top portion of the tunnel and the ambient part of the system was meshed into tetrahedral volumes. Despite that for short tunnels the airflow driven by the movement of vehicles (the 'piston effect') is normally adequate to

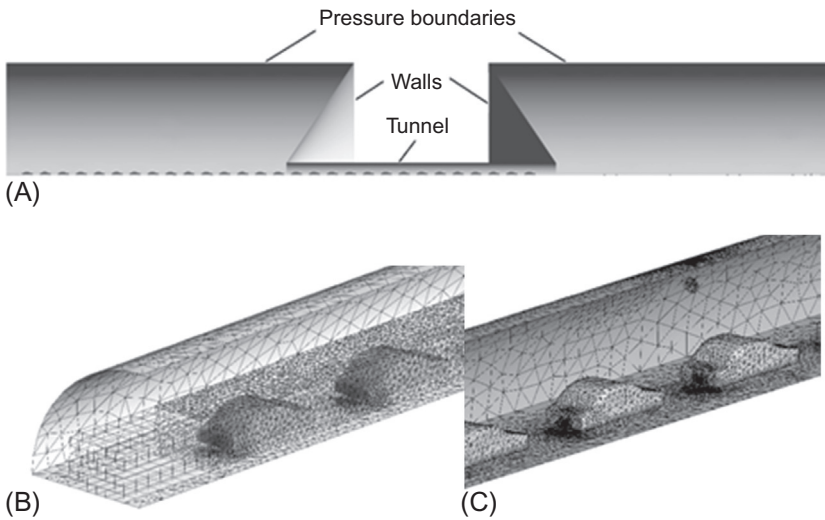


FIG. e1.46 (A) The computational domain, (B) the mesh generation for the moving and fixed part of meshes, and (C) the location of the fan.

manage in-tunnel air quality, the fan condition was designed in this case to generate an in-tunnel wind velocity to interact with the piston effect. The fan that was located 0.5 m to the ceiling of the tunnel (Fig. e1.46C), horizontally 40 m to the entrance and 80 m to the outlet, met the requirement of fan installation in long tunnels. The final mesh elements being used in the current case were 2.8 million.

❑ Boundary Conditions.

The non-slip stationary-wall boundary condition was used for the tunnel walls and car bodies. Two different traffic conditions under vehicle velocities of 10 km/h (low speed) and 40 km/h (medium speed) were considered to simulate possible scenarios when traffic congestion happened. Distances between vehicles were considered according to the safe following distance that allowed 2 s for vehicles to stop, thus 6 m for 10 km/h and 12 m for 40 km/h. Symmetry boundary was set at the midplane for the whole system. A pressure jump of 150 Pa in the driving direction was prescribed for the fan boundary, which generated a fan outlet velocity of 10 m/s and an average in-tunnel wind velocity of 1.47 m/s according to the simulation results. Opening boundary conditions were imposed on the atmosphere region as pressure inlet and pressure outlet. In order to control the flowing direction for all the cases, a slight pressure value of 0.1 Pa was imposed on the pressure inlet for all the cases, to generate a negligible velocity of around 0.3 m/s according to our simulation results (Table e1.9).

The exhausts were released at the outlet vent with a diameter of 0.06 m at the back of every vehicle. In the real condition, the tailpipe was located at the left, right, or both sides of the car. For simplicity, our case assumed the locations of tailpipes were in the middle for all the vehicles, set as a velocity inlet with a speed of 3 m/s under the traffic conditions. CO2 was chosen as the indication of in-tunnel air quality. The mass fraction of air components released from gasoline engines were $O2 = 0.02$, $CO2 = 0.17$, and $CO = 0.005$, and the other

TABLE e1.9 Boundary-Condition Settings

Name	Type	Value
Vehicles	Dynamic mesh zone (motion profile)	2.78 and 11.1 m/s
Exhaust vent	Velocity inlet	−3 m/s Species: $O_2 = 0.02$, $CO_2 = 0.17$, $CO = 0.005$
Ambient inlet	Pressure inlet	0.1 Pa, $CO_2 = 0.006$
Ambient outlet	Pressure outlet	0 Pa, $CO_2 = 0.006$

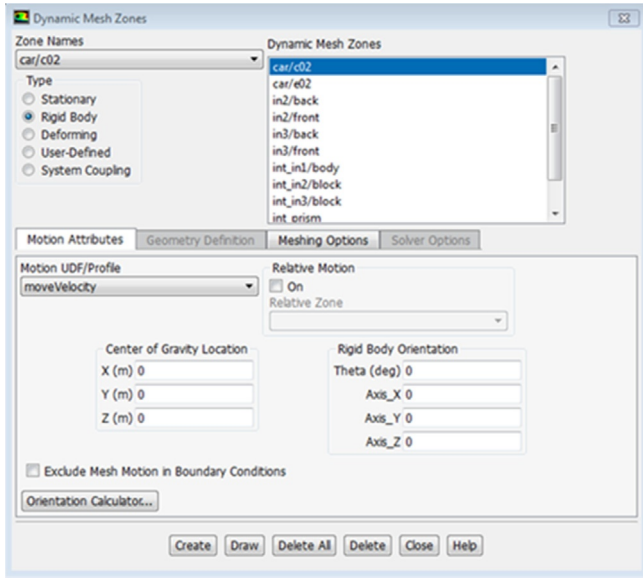


FIG. e1.47 Dynamic mesh settings in ANSYS Fluent.

component was regarded as N2, with an air temperature of 30°C. The air intake of the tunnel had a CO2 mass fraction of 0.006, with a temperature of 20°C.

The dynamic mesh setting was achieved by applying the velocity profile (moveVelocity) to the corresponding dynamic mesh zones (e.g. car/c02—the car bodies) as shown in Fig. e1.47.

❑ Solver settings

The standard k-ε turbulence model was adopted to predict the airflow pattern. All transport equations were discretized using second-order upwind scheme. The SIMPLE algorithm was used for pressure-velocity coupling. The convergence was judged as residuals decrease to 10^{-3} for all equations (continuity, momentum, turbulence, and species) except the energy equations, for which the criterion is 10^{-6}. The fluid flow was treated as transient state with a time-step size of 0.01 s, and the simulation was conducted by ANSYS-Fluent.

e1.3.4.4 Results and Discussion

For the vehicle motion, given the process of exhaust dispersion from running vehicles was time-dependent, we regarded the vehicles running through a tunnel length (120 m) as a baseline cycle during which vehicles were still fully occupying the tunnel. Once the vehicles finished a cycle, the results of the whole flow domain were interpolated as the initial condition for the original case to run again. In that way, the continuous running was approximated. The area-averaged CO_2 concentration at tunnel outlet was monitored to find the time

for the whole system to reach equilibrium. Vehicle speeds of 10 and 40 km/h with fan-on and fan-off conditions achieved nearly steady state at the fifth cycle. Therefore, the results after running for five cycles were used for the comparisons (results were obtained at the time 200 s for 10 km/h run and 50 s for 40 km/h).

❑ Velocity Distribution

The velocity and concentration distribution through the middle plane of the cars ($X = -2.1$ m) under vehicle moving conditions are shown in Fig. e1.48. The wind pushed by moving vehicles showed high velocities around the bodies, whilst the wind at the upper part of the tunnel was relatively stagnant. With an outlet velocity of 10 m/s, the fan-induced airflow generated confined jet-like airflow with high wind velocities at the ceiling, but the velocities were lower around the vehicles. Whilst as the vehicle speed increased, the fan-induced airflow showed minor effects on the whole tunnel's velocity distribution.

❑ CO_2 Concentration

The CO_2 distribution at the plane $X = -2.1$ m is shown in Fig. e1.49. When the discharging of vehicle emissions depended merely on the piston effect (Fig. e1.49A), the higher velocities around the moving vehicles pushed the exhausts to flow downstream the tunnel. However, vitiated air gradually accumulated at the downstream ceiling due to the thermal buoyancy and the low wind speed at the upper part of the tunnel. A higher vehicle speed (40 km/h) also occurred, the same problem that high concentration of CO_2 gathered at the outlet, but it discharged the contaminants considerably well, and only small regions with high CO_2 concentration were found at the portal.

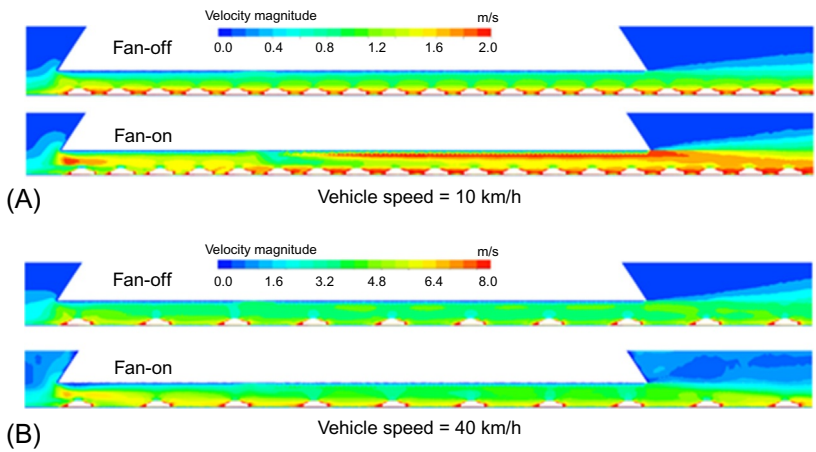


FIG. e1.48 Velocity field at the plane through the centre of car bodies ($X = -2.1$ m) under vehicle speeds of (A) 10 and (B) 40 km/h at fan-off and fan-on conditions.

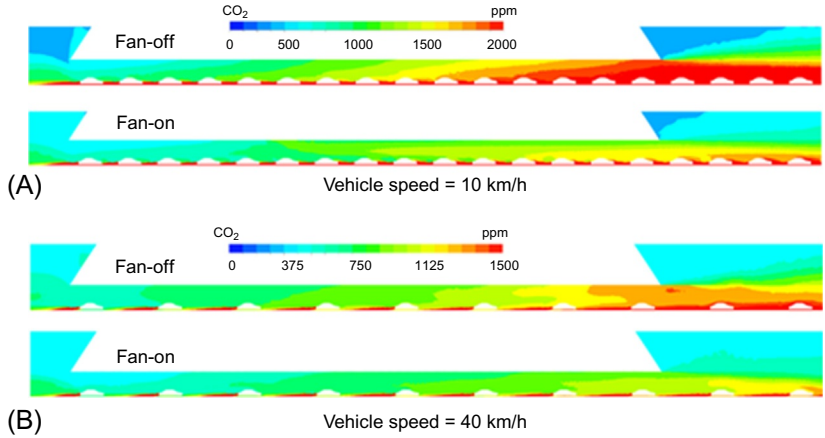


FIG. e1.49 Contour of CO_2 concentration at the plane through the centre of car bodies ($X = -2.1$ m) under vehicle speeds of (A) 10 and (B) 40 km/h at fan-off and fan-on conditions.

With the fan turned on and generated higher wind velocities near the roof, the high level of CO_2 concentration at the ceiling was discharged, and the ascending due to buoyancy effect was overwhelmed. Finally, the contaminants were controlled within a lower concentration at the exit portal and the surrounding environment. Under a higher vehicle speed of 40 km/h that the fan-induced airflow was comparatively weak compared with the motion-induced wind, the piston effect was already adequate for keeping the in-tunnel CO_2 concentration within an acceptable range. The mechanical-ventilation effects showed significance in assisting the discharge when it was comparable with the average piston wind generated by the vehicle motion. Whilst the piston wind became larger (at 40 km/h), the mechanical ventilation became dispensable.

Overall, the piston effect helped the elimination of emissions adequately under a vehicle speed of 40 km/h. But a lower vehicle speed of 10 km/h still encounters the high CO_2-concentration levels at the downstream part and the exit portal of the tunnel. The additional mechanical ventilation helped the discharge of emissions at the upper part of the tunnel that came from the thermal buoyancy and kept the remained CO_2 at the exit portal an acceptable level around the vehicles. Although normally the forced ventilation is not required for the short tunnels, it showed a significance to eliminate emissions when piston effect is not sufficient under complex traffic conditions.

Review Questions:

- What method was used to approximate the continuous running of vehicles in the tunnel?
- What are the differences of flow characteristics between the in-tunnel piston effect and the mechanical ventilation in this case?

Exploratory Questions:

- Apart from the assumptions in this case, are there any other influencing factors on the natural ventilation in the tunnel?
- Would other types of mechanical ventilation (i.e. stacks and horizontal ventilation) be more helpful to exhaust the vitiated air caused by slow vehicle motion in this case?

e1.3.5 Human-Induced Airflow in the Indoor Environment (Yao)

Yao Tao
RMIT University

e1.3.5.1 Case Introduction

Human activities have been identified to wield significant influences on indoor airflow patterns by producing distinct wake flow regions and unsteady vortex shedding over the body. The wake flow generated by human activities highly interests the assessment of air quality, as the human activity constitutes an important factor to influence the exposure to air pollutants in indoor workplaces. The influence of motion-induced wake on the indoor contaminant transport and dispersion received lots of attention especially in interior environments such as aircraft cabins, hospital wards, surgical rooms, and clean rooms, where occupants' exposure levels to airborne contaminants are highly valued.

The induced wake exhibits similarities to boundary-layer separation of flows over bluff bodies, where a mixing zone of vortices entraining air into a reverse flow region is formed. This case is to understand the fundamental fluid dynamics of the wake flow, in particular, for flow separation over bluff bodies in motion.

e1.3.5.2 Problem Description

Though simplified geometries such as cylinders and cuboids were used as substitutes of human bodies at earlier stages, discrepancies in flow features due to geometry differences were also found, i.e. the legs could be considered as two closely arranged cylinders whose wake flow interacted with each other depending on the gap width. On the other hand, many studies considered the body as stationary in a domain with a constant incoming flow. However, the assumption of relative motion between the flow and the stationary body neglected the flow disturbance caused by the manikin motion and hence partially represented the near wake characteristics of human wake during walking.

In the present study, numerical methods were adopted to investigate the details of wake flow induced by a thermal manikin in the indoor environment under two motion modes, focusing on the discrepancies in the flow field and vortex structures induced by motion with and without limbs swinging during and after the manikin moving. Techniques related to dynamic mesh modelling were applied in the simulation to achieve the motion. It is expected to improve the further assessment on contaminant levels for indoor air quality based on more accurate prediction of human-induced wake.

e1.3.5.3 Simulation

❑ Mesh Settings

A manikin with dimensions of 1.7 m (height) and 0.58 m (width) and an aspect ratio $H/D = 2.93$ was placed in a computational domain of 2.6 m (x coordinate) × 6.0 m (y coordinate) × 2.7 m (z coordinate). The coordinate system located the manikin at an initial standing position at $x = 0$ m and $y = 0$ m, facing the +y direction 1 m from the back wall (Fig. e1.50A). Unstructured tetrahedral cells and prism layers were generated for the domain (Fig. e1.50B). To capture the boundary-layer separation around the manikin, 10 prism layers were generated on the manikin surface to keep the dimensionless wall distance $y+ < 5$. For the dynamic meshing, the domain was remeshed at each time step to update the moving manikin.

❑ Boundary Conditions

The cadence (the number of steps per unit time) and the walking speed of a person are subject to various factors. We assumed a medium walking speed that two steps are finished in 1 s with a mean walking speed of 1.2 m/s (See Table e1.10). In order to reduce the calculation of dynamic meshes, the walking gestures were simplified as no bending of knees and elbows, only swung as pendulums starting from the root of big arms and thighs. Maximum joint-angle displacements for arms and elbows are 15° and 30°, respectively.

The surface temperature of the manikin was 32°C, and the air temperature was 22°C. Since our objective was to compare the thermal plume around the manikin during walking, the convective heat transfer from the body surface was the main contributor, and radiation, evaporation, and respiration were not considered. Likewise, clothing was not considered.

The gait cycle was achieved by defining the rotating velocities of limbs during each gait phase using User-Defined Function (UDF) in commercial CFD software ANSYS-Fluent. As an example of the UDF, the use of DEFINE_CG_MOTION macro to specify the movement of the right arm is shown in Table e1.11. As shown in Fig. e1.51, two steps are finished within

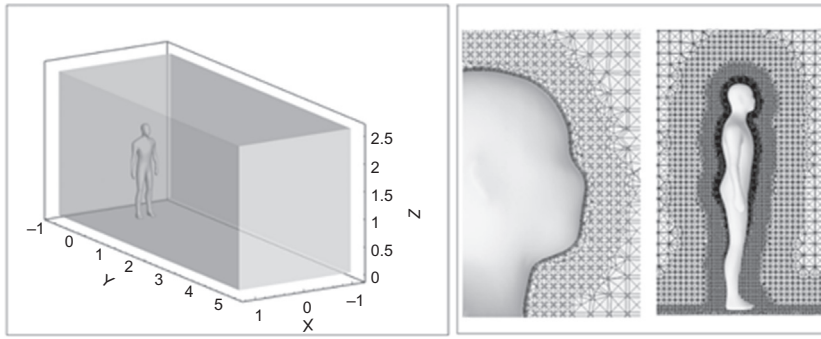


FIG. e1.50 (A) Computational domain of the room; (B) prism layers and mesh around the manikin.

TABLE e1.10 Boundary-Condition Settings

Name	Type	Value
	Dynamic mesh zone (UDF)	
Manikin body	Rigid velocity	1.2 (m/s)
	Angular velocity	1.3 (rad/s)
	Temperature	32
Room wall	Temperature	22

TABLE e1.11 An Example of UDF for the Movement of the Left Arm

```
#include "udf.h"
#include <math.h>
#include <stdio.h>
DEFINE_CG_MOTION(left_arm, dt, cg_vel, cg_omega, time, dtime)
{      real t,Rt;
    int t_cycle;
    t = CURRENT_TIME;
    t_cycle = (t*100)%100;
    if (t_cycle >= 0 && t_cycle < 50)
    {  DT_CG(dt)[0] = -0.2;
         DT_CG(dt)[1] = -0.07+1.2*t;
         DT_CG(dt)[2] = 1.205;
         cg_vel[1] = 1.2;
         cg_omega[0] = 1.3;
    }
    else if (t_cycle >= 50 && t_cycle < 100)
    { DT_CG(dt)[0] = -0.2;
         DT_CG(dt)[1] = -0.07+1.2*t;
         DT_CG(dt)[2] = 1.205;
         cg_vel[1] = 1.2;
         cg_omega[0] = -1.3;
    }
       }
```

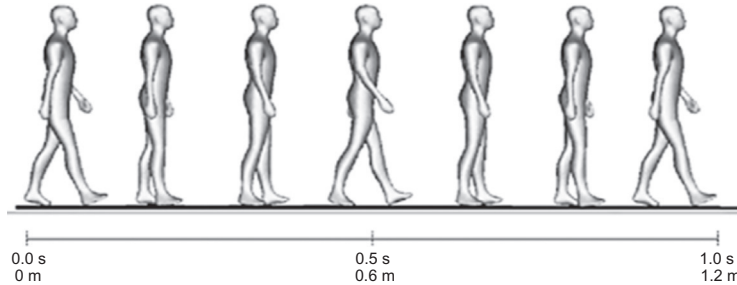


FIG. e1.51 Gait cycle in the simulation within a normal gait cycle (1 s). The walking speed is 1.2 m/s.

a gait cycle ($T = 1$ s). Taking the right arm as an example (Table 1), the DEFINE_CG_MOTION macro defined that in the first half of the cycle, the right arm and left leg were swinging forwards, whilst the opposite limbs were swinging backwards. In the second half of the cycle, the swinging of limbs reversed their direction and finished the second step at $T = 1$ s.

After compiling and loading the UDF, the movement of each limb (right arm, right leg, left arm, and left leg) could be assigned to the corresponding zones (Fig. e1.52).

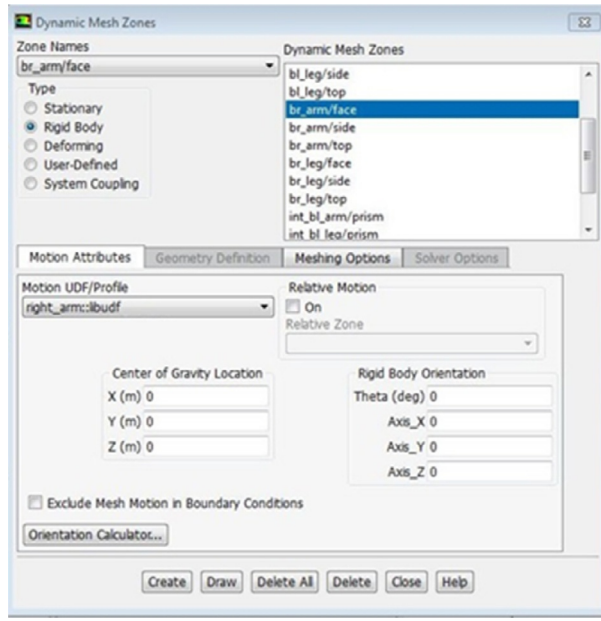


FIG. e1.52 Dynamic mesh settings in Fluent.

e1.3.5.4 Results and Discussion

Previous studies had showed that the unsteady RNG k-ε model was one of the best turbulence models to predict the velocity and total kinetic-energy fields for flow separation over a building in terms of accuracy, computing efficiency, and robustness. Thus, in this case, the RNG k-ε turbulence model was adopted. Enhanced wall treatment was used for the near-wall modelling. The discretization schemes used were the QUICK scheme for momentum, second-order upwind for the convection and diffusion terms, and the SIMPLE algorithm for pressure-velocity coupling. The time step was 0.001 s, and the mesh was updated at each time-step matching the manikin movement.

❑ Velocity Field

The effect of walking on the thermal plume was investigated under the swinging walking motion. Fig. e1.53 shows velocity contour and vectors on the midplane ($x = 0$ m) under the swinging motion at different time steps. The velocity contours are not shown for velocities below 0.10 m/s. The induced velocities were created from the relative motion between stationary and fixed stagnant fluids. To begin the modelling, the thermal environment around the body under steady

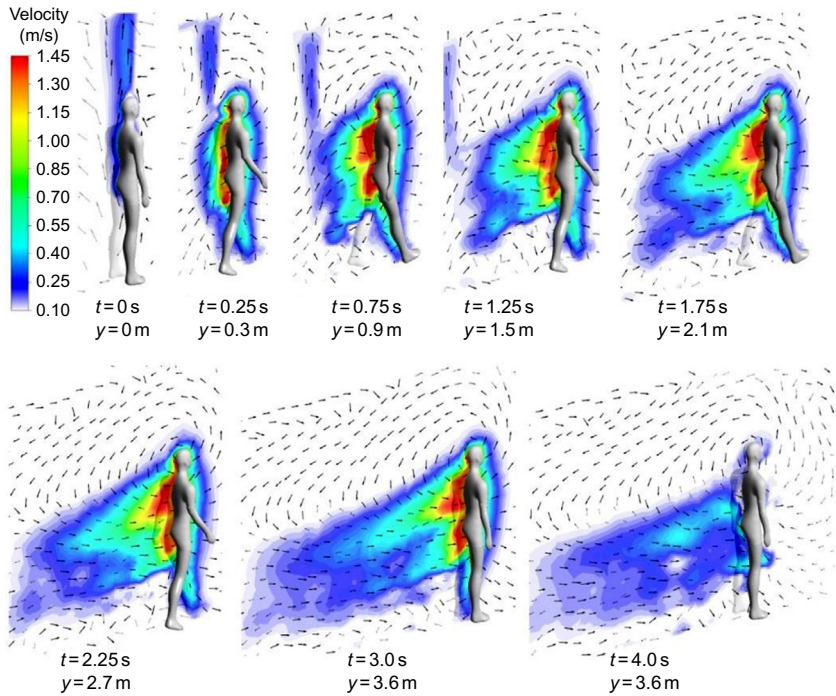


FIG. e1.53 Velocity contour and vectors on the centred plane ($x = 0$ m) under the swinging motion during $t = 0$–4.0 s (the motion stopped at $t = 3.0$ s).

state was established. A thermal plume was formed where it was weak at the bottom of the body and became stronger in the upper body. The plume rises vertically above the manikin head with a maximum velocity of 0.25 m/s at 0.18 m above the head. The swinging motion was then introduced into the thermal domain where the thermal plume does not move with the manikin. Instead, it trails behind slowly remaining connected to the manikin wake flow (based on flow velocities >0.1 m/s) until $t = 1.25$ s in the figure.

The velocity vectors in the thermal plume were directed upwards, and nearby flow was entrained in the plume. An anticlockwise recirculation was formed from the rising thermal plume that countered the clockwise recirculation coming from the downwash flow from the manikin. This led to a greater downwash flow, and the wake is narrowed compared with the isothermal case where the wake is more circular.

In the upper body, this is evident from the high velocities along the body, and a trailing wake forms. Vectors show the fluid moves upwards and around in a semi-circle from the head returning into the wake as it becomes entrained into the flow. Velocity vectors in the wake move back into the wake towards the manikin. In the front of the body, the vectors are directed forwards suggesting that the fluid is pushed away as the body moves through the flow field. In the lower body where the legs swing, the contours form around the swinging leg.

❑ Streamlines and Pressure Field

Streamlines originating from the body at different moments of the gait cycle for a walking speed of 1.2 m/s were used to determine the local flow behaviour around the manikin (Fig. e1.54). Streamlines originating from the front-right-hand side of the body wrap around and then curl back into the manikin body. This suggests strong flow entrainment caused by the moving manikin that pushes the air that is in front of it, making way for the manikin to occupy the space.

The displaced air then curls back around the body taking up the void space left behind by the manikin. We notice that the streamlines move furthest around the middle of the body, whilst it is thinnest near the head and feet. Generally, the streamlines don't show significant updraft to potentially redisperse floor-lying particles into the breathing region. The streamlines near the feet remain close to the floor, whilst streamlines at knee height will rise as it moves backwards.

❑ Vortex Structure

Coherent vortex structures of the manikin within a full gait cycle (1.75–2.75 s) are shown in Fig. e1.55 as isosurfaces of λ_2 coloured with velocity magnitude. Unlike the stationary bluff bodies where a long wake region is stretched downstream from an oncoming flow, the swinging walking motion generated small vortices that trailed the body. The vortex cores generate mainly behind the torso and on the legs during upright position. At the swinging limbs, larger vortices formed when the limbs finished the swinging phase. When manikin stopped moving ($t = 3$ s), the vortex cores propagated through the gaps between arms and thighs.

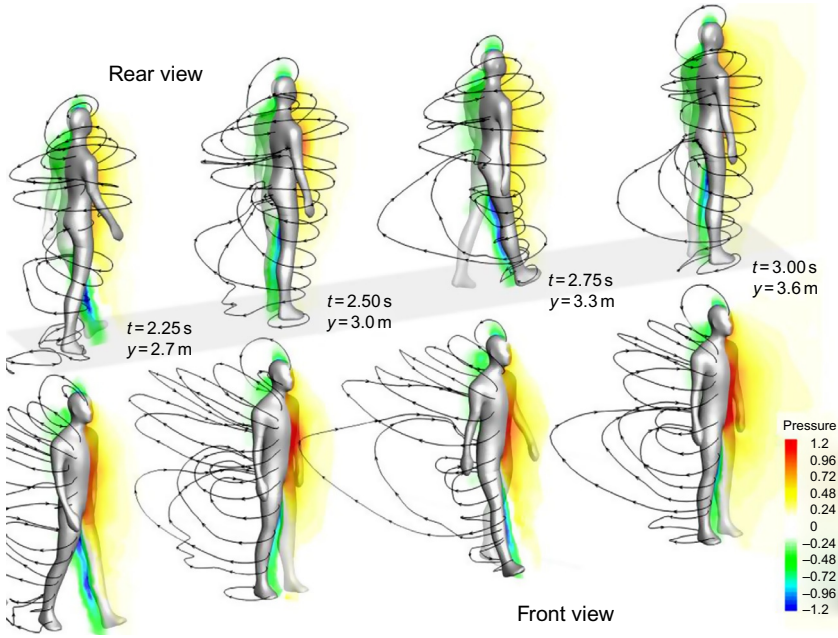


FIG. e1.54 Three-dimensional streamlines generated from the right side of the body. A pressure contour is overlaid to demonstrate the regions of high and low pressure, determining the flow direction.

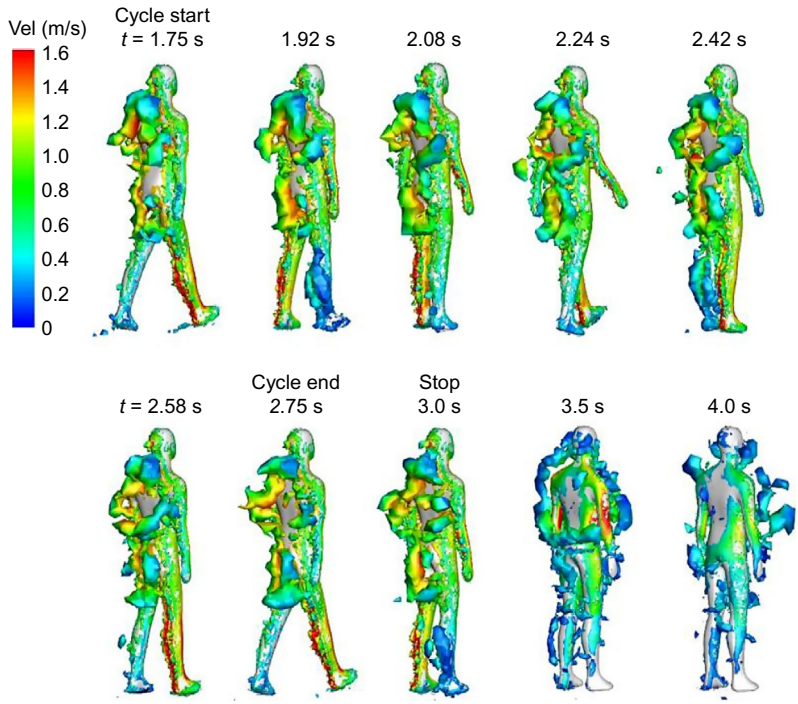


FIG. e1.55 The coherent vortex structures of the manikin within a full gait cycle (1.75–2.75 s) and after its stop (3.0–4.0 s).

Review Questions:

- Why did the thermal plume disappear during the walking process?
- How to change the UDF examples if the gait cycle/cadence changed?
- What prism-layer settings were applied on the manikin surface in this case, and what type of near-wall treatment was used?

Explore Questions:

➢ What are the differences between the three groups of mesh-motion methods in ANSYS-Fluent: smoothing, dynamic layering, and remeshing?

➢ What factors should be considered when determining the time-step size for simulating the flow over bluff bodies?

e1.3.6 Airflow and Pollutant Dispersion in Urban Street Canyons (Zijin)

Zijin Tan
Chang'an University

e1.3.6.1 Case Introduction

As a basic element of complex urban-built environment, urban street canyon has significant effect on both mesoscale and microscale environment. It is the source zone of motor-vehicle exhaust, the main occupied zone of urban residents, and also the source zone of indoor fresh air. Thus, it is necessary to have a better understanding of environmental characteristics in street canyons, which could benefit by not only improving urban and indoor environment but also removing pollutant and reducing energy consumption and, more importantly, ensuring safe and healthy environment for pedestrians.

Complicated environment inside urban street canyon is formed by heat transportation and momentum transportation, as the solid boundary of street canyon space and temperature conditions of street and sidewalls could significantly affect canyon flow structure, pollutant dispersion, and pedestrian comfort. Recently, studies focused on the differential surface heating due to atmospheric instability and solar tilt become an emerging research topic. Despite numerous studies that have been conducted, researches focusing on the seasonal difference considering the solar radiation and the anthropogenic heating from the building interiors remain limited, and their effects on airflow and pollutant transport are not clear. To reveal the seasonal differences of flow patterns and pollutant dispersion in street canyons between summer and winter, CFD simulations considering exterior solar radiation and interior anthropogenic heating were performed in this study. The results revealed that the seasonal variation significantly altered the street canyon microclimate. Compared with the summer situation, more evenly distributed surface temperature was found in winter. In addition, the summer case showed greater daily temperature and

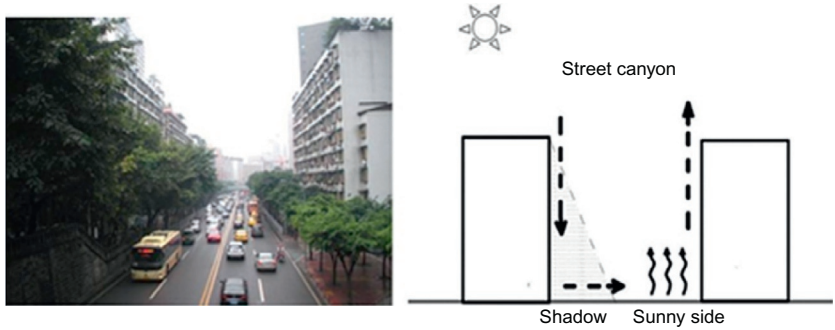


FIG. e1.56 Urban street canyon.

flow-pattern fluctuation than that of winter case. Consequently, the peak value of street canyon AER is found at winter morning and summer noon (Fig. e1.56).

e1.3.6.2 Problem Description

As two key impact factors of thermal process inside urban street canyons, the seasonal differences of atmospheric condition and indoor environment are considered. Length of the street canyon is assumed to be infinite, and roadside buildings are assumed to be solid without openings. Inertia ash particle with the density of 1 g/m^3 and diameter of 2e-6 m is used to represent PM2.5 pollutant in urban area.

e1.3.6.3 Simulation

❑ Computational Domain

In this study, a three-dimensional hypothetical street canyon model with an aspect ratio of unity was used (Fig. e1.57). The street axis was aligned with the x direction (from north to south). Both the building height (H) and street canyon width (W) were set as 20 m. The fluid domain is $5H$ (x direction) $\times$ $3H$(y direction) $\times$ $4H$(z direction). The prevailing ambient wind is introduced along the y direction, perpendicular to the axis of street canyon with constant velocity.

❑ Mesh Settings

On account of domain shape, size, and boundary conditions, structured mesh is adopted. The street canyon domain is discretized using the hexahedron mesh in ANSYS ICEM. Mesh-independency study was conducted over six grid scales. To address the buoyancy force in near-wall regions, six different first-layer grid thicknesses varying from 0.05 to 0.4 m were chosen, whilst the inflation-layer expansion ratio was kept as 1.1 in the whole domain. Accordingly, the mesh element number is 2,070,145 and 560,583 for the finest and coarsest grids considered, respectively. As listed in Table e1.12, the airflow velocity became

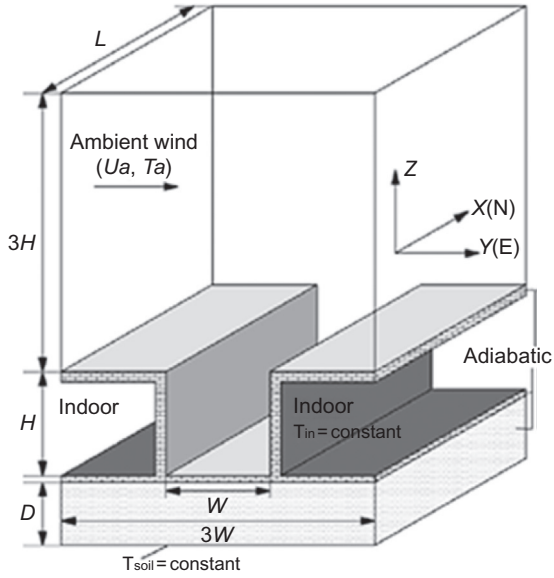


FIG. e1.57 Schematic diagram of the computational domain ($H = 20$ m, $W = 20$ m, $D = 2$ m, $L = 100$ m, Ua, ambient wind velocity, and Ta, ambient air temperature).

TABLE e1.12 Mesh-Independency Study

Element Number	First-Layer Thickness (m)	Grid Expansion Ratio	Maximum Element Size (m)	U (m/s)*
560,583	0.4	1.1	0.6	0.104
645,480	0.3	1.1	0.5	0.09
780,318	0.3	1.1	0.4	0.083
1,026,221	0.15	1.1	0.3	0.083
1,237,698	0.1	1.1	0.2	0.083
2,070,145	0.05	1.1	0.2	0.083

stable once the mesh element number exceeded 780,318. Taking the computational efficiency into consideration, the case having 1,026,221 mesh elements (the first layer thickness is 0.15 m, 0.75% of the street's width) was chosen for numerical analysis in this study (Tables e1.13 and e1.14).

TABLE e1.13 Velocity Boundary Conditions

Inlet	1 m/s
Outlet	Zero pressure gradient
Upper boundary	Zero pressure gradient
Side planes	Symmetry
Solid boundary	No slip

TABLE e1.14 Temperature Boundary Conditions

Inlet	Ambient air temperature was imposed, as shown in Fig. e1.58
Outlet	Ambient air temperature was imposed, as shown in Fig. e1.58
Upper boundary	Free-stream temperature is set as ambient air temperature, as shown in Fig. e1.58
Indoor surfaces	Summer, 299 K, and winter, 293 K
Underground	Daily-averaged air temperature

❑ Boundary Conditions

❑ Solution

The CFD model of this study is based on fluid flow and transport principles for incompressible turbulence flow in terms of mass, momentum, and energy-conservation equations. Reynolds number in all cases of this study is around 1e6. Equations for turbulent kinetic energy and turbulent dissipation rate are

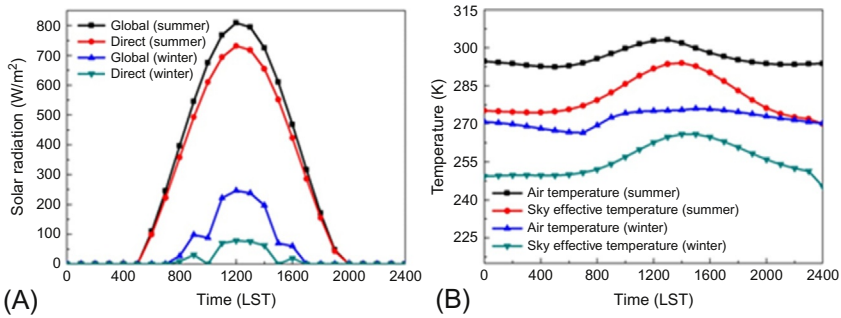


FIG. e1.58 Meteorological conditions, (A) Solar radiation, (B) Temperature.

solved with RNG k-epsilon closure scheme. Scalable wall function is adopted to solve the near-wall convection in this model. All governing equations were solved by the commercial CFD code ANSYS-Fluent (ANSYS, NH, the United States) with finite-volume method. The SIMPLE scheme is used for the pressure and velocity coupling. For all transport equations, the second-order scheme is used to provide better numerical accuracy, and the residual criterion for convergence is set as $1e-4$.

The solar ray tracing algorithm and the discrete ordinates (DO) model were chosen to include the diurnal solar radiation effect and radiation transfer between street canyon facets. Boussinesq approximation was employed to address temperature-induced density variation. Discrete phase model (DPM) was used to predict the particle dispersion characteristic, and all street canyon facets were set as reflect boundary for the particles.

e1.3.6.4 CFD Results and Discussion

❑ Surface Temperature

Temperature difference among street canyon surfaces or between solid surface and ambient air has remarkable influence on thermal flow inside street canyon. Fig. e1.59 compares absolute temperature differences among all facets, namely,

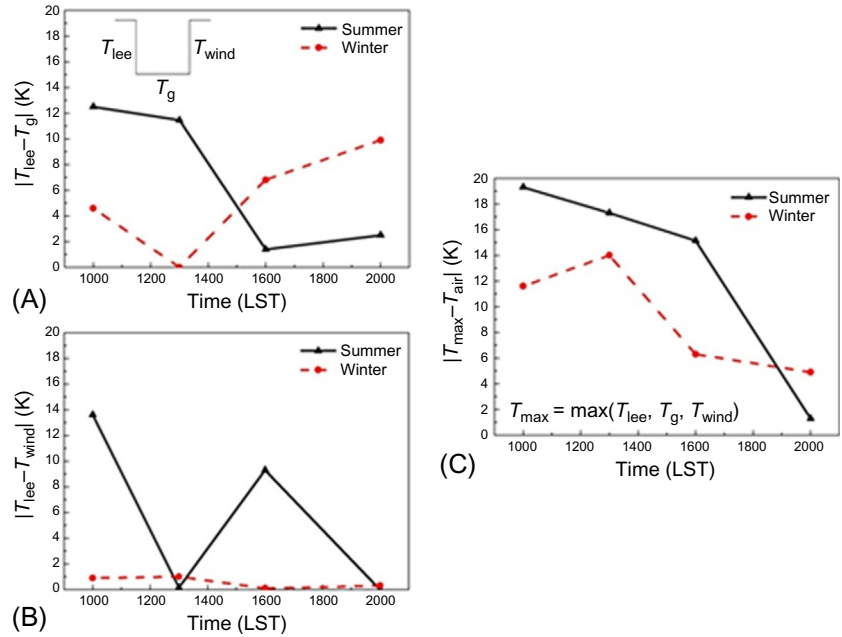


FIG. e1.59 Temperature comparison among canyon facets and ambient air for all time events (T_{lee}, leeward wall temperature; T_g, ground temperature; T_{wind}, windward wall temperature; T_{max}, maximum temperature among all canyon facets; and T_{air}, ambient air temperature).

leeward wall and ground, leeward wall and windward wall, the most heated facet, and ambient air under summer and winter. In general, greater temperature difference occurred in summer during most of the day than that of winter. Significant seasonal and diurnal variations were found for the canyon facet heating. More evenly distributed facet temperature with weak diurnal fluctuation is expected for winter condition due to the combined effect of solar radiation and anthropologic heating.

❑ Airflow Pattern

Fig. e1.60 details the wind-buoyancy-driven flow behaviour within the street canyon under different seasonal conditions. For the morning event (1000 LST) as shown in Fig. e1.60A and B, a clockwise rotating vortex centring close to the windward wall was observed under both seasons. However, a small secondary vortex was established at the bottom corner of the windward wall under winter condition (Fig. e1.60B). Similar flow patterns with two counter-rotating vortices were found for the noon event (1300 LST) for both seasons (Fig. e1.60C and D). For the afternoon case (1600 LST), completely different airflow patterns were found. For the summer condition, a complex airflow structure with multivortex was observed (Fig. e1.60E). Whilst for winter, a single vortex with intensified airflow along canyon facets was established (Fig. e1.60F). For the night event (2000 LST), a clockwise rotating vortex with slight disturbance of the ambient wind was observed under both seasons. These results suggest that flow patterns and its daily variation have significant difference between summer and winter. Maximum seasonal difference of street canyon flow structure is observed at afternoon and night when thermal effect of sidewalls is strongest. Weaker diurnal fluctuation is found in winter situation.

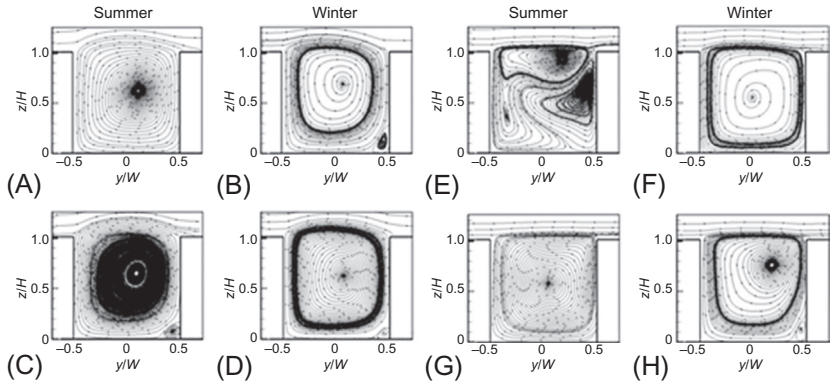


FIG. e1.60 Along-canyon averaged streamlines for all time events: (A) and (B) represent 1000 LST; (C) and (D) represent 1300 LST; (E) and (F) represent 1600 LST; (G) and (H) represent 2000 LST. The averaging calculation was taken from $x/L = 0.25$ to $x/L = 0.75$.

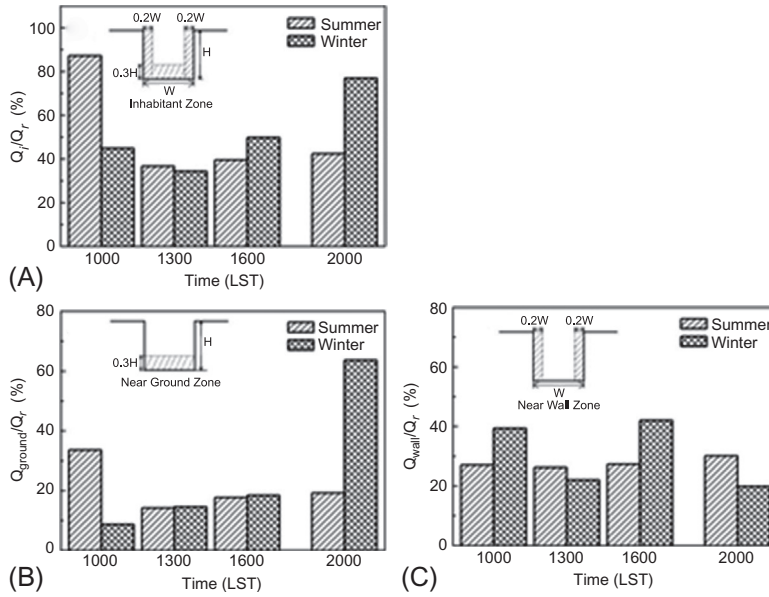


FIG. e1.61 Residual pollutant percentage within inhabitant zones (A) (Q_{wall}, residual pollutant mass in the near-wall zone; (B) Q_{ground}, residual pollutant mass in the near-ground zone; (C) Q_i, residual pollutant mass in the inhabitant zone; Q_r, total residual pollutant mass).

❑ Pollutant Dispersion Characteristics

Lastly, the relative residual pollutant percentages in the near-wall, near-ground, and inhabitant zone were calculated to quantify the air quality in human-occupied zones (Fig. e1.61). Fig. e1.61A summarizes the percentage of pollutants concentrated within all inhabitant zones, including near-ground zone and near-wall zone. The results showed a great increase for the morning event in summer with almost 90% of residual pollutant concentrating in these regions. In contrast, the winter condition showed a worst air quality with 75% of residual pollutant persisting in all inhabitant zones during the night event. These peaks indicate that the natural ventilation during summer morning and winter night is poor, and they are worst time slots for residents.

Through comparing the localized pollutant concentration (Fig. e1.61B and C) with the combined results (Fig. e1.61A), it is found that majority of the residual pollutant in winter night (65%) was accumulated in the near-ground zone due to weak ground ventilation. However, no apparent pollutant concentration differences were observed in near-wall zones for the summer condition.

Review Questions:

- Should wall functions be used for this type of case studies?
- How many layers should be used in the boundary layers?
- How the energy conservation was solved in this study (temperature-based, enthalpy-based, etc.)?

- Which solver should be used when buoyancy effect is considered?
- In terms of the requirements of the turbulence model, what's the threshold of the first-layer thickness?

Explore Questions:

➢ If gaseous emissions as CO_2 or SO_2 are concerned, which model should be adopted?

➢ If this numerical model is adopted for environment analysis under instantaneous ambient wind condition, what improvement should be made?

e1.3.7 Underground Thermal Performance of the Ground Heat Exchangers

Wenxin Li
RMIT University

e1.3.7.1 Case Introduction

As a renewable application in heating, ventilation, and air conditioning (HVAC) systems, the ground-source heat pump (GSHP) system can capitalize the geothermal energy to heat up or cool down buildings efficiently. Fig. e1.62 shows a typical vertical GSHP system, which generally consists of the distribution system, the heat pump unit, and the ground heat exchangers (GHEs) embedded in the soil, where water serves as the working fluid. When the system is working on a cooling mode, heat is collected from the building and then injected into the soil via the GHEs. On the contrary, heat is extracted from the soil and delivered to the building when the system is working on a heating mode. The vertical GHEs consist of two small-diameter U-tubes ranging from 20 to 40 mm nominal diameter, placed in a vertical borehole that is

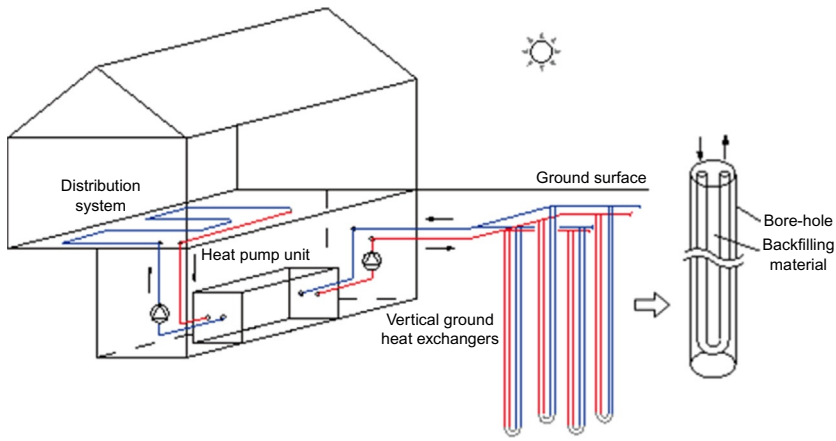


FIG. e1.62 Configuration of a typical vertical GSHP system and GHEs.

subsequently filled with backfilling material. The bore depths range from 15 to 180 m, and boreholes are typically 100–150 mm in diameter.

e1.3.7.2 Problem Description

As a vital role in the GSHP system, the GHE system was expected to transfer the waste heat load from the buildings to the ground in order to provide an appropriate indoor environment. If not, the system would operate inefficiently and even be paralyzed. Thus, a performance prediction is essential for the system design and assessment. Such heat-transfer efficiency is mainly affected by design parameters such as lengths and layouts and geological factors including ground-stratum structures and geological properties. In order to evaluate the operation performance of the system with the consideration of many influential factors, it is crucial to conduct a GHE model with consideration of the heat/mass transfer. Therefore, this case study aimed to utilize computational fluid dynamics (CFD) as the tool to obtain deep understanding of the underground heat-transfer process.

e1.3.7.3 Simulation

❑ Mesh Setting

The CFD simulation was conducted based on a small GSHP system, which consists of an 18.3 m-length GHE. To simplify the calculation, only half of the GHE was built in the CFD model with a computational domain of $1.826 \times 0.9 \times 18.32$ m. The model was discretized combining the structural and tetrahedral mesh in ANSYS Meshing, as shown in Fig. e1.63. As most

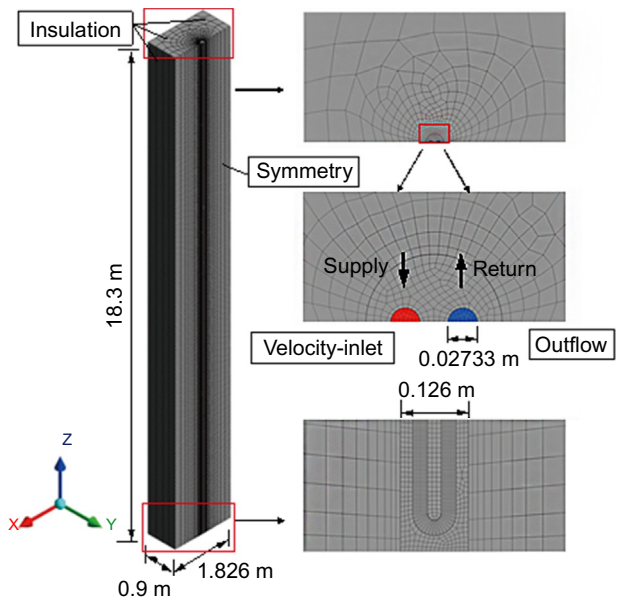


FIG. e1.63 Grid mesh of the computational model with boundary conditions.

TABLE e1.15 Mesh-Independency Study

Tube-Edge Size (m)	Borehole-Edge Size (m)	Element Number	Outlet Temperature (°C)
0.01	0.02	245,789	310.78
0.008	0.01	336,159	309.84
0.004	0.008	471,098	309.86
0.003	0.006	903,494	309.86

domains are solid and have a relative large dimension range, the mesh refinements were placed at the near-wall regions of the water tube and borehole. Prior to performing CFD simulations, grid-independency study was conducted. As listed in Table e1.15, once the mesh elements exceed 471,098, the water outlet temperature becomes stable. Considering the computational efficiency and accuracy, mesh with element numbers of 471,098 was used for further simulation in this study.

❑ Boundary conditions

Besides one wall of the soil domain was set as symmetry, the other sidewalls were set as adiabatic condition (Fig. e1.63). Thermal properties were assumed homogeneous for each material, and their initial temperature was identical and equal to the ground temperature.

The boundary conditions of the tube inlet and outlet are set as velocity inlet and outflow, respectively. At the time step t, water leaves the GHE with a temperature of T_{out} (t) and then absorbs the waste heat from the building, and the temperature is elevated to T_{in} (t). With water circulating in underground tubes, the absorbed heat is transferred into the ground as Q_g, and the water temperature reaches a new value of T_{out} $(t + 1)$, which serves as the starting temperature in the next time step of $t + 1$. Thus, the relationship between the inlet and outlet temperatures can be connected by

$$T_{in}(t) = T_{out}(t+1) + \Delta T(t) = T_{out}(t+1) + \frac{Q_g}{C_W \rho_W V_W} \tag{e1.1}$$

where C_W, ρ_W, and V_W represent the specific heat capacity, density, and volumetric flow rate of water.

In this case, to mimic a cooling situation, a slight heat load was inputted in the first minute, and a constant heat load of 1056 W was inputted continuously for 3 days, which serve as Q_g. Thus, the temperature difference between the GHE inlet and outlet is 0.08444°C for the first minute and 1.22°C for the rest. Eq. e1.1 serving as the water-temperature boundary condition was imposed at the water inlet via user-defined file (UDF), and the file was attached as appendix in the format of c file. First, the water temperature inlet was set with constant

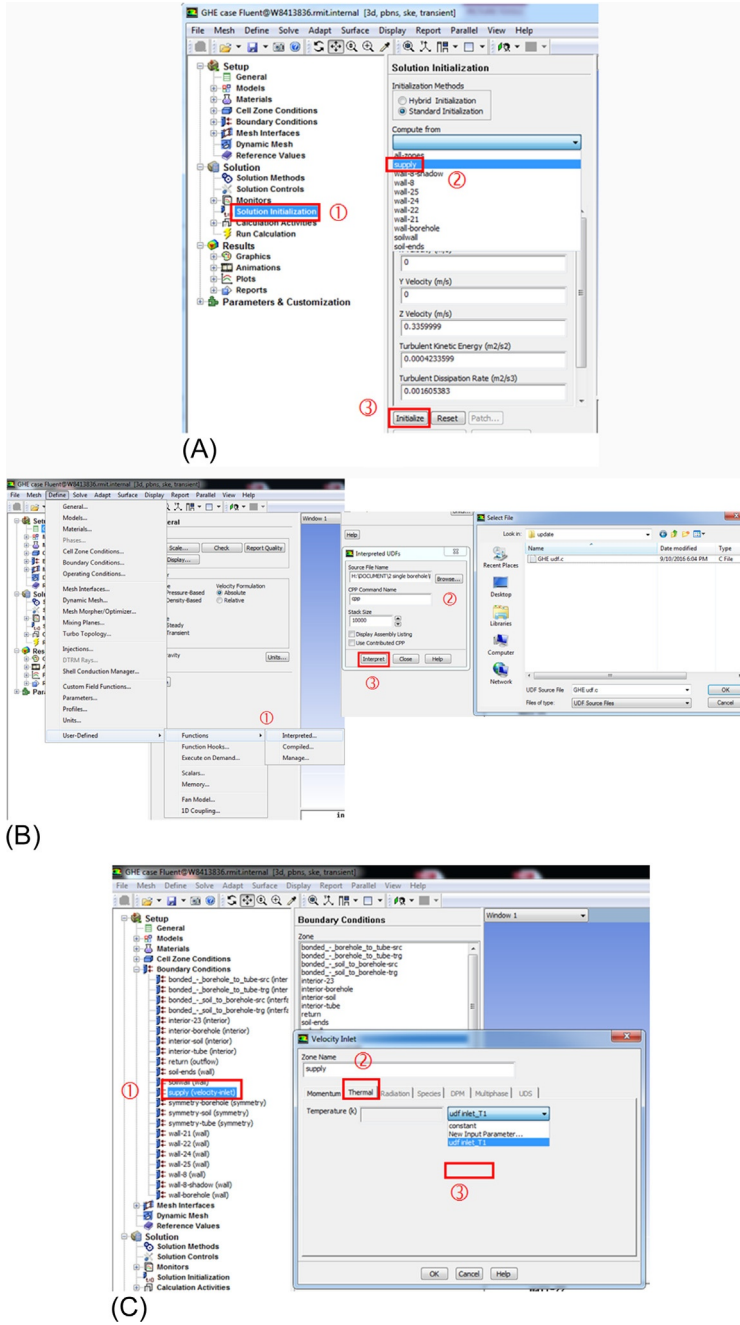


FIG. e1.64 Boundary-condition settings in Fluent: (A) initialization, (B) inputting UDF, and (C) velocity inlet.

initial temperature of 22°C, and after the initialization (Fig. e1.64A), the UDF was inputted (Fig. e1.64B), and the velocity inlet of the water inlet was set with the temperatures from UDF (Fig. e1.64C). Fig. e1.64 shows the process of inputting the UDF and changing the inlet boundary condition.

e1.3.7.4 CFD Results and Discussion

The CFD model of this study was based on governing equations of fluid flow and transport principles for incompressible turbulent flow in terms of mass, momentum, and energy-conservation equations; equations for turbulent kinetic energy and turbulent dissipation rate were solved with standard k-ε closure scheme. All governing equations were solved by using the commercial CFD code ANSYS-Fluent (ANSYS, NH, the United States). Unsteady simulation with a time step of 30 s was performed to predict the 72 h operating performance of GHE system. Convergence was achieved in every time step.

❑ Water Temperature Analysis

As the inlet and outlet temperatures are vital to the system operation, predictions of the inlet and outlet GHE water temperatures are shown in Fig. e1.65. Both the temperatures climb drastically at the beginning 30 h and then varied smoothly. The temperature was predicted to climb over 35°C in the first 4 h, which means the system starts to operate less efficiently than the expectation. For most commercially available heat-pump units, once the temperature of water flowing out of the GHE climbs over 40°C, the units would automatically shut down as a protective measure. The outlet temperature was predicted to rise over 40°C after 31 h, which indicates that the system would encounter the shutdown problem.

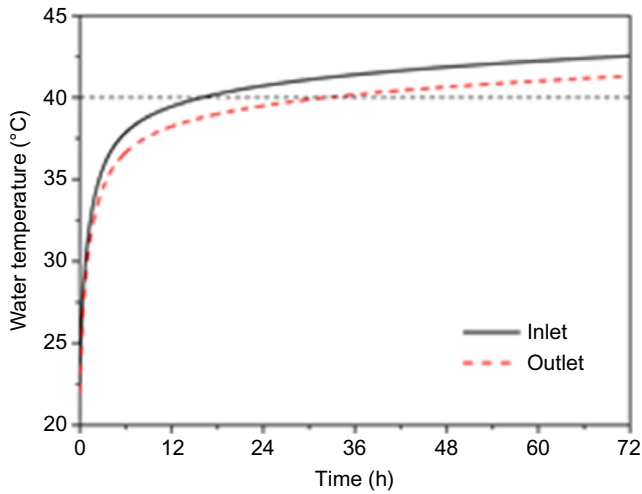


FIG. e1.65 The temperature variation of the inlet and outlet GHE water during a 72 h operation.

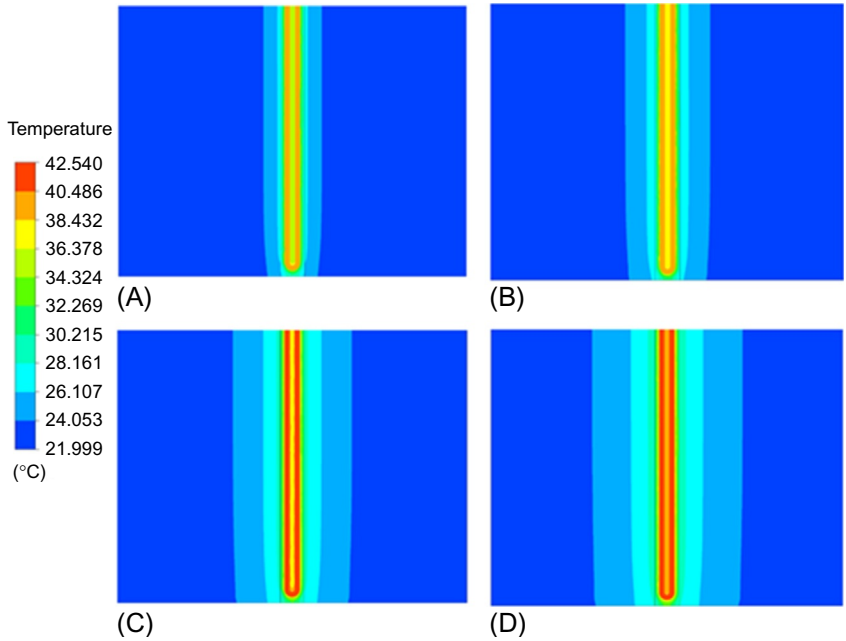


FIG. e1.66 The temperature distribution at the end of the GHE across Y plane ($y = 0.9$ m) over the 72 h operation. (A) $t = 12$ h. (B) $t = 24$ h. (C) $t = 48$ h. (D) $t = 72$ h.

❑ Temperature Distribution

Fig. e1.66 shows the temperature distributions at the end of the GHE. The fluid has the highest temperature and then follows the surrounding grout and soil. The temperatures of fluid and grout increased with the time, and as more heat was injected, 0.4 m outside the GHE was affected by the end of 72 h operation. The temperature varied slightly along the depth of the GHE due to a turbulent flow within the tubes. It should be noticed that the return water would be affected by the supply one, as the grout temperature amidst the two tubes also increased and became much higher than the surrounding grout on the other side.

The radial temperature distributions over 72 h are shown in Fig. e1.67. The temperature decreased in the radial direction from the tubes to the surrounding soil. Over the 72 h operation, the temperatures of the water and grout rose to over 42 and 30°C, respectively. With a slightly higher temperature, more surrounding soil outside the supply water was affected.

In all, for the system with one GHE, the heat-pump unit was predicted to operate less efficiently in the early 4 h and even shut down around 31 h, which definitely cannot meet the system design requirement. To satisfy the heating demand from the building, the GHE should be lengthened, or one more GHE should be added. If multiple GHEs are considered in the system, special attention should be paid to the distances between the GHEs, which should be far enough to guarantee an efficient heat-transfer process.

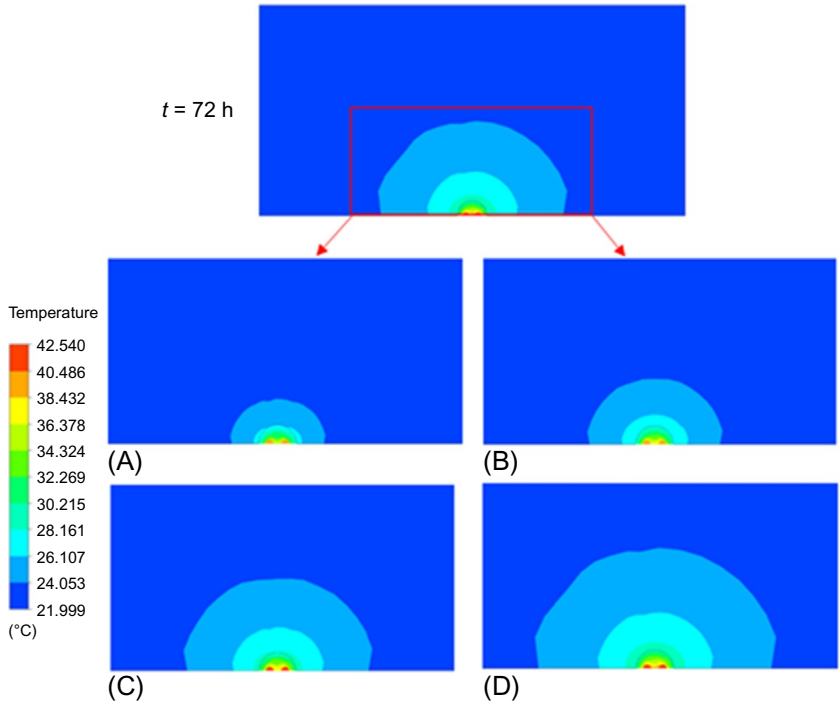


FIG. e1.67 The temperature distribution at the depth of 9.16 m over the 72 h operation. (A) $t = 12$ h. (B) $t = 24$ h. (C) $t = 48$ h. (D) $t = 72$ h.

Review Questions:

- What kinds of boundary conditions can be used to save the computational cost?
- How would you input the varied temperature though the boundary condition?
- To consider a constant heat flux imposed in the GHE, why do we impose the heat flux with a temperature difference rather than using the constant heat-flux boundary condition?
- What kinds of modifications should be added to the design of this case to enhance the efficiency?

Exploratory Questions:

➢ If the inputted heat load changed with time to consider both the cooling and heating modes, what should be done in the UDF to obtain the simulation results?

➢ If there is a large GHE filed with hundreds of GHEs, how to compose the UDF and add the boundary conditions?

➢ Since the main domains are solid, is it possible to simplify the model with ignorance of the fluid domain? And what about the accuracy?

e1.3.8 Bubble Behaviour and Size Distribution in a Continuous Casting Mould

Zhongqiu Liu
Northeastern University

e1.3.8.1 Case Introduction

Continuous casting (CC) has been widely accepted as the most important production process in the steel industry. In the casting process, molten steel from the ladle flows through the tundish into a mould. Within the mould, the molten steel freezes against the water-cooled copper mould walls forming a solid shell. Argon gas is injected into the molten steel that enters into the continuous casting mould through the submerged entry nozzle (SEN). After the SEN, due to intense shear forces exerted by molten steel, the argon gas disintegrates into swarm of bubbles with different diameters. As illustrated in Fig. e1.68, large bubbles have the tendency to escape from the liquid steel surface through the mould flux power layer, whilst smaller bubbles follow the main stream of molten steel flowing deep into the mould cavity. However, these small bubbles and non-metallic inclusions adhering to the surface of these bubbles may be entrapped

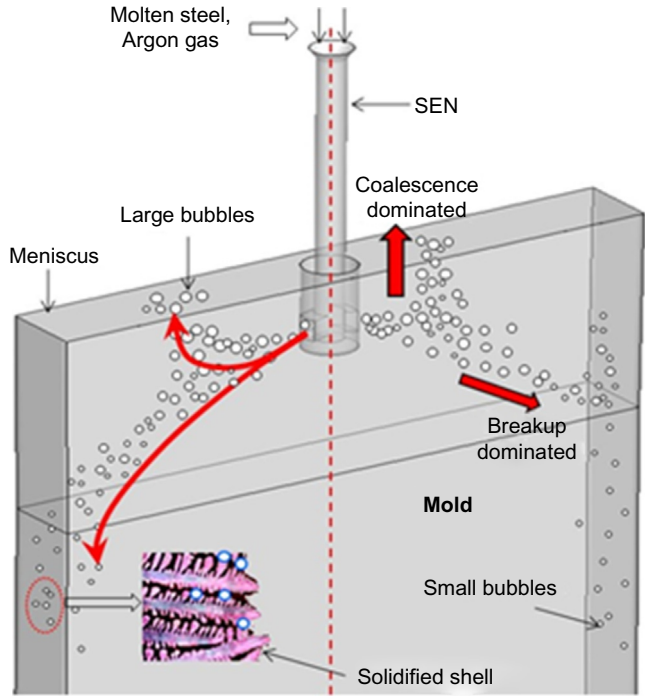


FIG. e1.68 Typical bubble motion in the continuous casting mould.

by solidified shell, forming defects in the final product, such as slivers, blisters, and other costly defects. In order to improve the quality of the final steel products, it is crucial to gain an in-depth understanding of the structure characteristics of molten steel-argon gas two-phase flows and the characteristics of bubble-size distribution and its related defects in the current continuous casting process.

e1.3.8.2 Problem Description

Owing to the importance of bubble size in two-phase flows, the predictions of argon bubble-size distribution become very important to understand the underlying physics and hydrodynamic in the continuous casting mould. Recently, the application of the population balance approach towards better describing complex bubbly flow inside the mould has received an increasing attention. The multiple-size group (MUSIG) model provides a framework in which the population balance equation can be incorporated into the generic computational fluid-dynamics solution procedures. Rather than prescribing a dispersed phase size as in the standard Eulerian treatment, the MUSIG model allows us to predict a mean bubble size based on fundamental considerations of coalescence and breakup mechanism. The evolution of the bubble-size distribution is determined by the relative magnitudes of bubble coalescence and breakage rates. Since the bubble-size distribution is discretized into multiple bubble class, the MUSIG model is capable to simulate polydispersed multiphase flows in which the dispersed phase features a large variation in its characteristic sizes. Fig. e1.69 shows the discrete bubble groups employed to characterize the multi-size bubbly flow.

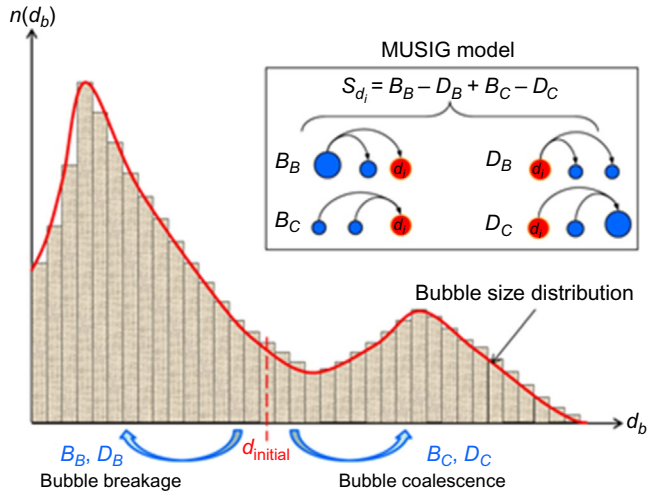


FIG. e1.69 Graphical presentations of the MUSIG model.

e1.3.8.3 Simulation

❑ Model Formation

The population balance model presented in this paper is based on the two-fluid model Eulerian-Eulerian approach. The liquid phase is treated as a continuum, whilst the gas phase is considered as dispersed phase. In bubbly flows, interfacial momentum transfer exhibits a dominant effect in the multiphase momentum equations. The total interfacial forces considered can be categorized into five main terms: drag, lift, virtual mass, lubrication, and turbulence dispersion. To account for non-uniform bubble-size distribution, the MUSIG model employs multiple discrete bubble-size groups to represent the population balance of bubbles. For bubble breakup, the Luo and Svendsen model is used to account for the so-called daughter bubble-size distribution, which is the size distribution of the fragments formed by the breakage process. The rate of bubble break in the flow is determined by examining the interaction of bubbles with turbulent eddies. Bubble coalescence would occur via collision of two bubbles that may be caused by wake entrainment, random turbulence, and buoyancy. However, only random turbulence collision is considered in the current work. The coalescence rate considering the turbulence collision is taken from Prince and Blanch model. The model proposed by Sato has been used to account for the turbulence induced by the movement of the bubbles. Fig. e1.70 shows the procedure details of solution methodology of this model.

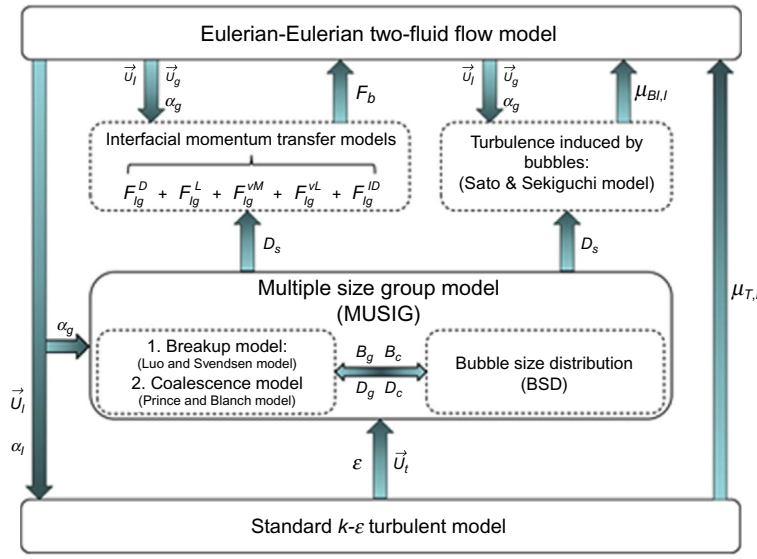


FIG. e1.70 Flow chart of solution methodology of this model.

❑ Numerical Details

The CFD code ANSYS-CFX was utilized to handle two sets of equations governing conservation of mass and momentum. The discrete bubble sizes prescribed in the dispersed phase were further tracked by solving additional transport equations, where these equations were coupled with the flow equations throughout the simulations. Sensitivity study on the number of size groups was performed through the consideration of equally dividing the bubble diameters into 5, 10, and 15 size groups, as shown in Fig. e1.71. The analysis revealed that no appreciable difference was found for the predicted maximum bubble Sauter diameter between the 10 and 15 bubble-size groups. In the view of computational resources and times, it was therefore concluded that the subdivision of the bubbles sizes into 10 size groups was deemed sufficient, and the following computational results are all based on the discretization of 10 bubble-size groups.

Due to the symmetry of the structure and reducing the computational cost, only a quarter of the actual mould was modelled, as shown in Fig. e1.72. A mass-flow boundary was set at the water inlet of the SEN based on the casting speed. A mass-flow boundary was set at the air inlet of the SEN; because the diameters of the injected bubbles were unknown, uniformly distributed bubble size was specified in accordance with the flow conditions, and all bubbles enter into the SEN with an initial bubble diameter of 1 mm.

The density of air is used with a constant density considering the conditions of pressure and temperature at the SEN port. A constant pressure-outlet condition at the bottom of the calculation domain is applied. The top surface of the mould cavity is modelled as degassing boundary condition, where dispersed bubbles are permitted to escape, but the liquid is not. Along the walls, wall functions are applied for standard k-ε model, whilst non-slip boundary condition is adopted. The velocity-pressure linkage was handled through the SIMPLE procedure. The hybrid-upwind discretization scheme was used for the convective terms. A fixed physical timescale of 0.001 s was adopted for all steady-state simulations.

e1.3.8.4 CFD Results and Discussion

❑ Gas Volume Fraction Analysis

Fig. e1.73A–D shows the effect of bubble size on the gas volume-fraction distribution inside the mould, which is obtained from the mono-size model. The bubble size is considered as 0.5, 1.0, 2.0, and 3.0 mm, respectively. A comparison between Fig. e1.73A and D clearly shows that smaller bubbles exhibited a more dispersed pattern and have a tendency to penetrate further across the mould. Subjected to stronger buoyancy forces, large bubbles show a less dispersed pattern and quickly float towards the water surface. Fig. e1.73E shows the predicted gas volume-fraction distribution inside the mould obtained from the MUSIG model that is used to validate against the measured bubble distribution obtained from the water model experiment. The predicted outlines of the

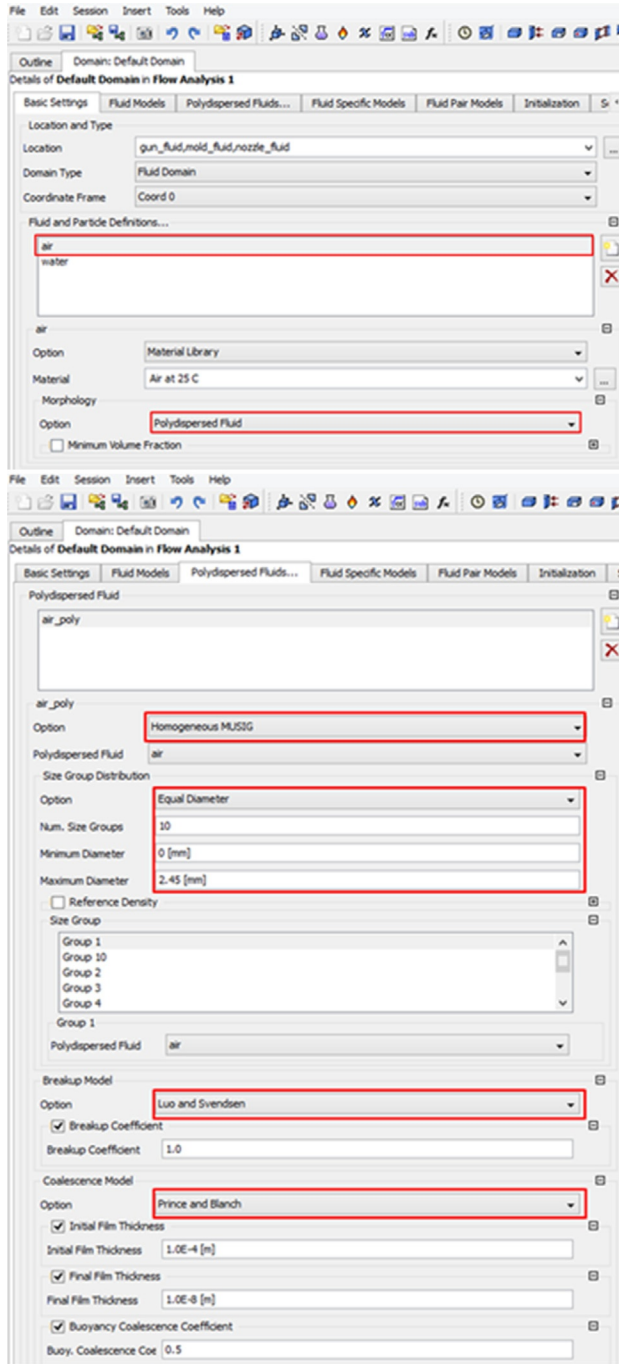


FIG. e1.71 MUSIG model settings in CFX.

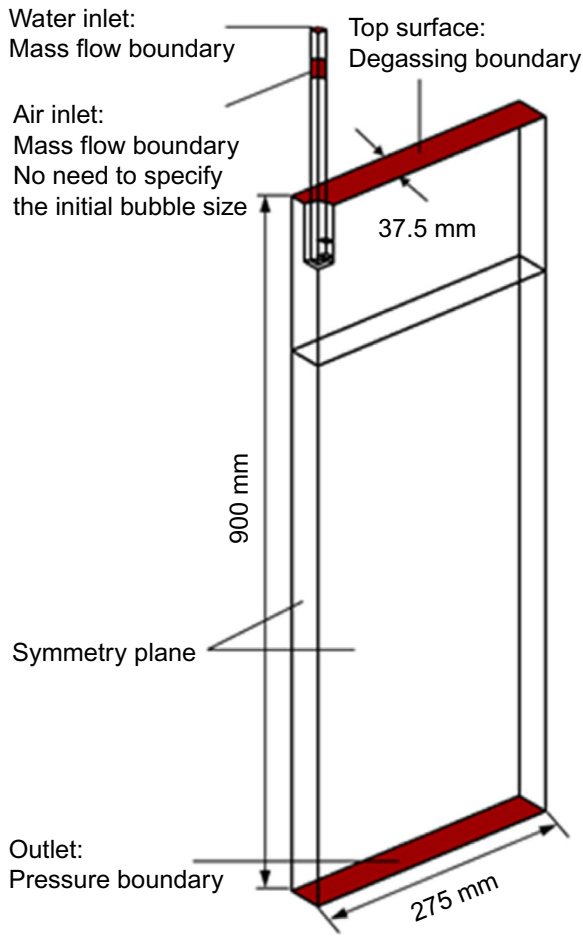


FIG. e1.72 The calculation domain and boundary conditions.

volume fraction are in satisfactory agreement with the measurement of water model experiment. After entering the mould with the water jet, most bubbles were concentrated at the vicinity of the SEN and float upwards through the upper recirculation zone and escape from the top surface sequentially. One may also notice that the maximum volume fraction exceed 0.2 in some locations. Meanwhile, some of the small bubbles may penetrate further across the upper recirculation zone and migrated to the middle of wide face.

❑ Flow Pattern Analysis

Gas injection affects the casting process in part through its influence on the liquid flow pattern. The extent of this effect depends on both the gas flow rate and the bubble size. The huge effects of gas flow rate and bubble size on the flow

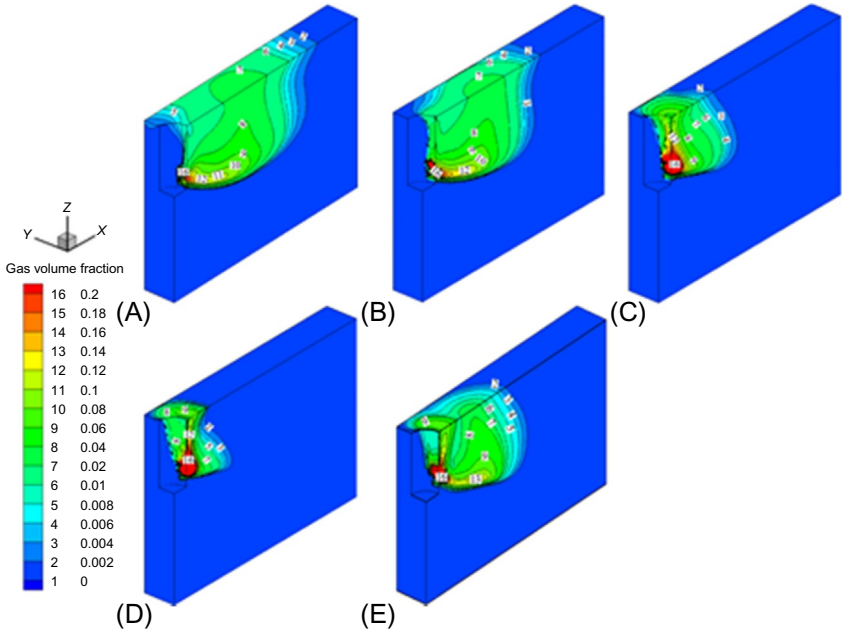


FIG. e1.73 Gas volume fractions in the mould with different bubble sizes (A, B, C, and D are 0.5, 1.0, 2.0, and 3.0 mm) and MUSIG model (E).

pattern in the mould have been studied in many previous works. The influence of the gas injection on the fluid flow pattern can be seen in Fig. e1.74A; it can be seen that part of fluid (upjet) moved up towards the top surface after leaving the SEN port; another part of fluid continues as a down-jet impinges at a slightly higher location on the narrow wall, forming a recirculation flow after the down-jet impinges on the narrow wall. Fig. e1.74B and C illustrates the fluid flow pattern predicted numerically using single-size Euler-Euler model with 0.5 and 3 mm bubble, respectively. Smaller bubbles (0.5 mm) can penetrate further across the mould and closer to the narrow face and have greater influence on the liquid flow pattern, but there is not recirculation flow from the down-jet, as shown in Fig. e1.74B. Larger bubbles (3 mm) are predicted to leave the mould more quickly and closer to the SEN and therefore have less influence on the liquid flow pattern, as shown in Fig. e1.74C. Both the two figures cannot represent the flow pattern obtained from water model. Fig. e1.74D shows the flow pattern in the mould obtained from the MUSIG model. It can be seen that the flow pattern in the upper recirculation zone is similar to the flow pattern observed in the water model experiment. Part of the jet flows upwards to the top surface when exiting the SEN port; another part of the fluid continues as a jet impinges on the narrow wall and then forms a recirculation flow. So, the prediction of bubble-size distribution in the mould is essential for more

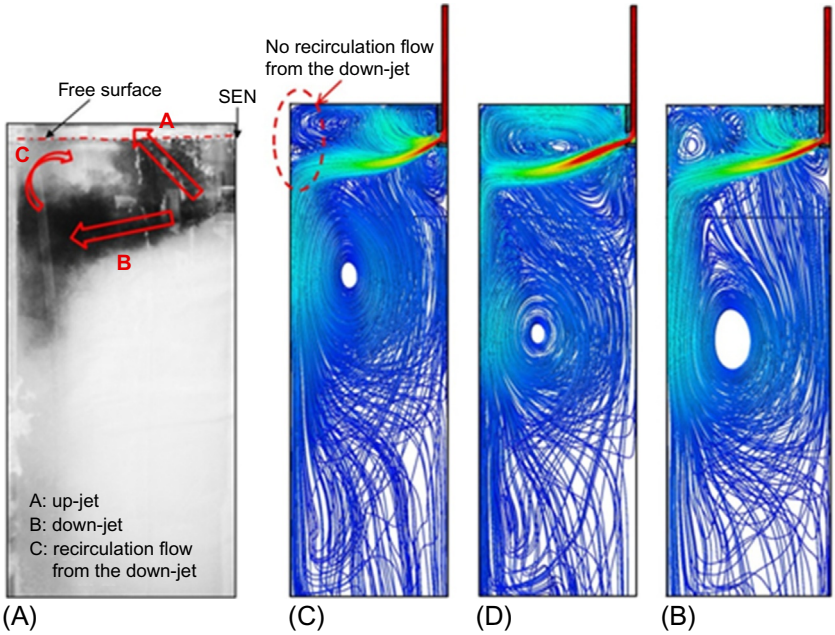


FIG. e1.74 Velocity-vector field across *Y* plane for isothermal and thermal case, (A) E-E 0.5 mm bubble, (B) E-E 3 mm bubble, (C) MUSIG model.

accurate understanding of multiphase fluid flow behaviour in the continuous casting process.

❑ Bubble Size Distribution Analysis

The predicted bubble Sauter mean-diameter distribution inside the SEN and mould is shown in Fig. e1.75, where the water and gas flow rate were 19 and 1.6 L/min, respectively. From the figure, it can be seen that the bubble diameter at the centre of SEN is larger than 2 mm. These large bubbles are then broken up into various smaller bubbles at the bottom of the SEN. According to the adopted bubble breakup model of Luo and Svendsen, bubble breakup can be expected in regions with high turbulent kinetic energy. The predicted maximum values of the turbulent kinetic energy are located at the bottom of the SEN. Furthermore, almost all bubbles in front of SEN port are <1.2 mm, indicating that the behaviour of bubble breakage is dominated at the bottom of the SEN. After escaping from the SEN port, large bubbles rise closer to the SEN due to enhanced buoyancy and drag forces, whilst smaller bubbles are carried deeper into the mould by the fluid jet. Along the bubble transport from the SEN port to the top surface, due to the effect of hydrostatic pressure and bubble coalescence, the diameters of bubbles would increase gradually. However, during the process of bubble transport from the SEN port to the narrow wall of the mould, high shearing force of fluid jet decreases the sizes of bubbles. In summary, the

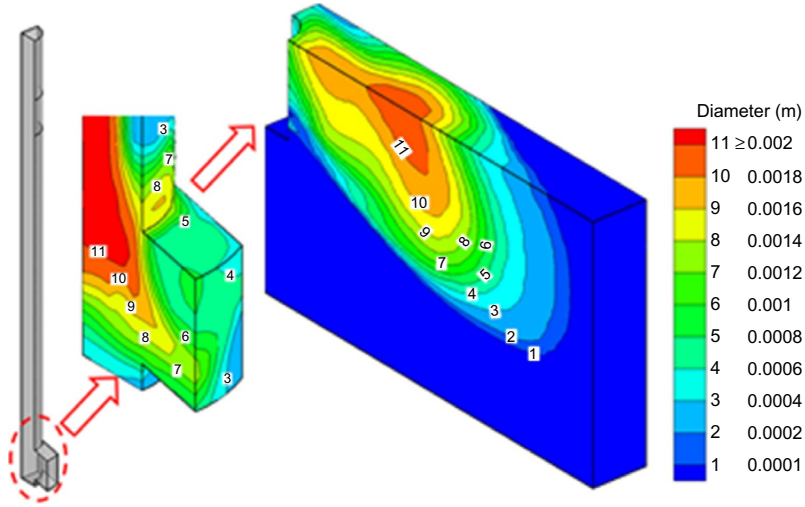


FIG. e1.75 Predicted bubble Sauter mean-diameter distribution inside the mould.

coalescence of bubbles is dominated during the bubbles rising to the top surface, and the breakage of bubbles is dominated during the bubble transport with the jet to the narrow wall.

Fig. e1.76 illustrates the predicted and measured bubble mean-diameter distributions at a constant gas injection rate (1.6 L/min) with different water flow rates (15, 19, and 21 L/min) along the centreline at 25 mm below the top surface. These results show a satisfactory agreement between predicted bubble

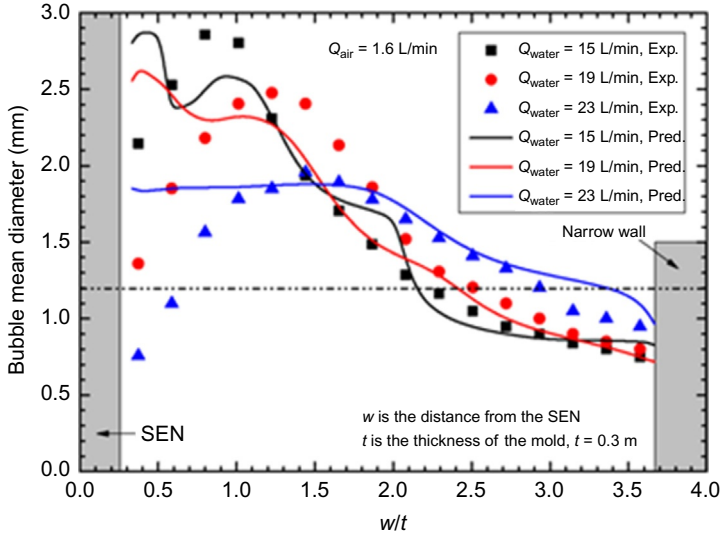


FIG. e1.76 Predicted bubble Sauter mean diameter with different water flow rates.

Sauter mean diameters and measured mean bubble sizes. Large bubbles are formed close to the SEN where highly concentrated bubbles having greater possibility to coalescence form bigger bubbles. Smaller bubbles are migrating towards the narrow wall of the mould. Due to the bubble sizes escaping from the SEN port being smaller than 1.2 mm, for water flow rate (19 L/min), the coalescence process of bubbles is prominent between $w/t = 0.3$ and 2.5 distance from the SEN. The net effect of bubble coalescence encourages the formation of larger bubbles after flowing out of the SEN ports. As the water flow rate increases, for a given gas flow rate, the bubble sizes in the width of the mould are distributed more uniformly. The maximum sizes of bubble are reduced slightly, and the position of maximum size moves towards to the narrow wall of the mould.

For two-phase flow inside the mould, another important operating parameter is the gas flow rate. Argon bubbles alter the flow pattern in the upper recirculation zone in proportion with increasing gas fraction, shifting the impingement point and recirculation zones upwards. Fig. e1.77 illustrates the predicted and measured bubble mean-diameter distributions at a constant water flow rate (21 L/min) with different gas flow rates (0.8, 1.6, and 2.4 L/min) along the centreline at 25 mm below the top surface. Stronger buoyancy due to the introduction of more bubbles not only changes the flow pattern to a larger extent but also increases the probability of bubble coalescence. The maximum size of bubbles is located approximately at $w/t = 1.25$ distance from the SEN when the argon gas flow rate is of 0.8 L/min. As the gas flow rate increases, with the same water flow rate, the maximum sizes of bubble increase gradually, whilst the position of maximum bubble sizes remains almost unchanged.

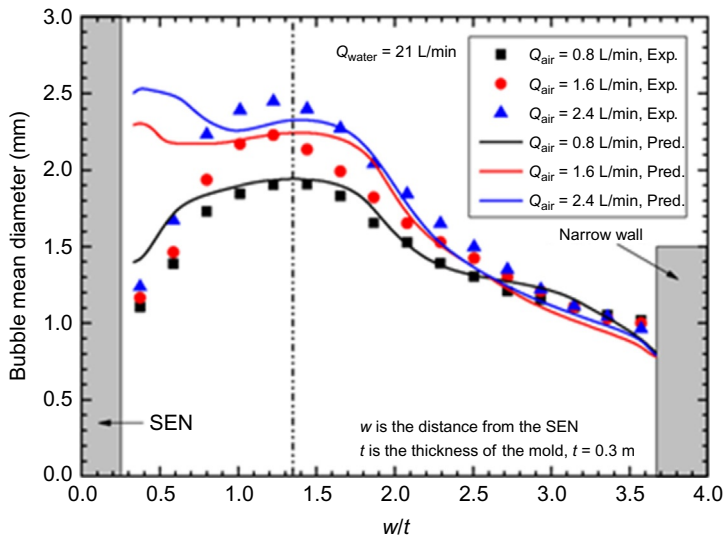


FIG. e1.77 Predicted bubble Sauter mean diameter with different gas flow rates.

Review Questions:

- What model can be used to simulate polydispersed multiphase flows with a large variation in its characteristic sizes?
- How many interfacial forces can be used in the Euler-Euler approach?
- What are the other approaches to model the bubble breakup and coalescence?
- What are the behaviours of bubble breakup and coalescence inside the mould?
- What are the differences between the homogeneous MUSIG and inhomogeneous MUSIG?

Explore Questions:

➢ There are at least four other factors that have not been discussed in the present work, which are worthy of further discussion:
  - The effect of the interfacial momentum transfer between gas and liquid
  - The bubble-induced turbulence flow
  - The effect of different breakup and coalescence model on the population balance of bubbles
  - The effect of surface waves at the top surface

e1.3.9 Influence of Back Pressure on the Steam Ejector Performance

Guangli Zhang
Northeastern University

e1.3.9.1 Case Introduction

With the global energy problem becoming more and more serious, the development and utilization of industrial-waste heat and solar energy and other heat-source equipment are particularly important. Steam-jet refrigeration system is one of the representatives. The steam ejector is a low-vacuum pump that carries the secondary gas by means of a high-speed jet of water vapour to obtain a certain degree of vacuum in pumped container. Schematic diagram of the structure and flow characteristics of the steam jet pump is shown in Fig. e1.78. Because the ejector utilizes low-grade thermal energy from inexpensive or even free sources and uses water, the most environmentally friendly substance, as its working fluid, its irreplaceable status has been focused by researchers for a long period. Especially in today's increasingly energy-saving and environmental-protection society, carrying out further research about steam ejector is even more necessary. However, because of the relatively low entrainment ratio and the complicated nature of flow structure and mixing process within a steam ejector, traditional theoretical and experimental research methods could not clearly describe these complications and give good determination and limit the development of the steam ejector largely.

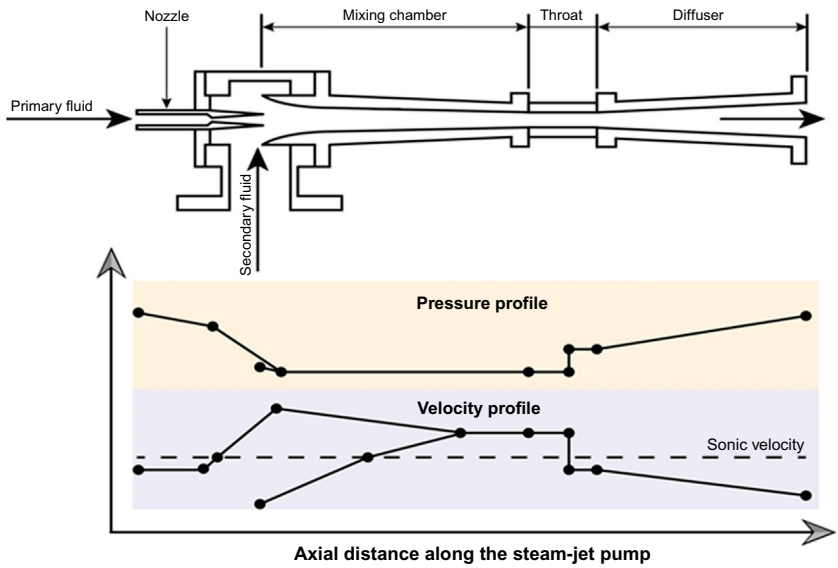


FIG. e1.78 Steam-jet pump structure and the internal flow characteristics.

In this case, numerical simulation method was used to simulate the internal flow of steam ejector by means of Fluent software platform. The influence of different operating parameters on the pumping performance of ejector was investigated, from the perspective of changes in the structure of the flow field to study the relationship between the operating parameters and the ejector performance, thus ensuring the stability of the ejector and improving the pumping performance of the ejector.

e1.3.9.2 Problem Description

The pumping performance of the steam ejector is mainly reflected in two aspects; one is entrainment ratio (the ratio of the mass flow rate of the secondary fluid to the mass flow rate of the primary fluid). The higher entrainment ratio leads to enhanced carrying capacity of the primary fluid and improved pumping performance. The other is critical pressure; when the back pressure is lower than critical pressure, the entrainment ratio is unchanged; therefore, the higher the critical pressure is, the more stable operating system becomes, and the lower the foreline pump requires. The pumping performance of ejector is influenced by the operating parameters; among them, the back pressure is a key factor affecting performance of ejector. In this case, the change law of entrainment ratio of ejector is researched by altering the back-pressure parameters of ejector. Then, the intrinsic cause of the change of the pumping performance is investigated by analysing the variety of the typical structure of the internal flow field of ejector. Fig. e1.79 describes the internal field structure of the steam ejector in

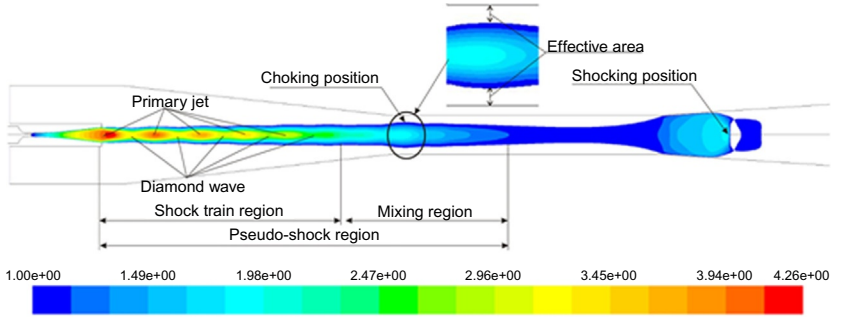


FIG. e1.79 The internal flow structure of the ejector.

which the choking phenomenon and the shock wave phenomenon directly affect the pumping performance of the ejector. The size of the effective area at the choking position and the mass flux of the secondary fluid influence the entrainment ratio; chocking position and strength affect the critical pressure of the ejector.

e1.3.9.3 CFD Simulation

❑ Geometric Model and Mesh Settings

In this case, the main ejector of the laboratory injection refrigeration system is used as the calculation model. The geometrical parameters of the ejector are shown in Table e1.16. The ICEM CFD meshing tool was utilized to construct

TABLE e1.16 Structure Size of Steam Ejector

Parameters	Size (mm)
Throat diameter of primary nozzle	2.5 mm
Export diameter of primary nozzle	11 mm
Length of primary nozzle throat to export	48 mm
Throat diameter of ejector	28 mm
Length of ejector throat	192 mm
Inlet diameter of mixing chamber	70 mm
Outlet diameter of diffuser	70 mm
Length of the convergent section (mixing chamber)	188 mm
Length of the divergent section (diffuser)	322 mm
Suction diameter of ejector	54 mm



FIG. e1.80 Structured grid of the ejector.

the grid of the ejector. The total number of grid elements initially was 45,344 (Fig. e1.80). In order to improve the accuracy of the calculation results and better capture the shock phenomena of the internal flow field, the mesh is locally intensive by grid-gradient adaptive technique. The number of locally intensive grids is 21,771, and the total number of final grids is 67,115 (Fig. e1.81).

❑ Boundary Conditions

Both the inlets of primary and secondary fluid are set as pressure inlet, and the outlet of ejector is set as the pressure outlet. The water vapour flow rate at the inlet is very low relative to the high-velocity flow in the jet pump, so the water vapour at the inlet is set as saturated stagnation state, that is, the given pressure value is the saturation pressure value; the temperature value is its corresponding saturation temperature value, and the gauge total pressure and initial gauge pressure at the boundary are equal. From the turbulence-intensity formula, $I = 0.16 * Re \wedge (-1/8)$, Reynolds number, the calculated turbulence intensity is about 5%, so the turbulence intensity at the inlet is preset to 5%. The ejector wall is set to non-slip condition, and the near wall is set to the standard wall function; boundary-condition settings in Fluent are shown in Fig. e1.82.

❑ Solve Settings

When it comes to the flow field inside the ejector, the realizable model can predict accurately the propagation velocity of the circular jet. Meanwhile, it displays better performance to predict the vortex and the separation of the boundary layer in the high reverse-pressure gradient than other models.

The solver chooses couple-implicit solver: using central difference discretization for the diffusion terms, utilizing Gauss-Seidel iterative method to calculate the discretization systems, choosing multiple Runge-Kutta explicit

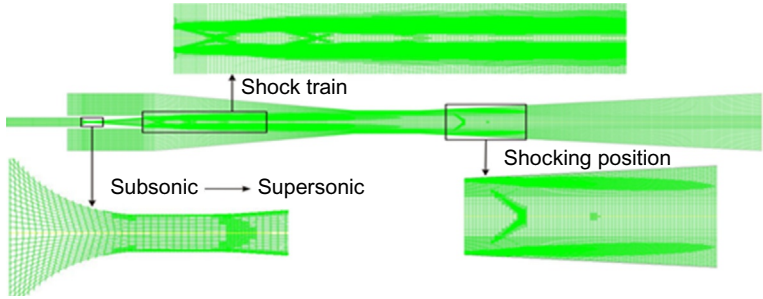


FIG. e1.81 Adaptive grid of the ejector.

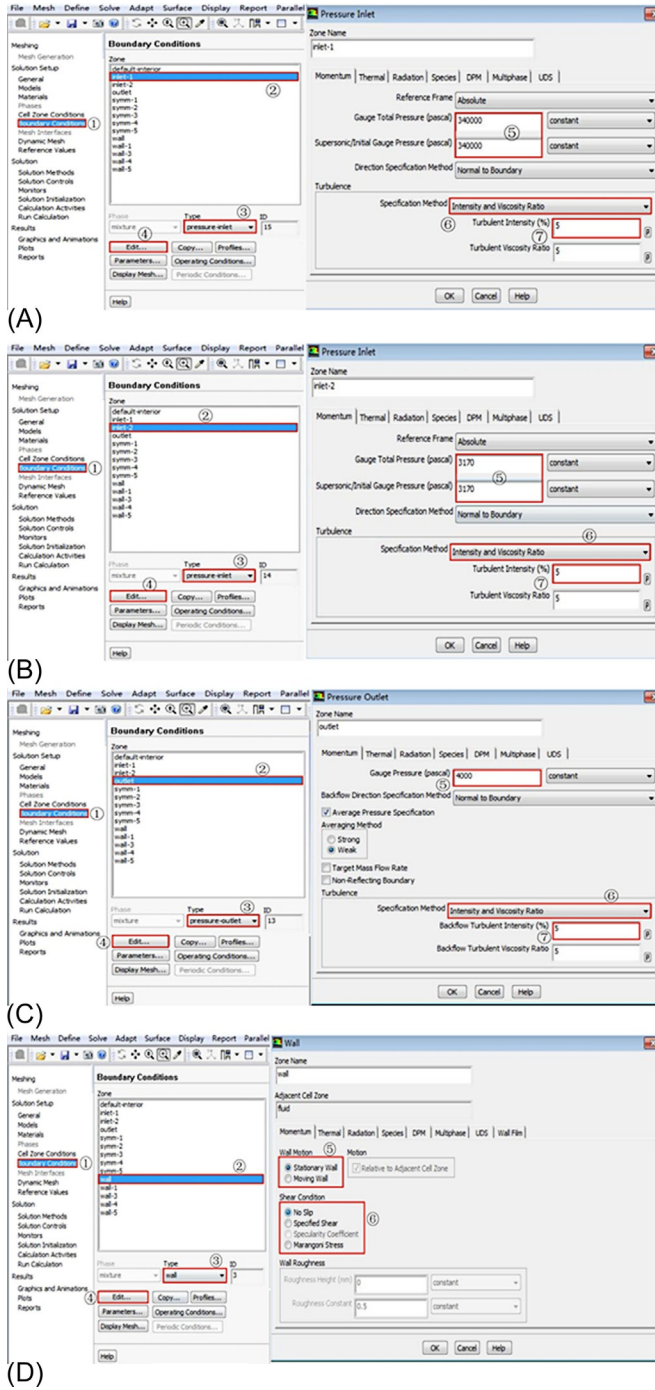


FIG. e1.82 Boundary-condition settings in Fluent. (A) Primary fluid boundary-condition settings in Fluent. (B) Secondary fluid boundary-condition settings in Fluent. (C) Outlet boundary-condition settings in Fluent. (D) Wall boundary-condition settings in Fluent.

iteration format for time discrete iteration, and adopting second-order upwind format to calculate all the convective terms on the basis of the first-order upwind format. The solver method settings in Fluent are displayed in Fig. e1.83.

Iteration termination condition:

(1) All residual items are below the specified value ($<10^{-6}$).
(2) The mass flow rate of both inlet and outlet keeps stability.
(3) The flow difference of inflow and outflow of the ejector is $<10^{-7}$ kg/s.

e1.3.9.4 CFD Results and Discussion

- The influence of back pressure on the pumping performance

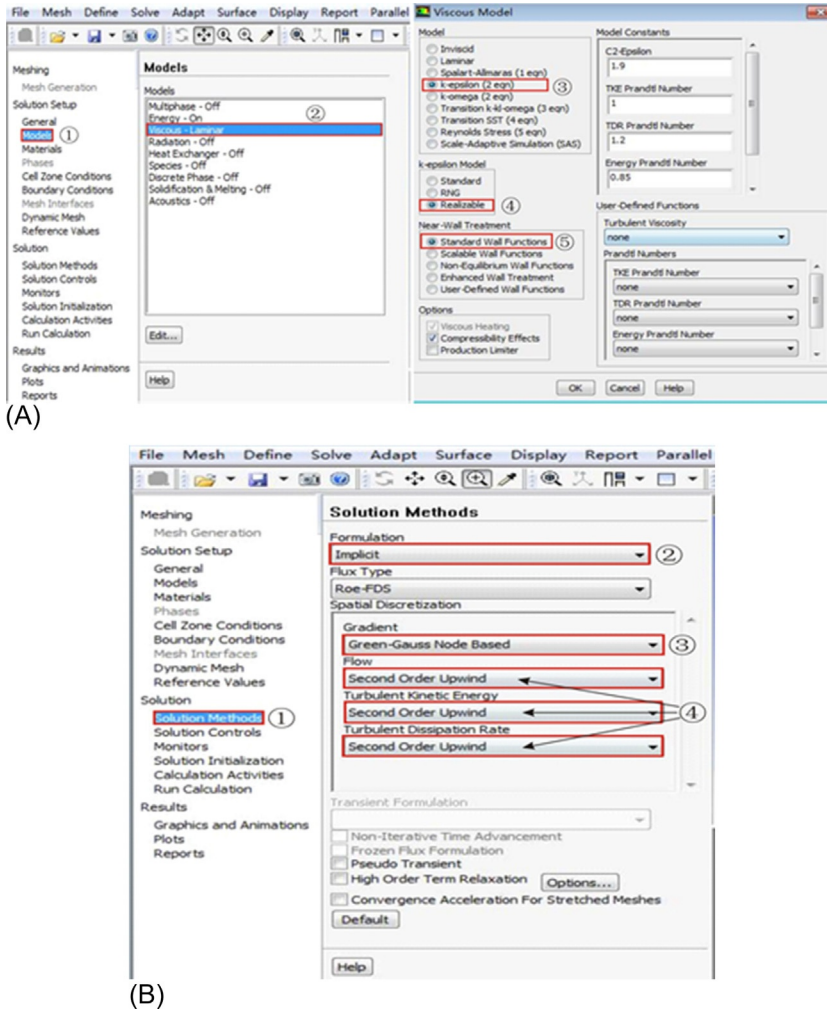


FIG. e1.83 The solver condition settings. (A) The turbulence model settings. (B) The solver settings.

When the primary fluid pressure is 0.34 MPa, the secondary fluid pressure is 3170 Pa; the influence of different back pressures on the entrainment ratio is described in Fig. e1.84. The critical pressure of the ejector is about 5000 Pa; when the outlet back pressure is lower than the critical pressure, the mass flow rate of the secondary and primary fluid does not change; consequently, the entrainment ratio keeps stable. When the outlet back pressure exceeds the critical pressure, the mass flow rate of the primary fluid is unchanged, and the mass flow rate of the secondary fluid decreases with the increase of the back pressure, which results in the decline of the entrainment ratio; when the outlet back pressure is close to 6100 Pa, the entrainment ratio is close to zero.

In order to explain the change of the pumping performance of the steam ejector, the internal flow field of the ejector is investigated. The pumping performance is affected by the effective area and the mass flux (mass flux, mass flow rate per unit area) at the choking position. The contours of Mach number of main fluid under different back pressure are shown in Fig. e1.85; only the flow structure of velocity range above 1 Mach is displayed. With the increase of the back pressure, the position of the shock wave measured at the outlet of diffuser extends to the upstream. In the presence of the shock, the supersonic main fluid prevents the disturbance caused by the back pressure from propagating to the upstream. At this time, the change of the back pressure does not affect the flow pattern and the choking position in the throat of the ejector; the choking position and effective area are unchanged. When the back pressure exceeds 5000 Pa, the relatively high back pressure compresses the main fluid to the throat of ejector; consequently, the choking flow is damaged; the pumping capacity of ejector decreases or is even lost.

Fig. e1.86 displays the mass-flux curve for the near-walled secondary fluid. It can be seen that when the back pressure is lower than the critical pressure (5000 Pa), the mass flux of the ejector is constant, and the effective area at the choking position is the same (Fig. e1.85); therefore, the entrainment ratio keeps stable. When the back pressure is higher than the critical pressure, the mass flux of the ejector is reduced; meanwhile, it can be seen from the mass-flux distribution in the convergent section of the ejector that the higher the back pressure is, the greater the mass flux will be, which indicates that the higher back pressure causes reverse flow for the secondary fluid, resulting in a sharp drop for pumping performance.

❑ The influence of back pressure on boundary layer separation

Fig. e1.87 shows the pathlines of the internal flow field of ejector under different back pressures. It can be seen that the change of back pressure induces different levels of boundary-layer separation. Among them, when back pressure is lower than the critical pressure (5000 Pa), the degree of separation of the boundary layer is small; when it exceeds the critical pressure, the boundary-layer separation is more and more obvious. Fig. e1.88 describes the streamlines of the internal flow field of ejector under different back pressures. As can be seen from

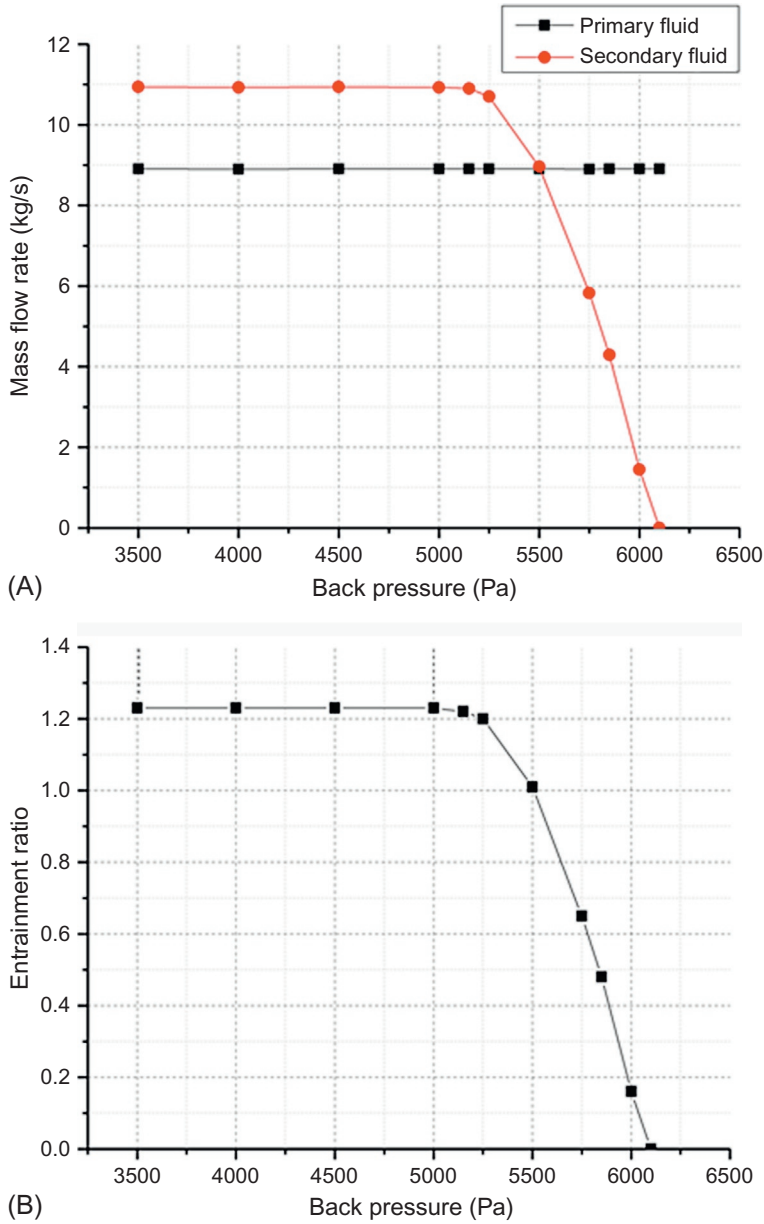


FIG. e1.84 The influence of different back pressure on pumping performance of the ejector. (A) The influence of different back pressure on mass flow rate. (B) The influence of different back pressure on entrainment ratio.

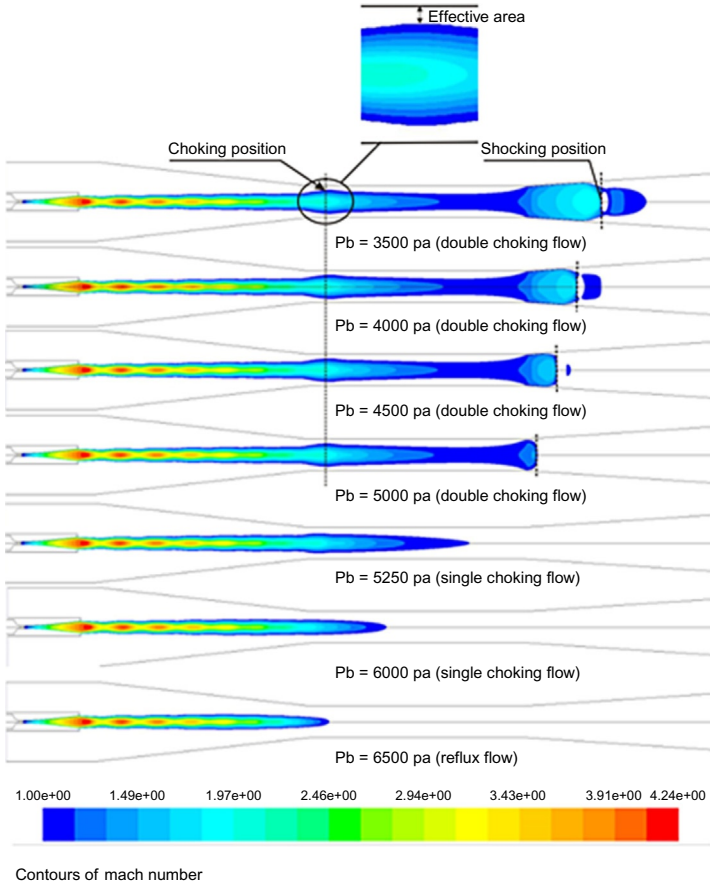


FIG. e1.85 Contours of Mach number of primary fluid with respect on different back pressures.

the figure in the area of boundary-layer separation, there is obvious vortex flow generated. Fig. e1.89 displays the variation of the wall pressure of ejector under different back pressures. It can be seen that when the back pressure is lower than the critical pressure, the near-wall pressure upstream of the chocking position is completely consistent and relatively small, and the degree of separation of the boundary layer is identical and not obvious (Fig. e1.87). When the back pressure is higher than the critical pressure, the static pressure of the wall gradually increases, and the degree of separation of the boundary layer is correspondingly enhanced (Fig. e1.87). In the analysis, the higher pressure-gradient effect leads to the separation of the boundary layer of the secondary fluid and produces a vortex in the area of boundary-layer separation, and this results in a decrease of the effective area for secondary fluid, which causes a sharp drop for the pumping performance of ejector.

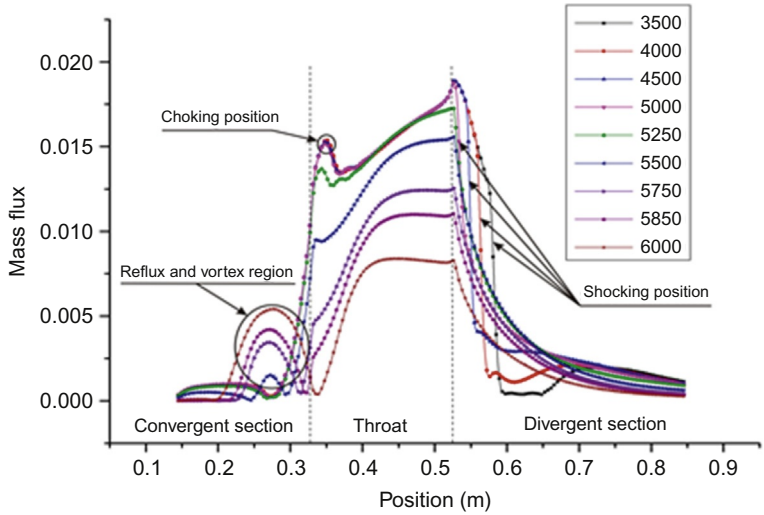


FIG. e1.86 The mass flux of the secondary fluid near the wall under different back pressures.

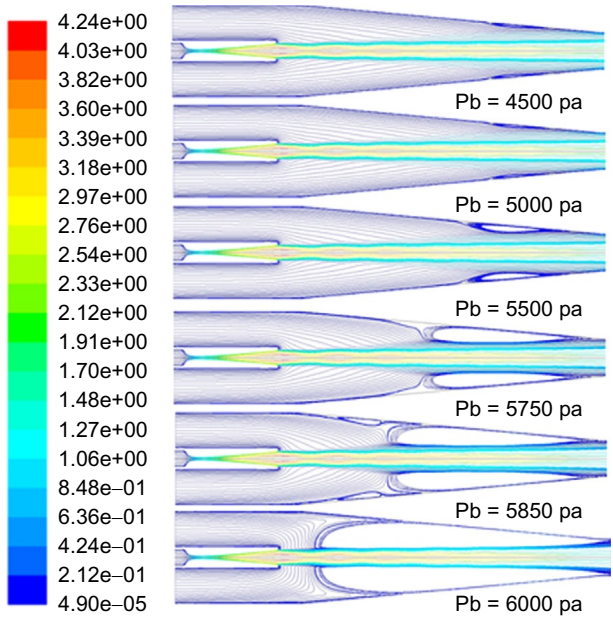


FIG. e1.87 The boundary-layer separation under different back pressures.

Review Questions:

- What are the advantages of grid-gradient adaptation, and what other methods does grid adaption include?
- When setting the boundary conditions, why would the inlet and outlet be set to the pressure inlet and the pressure outlet?

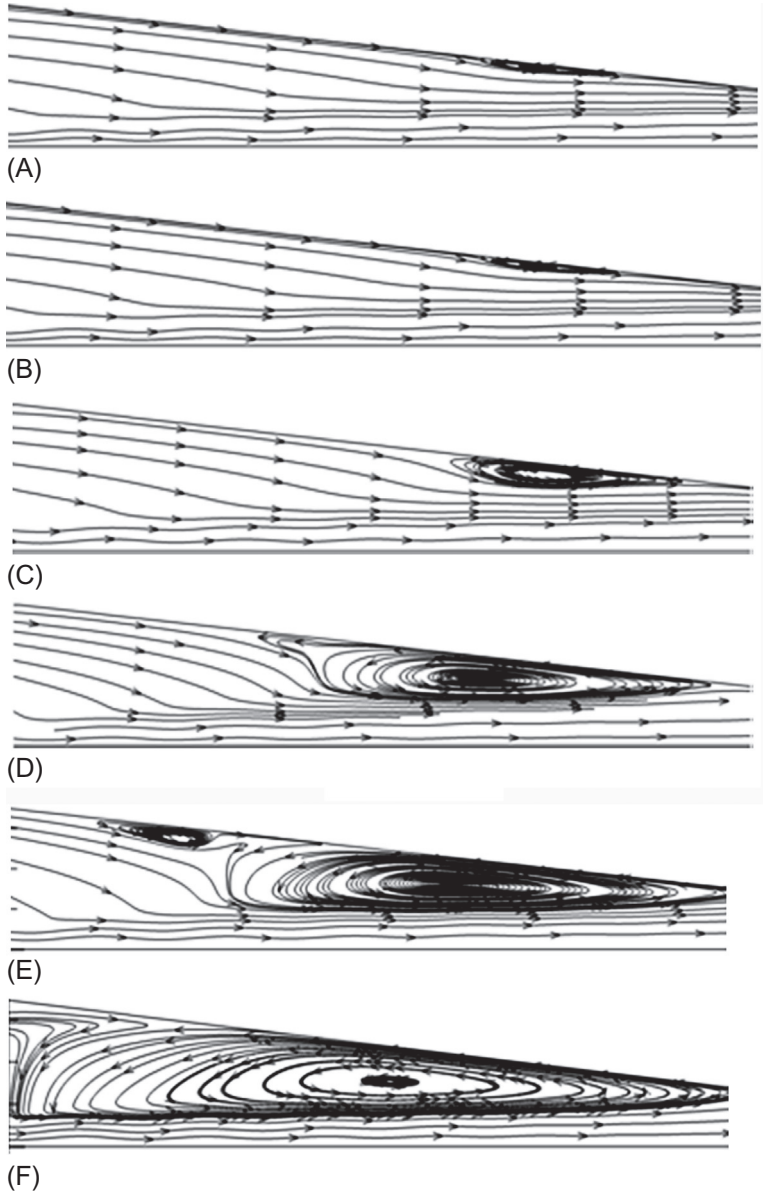


FIG. e1.88 The streamlines of convergent section of the ejector under different back pressures. (A) Pb = 4500 Pa. (B) Pb = 5000 Pa. (C) Pb = 5500 Pa. (D) Pb = 5750 Pa. (E) Pb = 5850 Pa. (F) Pb = 6000 Pa.

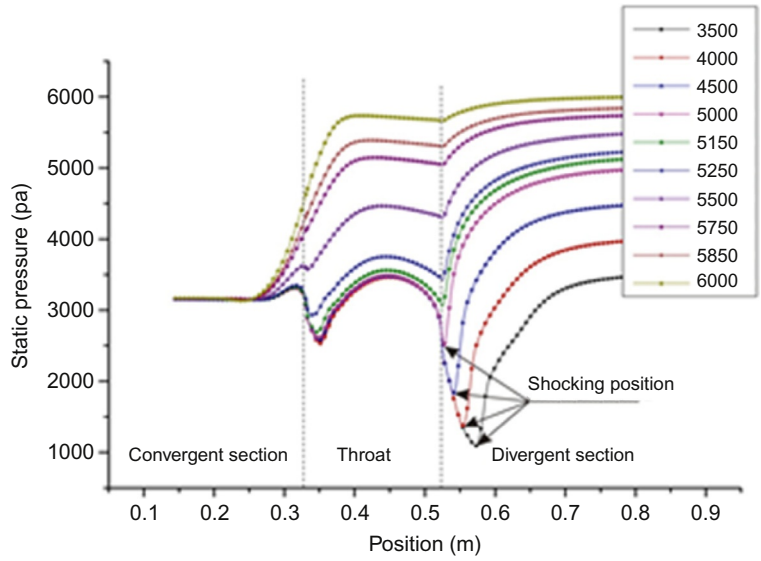


FIG. e1.89 The near-wall static-pressure distribution under different back pressures.

- What is the incentive for the separation of boundary layers, and how can this phenomenon be avoided?
- How does the vortex produced in the convergent section affect the pumping performance of the steam ejector?
- How does the choking phenomenon be determined, and what is the effect of choking on the pumping performance of the ejector?

Exploratory Questions:

➢ What are the effects on the critical pressure in changing operating parameters such as primary fluid pressure and secondary fluid pressure?
➢ Set the grid with different densities, investigate the influence of the grid number on the simulation results, and verify the grid independence.
➢ What is the effect of shock wave on the temperature, velocity, and pressure of the fluid? How to improve the pumping performance of ejector by utilizing shock wave?
➢ Conduct simulations for the wall-pressure distribution and entrainment ratio with different turbulence models, and compare with the experimental value to verify the correctness of turbulence model selection.

e1.3.10 Flow and Heat Mass Transfer in Shell-and-Tube Heat Exchanger

Simin Wang
Xi'an Jiaotong University

e1.3.10.1 Case Introduction

Shell-and-tube heat exchangers are widely used in oil refining, chemical industries, nuclear power plants, biopharmaceutical industries, etc. Baffles are important structural components in shell side, which have a significant influence on shell-side flow and heat-transfer performance. However, the experimental investigation can only obtain the inlet or outlet pressure and temperature, which can't show the flow and temperature distribution to carry out visualization research, as shown in Fig. e1.90. Hence, the numerical simulation is an effective method.

e1.3.10.2 Numerical Simulation

❑ Physical Model

The shell-and-tube heat exchangers with helical baffles consist of the cylinder, heat-transfer tubes, and baffles. The shell diameter of heat exchanger is 250 mm and 2500 mm in length. There are 40 tubes with the diameter of 19 mm to form the tube bundle, which are arranged squarely with the tube pitch of 25 mm. Four fan-shaped plain baffles are spirally arranged as shown in Fig. e1.91, whose main structural parameter helical angle and overlapped degree are 27° and 0.5°, respectively. And in order to simplify numerical simulation, the thickness of baffles, tubes, and shell are all neglected.

❑ Meshing

As illustrated in Fig. e1.92, there are two domains in shell-and-tube heat exchangers with fold helical baffles, shell-side and tube-side fluid. Owing to shell-side's complicated configuration, unstructured grids were used, whilst hexahedral grids were adopted in tube-side using ANSYS Meshing. The tube-side fluid selected the sweep method, and the sweep-element size is 5.8 mm. For the global mesh control, the minimized element size is

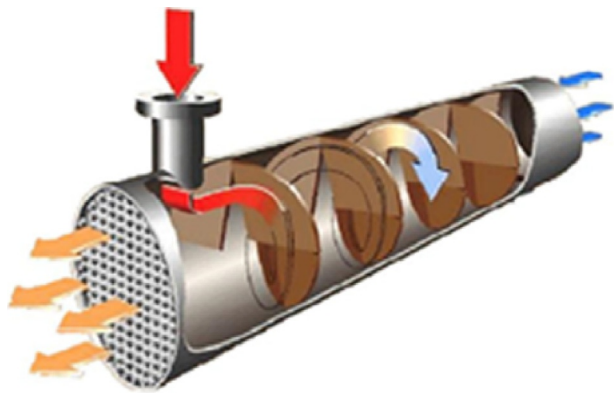


FIG. e1.90 Flow field of shell-and-tube heat exchangers with helical baffles.

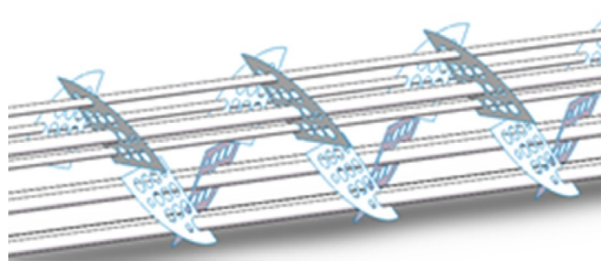


FIG. e1.91 Schematic diagram of the tube bundle.

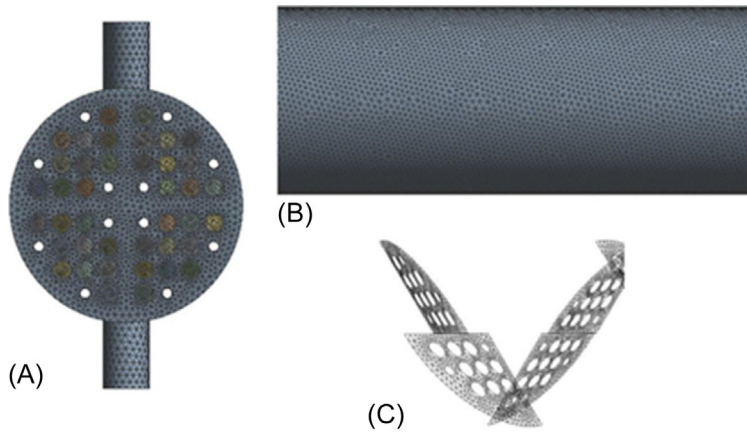


FIG. e1.92 Mesh: (A) tube and shell fluid (B) outside wall (C) baffles.

4.4 mm. At last, the number of elements in different helical angles and overlapped degrees is 9,178,293.

❑ Boundary Conditions

The turbulence model is RNG k-ε, as shown in Fig. e1.93. The boundary conditions of inlet and outlet are set as velocity inlet and pressure outlet, respectively. The shell-side inlet temperature of conductive oil is 358 K, and shell-side inlet velocity is between 2.84 $m \cdot s^{-1}$. The tube-side inlet temperature of water is 292 K, and tube-side inlet velocity is 0.92 $m \cdot s^{-1}$.

The boundary conditions of fold helical baffles and tubes are coupled wall, whilst other walls are non-slip, impermeable, and adiabatic. The governing equations are iteratively solved by SIMPLE velocity-pressure coupling algorithm based on finite-volume method. The convection term used first-order upwind scheme to calculate, as shown in Fig. e1.94. The convergence criterion is that the normalized residuals are $<1 \times 10^{-4}$ for mass and momentum equations and 1×10^{-6} for other equations.

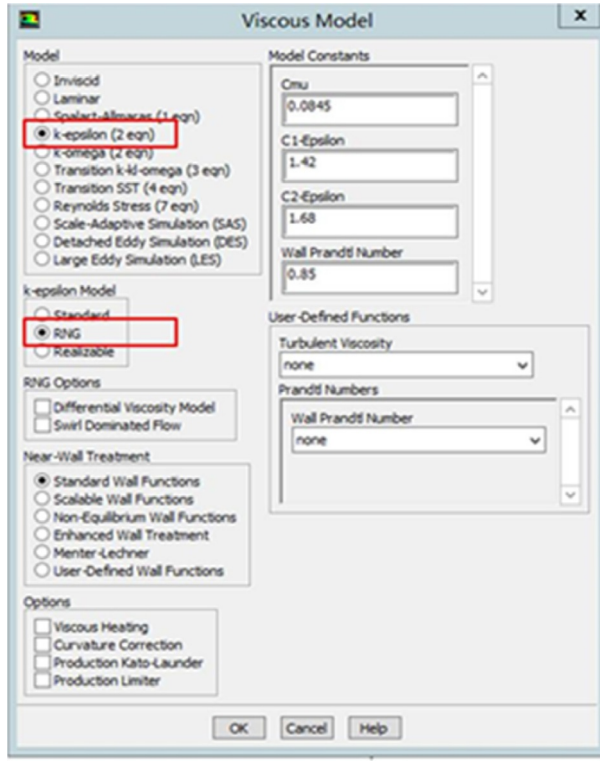


FIG. e1.93 The viscous model.

e1.3.10.3 CFD Results and Discussion

❑ Flow Field Analysis

Fig. e1.95 shows the streamline in shell side of shell-and-tube heat exchangers with helical baffles. It is clearly seen that the flow pattern in shell side is helical flow, which is beneficial to the mixing of shell fluid. And the streamline at outlet of shell side is more than that in other positions, which indicates that the velocity there is especially high. Hence it's meaningful to improve structure design at the inlet and outlet of shell side.

According to Fig. e1.96, the velocity in marginal region near shell side and in the centre of the shell is higher than that in other positions. In marginal region near shell side, the fluid sometimes flows through the holes between the baffles directly. As a result, a high velocity is conserved. And in the centre of the shell, a high velocity of the fluid is also kept because of the gaps between baffles. Therefore, lots of researches about the fluid flowing in marginal region near shell side and in the centre of the shell have been conducted in recent years.

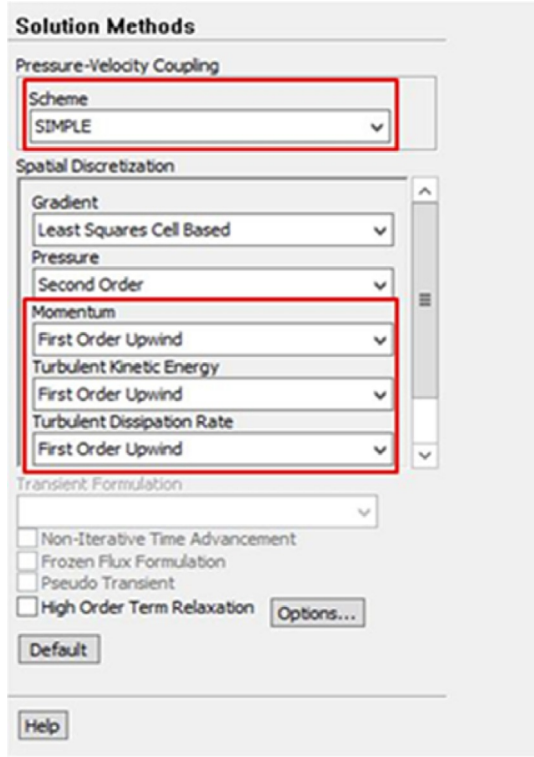


FIG. e1.94 The solution method.

❑ Pressure Distribution

In order to explore the pressure distribution of shell-and-tube heat exchangers with helical baffles clearly, the researchers analysed pressure fields of different positions. Figs. e1.97 and e1.98 show the pressure distribution in tube side and baffles of shell-and-tube heat exchangers with helical baffles, respectively. As is shown in them, with the fluid flowing, the pressure in both tubes and baffles reduces helically from inlet to outlet, which is caused by the helical flow in shell side. Furthermore, as the fluid flows in shell side, it collides with tubes, which results in velocity of the fluid decreasing and the pressure in shell sides falling.

Fig. e1.99 indicates that the pressure in inlet of shell side is extremely high, which is caused by the high-speed inflow. When the fluid flows into the shell, it crashes into block plate, and its velocity is so high that a local high-pressure area appears. Besides, these problems are often mentioned in heat-exchanger design manual. Therefore, it will be better that inflow velocity is limited when designing heat exchangers.

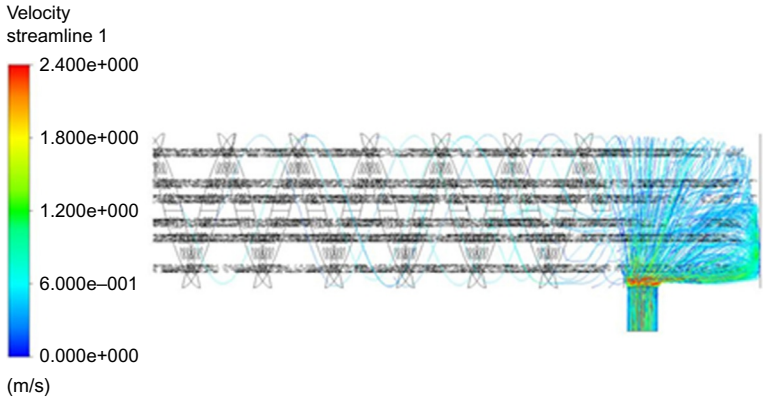


FIG. e1.95 Streamline in shell side.

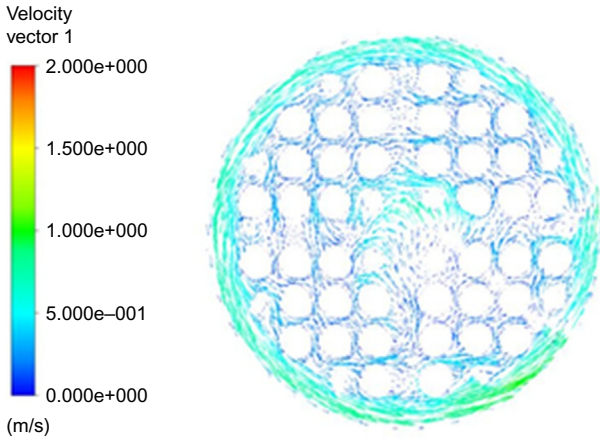


FIG. e1.96 Velocity vector of cross-section in shell side.

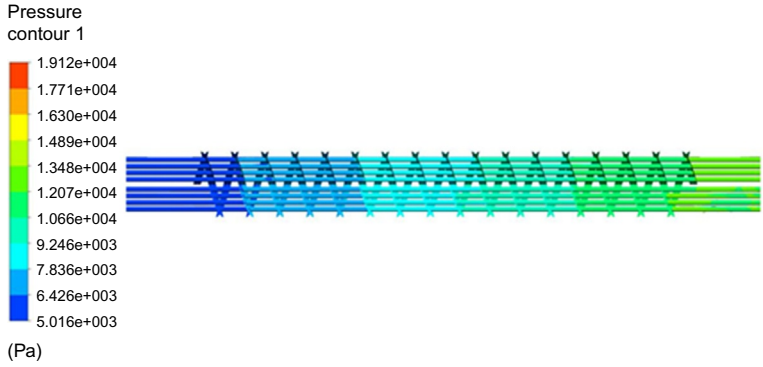


FIG. e1.97 Pressure of tube bundle.

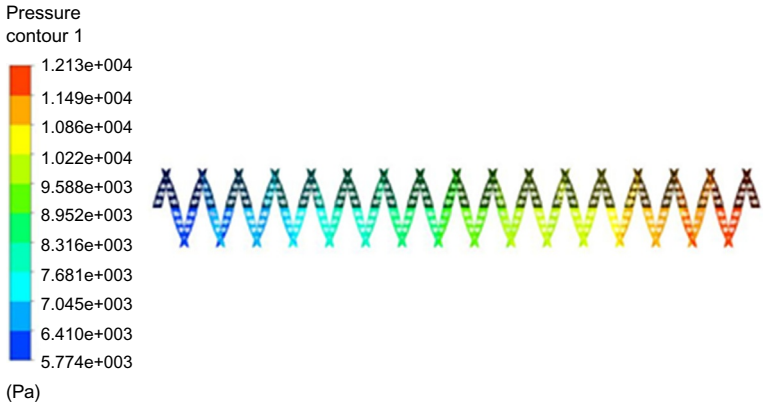


FIG. e1.98 Pressure of baffles.

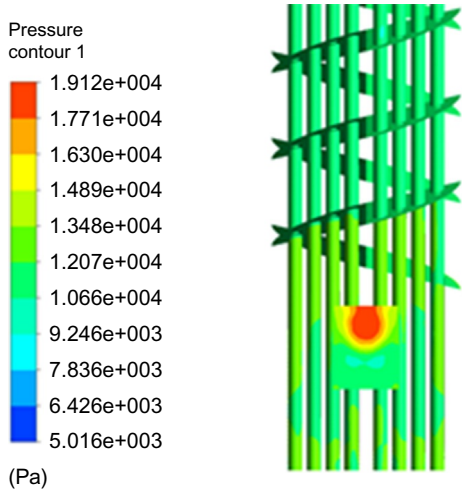


FIG. e1.99 Pressure in inlet of block plate.

❑ Temperature Field Analysis

As Fig. e1.100 shows, the temperature in baffles reduces gradually from the inlet of shell side to outlet. During the process of flowing, conductive oil in shell side and water in tube side exchange heat with each other constantly, and the temperature of hot fluid in shell side drops. Eventually, the temperature in inlet is obviously higher than that in outlet, which means heat exchanging is efficient. What's more, it can be seen from Fig. e1.100 that the temperature in central region is lower than that in marginal region near shell side. It's because the temperature of tube fluid is low, and conductive oil near them transfers more heat

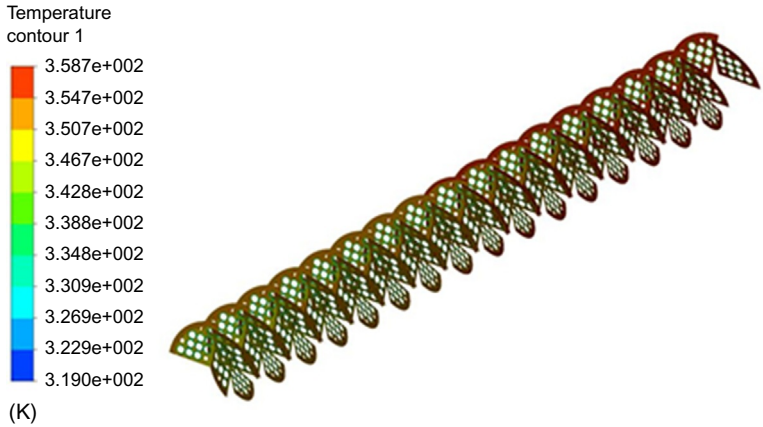


FIG. e1.100 Temperature of baffles.

out easily. Thus, the heater exchanging between tubes is stronger than that in marginal region near shell side.

Review Questions:

- What boundary conditions can be used to save the computational cost under complicated cases?
- What are the other possible approaches to save the computational resources?
- Where do the maximum pressure drop and temperature values occur for shell-and-tube heat exchanger with helical baffles?

Exploratory Questions:

➢ If the both fluid is non-Newtonian fluid, how would these be treated?
➢ Test different types of mesh (coarser mesh, finer mesh, etc.) and compare the results.
➢ If the mesh is coarsened, will the results change much?
➢ Conducting simulations with different turbulence models (k-ε, SST, etc.), compare the fluid field.
➢ Compare the streamline between the laminar flow and turbulence flow.

Appendix A

Full Derivation of Conservation Equations

The full derivation of the conservation equations for momentum and energy is presented in this appendix.

The concept of *substantial derivative* is described herein. It is conveniently acceptable to collect all the density terms together by expanding Eq. (3.10) by the chain rule. This gives

$$\frac{\partial \rho}{\partial t} + u\frac{\partial \rho}{\partial x} + v\frac{\partial \rho}{\partial y} + w\frac{\partial \rho}{\partial z} + \rho\left(\frac{\partial u}{\partial x} + \frac{\partial v}{\partial y} + \frac{\partial w}{\partial z}\right) = 0 \tag{A.1}$$

or

$$\frac{D\rho}{Dt} + \rho\left(\frac{\partial u}{\partial x} + \frac{\partial v}{\partial y} + \frac{\partial w}{\partial z}\right) = 0 \tag{A.2}$$

where D/Dt is the substantial derivative in Cartesian coordinates. The time derivatives of $D\rho/Dt$ and $\partial\rho/\partial t$ are physically and numerically different quantities. The reader should note that the former is the time rate of change following a moving fluid element whilst the latter is the time rate of change at a fixed location. Also, if we consider the general variable property per unit mass denoted as ϕ, the substantial derivative of ϕ with respect to time, written as $D\phi/Dt$, is

$$\frac{D\phi}{Dt} = \frac{\partial \phi}{\partial t} + u\frac{\partial \phi}{\partial x} + v\frac{\partial \phi}{\partial y} + w\frac{\partial \phi}{\partial z} \tag{A.3}$$

The above equation defines the rate of change of the variable property ϕ per unit mass. As in the case of mass conservation, we are interested in developing equations for the rates of change per unit volume. The rate of change of the variable property ϕ per unit volume can be obtained by multiplying the density ρ with the substantial derivative of ϕ that is given by

$$\rho\frac{D\phi}{Dt}=\rho\frac{\partial\phi}{\partial t}+\rho u\frac{\partial\phi}{\partial x}+\rho v\frac{\partial\phi}{\partial y}+\rho w\frac{\partial\phi}{\partial z} \tag{A.4}$$

It is recognized that Eq. (A.4) represents the *nonconservation form* of the rate of change of the variable property ϕ per unit volume.

The mass conservation equation derived in Section 3.2.1 defines the sum of the rate change of density and is called the advection term, which is

$$\frac{\partial\rho}{\partial t}+\frac{\partial(\rho u)}{\partial x}+\frac{\partial(\rho v)}{\partial y}+\frac{\partial(\rho w)}{\partial z}=0$$

It is conceivable that the generalization of these terms for the variable property ϕ in *conservation form* can be expressed as

$$\frac{\partial(\rho\phi)}{\partial t}+\frac{\partial(\rho u\phi)}{\partial x}+\frac{\partial(\rho v\phi)}{\partial y}+\frac{\partial(\rho w\phi)}{\partial z} \tag{A.5}$$

The above formula expresses the rate of change of ϕ per unit volume with the addition of the net flow of ϕ out of the fluid element per unit volume. It is now rewritten to illustrate the relationship between the conservative form of Eq. (3.16) and nonconservative form of Eq. (3.15):

$$\begin{aligned}&\frac{\partial(\rho\phi)}{\partial t}+\frac{\partial(\rho u\phi)}{\partial x}+\frac{\partial(\rho v\phi)}{\partial y}+\frac{\partial(\rho w\phi)}{\partial z}= \\ &\rho\frac{\partial\phi}{\partial t}+\rho u\frac{\partial\phi}{\partial x}+\rho v\frac{\partial\phi}{\partial y}+\rho w\frac{\partial\phi}{\partial z}+\phi\left[\frac{\partial\rho}{\partial t}+\frac{\partial(\rho u)}{\partial x}+\frac{\partial(\rho v)}{\partial y}+\frac{\partial(\rho w)}{\partial z}\right]=\rho\frac{D\phi}{Dt}\end{aligned} \tag{A.6}$$

Invoking the continuity equation $= 0$

Both of these forms can be used to express the conservation of a physical quantity. For brevity, the nonconservative form is adopted to derive the conservation equations for momentum and energy.

For the conservation of momentum, the net force in the x direction is the sum of the force components acting on the fluid element. Considering the velocity component u as seen in Fig. 3.4, the surface forces are due to the normal stress σ_{xx} and tangential stresses τ_{yx} and τ_{zx} acting on the surfaces of the fluid element. The net force in the normal x direction is

$$\left[\sigma_{xx}+\frac{\partial\sigma_{xx}}{\partial x}\Delta x\right]\Delta y\Delta z-\sigma_{xx}\Delta y\Delta z \tag{A.7}$$

whilst the net tangential forces acting along the x direction are, respectively, given by

$$\left[\tau_{yx} + \frac{\partial \tau_{yx}}{\partial y}\Delta y\right]\Delta x\Delta z - \tau_{yx}\Delta x\Delta z \tag{A.8}$$

and

$$\left[\tau_{zx} + \frac{\partial \tau_{zx}}{\partial z}\Delta z\right]\Delta x\Delta y - \tau_{zx}\Delta x\Delta y \tag{A.9}$$

The total net force per unit volume on the fluid due to these surface stresses should be equal to the sum of Eqs (A.7)–(A.9) divided by the control volume $\Delta x\ \Delta y\ \Delta z$:

$$\frac{\partial \sigma_{xx}}{\partial x} + \frac{\partial \tau_{yx}}{\partial y} + \frac{\partial \tau_{zx}}{\partial z} \tag{A.10}$$

It is not too difficult to verify that the total net forces per unit volume on the rest of the control volume surfaces in the y direction and z direction are given by

$$\frac{\partial \tau_{xy}}{\partial x} + \frac{\partial \sigma_{yy}}{\partial y} + \frac{\partial \tau_{zy}}{\partial z} \tag{A.11}$$

and

$$\frac{\partial \tau_{xz}}{\partial x} + \frac{\partial \tau_{yz}}{\partial y} + \frac{\partial \sigma_{zz}}{\partial z} \tag{A.12}$$

Combining Eq. (A.10) with the substantial derivative of the horizontal velocity component u and body forces, the x-momentum equation becomes

$$\rho\frac{Du}{Dt} = \frac{\partial \sigma_{xx}}{\partial x} + \frac{\partial \tau_{yx}}{\partial y} + \frac{\partial \tau_{zx}}{\partial z} + \sum F_x^{body\ forces} \tag{A.13}$$

In a similar fashion, the y-momentum and z-momentum equations, using Eqs (A.11) and (A.12), can be obtained through

$$\rho\frac{Dv}{Dt} = \frac{\partial \tau_{xy}}{\partial x} + \frac{\partial \sigma_{yy}}{\partial y} + \frac{\partial \tau_{zy}}{\partial z} + \sum F_y^{body\ forces} \tag{A.14}$$

and

$$\rho\frac{Dw}{Dt} = \frac{\partial \tau_{xz}}{\partial x} + \frac{\partial \tau_{yz}}{\partial y} + \frac{\partial \sigma_{zz}}{\partial z} + \sum F_z^{body\ forces} \tag{A.15}$$

If the fluid is taken to be Newtonian and isotropic—since all gases and majority of liquids are isotropic—the normal stresses σ_{xx}, σ_{yy}, and σ_{zz} appearing in Eqs (A.13)–(A.15) can be formulated in terms of pressure p and normal viscous stress components, τ_{xx}, τ_{yy}, and τ_{zz} acting perpendicular on the control volume. The remaining terms contain the tangential viscous stress components as also described from Eqs (A.13)–(A.15). In many fluid flows, a suitable model for the viscous stresses is introduced, which can be expressed as a function of the local deformation rate (or strain rate). Assuming that the fluid is Newtonian and isotropic since all gases and majority of liquids are isotropic, the rate of linear deformation on the control volume $\Delta x\,\Delta y\,\Delta z$ caused by the motion of fluid can usually be expressed in terms of the velocity gradients. The normal stress relationships can be expressed as

$$\sigma_{xx} = -p + \tau_{xx} \quad \sigma_{yy} = -p + \tau_{yy} \quad \sigma_{zz} = -p + \tau_{zz} \tag{A.16}$$

According to *Newton's law of viscosity*, the normal and tangential viscous stress components are given by

$$\begin{gathered}
\tau_{xx} = 2\mu\frac{\partial u}{\partial x} + \lambda\left[\frac{\partial u}{\partial x} + \frac{\partial v}{\partial y} + \frac{\partial w}{\partial z}\right] \quad \tau_{yy} = 2\mu\frac{\partial v}{\partial y} + \lambda\left[\frac{\partial u}{\partial x} + \frac{\partial v}{\partial y} + \frac{\partial w}{\partial z}\right] \\
\tau_{zz} = 2\mu\frac{\partial w}{\partial z} + \lambda\left[\frac{\partial u}{\partial x} + \frac{\partial v}{\partial y} + \frac{\partial w}{\partial z}\right] \\
\tau_{xy} = \tau_{yx} = \mu\left(\frac{\partial v}{\partial x} + \frac{\partial u}{\partial y}\right) \quad \tau_{xz} = \tau_{zx} = \mu\left(\frac{\partial w}{\partial x} + \frac{\partial u}{\partial z}\right) \\
\tau_{yz} = \tau_{zy} = \mu\left(\frac{\partial w}{\partial y} + \frac{\partial v}{\partial z}\right)
\end{gathered} \tag{A.17}$$

The proportionality constants of μ and λ are the (first) dynamic viscosity that relates stresses to linear deformation and the second viscosity that relates stresses to the volumetric deformation, respectively. To this present day, not much is known about the second viscosity. Nevertheless, Stokes' hypothesis of $\lambda = -2/3\mu$ is frequently used, and it has been found for gases to be a good working approximation.

When we combine Eqs (A.16) and (A.17) with Eqs (A.13)–(A.15), the equations for the velocity components u, v, and w in three dimensions can be rewritten as

$$\begin{aligned}
\rho\frac{Du}{Dt} = &-\frac{\partial p}{\partial x} + \frac{\partial}{\partial x}\left[2\mu\frac{\partial u}{\partial x} + \lambda\left(\frac{\partial u}{\partial x} + \frac{\partial v}{\partial y} + \frac{\partial w}{\partial z}\right)\right] \\
&+ \frac{\partial}{\partial y}\left[\mu\left(\frac{\partial u}{\partial y} + \frac{\partial v}{\partial x}\right)\right] + \frac{\partial}{\partial z}\left[\mu\left(\frac{\partial u}{\partial z} + \frac{\partial w}{\partial x}\right)\right] + \sum F_x^{body\ forces}
\end{aligned} \tag{A.18}$$

$$\rho\frac{Dv}{Dt}=-\frac{\partial p}{\partial y}+\frac{\partial}{\partial y}\left[2\mu\frac{\partial v}{\partial y}+\lambda\left(\frac{\partial u}{\partial x}+\frac{\partial v}{\partial y}+\frac{\partial w}{\partial z}\right)\right]+\frac{\partial}{\partial x}\left[\mu\left(\frac{\partial u}{\partial y}+\frac{\partial v}{\partial x}\right)\right]+\frac{\partial}{\partial z}\left[\mu\left(\frac{\partial v}{\partial z}+\frac{\partial w}{\partial y}\right)\right]+\sum F_y^{body\ forces} \tag{A.19}$$

$$\rho\frac{Dw}{Dt}=-\frac{\partial p}{\partial z}+\frac{\partial}{\partial z}\left[2\mu\frac{\partial w}{\partial z}+\lambda\left(\frac{\partial u}{\partial x}+\frac{\partial v}{\partial y}+\frac{\partial w}{\partial z}\right)\right]+\frac{\partial}{\partial x}\left[\mu\left(\frac{\partial u}{\partial z}+\frac{\partial w}{\partial x}\right)\right]+\frac{\partial}{\partial y}\left[\mu\left(\frac{\partial v}{\partial z}+\frac{\partial w}{\partial y}\right)\right]+\sum F_z^{body\ forces} \tag{A.20}$$

For the conservation of energy, the rate of work done on the control volume $\Delta x\ \Delta y\ \Delta z$ is equivalent to the product of the force and velocity component, which in the x direction is the velocity component u. From Fig. 3.5, the work done by the normal force in the x direction is

$$\left[u\sigma_{xx}+\frac{\partial(u\sigma_{xx})}{\partial x}\Delta x\right]\Delta y\Delta z-u\sigma_{xx}\Delta y\Delta z \tag{A.21}$$

whilst the work done by the tangential forces in the x direction is, respectively, given by

$$\left[u\tau_{yx}+\frac{\partial(u\tau_{yx})}{\partial y}\Delta y\right]\Delta x\Delta z-u\tau_{yx}\Delta x\Delta z \tag{A.22}$$

and

$$\left[u\tau_{zx}+\frac{\partial(u\tau_{zx})}{\partial z}\Delta z\right]\Delta x\Delta y-u\tau_{zx}\Delta x\Delta y \tag{A.23}$$

The net rate of work done by these surface forces acting in the x direction divided by the control volume $\Delta x\ \Delta y\ \Delta z$ is given by

$$\frac{\partial(u\sigma_{xx})}{\partial x}+\frac{\partial(u\tau_{yx})}{\partial y}+\frac{\partial(u\tau_{zx})}{\partial z} \tag{A.24}$$

Work done due to surface stress components in the y direction and z direction can also be similarly derived, and these additional rates of work done on the fluid are

$$\frac{\partial(v\tau_{xy})}{\partial x}+\frac{\partial(v\sigma_{yy})}{\partial y}+\frac{\partial(v\tau_{zy})}{\partial z} \tag{A.25}$$

and

$$\frac{\partial(w\tau_{xz})}{\partial x}+\frac{\partial(w\tau_{yz})}{\partial y}+\frac{\partial(w\sigma_{zz})}{\partial z} \tag{A.26}$$

For heat added, the net rate of heat transfer to the fluid due to the heat flow in the x direction is given by the difference between the heat input at surface at x and heat loss at surface $x+\Delta x$ as depicted in Fig. 3.5:

$$\left[q_x+\frac{\partial q_x}{\partial x}\Delta x\right]\Delta y\Delta z-q_x\Delta y\Delta z \tag{A.27}$$

Similarly, the net rates of heat transfer in the y direction and z direction may also be expressed as

$$\left[q_y+\frac{\partial q_y}{\partial y}\Delta y\right]\Delta x\Delta z-q_y\Delta x\Delta z \tag{A.28}$$

and

$$\left[q_z+\frac{\partial q_z}{\partial z}\Delta z\right]\Delta x\Delta y-q_z\Delta x\Delta y \tag{A.29}$$

The total rate of heat added to the fluid divided by the control volume $\Delta x\,\Delta y\,\Delta z$ results in

$$\frac{\partial q_x}{\partial x}+\frac{\partial q_y}{\partial y}+\frac{\partial q_z}{\partial z} \tag{A.30}$$

Combining Eqs (A.24)–(A.26) and (A.30) with the substantial derivative for a given specific energy E of a fluid, the equation for the conservation of energy becomes

$$\begin{aligned}\rho\frac{DE}{Dt}=&\frac{\partial(u\sigma_{xx})}{\partial x}+\frac{\partial(v\sigma_{yy})}{\partial y}+\frac{\partial(w\sigma_{zz})}{\partial z}\\&+\frac{\partial(u\tau_{yx})}{\partial y}+\frac{\partial(u\tau_{zx})}{\partial z}+\frac{\partial(v\tau_{xy})}{\partial x}+\frac{\partial(v\tau_{zy})}{\partial z}+\frac{\partial(w\tau_{xz})}{\partial x}\\&+\frac{\partial(w\tau_{yz})}{\partial y}-\frac{\partial q_x}{\partial x}-\frac{\partial q_y}{\partial y}-\frac{\partial q_z}{\partial z}\end{aligned} \tag{A.31}$$

Thus far, we have not defined the specific energy E of a fluid. Often, the energy of a fluid is defined as the sum of the internal energy, kinetic energy, and gravitational potential energy. We shall regard the gravitational force as

a body force and include the effects of potential energy changes as a source term. In three dimensions, the specific energy E can be defined as

$$E = \underbrace{e}_{internal\ energy} + \underbrace{\frac{1}{2}\left(u^2 + v^2 + w^2\right)}_{kinetic\ enertgy} \tag{A.32}$$

For compressible flows, Eq. (A.32) is often rearranged to give an equation for the *enthalpy*. The specific enthalpy h_{sp} and the specific (total) enthalpy h of a fluid are defined as

$$h_{sp} = e + \frac{p}{\rho}$$

and

$$h = h_{sp} + \frac{1}{2}\left(u^2 + v^2 + w^2\right)$$

Combining these two definitions with the specific energy E, we obtain

$$h = e + \frac{p}{\rho} + \frac{1}{2}\left(u^2 + v^2 + w^2\right) = E + \frac{p}{\rho} \tag{A.33}$$

Appendix B

Upwind Schemes

The first-order upwind scheme has been described in Chapter 5, Section 5.3. Here, we concentrate on the formulation of the second-order upwind and third-order QUICK schemes as illustrated below. As an improvement to the first-order upwind scheme, the idea is to incorporate additional variables located at the neighbouring grid nodal points indicated by the properties at points *WW* and *EE* as shown in Fig. B.1 in order to evaluate the interface values at the cell faces of *w* and *e*.

For the second-order upwind scheme, assuming uniform distribution of the grid nodal points, additional information of the fluid flow is introduced into the approximation by the consideration of an extra upstream variable point, namely,

$$\begin{aligned} \phi_w &= \frac{3}{2}\phi_W - \frac{1}{2}\phi_{WW} \\ \phi_e &= \frac{3}{2}\phi_P - \frac{1}{2}\phi_W \end{aligned} \quad \text{if } u_w > 0 \text{ and } u_e > 0 \tag{B.1}$$

$$\begin{aligned} \phi_w &= \frac{3}{2}\phi_P - \frac{1}{2}\phi_E \\ \phi_e &= \frac{3}{2}\phi_E - \frac{1}{2}\phi_{EE} \end{aligned} \quad \text{if } u_w < 0 \text{ and } u_e < 0 \tag{B.2}$$

For the third-order QUICK scheme, a quadratic approximation is introduced across two variable points at the upstream and one at the downstream depending

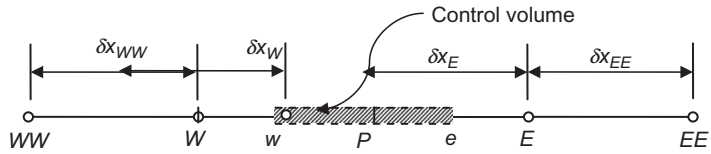


FIG. B.1 A schematic representation of a control volume around a node *P* in a one-dimensional domain with surrounding grid nodal points of *WW*, *W*, *E*, and *EE*.

on the flow direction. The unequal weighting influence of this particular scheme still hinges on the knowledge biased towards the upstream flow information. The interface values ϕ_w and ϕ_e based on a uniform grid nodal point distribution can be evaluated as

$$\begin{aligned} \phi_w &= -\frac{1}{8}\phi_{WW} + \frac{6}{8}\phi_W + \frac{3}{8}\phi_P \\ \phi_e &= -\frac{1}{8}\phi_W + \frac{6}{8}\phi_P + \frac{3}{8}\phi_E \end{aligned} \quad \text{if } u_w > 0 \text{ and } u_e > 0 \tag{B.3}$$

$$\begin{aligned} \phi_w &= -\frac{1}{8}\phi_E + \frac{6}{8}\phi_P + \frac{3}{8}\phi_W \\ \phi_e &= -\frac{1}{8}\phi_{EE} + \frac{6}{8}\phi_E + \frac{3}{8}\phi_P \end{aligned} \quad \text{if } u_w < 0 \text{ and } u_e < 0 \tag{B.4}$$

Appendix C

Explicit and Implicit Methods

The first-order explicit and implicit methods have been described in Chapter 5, Section 5.3. Here, we further concentrate on the formulation of the second-order *explicit* Adams–Bashforth and *semi-implicit* Crank–Nicolson methods as illustrated below.

As illustrated from the sketch in Fig. C.1, the extension of the first-order *explicit* method to the second-order *explicit* Adams–Bashforth requires the values not only at time level n but also at time level $n-1$. The unsteady one-dimensional convection–diffusion of Eq. (5.58) can be recast in the form of

$$\begin{aligned}\frac{\phi_P^{n+1}-\phi_P^n}{\Delta t} &= \frac{3}{2}\frac{\partial\phi}{\partial t}\bigg|^n - \frac{1}{2}\frac{\partial\phi}{\partial t}\bigg|^{n-1} \\ &= \frac{3}{2}\left[-u_e A_E \frac{1}{2}(\phi_W+\phi_P) + u_w A_W \frac{1}{2}(\phi_P+\phi_E)\right. \\ &\quad \left. + \Gamma_e A_E \frac{1}{\rho}\left(\frac{\phi_E-\phi_P}{\delta x_E}\right) - \Gamma_w A_W \frac{1}{\rho}\left(\frac{\phi_P-\phi_W}{\delta x_W}\right) + \frac{S_\phi}{\rho}\Delta V\right]^n \\ &\quad - \frac{1}{2}\left[-u_e A_E \frac{1}{2}(\phi_W+\phi_P) + u_w A_W \frac{1}{2}(\phi_P+\phi_E)\right. \\ &\quad \left. + \Gamma_e A_E \frac{1}{\rho}\left(\frac{\phi_E-\phi_P}{\delta x_E}\right) - \Gamma_w A_W \frac{1}{\rho}\left(\frac{\phi_P-\phi_W}{\delta x_W}\right) + \frac{S_\phi}{\rho}\Delta V\right]^{n-1}\end{aligned} \tag{C.1}$$

For the second-order Crank–Nicolson method, this special type of differencing in time requires the solution of ϕ_P^{n+1} to be obtained through averaging the properties between time levels n and $n+1$. There are many versions of the Crank–Nicolson form in CFD. Some may only include the implicit evaluation of the diffusive term, whilst others may even choose to consider the convective term in addition to the diffusive term to be implicitly determined, but the source term remains in the previous time level n regardless. The authors present the latter form as depicted below:

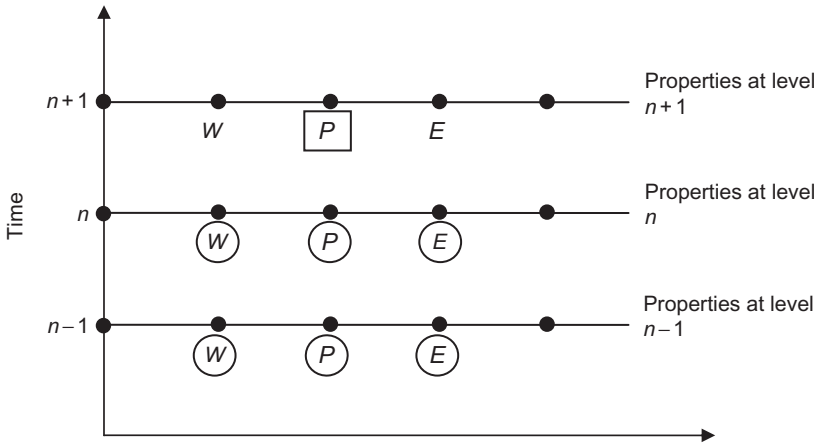


FIG. C.1 An illustration for the second-order Adams–Bashforth.

$$\begin{aligned}\frac{\phi_P^{n+1}-\phi_P^n}{\Delta t} = &-\frac{u_e^n A_E}{2}\left[\frac{1}{2}\left(\phi_W^{n+1}+\phi_W^n\right)+\frac{1}{2}\left(\phi_P^{n+1}+\phi_P^n\right)\right]\\ &+\frac{u_w^n A_W}{2}\left[\frac{1}{2}\left(\phi_P^{n+1}+\phi_P^n\right)+\frac{1}{2}\left(\phi_E^{n+1}+\phi_E^n\right)\right]\\ &+\frac{\Gamma_e^n A_E}{\rho}\left[\frac{\frac{1}{2}\left(\phi_E^{n+1}+\phi_E^n\right)-\frac{1}{2}\left(\phi_P^{n+1}+\phi_P^n\right)}{\delta x_E}\right]\\ &-\frac{\Gamma_w^n A_W}{\rho}\left[\frac{\frac{1}{2}\left(\phi_P^{n+1}+\phi_P^n\right)-\frac{1}{2}\left(\phi_W^{n+1}+\phi_W^n\right)}{\delta x_W}\right]+\frac{S_\phi^n}{\rho}\Delta V\end{aligned} \tag{C.2}$$

The above equation represents an example of a *semi-implicit* approach. Like the *fully implicit* approach, it also requires a simultaneous solution of the unknowns at *all* grid nodal points in the respective difference equations for a given time level of $n+1$.

Appendix D

Learning Program

The materials presented in this book have been partially designed from teaching the course of *Introduction to Computational Fluid Dynamics* for senior undergraduate students in the School of Aerospace, Mechanical and Manufacturing Engineering at RMIT University, Australia. This learning program can be adopted by an instructor to conduct either a one-semester (6–8 h/week) or two-semester (3–4 h/week) CFD course in any engineering department. For example, the instructor may wish to assign 3 or 4 h/week on lectures and 3 or 4 h/week on CFD labs for a one-semester course. The appropriate allocation of hours for lectures or CFD labs is entirely up to the instructor. He/she may reduce the number of hours for lectures and concentrate more on CFD labs to allow students to attain more practical experiences in handling real fluid flow problems through CFD methods.

This program consists of the student's own reading of the relevant chapters described below, working out the assignments and completing a final CFD project as will be presented in Appendix E. The teaching approach has worked very well in facilitating students to better engage in various real problem-based assignments and projects. From the students' perspective, an air of excitement is exuberated from the beginning of the course through working relatively easier problems in early assignments towards solving a real-life fluid dynamics problem chosen by the student at the final stage of this course. Details with regard to mathematical formulations are kept to a minimum, and computer programming is avoided during the teaching of this course. Rather, the basic and practical knowledge in the ability of analysing CFD solution is emphasized within this program. The lectures are thus directed primarily to present the major theories and methodologies used in CFD and guide the students as to where their learning efforts should be concentrated. The CFD labs, as indicated below, are to facilitate the learning of the basic theories, development of analysis capability, and ability to resolve practical engineering problems through the use of CFD software. During the CFD labs, tutorials will also be used to introduce and discuss the problems in assignments and to provide the hands-on assistance and feedback to the students. The final CFD project allows the student to attain

experience in the application of CFD methods and analysis to real-world engineering problems.

Learning Program for a One-Semester CFD Course		
Week 1	Lecture:	Introduction to CFD and CFD procedure
	Reading:	Chapters 1 and 2
	CFD lab:	Introduction to CFD software
		Assignment 1 (Introduction)
Week 2	Lecture:	Basic CFD equations
	Reading:	Chapter 3
	CFD lab:	Assignment 1 (Discussion)
Week 3	Lecture:	Mesh generation and boundary conditions
	Reading:	Chapters 4 and 7
	CFD lab:	Assignment 1 (Finalization)
Week 4	Lecture:	Basic numerical methods
	Reading:	Chapter 5
	CFD lab:	Assignment 2 (Introduction)
Week 5	Lecture:	Basic numerical techniques
	Reading:	Chapter 5
	CFD lab:	Assignment 2 (Discussion)
Week 6	Lecture:	CFD solution analysis
	Reading:	Chapter 6
	CFD lab:	Assignment 2 (Finalization)
Week 7	Lecture:	Turbulence modelling
	Reading:	Chapter 7
	CFD lab:	Assignment 3 (Introduction)
Week 8	Lecture:	Practical guidelines and case study
	Reading:	Chapter 7
	CFD lab:	Assignment 3 (Discussion)
Week 9	Lecture:	CFD applications
	Reading:	Chapter 8
	CFD lab:	Assignment 3 (Finalization)

Learning Program for a One-Semester CFD Course—cont'd		
Week 10	Lecture:	Invited seminar: Engineering design and optimization using CFD
	Reading:	Chapter 8
	CFD lab:	Introduction to CFD project
Week 11	Lecture:	Advanced CFD topics
	Reading:	Chapter 9
	CFD lab:	CFD project (Discussion)
Week 12		CFD project (Feedback)
Week 13		CFD project (Finalization)
Week 14		Revision and final examination

Appendix E

CFD Assignments and Guideline for CFD Project

A sample of three assignments and a guideline for a CFD project clarifying the aim and objectives are described in this appendix. For students who do not possess their own project topics, they are most welcomed to select one from the attached project topics (CFD projects A–C) exemplified herein.

E.1 ASSIGNMENT 1

E.1.1 Background and Aim

The backward-facing step is commonly used as a benchmark for validating numerous flow characteristics, including flow recirculation and reattachment, and testing of numerical models and methods. This problem has numerous applications in industry, such as for HVAC and combustion chamber.

The aims of this problem are as follows:

1. To learn the process of creating and exporting a mesh by using any available mesh generation software packages. For this assignment, the mesh generator in ANSYS Workbench is employed.
2. To learn how to set suitable boundary conditions and numerical models using any available CFD software packages. ANSYS-FLUENT is used to solve the flow problem in this assignment.
3. To explore the postprocessing facilities of the CFD code to analyse the numerical results.
4. To formulate concise professional reports.

E.1.2 Problem Description

The student is required to compute laminar flows through a backward-facing step as detailed below. The coordinates given for the geometry are normalized against the characteristic length scale. For the case of backward-facing step, the characteristic length scale is the *step height* (in this case, a length of unity is

assumed). The normalized fluid properties at the *velocity inlet* are given as follows:

Inlet velocity: $u_x = 1$ and $u_y = 0$
Fluid properties: Density, $\rho = 1$ and dynamic viscosity, $\mu = 1/Re$, where Re is the Reynolds number

The outlet boundary is defined as an outflow condition, whilst the no-slip condition is invoked for the rest of the computational walls. Turbulence is ignored, and no heat transfer exists within the system. It is noted that the dimensions of the computational domain may need to be altered to ensure that the flow is sufficiently developed at the outlet boundary (Fig. E.1).

E.1.3 Instructions

1. Initiate ANSYS Workbench to create a mesh for the backward-facing step. Assign appropriate boundary conditions to the computational domain. Structured mesh is preferred, but the user may alternatively generate the geometry with an unstructured mesh. Ensure that proper mesh quality is achieved. Provide explanations for areas that require further mesh refinement. Export the two-dimensional mesh to ANSYS-FLUENT, Version 17.
2. Using ANSYS-FLUENT, solve the simulation to obtain the velocity and pressure contours and the velocity vectors for $Re = 100$. Ensure that the flow is fully developed (ensuring no flow reversal) or close-to-developed flow at the outlet boundary. Discuss any observed flow characteristics using the physical parameters.
3. Repeat steps 2 and 3 for other meshes of varying densities. Use the same flow settings for $Re = 100$ to determine the sensitivity of the mesh to the reattachment point of the recirculation zone. Plot a graph relating the mesh size against the reattachment location, highlighting the most economical mesh for numerical computations (hint, when grid independence is achieved, the reattachment point will not vary with increasing mesh density).
4. Using the mesh determined from step 3, perform simulations for other Reynolds numbers of 50, 150, and 200. Compile your results and create a graph illustrating the relationship between the Reynolds numbers and reattachment points. Explain the phenomenon and provide your own conclusions.

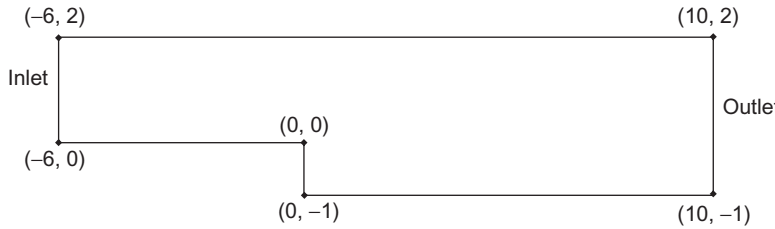


FIG. E.1 A schematic illustration of two-dimensional geometry of a backward-facing step.

E.2 ASSIGNMENT 2

E.2.1 Background and Aim

One common CFD application is the study of flows over external structures. In the automotive industry, it is important to determine the aerodynamic effects of the spacing between adjacent motor vehicles. The Ahmed model is often used in experiments as a representation of the motor vehicle due to its simple geometry and the ease of varying a number of important parameters.

The aims of simulating these models are as follows:

1. To create a CFD simulation of a single Ahmed model and extract meaningful data
2. To obtain CFD simulations and study the effects of spacing between two Ahmed models
3. To gain an understanding on the model requirements for turbulent flow and the importance of the distribution of y^+ values
4. To better understand boundary-layer flows
5. To learn how to distinguish and access results with available published experimental results

E.2.2 Problem Description

E.2.2.1 Single Car Configuration

The geometry of a typical Ahmed configuration is shown below. Students are required to develop a model simulation of a single two-dimensional Ahmed configuration model (Fig. E.2).

The coordinates for the Ahmed model are given as follows:

x	*y*
−0.94400	0.00000
0.00000	0.00000
−1.04400	0.10000
0.00000	0.17700
−1.04400	0.18800
−0.94400	0.28800
−0.19226	0.28800

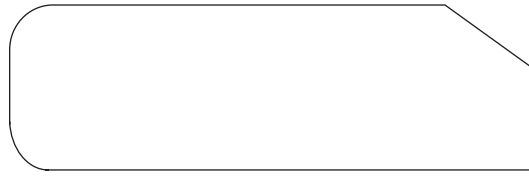


FIG. E.2 A two-dimensional geometry of an Ahmed model.

Note that the characteristic length (taken as the length of the vehicle) of the Ahmed configuration is not equivalent to unity. You will need to take into consideration when normalizing the Reynolds number and the spacing between adjacent vehicles.

Simulations are to be performed in air. The outer domain for the *single-model case* should be constructed according to the following Cartesian coordinates below, which should allow any wakes and vortices to be properly resolved within the computational domain:

x	*y*
−9.39600	−0.05000
−9.39600	4.12600
19.83600	−0.05000
19.83600	4.12600

At the inlet, the velocity should be set according to the *Reynolds number* (with respect to the car length) of 2.3×10^6. The flow *turbulence intensity* is assumed to be *1.8%*.

Instructions

1. Students are required to generate another mesh for a second *vehicle trailing the one created above* (hint, the domain may need to be purposefully extended to accommodate the additional vehicle).
2. Appropriate meshing should be employed, preferably similar to above. The same meshing methods and boundary conditions as used in previous section should be used herein.
3. *Vary the distance* between the trailing and leading vehicles. Formulate at least three additional cases. Discuss the flow characteristics and compare the drag and lift coefficients for both the lead and the rear car models (Figs E.3 and E.4).
4. Compare the drag and lift coefficients against experimental results (Figs E.3 and E.4).
5. Discuss the flow physics obtained from the predicted drag and lift coefficients.

E.2.2.2 Drafting Configuration

Instructions

1. Generate a mesh of sufficient quality (keeping in mind the numerical considerations of aspect ratios and grid skewness). Ensure *mesh independence* is reached (hint, use two or three different types of mesh densities).
2. Students must apply the attained knowledge gained from tutorials and the previous assignment to determine *suitable boundary conditions* (note that

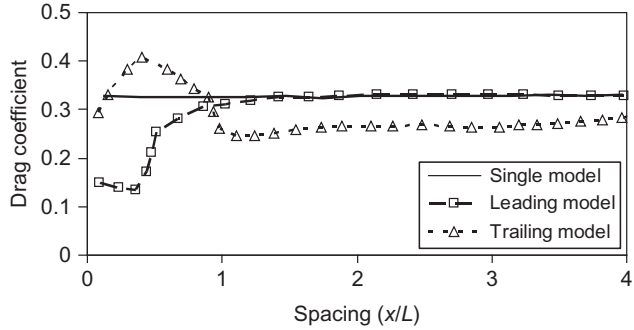


FIG. E.3 Drag coefficient for single Ahmed model and two Ahmed models at different vehicle spacing. *(From Watkins, S., Vino, G., 2004. On vehicle spacing and its effect on drag and lift. In: Proceedings of the 5th International Colloquium on Bluff Body Aerodynamics and Applications (BBAA5), Ottawa, Canada.)*

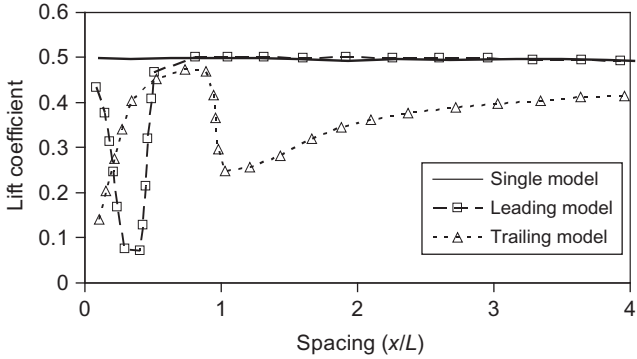


FIG. E.4 Lift coefficient for single Ahmed model and two Ahmed models at different vehicle spacing. *(From Watkins, S., Vino, G., 2004. On vehicle spacing and its effect on drag and lift. In: Proceedings of the 5th International Colloquium on Bluff Body Aerodynamics and Applications (BBAA5), Ottawa, Canada.)*

simulations can be performed by allowing the *floor* to *travel in the same speed as the air*).

3. Discuss the importance of y^+ values in turbulent flows. Students must ensure that acceptable values are achieved. If otherwise, provide an explanation on this.

E.3 ASSIGNMENT 3

E.3.1 Background and Aim

CFD has the ability to model fluid flows coupled with heat transfer. Basic understanding of the thermal and hydrodynamic behaviour of fluid within a

channel has long been an established area of research. CFD simulations can provide important insights into the flow behaviour and heat transfer to improve the heat transfer within a complex channel geometry having a waved-shaped wall (depicted below), which are increasing being explored in industrial heat exchangers.

The aims of this assignment are as follows:

1. To create a wavy channel consisting of a sufficient number of complete waves as to provide developed flow conditions
2. To create a wavy channel segment using the periodic boundary conditions
3. To investigate the effect of different turbulence models and wall functions on the solution
4. To implement a constant surface temperature and a constant surface heat flux on the wavy wall and determine the relationship between the Reynolds number and thermal properties
5. To compare and discuss simulation results with experimental results

E.3.2 Problem Description

The channel consists of a repeated section consisting of a straight wall at the top and a sine-wave-shaped wall at the bottom (Fig. E.5).

The *coordinates* for the geometry are given as follows:

0	0
0.25	0.1
0.5	0
0.75	−0.1
1	0
1	0
0	1
1	1

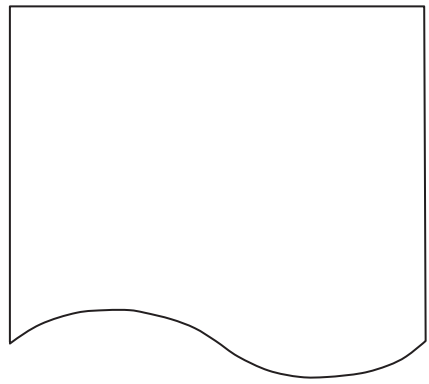


FIG. E.5 A section of the wavy channel.

The *flow properties* of the air are as follows:

Mass flow rate: $\dot{m} = 0.816$ kg/s
Density: $\rho = 1$ kg/m^3
Dynamic viscosity: $\mu = 0.0001$ kg/m s
Bulk fluid temperature: $T_b = 300$ K

Other thermal fluid properties are set as default.

The flow is *initialized* according to the following:

X velocity $= 0.816$ m/s
Turbulence kinetic energy $= 1$ m^2/s^2
Turbulence dissipation rate $= 1 \times 10^5$ m^2/s^3

Enhanced wall treatment is applied for all turbulence models (suitable y^+ values are adjusted accordingly as discussed in Chapter 6).

E.3.3 Instructions

1. Create a channel consisting of sufficient numbers of the section given above to provide developed flow conditions (hint, approximately 12 sections).
2. Compare the *NORMALIZED* axial velocity at the crest and the trough of the full model where the flow has become fully developed with the experimental results.
3. Create a section as described above using periodic boundary conditions (see Chapter 7).
4. Compare the *NORMALIZED* axial velocity at the crest ($x = 0.25$) and the trough ($x = 0.75$) of the periodic model with the experimental results. Discuss the relationship between the full model, periodic model, and experimental results.
5. Using the periodic model, investigate the accuracy of using the standard k–ε, RNG, and realizable turbulence models and compare them against the experimental results. Discuss which turbulence model is the most aptly suited for such a complex configuration.
6. Implement a *constant wall temperature of 500 K* on the wavy wall surface for a full model and discuss the thermal characteristics. Vary the flow to provide Reynolds numbers of 10,000 and 5400. Compare and discuss the effect of changing the flow rate.
7. Implement a *constant wall heat flux of 1000 W/m^2* on the wavy wall surface for a full model and discuss the thermal characteristics. Use only the initial Reynolds number.
8. Generate other results of interest: velocity, turbulence parameters, temperature distribution (wall and fluid), total heat transfer, and Nusselt number.

E.4 PROJECT GUIDELINE

E.4.1 Aim

The aim of the CFD project is to provide an opportunity for students to demonstrate their understanding of the fundamentals and usage of CFD software and to introduce them to the numerous applications within the software. Students are allowed to freely determine any topic of interest. It may be desirable that the intended CFD project topic coincides with the undertaking of your final year project, keeping in mind the many constraints and complexity of the flow problem to be simulated. Students are therefore strongly encouraged to consult and discuss the project proposal with the lecturer/instructor before embarking on the next stage of their numerical study.

E.4.2 Objectives

The following abilities should be demonstrated and explained in your project report:

1. The ability to use the commercial CFD software packages
   - Mesh generation and grid quality
   - Defining the settings of a flow problem, that is, boundary conditions and solver settings
   - Selecting appropriate CFD models, that is, turbulence models, heat transfer, or other types of simulations
2. The ability to use CFD as a tool for engineering design
   - Reduction of drag or increase of lift for flow over geometries, for example, car body or aerofoils
   - Increase of heat transfer for cooling of a car engine or reduction of heat transfer to prevent heat loss
   - To create desired flow control, that is, the ability to cause flow to move within a desired region
3. The ability to apply CFD knowledge to analyse numerical results
   - Discussions of the flow patterns and behaviours (e.g. wake flow, flow separation, boundary layer, and convective effects)
   - Discussions of the accuracy of the CFD solution with regard to the mesh quality, flow models chosen, and boundary/domain setting
   - Assumptions made on the actual model to allow for modelling simplifications to the original geometry

Note that not all the items listed above are applicable to all types of CFD problems. Please consult with lecturers or tutors concerning the above and ascertaining the suitability of the project. A brief project proposal outlining aims and scopes of the project, problem description, and objectives of the project should be prepared and submitted to the lecturers, which will be accounted for 5% of your project mark.

Examples of past CFD project topics:

- Effect of vehicle spacing on vehicles in convoy
- CFD analysis of wing in ground effect
- Investigation of the effect of winglet design on the lift and drag performance
- CFD simulation of flow over a bicycle helmet
- Study of the reduction of aerodynamic drag on a car–caravan combination
- Turbulent flow analysis over two two-dimensional wings of variable horizontal separation
- Investigation of flow field in areas of different hydropower plants
- Modelling of car air intake system and comparison of different designs
- Numerical investigation of trailing-edge flows
- Comparison of fowler flap systems through CFD

E.5 EXAMPLE—CFD PROJECT PROPOSAL PREPARED BY THE STUDENT

E.5.1 Introduction

Aerofoil design plays a pivotal role in the wing and control surface performance in aerospace engineering. Whilst wind-tunnel testing can be rather time-consuming and expensive, CFD provides an attractive alternative. Modelling of flow over an aerofoil is an important CFD problem. Amongst the many aerofoil design features, the flap (Fig. E.6) that when deployed increases the camber of the wing to give increased lift (and drag). This phenomenon is being utilized during takeoff and landing in most aircraft as lift (and drag)-enhancing devices (Fig. E.7).

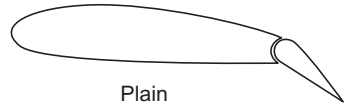


FIG. E.6 Plain flap.

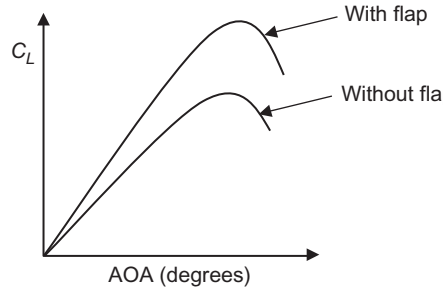


FIG. E.7 Lift curve slope.

E.5.2 Scope

The project will focus on the aerodynamic characteristics of a two-dimensional NACA 23012 aerofoil with a 20% scaled NACA 23012 plain flap. The aerofoil will be modelled at 0 degree angle of attack with flap settings of 0, 10, 20, 30, and 40 degrees. The Reynolds number of 1,400,000 helps to study the turbulent characteristics of the combo. The lift and drag coefficient and flow separation will be determined using the standard RNG k–ε and realizable k–ε turbulence models to assess the most appropriate model to be applied.

Results will be validated against benchmark experimental data of Carl Wenzinger (*Carl J. Wenzinger, 1937, Pressure distribution over an NACA 23012 Airfoil with an NACA 23012 external-airfoil flap. NACA Report No. 614*).

E.5.3 Objectives

- Create a quality mesh around the aerofoil/flap.
- Model the airflow around the aerofoil/flap at $Re = 1{,}400{,}000$ and SSL conditions with flap settings varying from 0 to 40 degrees using standard k–ε turbulence model.
- Measure the lift and drag coefficient and pressure and velocity distribution of the aerofoil/flap.
- Repeat with RNG k–ε and realizable k–ε turbulence models.
- Compare and discuss the results of the three turbulence models.
- Evaluate the accuracy of the results against experimental data.

E.6 OTHER TOPICS FOR CFD PROJECTS

E.6.1 CFD Project A: CFD Simulation of Turbulent Flow Over a Backward-Facing Step

E.6.1.1 Background

The backward-facing step is commonly used as a benchmark for the validation of numerous flow characteristics, including turbulence model, multiphase flows, and fundamental numerical methods. This model also has applications in industry, such as for combustion and HVAC.

E.6.1.2 Objectives

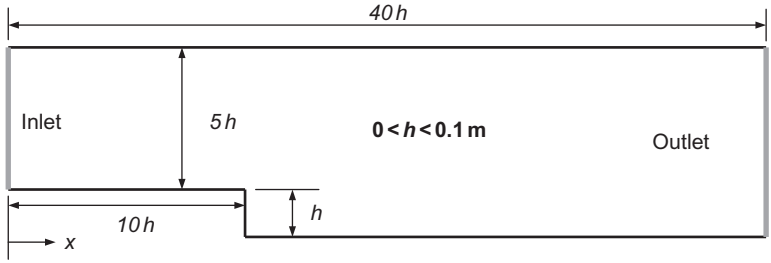
The aims of this simulation are the following:

1. Create a backward-facing step simulation appropriate for turbulence modelling.
2. Determine the effects of different meshing scheme.
3. Simulate turbulent flow and compare with the benchmark data.
4. Determine the effects of different turbulence models.

5. Understand the relevant flow characteristics.
6. Prepare a concise and well-written professional report.

E.6.1.3 Problem Description

Dry air at 27°C flows through a 2D duct with a backward-facing step at a Reynolds number, $Re_h = 5100$, based on the step height, h. The dimensions of this flow configuration are shown below. 'No-slip' conditions are applied at the walls, and it can be assumed that they are perfectly smooth (i.e. roughness height = 0 m). The turbulence intensity of the incoming flow can be assumed to be 0.01%, and thermal interaction between the walls and the fluid is assumed adiabatic (i.e. no heat transfer). For the purpose of this assignment, it is expected that no vortex shedding will occur (i.e. steady-state analysis). From extremely accurate direct numerical simulations (DNS), it has been determined that the reattachment of the separated boundary layer occurs on the bottom wall at $x = 16.28h$.



E.6.1.4 Required Discussions

1. Compare the following meshing schemes: (a) uniform structured quadrilateral mesh, (b) nonuniform structured quadrilateral mesh with mesh refinement in appropriate regions (with similar number of cells), and (c) unstructured triangular mesh with refinement in appropriate regions (with similar number of cells). Discuss the differences and the necessity of mesh refinement.
2. Using the best mesh determined from (1), run the case using appropriate settings for (a) a *standard* k–ε turbulence model and (b) a *realizable* k–ε turbulence model. Determine which model gives the better prediction. Discuss the differences of the k–ε models, referring to their characteristic equations.
3. Using the best model determined from (1) and (2), replace the dry air with ethylene glycol at 37°C flowing at the same Reynolds number ($Re_h = 5100$). Discuss any similarities or differences with the dry air simulation.
4. Discuss the relevant flow characteristics of the simulation.

E.6.2 CFD Project B: CFD Simulation of Pickup Trucks With Open/Closed Tubs

E.6.2.1 Background

CFD has been a vital tool in studying vehicle aerodynamics. These simulations aim to provide a better understanding on the flow behaviour over the complex geometries and give insights on the methods of increasing vehicle efficiency.

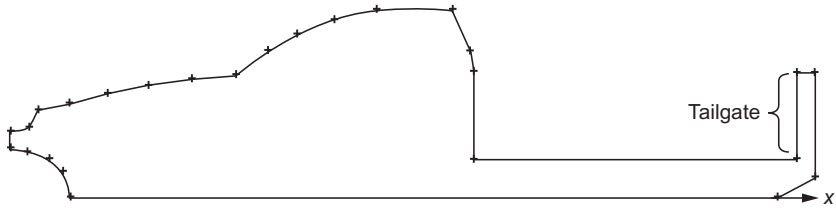
E.6.2.2 Objectives

The aims of this simulation are the following:

1. Create two-dimensional models of a pickup truck with the tub open and closed.
2. Create a mesh of sufficient quality to achieve grid independence.
3. Simulate turbulent flow and compare with benchmark data.
4. Understand and discuss the relevant flow characteristics, such as flow velocity and pressure, to design parameters, such as drag and lift forces.
5. Create a trailing pickup truck and investigate the effect of different distances on flow characteristics.
6. Prepare a concise and well-written report.

E.6.2.3 Problem Description

A truck as shown below (dimensions provided in addendum) is to be modelled (with tailgate closed). The moving truck is simulated travelling at a Reynolds number of 3.3×10^6 (based on the truck length). The standard k–ε turbulence model and standard wall functions are employed. Students are to create a sufficiently large domain to capture the generated wake. The inlet should have a turbulence intensity of 2%, and the lower boundary (parallel to the x-axis) should be set to a nonmoving smooth wall, so as to simulate wind-tunnel conditions. The system is assumed to be adiabatic and time-independent. For a single pickup truck with a closed tailgate, the drag coefficient was found to be 0.44.



E.6.2.4 Required Discussions

1. Determine appropriate boundary-layer settings to provide a mesh of sufficient quality for this simulation, including the calculations of the first-layer thickness for a standard wall model turbulence case.

2. Compare the simulation drag coefficient with the benchmark data to determine mesh independence.
3. Compare and discuss the flow characteristics of a single truck with the *tailgate open* with one with the *tailgate closed* to determine if this has an effect on the overall drag of the vehicle.
4. Compare and discuss the effect of adding a trailing truck of variable distance (recommended you do not exceed 3 lengths of the truck) on both the leading and trailing vehicles. You may set either truck to have an open or closed tailgate for this investigation. Plot and compare the drag and lift coefficients for both trucks against different separation lengths on a graph and discuss.

Note that you may need to extend the length of the domain to incorporate the extra truck.

E.6.2.5 Addendum

Coordinates for the pickup truck with closed tailgate are as follows:

x	*y*
0	0.354
0	0.224
0.0215	0.246
0.0215	0.354
0.045	0.199
0.4226	0.246
0.4226	0.354
0.4264	0.38
0.4504	0.432
0.5458	0.432
0.5981	0.419
0.6438	0.402
0.6795	0.38
0.7185	0.35
0.7743	0.346
0.8284	0.337
0.8792	0.328
0.9263	0.199
0.9263	0.199
0.9267	0.315
0.935	0.229
0.9518	0.246
0.966	0.307
0.9771	0.285
0.9798	0.255
1	0.26
1	0.281

E.6.3 CFD Project C: Investigation of Cooling Electronic Components Within a Computer

E.6.3.1 Background

CFD is a powerful tool in optimizing applications involving heat transfer. The cooling of electronic components within a computer has recently become an important issue. Particularly, increased processing power tends to generate more heat, which may cause hardware damage or failure.

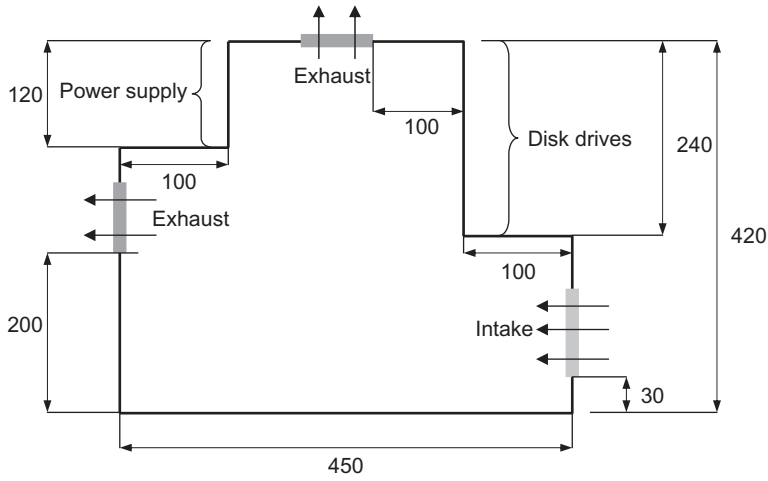
E.6.3.2 Objectives

The aims of this simulation are the following:

1. To prepare a suitable mesh of sufficient quality to analyse the thermal and flow characteristics of air cooling within a computer.
2. To understand the requirements for cooling electronic components within the system.
3. To design the system by placing the components in optimal positions to allow operation within the safety range through the understanding of the thermal and flow behaviour.
4. To determine the best positions for the electronic components.

E.6.3.3 Problem Description

A system case is shown below with the dimensions listed in millimetres. There are two exhaust openings (50 mm wide) and one air intake (80 mm wide). Air is to enter the system at a temperature of 20°C at a rate of 0.1 m^3/s with a turbulence intensity of 5%. The walls of the system are assumed to be adiabatic and smooth. Within the system, add (a) one processor with dimensions 25×25 mm with a heat output of 800 W/m^2, (b) three RAM modules with dimensions 135×30 mm with a heat output of 60 W/m^2, and (c) three other components of dimensions 100×50 mm with a heat output of 150 W/m^2. Use the standard k–ε turbulence model to simulate the flow turbulence.



E.6.3.4 Required Discussions

Arrange the components listed above within the system casing with the given boundary conditions in at least three different designs. Additionally, analyse the fluid flow and thermal characteristics to determine the most optimum locations for your components, bearing in mind that no component surface should exceed 80°C.

REFERENCES

Ahmed, S.R., Ramm, G., Faltin, G., 1984. Some Salient Features of the Time-Averaged Ground Vehicle Wake, SAE Paper 840300.

Aiba, S., Tsuchida, H., Ota, T., 1982a. Heat transfer around tubes in in-line tube banks. Bull. JSME 25, 919–926.

Aiba, S., Tsuchida, H., Ota, T., 1982b. Heat transfer around tubes in staggered tube banks. Bull. JSME 25, 927–933.

American Institute of Aeronautics and Astronautics, 1998. Guide for the Verification and Validation of Computational Fluid Dynamics, AIAA G-077-1998. American Institute of Aeronautics and Astronautics, Reston, USA.

Anderson, W., Thomas, J.L., Van Leer, B., 1986. Comparison of finite volume flux vector splittings for the Euler equations. AIAA J. 24, 1453–1460.

Anderson, J., Lorenz, C., Travesset, A., 2008. General purpose molecular dynamics simulations fully implemented on graphics processing units. J. Comput. Phys. 227, 5342–5359.

Apsley, D., Chen, W.-L., Leschziner, M., Lien, F.-S., 1997. Nonliner eddy viscosity modelling of separated flows. IAHR J. Hydraul. Res. 35, 723–748.

Archaya, S., Moukalled, F., 1989. Improvements to incompressible flow calculation on a non-staggered grid. Numer. Heat Transfer, Part B 15, 131–152.

Arcilla, A.S., Häuser, J., Eiseman, P.R., Thompson, J.F. (Eds.), 1991. Numerical Grid Generation in Computational Fluid Dynamics and Related Fields. North-Holland, Amsterdam.

Baker, A.J., 1983. Finite Element Fluid Mechanics. McGraw-Hill, New York.

Balaras, E., Benocci, C., Piomelli, U., 1996. Two-layer approximate boundary conditions for large-eddy simulations. AIAA J. 34, 1111–1119.

Baldwin, W.S., Lomax, H., 1978. Thin-Layer Approximation and Algebraic Model for Separated Turbulent Flow, AIAA Paper 87-257.

Bassi, F., Rebay, S., 2000. GMRES discontinuous Galerkin solution of the compressible Navier-Stokes equations. In: Cockburn, B., Karniadakis, G.E., Shu, C.W. (Eds.), Discontinuous Galerkin Methods. Lecture Notes in Computational Science and Engineering. vol. 11. Springer, Berlin, Heidelberg.

Battan, P., Goldberg, U., Chakravarthy, S., 2004. Interfacing statistical turbulence closures with large-eddy simulation. AIAA J. 42, 485–492.

Baum, H.R., McCaffrey, B.J., 1989. Fire induced flow field-theory and experiment. In: Proceedings of the 2nd International Symposium on Fire Safety Science, pp. 129–148.

Beam, R.M., Warming, R.F., 1978. An implicit factored scheme for the compressible Navier-Stokes equations. AIAA J. 16, 393–402.

Belytschko, T., Krongauz, Y., Organ, D., Fleming, M., Krysl, P., 1996. Meshless methods: an overview and recent developments. Comput. Methods Appl. Mech. Eng. 139, 3–47.

Benson, R.A., McRae, D.S., 1991. A solution adaptive mesh algorithm for dynamic/static refinement of two and three dimensional grids. In: 3th International Conference on Numerical Grid Generation in Computational Fluid Dynamics and Related Fields, Barcelona, Spain.

Benzi, R., Struglia, M.V., Tripiccione, R., 1996. Extended self-similarity in numerical simulations of three-dimensional anisotropic turbulence. Phys. Rev. E 53, 5565–5568.

Bertrand, F., Leclaire, L.-A., Levecque, G., 2005. DEM-based models for the mixing of granular materials. Chem. Eng. Sci. 60, 2517–2531.

Bhatnagar, P.L., Gross, E.P., Krook, M., 1954. A model for collision processes in gases. I: small amplitude processes in charged and neutral one-component system. Phys. Rev. 94, 511–525.

Bird, G.A., 1986. Direct simulation of gas at the molecular level. In: First World Congress on Computational Mechanics, Austin, TX.

Bird, G.A., 1994. Molecular Gas Dynamics and the Direct Simulation of Gas Flows. Oxford Press, Clarenden, UK.

Bourgoyne, D.A., Ceccio, S.L., Dowling, D.R., Jessup, S., Park, J., Brewer, W., Pankajakshan, R., 2000. Hydrofoil turbulent boundary layer separation at high Reynolds numbers. In: 23rd Symposium on Naval Hydrodynamics, Val de Reuil, France, September 17–22.

Boussinesq, J., 1868. Memoire sur l'influence des frottements dans les mouvements reguliers des fluides. J. Math. Pures Appl. 2 (13), 377–424.

Bradshaw, P., 1994. Turbulence: the chief outstanding difficulty of our subject. Exp. Fluids 16, 203–216.

Briley, W.R., McDonald, H., 1977. Solution of the multidimensional compressible Navier-Stokes equations by a generalized implicit method. J. Comput. Phys. 24, 372–379.

Canuto, C., Hussaini, M.Y., Quateroni, A., Zang, T.A., 1987. Spectral Methods in Fluid Dynamics. Springer-Verlag, Berlin.

Chang, J.L.C., Kwak, D., 1984. On the Method of Pseudo Compressibility for Numerically Solving Incompressible Flows, AIAA Paper 84-0252.

Chen, S., Doolen, G.D., 1998. Lattice Boltzmann method for fluid flows. Annu. Rev. Fluid Mech. 30, 329–364.

Chen, L., Tu, J.Y., Yeoh, G.H., 2003. Numerical simulation of turbulent wake flows behind two side-by-side cylinders. J. Fluids Struct. 18, 387–403.

Cheng, H.K., 1993. Perspectives on hypersonic viscous flow research. Annu. Rev. Fluid Mech. 25, 455–484.

Cheng, H.K., Emmanual, G., 1995. Perspectives on hypersonic nonequilibrium flow. AIAA J. 33, 385–400.

Cheung, S.C.P., Yeoh, G.H., Cheung, A.L.K., Yuen, R.K.K., 2007. Flickering behaviour of turbulent fires using large eddy simulation. Numer. Heat Transfer Part A: Appl. (in press).

Chew, P.L., 1989. Guaranteed-Quality Triangular Meshes, TR 89-983. Dept. Comp. Sci., Cornell University, NY.

Chiesa, M., Mathiesen, V., Melheim, J.A., Halvorsen, B., 2005. Numerical simulation of particulate flow by the Eulerian-Lagrangian and the Eulerian-Eulerian approach with the application to a fluidized bed. Comput. Chem. Eng. 29, 291–304.

Chorin, A.J., 1968. Numerical solution of Navier-Stokes equations. Math. Comput. 22, 745–762.

Choy, Y.-H., Merkle, C.L., 1993. The application of preconditioning in viscous flows. J. Comput. Phys. 105, 207–223.

Colburn, A.P., 1933. A method of correlating forced convection heat transfer data and a comparison with fluid friction. Trans. American Institute of Chemical Engineers. vol. 29 American Institute of Electrical Engineers, New York, pp. 174–210.

Colella, P., Woodward, P., 1984. The piecewise parabolic method for gas-dynamical simulations. J. Comput. Phys. 54, 174.

Cottet, G.H., Poncet, P., 2004. Advances in direct numerical simulations of 3D wall-bounded flows by vortex-in-cell methods. J. Comput. Phys. 193, 136–158.

Cox, G., Chitty, R., 1980. A study of the deterministic properties of unbounded fire plumes. Combust. Flame 39, 191–209.

Crowe, C., Sommerfield, M., Tsuji, Y., 1998. Multiphase Flows with Droplets and Particles. CRC Press, Florida.

Cundall, P.A., Strack, O.D.L., 1979. A discrete numerical model for granular assemblies. Geotechnique 29, 47–65.

Daru, V., Tenaud, C., 2004. High order one-step monotonicity-preserving schemes for unsteady compressible flow calculations. J. Comput. Phys. 193, 563–594.

Davidson, L., Peng, S.-H., 2003. Hybrid LES-RANS: a one-equation SGS model combined with a k-ω model for predicting recirculating flows. Int. J. Numer. Methods Fluids 43, 1003–1018.

De Berg, M., van Kreveld, M., Overmars, M., Schwarzkopf, O., 2000. Computational Geometry: Algorithms and Applications, second ed. Springer-Verlag, Berlin.

de Langhe, C., Merci, B., Dick, E., 2005a. Hybrid RANS/LES modelling with an approximate renormalization group. I. Model development. J. Turbul. 6, 1–18.

de Langhe, C., Merci, B., Lodefier, K., Dick, E., 2005b. Hybrid RANS/LES modelling with an approximate renormalization group II applications. J. Turbul. 6, 1–16.

Deen, N.G., Van Sint Annaland, M., Van Der Hoef, M.A., Kuipers, J.A.M., 2007. Review of discrete particle modeling of fluidized beds. Chem. Eng. Sci. 62, 28–44.

Demirdzic, I., Muzaferija, S., Peric, M., Schreck, E., 1997. Numerical method for simulation of flow problems involving moving and sliding grids. In: Proceedings of the 7th International Symposium on Computational Fluid Dynamics. Int. Academic Publishers, Beijing, China.

Deng, S., Jiang, L., Liu, C., 2007. DNS for flow separation control around airfoil by steady and pulsed jets. Comput. Fluids (in press).

Desjardin, P.E., Frankel, S.H., 1999. Two-dimensional large eddy simulation of soot formation in the near-field of a strongly radiating nonpremixed acetylene-air turbulent jet flame. Combust. Flame 119, 121–132.

Di Renzo, A., Di Maio, F.P., 2005. An improved integral non-linear model for the contact of particles in distinct element simulations. Chem. Eng. Sci. 59, 3461–3475.

Dopazo, C., 1993. Recent development in PDF methods. In: Libby, P.A., Williams, F.A. (Eds.), Turbulent Reacting Flows. Academic Press, New York.

Drikakis, D., 2002. Embedded turbulence model in numerical methods for hyperbolic conservation laws. Int. J. Numer. Methods Fluids 39, 763–781.

Duarte, C.A., Oden, J.T., 1996. AN H-P adaptive method using clouds. Comput. Methods Appl. Mech. Eng. 139, 237–262.

Dufort, E.C., Frankel, S.P., 1953. Stability conditions in the numerical treatment of parabolic differential equations. Math. Tables Other Aids Comput. 7, 559–573.

Ellero, M., Kröger, M., Hess, 2002. Viscoelastic flows studied by smoothed particle dynamics. J. Non-Newtonian Fluid Mech. 105, 35–51.

Elsen, E., LeGresley, P., Darve, E., 2008. Large calculation of the flow over a hypersonic vehicle using a GPU. J. Comput. Phys. 227, 10148–10161.

Fanelli, M., Feke, D.L., Manas-Zloczower, I., 2006. Prediction of the dispersion of particle clusters in the nano-scale, part I: steady shearing responses. Chem. Eng. Sci. 61, 388–473.

Farhat, C., 2005. CFD on moving grids: from theory to realistic flutter, maneuvering, and multidisciplinary optimization. Int. J. Comput. Fluid Dyn. 19, 595–603.

Fauci, L.J., McDonald, A., 1994. Sperm moltility in the presence of boundaries. Bull. Math. Biol. 57, 679–699.

Fletcher, C.A.J., 1984. Computational Galerkin Methods. Springer-Verlag, Berlin.

Forum, H.P.F., 1993. High performance Fortran language specification. Sci. Prog. 2, 1–70.

Forum, M.P.I., 1994. MPI: a message-passing interface standard. J. Supercomput. Appl. 8.

Fujii, K., 2005. Progress and future prospects of CFD in aerospace – wind tunnel and beyond. Prog. Aerosp. Sci. 42, 455–470.

Fujii, K., Obayashi, S., 1987a. Navier-Stokes simulations of transonic flows over a practical wing configuration. AIAA J. 25, 368–370.

Fujii, K., Obayashi, S., 1987b. Navier-Stokes simulations of transonic flows over a wing fuselage configuration. AIAA J. 25, 1587–1596.

Garnier, E., Mossi, M., Sagaut, P., Comte, P., Deville, M., 1999. On the use of shock-capturing schemes for large-eddy simulation. J. Comput. Phys. 153, 273–311.

Germano, M., Piomelli, U., Moin, P., Cabot, W., 1991. A dynamic subgrid-scale eddy viscosity model. Phys. Fluids 3, 1760–1765.

Ghias, R., Mittal, R., Lund, T.S., 2004. A Non-Body Conformal Grid Method for Simulation of Compressible Flows with Complex Immersed Boundaries, AIAA Paper 2004-0080.

Giles, M.B., 1990. Non-reflecting boundary conditions for Euler equation calculations. AIAA J. 28, 2050–2058.

Godunov, S.K., 1959. A finite difference method for the numerical computation of discontinuous solutions of the equations of fluid dynamics. Mat. Sbornik 47, 357.

Gordon, W.J., Thiel, L.C., 1982. Transfinite mappings and their application to grid generation. In: Thompson, J.F. (Ed.), Numerical Grid Generation. North-Holland, Amsterdam, pp. 171–192.

Gresho, P.M., 1991. Incompressible fluid dynamics: some fundamental formulation issues. Annu. Rev. Fluid Mech. 23, 182–188.

Gresho, P.M., Sani, R.L., 1990. On pressure boundary conditions for the incompressible Navier-Stokes equations. Int. J. Numer. Methods Fluids 7, 11–46.

Grotberg, J.B., Jensen, O.E., 2004. Biofluid mechanics in flexible tubes. Annu. Rev. Fluid Mech. 36, 121–147.

Guerts, B.J., 2001. Modern Simulation Strategies for Turbulent Flow. Edwards, Inc., Philadelphia.

Gumbert, C., Lohner, R., Parikh, P., Pirzadeh, S., 1989. A package for unstructured grid generation and finite element flow solvers. AIAA Pap. 89-2175.

Gunzburger, M.D., Nicolades, R.A. (Eds.), 1993. Incompressible Computational Fluid Dynamics Trends and Advances. Cambridge University Press, UK.

Gustafsson, B., Lotsedt, P., Goran, A., 2002. A Fourth-Order Difference Method for the Incompressible Navier-Stokes Equations. Numerical Simulation of Incompressible Flows. World Scientific Press, Washington.

Hafez, M., 2002. Numerical Simulation of Incompressible Flows. World Scientific Press, Washington.

Hahn, M., Drikakis, D., 2005. Large eddy simulation of compressible turbulence using high-resolution methods. Int. J. Numer. Methods Fluids 47, 971–977.

Hájek, J., Kermes, V., Stehlík, P., Šikula, J., 2005. Utilizing CFD as an efficient tool for improved equipment design. Heat Transfer Eng. 26, 15–24.

Harlow, F.H., Welch, J.E., 1965. Numerical calculation of time-dependent viscous incompressible flow with free surface. Phys. Fluids 8, 2182–2189.

Harten, A., 1989. ENO schemes with subcell resolution. J. Comput. Phys. 83, 148.

Hartwich, P.M., Agrawal, S., 1997. Method for Perturbing Multi-Block Patched Grids in Aeroelastic and Design Optimization Applications, AIAA Paper 91-2038.

Hassan, O., Probert, E.J., 1999. Grid control and adaptation. In: Thompson, J.F., Soni, B.K., Wetherhill, N.P. (Eds.), Handbook of Grid Generation. CRC Press, Florida, pp. 35.1–35.29.

Hazel, A.L., Heil, M., 2003. Steady finite-Reynolds-number flows in three-dimensional collapsible tubes. J. Fluid Mech. 486, 79–103.

He, X., Doolen, G.D., 1997. Lattice Boltzmann method on curvilinear coordinates system: vortex shedding behind a circular cylinder. Phys. Rev. E 56, 434–440.

He, X., Luo, L.-S., 1997. A priori derivation of the lattice Boltzmann equation. Phys. Rev. E 55, 6333–6336.

Heil, M., 1997. Stokes flow in collapsible tubes: computation and experiment. J. Fluid Mech. 353, 285–312.

Heil, M., Pedley, T.J., 1996. Large post-buckling deformations of cylindrical shells conveying viscous flow. J. Fluids Struct. 10, 565–599.

Hertz, H., 1882. Über die berührung fester elatischer körper. J. Reine Angew. Math. 92, 156–171.

Hieber, S.E., Koumoutsakos, P., 2005. A Lagrangian particle level set method. J. Comput. Phys. 210, 342–367.

Hirt, C.W., Nichols, B.D., 1981. Volume of fluid (VOF) method for dynamics of free boundaries. J. Comput. Phys. 39, 201–225.

Höhne, T., Krepper, E., Rohde, U., 2010. Application of CFD codes in nuclear reactor safety analysis. Sci. Technol. Nucl. Ins. (Article ID 198758).

Hoomans, B.P.B., Kuipers, J.A.M., Briels, W.J., Swaaij, W.P., 1996. Discrete particle simulation of bubble and slug formation in a two-dimensional gas-fluidized bed: a hard-sphere approach. Chem. Eng. Sci. 51, 99–118.

Hörschler, I., Meinke, M., Schröder, W., 2003. Numerical simulation of the flow field in a model of the nasal cavity. Comput. Fluids 32, 39–45.

Hou, S., Zuo, Q., Chen, S., Doolen, G., Cogley, A.C., 1995. Simulation of a cavity flow by the lattice Boltzmann method. J. Comput. Phys. 118, 329–347.

Hou, S., Sterling, J., Chen, S., Doolen, G., 1996. A lattice Boltzmann subgrid model for high Reynolds number flows. Fields Inst. Commun. 6, 151–166.

Hu, F.Q., Hussaini, M.Y., Manthey, J.L., 1996. Low-dissipation and low-dispersion Runge-Kutta schemes for computational acoustics. J. Comput. Phys. 124, 177–191.

Huang, W., 2001. Practical aspects of formulation and solution of moving mesh partial differential equations. J. Comput. Phys. 171, 753–775.

Huang, W., Russel, R.D., 1999. Moving mesh strategy based on a gradient flow equation for two-dimensional problems. SIAM J. Sci. Comput. 20, 998–1015.

Huang, W., Ren, Y., Russel, R.D., 1994. Moving mesh methods based on moving mesh partial differential equations. J. Comput. Phys. 113, 279–290.

Hubbard, B.J., Chen, H.C., 1994. A Chimera Scheme for Incompressible Viscous Flows with Applications to Submarine Hydrodynamics, AIAA Paper 94-2210.

Hubbard, B.J., Chen, H.C., 1995. Calculation of unsteady flows around bodies with relative motion using a chimera RANS method. In: Proceedings of the 10th ASCE Engineering Mechanics Conference, May 21–24, vol. II. Univ. of Colorado at Boulder, Boulder, CO, pp. 7832–7852.

Hucho, W.H., 1996. Road Vehicle Aerodynamic Design, An Introduction. Addison Wesley Longmann Ltd., Edinburgh, Harlow.

Humphrey, J.A.C., Whitelaw, J.A., Yee, G., 1981. Turbulent flow in a square duct with strong curvature. J. Fluid Mech. 102, 443–463.

Iaccarino, G., Kalitzin, G., Elkins, C.J., 2003. Numerical and experimental investigation of the turbulent flow in ribbed serpentine passage. Ann. Res. Briefs Cent. Turb. Res. 379–388.

Ince, N.Z., Launder, B.E., 1995. Three-dimensional and heat-loss effects on turbulent flow in a nominally two-dimensional cavity. Int. J. Heat Fluid Flow 16, 171–177.

Incropera, F.P., DeWitt, D.P., 1985. Fundamentals of Heat and Mass Transfer, second ed. Wiley, New York.

Ingram, C.L., McRae, D.S., Benson, R.A., 1993. Time accurate simulation of a self-excited oscillatory supersonic external flow with a multi-block solution adaptive mesh algorithm, AIAA 93-3387. In: 11th Computational Fluid Dynamics Conference, Orlando, FL.

Inthavong, K., Tian, Z.F., Li, H.F., Tu, J.Y., Yang, W., Xue, C.L., Li, C.G., 2006. A numerical study of spray particles deposition in a human nasal cavity. Aerosp. Sci. Technol. 40, 1034–1045.

Ishii, M., Hibiki, T., 2006. Thermo-Fluid Dynamics of Two-Phase Flows. Springer-Verlag, Berlin.

Issa, R.I., 1986. Solution of the implicitly discretised fluid flow equations by operator-splitting. J. Comput. Phys. 62, 40–65.

Jiang, G.-S., Shu, C.-W., 1996. Efficient implementation of weighted ENO schemes. J. Comput. Phys. 126, 202–228.

Jiang, L., Choudari, M., Chang, C., Liu, C., 2006. Numerical Simulations of Laminar-Turbulent Transition in Supersonic Boundary Layers, AIAA Paper 2006-3224.

Johansen, S.T., 2003. Mathematical modeling of metallurgical processes. In: 3rd International Conference on CFD in the Minerals and Process Industries. CSIRO, Melbourne, Australia.

Jones, W.P., 1979. Models for turbulent flows with variable density. In: Kollmann, W. (Ed.), Prediction Methods for Turbulent Flows. VKI Lecture Series. Hemisphere Publishing Corporation, New York, pp. 378–421.

Kadanoff, L., 1986. On two levels. Phys. Today 39, 7–9.

Kader, B., 1993. Temperature and concentration profiles in fully turbulent boundary layers. Int. J. Heat Mass Transfer 24, 1541–1544.

Kallinderis, Y. (Ed.), 2000. Adaptive Methods for Compressible CFD. Comput. Methods Appl. Sci. Eng., vol. 189. (Preface).

Kamakoti, R., Shyy, W., 2004. Fluid-structure interaction for aeroelastic applications. Prog. Aerosp. Sci. 40, 535–558.

Kampolis, I., Trompoukis, X., Asouti, V., Giannakoglou, K., 2010. CFD-based analysis and two-level aerodynamic optimization on graphics processing units. Comput. Methods Appl. Mech. Eng. 199, 712–722.

Kandil, O.A., Chung, H.A., 1988. Unsteady vortex-dominated flows around maneuvering wings over a wide range of mach numbers, AIAA Paper No. 88-0317. In: AIAA 26th Aerospace Sciences Meeting & Exhibit, Nevada, Reno.

Kato, M., Launder, B.E., 1993. Three-dimensional modelling and heat-loss effects on turbulent flow in a nominally two-dimensional cavity. Int. J. Heat Fluid Flow 16, 171–177.

Keyhani, K., Scherer, P.W., Mozell, M.M., 1995. Numerical simulation of airflow in the human nasal cavity. J. Biomech. Eng. 117, 429–441.

Khan, W.A., Culham, J.R., Yovanovich, M.M., 2006. Analytical model for convection heat transfer from tube banks. J. Thermophys. Heat Transf. 20, 720–727.

Kim, S.E., Choudbury, D., 1995. A near-wall treatment using wall functions sensitized to pressure gradient. ASME FED, Vol. 217, Separated and Complex Flows. ASME.

Kiris, C., Kwak, D., Rogers, S., 2002. Incompressible Navier-Stokes solvers in primitive variables and their applications to steady and unsteady flow simulations. In: Numerical Simulation of Incompressible Flows. World Scientific Press, Washington.

Kliafas, Y., Holt, M., 1987. LDV measurements of a turbulent air-solid two-phase flow in a 90° bend. Exp. Fluids 5, 73–85.

Knio, O.M., Ghoniem, A.F., 1992. The three-dimensional structure of periodic vorticity layers under non-symmetrical conditions. J. Fluid Mech. 243, 353–392.

Koelbel, C., Loveman, D., Schreiber, R., Steele, G., Zosel, M., 1994. The High Performance Fortran Handbook. MIT Press, Cambridge, MA.

Kolev, N.I., 2005. Multiphase Flow Dynamics 1. Springer-Verlag, Berlin.

Komatitsch, D., Erlebacher, G., Göddeke, D., Michéa, D., 2010. High-order finite-element seismic wave propagation modeling with MP on a large GPU cluster. J. Comput. Phys. 229, 7692–7714.

Koobus, B., Tran, H., Farhat, C., 2000. Computation of unsteady viscous flows around moving grids using k-ε turbulence model on unstructured dynamics grids. Comput. Methods Appl. Mech. Eng. 190, 1441–1466.

Koumoutsakos, P., 2005. Multiscale flow simulations using particles. Annu. Rev. Fluid Mech. 37, 457–487.

Koumoutsakos, P., Leonard, A., 1995. High resolution simulation of the flow around an impulsively started cylinder using vortex methods. J. Fluid Mech. 296, 1–38.

Krasny, R., 1986. A study of singularity formation in a vortex sheet by the point vortex approximation. J. Fluid Mech. 167, 65–93.

Kruggel-Emden, H., Wirtz, S., Scherer, V., 2009. Applicable contact force models for the discrete element model: the single particle perspective. ASME J. Press. Vessel. Technol. 131, 1–11.

Ku, D., 1997. Blood flow in arteries. Annu. Rev. Fluid Mech. 29, 399–434.

Kuwabara, G., Kono, K., 1987. Restitution coefficient in collision between two spheres. Jpn. J. Appl. Phys. Part 1 26, 1230–1233.

Kuzan, J.D., 1986. Velocity Measurements for Turbulent Separated and Near-Separated Flows Over Solid Waves (Ph.D. Thesis). Dept. Chem. Eng., Univ. Illonois, Urbana, IL.

Kwak, D., Kiris, C., 1991. Steady and unsteady solutions of the incompressible Navier-Stokes equations. AIAA J. 29, 603–610.

Kwak, D., Kiris, C., Kim, C.S., 2005. Computational challenges of viscous incompressible flows. Comput. Fluids 34, 283–299.

Labournasse, E., Sagaut, P., 2004. Advance in RAN-LES coupling, a review and an insight on the NLDE approach. Arch. Comput. Meth. Eng. 11, 199–256.

Launder, B.E., 1989. Second-moment closures: present and future? Int. J. Heat Fluid Flow 10, 282–300.

Launder, B.E., Spalding, D.B., 1974. The numerical computation of turbulent flows. Comput. Methods Appl. Mech. Eng. 3, 269–289.

Launder, B.E., Reece, G.J., Rodi, W., 1975. Progress in the development of a Reynolds stress turbulence closure. J. Fluid Mech. 86 (3), 537–566.

Lax, P.D., Richtmyer, R.D., 1956. Survey of the stability of linear finite difference equations. Commun. Pure Appl. Math. 9, 267–293.

Lee, J., Herrmann, H.J., 1993. Angle of repose and angle of marginal stability – molecular dynamics of granular particles. Phys. Rev. E 52, 3288–3291.

Lei, M., Archie, J., Kleimstreuer, C., 1997. Computational design of a bypass graft that minimizes wall shear stress gradients in the region of the distal anastomosis. J. Vasc. Surg. 25, 637–646.

Leonard, B.P., 1991. The ULTIMATE conservative difference scheme applied to unsteady one-dimensional advection. Comput. Methods Appl. Mech. Eng. 88, 17.

Lilek, Z., Muzaferija, S., Peric, M., Sedil, V., 1997. Computation of unsteady flows using non-matching blocks of structured grids. Numer. Heat Transfer Part B: Fundam. 23, 369–384.

Lilly, D.K., 1992. A proposed modification of the Germano subgrid-scale closure model. Phys. Fluids 4, 633–635.

Liseikin, V.D., 1999. Grid Generation Methods. Springer-Verlag, Berlin.

Liu, X., Osher, S., Chan, T., 1994. Weighted essentially non-oscillatory schemes. J. Comput. Phys. 115, 200–212.

Lo, S.H., 1985. A new mesh generation scheme for arbitrary planar domains. Int. J. Numer. Methods Eng. 21, 1403–1426.

Lockwood, F.C., Naguib, A.S., 1975. The prediction of fluctuations in the properties of free, round jet turbulent diffusion flames. Combust. Flame 24, 109–124.

Loner, R., Yang, C., Cebral, J., Soto, O., Camelli, F., 2002. On Incompressible Flow Solvers. Numerical Simulation of Incompressible Flows. World Scientific Press, Washington.

Luan, B., Robbins, M.O., 2005. The breakdown of continuum model for mechanical contacts. Nature 435, 929–932.

Luo, L., 1997. Symmetry breaking of flow in 2-D symmetric channels: simulations by lattice Boltzmann method. Int. J. Mod. Phys. C 8, 859–867.

MacCormack, R.W., 1969. The Effect of Viscosity in Hypervelocity Impact Cratering, AIAA Paper 60-354.

MacCormak, R.W., Paullay, A.J., 1972. Computational Efficiency Achieved by Time Splitting of Finite Difference Operators, AIAA Paper 72-154.

Magnussen, B.F., Hjertager, B.H., 1976. On mathematical modelling of turbulent combustion with special emphasis on soot formation and combustion. In: 16th Symposium (International) on Combustion. The Combustion Institute, pp. 1405–1414.

Malalasekera, W.M.G., Versteeg, H.K., Gilchrist, K., 1996. A review of research and an experimental study of the pulsation of buoyant diffusion flames and pool fires. Fire Mater. 20, 261–271.

Marcum, D.L., Weatherill, N.P., 1985. Unstructured grid generation using iterative point inserton and local reconnection. AIAA J. 33, 1619–1625.

MATLAB, 1992. The Student Edition of MATLAB. The Math Works Inc/Prentice Hall, Englewood Cliffs/New Jersey.

Mattson, T., 1995. Progamming environments for parallel and distributed computing: a comparison of p4, PVM, Linda and TCGMSG. Int. J. Supercomput. 9, 138–161.

Mavriplis, D., 1988. Multigrid solution of the two-dimensional Euler equations on unstructured triangular meshes. AIAA J. 26, 824–831.

Mavriplis, D.J., 1997. Unstructured grid techniques. Annu. Rev. Fluid Mech. 29, 473–514.

Maw, N., Barber, J.R., Fawcett, J.N., 1976. Oblique impact of elastic sphere. Wear 38, 101–114.

McCaffrey, B.J., 1979. Purely Buoyant Diffusion Flames: Some Experimental Results, NBSIR 79-1910. NIST.

McCaffrey, B.J., 1983. Momentum implications for buoyant diffusion flames. Combust. Flame 52, 149–216.

McDonald, P.W., 1971. The computation of transonic flow through two-dimensional gas turbine cascades, ASME Paper 71-GT-89. In: Gas Turbine Conference and Products Show, Houston, TX.

McRae, D.S., 2000. R-refinement grid adaptation and issues. Comput. Methods Appl. Sci. Eng. 189, 1288–1294.

Meneveau, C., Lund, T.S., Cabot, W.H., 1996. A Lagrangian dynamic subgrid-scale model of turbulence. J. Fluid Mech. 319, 353–385.

Menter, F.R., 1994a. Two-equation eddy-viscosity turbulence models for engineering applications. AIAA J. 32, 1598–1605.

Menter, F.R., 1994b. Eddy-Viscosity Transport Equations and Their Relation to the k-ε Model, NASA-TM-108854.

Métais, O., Lesieur, M., 1992. Spectral large-eddy simulation of isotropic and stably stratified turbulence. J. Fluid Mech. 256, 157–194.

Mishra, B.K., 2003a. A review of computer simulation of tumbling mills by the discrete element method, part I – contact mechanics. Int. J. Miner. Process. 71, 73–93.

Mishra, B.K., 2003b. A review of computer simulation of tumbling mills by the discrete element method, part II – practical applications. Int. J. Miner. Process. 71, 95–112.

Mittal, R., Iaccarino, G., 2005. Immersed boundary methods. Annu. Rev. Fluid Mech. 37, 239–261.
Mittal, R., Moin, P., 1997. Suitability of upwind-biased finite difference schemes for large-eddy simulation of turbulent flows. AIAA J. 35, 1415.
Mittal, R., Utturkar, Y., Udaykumar, H.S., 2002. Computational Modeling and Analysis of Biomimetric Flight Mechanisms, AIAA Paper 2002-0865.
Mittal, R., Seshadri, V., Udaykumar, H.S., 2004. Flutter, tumble and vortex induced autorotation. Theor. Comput. Fluid Dyn. 17, 165–170.
Monaghan, J.J., 1988. An introduction to SPH. Comput. Phys. Commun. 48, 89–96.
Morris, P.J., Long, L.N., Wang, Q., Lockard, D.P., 1997. Numerical Prediction of High-Speed Jet Noise, AIAA Paper 91-1958.
Morris, P.J., Long, L.N., Wang, Q., Pilon, A.R., 1998. High-Speed Jet Noise SImulations, AIAA Paper 98-2290.
Morsi, S.A., Alexander, J.A., 1972. An investigation of particle trajectories in two-phase systems. J. Fluid Mech. 55, 193–201.
Morsi, Y.S., Tu, J.Y., Yeoh, G.H., Yang, W., 2004. Principal characteristics of turbulent gas-particulate flow in the vicinity of single tube and tube bundle structure. Chem. Eng. Sci. 59, 3141–3157.
Muntz, E.P., 1989. Rarefied gas dynamics. Annu. Rev. Fluid Mech. 21, 387–417.
Murakami, S., 1993. Comparison of various turbulence models applied to a bluff body. J. Wind Eng. Ind. Aerodyn. 46–47, 21–36.
Najm, H.H., Wyckoff, P.S., Knio, O.M., 1998. A semi-implicit numerical scheme for reacting flow: I. Stiff chemistry. J. Comput. Phys. 143, 381–402.
Nakayama, Y. (Ed.), 1998. Visualised Flow. Pergamon Press, Oxford.
Oberkampf, W.L., Trucano, T.G., Hirsch, C., 2002. Verification, validation and predictive capability in computational engineering and physics. In: 21st Century Workshop. John Hopkins University/Applied Physics Laboratory, MA, USA.
Oran, E.S., Oh, C.K., Cybyk, B.Z., 1998. Direct simulation Monte Carlo: recent advances and applications. Annu. Rev. Fluid Mech. 30, 403–441.
Orszag, S.A., Israeli, N., Deville, M.O., 1986. Boundary conditions for incompressible flow. J. Sci. Comput. 1, 75–111.
Papadrakakis, M., Stavroulakis, G., Karatarakis, A., 2011. A new ear in scientific computing: domain decomposition methods in hybrid CPU-GPU architectures. Comput. Methods Appl. Mech. Eng. 200, 1490–1508.
Park, N., Yoo, J.Y., Choi, D., 2004. Discretisation errors in large-eddy simulation on the suitability of centered and upwind-biased compact difference schemes. J. Comput. Phys. 198, 580–616.
Patankar, S.V., Spalding, D.B., 1972. A calculation procedure for heat, mass and momentum transfer in three-dimensional parabolic flows. Int. J. Heat Mass Transfer 15, 1787–1806.
Patel, V.C., Rodi, W., Scheuerer, G., 1985. Turbulence model for near-wall and low Reynolds number flows: a review. AIAA J. 23, 1308–1319.
Patera, A.T., 1984. A spectral element method for fluid dynamics: laminar flow in a channel expansion. J. Comput. Phys. 54, 468–488.
Peaceman, D.W., Rachford, H., Jr, H., 1955. The numerical solution of parabolic and elliptic differential equations. J. Soc. Ind. Appl. Math. 3 (1), 28–41.
Perktold, K., Resch, M., Peter, R.O., 1991. Three-dimensional numerical analysis of pulsatile flow and wall shear stress in the carotid artery bifurcation. J. Biomech. 24, 409–420.
Peskin, C.S., 1972. Flow Patterns Around Heart Valves: A Digital Method for Solving the Equations of Motion (Ph.D. Thesis). Physiol., Albert Einstein Coll. Med., Univ. Microfilms 72-30, p. 378.

Peters, N., 2000. Turbulent Combustion. Cambridge University Press, Cambridge, UK.

Piomelli, U., Ferziger, J.H., Moin, P., 1987. Models for Large Eddy Simulation of Turbulent Channel Flows Including Transpiration, Technical Report, Report TF-32, Dept. Mech. Eng., Stanford University.

Piomelli, U., Ferziger, J.H., Moin, P., Kim, J., 1989. New approximate boundary conditions for large eddy simulations of wall-bounded flows. Phys. Fluids A 1, 1061–1068.

Pope, S.B., 1994. Lagrangian PDF methods for turbulent flows. Annu. Rev. Fluid Mech. 26, 23–63.

Portscht, R., 1975. Studies on characteristic fluctuations of the flame radiation emitted by fires. Combust. Sci. Technol. 10, 73–84.

Posner, J.D., Buchanan, C.R., Dunn-Rankin, D., 2003. Measurement and prediction of indoor air flow in a model room. Energ. Buildings 35, 269–289.

Rai, M.M., Moin, P., 1991. Direct simulation of turbulent flow using finite-difference schemes. J. Comput. Phys. 96, 15–53.

Rajamani, G.K., 2006. CFD Analysis of Air Flow Interactions in Vehicle Platoons (M.Eng. Thesis). RMIT University, Australia.

Rappitsch, G., Perktold, K., 1996. Pulsatile albumin transport in large arteries. J. Biomech. Eng. 118, 511–519.

Rhie, C.M., Chow, W.L., 1983. A numerical study of the turbulent flow past an isolated airfoil with trailing edge separation. AIAA J. 21, 1525–1532.

Richards, K., Bithell, M., Dove, M., Hodge, R., 2004. Discrete-element modelling: methods and applications in the environmental sciences. Philos. Trans. R. Soc. Lond. A 362, 1797–1861.

Rizzi, A.W., Inuoye, M., 1973. Time split finite volume method for 3D blunt body flows. AIAA J. 11, 1478–1485.

Roache, P.J., 1997. Quantification of uncertainty in computational fluid dynamics. Annu. Rev. Fluid Mech. 29, 123–160.

Rodi, W., 1980. Turbulence Models and Their Application in Hydraulics – A State of the Art Review. IAHR, Delft, The Netherlands.

Rodi, W., 1991. Experience with Two-Layer Models Combining the k-ε Model With a One-Equation Model Near the Wall, AIAA Paper 91-0216.

Rodi, W., 1993. Turbulence Models and Their Application in Hydraulics. Balkema, Rotterdam.

Roe, P.L., 2005. Computational fluid dynamics – retrospective and prospective. Int. J. Comput. Fluid Dyn. 19, 581–594.

Rogers, S.E., Kwak, D., Kiris, C., 1991. Steady and unsteady solutions of the incompressible Navier-Stokes equations. AIAA J. 29, 603–610.

Roma, A.M., Peskin, C.S., Berger, M.J., 1999. An adaptive version of the immersed boundary method. J. Comput. Phys. 153, 509–534.

Rosenfeld, M., Kwak, D., Vinokur, M., 1991. A fractional-step method for unsteady incompressible Navier-Stokes equations in generalized coordinate systems. J. Comput. Phys. 94, 102–137.

Rosenhead, L., 1930. The spread of vorticity in the wake behind a cylinder. Proc. R. Soc. Lond. A 127, 512–590.

Ruppert, J., 1993. A new and simple algorithm for quality two-dimensional mesh generation. In: Proceedings of Fourth ACM-SIAM Symposium on Discrete Algorithms, pp. 83–92.

Ryck, B., Makiola, B., 1988. Particle dispersion in a single-sided backward facing step flow. Int. J. Multiphase Flow 14, 787–800.

Saad, Y., Schultz, M., 1985. Conjugate gradient-like algorithms for solving nonsymmetric linear systems. SIAM J. 44, 417–424.

Sadd, M.H., Tai, Q.M., Shukla, A., 1993. Contact law effects on wave-propagation in particulate materials using distinct element modeling. Int. J. Non-Linear Mech. 28, 251–265.

Sagaut, P., 2004. Large-Eddy Simulation for Incompressible Flows – An Introduction. Springer-Verlag, Berlin.

Sethan, J.A., 1996. Level Set Methods. Cambridge University Press, Cambridge, UK.

Shah, K.B., Ferziger, J.H., 1997. A fluid mechanisms view of wind engineering: large eddy simulation of flow over a cubical obstacle. In: Meroney, R.N., Bienkiewicsz, B. (Eds.), Computer Wind Engineering. vol. 2. Elsevier, Amsterdam, pp. 211–236.

Shan, X., 1997. Simulation of Rayleigh-Bénard convection using a lattice Boltzmann method. Phys. Rev. E 55, 2780–2788.

Shan, H., Jiang, L., Liu, C., 2005. Direct numerical simulation of flow separation around a NACA0023 airfoil. Comput. Fluids 34, 1096–1114.

Shepard, M.S., Georges, M.K., 1991. Three-dimensional mesh generation by finite octree technique. Int. J. Numer. Methods Eng. 32, 709–749.

Shewchuk, J.R., 2002. Delaunay refinement algorithms for triangular mesh generation. Comput. Geom. 22, 21–74.

Shih, T.-H., Liou, W.W., Shabbir, A., Yang, Z., Zhu, J., 1995. A new k-ε eddy viscosity model for high Reynolds number turbulent flows. Comput. Fluids 24, 227–238.

Shu, C.-W., Osher, S., 1988. Efficient implementation of essentially non-oscillatory schemes. I. J. Comput. Phys. 77, 439–471.

Shu, C.-W., Osher, S., 1989. Efficient implementation of essentially non-oscillatory schemes. II. J. Comput. Phys. 83, 32–78.

Simon, H., 1992. Parallel Computational Fluid Dynamics. MIT Press, Cambridge, MA.

Smagorinsky, J., 1963. General circulation experiments with the primitive equation, part 1: the basic experiment. Mon. Weather Rev. 91, 99–164.

Smith, R.E., 1982. Algebraic grid generation. In: Thompson, J.F. (Ed.), Numerical Grid Generation. North-Holland, Amsterdam, pp. 137–170.

Soni, B., Thompson, D., Koomullil, R., Thornburg, H., 2001. GGTK: A tool kit for static and dynamic geometry-grid generation, AIAA 2001-1164. In: AIAA 39th Aerospace Science Meeting, Reno, Nevada.

Spaid, M.A.A., Phelan Jr., F.R., 1997. Lattice Boltzmann methods for modeling microscale flow in fibrous porous media. Phys. Fluids 9, 2468–2474.

Spalart, P.R., Jou, W.H., Strelets, M., Allamaras, S.R., 1997. Comments on the feasibility of LES for wings, and on a hybrid RANS/LES approach. In: Liu, C., Liu, Z. (Eds.), Advances in DNS/LES. Greyden Press, Columbus, pp. 137–148.

Spalding, D.B., 1971. Mixing and chemical reaction in steady confined turbulent flames. In: 13th Symposium (International) Combustion. The Combustion Institute, pp. 649–657.

Spalding, D.B., 1972. A novel finite-difference formulation for differential expressions involving both first and second derivatives. Int. J. Numer. Methods Eng. 4, 551–559.

Spalding, D.B., 1980. Numerical computation of multi-phase fluid flow and heat transfer. In: Taylor, C., Morgan, K. (Eds.), Recent Advances in Numerical Methods in Fluid. vol. 1, pp. 139–167.

Speziale, C.G., 1998. Turbulence modeling for time-dependent RANS and VLES: a review. AIAA J. 36, 173–184.

Squires, K.D., Constantinescu, G.S., 2003. LES and DES investigations of turbulent flow over a sphere at $Re = 10{,}000$. Flow Turbul. Combust. 70, 267–298.

Stone, H.L., 1968. Iterative solution of implicit approximations of multidimensional partial differential equations. SIAM J. Numer. Anal. 5 (3), 530–558.

Strelets, M., 2001. Detached Eddy Simulation of Massively Separated Flows, AIAA Paper 2001-0879.

Sunarso, A., Tsuiji, T., Chono, S., 2010. GPU-accelerated molecular dynamics simulation for study of liquid crystalline flows. J. Comput. Phys. 229, 5486–5497.

Sunderam, V., Geist, G., Dongarra, J., Manchek, R., 1990. PVM: a framework for parallel distributed computing. J. Concurrency: Prac. Exp. 2, 315–339.

Suresh, A., Huynh, H.T., 1997. Accurate monotonicity-preserving schemes with Runge-Kutta time stepping. J. Comput. Phys. 136, 83–99.

Sutera, S.P., Skalak, R., 1993. The History of Poiseuille's Law. Annu. Rev. Fluid Mech. 25, 1–19.

Sweby, P.K., 1984. High resolution schemes using flux limiters for hyperbolic conservation laws. SIAM J. Numer. Anal. 21, 995–1011.

Sweet, R.A., 1973. Direct methods for the solution of Poisson's equation on a staggered grid. J. Comput. Phys. 12, 422–428.

Taylor, C.A., Draney, M.T., 2004. Experimental and computational methods in cardiovascular fluid mechanics. Annu. Rev. Fluid Mech. 36, 197–231.

Taylor, C.A., Draney, M.T., Ku, J.P., Parker, D., Steele, B.N., et al., 1999. Predictive medicine: computational techniques in therapeutic decision-making. Comput. Aided Surg. 4, 231–247.

Temmerman, L., Hadziabdic, M., Leschziner, M.A., Hanjalic, K., 2005. A hybrid two-layer URANS-LES approach for large eddy simulation at high Reynolds numbers. Int. J. Numer. Methods Fluids 26, 173–190.

Tennekes, H., Lumley, J.L., 1976. A First Course in Turbulence. MIT Press, Cambridge, MA.

Tezduyar, T.E., 2001. Finite element methods for flow problems with moving boundaries and interfaces. Arch. Comput. Meth. Eng. 8, 83–130.

Thomas, J.L., Diskin, B., Brandt, A., 2003. Textbook multigrid efficiency for fluid simulations. Annu. Rev. Fluid Mech. 35, 317–340.

Thomasset, F., 1981. Implementation of Finite Element Methods for Navier-Stokes Equations. Springer-Verlag, Berlin.

Thompson, J.F., Warsi, S.U.A., Mastin, C.W., 1982. Boundary-fitted coordinate systems for numerical solution of partial differential equations – a review. J. Comput. Phys. 47, 1–108.

Thompson, J.F., Warsi, Z.U.A., Mastin, C.W., 1985. Numerical Grid Generation – Foundations and Applications. Elsevier, New York.

Thompson, J.F., Soni, B.K., Weatherhill, N.P., 1999. Handbook of Grid Generation. CRC Press, Florida.

Thornton, C., 1997. Coefficient of restitution for collinear collisions of elastic perfectly plastic spheres. J. Appl. Mech. Trans. ASME 64, 383–386.

Tian, Z.F., Tu, J.Y., Yeoh, G.H., 2005. Numerical simulation and validation of dilute gas-particle flow over a backward facing step. Aerosp. Sci. Technol. 39, 319–332.

Tian, Z.F., Tu, J.Y., Yeoh, G.H., 2006. On the numerical study of contaniminat particle concentration in indoor airflow. Build. Environ. 41, 1504–1514.

Tian, W., Sevilla, T.A., Zuo, W.D., 2016. A systematic evaluation of accelerating indoor airflow simulations using cross-platform parallel computing. J. Build. Perform. Simul. https://doi.org/10.1080/19401493.2016.1212933.

Timmermann, G., 2000. A cascadic multigrid algorithm for semilinear elliptic problems. Numer. Math. 86, 717–731.

Tomas, J., 2003. Mechanics of nanoparticle adhesion – a continuum approach. In: Mittal, V.L. (Ed.), Particles on Surfaces 8: Detection Adhesion and Removal. VSP, Utrecht, pp. 183–229.

Toro, E.F., 1997. Riemann Solvers and Numerical Methods for Fluid Dynamics: A Practical Introduction. Springer-Verlag, Berlin.

Tsuji, Y., Tanaka, T., Ishida, T., 1992. Lagrangian numerical simulation of plug flow of cohesionless particles in a horizontal pipe. Powder Technol. 71, 239–250.

Tsuji, Y., Kawaguchi, T., Tanaka, T., 1993. Discrete particle simulation of two-dimensional fluidized bed. Powder Technol. 77, 79–87.

Tu, J.Y., 1997. Computational of turbulent two-phase flow on overlapped grids. Numer. Heat. Transfer Part B: Fundam. 32, 175–195.

Tu, J.Y., Fletcher, C.A.J., 1995. Numerical computation of turbulent gas-solid particle flow in a 90° bend. AICHE J. 41, 2187–2197.

Tu, J.Y., Fuchs, L., 1992. Overlapping grids and multigrid methods for three-dimensional unsteady flow calculations in IC engines. Int. J. Numer. Methods Fluids 15, 693–714.

Tu, J.Y., Abu-Hijleh, B., Xue, C., Li, C.G., 2004a. CFD simulation of air/particle flow in the human nasal cavity. In: Proceedings of the 5th International Conference on Multiphase Flow, Yokohama, Japan.

Tu, J.Y., Yeoh, G.H., Morsi, Y.S., Yang, W., 2004b. A study of particle rebounding characteristics of gas-particle flow over curved surface. Aerosp. Sci. Technol. 38, 739–755.

Tucker, P., 2003. Differential Equation Based Length Scales to Improve DES and RANS Simulations, AIAA Paper 2003-3968.

Tucker, P.G., Davidson, L., 2004. Zonal *k-l* based large eddy simulation. Comput. Fluids 33, 267–287.

Turkel, E., 1999. Preconditioning techniques in computational fluid dynamics. Annu. Rev. Fluid Mech. 31, 385–416.

Unverdi, S., Tryggvason, G., 1992. A front-tracking method for viscous, incompressible, multifuild flows. J. Comput. Phys. 100, 25–42.

Valino, L., 1998. A field Monte-Carlo formulation for calculating the probability density function of a single scalar in a turbulent flow. Flow Turbul. Combust. 60, 151–172.

Van Doormal, J.P., Raithby, G.D., 1984. Enhancements of the SIMPLE method for predicting incompressible fluid flows. Numer. Heat Transfer 7, 147–163.

Van Doormal, J.P., Raithby, G.D., 1985. An evaluation of the segregated approach for predicting incompressible fluid flows, ASME Paper 85-HT-9. In: National Heat Transfer Conference, Denver, Colorado.

Van Drient, E.R., 1952. Investigation of Laminar Boundary Layer in Compressible Fluids Using the Crocco Method, NACA Tech. Note 2597.

Van Driest, E.R., 1956. On turbulent flow near a wall. J. Aerosol Sci. 23, 1007–1011.

Van Leer, B., 1974. Towards the ultimate conservative difference scheme, II. Monotonicity and conservation combined in a second-order scheme. J. Comput. Phys. 14, 361–370.

Van Leer, B., 1977a. Towards the ultimate conservative difference scheme, III. Upstream-centered finite difference schemes for ideal compressible flow. J. Comput. Phys. 23, 263–275.

Van Leer, B., 1977b. Towards the ultimate conservative difference scheme, IV. A second order sequel to Godunov's method. J. Comput. Phys. 23, 276–299.

Van Leer, B., 1979. Towards the ultimate conservative difference scheme, V. A new approach to numerical convection. J. Comput. Phys. 32, 101–136.

Verlet, L., 1967. Computer experiments on classical fluids, I. Thermodynamical properties of Lennard-Jones molecules. Phys. Rev. E 55, 3546–3554.

Vino, G., Watkins, S., Mousley, P., Watmuff, J., Prasad, S., 2004. The unsteady near-wake of a simplified passenger car. In: 15th Australasian Fluid Mechanics Conference, Sydney, Australia.

Vu-Quoc, L., Zhang, X., 1999. An elastoplastic force-displacement model in the normal direction: displacement-driven version. Proc. R. Soc. Lond. Ser. A 455, 4013–4044.

Walton, O.R., Braun, R.L., 1986. Computer-simulation of the mechanical sorting of grains. Powder Technol. 48, 239–245.

Wang, M., Moin, P., 2002. Dynamic wall modeling for large-eddy simulation of complex turbulent flows. Phys. Fluids 14, 2043–2051.

Wang, Y.Q., Jackson, P., Phaneu, T.J., et al., 2006. Turbulent flow through a staggered tube bank. J. Thermophys. Heat Transf. 20, 738–747.

Watkins, S., Vino, G., 2004. On vehicle spacing and its effect on drag and lift. In: Proceedings of the 5th International Colloquium on Bluff Body Aerodynamics and Applications (BBAA5), Ottawa, Canada.

Wesseling, P., 1995. Introduction to Multi-Grid Methods, CR-195045 ICASE 95-11. NASA.

Wilcox, D.C., 1998. Turbulence Modelling for CFD. DCW Industries Inc.

Wilson, N.M., 2002. Geometric Algorithms and Software Architecture for Computational Prototyping: Applications in Vascular Surgery and MEMS (Ph.D. Thesis). Stanford Univ., Stanford.

Witry, A., Al-Hajeri, M.H., Bondok, A.A., 2005. Thermal performance of automotive aluminium plate radiator. Appl. Therm. Eng. 25, 1207–1218.

Wolfshtein, M.W., 1969. The velocity and temperature distribution in a one-dimensional flow with turbulence augmentation and pressure gradient. Int. J. Heat Mass Transfer 12, 301–312.

Yakhot, V., Orszag, S.A., 1986. Renormalization group analysis of turbulence. I. Basic theory. J. Sci. Comput. 1, 1–15.

Yakhot, V., Prszag, S.A., Tangham, S., Gatski, T.B., Speciale, C.G., 1992. Development of turbulence models for shear flows by a double expansion technique. Phys. Fluids A 4, 1510–1520.

Yanenko, N.N., 1971. The Method of Fractional Steps. Springer-Verlag, Berlin.

Yang, Z.L., Dinh, T.N., Nourgaliev, R.R., Sehgal, B.R., 2000. Numerical investigation of bubble coalescence characteristics under nucleate boiling condition by a lattice Boltzmann model. Int. J. Therm. Sci. 389, 1–17.

Yang, Y.X., Zhou, B., Post, J.R., Scheepers, E., Reuter, M.A., Boom, R., 2006. Computational fluid dynamics simulation of pyrometallurgical processes. In: 5th International Conference on CFD in the Minerals and Process Industries. CSIRO, Melbourne, Australia.

Yeoh, G.H., Tu, J.Y., 2005. Thermal-hydrodynamics modelling of bubbly flows with heat and mass transfer. AICHE J. 51, 8–27.

Yeoh, G.H., Tu, J.Y., 2006a. Numerical modelling of gas-liquid with and without heat and mass transfer. Appl. Math. Model. 30, 1067–1095.

Yeoh, G.H., Tu, J.Y., 2006b. Two-fluid and population balance models for subcooled boiling flow. Appl. Math. Model. 30, 1370–1391.

Yeoh, G.H., Behnia, M., de Vahl Davis, G., Leonardi, E., 1990. A numerical study of three-dimensional natural convection during freezing of water. Int. J. Numer. Methods Eng. 30, 899–914.

Yeoh, G.H., Lee, E.W.M., Yuen, R.K.K., Kwok, W.K., 2002. Fire and smoke distribution in a two-room compartment structure. Int. J. Numer. Methods Heat Fluid Flow 12, 178–194.

Yerry, M.A., Shepard, M.S., 1984. Three-dimensional mesh generation by modified octree technique. Int. J. Numer. Methods Eng. 20, 1965–1990.

Yu, G., Xhang, Z., Lessmann, R., 1998. Fluid flow and particle diffusion in the human upper respiratory system. Aerosp. Sci. Technol. 28, 146–158.

Yun, G., Kim, D., Choi, H., 2006. Vortical structures behind a sphere at subcritical Reynolds numbers. Phys. Fluids 18 (015102), 1–14.

Zang, Y., Street, R.L., Koseff, J.R., 1993. A dynamic mixed subgrid-scale model and its application to turbulent recirculating flows. Phys. Fluids A 5, 3186–3196.

Žukauskas, A., Ulinskas, R., 1988. Heat Transfer in Tube Banks in Crossflow. Hemisphere, Washington.
Zukoski, E.E., Cetegen, B.M., Kubota, T., 1984. Visible structures of buoyant diffusion flames. In: 20th Symposium (International) Combustion. The Combustion Institute, pp. 361–366.
Zwartz, G.J., Guilmette, R.A., 2001. Effect of flow rate on particle deposition in a replica of a human nasal airway. Inhal. Toxicol. 13, 109–127.

FURTHER READING

Anderson Jr., J.D., 1995. Computational Fluid Dynamics – The Basics With Applications. McGraw-Hill, New York.
Çengel, Y.A., 2003. Heat Transfer: A Practical Approach. McGraw-Hill, New York.
Çengel, Y.A., Turner, R., 2005. Fundamentals of Thermal-Fluid Science, second ed. McGraw-Hill, New York.
Chung, T.J., 2002. Computational Fluid Dynamics. Cambridge University Press, Cambridge, UK.
Crowe, T.C., Elger, D.F., Roberson, J.A., 2005. Engineering Fluid Mechanics, eighth ed. Wiley, New York.
Drikakis, D., Rider, W., 2005. High-Resolution Methods for Incompressible and Low-Speed Flows. Springer-Verlag, Berlin.
Ferziger, J.H., Perić, M., 1999. Computational Methods for Fluid Dynamics. Springer-Verlag, Berlin.
Fletcher, C.A.J., 1991. Computational Techniques for Fluid Dynamics. vols. I and II. Springer-Verlag, Berlin.
Incropera, F.P., De Witt, D., 2005. Fundamentals of Heat and Mass Transfer, sixth ed. Wiley, New York.
Lomax, 2001. Fundamentals of Computational Fluid Dynamics.
Patankar, S.V., 1980. Numerical Heat Transfer and Fluid Flow. Hemisphere Publishing Corporation, Taylor & Francis Group, New York.
Roach, P.J., 1998. Fundamental of Computational Fluid Dynamics. Hermosa Publishers, Albuquerque, NM.
Versteeg, H.K., Malalasekera, W., 1995. An Introduction to Computational Fluid Dynamics – The Finite Volume Method. Prentice Hall, Pearson Education Ltd., England.
Zikanov, 2015. Essential Computational Fluid Dynamics.

Index

Note: Page numbers followed by *f* indicate figures, and *t* indicate tables.

A

Acceleration, 77–78
  force balance, 73
  stagnation streamline, 80, 80*f*
Accuracy
  channel flow, 242–244
  grid convergence, 230
  solution errors
    control, 236–238
    discretisation error, 231–234, 232–233*f*
    human error, 236
    iteration/convergence error, 235
    physical modelling error, 235–236
    round-off error, 234–235
    verification and validation, 238–239
  truncation error, 229
Adaptive mesh, 145–146
  redistribution, 145–146
  refinement, 145–146
Adiabatic wall temperature, 119
Advantages, 4–5
Advection, 66–67, 77–78, 156, 420
Aerodynamic helmet, 26–27, 27*f*
Aerodynamics, 10, 11*f*
Aerofoil, 348–349, 350*f*, 443
  lift curve slope, 443, 443*f*
  plain flap, 443, 443*f*
Aerospace, 9–10, 9*f*
Ahmed model, 325–326, 326*f*, 437
  drag coefficient for, 438, 439*f*
  lift coefficient, 438, 439*f*
  two-dimensional geometry of, 437, 437*f*
Algebraic equations
  direct methods, 185–189
  iterative methods, 189–193
Algebraic multigrid (AMG) algorithm, 47–48
Alternating direction implicit (ADI), 193, 371
Animation, 60–61
ANSYS CFX software, 35–36, 36*f*
ANSYS FLUENT software, 35–36, 37*f*, 268
Applications
  aerospace, 9–10, 9*f*
  air/particle flow in human nasal cavity, 331–337, 332–337*f*
  automotive engineering, 10–12, 11*f*
  biomedical science and engineering, 12–15, 12–14*f*
  buoyant free-standing fire, 320–325, 321*f*, 323–324*f*
  chemical and mineral processing, 15–17, 16–17*f*
  civil and environmental engineering, 17–19, 18–19*f*
  conjugate and radiation heat transfer, 312–320, 313–315*f*, 319*t*, 319–320*f*
  as design tool, 8–9
  as educational tool, 7–8
  flow over vehicle platoon, 325–330, 326–327*f*, 329–331*f*
  heat exchanger, 305–312, 306*f*, 308*f*, 309*t*, 310–312*f*
  high speed flows, 338–360, 339–340*f*, 341*t*, 342*f*, 344–360*f*, 344*t*
  indoor airflow distribution, 292–298
  metallurgy, 19–20, 20–21*f*
  nuclear safety, 20–22, 22*f*
  power generation and renewable energy, 22–25, 23–25*f*
  as research tool, 6–7
    gas-particle flow in 90 degrees bend, 299–305, 300*f*, 301*t*, 303–304*f*
  sports, 25–27, 26–27*f*
Artificial compressibility, 371
Automotive engineering
  aerodynamics, 10, 11*f*
  CFD in, 10
  diesel internal combustion engine, 10–12, 11*f*
  numerical simulations, 10–12

B

Backward-facing step geometry, 142, 143*f*, 435
  local mesh refinement, 142, 143*f*
  turbulent flow over, 444–445
Bernoulli's equation, 79

Black boxes, 33
Block-structured grids, 144–145
Body-fitted mesh, 128–133
  Cartesian coordinates, 131
  computational geometry, 130*f*
  elliptic grid generation method, 132–133
  Hermite interpolation, 132
  staircase-like steps, 130*f*
  transfinite interpolation method, 131
Body forces, 74
Boundary conditions
  for an external flow problem, 43–44, 43*f*
  buoyancy driven flows, 44
  combusting flows, 44
  cyclic, 44, 45*f*
  for external flows, 278
  inflow and outflow boundaries, 42
  inlet, 258–260, 259–260*f*
  for internal flows, 42–43, 43*f*, 278
  for k–ω model, 278
  outlet, 260–261, 261*f*
  overview, 256–258
  periodic, 262–263, 263–264*f*
  solid walls, 43–44
  for solid walls, 278
  subsonic fluid flows, 44–45
  supersonic fluid flows, 44–45
  symmetry, 44, 45*f*, 262–263, 263–264*f*
  turbulent kinetic energy, 277–278
  wall, 261–262, 262*f*
Boundedness, 180
Bronchial tree geometry, pulmonary system, 13, 14*f*
Buoyant fire
  bulge structure, 321–322
  buoyant plume, 320–321, 321*f*
  CFD simulation, 322
  flickering behaviour, 322–324, 323*f*
  intermittent flame, 320–321, 321*f*
  LES, 322
  persistent flame, 320–321, 321*f*
  puffing effect, 321–322, 323*f*
  SGS, 322
  soot model, 322, 324*f*, 325
  vortex, 321–322
Buoyant plume, 320–321, 321*f*

C

Carbon dissolution, 20
Cartesian mesh, 127–129
Central processing units (CPUs), 241, 384, 387
Channel flow
  accuracy, 242–244
  collocated grid arrangement, 242
  consistency, 242–244
  double precision, 244
  grid convergence, 242
  horizontal velocity, convergence histories of, 242, 243*f*
  SIMPLE scheme, 242
  single-precision, 244
  solution error, 244, 244*t*
Channel length
  horizontal velocity, 71*f*
  vertical velocity, 71–72, 72*f*
Chebyshev polynomials, 156
Chimera grids. *See* Block-structured grids
Codes
  commercial CFD, 35–36
  elements, 34
  Shareware CFD, 34
Combustion, 400–402
Commercial CFD codes, 35–36, 51–52
  internet links, 35–36, 36*t*
Compressible flows, 6
  adaptive meshing, 378–380, 379*f*
  embedded shock waves, 373
  explicit method, 373
  high resolution schemes
    MUSCL, 375
    PPM, 375
    propagating wave, 374–375, 374*f*
    TVD, 375
  implicit method, 373
  pressure drag, 373
  r-refinement technique, 378–380, 379*f*
  wave drag, 373
Computational aeroelasticity (CAE), 402–403
Computational domain, 36–38
Computational efficiency, 372
Computational models, advances in
  combustion, 400–402
  DEM, 413–415
  DNS, 390–393
  fluid–structure interaction, 402–404
  LBM, 407–408
  LES, 393–396
  Monte Carlo method, 409–410
  multiphase flows, 398–400
  particle methods, 411–413
  physiological fluid dynamics, 404–406
  RANS–LES coupling, 396–398
Computational simulations, 3–4

Computational solutions, 155, 157–158, 157*f*
channel flow, 242–245
consistency, 212–216
convergence
accelerating, 228–229
definition, 222–224
difficulty, 227–228
residuals and, 224–226
underrelaxation factors, 227–228
efficiency, 239–241
flow over 90° bend, 245–250, 245*f*
solution errors
control, 236–238
discretisation error, 231–234, 232–233*f*
human error, 236
iteration/convergence error, 235
physical modelling error, 235–236
round-off error, 234–235
verification and validation, 238–239
stability, 216–222
Compute unified device architecture (CUDA), 241
Conservation equations
advection term, 420
control volume, 421
Newton's law of viscosity, 422
Stokes' hypothesis, 422
substantial derivative, 419
Conservativeness, 181
Consistency
control volume, for two-dimensional structured grid, 213, 213*f*
face velocities, 213
one-dimensional transient diffusion equation, 214
steady-state solutions, 215, 215–216*f*
Taylor series expansion, 213–215
truncation error, 212
Continuity equation
comments, 72–73
mass conservation, 65–68
physical interpretation, 69–72
Continuous forcing approach, 389
Contour line, 56
Contour plots
flooded contours, 56, 56–57*f*, 59*f*
isolines, 56
isosurface, 56
line contours, 58*f*
rainbow-scale colour map, 56, 56–57*f*
Convergence
acceleration, 228–229
ANSYS CFX GUIs, 48–50, 49*f*
definition, 222–224
difficulty, 227–228
error(s), 235
error estimation, 50
FLUENT GUIs, 48–50, 49*f*
grid, 223–224
imbalances, 48–50
iterative, 223–224
lift coefficient, 48–50
one-dimensional transient diffusion equation, 223, 223*f*
parabolic laminar velocity, 51*f*
residuals and, 48–50, 223–226
tolerance values, 48–50
underrelaxation factors, 50, 227–228
Cooling, electronic components within computer, 448–449
Cooling tower, plume dispersion, 18*f*
Courant–Friedrichs–Lewy (CFL) condition, 218
Courant number, 228–229
CPUs. *See* Central processing units (CPUs)
Crank–Nicolson methods, 429–430
CUDA processing flow paradigm, 386, 386*f*
Cyclic boundary condition, 44, 45*f*

D

Delaunay triangulation, 134
Density fluctuation, 347–348, 348*f*
Design tool, 8–9
Diesel internal combustion engine, 10–12, 11*f*
Diffuser grill, 296, 297*f*
Direct methods
back substitution process, 186–187
forward elimination, 186–187
Gaussian elimination, 185
Thomas algorithm, 186–188
Direct numerical simulation (DNS), 28, 264–265
explicit methods, 391–392
implicit methods, 391–392
k-ε two-equation turbulence model, 100–101
Kolmogorov microscales, 390
numerical issues, 391
RANS, 392–393
Reynolds number, 391
supersonic flow, over flat plate, 340–341, 347, 347*f*
turbulence models, 264–265
turbulent flow, 390

Direct simulation Monte Carlo (DSMC), 409–410
Dirichlet boundary condition, 118, 256–257
Disciplines, 1–2, 2*f*
Discontinuous Galerkin method, 156
Discrete element method (DEM), 413–415
Discrete forcing approach, 389
Discrete random walk (DRW) model, 302
Discretisation approach, 126
Discretisation error, 237, 237*f*
  convection-type equation, 233*f*
  Euler explicit method, 232
  global, 231, 232*f*
  leapfrog method, 233
  local, 231, 232*f*
Distorted air diffusion, 296, 297*f*
Diverging residuals, 227
DNS. *See* Direct numerical simulation (DNS)
Domain decomposition, 384–385
Donor-cell concept, 178–179
Drag coefficient, 328–330, 328*f*, 438–439, 439*f*
DSMC. *See* Direct simulation Monte Carlo (DSMC)
Dynamic mesh model, 18–19

E

Eddy-lifetime model, 301
Efficiency
  CPUs, 241
  explicit marching methods, 240
  GPUs, 241
  implicit methods, 240–241
  parallel computing, 240
  steepest descent methods, 239–240
Elliptic grid generation method, 132–133
Embedded Cartesian mesh, 144, 144*f*
Energy cascade, 99–100
Energy conservation
  for compressible flow, 90
  conservative form, 90
  dissipation function, 90
  energy fluxes, 89
  first law of thermodynamics, 88
  for incompressible flow, 90–91
  nonconservative form, 88–89
  surface forces, 88, 89*f*
Energy equations
  acceleration, 91–97
  advection, 91, 97
  comments, 88–91
  diffusion, 91, 97
  dimensionless temperature profiles, 95–96, 95–96*f*
  energy conservation, 87–88
  friction, 97
  physical interpretation, 88–98
Errors
  defined, 230–231
  discretisation, 231–234, 232–233*f*
  high frequency, 382–383
  human, 236
  iteration/convergence, 235
  low-frequency, 382–383
  physical modelling, 235–236
  round-off, 234–235
Essentially non-oscillatory (ENO) schemes, 376
Explicit methods, 182, 183*f*, 429–430
  compressible flows, 373
  DNS, 391–392
  Stability, 222
External flow, 38

F

Finite difference method
  algebraic equation system, 170–171
  backward difference, 161–162
  Cartesian grids, 158–159
  central difference, 160–161
  forward difference, 161–162
  grid lines, 159
  partial differential equations, 159–160
  second-order derivative, 162
  Taylor series expansions, 158, 160, 162
  truncation error, 160–161
  uniform grid spacing, 170*f*
  uniform spacing, 159–160
Finite element method
  Galerkin method, 168–169
  governing equations, 168–169
  linear shape functions, 168–169
Finite-volume discretization
  control volumes, 174–175, 175*f*
  of large brick plate domain, 174–175, 175*f*
Finite volume method, 47
  algebraic equation system, 171–173
  control volume, 163–165, 171, 171*f*
  diffusive fluxes, 172
  discretized continuity equation, 166
  first-order derivative, 164–167
  Gauss's divergence theorem, 164–167
  heat conduction problem, 174
  interpolation, 163
  second-order derivative, 167

structured mesh, 163–164, 164*f*, 168*f*
two-dimensional structured grid, 165, 166*f*
unstructured mesh, 163–164, 164*f*
F18 jet, 9, 9*f*
Flat plate
boundary layer thickness, 70, 70*f*
two-dimensional flow, 69, 69*f*
velocity ratio, 70, 70*f*
Flickering behaviour, 322–324, 323*f*
Flooded contours
on grey-scale colour map, 57–58, 59*f*
on rainbow-scale colour map, 56, 56–57*f*
Flow
external, 38
internal, 38
Fluid flow
flow between two stationary parallel plates, 36–38, 37*f*
heat transfer coupled with, 305–320
passing over two cylinders, 36–38, 38*f*
vehicle platoon, 325–330
Fluidized coal bed, 23–24, 24*f*
Fluid motion
circular cylinder, 78, 78*f*
in piston mechanism, 77, 77*f*
venturi, 77–78
Fluid–structure interaction, 402–404
Force balance
body forces, 74
substantial derivative, 75
surface forces, 74, 74*f*
Friction coefficients, 115–116, 116*f*
Friction forces, 87
Fully coupled model, 403

G

Gaphical user interface (GUI)
ANSYS CFX software, 35–36, 36*f*
ANSYS FLUENT software, 35–36, 37*f*
Gas cyclones, 15–16, 17*f*
Gas-particle flows, 298–299
in 90 degrees bend
ANSYS FLUENT, 299
computational meshes, 299, 300*f*
DRW model, 302
eddy-lifetime model, 301
Eulerian approach, 301–305
gas tracers, 304
grid, 299
Lagrangian approach, 300–301
LDA system, 299
mean streamwise gas velocity, 303, 303*f*
Reynolds number, 301
Stokes number, 302–304, 304*f*
transport equations, 301, 301*t*
solid particles, 298–299, 298*f*
Gas-sparged stirred tank reactor, 15, 16*f*
Gas tracers, 304
Gaussian elimination, 185
Gauss's divergence theorem, 65–66, 164–167
Gauss–Seidel method, 190–192
Geometry creation
computational domain, 36–38
fluid flow cases, 36–38, 37*f*
Global solution algorithm, 285–286
Governing equations
for compressible flow in Cartesian coordinates, 109, 112*t*
continuity
comments, 72–73
mass conservation, 65–68
physical interpretation, 69–72
conversion to algebraic equation system
finite difference method, 170–171
finite difference *vs*. finite volume discretizations, 173–184
finite volume method, 171–173
discretization
finite difference method, 158–163
finite element method, 168–169
finite volume method, 163–167
spectral method, 169
energy
comments, 88–91
energy conservation, 87–88
physical interpretation, 88–98
generic form, 108–117
for incompressible flow in Cartesian coordinates, 109, 110*t*, 112*t*
momentum
comments, 77–87
force balance, 73–88
physical interpretation, 73–76
numerical solutions
direct methods, 185–189
iterative methods, 189–193
multigrid method, 204–206
pressure–velocity coupling, 193–204
physical boundary conditions, 117–120
turbulent flow
comments, 108
k-ε two-equation turbulence model, 100–107
turbulence, 98–100

Graphics processing units (GPUs), 241, 385–387
Grid distortion, 150
GRIDGEN, 126–127
Grid generation, 148
Grid independence, 151–152, 237–238
GRIDPRO, 126–127
Guidelines
  for boundary conditions
    inlet, 258–260, 259–260*f*
    outlet, 260–261, 261*f*
    overview, 256–258
    symmetry and periodic, 262–263, 263–264*f*
    wall, 261–262, 262*f*
  global solution algorithm, 285–286
  on problem definition, 284–285
  on solution strategy, 285–286
  for turbulence modeling
    hydrofoil flows, two-equation turbulence modeling for, 279–284
    near wall treatments, 273–277, 275*f*
    overview, 264–267, 265*f*
    selection strategy, 267–273
    setting boundary conditions, 277–279
  on validation, 286

H

Hagen–Poiseuille flow, 83–84
Hard-sphere model, 414
Heat conduction, 174
  solid slab, 91–92, 92*f*
Heat exchanger
  CFD simulation, 315–316
  conjugate, 312–320
  cyclic boundary conditions, 307
  dimensionless parameters, 305
  hybrid mesh, 308–309
  in-line arrangement, 305–307, 306*f*, 309*t*, 310*f*
  momentum equation, 316
  radiation, 312–320
  Reynolds number, 310–311, 310–311*f*
  single plate-type molybdenum target, 312–313, 313*f*
  smoke seeding, 318–319
  smoke traces, 318–319, 318*f*
  SST model, 317–318
  staggered arrangement, 305–307, 306*f*, 309*t*, 311*f*
  symmetric boundary conditions, 307
  target plate, 313–315, 314–315*f*
  temperature contours, 319, 319*f*
  tube banks, 305, 306*f*
Hermite interpolation, 132
H-grid, 136–137, 138*f*
High speed flows
  subsonic and supersonic flows over wing aerofoil, 348–349, 350*f*
    boundary conditions, 357
    CFD simulation, 351
    C-type mesh scheme, 351–352, 352*f*
    free-slip condition, 351–352
    instantaneous spanwise vorticity, 357–360, 357*f*, 359*f*
    local Mach number, 352–354, 353–354*f*
    multiblock mesh, 351, 351*f*
    no-slip condition, 351–352
    RANS, 350–351
    stall position, 354–356
    temperature contours, 356–357, 356*f*
    velocity vectors, 354–356, 355*f*
  supersonic flow, over flat plate
    boundary conditions, 342–343, 342*f*
    boundary layer, 338
    CFD simulation, 341
    density fluctuation, 347–348, 348*f*
    DNS, 340–341, 347, 347*f*
    laminar flow, 339–340, 343, 344*t*
    local Mach number, 343–346, 346*f*
    Navier–Stokes equations, 341
    normalized component velocity, 343–346, 345*f*
    normalized temperature, 343–346, 345*f*
    parameters, 341*t*
    Reynolds number, 339–340
    Sutherland's law, 342
    temperature contours, 343, 344*f*
    three-dimensional computational domain, 340–341, 340*f*
    two-dimensional computational domain, 339–340, 339*f*
    velocity vectors, 343, 344*f*
    viscous dissipation, 338
    wall-normal vorticity, 349*f*
Human error
  computer programming, 236
  usage, 236
Human nasal cavity
  airflow rate, 335–336
  air/particle flow in, 331–337
  CFD simulation, 333–334
  internal walls, 334
  QUICK scheme, 333–334

spray cone angles, 336–337, 336–337*f*
spray particle deposition, 331
surface topology, 332, 333*f*
velocity profiles, 332–333, 334*f*
Hybrid grids, 140
Hybrid RANS–LES models, 397–398
Hydrocyclone, 15–16, 17*f*
Hydrodynamic entry length, 84, 84*f*

I

Ice–water interface, 381, 382*f*
Immersed boundary methods, 387–390
Implicit method, 183, 184*f*, 429–430
compressible flows, 373
DNS, 391–392
efficiency, 240–241
residuals, 226–227
stability, 222
Incompressible flows, 6
artificial compressibility approach, 371
definition, 369–370
fractional step procedure, 370–371
Poisson's equation, 370
pressure iteration, 370
Indoor airflow
computational mesh, 293, 294*f*
diffuser grill, 296, 297*f*
distorted air diffusion, 296, 297*f*
grid, 293
LES, 293–294
LRN turbulence, 292–293
model room, 293, 293*f*
model validation, 294–295
pressure–velocity coupling, 293–294
RANS approach, 293–294
RNG-based LES model, 295–296
room ventilation system, 296
simulation features, 293–294
symmetrical air diffusion, 296, 297*f*
ventilated compartment, 296, 296*f*
vertical inlet velocity, 293–296, 295*f*
Inhomogeneous multiphase model, 20–22
Inlet boundary conditions
backward-facing step geometry, 259–260, 260*f*
flow between two stationary parallel plates, 258–259, 259*f*
parameters, 258
Intelligent transport systems (ITS), 325
Interface capturing, 399–400
Interface-tracking methods, 399–400
Intermittent flame, 320–321, 321*f*
Internal flow, 38
Intervehicle spacing, 328–329, 329*f*
Inviscid fluid flows, 41–42
Iteration errors, 235
Iterative methods
Gauss–Seidel method, 190–192
Jacobi method, 189
steady heat conduction problem, 190
successive overrelaxation, 192–193
Iterative solvers, 47–48
Itsukushima torii, 18–19, 19*f*

J

Jacobi method, 189

K

k-ε two-equation turbulence model
Cartesian tensor notation, 102
conservative form, 104
DNS, 100–101
laminar velocity profiles, 105–108, 106*f*
laminar viscosity, 105–108, 106*f*
Newton's law of viscosity, 102
nonconservative form, 104
Reynolds stresses, 100–102
turbulent momentum transport, 102
turbulent velocity profiles, 105–108, 106*f*
turbulent viscosity, 105–108, 106*f*
Kolmogorov microscales, 390
k–ω model, 272–273

L

Laminar viscosity, 105–108, 106*f*
Large-eddy simulation (LES), 28, 264–265, 389, 393–396
Laser Doppler anemometry (LDA) system, 299
Lattice Boltzmann equation (LBE), 407–408
Lattice Boltzmann method (LBM), 407–408
operations, 408
Lax method, 218
Lead model, 326–328, 327*f*
Learning program, 431–434
LES. *See* Large-eddy simulation (LES)
Lift coefficient, 48–50
Load balancing, 384–385
Local mesh refinement
backward-facing step geometry, 142, 143*f*
boundary layer, 141
embedded Cartesian mesh, 144, 144*f*
stretched grid, 140–141
truncation error, 141–142
upward stagnation flow, 142
viscous-like velocity profile, 141

Log-law layer, 274
Longitudinal mean velocity, 246–247, 247*f*
Loosely coupled model, 403
Low-Reynolds-number (LRN), 292

M

Marker-and cell (MAC) method, 370–371
Mass conservation, 65–68, 66–67*f*
Mass residual, 199
  convergence history of the, 202*f*
Medical simulations, 12–13
Menter's model, 272–273
Mesh generation, 39–40
  adaptive mesh with solution, 145–146, 146*f*
  definition, 125
  discretization approach, 126
  local refinement, 140–144, 142–144*f*
  moving meshes, 146–148, 148*f*
  overlapping grids, 144–145, 145*f*
  quality and design, 148–152, 150–151*f*
  rectangular Cartesian meshes, 126
  topology, 136–140, 137–141*f*
  types
    body-fitted, 128–133, 130*f*
    structured, 127–128, 128–129*f*
    unstructured, 133–135, 133*f*, 136*f*
Metallurgy, 19–20
Mineral processing, 15–16
Molten iron, flow pattern of, 20
Momentum equations
  comments, 77–87
  force balance, 73–88
  physical interpretation, 73–76
Monitor function, 147
Monotone upwind scheme for conservation laws (MUSCL), 375
Monte Carlo method, 409–410
Moving grids, 380–381
Moving meshes, 146–148, 148*f*
  for swinging limb, 147, 148*f*
Multiblock mesh, 136–137, 138*f*, 351, 351*f*
Multigrid methods, 381–384
  highfrequency errors, 382–383
  low-frequency errors, 382–383
  Poisson-like pressure, 204
  V-cycle, 204–206, 205*f*, 381–383
  W-cycle, 204–206, 383–384
Multiphase flows, 398–400

N

Nasal cavity, particle transport/deposition, 13, 14*f*
Nasal sprayers, particle formation/dispersion, 13, 14*f*
Navier–Stokes equations, 156, 174–177
  physical modelling error, 235–236
Near-wall models, 273
Neumann boundary condition, 118, 257
Newton's law of viscosity, 102
Non-linear disturbance equation (NLDE) approach, 397
Nonuniform grid distribution, 173
Nonuniform rectangular mesh, 127–128, 129*f*
No-time-counter technique, 410
Nuclear safety, 20–22
Numerical errors, 236–237
Numerical methods
  compressible flows, 373–380
  CUDA processing flow paradigm, 386–387, 386*f*
  GPU, 385–387
  immersed boundary methods, 387–390
  incompressible flow, 369–372
  LBM, 407–408
  moving grids, 380–381
  multigrid methods, 381–384
  parallel computing, 384–385
Numerical solutions
  to algebraic equations
    direct methods, 185–189
    iterative methods, 189–193
  convergence, monitoring, 48–51, 49–51*f*
  initialization and solution control, 46–48

O

Off-gas combustion, 20, 21*f*
O-grid, 136–137, 139*f*
Olympic bikes, 26–27
Optimum stroke, 25–26, 26*f*
Ordinary differential equations (ODEs), 411
Outlet boundary conditions, 260–261, 261*f*
Overlapping grids, 144–145, 145*f*
Overlapping mesh techniques, 144–145, 145*f*

P

Parabolic laminar velocity, 51*f*
Parabolic profile, 83–84
Parallel computing, 240, 384–385
Partial differential equations, 155, 159–160
Particle methods, 411–413
  ODEs, 411
  SPH, 411
  truncation errors, 411
  VMs, 411–412
Peclet numbers, 180–181

Periodic boundary conditions, 263, 264*f*
Persistent flame, 320–321, 321*f*
Physical modelling error, 235–236
Physiological fluid dynamics, 404–406
Pickup trucks
  with open/closed tubs, 446–447
  recirculation flow region, 330, 331*f*
Piecewise parabolic method (PPM), 375
Poisson's equation, 199
Poject-based learning (PBL), 8
Polyhedral cells, 135, 136*f*, 145–146
Population balance approach, 399
Power generation, 22–25
Power-law differencing scheme, 181
Prandtl number, 97–98
Pressure
  coefficient values for patient with and without asthma, 13, 14*f*
  convergence history of, 201*f*
  correction, 202*f*
  drag, 373
  iteration, 370
Pressure–velocity coupling, 293–294
  collocated grid arrangement, 195–196, 195*f*
  control volume, velocity components on, 195–196, 195*f*
  pressure-correction equation, 196
  SIMPLE, 194, 197*f*
    iterative steps, 196–203
    pressure-correction equation, 196
  staggered grid arrangement, 194, 195*f*
Problem definition, 284–285
Problem setup
  boundary conditions, 42–45, 43*f*, 45*f*
  geometry creation, 36–39
  mesh generation, 39–40
  physics and fluid properties selection, 40–42, 41*f*
Puffing effect, 321–322, 323*f*
Pure diffusion process, 170

Q

Quadratic upstream interpolation convective kinetics (QUICK), 47
Quadrilateral cell, 149–150, 150*f*
QUICK schemes, 427–428

R

Realizable k-ε model, 269–271
Rectangular Cartesian meshes, 126
Research tool, 6–7
Residuals
  in CFD, 224
  convergence tolerance, 225–227
  implicit methodology, 226–227
  qualitative convergence, 225–227
  quantitative convergence, 225–227
Reynolds averaged Navier-Stokes (RANS), 100–101
Reynolds stresses, 100–102
Reynolds stress model, 246–250, 266
RNG k-ε model, 268–271
Robust solvers, 47–48
Round-off error, 234–235, 237, 237*f*
  double precision, 234
  single precision, 234

S

Scalability, 384
Semi-implicit method for pressure-linkage equations (SIMPLE)
  iterative steps, 196–203
  pressure-correction equation, 196
Shareware CFD, 34
Shear-stress transport (SST), 273, 317–318
Side-by-side cylinders, CFD simulations, 6–7, 6–7*f*
Simple chemical reacting system (SCRS), 401–402
SIMPLE-consistent (SIMPLEC) algorithm, 203–204
SIMPLE-revised (SIMPLER) algorithm, 203–204
Single instruction multiple data (SIMD), 386–387
Skewness, 150
Smagorinsky subgrid-scale (SGS) turbulence model, 322
Smoke seeding, 318–319
Smoke traces, 318–319, 318*f*
Smooth particle hydrodynamics (SPH), 411–413
Soft-sphere model, 413–414
SolarFox 3, 25, 25*f*
Solid modeller packages, 39
Solution errors
  control, 236–238
  discretisation error, 231–234, 232–233*f*
  human error, 236
  iteration/convergence error, 235
  physical modelling error, 235–236
  round-off error, 234–235
  verification and validation, 238–239

Solution strategy, 285–286
Solvers, 46
  iterative, 47–48
  robust, 47–48
Soot model, 322, 324*f*, 325
Spectral method, 169
Sports Engineering Research Group (SERG), 26–27
Stability
  convection-type equation, 220
  Courant–Friedrichs–Lewy condition, 218, 220–222
  Euler method, 218–220
  explicit method, 222
  finite-difference discretization, 218–220
  implicit method, 222
  latter criterion, 217–218
  Lax method, 218
  for linear problems, 216–222
  matrix method, 216–222
  one-dimensional transient diffusion equation, 218–219
  time advancement, 219*f*, 220, 221*f*, 222
  von Neumann method, 216–222
Stagnation streamline
  acceleration, 80, 80*f*
  pressure difference, 80, 80*f*
  velocity profile, 79–80, 79*f*
Standard k–ε model, 266–267, 271–272
  weakness, 267–272
STAR-CD, 51–52
Steady convection-diffusion process, 177
Steady heat conduction problem
  Gauss–Seidel method, 191–192
  Jacobi method, 190
  in large brick plate, 174, 174*f*
  Thomas algorithm, 188
Stenosed artery, 12–13, 12*f*
Stokes number, 302–304, 304*f*
Streamlines, 58–59
Stress–strain relationships, 75–76
Strongly implicit procedure (SIP), 47–48, 193
Structured mesh, 127–128, 157–158, 163–164, 164*f*, 168*f*
  elemental cells, 136, 137*f*
  H-grid, 136–137, 138*f*
  multiblock, 136–137, 138*f*
  nonuniform rectangular mesh, 127–128, 129*f*
  O-grid, 136–137, 139*f*
  uniform rectangular mesh, 127, 128*f*
Subgrid-scale (SGS) model, 393–394
Subsonic fluid flows, 44–45
Successive overrelaxation, 192–193
Supersonic fluid flows, 44–45
Surface forces, 74, 74*f*
Sutherland's law, 342
Symmetry boundary condition, 44, 45*f*, 262–263, 263*f*

T

Taylor series expansion, 155–156, 178
TECPLOT, 51–53
Test runs, 148–149. *See also* Mesh generation
Thermal entry length, 94–95, 94*f*
Thomas algorithm, 184–185
  direct methods, 186–188
Three-dimensional turbulent flow, over 90° bend, 245–250, 245*f*
Total error, 237, 237*f*
Transfinite interpolation method, 131
Transportiveness, 179–180
Triangular mesh, 133*f*
Truncation error, 141–142
  accuracy, 229
  consistency, 212
  finite difference method, 160–161
  local mesh refinement, 141–142
  particle methods, 411
Turbulence, 98–100
  random fluctuations, 98–100
Turbulence models
  advanced techniques, 264–265
  DNS, 264–265
  hydrofoil flows, two-equation turbulence modeling for, 279–284
  LES, 264–265
  near wall treatments, 273–277, 275*f*
  practical techniques, 265–267
  selection strategy, 267–273
  setting boundary conditions, 277–279
  turbulent motion, 264–265, 265*f*
  two-dimensional hydrofoil geometry
    boundary conditions, 281
    grid, 280
    model description, 280
    pressure-surface boundary-layer velocity profiles, 282–284, 283*f*
    simulation features, 280–281
    wall treatment analysis, 282, 282–283*f*
Turbulent boundary layer, 273–274, 275*f*
Turbulent flow
  comments, 108
  k-ε two-equation turbulence model, 100–107
  RANS-LES coupling for, 396–398
  turbulence, 98–100

Turbulent fluctuations, 99–100
Turbulent viscosity, 394
Two-dimensional laminar flow, 200, 200*f*

U

Underrelaxation factors, 149–150, 227–228
Uniform rectangular mesh, 127, 128*f*
Unsteady convection-diffusion process, 181
Unstructured mesh, 137–139, 157–158, 163–164, 164*f*
  for circular cylinder, 140*f*
  Delaunay triangulation, 134
  polyhedral, 135, 136*f*
  quadtree/octree method, 135
  vs. structured mesh, 139–140
  for three-dimensional grid generation, 135
  triangular mesh, 133*f*
Upwind differencing scheme, 179–180, 180*f*
Upwind schemes, 427–428

V

Validation, 239
  guidelines, 286
V-cycle, 204–206, 205*f*, 381–383
Vector plots
  localized wake recirculation zones, 55–56, 55*f*
  parallel-plate channel, fluid flow, 54–55, 55*f*
Vehicle platoon
  Ahmed car geometry, 325–326, 326*f*
  drag coefficient, 328–330, 328*f*
  Ford Falcon EXT 2003 model, 330, 330*f*
  high drag configuration, 329, 329*f*
  intervehicle spacing, 328–329, 329*f*
  ITS, 325
  lead model, 326–328, 327*f*
  pressure pathlines, 329–330, 330*f*
  recirculation flow region, pickup truck, 330, 331*f*
  trailing model, 327–328
  turbulent flow, 328
  wind-tunnel configuration, 327–328
Velocity profile
  downstream locations, 84–86, 85–86*f*
  stagnation streamline, 79–80, 79*f*
Verification, 239
Vertical inlet velocity, 293–296, 295*f*
Virtually stented arteries, 12–13, 12*f*
Viscous dissipation, 338
Viscous fluid flows, 41–42
Viscous sublayer, 272, 274
VMs. *See* Vortex methods (VMs)
Volume of fluid (VOF), 399–400
von Neumann method, 216–222
Vortex methods (VMs), 411–412
Vortex stretching, 99–100

W

Wall boundary conditions
  fluid flow with moving or rotating walls, 262, 262*f*
  solid walls, 261
  stationary walls, 261–262
Wall functions
  with low-Reynolds-number turbulence models, 277
  near-wall meshing guidelines on, 276
Wall shear stress (WSS), 12*f*
Warp angles, 151
Water tank, CFD simulation, 18*f*
Water turbulence, 25–26
Wave drag, 373
Wavy channel, 440, 440*f*
W-cycle, 204–206, 383–384
Weighted ENO (WENO), 376
Wind-tunnel configuration, 327–328
Wind-tunnel testing, 5
Wind turbine, 22–23, 23*f*

X

X–Y plots
  laminar velocity profile, 51*f*, 53–54
  normalized horizontal velocity, 53–54, 54*f*
  two-dimensional velocity profiles, 53–54, 53*f*

Z

Zero prototype engineering, 27–28

THIRD EDITION

Computational Fluid Dynamics
A Practical Approach

Jiyuan Tu, Guan-Heng Yeoh, and Chaoqun Liu

An introduction to understanding CFD and using CFD codes to solve engineering problems, designed for the CFD user rather than CFD developer.

Computational Fluid Dynamics: A Practical Approach is an introduction to CFD fundamentals and commercial CFD software to solve engineering problems, designed for the wide variety of engineering students new to CFD and for practicing engineers learning CFD for the first time. Combining an appropriate level of mathematical background, worked examples, computer screenshots, and step-by-step processes, this book walks the reader through modelling and computing, as well as interpreting CFD results. This new edition has been updated throughout, with new content and improved figures, examples, and problems.

Key Features:
- Includes a new chapter on practical guidelines for mesh generation.
- Provides full coverage of high-pressure fluid dynamics and meshless approach to provide a broader overview of the application areas where CFD can be used.
- Online resources include a new bonus chapter featuring detailed case studies and the latest developments in CFD.

Related Titles

Blazek / Computational Fluid Dynamics: Principles and Applications, Third Edition / 9780080999951

Hirsch / Numerical Computation of Internal and External Flows: The Fundamentals of Computational Fluid Dynamics, Second Edition / 9780750665940

Yeoh and Yuen / Computational Fluid Dynamics in Fire Engineering / 9780750685894

About the Authors

Jiyuan Tu, Distinguished Professor, Tsinghua University, P.R.China, Adjunct Professor, University of NSW, Australia, and Professor, RMIT University, Australia

Guan-Heng Yeoh, Principal Research Scientist, ANSTO (Australian Nuclear Science and Technology Organization), Professor, University of NSW, Australia, and Visiting Professor at the Zhejiang University and City University of Hong Kong

Chaoqun Liu, Director of the Center for Numerical Simulation and Modeling, and Distinguished Professor, University of Texas at Arlington, USA

Engineering, Fluid Dynamics

ISBN 978-0-08-101127-0

9 780081 011270

ELSEVIER

Butterworth-Heinemann
An imprint of Elsevier
elsevier.com/books-and-journals